Development of an Electrical Impedance Computed Tomographic Two–Phase Flows Analyzer

Final Report

DOE/ER/13032--T3

Levent Ovacik, Graduate Student
Owen C. Jones, Professor and Principal Investigator
Center for Multiphase Research
Department of Nuclear Engineering and Engineering Physics
Rensselaer Polytechnic Institute
Troy, New York 12180–3590 U.S.A.

August, 1998

Prepared for the U.S. Department of Energy, Energy Research Office, Nuclear Engineering Research Program, Contract Agreement No. DE–FG07–90ER13032, Initiated October, 1990. Cooperative Research Program with Hitachi, Ltd., Energy Research Laboratory, 1168 Moriyama–cho, Hitachi–shi, Ibaraki–ken, Japan 316.

DISCLAIMER

TABLE OF CONTENTS

LIST OF TABLES

LIST OF FIGURES

NOMENCLATURE

Notation used for formutations in electromagnetic field theory, numerical optimization, and linear algebra sometimes leads to confusion when representing vector quantities. To prevent this, all vectors and matrices of linear algebra represented by *bold–faced* characters, such as A, $\boldsymbol{a}$, and the vectors of field theory are represented by *bold–faced* characters with an *over–bar* sign, such as $\overline{A}$ and $\overline{\boldsymbol{a}}$.

English

a	conductivity model coefficient
A	system modeling operator
$\boldsymbol{A}$	preconditioning matrix of size $N \times N$
$\boldsymbol{A}_{11}$	subspace corrector matrix of size $E \times E$
b	conductivity model coefficient
$\boldsymbol{B}$	backprojection operator
$\tilde{\boldsymbol{B}}$	filtered backprojection operator
c_i	current applied to the i–th port
C	number of current sensing electrodes
$\boldsymbol{C}$	global current matrix of size $N \times P$
$\boldsymbol{C}_e$	electrode current matrix of size $E \times P$
C_B	best contour level of a target
$C_{\min}$, $C_{\max}$	minimum and maximum contrast levels of a target
d	distinguishability, distance from pixel to phantom center, thickness of nonuniform current density region
d_c	distinguishability in the sense of excitation by a current source
d_t	separation distance between two cylindrical targets
$d_{\max}$	maximum distinguishability
d_v	distinguishability in the sense of excitation by a voltage source
D	distinguishability matrix
D_t	cylindrical target diameter
$\overline{\boldsymbol{D}}$	electric flux density vector
E	number of electrodes
$\overline{\boldsymbol{E}}$	electric field intensity vector
f	X–ray absorptivity, logarithmic transformation function, frequency

f	computed electrode voltage array of size $EP \times 1$
F	energy functional
$\boldsymbol{F}$	backprojection filtering operator
g	matrix including relative changes in boundary potentials
$\boldsymbol{G}$	matrix of size $E \times M_c$ holding global node indices of element nodes
$\boldsymbol{G}_p$	phantom conductance matrix of size $E \times E$
h	deviation function relative to the element center
$\boldsymbol{H}$	Hessian matrix of size $M \times M$, Walsh–Hadamard matrix of size $E \times E$
$\overline{\boldsymbol{H}}$	magnetic field intensity vector
$\bar{i}$	Cartesian coordinate system unit vector
$\boldsymbol{I}_M$	identity matrix of size $M \times M$
j	complex unit, $\sqrt{-1}$
$\bar{j}$	Cartesian coordinate system unit vector
J	Jacobian of coordinate transformation
J_n	component of current density vector on n–coordinate
J_r	component of current density vector on r–coordinate
$\boldsymbol{J}$	Jacobian matrix of size $EP \times M$
$\overline{\boldsymbol{J}}$	current density vector
$\overline{\boldsymbol{J}}_E$	current density vector on electrode surface
k	overrelaxation factor, iteration number
k_y	admittance matrix normalization factor
$k_{c,p}$	normalization factor for the p–th column of current matrix
$k_{v,p}$	normalization factor for the p–th column of voltage matrix
$\bar{k}$	Cartesian coordinate system unit vector
K	condition number of a matrix
ℓ	distance between pixel and dipole
ℓ_e	submerged length of electrodes
L	size of 3D electrode, number of layers
M	number of elements
M_c	number of corner nodes for an element
n	coordinate, normal direction
N	number of nodes, element shape function, number of fitted points
p	system modeling parameter

P	number of excitations or projections, pixel density
$\overline{q}^e$	current density on the e–th element boundary
r	radial distance, coordinate, accuracy index
R	squared sum of residual errors
$\boldsymbol{R}_m$	measurement–resistor transfer impedance matrix of size $E \times E$
$\boldsymbol{R}_p$	phantom impedance matrix of size $E \times E$
s	radial distance in the transformed plane
$\boldsymbol{S}$	sensitivity coefficient matrix
t	time
T	transpose of a matrix, cycle ($= 1/f$)
$\boldsymbol{T}$	transformation matrix of size $EP \times NP$, sensitivity matrix
u	system output
$\boldsymbol{U}$	orthogonal matrix in singular value decomposition (SVD)
V	voltage, volume
$\boldsymbol{V}$	global voltage matrix of size $N \times P$, orthogonal matrix in singular value decomposition (SVD)
$\boldsymbol{V}_e$	electrode voltage matrix of size $E \times P$
$\boldsymbol{V}'$	true voltage matrix of size $N \times P$
$\boldsymbol{V}_o$	measured electrode voltage array of size $EP \times 1$
$\boldsymbol{V}_o'$	preconditioned electrode voltage array of size $EP \times 1$
w	pixel weight, integration weights for Gauss–Legendre quadrature
x	Cartesian coordinate
x_o	x –coordinate at element center
$\overline{x}_{n,1}$	average of n data in Block 1
y	Cartesian coordinate, element admittance matrix entry
y_o	y –coordinate at element center
$\boldsymbol{Y}$	global admittance matrix of size $N \times N$
z	system input, Cartesian coordinate
z_{ij}	transfer impedance between the i–th and j–th ports

Greek

α	coefficient of bilinear coordinate transformation
β	coefficient of bilinear coordinate transformation

γ	Marqurdt's conditioning number
$\boldsymbol{\Gamma}$	true global admittance matrix of size $N \times N$
$\delta\lambda$	fluctuation in eigenvalues
$\delta\boldsymbol{G}$	fluctuation in phantom conductance matrix of size $E \times E$
Δ	difference operator
ΔV	potential difference between adjacent electrodes
Δv	voltage change at the i–th port
$\Delta\varrho$	resistivity deviation
ε	dielectric permittivity, tolerance for stopping criterion
ε_n	relative error between the averages of two blocks after n measurements
ε_o	dielectric permittivity of vacuum
ε_r	relative dielectric permittivity
η	transformed coordinate
η_n	comparison indicator after n measurements
θ	angle between the current density vector and the r–coordinate
λ	eigenvalues of the sensitivity matrix
$\lambda_{\min}$, $\lambda_{\max}$	minimum and maximum eigenvalue of the sensitivity matrix
ν	degrees of freedom for population of $\nu + 1$ data
ξ	transformed coordinate
π	pi (=3.1416)
ϱ	electric resistivity
σ	electric conductivity
σ_e	element conductivity
σ_o	conductivity at element center
σ_{ave}	average conductivity
$\boldsymbol{\sigma}$	conductivity matrix of size $M \times M$
$\boldsymbol{\Sigma}$	diagonal matrix in singular value decomposition (SVD)
ϕ	electric potential
Φ	least–squares error
ψ	shape function for electric potential
ω	angular frequency ($= 2\pi f$)
Ω	domain
Ω_e	element domain
Ω_E	zones of electrodes

Ω_H	zones of homogeneous boundary condition

Mathematical

∇	gradient operator
∂	partial
$\partial\Omega$	boundary of Ω
$\times$	curl operator
$\otimes$	Kronecker matrix product

Executive Summary

Development of an Electrical Impedance Computed Tomographic Two–Phase Flows Analyzer

Final Report

Summary

This report summarizes the work on the research project on this cooperative program between DOE and Hitachi, Ltd. Major advances were made in the computational reconstruction of images from electrical excitation and response data with respect to existing capabilities reported in the literature. A demonstration is provided of the imaging of one or more circular objects within the measurement plane with demonstrated linear resolution of six parts in two hundred. At this point it can be said that accurate excitation and measurement of boundary voltages and currents appears adequate to obtain reasonable images of the real conductivity distribution within a body and the outlines of insulating targets suspended within a homogeneous conducting medium.

The quality of images is heavily dependent on the theoretical and numerical implementation of imaging algorithms. The overall imaging system described has the potential of being both fast and cost effective in comparison with alternative methods. The methods developed use multiple plate–electrode excitation in conjunction with finite element block decomposition, preconditioned voltage conversion, layer approximation of the third dimension and post processing of boundary measurements to obtain optimal boundary excitations.

Reasonably accurate imaging of single and multiple targets of differing size, location and separation is demonstrated and the resulting images are better than any others found in the literature.

Recommendations for future effort include the improvement in computational algorithms with emphasis on internal conductivity shape functions and the use of adaptive development of quadrilateral (2–D) or tetrahedral or hexahedral (3–D) elements to coincide with large discrete zone boundaries in the fields, development of a truly binary model and completion of a fast imaging system. Further, the rudimentary methods shown herein for three–dimensional imaging need improving.

The overall program was jointly supported by both the U.S. Department of Energy, Contract Agreement No. DE–FG07–90ER13032, Initiated October, 1990, and Hitachi, Ltd. The results achieved were due to the joint effort of a number of persons of differing disciplines, and could not have been undertaken otherwise.

1. INTRODUCTION

Composites of static or flowing binary media are pervasive throughout the engineering field and include such diverse situations as voids in castings, cracks in pressure vessel walls, food processing, steam power generation, oil well flows. In this work the emphasis is placed on application to binary media consisting of a continuous, electrically conducting, homogeneous medium in which insulating discontinuous regions are to be imaged. Such situations may be either static or moving, and the moving fields may also be distorting such as is the case in gas–liquid flows.

Virtually all present methods of predicting two–phase, gas–liquid flow behavior for design, optimization, and safety analyses use models where the two media are modeled as

separate fields, then coupled at mutual interfaces—the two–fluid model. As with any physical model, the two–fluid model is generally constructed by considering separately the appropriate field equations for the phases together with reasonable boundary and initial conditions. Closure, that is the ability to utilize the field equations in computation of flow field behavior, is obtained by using appropriate constitutive equations to describe interactions at phase boundaries—both solid and fluid. Such closure required knowledge of the structure of both fields.

Reasonable descriptions are currently in hand for the fluid–solid boundary interactions because of their representation in terms of global behavior which is readily measured. Nothing of practical value is known in general about fluid–fluid boundary interactions except in the most simple of cases involving fixed geometric elements such as planes or spheres. This is because of a near complete lack of measurement ability relative to complex interfacial interactions.

A description of interfacial structure and evolution, as well as the gradients which control transfer of mass, momentum, and energy at these phase boundaries is a critical challenge for the future of two–phase flow analysis. Indeed, measurement and prediction of phase boundary structure and gradients is the key element impeding development of true predictive capability for systems involving flows of liquid and vapor or gas mixtures.

The development and application of electrical impedance imaging would provide a major step forward in this area by providing the ability to quantitatively determine interfacial structure and evolution in areas where phasic interactions at boundaries is rate limited. In such cases, significant nonequilibrium can exist between phases and the problem of properly partitioning momentum and energy between the phases becomes paramount in a field description of multiphase system behavior.

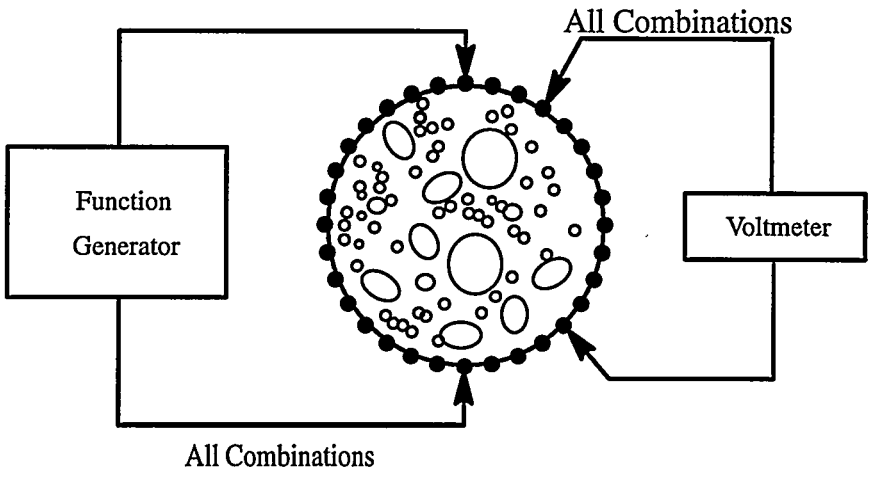

Figure 1. Schematic of excitation and measurement system.

The concept of impedance imaging is relatively straight forward. A volume of a liquid–vapor flow is excited electrically through means of boundary electrodes (Fig. 1). the response is measured and the internal distribution of electrical properties is determined which best matches the measured response. Since the electric field behavior of any medium or composite follows Maxwell's equations, the multi–fluid field must respond to

$$\nabla \cdot (\sigma \nabla \phi) = 0$$

where σ is the fluid conductivity and ϕ is the potential field, and where the boundary conditions specify the injection of electrical current through the boundary or the potential field placed onto the boundary by some means. The standard, or "forward," problem is to solve for the potential field distribution given the appropriate boundary conditions and specification of the conductivity distribution. Since the equation above is found in many areas of mathematical physics, this type of problem is solved both analytically and numerically in many widespread and diverse applications of engineering and physics.

The alternate problem, and the one which concerns us here, is to determine the distribution of conductivity, σ, which provides the best match between the boundary conditions and the potential field, the latter being determined only on the boundary. This "inverse problem,"

where the potential field is electrical, is variously called electrical impedance imaging or electrical impedance computed tomography. Since both electrical resistivity and permittivity of water and vapor are significantly different in each fluid, development of this method having sufficient rapidity will allow interfacial structure and evolution to be determined for two–phase flows.

Methods for solution to this nonlinear problem are iterative in nature. A property distribution is assumed, response to the applied excitation is calculated and compared with the measured response, and variations in the original distribution are undertaken which push the calculations in the direction of the measurements. This computationally intensive process is continued until the total mean square error between measured and computed boundary response is reduced below some predetermined value such that the resultant conductivity distributions, images, become static.

Electrical impedance imaging is a relatively new field, the earliest paper on the subject being less than two decades old. Over the past 15 years, the emphasis has been predominantly in the biomedical field for imaging organic structure. It is the purpose of this report, based on the PhD thesis of Ovacik[1], to summarize the present research which, building on the methods used primarily in the biomedical field, now stands at the forefront of this overall field of research.

2. SIGNIFICANCE OF RESULTS

Measurement and modeling the interfacial structure and evolution of complex, two–phase, gas–liquid flows is only the first part of the problem required to provide closure

1. Ovacik, L., *Extensions To The Finite Element Method For The Analysis Of Inverse Problems In Electromagnetic Devices*, PhD thesis, Rensselaer Polytechnic Institute, Troy, New York, 1998.

for the two–fluid model. Determination and modeling of gradients follows, and modeling the combined transfer laws in local and integral form must be undertaken to allow for complete closure. With this in hand, true prediction of multiphase system behavior will be much closer to reality. The overall research program of which the DOE–Hitachi Cooperative Research Program is an important part, provides the cornerstone for this effort. The results definitively show that reasonably accurate determination can be made of the size, shape and location of discrete resistive objects in a continuous field. Furthermore, the research results should have major implications outside the immediate field of two–phase flow analysis: biomedical, nondestructive testing and quality assurance, geological assay, and general internal diagnostics, to name a few. Extension of the work being reported can be expected to ultimately lead to transient imaging of a flowing gas–liquid flow field and determination of the interfacial structure of this field.

3. SUMMARY OF THE RESULTS OF THIS RESEARCH

The material presented in this report summarized the effort expended in the course of developing a finite element electrical impedance imaging system for obtaining images of binary mixtures of fluids, such as liquid and gas, using electrical measurements obtained on the boundary. The outline of the report is as follows:

- Chapters 1 and 2: Introductory material and historical background including an overview for inverse problems arising from various fields of engineering, and described inverse problems within the context of mathematics. Issues related to ill–posedness and regularization of inverse problems were also briefly discussed.
- Chapter 3: presents an extended overview which places impedance imaging in perspective relative to other imaging methods, and provided detailed background information for alternative imaging techniques.

- Chapter 4: summarizes the theory of basic electrical impedance methods. The concept of electrical impedance imaging is explained and, starting with Maxwell's equations, the field equations were derived. Various sources of error affecting experimental measurements and reconstruction procedures were also identified.
- Chapter 5: introduces several analytical and numerical innovations which can also be considered as extensions to the basic Newton–Raphson algorithm to be used for both two– and three–dimensional conductivity imaging, and which, in some cases, mean the difference between obtaining an acceptable image or not.
- Chapter 6: summarizes various experimental features used in the development of static, high–accuracy data acquisition system.
- Chapter 7: summarizes all the experimental results obtained and compares the effects of all experimental and numerical methods developed.
- Chapter 8: presents the overall report summary, the major accomplishments and conclusions reached, and points towards future research required.

4. MAJOR ACCOMPLISHMENTS

There have been a number of major modeling innovations required to achieve reasonable success in imaging of binary mixtures (mixtures having basically two, widely disparate sets of electrical properties). Once the basic method was selected and implemented, there were numerous innovations necessary to enable us to image binary fluids in an acceptable manner. These include:

1. Determined methods to directly compute the Hessian matrix rather than indirectly through the Jacobian (the full sensitivity matrix which relates the changes in elemen-

tal conductivity to the individual boundary measurements) resulting in an order–of–magnitude savings in computational resources;

2. Developed a method of undertaking preconditioned voltage conversion (PVC), corrections of experimental boundary data, which enabled us to account for errors and inaccuracies in numerical and experimental factors which distort the boundary computations.

3. Developed a block decomposition model for the field to be imaged thus reducing the computational times by three orders of magnitude. This model incorporates the following attributes:

   - use of exponential shape functions to define the behavior of the field potential within individual finite elements and especially adjacent to electrodes;
   - use of biquadratic exponential shape functions to define the variations of electrical conductivity within each finite element relative to that at the element center;
   - improved modeling of the electrodes themselves in the case of plate electrodes;

4. Developed a layer reduction method for folding unexcited three–dimensional image layers into an equivalent two–dimensional layer thereby making real quasi–three–dimensional images possible;

5. Determined the numerical sensitivity as affected by the number of elements in the finite element model and the limits of contrast sensitivity in the model;

6. Determined the boundary excitation patterns which optimize the resolution of the imaging system.

These developments allow imaging data to be obtained and images to be computed with a minimum of experimental and numerical effort.

Additional developments which have had an important and enabling effect on our ability to clearly and accurately image single and multi–sized binary targets in homogeneous media involve

7. Clearly determined that plate electrodes were superior to rod (point) electrodes for use in exciting the phantom and obtaining images;

8. Adopted the use of multiply–excited, plate electrodes for significant increase in both sensitivity and image quality;

9. Determined error variation with fluid conductivity and demonstrated the lack of contact impedance effect on the data for conductivities below 1000 μS/cm;

10. Showed it was possible to use incomplete measurement sequences combined with Walsh–function boundary excitation to minimize the acquisition effort and demonstrate methods which will be utilized in high–speed imaging;

11. Extended and adapted theoretical distinguishability concepts in the literature to experimental data through the use of differential eigenvalues to determine the minimum target sizes and multiple target separations which could be imaged;

12. Developed a *post–facto* application of boundary excitation pattern optimization to experimental data to significantly improve quality of images obtained;

13. Differentially filtered targets of varying sensitivity to allow simultaneous imaging of multiple targets of differing size and location;

14. Development of a "best contour" algorithm for explicitly determining the location, shape and size of the boundary of any discrete component based on its contrast ratio in the image.

This report described the details of these accomplishments, all of which were integral in the success we have obtained, some enabling and some incremental, for accurate imaging of single and multiple, two–dimensional and three–dimensional insulating targets in a homogeneous conducting medium.

5. CONCLUSIONS

The *first major conclusion* that can be drawn from this work is that accurate excitation and measurement of boundary voltages and currents appears to be sufficient to obtain images of the real conductivity distribution of a binary, multiply connected field within a measuring volume. Figure 2 shows just two examples of this while at the same time showing the imaging of a very small object of 6–mm diameter inside a 200–mm square tank, a demonstrated linear resolution of three parts in 100. Furthermore, we have shown that the quality of these images, and in fact the ability to obtain an image itself, is heavily dependent on both excitation/measurement techniques and the theoretical and numerical implementation of imaging algorithms. It is shown in this report that electrical impedance imaging method *has the potential* of being both fast and cost effective in comparison with alternative methods.

The *second major conclusion* drawn is that at this point, even after seven years of development effort, considerably more work must be expended before the the potential becomes reality. It has been found that excellent images of objects within a homogeneous region can be obtained with a demonstrated linear resolution of six parts in 200, and potential resolution based on distinguishability results perhaps better than one part in more than five hundred; however, the ability to correctly determine the boundary of the object depends on its shape, its relationship to the finite element geometry, the algorithm(s) chosen to represent the conductivity behavior within the elements, the image enhancement algorithms uti-

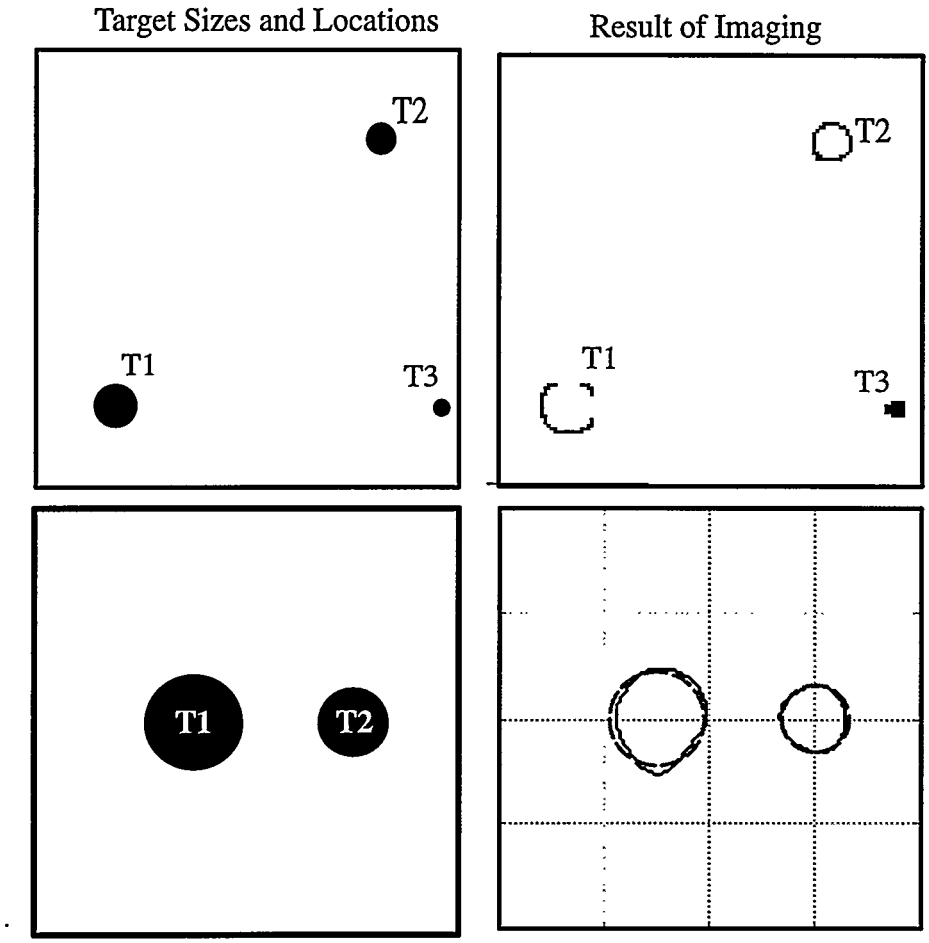

Figure 2. Examples of imaging of various targets of differing positions and sizes. Dashed grey circles indicate actual size and position of targets.

lized to treat the image before reconstructive iteration, and even the basic numerical model itself. Furthermore, the limits of resolution implied by the distinguishability data can probably approached only with an accurate, discrete–property, adaptive mesh, field computation model rather than using a conductivity continuum as undertaken herein. This will require a significant new development effort.

Specific conclusions may be drawn from this study as itemized below:

1. It is impossible using the Newton–Raphson, finite element, inverse computations methods developed herein to obtain perfect delineation of target contrast (ratio of target conductivity to background conductivity) if it varies by more than approximately a factor of ten from the homogeneous values and that computational, S–curve saturation ultimately occurs with increasing true contrast.

2. The computed boundary sensitivity to perturbations diminishes as the size of the elements used in the model decreases making our model increasingly ill posed as the number of elements used to represent a given situation increases. Nevertheless, this model was judged as that having the best potential to ultimately yield accurate phase boundary images.

3. The computational times for conductivity reconstructions using Newton–Raphson methods increase with 3.3 power of the number of elements used in the model, thus limiting the use of large number of elements in practical situations, especially three–dimensional models.

4. Numerous methods were utilized to minimize the compute times and resources. In particular, block decomposition reconstruction methods developed in this program yielded the ability to rapidly compute a converged image with a reasonable accuracy and resolution. A 50 iterations, two–dimensional, 16×16 mesh model using 16–plate–electrodes now requires approximately 37.5 minutes (45 seconds/iteration) on a Silicon Graphics INDY Unix workstation.

5. In comparison with a constant conductivity element model or one using a bilinear exponential shape function, the use of a biquadratic–exponential conductivity shape

function with the plate–electrode model produced excellent results seen in Fig. 3 for the case of the two circular–target case shown in Fig. 2.

6. Phase–timed (PT) boundary measurement methods (measuring the peak of square–pulse signals) using an accuracy of one part in 1000 is an excellent alternate to frequency locking methods (measuring rms of sinusoidal signals). PT was found to produce images as accurate as low–noise rms methods and is ten times faster. PT methods also have the advantage of eliminating broad–band noise and is more suited to high–speed applications.

7. Increasing liquid background conductivity has the effect of increasing the current magnitude and therefore improving the signal–to–noise ratio of the data and ultimately reducing the overall error in any image as seen in Fig. 4. No effect of liquid–electrode contact impedance was noted in the range of conductivities utilized.

8. The computed relative contrast (resistivity relative to the background) of any insulating target is not only a function of the model itself, but also of the target size and location within the field of interest. This is clearly shown in the relief and contour maps of Fig. 5 where targets identical to those shown in the two–target image of Fig. 2 have differing contrasts.

9. An algorithm was required and developed to determine the actual contrast ratio depicting the true size of a given object (Figure 6) behavior once the conductivity contours are known. Applying this algorithm to the two–target case yields reasonable results seen in Fig. 7. Figure 8 demonstrates that this algorithm works for circular targets of various sizes from 6–mm to 88 mm in diameter. Even with one of the most difficult challenges, imaging numerous targets of differing size and locations, Figure 9 shows that the targets can be imaged if the correct contrast ratio is utilized.

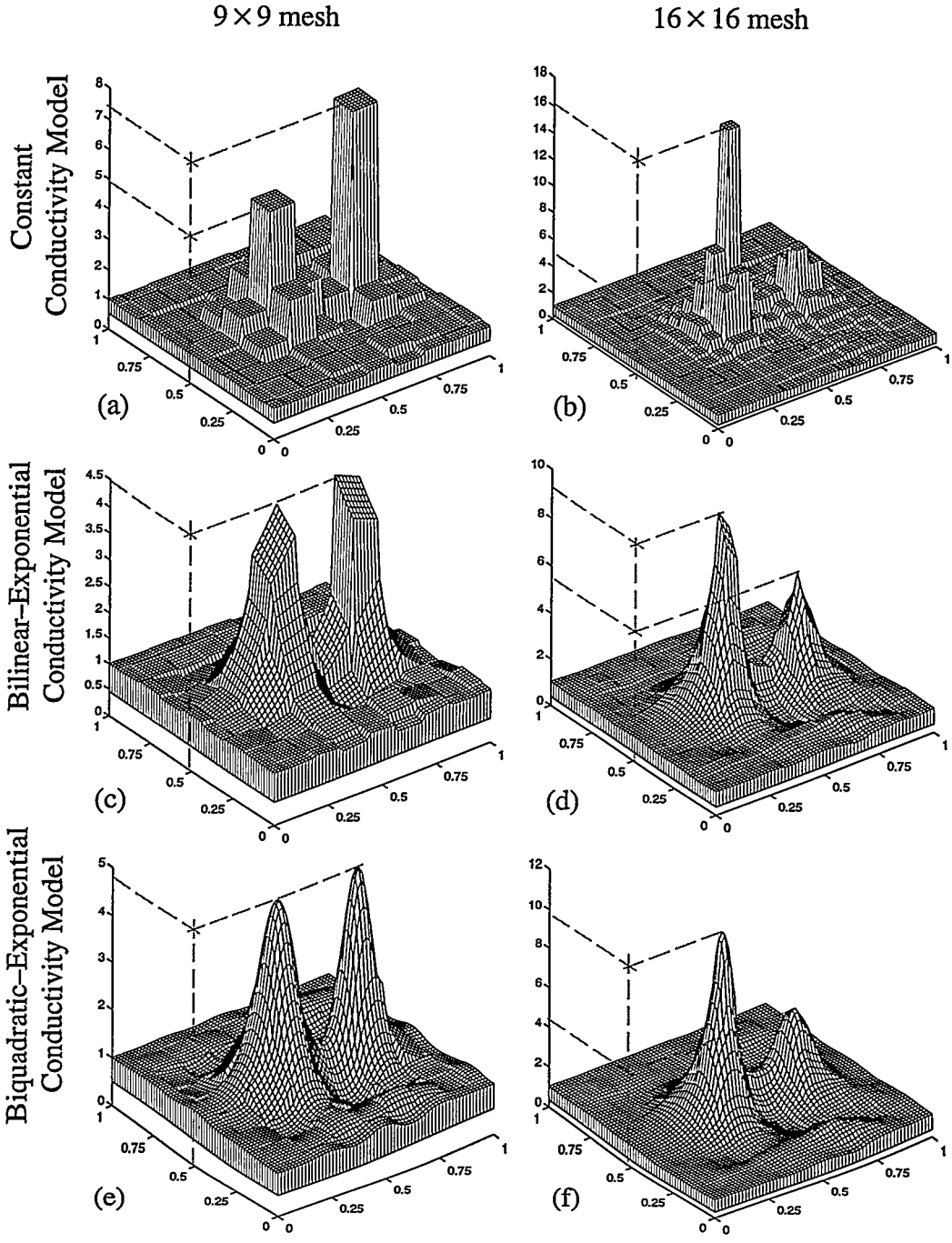

Figure 3. Comparison of element conductivity shape functions; (a), (b) constant: (c), (d) bilinear– and (e), (f) biquadratic–exponential schemes.

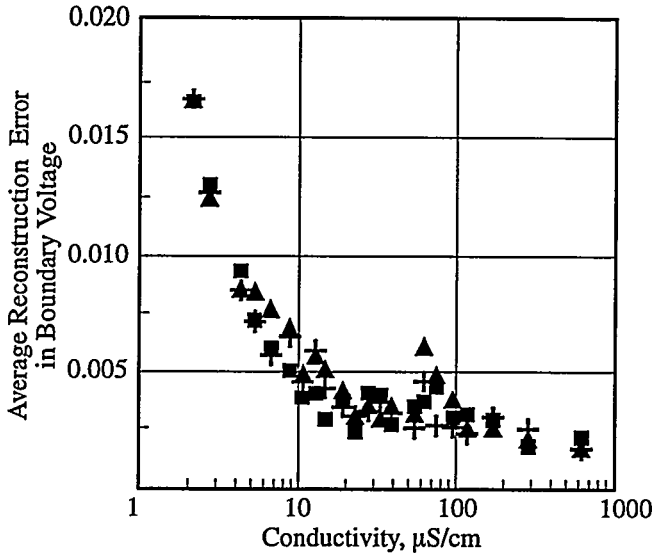

Figure 4. Liquid conductivity effect on reconstruction error.

10. Numerous different methods were utilized to improve experimental measurements. Some of the most significant include:

    - increasing the number of single–pair electrode excitations up to a point;
    - increasing the number of electrodes;
    - using multiple simultaneous excitations of electrodes rather than sequential single–pair excitation;
    - using the Preconditioned Voltage Conversion (PVC) method to correct noise and modeling errors. In many cases made the difference between obtaining a good image and no image at all;
    - using *post–facto* boundary measurement optimization to increase sensitivity of measurements.
    - correcting for quasi–three–dimensional effects in two–dimensional reconstructions using finite–length, boundary–electrode elements and a new layer model.

11. Use of Walsh–function excitations patterns (alternate, plus/minus, constant amplitude, electrode excitation) not only yielded superior results compared with single–

Figure 5. Two–target case of Fig. 2 showing relief and contour relative conductivity maps.

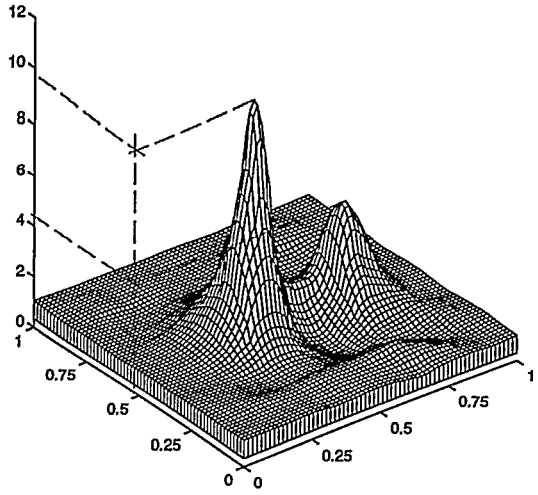

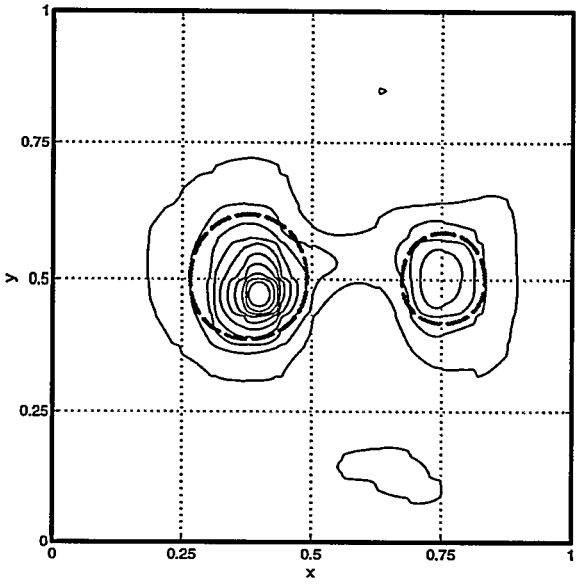

Figure 6. Correlation of differential discrimination level for individual targets taken from multiple–target images: ● 2–D data; ◆ 3–D cylinder data; ▲ 3–D flask data; × 3–D sphere data (60–mm and 115–mm diameter).

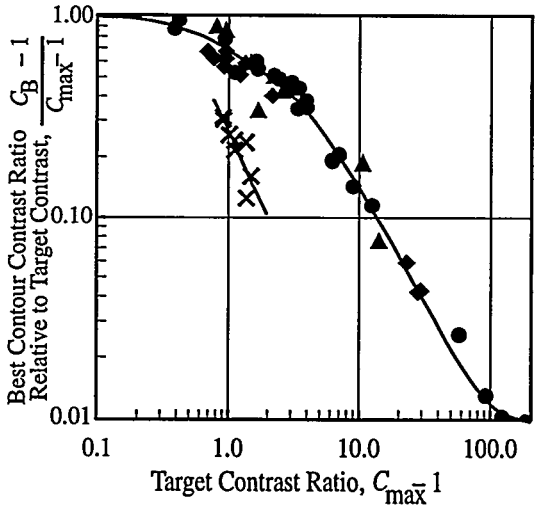

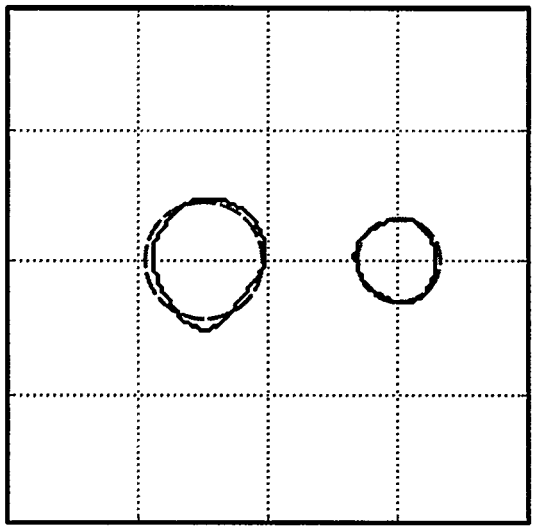

Figure 7. Application of best contour result from Fig. 6 as applied to the two–target case of Fig. 2.

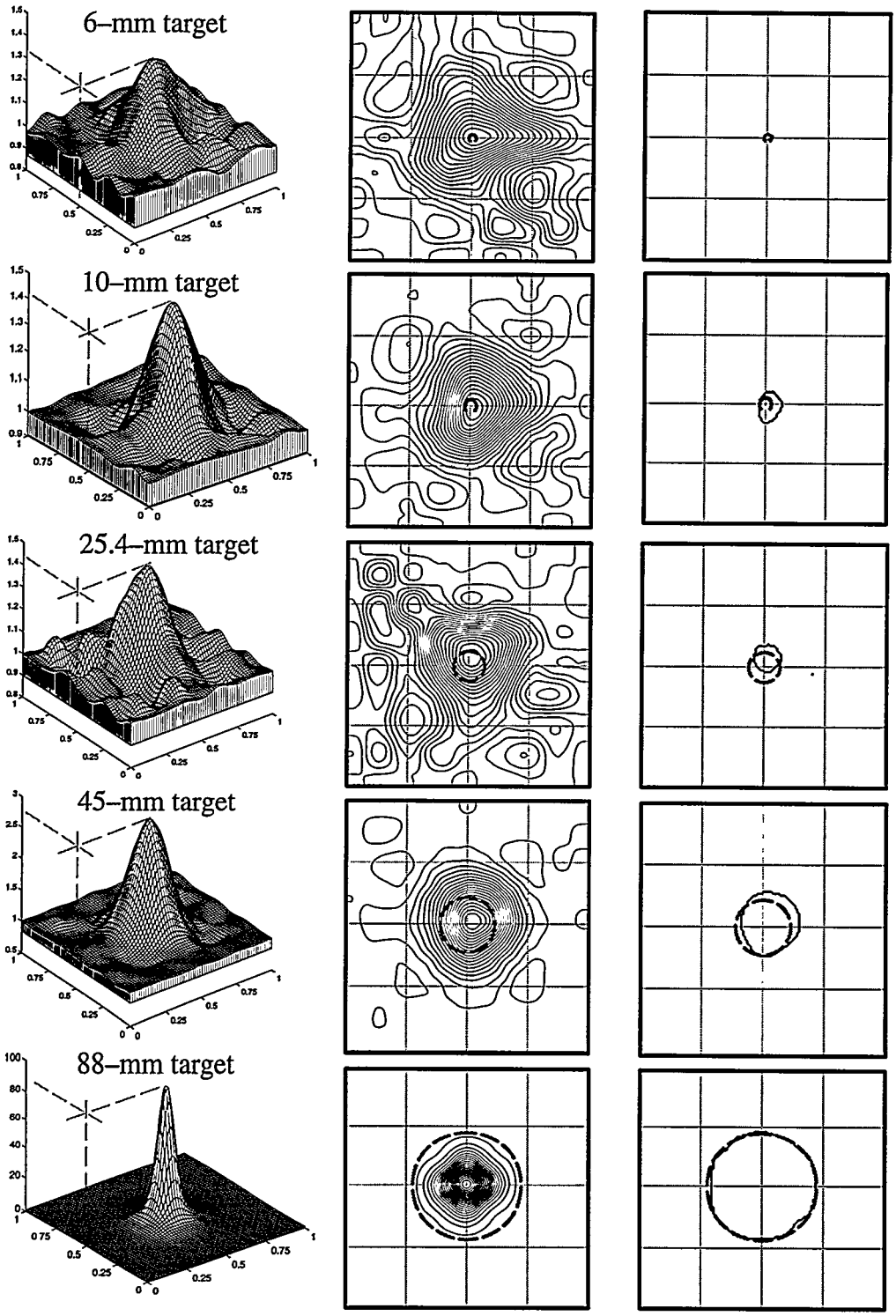

Figure 8. Relief, contour and best contour relative resistivity plots for distinguishability tests on centrally–located circular targets. Dashed grey scale circles depict actual target size and location.

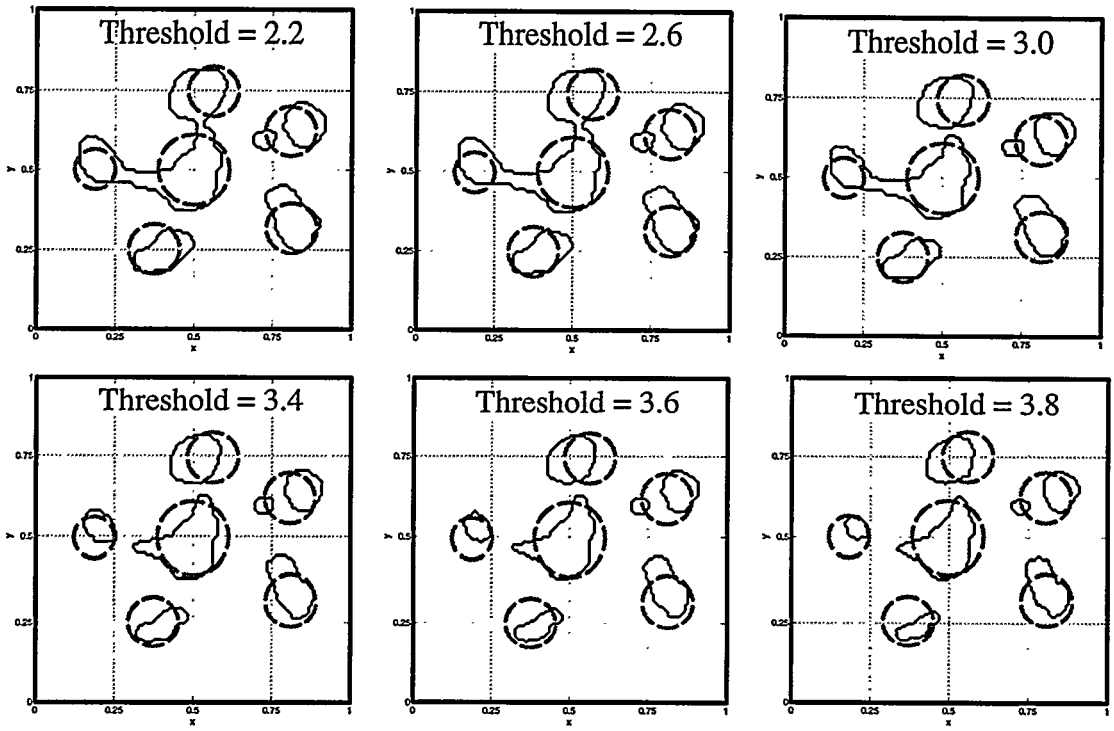

Figure 9. Best contour algorithm applied to six targets of differing size using differing contrast threshold: 2.2, 2.6, 3.0, 3.4, 3.6 and 3.8.

pair excitation acquired in the same amount of time, but also allowed phantom conductance matrices to be computed more accurately.

12. Plate electrodes were consistently better than rod electrodes in producing quality, low–noise images, the former failing in many instances to produce anything acceptable or simply failing to produce any converged image. Figure 10 depicts typical results comparing the two test geometries.

13. Multiple targets which are very close together or touching may not be separated in the image but the degree of separation required for separation is small as shown in Fig. 11.

14. While strictly applicable only to two–dimensional or quasi–three–dimensional situations, images were obtained of two spherical targets shown in Fig. 12, the contours being flattened due to three–dimensional current flow not accounted for in the model.

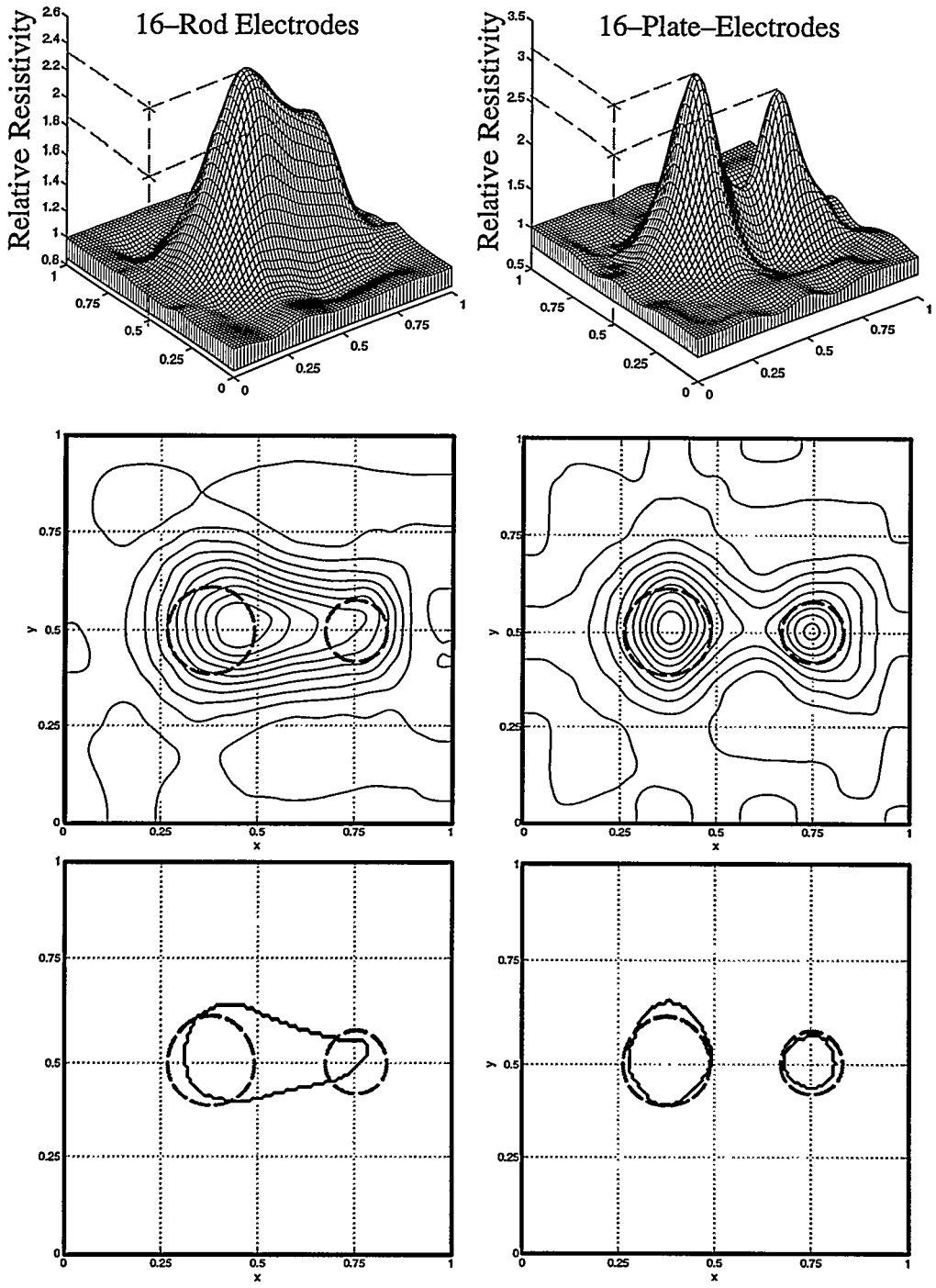

Figure 10. Relief, contour and best contour plots for the two–target case shown in Fig. 2 comparing the 16–rod–electrode phantom (left column) and the 16–plate–electrode phantom.

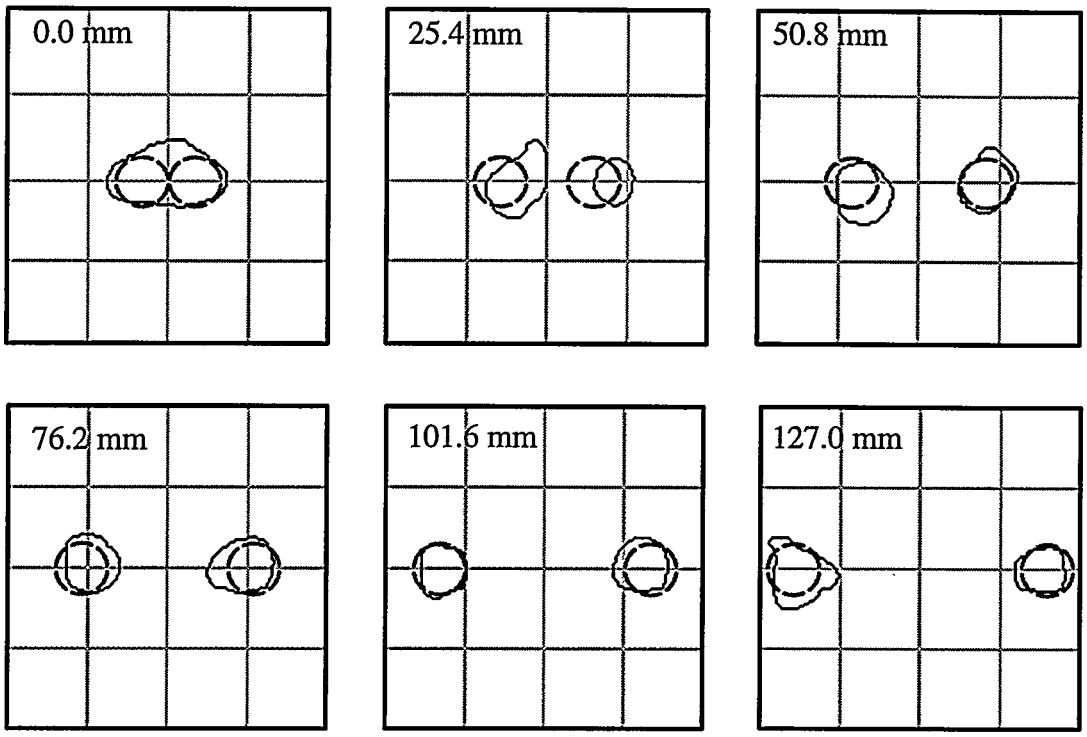

Figure 11. Horizontal distinguishability test results for various amounts of separation.

15. The first, crude images of a moving target were obtained showing that sequential slicing of a three–dimensional target (Fig. 13) may be possible to build three–dimensional images.

16. In comparison with other electrical impedance imaging methods described in the literature, it is concluded that the finite element model, among of all those known and examined to date, provides the best possibility of those currently in existence of yielding the best quality (size, shape and position of targets) impedance images of binary media.

17. It is further concluded that the finite element model has limitations which will mean its ultimate replacement by a true binary field model where the limitations associated with best contour algorithms no longer limit the accuracy of the results.

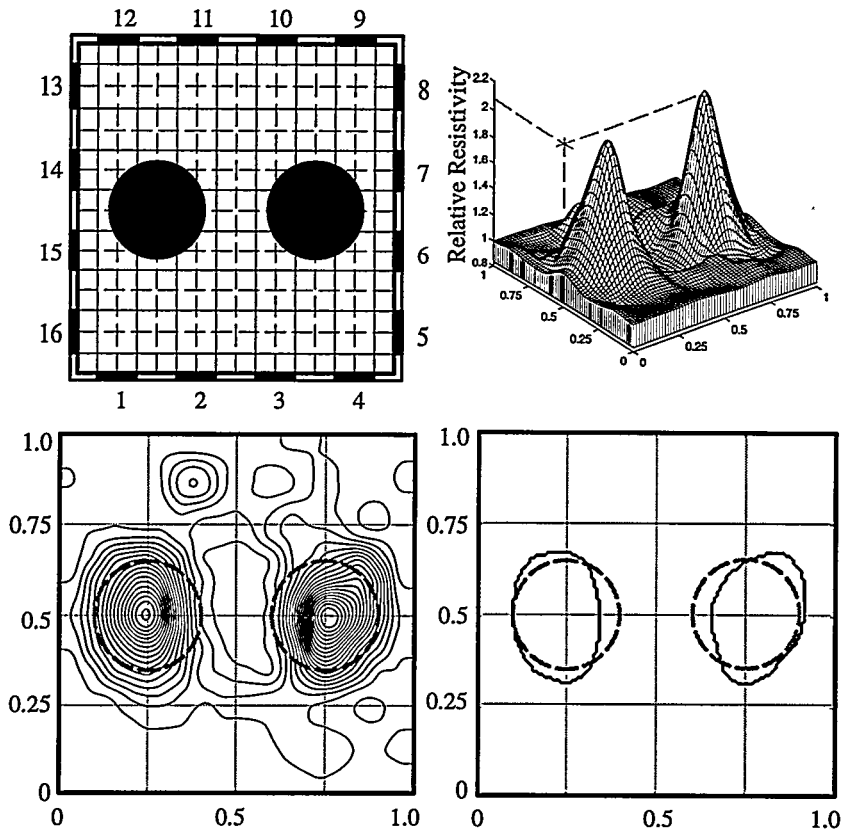

Figure 12. Image of two 60–mm diameter spheres centered vertically in the imaging plane of the three–dimensional phantom.

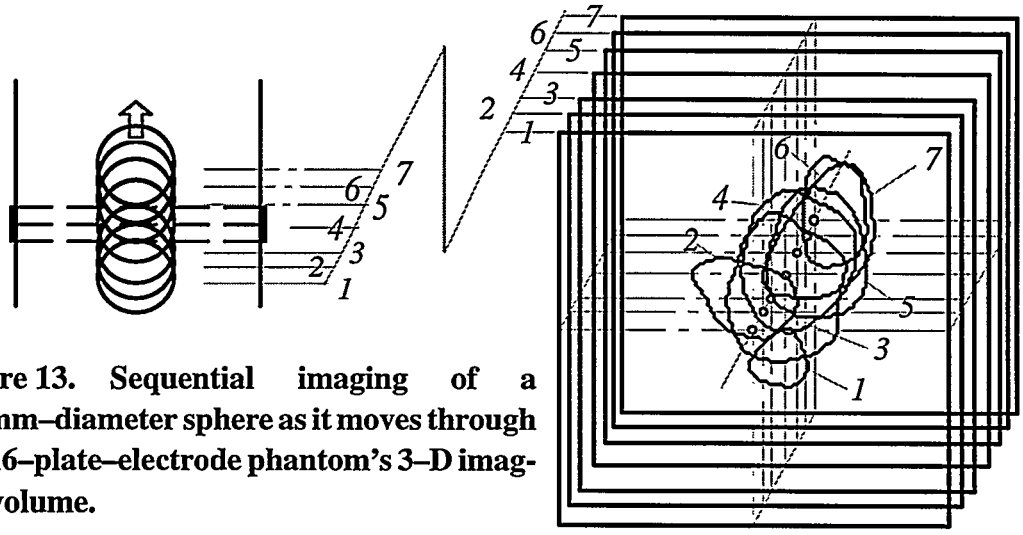

Figure 13. Sequential imaging of a 60–mm–diameter sphere as it moves through the 16–plate–electrode phantom's 3–D imaging volume.

18. In general, it is concluded that the information necessary to obtain accurate images of three–dimensional binary media is available using electrical impedance imaging methods described herein, and that these methods should allow image framing rates of at least 1000 images per second using relatively inexpensive electronics. Faster imaging should be possible limited only by the cost and accuracy of available high–speed data acquisition hardware.

6. RECOMMENDATIONS FOR FUTURE WORK

The research undertaken in electrical impedance imaging (EII) has put the Rensselaer Multiphase Imaging Laboratory at the forefront of the low–cost imaging field with capabilities which in most cases far surpass those currently extant. However, there is still much left to be done for the goal of using EII for interfacial reconstruction of gas–liquid flows to become a reality. It is recommended that future research should place the emphasis particularly on software development, and design of a high–speed data acquisition system. In the near term, the finite element model will be the work house of electrical impedance imaging in this field. For liquid–gas system imaging, a truly three–dimensional result will ultimately be needed and this will probably require one of the new generation of vector machines. This section outlines major developmental items which are necessary to further improve performance of the finite element schemes and iterative reconstruction schemes.

6.1 Two–Dimensional, Continuous Conductivity Model

6.1.1 Generalized geometry

This research report presents a detailed summary of the exponential finite element scheme for rectangular or brick elements. These elements however are limited to accurately representing only rectangular geometries. The first recommendation is to:

1. *Extend the exponential finite element scheme to quadrilateral (2–D) and/or tetrahedral or hexahedral (3–D) elements to represent more general boundary geometries.*

6.1.2 Adaptive mesh

Although the biquadratic–exponential conductivity function does not represent the most general case, this model has probably reached its ultimate limit of applicability. Because of the criterion which is necessary for obtaining a closed form solution to the potential function inside each element, exponential functions are very attractive because of both their separability in each coordinate direction and their ability to approximate discontinuity in conductivity variations. Considering a bicubic or a higher order exponential model is not recommended because closed solutions for such models do not exist. Rather, the conductivity distribution could be first estimated by using the existing block decomposition algorithm, and then the mesh coordinates could be moved to the contours where very rapid conductivity variations occur.

2. *Develop an adaptive, mesh–moving scheme which can place element boundaries along the edges of "large" discontinuities in the field.*

6.1.3 Reactive–continuum modeling

Since only continuous conducting media are considered herein, such media being in electrical contact with the boundary, the ultimate extension to this method will involve the ability to completely image a field where the continuum may, in fact, be nonconducting. This would be enabling for imaging of resistive media surrounded by purely reactive media. Therefore, the recommendation is to:

3. *Extend the methods developed to consider both the resistive and reactive parts of the electrical field to enable the entire field to be determined under circumstances where the reactive field surrounds or contains, at least in part, the resistive field.*

6.2 Three–Dimensional, Continuous Conductivity Model

6.2.1 Variable–conductivity layer model

The original idea in developing the layer reduction method was to provide reconstructions from a single scan. However, a single scan data set does not contain the conductivity information in layers below and above the scanning plane and so variable conductivity in the axial dimension could not be considered. While this was adequate for three–dimensional objects having slowly varying axial conductivity, it was not adequate where the variations were large or rapid. Thus, although successful results were obtained for 60–mm–diameter spherical targets, this method did not produced the same successful results when smaller spherical targets such as 32–mm–diameter spheres were used. Therefore, the next step should:

4. *Improve element conductivity model (in brick or quadrahedral elements) which can also model conductivity variation in the phantom's axial direction (z–direction).*

6.2.2 Automatic Tomographic Capability

The development of three–dimensional imaging methods has as its goal the computation of true tomographs using slices which can then be pieced together to display the whole field. Such layering tomography is characteristic of every tomographic method currently in existence such as magnetic resonance and x–ray tomography methods. Whether approximate three–dimensional methods are used or true three–dimensionality is developed, slice tomography must be developed. Therefore:

5. *Automate the layer reduction method to develop a three–dimensional, slice–by–slice, tomographic and three–dimensional reconstruction capability which uses multiple–scan data acquired in successive time intervals as the conductivity field passes through the scanning plane.*

6.2.3 True Three–Dimensional Model

Faster, more powerful computers continue to become available. The limiting factor for using currently reported methods in three–dimensions was the 3.3 power variation of computer time and storage required as the size of the model gets larger. Thus, taking a 16 x 16 model into the third dimension by the same factor increase the compute time by approximately 10,000 times. The availability of new vector machines having large numbers of parallel processors, coupled with further improvements and innovations, may make true three–dimensional imaging possible. Therefore,

6. *Begin development of both software and hardware for a truly three–dimensional imaging FEM system adapting the current methodology to advanced, high speed, vector computers.*

6.2.4 True binary modeling

In the longer term, a true three–dimensional model which can handle a combination of continuous and discontinuous conductivities will be required. The continuous field capability will be needed where imbedded discontinuities are so small as to make the field a quasi–homogeneous mixture such as a froth, foam or slurry. The discontinuous field is required to image large imbedded discontinuities such as large bubbles in a foam or slurry, or large liquid masses or columns imbedded in a gaseous continuum such as inverted annular flow. The size of discrete elements is a consideration because it is generally where the elements are large that they present impediments to interfacial energy or momentum transfer. Otherwise, discrete elements simply make the flow appear as homogeneous with mixture properties somewhere between those of the continuum and discrete phase.

Such a model was attempted early on in the research program being discussed but was found to be inherently unstable within the confines of our FE model due in part to the lack of coincidence of the phase boundaries with the element boundaries. However, in the long run, this type of computational system will be required and its implementation will immediately eliminate the necessity of heuristic algorithms such as the best contour method of shape determination. Thus, under conditions where the discreteness is both important and limiting in some form of multiphase behavior, the last two recommendations are:

7. *Develop a true binary model using piecewise analytic solutions for potential field variations near electrode and conductivity field discontinuities occur.*

8. *Develop a combination model which can handle both fields with a variable conductivity continuum and discontinuous fields capable of handling pure conductors or pure insulators.*

7. CONTRIBUTORS

The following personnel have been principally involved in the various stages of this project:

- Dr. O.C. Jones, Professor of Nuclear Engineering and Engineering Physics, principal investigator and overall project coordinator.
- Dr. J.T. Lin, first as Post–Doctoral Research Associate and then as Assistant Research Professor has been the major lead contributor in the day–to–day operation of the program, in the development of the finite element model, the block decomposition method, and the overall numerical effort in the program.
- Mr. L. Ovacik, graduate student in Electric Power Engineering, is the lead student researcher in the finite element method and numerical imaging methods development effort.
- Mr. Hongjun Shu, graduate student in Engineering Physics, was responsible for designing and constructing the high accuracy imaging electronic system and is the lead student responsible for design and construction of the PACIFIC–1 high speed system.

Others who contributed to the success of this research project include:

- Dr. J.C. Newell, Professor of Biomedical Engineering and leader of the Rensselaer Biomedical Imaging Team, provided valuable assistance and information in the initial organization of the effort and in the early stages of the research.
- Dr. D. Isaacson, Professor of Mathematical Science, provided guidance in mathematical modeling.
- Dr. M. Cheney, Associate Professor of Mathematical Science, provided early guidance and information relative to the NOSER method of image reconstruction.

- Dr. G.J. Saulnier, Assistant Professor of Electrical, Computer, and Systems Engineering, has provided valuable guidance in development of the high speed electronic design.
- Dr. J. Goble, Post Doctoral Research Associate provided assistance in initial image treatment especially using ImageTool.
- Dr. K. Kiymik, Visiting Scientist, was responsible for the frequency multiplexing work.
- Ms. Yingchao He, graduate student in Nuclear Engineering, is the lead student responsible for developing the back projection imaging methods.
- Mr. Y. Danon, graduate student in Engineering Physics, was instrumental in assisting the setup of our overall computational system network.
- Mr. B. Dunsmoor, undergraduate student in Mechanical Engineering, is the lead person responsible for design and construction of the three–dimensional phantoms.
- Mr. R. Parker, undergraduate student in Engineering Physics, is the person responsible for design and construction of the natural convection test.

8. PUBLICATIONS

The following is a list of publications which resulted from this research:

[1] Lin, J.T., Ovacik, L., Jones, O.C., Newell, J.C., and Cheney. M., and Suzuki, H., [1991] Use of Electrical Impedance Imaging in Two–Phase, Gas–Liquid flows. Presented at the 1991 National Heat Transfer Conference, Minneapolis, July 28–31.

[2] Jones, O.C., [1991] Developments in Impedance Imaging of Two–Phase Flows. **Proc. Int. Conf. on Multiphase Flows**, Tsukuba, Japan, Sept. 24–27.

[3] Jones, O.C., Lin, J.T., and Ovacik, L., [1991] Electrical Impedance Imaging in Two–Phase, Gas–Liquid Flows: 1. Initial Investigation. **Proc. Conf. on Inverse Design Concepts and Optimization in Engineering Sciences–III**, Washington, Oct. 23–25.

[4] Jones, O.C., Lin, J.T., and Ovacik, L., [1991] Electrical Impedance Imaging of Two–Phase Flows. Presented at the annual AIChE meeting, session on Fundamental Research in Multiphase flows, Los Angeles, Nov. 17–21.

[5] Lin, J.T., Ovacik, L., and Jones. O.C., [1991] Impedance Imaging for Two–Phase Flows. **Trans. ANS, 64**, pg. 718.

[6] Lin, J.T., Ovacik, L., and Jones, O.C., [1992] Investigation of Electrical Impedance Imaging for Two–Phase, Gas–Liquid Flows. **Chemical Engineering Communications, 118**, pg. 299–325.

[7] Lin, J.T., Ovacik, L., and Jones, O.C., [1992] Progress in Electrical Impedance Imaging of Two–Phase Flows. Presented at the 1992 National Heat Transfer Conference, San Diego, Aug. 9–12.

[8] Jones, O.C., [1992] On imaging of two–phase flows using electrical impedance methods. Proc. First European Thermal–Sciences and Third U.K National Heat Transfer Conference, 16–18 September 1992.

[9] Jones, O.C., Lin, J.T., Ovacik, L., and Shu, H., [1992] Advances in Impedance Imaging of Gas–Liquid Systems. **Proc. Japan–U.S. Seminar on Two–Phase Flow Dynamics**, V. Schrock and T. Sakaguchi, Eds., July 4–11.

[10] Jones, O.C., Lin, J.T., and Ovacik, L., [1992] Investigation of Electrical Impedance Imaging Relative to Two–Phase, Gas–Liquid Flows. **Chemical Engineering Communications, 118**, 299–326.

[11] Lin, J.T., Jones, O.C., Ovacik, L., and Shu, H., [1992] Developments in Impedance Imaging relative to Gas–Liquid Systems. Proc. National Heat Transfer Conf, Lagrange Park, IL, pg. 68–75.

[12] Ovacik, L., Shu, H, Lin, J.T., Jones, O.C., [1993] Progress in Impedance Imaging for Gas–Liquid Flows: Analytical and Numerical Developments. Presented at the First International Conference on Inverse Problems in Engineering: Experimental Developments, Palm Coast, Florida, June 13–18.

[13] Lin, J.T., Jones, O.C., [1993] Progress in Impedance Imaging for Gas–Liquid Flows: Experimental Developments. Presented at the First International Conference on Inverse Problems in Engineering: Theory and Practice, Palm Coast, Florida, June 13–18.

[14] Lin, J.T., Jones, O.C., [1993] Progress in Impedance Imaging for Gas Liquid Flows: Analytical and Numerical Development. **Proc. 1st Int. conf. on Inverse Problems in Engrg.**, Palm Coast, Florida, June 13–18.

[15] Lin, J.T., Jones, O.C., Ovacik, L., and Shu, H–J, [1993] Advances in Impedance Imaging Relative to Two–Phase Flow, Presented at the National Heat Transfer Conference, Minneapolis.

[16] Jones, O.C., Lin, J.T., Ovacik, L., and Shu, L., [1993] Impedance Imaging Relative to Gas–Liquid Systems. **Nucl. Eng. Des., 141**, pg 159–176.

[17] Jones, O.C., Lin, J.T., Shu, H. and Ovacik, L, [1994] Impedance Imaging Relative to Binary Mixtures. Proc. 5th Int. Sym. on Liquid–Solid Flows, Fluids Engineering Conf., June 19–23, Lake Taho.

[18] Jones, O.C., Lin, J.T., Shu, H., [1994] Impedance Imaging Relative to Binary Mixtures. Proc. 5th Int. Sym. on Liquid–Solid Flows, Fluids Engineering Conf., June 19–23, Lake Taho.

[19] Jones, O.C., Ovacik, L., Lin, J–T and Shu, H–J, [1996] Electrical Impedance Imaging for Gas–Liquid Mixtures.1: Basic Analytical Methods Development, presented at the Japan–U.S. Seminar on Two–Phase Flow Dynamics, Fukuoka, Japan, July 7–13.

[20] Jones, O.C., Ovacik, L., Lin, J–T and Shu, H–J, [1996] Electrical Impedance Imaging for Gas–Liquid Mixtures.2: Preconditioning and Numerical Sensitivity, presented at the Japan–U.S. Seminar on Two–Phase Flow Dynamics, Fukuoka, Japan, July 7–13.

[21] Jones, O.C., Ovacik, L., Lin, J–T and Shu, H–J, [1996] Electrical Impedance Imaging for Gas–Liquid Mixtures.3: Experimental Methods and Results, presented at the Japan–U.S. Seminar on Two–Phase Flow Dynamics, Fukuoka, Japan, July 7–13.

[22] Ovacik, L., Lin, J–T, and Jones, O.C., [1997], Progress in Electrical Impedance Imaging of Binary Media:1: Analytical and Numerical Methods, **Proc. OECD/ CSNI Meeting**, Santa Barbara, CA, March 17–20.

[23] Ovacik, L., and Jones, O.C., [1997], Progress in Electrical Impedance Imaging of Binary Media:2: Experimental Developments and Results, **Proc. OECD/CSNI Meeting**, Santa Barbara, CA, March 17–20.

[24] Ovacik, L., Jones, O.C., Lin, J–T, and Shu, H., [1998] "A Finite Element Electrical Impedance Imaging System for Binary Media: 1: Analytical and Numerical Methods," **Inverse Problems in Engineering, 6**, 1, pg. 33–77.

[25] Ovacik, L., Jones, O.C., [1998] "A Finite Element Electrical Impedance Imaging System for Binary Media: 2: Experimental Methods in Two Dimensions with Emphasis on Distinguishability," **Inverse Problems in Engineering, 6**, 2, pg. 125–154.

[26] Ovacik, L., Jones, O.C., [1998] "A Finite Element Electrical Impedance Imaging System for Binary Media: 3: Differential Discrimination and Separate Effects for 2–D and 3–D Objects," **Inverse Problems in Engineering, 6**, 3, pg. 227–253.

[27] Jones, O.C., Ovacik, L., Lin, J–T, and Shu, H., [1998] "Electrical Impedance Imaging for Gas–Liquid Mixtures: 1: Basic Analytical Methods Development," submitted for publication in the **Trans. ASME, J. Fluids Eng.**

[28] Jones, O.C., Ovacik, L., Lin, J–T, and Shu, H., [1998] "Electrical Impedance Imaging for Gas–Liquid Mixtures: 2. Extension to 3–D, Preconditioning and Numerical Sensitivity," submitted for publication in the **Trans. ASME, J. Fluids Eng.**

[29] Jones, O.C., Ovacik, L., Lin, J–T, and Shu, H., [1998] "Electrical Impedance Imaging for Gas–Liquid Mixtures: 3. Experimental Methods and Results," submitted for publication in the **Trans. ASME, J. Fluids Eng.**

CHAPTER 1

INTRODUCTION

1.1 Introduction

For the last twenty years, with the advent of increasing computational power, many physical phenomena arising from various fields of engineering have been successfully modelled by means of accurate and fast numerical analysis techniques. As these techniques developed, inverse problems have increasingly become of interest in many fields of science and engineering, ranging from medical tomography and nondestructive evaluation to optimal design problems. Inverse problems are involved in such diverse disciplines as [1]: mechanics, geophysics, electromagnetics, acoustics, heat transfer, fluid mechanics. However, almost all applications are problem dependent. For their solutions, implementation of different techniques and instrumentation are required together with an expert's interpretation of the problem in that field. In electromagnetics, for example, the interest in inverse problems stems from a desire to determine electrical or geometrical characteristics of an electromagnetic system from either measured (observed) or specified response of an electromagnetic phenomenon. This measured or specified system response may be either in the form of potentials or gradients of potentials describing the electromagnetic behavior of the system.

It is the purpose of this report, based on the PhD thesis of Ovacik [2][2], to summarize the results of the research undertaken under the DOE contract. This introductory chapter is intended to provide a background information for various types inverse problems arising

2. Numbers in brackets refer to references listed at the end of this thesis.

from different fields of engineering and science. First, the classification of inverse problems are discussed and then these problems are explained within the mathematical context. Finally, the problem of *ill–posedness* effecting the behavior and efficiency of most inverse solution procedures is explained and discussed briefly.

1.2 Classification of Inverse Problems

It has been noted that there is not a common criterion for classification of inverse problems in literature: different authors used different criteria based on the way which parameters are defined as the unknowns, the way by which the system input and output data is obtained, or the way by which the inverse problem is formulated. In this report, the inverse problems are classified based on whether or not the system physically exists, i.e., whether the data are experimentally measured from an existing system or they are specified a *priori* describing a system which does not exist. In this regard, an inverse problem may belong to either of the following categories:

1. Nondestructive Test Problems (NDTP);

- Identification Problems (IP)
- Reconstruction Problems (RP)

2. Synthesis Problems (SP).

Every inverse problem, in common, has given data which may be in the form of system input (or excitation), system output (or response), and a set of parameters describing the system itself. In some problems the system physically exists, and the system's input–output relation is experimentally determined by measurements. These problems are called nondestructive test problems (NDTP). In the problems of this class, either the input–output relationship is given and the system parameters are determined (identification problem, IP)

or the output and the system is given and the input is determined (reconstruction problem, RP). In contrast, there is another type of inverse problem in which the system does not physically exist and the input–output data are specified rather than measured. In this case, the problem is to synthesize the system which can yield the given input–output relation. The problems of this kind are called synthesis problems (SP). Synthesis problems in general deal with finding geometrical coefficients or location and magnitude of system excitation sources under specified input–output relations of the system. However, it is quite important to know that since the data is not obtained from an existing system, a unique solution to the inverse synthesis problem may not always exist.

1.3 Mathematical Statement of Inverse Problems

To describe inverse problems from the mathematical point of view, first consider a system model $A(p)$ describing the behavior of a constitutive field. The model is given in the form of an "operator equation" [3]: $A(p)z = u$; $p \in P$; $z \in Z$; $u \in U$, where A, z, u and p are system modeling operator, system input excitation, system response, and system modeling parameters defined in spaces Z, U, and P, respectively. The forward problem is to find the system response, $u \in U$, for given: $z \in Z$, and $p \in P$, as outlined in Figure 1.1. In contrast to the forward problem, a typical inverse problem may be of either of two types. The first type is called a "reconstruction problem" which finds the input excitation, $z \in Z$, for given: $u \in U$ and $p \in P$ (see Figure 1.2(a)). The second type which is a well–known "identification problem" concerns estimation of system parameters, $p \in P$, for given: $z \in Z$ and $u \in U$, as shown in Figure 1.2(b).

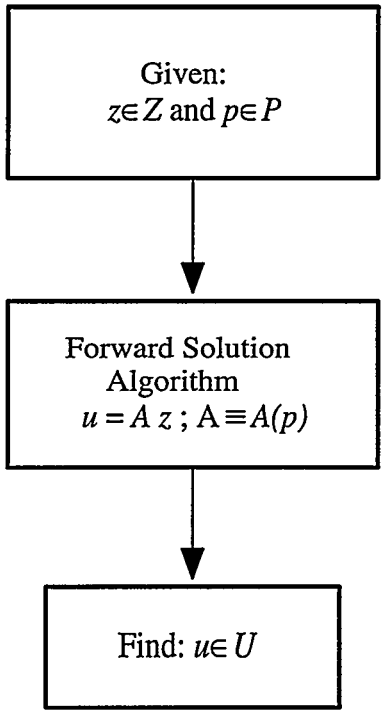

Figure 1.1 Flow chart for solution of a forward problem.

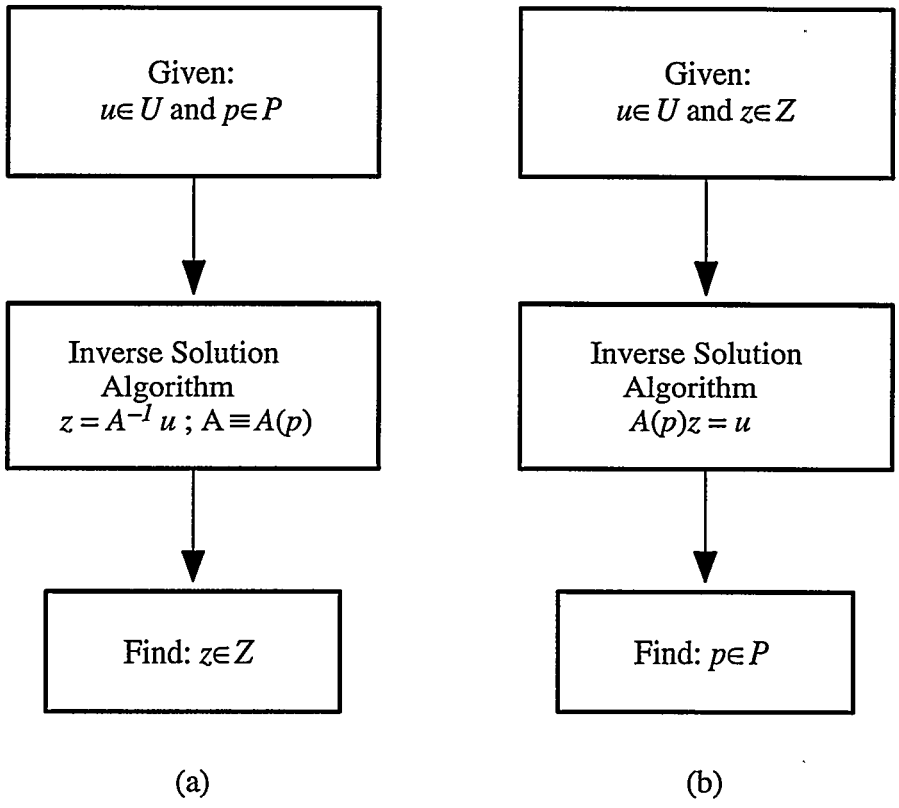

Figure 1.2 Flow chart for solution of two inverse problem types: (a) reconstruction problem; (b) identification problem.

1.4 Ill–Posedness of Inverse Problems

In general, solution of inverse problems is inherently *ill–posed* or *nonunique* in the case of the system's low sensitivity to the system parameters. In the sense of Hadamard,[3] "well–posedness" of a problem is defined as follows [5]: 1) the problem represented by $A(p)\ z = u(z \in Z, u \in U, p \in P)$ is solvable over the entire space U, 2) the solution is unique, 3) the solution is stable (i.e., small perturbations of u result in small perturbations of the solution). Even if one of these three conditions are not satisfied, the problem is said to be *ill–posed.* In solution of *ill–posed* problems, an instability issue arises because of the fact that measurements of system output are contaminated by noise. In this case, solution is unstable and wildly oscillating. Instabilities can be avoided by constructing "well–posedness" employing regularizing algorithms[4] [6]. These algorithms simply smooth the "sharpness" of the mapping between the true and estimated solution (i.e., goodness of agreement between data and solution). The *trade–off* here is between stability of the solution and agreement with the data. The more the stability of solution is desired, the more the goodness of agreement is forfeited, or the other way around.

1.5 Summary

Inverse problems appear in many applications of nondestructive test and design problems and they are increasingly becoming popular in parallel to the unprecedented advancements achieved in software and computer resources. Efficiency of most numerical solution schemes severely suffer from the consequences of ill–posedness arising from the

---

[3] J. S. Hadamard first mentioned the concept in 1902 and later in 1923, and formalized the notion with the definition given in the text which follows [4].

[4] Very little was advanced regarding a general theory of ill–posed problems prior to the 1950's at which time A. N. Tikhonov began his investigations of ill–posed problems associated with geophysical exploration.

lack of sensitivity due to the nonlinear nature of inverse problems. It is therefore extremely important to understand the causes of ill–conditioning and to incorporate regularization strategies into the numerical schemes in order to obtain a stable solution. These will be discussed in more detail in the subsequent chapters.

CHAPTER 2

HISTORICAL BACKGROUND AND CONTRIBUTION

2.1 Introduction

The work throughout this report is mainly devoted to development of inverse finite element methodologies for numerical solution of inverse problems based on the least–squares minimization type of optimization methods. The scope of this work concentrates on investigation of two specific type of inverse problems. These two problems belong to the class of aforementioned *identification* problems. The inverse conductivity problem arising from the area of electrical impedance computed tomography (EICT) is a potentially useful technique for medical as well as nonmedical (industrial) applications (industrial applications can be envisioned in geological surveying, imaging two–phase flows, and determining locations and shapes of cracks in metallic bodies [7]–[9]). This technique noninvasively determines electrical properties in a body (conductivity, permittivity, or both) from measurements on its surface. In the following sections of this chapter, first, a historical overview of recent developments is given, and then the contributions made to those areas are summarized.

2.2 Previous Work

Description of interfacial structure, as well as the measurement of the gradients which control the transport of mass, momentum, and energy at these phase boundaries, is a critical challenge for the future of two–phase flow analysis. Indeed, the measurement and prediction of phase boundary structure and gradients is the key element impeding develop-

ment of true predictive capability for systems involving flows of liquid and vapor or gas mixtures.

In contrast to other imaging systems available,[5] impedance methods have the potential of obtaining up to 1000 or more images per second (ips) which could be very valuable in imaging two–phase flows. The challenge in impedance imaging is to obtain high quality, high resolution, three–dimensional images using reasonable computer resources. The first part of the report describes the development of computationally efficient, electrical impedance imaging algorithms evolved from inverse techniques based on a finite element method. Both two–dimensional and three–dimensional imaging techniques are described in detail.

In the early 1980's, research in the development of electrical impedance computed tomography (EICT) started in the geological area (Dines and Lytle [10]), and in the biomedical field (c.f. Price [11], Barber and Brown [12], [13], Seagar, Barber, and Brown [14], Yorkey [15], [16], Yorkey et al.[17]–[21], Cheney et al. [22], Fuks [23], Fuks et al. [24], Hua [25], Hua et al. [26]–[29], Woo [30], and Woo et al. [31], [32]). Most methods have used the resistive field because the resistivities of relevant materials are low. To date, the best of applications applied to real systems produce a somewhat fuzzy planar "picture" of resistivity or permittivity variations which has not been significantly improved in the past five years.

The early attempts of Price [11], and Dines and Lytle [10] used impedance network methods. Price's method, although unsuccessful, appears to have been the first in the

[5] See other imaging techniques in Chapter 3.

biomedical field to attempt to obtain impedance tomograms using the guard–electrode method. His suggestions of the use of "guarding" methods was aimed at creating a beam–like current line, expecting to minimize nonlinearity of current paths. Unfortunately his reported work failed. Dines and Lytle [10], however, devised an iterative process by linearizing the network equations and demonstrated successful reconstruction of resistors in a 7×7 array. When the size of the network was increased, computational limitations to this method evolved from complex Jacobian matrix calculations. Starzyk and Dai [33] proposed a "layer–by–layer" method which only solves one concentric layer at a time, starting from outside to inner layers. This method decreased the computational effort of the Jacobian matrix by an order of magnitude.

Barber and Brown [12], [13] developed a back projection method based on linearization around a constant conductivity. This method was subsequently improved upon by Santosa and Vogelius [34] but with mixed results. Beck and his co–workers (Huang et al. [35], Beck and Williams [36]) have also developed back–plane projection methods for analysis of gas–liquid pipe flows of gas and oil. A variational method developed by Kohn and Vogelius is similar to that of Wexler et al. [37]. It was shown by Kohn and McKenney [38], however, to produce results no better than those of Wexler et al. [37].

Yorkey [15], [16], Yorkey and Webster [19], and Yorkey, Webster, and Tompkins [20],[21], Kim, Tompkins, and Webster [39], and Kim, Webster and Tompkins [40], followed a different approach based on a finite element method and using Marquardt's conditioning which they stated to be better than Akaike's method [41] to improve ill–conditioning in the overall problem. This method is here refer as the YWT method (using the initials of Yorkey, Webster and Tompkins). Their results appear singularly successful in inversion of carefully chosen numerical experiments, but a recurring criticism (c.f. Kohn and McKenney [38]) is that their variations in conductivity were carefully chosen to

be aligned with model cell boundaries. Others following the finite element approach include Dines and Lytle [10], Murai and Kagawa [42], [43], Kagawa, Murai and their co–workers [44], Hua [25], Hua et al. [26]–[29], Woo [30], Woo et al. [31], [32], and Jones, Lin and their co–workers [45]–[50].

Yorkey et al. [15] examined several other methods including the perturbation method used by Kim et al. [39], [40], the equipotential lines method used by Barber and Brown [12], [13], the iterative equipotential lines method (the original one proposed was not iterative), and the method used by Wexler et al. [37], and similarly by Kohn and Vogelius [51] (referenced by YWT). Of the five methods tried, only the YWT method converged to zero error in overall resistivity, and seemed to obtain the correct result locally, in spite of the fact that they only utilized adjacent electrodes for excitation—a pattern guaranteed to produce the most difficult problems with sensitivity and ill–conditioning. Other methods either did not converge or converged with some error.

On a completely separate track, Newell, Gisser, and Isaacson and their co–workers at Rensselaer developed the multi–pole current distribution (MPCD) method based on an optimal application of electrical current: $\sin(k\theta)$ and $\cos(k\theta)$, $k = 1, ..., K$ where K is half the number of circumferential electrodes (Newell et al. [52], Fuks et al. [24], Isaacson and Cheney [53], Cheng et al. [54]). This distribution is optimum in effect because at any instant all electrodes are simultaneously excited and the total input current is the sum of individual electrode–pair currents thereby increasing the sensitivity and decreasing the effects of noise in the system. Results on two–dimensional electrode arrays without iteration (Newton's One Step Error Reconstructor, NOSER, method [22]) are quite fuzzy, but are the equal of others described in the literature.

Isaacson and Newell and their Rensselaer co–workers (Isaacson [55], Gisser, Isaacson and Newell [56], and Isaacson and Cheney [53]) described a method to estimate the conditions necessary to distinguish a homogeneous cylindrical body of one size, centered in a cylinder of a larger size with the region between the two also of homogeneous electrical field structure. This was followed by Fuks et al. [24], who also provided methods of estimating the degree of accuracy to be obtained with digital conversion of data. In general, they found that increasing the number of electrodes can improve the image only up to a point after which better imaging comes only by improving accuracy of measurement. Hua [25] and Woo [30] followed the distinguishability theory developed by Isaacson [55] by investigating direct calculation of optimal excitation patterns from singular value–decomposition (SVD) of the phantom resistance matrices. They concluded that Fourier and Walsh excitation bases are superior to the neighboring and diagonal bases when used to accurately calculate phantom resistance matrices.

Most recently, Jones, Lin, and their co–workers [46] created an algorithm within the finite element, Newton–Raphson method which they termed the "block decomposition method" (BDM). This algorithm applied locally analytic solutions as the shape functions inside the element which allowed significantly decreased number of elements in a finite element structure. In addition, they applied a method termed the "preconditioned voltage conversion" (PVC) to minimize the effects of noise and errors caused by both measurement errors and physical modelling.

The accuracy and the detail obtained in the process of impedance tomography is dependent on test construction, experimental measurements and accuracy of computational methods including both analytical and numerical models. Experimentally, the number of boundary electrodes, the accuracy of the measurements, and the speed at which a transient field is imaged are controlling factors. However, the experiment must also be constructed

accurately so that a closely controlled geometry is used in the experiment and duplicated in the numerical model. Analytically, the modeling of features such as electrodes is important. Numerically, the choice of algorithms such as finite element, finite difference, back projection method or others plays in important role, but more importantly, the limitations in any given model due to limitations in computational systems of memory and speed are also important. While it has been found that the finite element method appears to hold excellent promise in comparison with other methods, computational times and memory limitations, increasing as the 3.3 power of the number of elements, have heretofore placed insurmountable constraints on the development of this method. This report describes an approach for surmounting these difficulties.

The research for improvement in electrical impedance imaging has been undertaken in computer program (numerical) and data acquisition (experimental) development. The numerical effort, which is partly the area of concentration in this study, concentrates on accurate mathematical modelling of the imaging domain with appropriate boundary conditions and geometries, numerical stability aspects in inverse solution step, and increasing image resolution with appropriate modelling of elemental conductivities. The experimental effort is aimed at increasing the measurement accuracy in data acquisition of excitation currents and their response as electrode voltages.

2.3 Overview

Chapter 1 and Chapter 2 (this chapter) are prepared to provide an introduction of the topics studied in this report. Chapter 1 informs the reader about the mathematical description and classification of inverse problems, and their ill–posedness. Chapter 2 discusses on the previous work undertaken in the field of electrical impedance imaging by other individuals and research groups.

Chapter 3 provides a review of general imaging methods used in various fields of science and engineering. Brief discussion on each of the imaging methods are provided in terms of their basic principles, capabilities such as resolution, cost and their practical use for designing a flow monitoring system.

Chapter 4 gives an overview of presently available reconstruction algorithms for electrical impedance imaging methods (the backprojection method, the perturbation method, the double constraint method, the compensation theorem method, Yorkey's Newton–Raphson method, the NOSER method, and capacitive imaging methods). In the remaining sections of this chapter, the further analytical development and implementation of Yorkey's method wherein two–dimensional quadrilateral elements (with constant conductivity variation) are used. Numerical simulation results including converged test results on various conductivity patterns are presented. The convergence characteristics of Yorkey's standard method are also tested on data artificially contaminated with additive Gaussian noise.

Chapter 5 deals with the extension of Yorkey's standard Newton–Raphson method to a high–resolution, three–dimensional reconstruction algorithm. A new finite element scheme assuming exponentially bilinear or biquadratic spatial conductivity models in each element are developed for two–dimensional rectangular elements and three–dimensional brick–elements used for the layer–model representation of three–dimensional phantoms. Reduction of multiple layers into a single planar impedance network (the layer reduction method, LRM), and its implementation in the Hessian matrix calculations are also presented. A method called "preconditioned voltage conversion" (PVC) is introduced. This method reduces the effects of errors caused by experimental measurements and numerical modeling. Finally, all the new methods are implemented and incorporated in the block decomposition method (BDM).

Chapter 6 is devoted to the experimental set–up and measurements for electrical impedance imaging. The basic principles and design details of the data acquisition hardware used in the experiments are explained. Design of two– and three–dimensional experimental phantoms and their electrodes, and numerical sensitivity analysis of the phantoms to compare rod electrodes with plate electrodes are presented. After reviewing general excitation methods, Walsh–voltage excitation patterns are introduced and their advantages are discussed. The theory of optimal excitation patterns to improve distinguishability is presented. Methodologies for elimination of statistical noise in measurements are also introduced and discussed in this chapter.

Chapter 7 provides a set of computational results obtained from three groups of experiments, each group including a sequence of carefully selected experiments. The first group of experiments are undertaken to verify, compare, and evaluate the performances of the overall numerical methods (described in Chapter 5), and design and measurement methods developed for the high–accuracy data acquisition system (described in Chapter 6). The best capabilities determined by comparing the results from the first group of experiments are utilized later in the second and the third group of experiments. The second group of experiments are undertaken to determine the resolution limits of the imaging system. Using the methods introduced in Chapter 6 for analyzing the eigenvalues of the system, the system's ability to distinguish the minimum size of a center cylindrical target, and the minimum separation distance between two cylindrical targets centered a two–dimensional phantom are determined. The third group of experiments are undertaken to demonstrate that the system is capable of imaging both single and multiple insulating targets with changing size, geometry and location in both two– and three–dimensional phantoms. In addition, a new algorithm called the "best contour" algorithm is introduced. This algorithm is capable of determining the best–matching contour level describing the actual boundaries of

each target from the computed conductivity distribution given in a 128 × 128–pixel image.

Finally, Chapter 8 provides a general discussion on the overall results presented in this study. Based on the results obtained using best capabilities, a future work is however still needed to be done for the development of a real–time, liquid–gas flow imaging system. Several recommendations are outlined for the future research in this field.

CHAPTER 3

OVERVIEW OF GENERAL IMAGING TECHNIQUES

3.1 Introduction

In this chapter, an overview of conventional tomography techniques in terms of their basic principles is presented. At the end of this section, a comparison of these techniques is provided.

The techniques currently available to construct images within a body are:

1. X–ray computerized tomography (CT);
2. nuclear magnetic resonance (NMR) tomography;
3. ultrasonic imaging;
4. neutron tomography;
5. radiation scattering tomography;
6. electric impedance tomography (EIT).

Although these techniques require different type of equipment, different data–collection strategies, and different data–processing (reconstruction) algorithms, they have a common objective, and all produce the same result, they have widely differing functional characteristics (i.e., cost, speed, resolution, portability and safety).

3.2 X–ray Computerized Tomography

X–ray CT scanners were developed to construct high resolution transverse plane images based on attenuation characteristics (or absorptivity) of the plane [57]. The reconstruction of an X–ray CT image is a relatively straight forward process because an X–ray beam passes through an object without a significant divergence or deviation. The image basically displays the spatial distribution of X–ray absorptivity in the region of interest. The X–ray source–detector pair turns around the body and take projections at M distinct locations. The measurement obtained by the detector, which is placed in the opposite side of the source, is expressed in the the form of a line integral $\int f(r,\phi)\ dz$, where dz is the incremental distance from source to detector and $f(r,\phi)$ is an unknown function of spatial X–ray absorptivity of the medium. The image is reconstructed by solving the following problem: *given* the estimates of integrals of an unknown functions of two variables along a number of lines of known locations, *estimate* the values of the function at a number of points of given locations.

3.3 Nuclear Magnetic Resonance Tomography

The principle of Nuclear Magnetic Resonance Imaging [58], [59] is based on measuring the electric and magnetic fields using detectors placed around the body and determining the spin relaxation times of nuclei in a strong magnetic field created by magnets. The most commonly used nuclei are protons, most of which are contained in the hydrogen of water. The proton is considered as a small rotating sphere with an electric charge. A rotating or spinning electric charge creates a magnetic field around it. Therefore, each nucleus has a magnetic moment. In the absence of a magnetic field the magnetic moments of nuclei are equally distributed in all directions. In this case, the net magnetic moment is zero. In a

strong external magnetic field the situation changes: the protons align either parallel or antiparallel to the magnetic field. The summation of these magnetic moments leads to a relatively large magnetic moment parallel to the main magnetic field. Relatively weak radio–frequency pulses can change the orientation of the nuclei relative to the direction of the main magnetic field. The different magnetic moments of nuclei of different isotopes can be discriminated and various properties of this dynamic behavior measured, such as relaxation times (relaxation time is defined as the time for the nucleus to return to equilibrium state from a disturbed state). A reconstruction, therefore, is simply obtained by the inverse Fourier transform. Contrast in image depends on the differences in the proton density, longitudinal and transverse relaxation times (T_1 and T_2 respectively). Three different kinds of magnets are used to create magnetic field. These are permanent magnets, electromagnets and cryomagnets (electromagnets with superconducting coils). Resistive electromagnets can create magnetic fields up to 0.15 Tesla. However, 1.5–2.0 Tesla has been achieved by using cryogenic magnets. Data collected in very high magnetic fields help improve the quality of images [58].

3.4 Ultrasonic Imaging

Ultrasonic imaging techniques derive from SONAR technology [60], [61]. They are widely used in biomedical applications when X–rays may be potentially or critically harmful to a patient. By these techniques, the material properties are assessed by measuring reflection and scattering times of ultra sonic waves, which are a function of the material density and other mechanical properties. An ultrasonic wave is deviated by refraction and diffraction in travelling across interfaces of different materials, so that the attenuation profiles may not be the true representation of line–of–sight tissue elements. Therefore, ultrasonic CT images tend to be quite distorted due to the assumption that line–of–sight

propagation is maintained across the object being scanned. The ultrasonic images are a product of acoustic impedance, frequency shift, velocity and attenuation. While ultra–sound is quite safe and clean, and of reasonable in cost, in multi–phase flow systems, the significant scattering due to multiple interfaces renders the method relatively useless for anything but gross qualitative information.

3.5 Neutron Tomography

The idea of using fast and thermal neutrons in computerized tomography was introduced by Pfister et al. [62]. They presented results of several technical applications such as determination of cracks in metallic objects, detection of density and material variations, and determination of molten zones in reactor fuel elements are presented. Although successfully used in clinical applications, X–ray CT is not suitable for finding small, possibly nonmetallic, bodies near large metallic objects due to large attenuation in metals. A judicious use of all characteristic features of neutron cross sections provides much more information about the internal structure of a test object that is unique or highly complementary to the information obtainable from classic X–ray CT. Most imaging studies in radiography have been done by using thermal neutrons. Typical applications of thermal neutrons are the investigation of ceramic materials and detection of corrosion products in aluminum. Heavy atoms have smaller cross sections for scattering thermal neutrons than for attenuating X–rays. Therefore, fast neutrons are outstandingly useful for imaging light materials in the presence of large metallic objects. For the image reconstructions, the inverse Radon transformation is used. The data acquisition time for 20 neutron detectors, for an approximately 200 x 200–mm cross section, is reported to take 30 minutes.

3.6 Radiation Scattering Tomography

Radiation scattering has been considered for medical and industrial imaging applications for many years. Hussein et al. [63], [64] used Single Exposure Neutron Scattering Technique (SENT) for multiphase flow imaging. A path of single scattered ray (from the source to a detector) is identified by appropriate collimation by utilizing the unique energy–angle relationship of gamma Compton or neutron elastic scattering. The basic principle of this technique is that the radiation scattered from a monoenergetic isotropic source is measured by a detector that is capable of providing the radiation energy spectrum. This spectrum is divided into M energy groups, providing M different radiation influence. Using direct mapping technique, the density inside N fictitious cells can be estimated. In order to make the problem overdetermined, the number of energy groups is chosen greater then the number of cells. This method of analysis has been successfully applied to measuring gas volume fraction distribution in gas–liquid flows, and experimental and simulation results are illustrated in [63].

3.7 Electrical Impedance Imaging

Finally, electric impedance imaging techniques are also used noninvasively to reconstruct impedance distribution in a region. EII methods, sometimes termed Electric Impedance Computed Tomography or EICT, work by driving independent current excitation patterns into the electrodes on the boundary of the region, and measuring the electrode voltages for every independent current excitation. Unlike X–ray CT scanners, the current does not cross the electrodes in a straight line, i.e., the current distribution is a function of impedance distribution inside the region [15]. Because of this fact, the inverse Fourier transform, like that used in other techniques, cannot be used effectively to reconstruct images. While EII [11] requires relatively simple and inexpensive hardware, image reconstruction algo-

rithms must be more sophisticated compared with other imaging techniques. For better images, the voltage and current measurements must be very accurate and this makes the measurement equipment also more sophisticated. The reconstructed image is produced by computed variation in spatial resistivity/conductivity or permittivity [65]–[75] (capacitive) distribution or both [23], [76].

3.8 Cost Comparisons

Regarding the costs of various techniques, NMR is considered the most expensive technique due to its requirement of very complex and expensive equipment which has a strong influence on the quality of imaging. The cost of such a system with today's technology is in the order of $10M or more. The second most expensive one is X–ray CT which costs approximately $1M or more. X–ray and γ–ray CT methods provide a fairly good resolution and clear images when biological hazard becomes less of a concern such as for industrial applications, but their data are generally obtained at low acquisition speed because of safety considerations and source strength limitations. The cost is the major limitation for dynamic imaging applications as is the dynamic imaging rate limitations due to limited photon flux density and/or energy limitations.

The ultra–sound imaging technique is reasonably fast being capable of producing images obtained in the order of seconds or faster, the imaging rate of this technique limited to sonic velocities; however, scattering makes it difficult to obtain definitive images. Ultra–sound and electric impedance imaging techniques are 1–2 order of magnitude less expensive than X–ray CT systems. Table 3.1 gives a comparison of general tomography techniques in terms of their costs, resolutions, speeds, and performances. The terms "very

slow," "slow," and "fast" used for data acquisition speed are referred to *minutes*, *seconds*, and *milliseconds*, respectively.

Table 3.1 Comparison of Different Tomography Techniques [23], [77].

Imaging Technique	Cost ($)	Mechanism of measurement	Physical Characteristic	Resoln. (%)	Comp. Complexity	Data acquisition speed
NMR	10^7	magnetic and electric field	spin relaxation times, proton density	<0.1	<1	slow
X–ray CT	10^6	transmission of X–ray	X–ray absorptivity	<1	1 (Reference)	very slow
Gamma	10^5	nuclear particle emission	density of administered isotopes(2–D scan)	>3	>1	very slow
Ultra–Sound	10^4	reflection and scattering	acoustic impedance	1	>1	slow
EICT	10^4	currents and voltages	electrical conductivity	1	>>1	fast

CHAPTER 4

GENERAL THEORY OF ELECTRICAL IMPEDANCE TOMOGRAPHY

4.1 Introduction

This chapter is devoted to the establishment of a theoretical groundwork for the solution of the inverse conductivity problem, electrical impedance tomography (EIT). The basic principles of two–dimensional image reconstruction techniques are introduced in three parts.

In the first part, the impedance imaging concept and its possible application to two–phase flow visualization is explained at an introductory level. As a background for the progress of Chapter 5 and Chapter 6, conventionally used reconstruction algorithms and their major steps are briefly outlined with discussions on their advantages and disadvantages.

The second part deals with Yorkey's implementation of the standard Newton–Raphson algorithm, one of the reconstruction methods introduced herein. It is shown to be a potentially useful algorithm which may be adapted to development of a high–resolution, three–dimensional reconstruction method. The analytical derivation and computer implementation of Yorkey's algorithm is presented in detail. This implementation is a rudimentary step for the development of a three–dimensional imaging method to be presented later in Chapter 5. In this implementation, the forward problem is formulated by employing the finite element method using quadrilateral elements and bilinear polynomial approximations to the potential function. These constant–conductivity elements are capable of modelling two–dimensional phantoms with arbitrary target geometries.

Finally, the third part describes verification of the two–dimensional Yorkey's method implementation of image reconstruction. The stability and the reconstruction performance of the method implemented is numerically tested by adding different quantities of Gaussian noise to the computer–generated boundary data.

4.2 Concept

Impedance tomography would ideally provide non–intrusive, relatively instantaneous, piecewise, two–dimensional images of complex conductivity ($\sigma + j\omega\varepsilon$) distribution, for instance in any multiphase or multiregion industrial, geological or biological field. To this extent, the regions or phases could be distinguished by their differences in permittivity, ε, and/or conductivity, σ. A field could thus be mapped by sequential images which could then be pieced together as thin, approximately two–dimensional, slices to form the whole structure. This could be done spatially for a stationary field, or temporarily at one or more locations as a field evolves in time.

The concept of electrical impedance imaging includes a body of unknown internal electrical field properties of conductivity and/or permittivity surrounded by electrodes placed on the bounding surface (Figure 4.1) . These electrodes are electrically excited either in pairs or groups, and the response on the boundary electrodes is measured. The excitations are applied by a current/voltage source (both can give the same response). The excitations are chosen as linearly independent combinations which provide enough information to predict parameters representing the body's internal impedance distribution. To approach this problem, the imaging domain is divided into subregions in which the electrical material properties are determined. The imaging problem basically includes *forward* and *inverse* solution steps. In the forward solution, Maxwell's equations representing the behavior of the electric field are utilized to determine internal and boundary electric poten-

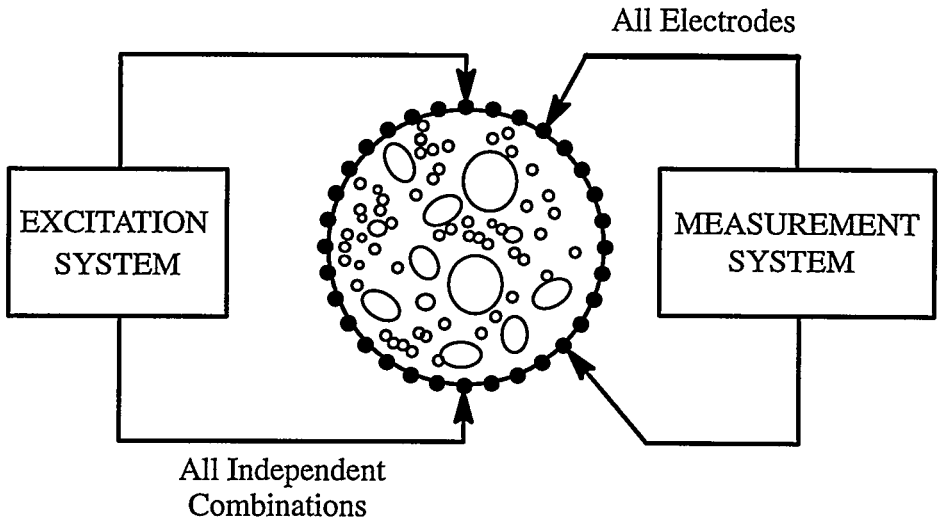

Figure 4.1 Schematic of excitation and measurement system.

tial calculations with assumed or pre–computed electrical field properties. Inverse solution calculates and applies perturbations to these assumed electrical material properties and the process is repeated until the differences between the computed and measured potentials on the boundary are minimized in the least–square sense. The impedance imaging problem is called as an *inverse problem* since it is directly *inverse* to the *forward* problem which seeks a solution to the internal electrical field with known electrical material properties and boundary conditions. For the inverse solution, there is no known method of directly computing the property distribution. Rather, the electrical material properties are determined in a way which minimizes the differences between calculated and measured electrode potentials.

4.3 Number of Measurements Required

Since finite number of electrodes are used in electrical impedance imaging systems, there is only a finite number of degrees of freedom which can be uniquely reconstructed. For an E–electrode imaging system, $(E-1)$ independent excitations can be applied and the linear relationship between current and voltage can be given by an $(E-1) \times (E-1)$ operator matrix which describe the current–voltage relationship of the phantom (Gisser et al. [78]). The operator matrix is symmetric and self–adjoint (because of the reciprocal impedance network) with $E\ (E-1)/2$ degrees of freedom (this number is the number of upper diagonal entries of the operator matrix). These upper diagonal entries of the operator matrix represent the admittances between the boundary electrodes and these elements are the nonlinear function of the conductivity distribution inside the phantom. Thus, M unknown element conductivities should be chosen as

$$M \leq \frac{E\ (E-1)}{2}. \tag{4.1}$$

to avoid the problem being under determined,

Since each degrees of freedom yields an equation with M unknown parameters, the equation system needs at least $E\ (E-1)/2$ independent measurements to obtain an approximate solution of these equations. If the the number of unknown element conductivities is chosen as the number of degrees of freedom, all element conductivities are uniquely determined.

4.4 Field Equation in Conductive and Dielectric Medium

The governing partial differential equation is derived by considering the following equation from Maxwell's set [79]:

$$\nabla \times \overline{H} = \overline{J} + \frac{\partial \overline{D}}{\partial t} \tag{4.2}$$

where $\overline{H}, \overline{J}$, and $\overline{D}$ are the magnetic field intensity, current density, and electric flux density, respectively. Multiplying both sides by the divergence operator, and using the vector identity $\nabla \cdot (\nabla \times \overline{A}) \equiv 0$ (where $\overline{A}$ is any vector), the conservation of current density is expressed by

$$\nabla \cdot \left(\overline{J} + \frac{\partial \overline{D}}{\partial t} \right) \equiv 0. \tag{4.3}$$

Using Ohm's law, the current density is obtained by

$$J = \sigma\, \overline{E}, \tag{4.4}$$

with σ the electrical conductivity. If the excitation is a sinusoidally varying in time, the electric field intensity is written in phasor notation

$$\overline{E} = E_0\, e^{-j\omega t}, \tag{4.5}$$

where E_0 is the magnitude and ω is the angular frequency. Therefore, the time derivative of the electric field displacement vector is expressed by

$$\frac{\partial \overline{D}}{\partial t} = -j\omega\varepsilon\,\overline{E}, \tag{4.6}$$

and for a conservative field the electric field intensity is written in terms of the gradient of the electric potential, ϕ,

$$\overline{E} = -\nabla\phi. \tag{4.7}$$

Finally, substituting Equation (4.7) into Equations (4.4) and (4.6) and then substituting these equations into Equation (4.3), the problem of solving the electrical properties in a domain Ω is governed by the equation:

$$\nabla \cdot (\sigma + j\omega\varepsilon\ )\nabla\phi = 0, \tag{4.8}$$

with the boundary conditions:

$$-(\sigma + j\omega\varepsilon)\frac{\partial\phi}{\partial n} = \begin{cases} \pm\,\overline{J}_E & \text{on } \partial\Omega_E \\ 0 & \text{on } \partial\Omega_H, \end{cases} \tag{4.9}$$

where the complex conductivity (also called "admittivity") is $(\sigma + j\omega\varepsilon)$, consisting of the conductivity and the permittivity. In Equation (4.9), n denotes the outward normal vector on the surface $\partial\Omega = \partial\Omega_E \cup \partial\Omega_H$, bounding the domain of interest, while $\partial\Omega_E$ and $\partial\Omega_H$ represent the surface of the electrodes and homogeneous zones of the boundary condition, respectively. Here, $\overline{J}_E$ denotes the current density vector of injected excitation.

Uniqueness of the piecewise analytic inverse solution of Equation (4.8) subject to the boundary conditions in Equation (4.9) for conductivity was established in 1985 by Kohn and Vogelius [51]. Later, Sylvester and Uhlmann demonstrated uniqueness of the in-

verse problem for a continuous conductivity distribution [80] whereas Isakov proved uniqueness for the case where the conductivity was discontinuous [81].

An electrically excited medium in Figure 4.1 consists of both *conductive* and *dielectric* properties. The dielectric permittivity in water and air regions can be assumed an isotropic constant and can be expressed as $\varepsilon = \varepsilon_r \varepsilon_o$, where ε_r is the relative permittivity and ε_o is the permittivity of vacuum ($\varepsilon_o \approx 8.86 \times 10^{-12}$ F/m). Since the relative permittivity of water, $\varepsilon_{r,water}$, is about 80 times larger than that of air ($\varepsilon_{r,air} = 1$), the capacitive admittivity of regions of air and water can be distinguished from each other. Figure 4.2 shows the capacitive reactance to conductivity ratio ($\omega\varepsilon/\sigma$) versus applied excitation frequency. This figure shows that this relatively high contrast ratio can be distinguished in applications using high excitation frequencies. Figure 4.3 shows the phase angle between the applied current and voltage response versus applied frequency. In low frequency applications, the effect of dielectric constant becomes negligible compared to high conductivity values, and thus, the phase shift between current and voltage measurements is very small when the real part of the complex conductivity dominates the imaginary part ($\omega\varepsilon \ll \sigma$).

Realizing this effect in phase shift, the dielectric property will be omitted in further analytical developments for low frequency applications in 1–10 kHz range with high background (water) conductivity values varying in the range of 0.01–0.1 S/m.

4.5 Background Theory of Reconstruction Methods

The inverse problem is nonlinear in nature. Approaches for solving this nonlinear problem can be categorized as direct and iterative methods. Direct analytical solution methods are generally obtained using simplifying assumptions that limit the scope of their use to few problems of practical interest, usually with limited accuracy. These techniques

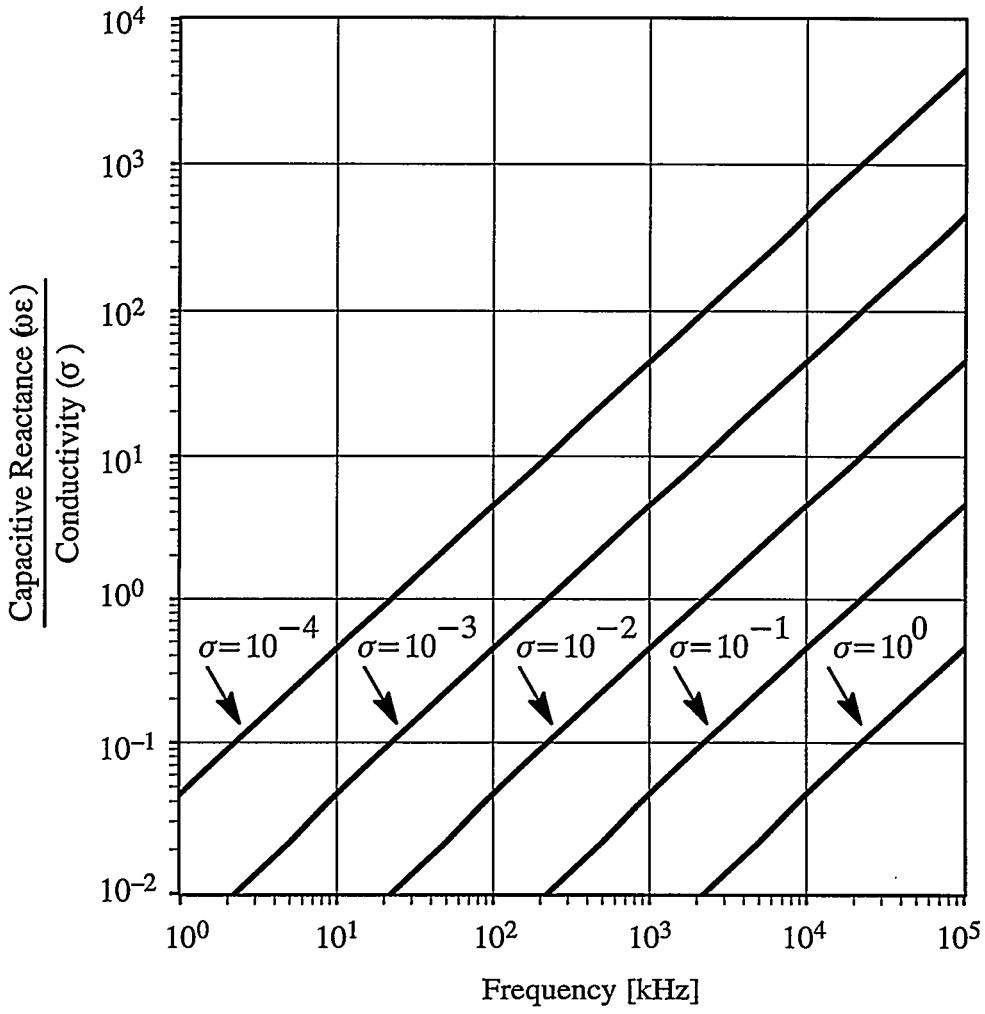

Figure 4.2 Variation of capacitive reactance to conductivity ratio versus applied excitation frequency.

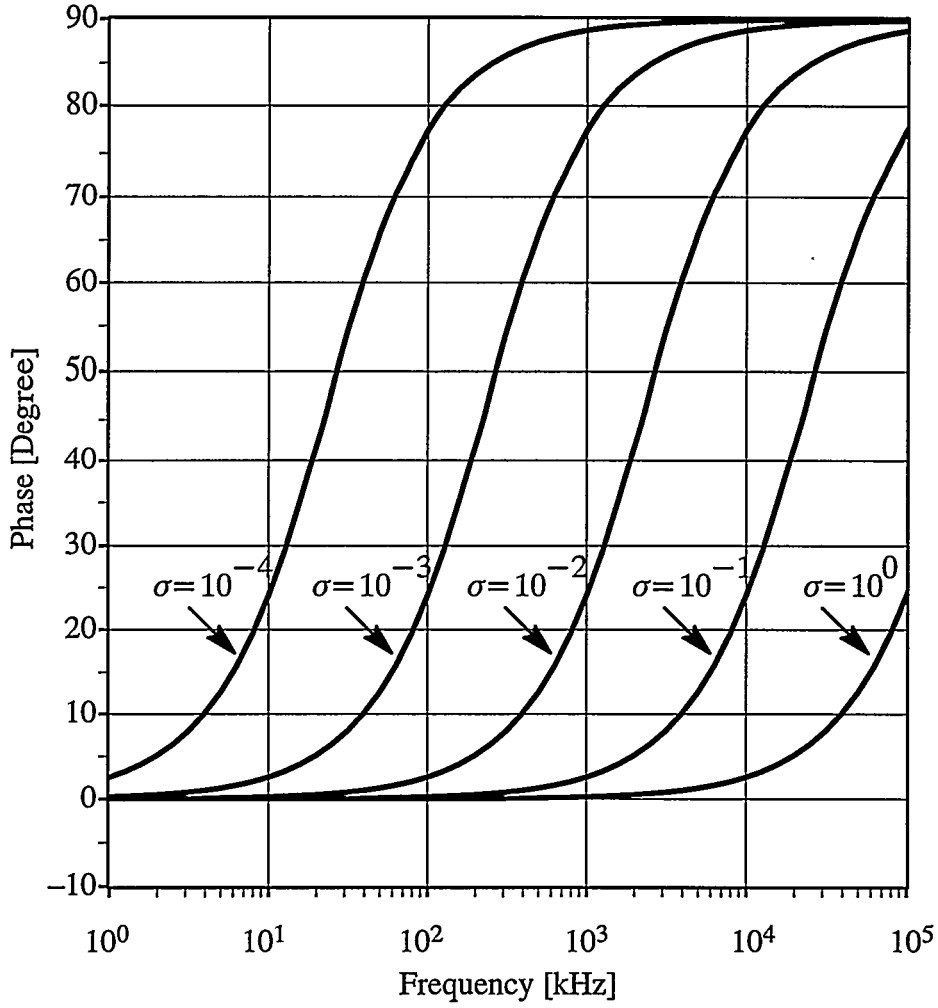

Figure 4.3 Variation of phase angle between current and voltage measurements versus applied excitation frequency.

can be considered to offer exact solutions that solve an approximation to the given problem. Iterative approaches are new and inherently approximate. Care has to be taken to be sure that the method used produces results which converge to the correct solution. However, iterative methods require relatively fewer assumptions and therefore yield good approximate solutions to the desired problem. Moreover, because of the ease of construction of iterative solutions, these approximate solutions have a wider range of application.

4.5.1 Backprojection Method

The backprojection methods developed to date are intrinsically based on the assumption that the relationship between unknown resistivity values and measured boundary potentials is approximately linear due to small changes in resistivity distribution. This also implies that the resistivity of the nonhomogeneous medium is close to the resistivity of the homogeneous medium, and the potential lines do not change significantly due to small deviations of the resistivity distribution from the resistivity of the homogeneous medium. Under this assumption, the electric potential for the homogeneous medium is obtained by using either analytical or numerical methods. Then, an algebraic set of equations to obtain an approximate resistivity distribution is constructed by comparing the potential solution on the boundary electrodes to the measurements obtained from the nonhomogeneous medium. Images obtained for each excitations (projections) are averaged to approximate actual resistivity distribution. The following outlines the basic principles of backprojection algorithms developed for electrical impedance imaging used in different applications.

The Basic Backprojection Method. This method is a direct reconstruction method originally developed by Barber and Brown [82] to be used for biomedical applications. Figure 4.4(a) shows the excitation–measurement schematic used for backprojection of the resistivity distribution of the homogeneous region (shaded area) between the potential lines

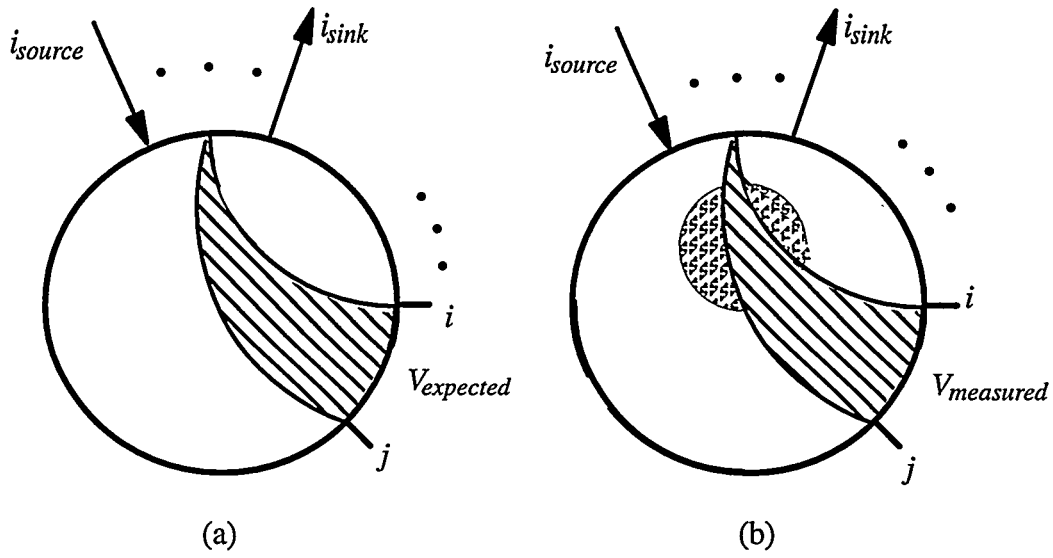

Figure 4.4 Schematic of projections for the backprojection method: (a) excitation of neighboring electrodes for a uniform resistivity field and the region between two equipotential lines; (b) an inserted object into the region between the equipotential lines (if the measured voltage is higher than the calculated voltage, multiply the resistivity in the shaded area by that factor).

V_i and V_j ending at the i–th and j–th electrodes. Let ϱ_o be the resistivity of the homogeneous medium from which the expected potential difference is obtained by solving the Laplace's equation by using either analytical or numerical methods. If a target is inserted into the homogenous region as shown in Figure 4.4(b), the resistivity of the shaded area is calculated by

$$\varrho = \varrho_o \frac{(V_i - V_j)_{measured}}{(V_i - V_j)_{expected}}. \tag{4.10}$$

The computed resistivities of the shaded regions for all projections and measurement electrode pairs are averaged to obtain the resistivity image of the nonhomogeneous medium. Then, the averaged image is filtered by a ramp filter to reduce blurring inherent in this method. Figure 4.5 shows a typical result of the basic backprojection method applied to a human arm.

Capacitive Imaging Using Basic Backprojection. Determining unknown permittivity distribution based upon capacitive measurements from a multi–electrode phantom is another alternative for multiphase flow imaging purpose. It is suitable for different permittivities such as gas–solid, gas–oil and water–oil flow mixtures. Its advantages are: noninvasive, inexpensive, simple to construct and it provides very fast capacitive measurements.

Halow et al. [65] developed a capacitive imaging system applied to a fluidized bed. The bed contains four rings of sensing electrodes mounted flush with the walls of the fluidized bed. Each ring electrodes consists of 16 individual sensing electrodes placed symmetrically on the interior circumference of the bed. The sensing electrodes are energized in pairs and resultant current is measured. Rapid switching of the energized pairs generates data related to the dielectric constants of the material along the "flux tubes." The other pairs of electrodes are then energized which provided "flux tubes" that intersect the first set of

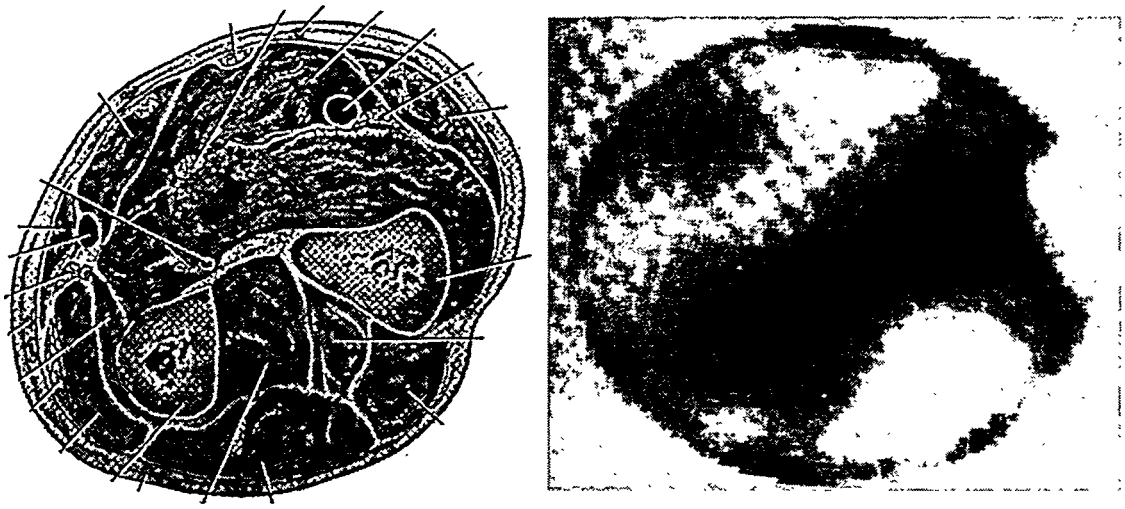

(a) (b)

Figure 4.5 **Result of the basic backprojection method applied to a human arm by Barber and Brown [82]: (a) diagrammatic cross–section of the human arm at the level of imaging; (b) resistivity distribution obtained (increasing blackness denotes increasing resistivity).**

flux tubes. The unknown dielectric constants can be calculated from the combined data sets. This procedure is repeated rapidly at each of the four levels to provide the measurements within time.

Xie et al. [69], [70], [71] proposed an 8–electrode capacitance flow imaging system which utilizes stray–immune capacitance measuring circuits developed by Huang et al. [67] (see Huang [66] for more detail). The 8 electrodes are placed in a dielectric pipe whose outside is shielded by a conductive screen to eliminate external capacitive effects. This prevents leakage effects due to external capacitive coupling in leads, for instance, and to provide insulation between the electrodes and the screen. The number of electrode pair excitations for the 8–electrode system is 28. Basically, the electrode pairs are divided into four groups: adjacent, one–electrode separation, two–electrode separation and three–electrode separation. The sensitivity areas for the elements in each group are identical.

Using a two–dimensional finite element model, the system capacitance and the sensitivity distribution of all possible excited electrode pairs are calculated. The relationship between measured data and unknown permittivity distribution is nonlinear, and the problem should be linearized. Then, a linear backprojection algorithm is used to find a grey level representation of permittivity change on the cross section of the pipe. Assuming a constant sensitivity level in each sensitivity region corresponding to electrode pairs, and summing up all 28 grey areas on the cross section of the pipe, grey levels in the areas where the objects with higher permittivity are enhanced. Xie et al. [70] proposed using a threshold filter incorporated into a linear backprojection algorithm to improve capacitive imaging results.

Figure 4.6 shows capacitive imaging results obtained by Huang et al. [67]. Figure 4.6(a) shows the 8–electrode capacitive phantom of a 76–mm–diameter Perspex pipe

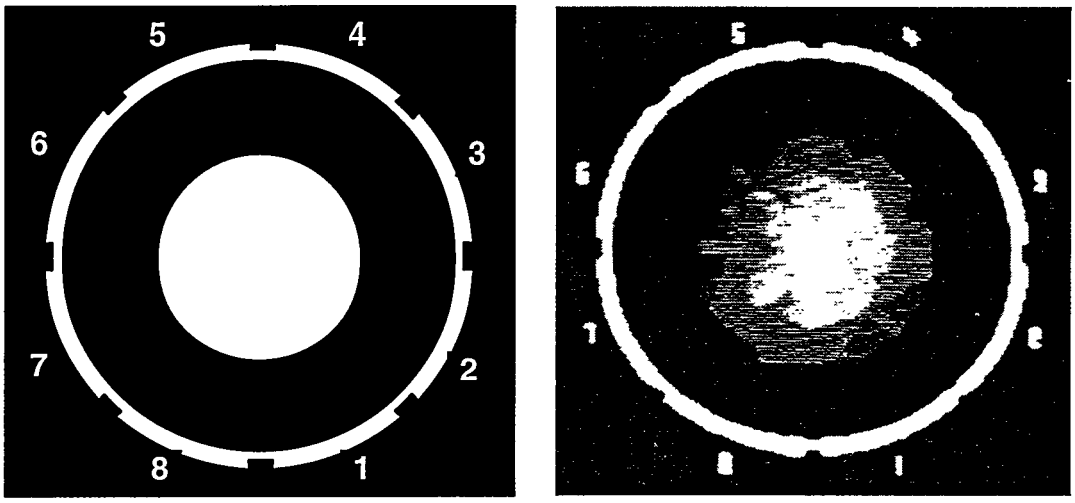

(a) (b)

Figure 4.6 **Result of the basic backprojection method adapted for capacitive imaging problems by Huang et al. [67]: (a) capacitive phantom containing 8 brass electrodes arranged around a 76–mm–diameter (5–mm wall thickness) Perspex pipe, and an empty cylindrical tube having half the diameter of that pipe centered in the phantom (the gap between the tube and the pipe is filled with sand); (b) computed relative permittivity image enhanced by a simple threshold filter.**

(5–mm wall thickness) and empty tube having half the diameter of the pipe inserted into the phantom (the gap between the pipe and the tube is filled with sand). Figure 4.6(b) shows the image of the empty tube backprojected and enhanced by a threshold filter.

Using an 8–electrode system gives low–resolution images. However, in industrial applications, an 8–electrode imaging system is found to be adequate to identify different flow regimes, such as bubbly, slug, stratified or annular flow regimes. To obtain higher resolutions more electrodes should be used to produce more independent measurements. On the other hand, using more electrodes decreases the size of the electrodes, decreasing the measurement sensitivity (see [35], [66], [67]).

The developers of the capacitance imaging system have also applied this method to several industrial process applications (Dickin et al. [73], [74], [75]) including measurement of component concentration profiles, phase boundaries, component velocities and component flow rates. Shi et al. [72] applied the same imaging system to measurement of multiple interfaces.

The Fast Filtered Backprojection Method. Barber and Brown [83], and Barber and Seagar [84] developed a fast backprojection algorithm based on the principles widely used in X–ray tomography. This method uses the same linearity assumption as stated in the basic backprojection method but pixel resistivities are backprojected along equipotential lines.

Linearization of the problem is based on the fact that if the resistivity of the nonhomogeneous medium is deviated from ϱ_o to $\varrho_o + \Delta\varrho$, the potential measurements between the adjacent electrodes deviate from V_o to $V_o + \Delta V$. Since deviations are small compared to the reference quantities, i.e. $\Delta\varrho \ll \varrho_o$ and $\Delta V \ll V_o$, the relation between the resistivity and the voltage measurements for the linearized problem can be expressed by

$$\frac{\Delta\varrho}{\varrho_o} \approx -\frac{\Delta V}{V_o}, \tag{4.11}$$

where $\Delta V/V_o$ and $\Delta\varrho/\varrho_o$ are the relative deviation in differential voltage measurements between the adjacent electrodes and the relative change in the resistivity distribution, respectively.

The potential function for the circular, isotropic, homogeneous resistivity distribution is obtained by analytical solution of Laplace's equation for applied boundary current injections. If the excited electrodes are sufficiently close to each other, the analytical solution to the electric potential can be obtained by using the "dipole approach." In this case, an approximate solution to the electric potential can be analytically obtained by using the conformal mapping technique transforming the circular region (due to the excitation of adjacent electrodes, or drive dipole) to a semi–infinite region. Figure 4.7(a) shows the equipotential line staring from a drive dipole–D, passing through the pixel–P, and ending at the boundary point–Q. The resistivity of each pixel corresponding to the j–th drive dipole excitation is backprojected along the potential line by

$$\boldsymbol{B}_j = \boldsymbol{W}_j \, \boldsymbol{g}_j \tag{4.12}$$

where $\boldsymbol{B}$ is the backprojection operator including the backprojected pixel resistivities for the j–th drive dipole, and $\boldsymbol{g}$ includes the relative change in boundary potentials between the adjacent electrodes. $\boldsymbol{W}$ includes the pixel weights whose p–th row corresponds to the p–th pixel and the j–th projection is calculated as $w_{pj} = [0\ 0 \cdots w_{pj} \cdots 0\ 0]$. The p–th weight w_{pj} is calculated as described below.

For backprojection in the circularly symmetric geometries, the potential lines are not symmetric for each pixel except for the central one. Therefore, contribution of each pixel along the potential line is not necessarily uniform. Failure to achieve uniformity of

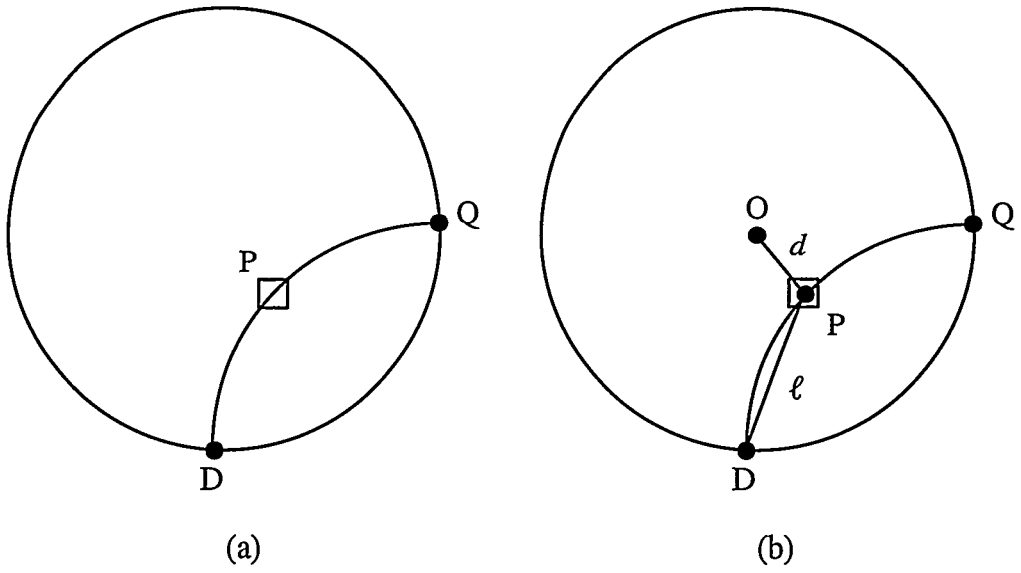

Figure 4.7 **The backprojection method applied to a circularly symmetric medium: (a) excited dipole Q and pixel element P lying on the equipotential line ending at the boundary point Q; (b) schematic to determine weights of pixels based on its distance to the excited electrode–pair and to the center O of the circular medium.**

each pixel results in unacceptable reconstruction artifacts. Therefore, the uniformity of each pixel is achieved by a proper weighting suggested by Barber and Brown [83], and Seagar et al. [85]:

$$w_{pj} = \frac{1 - d^2}{\ell^2}, \tag{4.13}$$

where d is the distance of the pixel to the center O and ℓ is the distance of this pixel to the drive dipole D as shown in Figure 4.7(b).

If E is the number of electrodes used in the measurements, it is possible to chose E adjacent electrode pairs for projections. Then, the backprojections computed for each drive pair are added together and averaged to form the final relative resistivity image

$$\boldsymbol{B} = \frac{1}{E} \sum_{j=1,}^{E} \boldsymbol{B}_j. \tag{4.14}$$

Seagar et al. [85] pointed out that image resolution is dependent on the position of an object in the circular medium. In order to minimize the artifacts of position dependence, they implemented an empirical restoration filter. They first applied a nonlinear radial transformation to the image to make the filtration problem position independent. Then, they applied the inverse radial transform to the result. The nonlinear radial transform and its inverse are

$$s = \tanh(r) \tag{4.15a}$$

$$r = 0.5 \cdot \ln\left(\frac{1 + s}{1 - s}\right), \tag{4.15b}$$

where r is the radial distance in the original image and s is the radial distance in the transformed space.

Since the problem is linearized, the filtering and backprojection operations are combined into a single algorithm called the "fast filtered backprojection:"

$$\tilde{\boldsymbol{B}} = \boldsymbol{F}\,\boldsymbol{B}, \tag{4.16}$$

where $\boldsymbol{F}$ denotes the filtering operation describes in Equation (4.15a). Details in implementing this algorithm are described by Eyuboglu [86], and by Santosa and Vogelius [87].

Barber and Seagar [84] compared the result of unfiltered backprojection to that of the filtered backprojection. The two images in Figure 4.8(a) show the effects of the filtering for a point object placed at the center of a circular phantom. The left image in this figure shows the reconstructions without using a radial filter. The right image is obtained using the same data but using the radial filter given in Equations (4.15a) and (4.15b). Figure 4.8(b) shows the results obtained in a similar way but this time the point target is placed 0.67 of unit radius from the center. The results in Figure 4.8 indicate that filtered backprojection remarkably reduces the blurring for the center target while it causes some filtering artifacts for the off–center target.

Sensitivity Coefficient Matrix in Backprojection. Breckon and Pidcock [88] pointed out that backprojection between equipotential lines uses only the diagonal elements of the sensitivity matrix. The image quality can be further improved if the other elements of the sensitivity matrix is utilized. Based on their suggestions, Kotre [89] modified the backprojection algorithm, and called it the sensitivity coefficient method using all the sensitivity coefficients as weights. Figure 4.9 shows the excitation–measurement schematic to obtain data for this method.

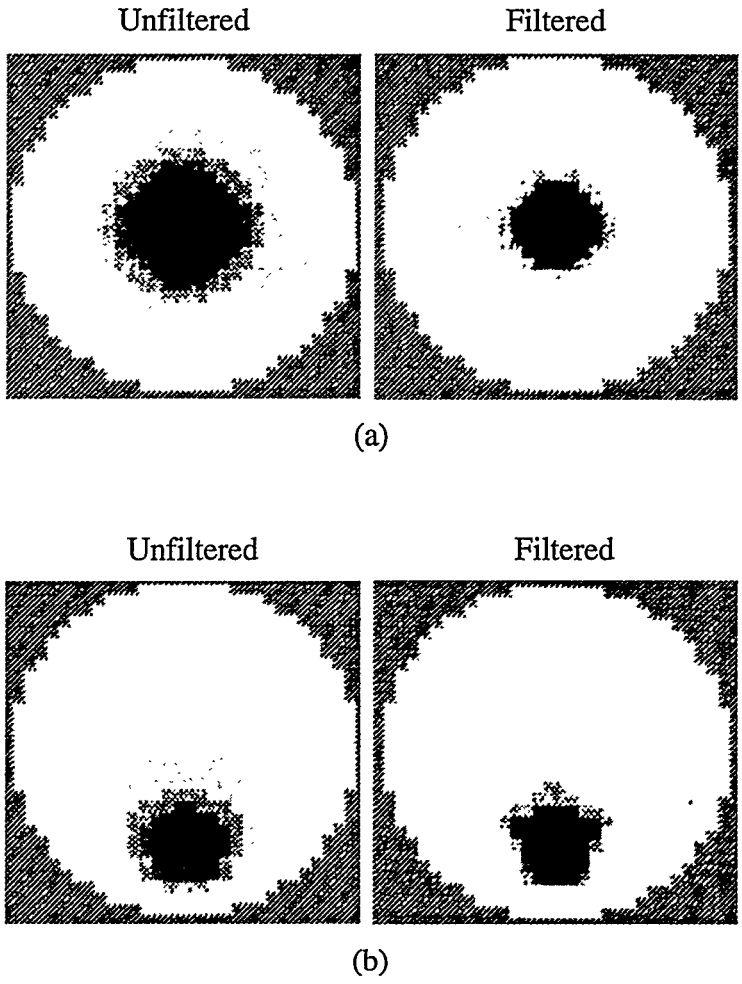

Figure 4.8 **Results showing the effects of the radial filter in the backprojection method (Barber and Seagar [84]): (a) resistivity distribution of a point object placed at the center of the circular phantom; (b) resistivity distribution of a point object is placed at the 0.67 of unit radius.**

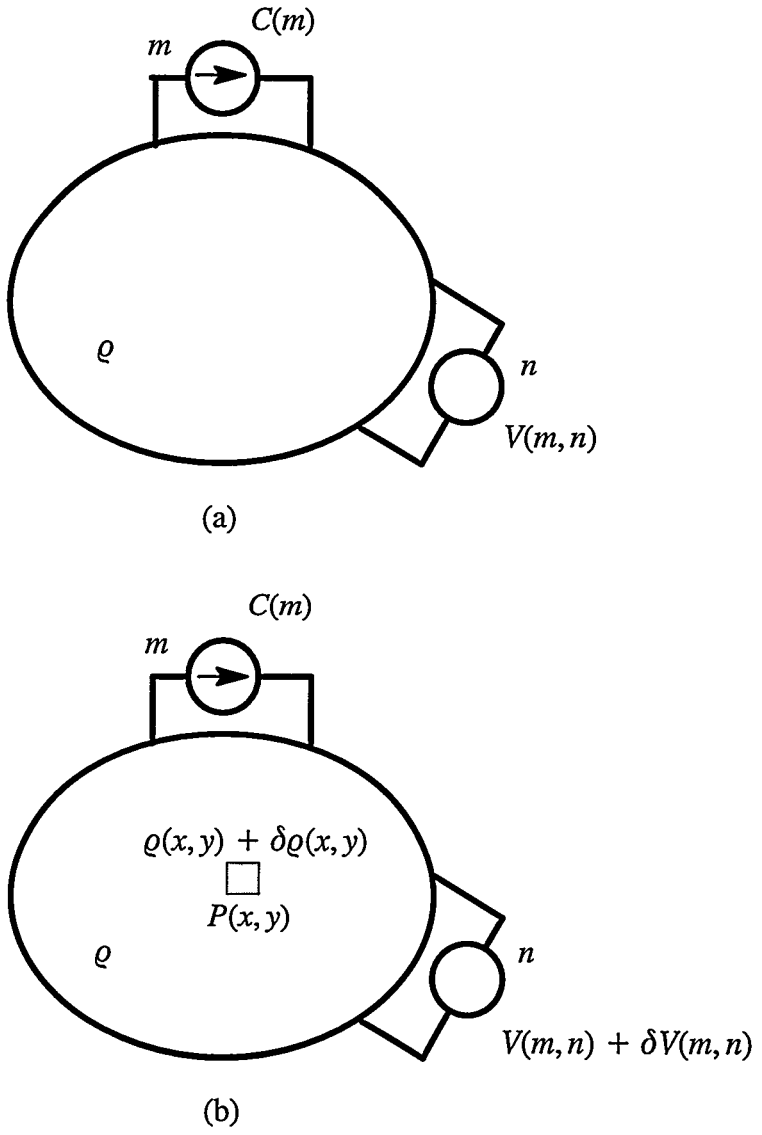

Figure 4.9 **Schematic diagram using adjacent electrode pairs for the sensitivity coefficient method (Kotre [89]): (a) measurements from homogeneous resistivity distribution; (b) measurements from perturbed pixel resistivity.**

If the resistivity of the pixel element located at (x, y) is increased by $\delta\varrho$, the element of the sensitivity coefficient matrix related to the excitation–m and measurement–n is calculated by

$$S_{m,n,x,y} = \frac{\delta V(m,n)}{\delta\varrho(x,y)} = \int\int_{S(\Omega_p)} \nabla\phi_m \cdot \nabla\phi_n \; dS, \tag{4.17}$$

where $S(\Omega_p)$ denotes the area of the pixel element–P, and $\nabla\phi_m$ and $\nabla\phi_n$ denote the gradient of the electric potential when the electrode pairs m and n are excited by the unit current sources $C(m)$ and $C(n)$, respectively. Using the sensitivity matrix coefficients, Kotre calculated the pixel densities by

$$P(x,y) = \sum_{m=1}^{M}\sum_{n=1}^{N} S_{m,n,x,y} \; \ln\left(\frac{V'(m,n)}{V(m,n)}\right), \tag{4.18}$$

where M is the number of excitations, N is the number of differential measurements for each excited pair, and $V'(m,n) = V(m,n) + \delta V(m,n)$ denotes the differential potential measured on the phantom boundary for the target case.

Figure 4.10 shows a typical result obtained the sensitivity coefficient method by Kotre [89]. Figure 4.10(a) shows the original image of a Perspex/aluminium rod target placed in a circular phantom. The boundary voltage profile measurements are obtained from 16 electrodes by a high–input–impedance averaging voltmeter. A constant 1 mA current at 20 kHz is injected to the adjacent electrodes for each excitation. Figure 4.10(b) shows the image obtained by reconstructions using Equations (4.17) and (4.18).

Iterative Equipotential Lines Method. Since the original equipotential lines are no longer valid after the correction of resistivities, the sensitivity matrix is not valid for a second iteration. Yorkey et al. [19] and Ider et al. [90] implemented an iterative backprojec-

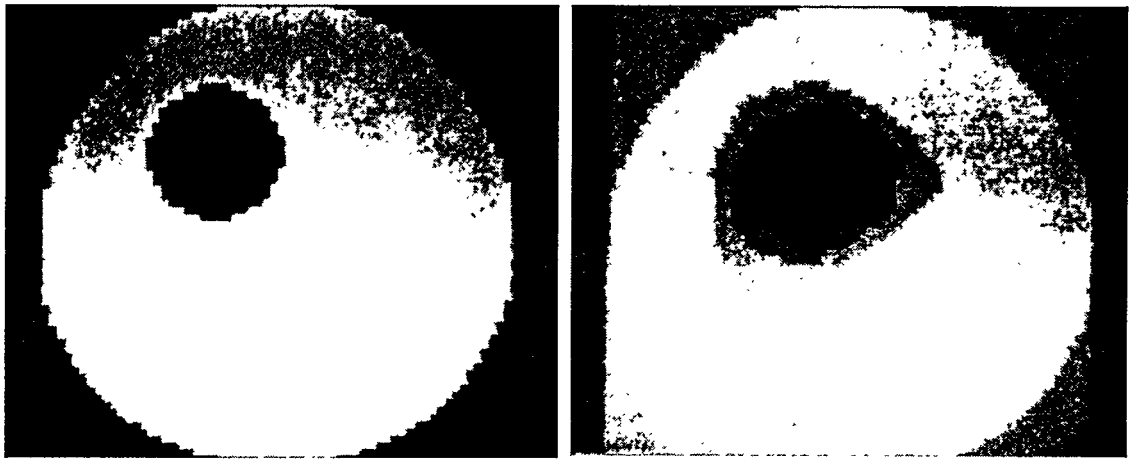

(a) (b)

Figure 4.10 Result of the sensitivity coefficient method (Kotre [89]): (a) original image of a Perspex/aluminium rod target inserted in a cylindrical phantom; (b) obtained image.

tion method, iteratively calculating new equipotential lines after each backprojection. They reported that the iterative equipotential lines method showed better performance (i.e., less error and better picture quality over noniterative equipotential lines methods).

Figure 4.11 shows how images can be iteratively improved after the conductivity distribution is updated after the first step (Ider et al. [90]). Figure 4.11(a) shows a 90–mm–diameter, 0.6 S/m agar object placed at the center of a 16–electrode, 260–mm–diameter phantom filled with 0.2 S/m saline. The equipotential lines are calculated by the finite element solver and used in backprojection repetitively. Figure 4.11 (b and c) shows the computed conductivity images after the 1st and the 10th iterations, respectively. The result obtained in further iterations improve significantly.

To date, while the methods of backprojection are only approximate and their results are not considered unique, the rapidity of computations combined with the reasonableness of the results for the intended purposes has made this the method of choice in the biomedical area. However, for the purposes of definitely determining the boundaries of three–dimensional nonhomogeneous conductivity fields this method appears to hold little promise.

4.5.2 Perturbation Method

The perturbation method is based on measurement of relative changes of electrode currents caused by an inserted object into the resistivity field for applied excitation voltages on the electrodes. The perturbation matrix is calculated by solving the electrical potential field for perturbed element resistivities, and thus the changes in current values are backprojected by using the perturbation matrix to estimate the resistivity distribution.

Kim et al. [40] proposed a two–electrode perturbation method which used 8 projection angles for two different projection methods, called "parallel–beam–like projection"

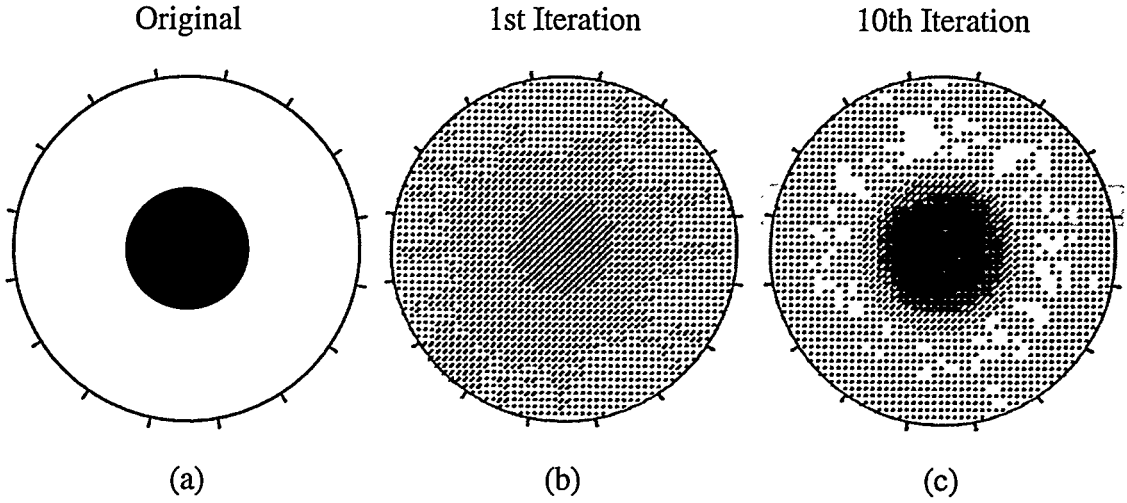

Figure 4.11 Improved results obtained by using iterative equipotential lines method developed for backprojection along the equipotential lines by Ider et al. [90]: (a) original image of a 90–mm–diameter circular 0.6 S/m agar object centered in a 16–electrode, two–dimensional 260–mm–diameter circular phantom filled with 0.2 S/m saline; computed results obtained after (b) the 1st; and (c) the 10th iteration.

and "fan–beam–like projection." Their measurement design is described by the schematic diagram in Figure 4.12. Each projection uses two type of electrodes which are called the "voltage–supplying electrode" and the "current–sensing electrode."

In parallel–beam–like projection, the voltage–supplying electrode consists of 11 nodes at one level of a three–dimensional body. The current–sensing electrode covers 22 elements on the opposite side. In fan–beam–like projection, the voltage–supplying electrode consists of one node and the current–sensing electrode covers 22 elements.

They pointed out that the sequence of the projection angles played an important role when determining the necessary number of iterations. For both methods, they made each current projections 45 degrees apart. For example, if the first projection current is chosen in a main position from top to bottom, then projection angles 2, 3 and 4 are rotated 90, 180 and 270 respectively. The projection angle 5 is located in the midway between 1–2 by rotating 45 degrees from 1. Accordingly 6, 7, and 8 are rotated by 135, 225 and 315 degrees, respectively. They used a three–dimensional cylindrical model with multiple layers. Each layer in their computational grid contained 332 hexahedral elements with the total number of 361 nodes. The data were synthetically generated by simulating the objects in the model grid.

To reconstruct the impedance image, the exit currents for a homogenous resistivity distribution are calculated for a particular projection angle. The resistivity values of each element are changed (for example, by a factor of 10), and then the percentage change in exit currents are observed. This process forms the entry of the sensitivity matrix, $T_{ij\ell}$, for the i–th element number, j–th current–sensing electrode, and the ℓ–th projection angle, respectively. If the initial guess for the element resistivities are not correct, the differences between calculated and measured current densities are back projected by modifying each

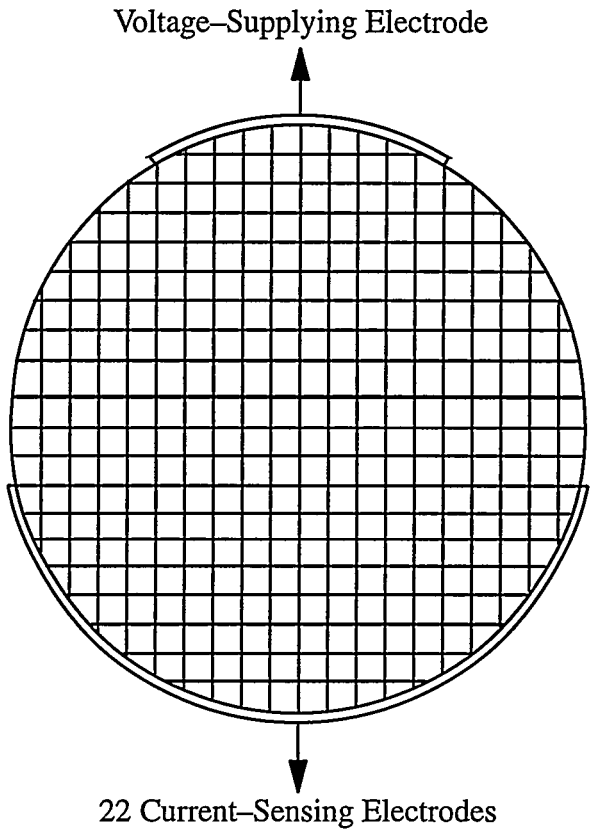

Figure 4.12 Measurement schematic used for fan–beam–like and parallel–beam–like projections by Kim et al. [40]. In parallel–beam–like projections, the voltage–supplying electrode consists 11 boundary nodes. The current sensing electrodes cover 22 boundary elements in the opposite side. In fan–beam–like projections, voltage–supplying electrode consists of only one node on the boundary.

element's resistivity according to the relationship of each element's sensitivity to each electrode:

$$\varrho_i^n = \varrho_i^{n-1} + k \cdot \frac{\sum_{j=1}^{C} RC_{j\ell}^n \; T_{ij\ell} \; \varrho_i^{n-1}}{\sum_{k=1}^{C} |T_{ik\ell}|}, \tag{4.19}$$

where k is an overrelaxation factor which sets the rate of convergence, $RC_{j\ell}^n$'s are the percentage difference between measured and calculated current densities at the j–th current–sensing electrode for the n–th iteration and ℓ–th projection angle, and C is the number of current sensing electrodes.

Figure 4.13 shows the reconstructed images using the perturbation method obtained by Kim et al. [40]. Figure 4.13(a) and (b) are obtained by using the parallel–beam–like and the fan–beam–like projection methods, respectively. With both projection methods, the rectangular image in the upper–center region of the phantom can be shown easily.

Kim et al. [40] calculated the exit currents by calculating the current densities in the boundary elements and multiplying these values by electrode areas. This approach used for the electrode currents is in error when there are large electrodes nearby. Yorkey [15] and Yorkey et al. [20], however, proposed a nodal electrode model to calculate electrode currents more accurately. Yorkey decreased the size of the electrodes until they just cover the nodes, but not the whole elements. He found that this was a better predictor for the exit currents.

Yorkey [15] proposed an improved perturbation technique and compared it with the original method proposed by Kim et al. [40]. Since this backprojection scheme corrects the

Legend for the Images

80 ≤ "1" < 120 ohm–cm	340 ≤ "6" < 400 ohm–cm
120 ≤ "2" < 160 ohm–cm	400 ≤ "–" < 460 ohm–cm
160 ≤ "3" < 220 ohm–cm	460 ≤ "*" < 540 ohm–cm
220 ≤ "4" < 280 ohm–cm	540 ≤ "+" < 600 ohm–cm
280 ≤ "5" < 340 ohm–cm	600 ≤ "7" < 660 ohm–cm

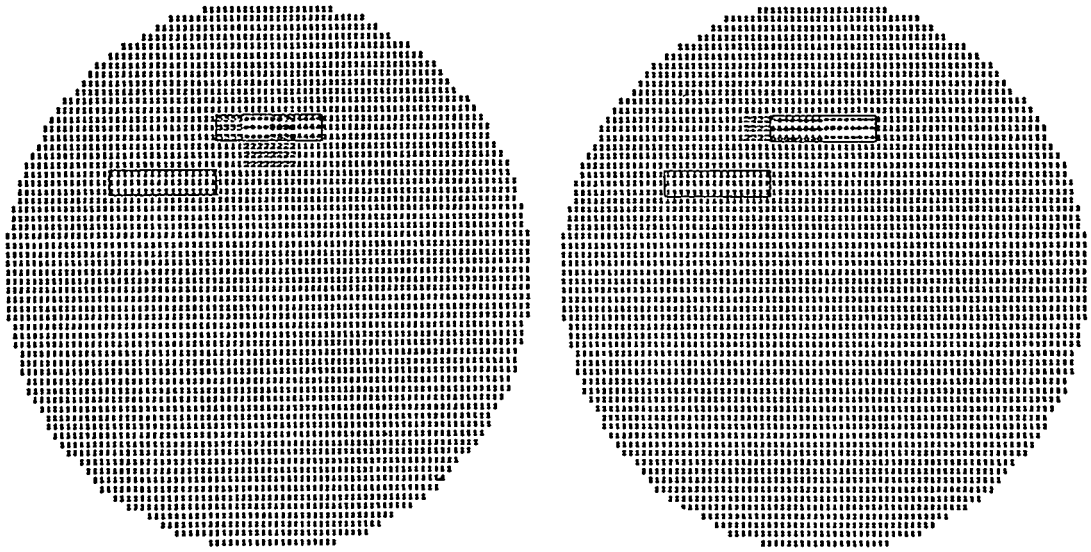

(a) (b)

Figure 4.13 Reconstructions obtained by using the perturbation method (Kim et al. [40]): (a) using the parallel–beam–like projection method; (b) using the fan–beam–like projection method. The object (rectangle upper–center region) and background resistivities are 500 ohm–cm and 100 ohm–cm, respectively.

image after each projection angle, he called this technique the "ART–like method" (ART, algebraic reconstruction technique[6]).

Yorkey improved the convergence behavior by his modified method which corrects the resistivities after the data for all P projections are acquired:

$$\varrho_i^n = \varrho_i^{n-1} + k \cdot \frac{\sum_{\ell=1}^{P} \sum_{j=1}^{C} RC_{j\ell}^n \; T_{ij\ell} \; \varrho_i^{n-1}}{\sum_{\ell=1}^{P} \sum_{k=1}^{C} |T_{ik\ell}|} \cdot \qquad (4.20)$$

Since this method is similar to the simultaneous iterative reconstruction technique[6] (SIRT), he called it the "SIRT–like method." This projection method used by Yorkey is similar to "fan–beam–like projection" proposed by Kim et al [40].

In the SIRT–like method, Yorkey used a two–dimensional square model with 64 elements and with equally spaced electrodes on the periphery of the square model. For each projection, starting from a corner, a constant voltage is applied to one electrode and the remaining electrodes are grounded. Exit currents of 15 electrodes are then measured. The voltage distribution is rotated clockwise by one electrode to obtain measurements for the other projection angles. Figure 4.14 shows the computed results of the SIRT–like method. The 375–ohm–cm rectangular object is aligned to the element boundaries of a 64–element square computer model (see Figure 4.14(a)). The resistivity image shown in Figure 4.14(b) is obtained after the 20th iteration.

---

[6] These iterative reconstruction algorithms are often utilized by X–ray and magnetic resonance scanners in medical tomography [59], [60].

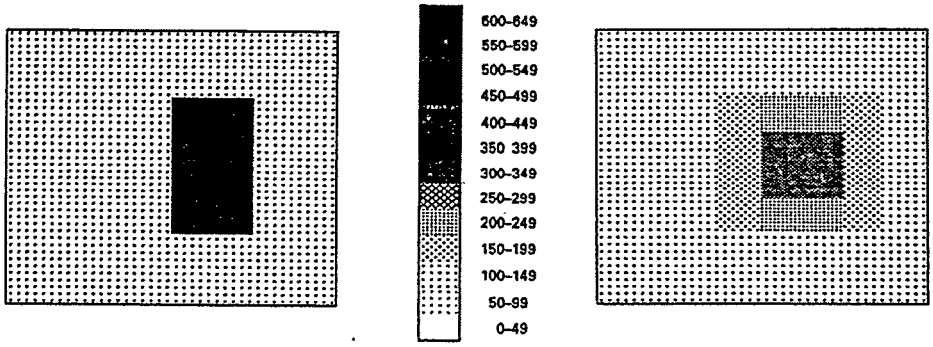

Figure 4.14 Reconstruction obtained by using the improved perturbation method (the SIRT–like method, Yorkey [15]): (a) original resistivity distribution of a 375–ohm–cm rectangular object aligned to element boundaries of a 64–element, 16–electrode square model (the background resistivity is 125 ohm–cm); (b) computed image after the 20th iteration.

Yorkey [15] reported that the results did not converge when outer layer of the square model was included in the resistivity corrections. He concluded that it might be due to the higher sensitivity in this region. However, when enough layers were constrained, the ART–like method converged. Comparing the ART–like method with the SIRT–like method, he pointed out that the SIRT–like method had less error than that of the ART–like method for the same number of corrections. He also showed that the perturbation matrix was image dependent. Once the resistivity profile is changed, the perturbation matrix does not hold causing inaccurate corrections based on an incorrect perturbation matrix. Yorkey reported that calculating the perturbation matrix after each iteration did not improve the convergence rate.

The values of entries in the perturbation matrix are functions of element size, element distance from current–sensing electrodes, and background resistivity [15], [20], [42]. Sensitivity element value increased with increasing size, decreasing distance to the current–sensing electrodes, and lowering background resistivity. Kim and Woo [91] modified the perturbation method by this observation that simplifies the sensitivity to become a linear function of the element distance from the current–sensing electrodes. Therefore, the modified method rapidly calculates the perturbation matrix, without storing the entire perturbation matrix.

4.5.3 Double Constraint Method

The double constraint method proposed by Wexler et al. [37] is based on the comparison of the finite element solutions of Poisson's equation subject to the experimentally measured boundary conditions of surface voltages (Dirichlet conditions) and surface currents (Neumann conditions). Starting with a homogenous conductivity distribution, the conductivity distribution is iteratively changed to satisfy the compatibility between the solutions for two type of boundary conditions.

The double constraint method first constraints the finite element method with the known surface current values. Then, the potential distribution, V, on the interior nodes is solved, and then the current densities in the computer model elements are calculated by $\boldsymbol{J} = \sigma\, \boldsymbol{E} = -\sigma\, \nabla\phi$. The conductivity distribution used in this step is different from the actual conductivity distribution. If the error between the calculated surface voltages and the measured surface voltages is less than a small value, the iterative procedure is stopped and the conductivity distribution is obtained. If the error is still above a certain value, the finite element solution is constrained with the observed voltages and then a new potential solution is obtained. The element current densities are calculated again for the new potential solution. The sum of the squared residual errors between the electric current densities of the first and second steps is expressed by

$$R(\sigma) = \sum_{i}^{all\ elements} \iiint_{\Omega_i} (\boldsymbol{J}_i + \sigma_i \nabla\phi_2) \cdot (\boldsymbol{J}_i + \sigma_i \nabla\phi_2)\ dV, \tag{4.21}$$

where $\boldsymbol{J}_i$ is the current density of elements calculated by the potential solution subject to the Neumann boundary conditions, and $-\sigma_i \nabla\phi_2$ is the element current density calculated from the potential solution subject to the Dirichlet boundary conditions (the second solution step).

Assuming both solutions are unique for both type of boundary conditions, the new element conductivities are calculated by minimizing the residual sum in Equation (4.21) with respect to each element's conductivity

$$\frac{\partial R}{\partial \sigma_i} = \int\int\int_{\Omega_i} (2\, \boldsymbol{J}_i \cdot \nabla\phi_2 + 2\, \sigma_i \nabla\phi_2 \cdot \nabla\phi_2)\, dV = 0 \qquad (4.22)$$

and solving for σ_i yields the expression to calculate the new element conductivity values by

$$\sigma_i = \frac{-\int\int\int_{V(\Omega_i)} \boldsymbol{J}_i \cdot \nabla\phi_2 \, dV}{\int\int\int_{V(\Omega_i)} \nabla\phi_2 \cdot \nabla\phi_2 \, dV}. \qquad (4.23)$$

After the new element conductivity values are calculated, the the procedure is continued until the error is below a certain small value.

For large number of excitations, the forward solution step may become computationally intensive. The convergence is very slow (taking thousands of iterations) in reported results of Wexler et al. [37] in Figure 4.15. Some scheme to reduce the number of iterations is needed for practical applications. Improvement of modeling field near the electrodes is necessary for image enhancement. The relaxed variational method suggested by Kohn and Vogelious [51] may improve the field near the electrodes, because the relaxed functional method on a coarse mesh is reported to be equivalent of the original method on a finer mesh.

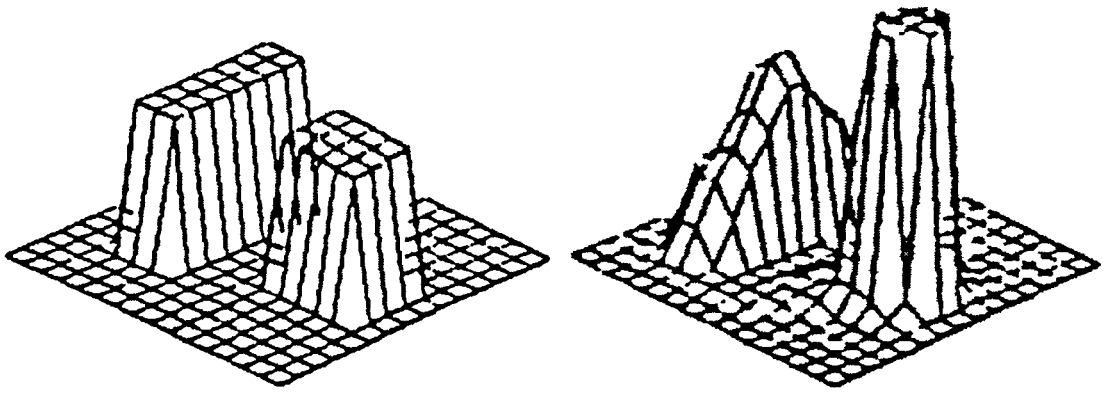

(a) (b)

Figure 4.15 Result obtained using the double constraint method (Wexler et al. [37]): (a) relief plot of the original conductivity distribution; (b) converged result obtained after 1700 iterations.

4.5.4 Newton–Raphson Method: Yorkey's Method

The Newton–Raphson method is an iterative reconstruction algorithm originally developed for solution of nonlinear problems. Yorkey [15] described a Newton–Raphson–based reconstruction algorithm minimizing the least–squares error formed by the squared differences between the the calculated and the observed electrode voltages. The least–squares error function is minimized with respect to the unknown conductivity distribution, and the resulting nonlinear equation system is iteratively solved by the Newton–Raphson method.

The Newton–Raphson method has been accepted as the most accurate reconstruction technique. This method, however, requires intensive computations in computer, with most of the computational effort required for forming the Jacobian matrix. This is the method adopted for further developments in this study as most likely to provide information regarding interfacial area density. More theoretical details will be discussed in the following sections.

4.5.5 NOSER Method

An analytical approach to the forward and inverse solution steps of the inverse conductivity problem is used in *Newton's one step error reconstructor* (NOSER) algorithm [22]. In the NOSER method, spatial distributions of trigonometric current patterns are applied to a 32–electrode axisymmetric test phantom. Such current patterns have been shown to be optimum in forming conductivity distributions in a circular phantom [56], [54]. By radial and angular subdivisions, the circular phantom area is divided into 496 equal–area elements in such a way that the elements near the boundary are smaller in radial direction, but all the elements cover the same area. Assuming a homogeneous starting guess for the

element conductivities and given the geometry and excitation current patterns, an analytical solution of the potential function can be obtained by the method of separation of variables. In the inverse solution, one step of Newton's method is used because the differentials of the voltages are analytically evaluated for the first iteration. Using the analytical expressions of the potential function, the Jacobian matrix is evaluated by integrating potential gradients over the area of the elements. After the first iteration of Newton's procedure, element conductivities are updated and the image is displayed. The NOSER method is thus seem to be a noniterative reconstruction method which uses exact solutions of the uniform field problem and exact computations of the first Taylor–series corrections in the iterative process.

Resistivity reconstructions using the NOSER method (Cheney et al. [22]) is shown in Figure 4.16. The data used in these reconstructions are analytically derived from 50 Ω cm, 20–, 40–, 80–, and 160–mm–diameter cylindrical targets placed in the center of a 300–mm–diameter, 500–Ω cm homogeneous medium. The top row in this figure shows the actual locations and sizes of the circular targets. The darker regions in the gray–scale images in the bottom row of Figure 4.16 indicates the low–resistivity regions.

The methodology of the NOSER algorithm is equivalent of the first iteration of the Newton–Raphson algorithm. Once the element conductivities are updated, the conductivity distribution is no longer homogenous. Therefore, an analytical solution cannot be obtained to perform more iteration steps. The magnitude of computed conductivities are not realistic since only one iteration of Newton's minimization procedure is applied and no analytical estimates of anticipated errors have been published. Another disadvantage is that this algorithm is very strictly dependent on the mesh geometry. This is a limitation for using moving mesh methodologies which may be desired to fit to the boundaries of model objects in the imaging domain.

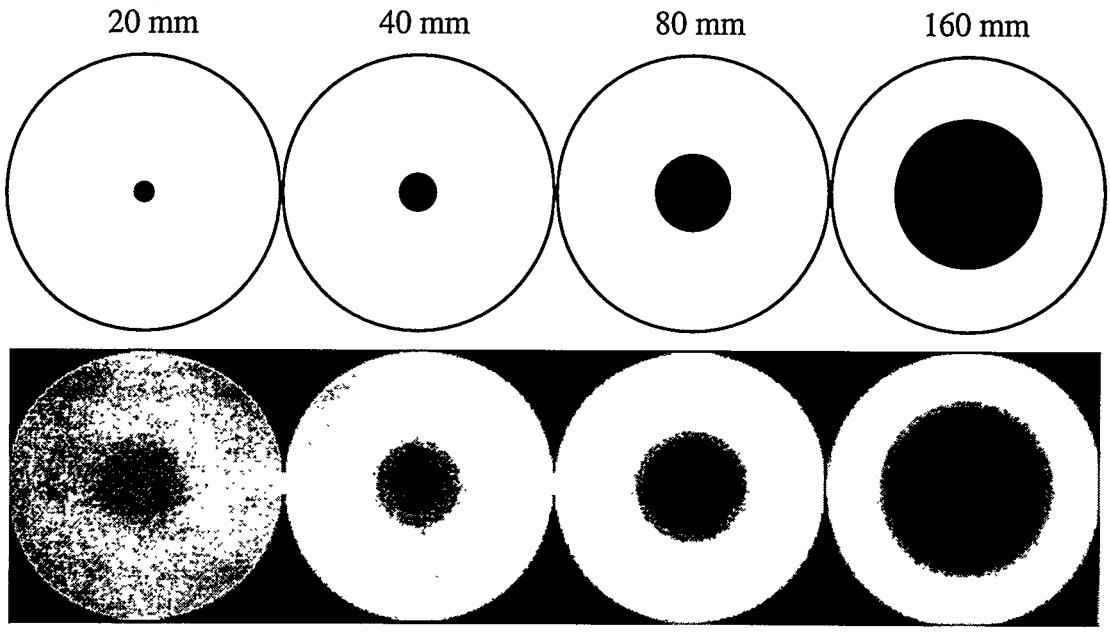

Figure 4.16 Example of the NOSER method reconstructions using analytically derived data sets from 20, 40, 80, and 160–mm–diameter targets placed in the center of a 500 Ω cm, 300–mm–diameter circular homogeneous medium (Cheney et al. [22]). The top and the bottom rows show the actual size and locations of the targets, and the reconstructed resistivity gray–scale images, respectively (black represents the low–resistivity regions).

To overcome the limitations present in the original (noniterative) version of the NOSER method, a precise numerical solution to the forward problem in further iterations can be obtained by using the finite element or the boundary element methods. The earlier study for this methodology is reported in References [92] and [93]. Following this idea, Jain et al. [94] developed an iterative version of the NOSER algorithm using the finite element and boundary element methods (with 0.05% error) to reconstruct admittivity (complex conductivity) reconstructions in noncircular mediums.

They reported that significant artifacts can occur in the obtained images due to a circular–geometry assumption for noncircular geometries (such as a human chest). These artifacts include both distortion of the computed target shapes and inaccurate conductivity and permittivity values. Both the conductivity error and shape distortion magnify as the actual phantom geometry deviates from a circle. They reported that the error in conductivity value is 20% for an axis ratio of 0.73 (for an elliptic body). This error increases further to 37% as the the axis ratio is decreased to 0.64.

More recently, Edic et al. [95] developed a complex, iterative version of the original NOSER algorithm, and they called this algorithm *complex Newton's recursive–step error reconstructor* (CNRSER). A typical result reconstructed using the algorithm is shown in Figure 4.17. The reconstructions shown in this figure are undertaken using data obtained from a finite element model of a simulated human chest geometry shown in Figure 4.17(a). The ideal conductivity distribution of the model is shown in Figure 4.17(b), where the actual conductivity values are: 150 mS/m (background), 100 mS/m (lungs L_1 and L_2), and 200 mS/m (heart, H). The reconstructed conductivity distributions are shown in Figures 4.17(c) and (d) after the first and fourth iterations, respectively.

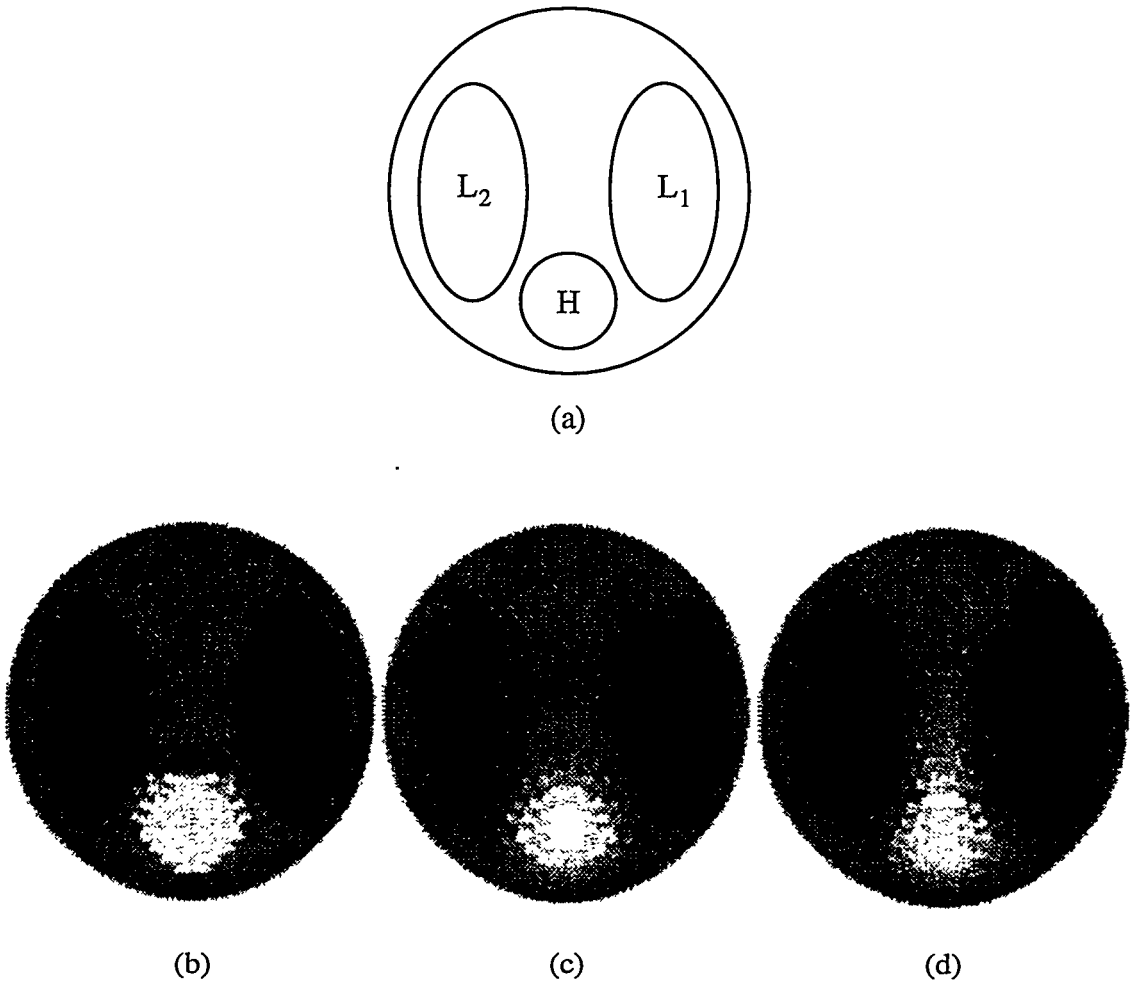

Figure 4.17 **Conductivity reconstructions using the CNRSER method (Edic et al. [95]). The data is numerically obtained from a simulated human chest model: (a) the geometry of a human chest model (L_1, L_2, and H represent the lungs and the heart respectively). The actual conductivity values are 150 mS/m (background), 100 mS/m (L_1 and L_2), and 200 mS/m (H); (b) the ideal conductivity distribution of the model; the result after the (c) first iteration; (d) fourth iteration.**

4.5.6 Compensation Theorem Method

The compensation theorem method is based on a linear network analogy of a continuum conductivity field discretized by finite elements. The elemental coefficient matrix entries are equivalent to the admittances between the nodes of the elements. Therefore, the entire imaging domain is represented by an admittance network. The sensitivity of the voltage between an electrode pair can be calculated by Geselowitz's sensitivity theorem [96].

Using Geselowitz's sensitivity theorem, Murai and Kagawa [42] showed that the change in voltage of a port in an admittance network with respect to the change in conductivity of an admittance element can be expressed by a linear relationship. Figure (4.18) illustrates such a network with three ports. If a current source is applied to port k and the admittance element connected to the port–j is changed by a small increment of Δy, the voltage change at the port–i is expressed in terms of the applied current c_k, the change in the admittance element and the transfer impedance of the ports by

$$\Delta v_i = -c_k \, \Delta y_j \, z_{ij'} \, z_{kj} \tag{4.24}$$

where $z_{ij'}$ is the transfer impedance between ports i and j', j' denoting the new port (after Δy is added to the port–j). Yorkey [15] adapted the findings of Murai and Kagawa's work to his finite element model which uses piecewise constant conductivity elements. If each element is made of L admittance elements, Equation (4.24) can be modified as

$$\Delta v_i = -c_k \sum_{\ell=1}^{L} \Delta y_{j(\ell)} \, z_{ij'(\ell)} z_{kj(\ell)} \tag{4.25}$$

where subscript ij' is a function of ℓ. The ℓ–th admittance is a product of element's conductivity σ_j and a finite element constant s_ℓ. Thus, Equation (4.25) is written as

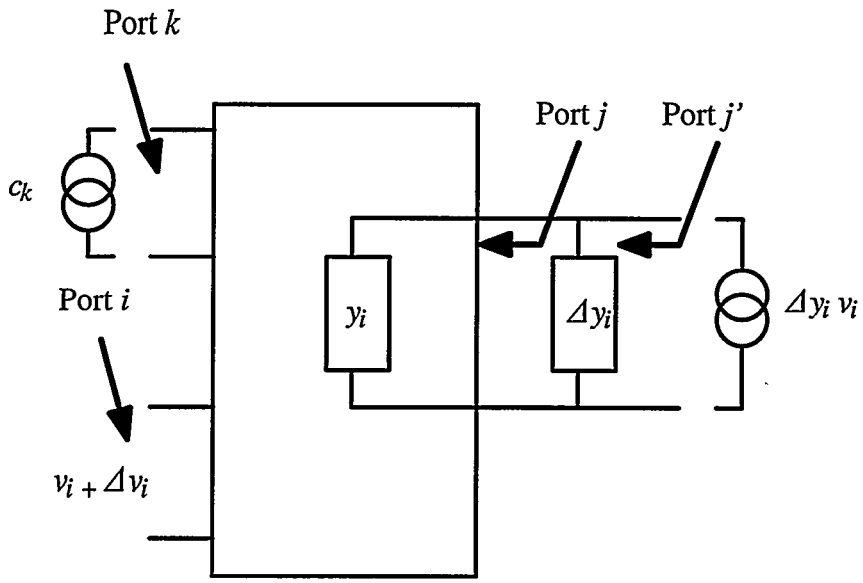

Figure 4.18 The admittance network model to explain the compensation theorem.

$$\Delta v_i = -\Delta\sigma_j \; c_k \sum_{\ell=1}^{L} s_\ell \; z_{ij(\ell)} \; z_{kj(\ell)} \tag{4.26}$$

Substituting $z_{ij'} = z_{ij}$, $\varrho_j = \sigma_j^{-1}$, $c_k = c$, and $z = vc^{-1}$ into Equation (4.26) results in

$$\frac{\partial v_i}{\partial \varrho_j} = \frac{1}{c\varrho_j^2} \sum_{\ell=1}^{L} s_\ell \; v_{ij(\ell)} \; v_{kj(\ell)}. \tag{4.27}$$

Equation (4.27) is equivalent of the (i,j)–th entry of the Jacobian matrix.

Yorkey [15] used a compensation theorem to compute the entries of the Jacobian matrix, which includes the sensitivity information in the form of derivatives of boundary potentials of electrodes with respect to element conductivity or resistivity values. He found it was computationally more efficient than the standard Jacobian matrix computation, and more accurate than Geselowitz's sensitivity theorem. Yorkey's reported numerical experiments in Figure 4.19 show that the reconstructions using the compensation theorem method gives good converged results, being close to Yorkey's method based on standard Newton–Raphson minimization.

4.6 Finite Element Formulation of the Forward Problem

There are number of methods for solving the well known forward problem of impedance imaging. Analytical solutions may be based on series expansion methods which can be further simplified by the phantom exhibiting axes of symmetry and a regular boundary profile and conformal mapping. For complex geometry and boundary conditions, however, the numerical methods such as the finite difference method (FDM) or the finite element method (FEM) may be utilized to obtain an approximate solution to the field potential for the forward solution. In this study, the finite element method is chosen for this purpose because of its potential to accurately model arbitrary geometries, applied

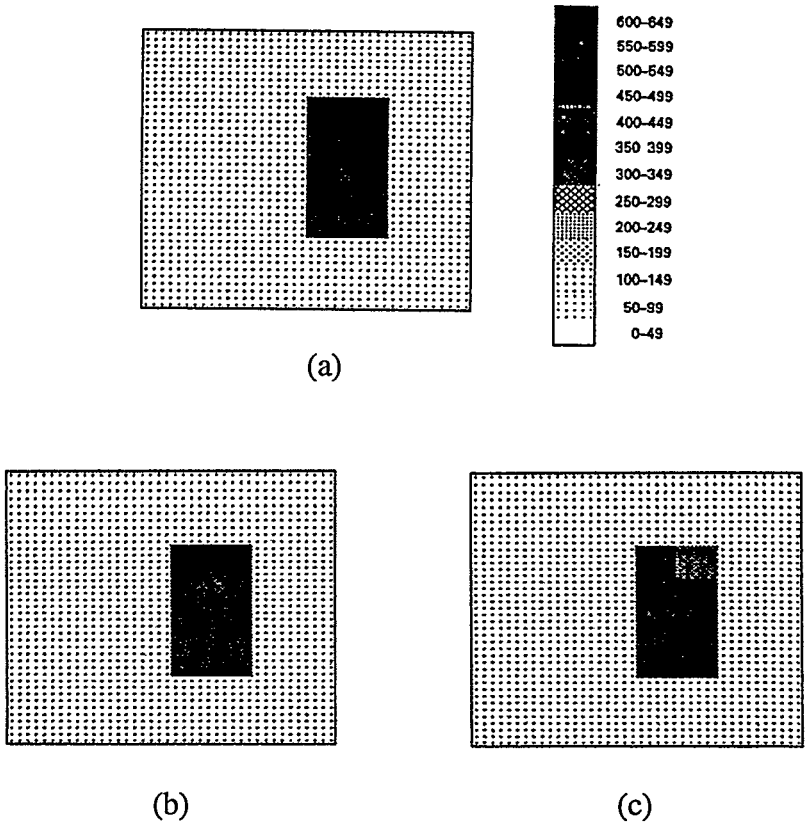

Figure 4.19 Comparison of results obtained by using the Jacobain matrix calculated by the standard method and by the compensation theorem method (Yorkey [15]): (a) original resistivity distribution of a 375–ohm–cm rectangular object aligned to element boundaries of a 64–element, 16–electrode square model (the background resistivity is 125 ohm–cm); computed images after the 20th iteration using (b) the standard method; (c) the compensation theorem method.

excitation patterns, and conductivity distributions in the domain of the conductivity field. In this section, the basic steps of formulating the forward problem by using the finite element method with the constant–conductivity quadrilateral elements are delineated.

4.6.1 Quadrilateral Elements

To easily model geometries having curved surfaces, a transformation from quadrilateral to square elements was included both for preprocessing and postprocessing of computed results.

Consider the sketch in Figure 4.20. A shape function $N_i = N_i(\xi, \eta)$ is chosen with the values of ξ and η defined in the figure such that the mapping from the parent domain Ω_e into the square–element domain is given by

$$\begin{aligned} x(\xi, \eta) &= \sum_{i=1}^{4} x_i \, N_i(\xi, \eta) \\ y(\xi, \eta) &= \sum_{i=1}^{4} y_i \, N_i(\xi, \eta). \end{aligned} \tag{4.28}$$

An infinitesimal small area is transformed in the usual manner as

$$dx \, dy = |J| \, d\xi \, d\eta, \tag{4.29}$$

where $|J|$ denotes the determinant of the Jacobian of the coordinate transformation.

The shape functions N_i are given as

$$\begin{aligned} N_1 &= (1/4)(1 - \xi)(1 - \eta) \\ N_2 &= (1/4)(1 + \xi)(1 - \eta) \\ N_3 &= (1/4)(1 + \xi)(1 + \eta) \\ N_4 &= (1/4)(1 - \xi)(1 + \eta) \end{aligned} \tag{4.30}$$

and a bilinear expansion form is utilized such that

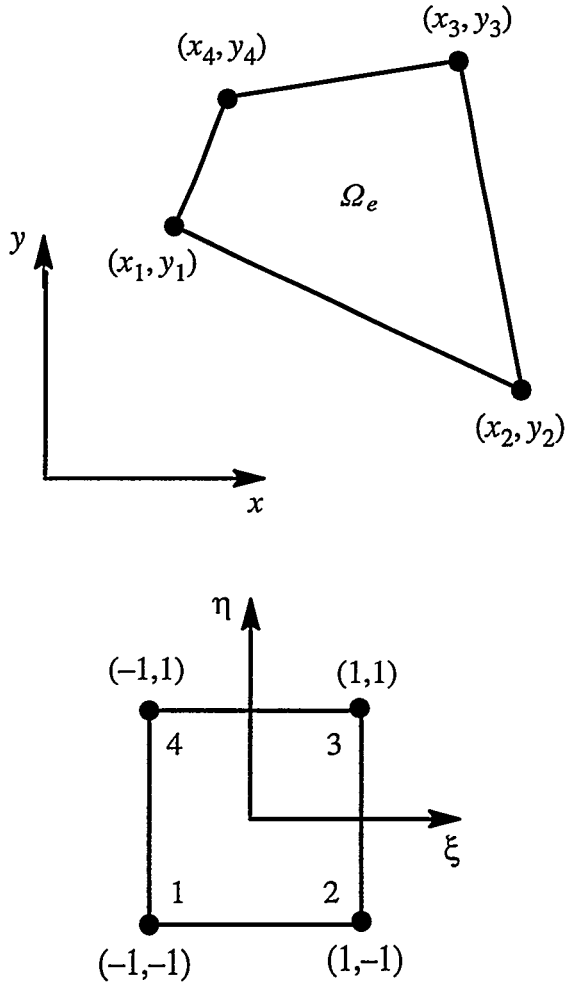

Figure 4.20 Quadrilateral element and its transformation geometry in the (ξ,η)–coordinate system.

$$x(\xi,\eta) = \alpha_0 + \alpha_1\xi + \alpha_2\eta + \alpha_3\xi\eta$$
$$y(\xi,\eta) = \beta_0 + \beta_1\xi + \beta_2\eta + \beta_3\xi\eta, \tag{4.31}$$

where the α's and β's are determined by the Jacobian of the coordinate transformation

$$[J] = \begin{bmatrix} \alpha_1 + \alpha_3\eta & \alpha_2 + \alpha_3\xi \\ \beta_1 + \beta_3\eta & \beta_2 + \beta_3\xi \end{bmatrix}. \tag{4.32}$$

Now the problem to be solved is Equation (4.8). It is assumed that the conductivity is piecewise continuous being constant in each element such that Poisson's equation is solved element–by–element. Thus, the potential function and its gradient inside an element is approximated by

$$\phi(\xi,\eta) = \sum_{i=1}^{4} \phi_i \, N_i(\xi,\eta)$$
$$\nabla\phi = \sum_{i=1}^{4} \phi_i \; \nabla N_i(\xi,\eta). \tag{4.33}$$

Solving Equation (4.8) is equivalent to minimizing the functional

$$F = \frac{\sigma_e}{2} \int\int_{S(\Omega_e)} |\nabla\phi|^2 \, dS, \tag{4.34}$$

where σ_e is element conductivity (assumed constant inside the e–th element), and Ω_e designates the region occupied by the individual elements for which Equation (4.34) applies. Thus,

$$\frac{\partial F}{\partial \phi_i} = 0 \qquad \text{for} \qquad i = 1,\ldots,4 \tag{4.35}$$

which, after minimizing, results identically in Equation (4.8). The entries of element admittance matrix are given by the transformation,

$$y_{ij} = \sigma_e \int_{-1}^{1} \int_{-1}^{1} F_{ij}\,(\xi,\eta)\; d\xi d\eta \qquad \text{for} \quad \begin{matrix} i = 1,\ldots,4 \\ j = 1,\ldots,4, \end{matrix} \tag{4.36}$$

and where

$$F_{ij}(\xi,\eta) = \left[\left(J_{11}^{-1}\frac{\partial N_i}{\partial \xi} + J_{12}^{-1}\frac{\partial N_i}{\partial \eta}\right)\left(J_{11}^{-1}\frac{\partial N_j}{\partial \xi} + J_{12}^{-1}\frac{\partial N_j}{\partial \eta}\right) + \left(J_{21}^{-1}\frac{\partial N_i}{\partial \xi} + J_{22}^{-1}\frac{\partial N_i}{\partial \eta}\right)\left(J_{21}^{-1}\frac{\partial N_j}{\partial \xi} + J_{22}^{-1}\frac{\partial N_j}{\partial \eta}\right)\right] |J| \cdot \tag{4.37}$$

The double integral in Equation (4.36) is numerically calculated by the Gauss–Legendre quadrature formula:

$$\int_{-1}^{1}\int_{-1}^{1} F_{ij}(\xi,\eta)\; d\xi d\eta = \sum_{m=1}^{6}\sum_{n=1}^{6} F_{ij}(\xi_m,\eta_n)\; w_m\; w_n, \tag{4.38}$$

where w_m and w_n's are the integration weights of six points (a grid of 6×6 points from six selected points in each direction [97]) from Table A.1 in Appendix A.

4.6.2 Assembling the Global Admittance Matrix

After calculating the local element admittance matrices, the global admittance matrix for the whole finite element structure is assembled, and Equation (4.8) for the potential field is approximated by solving the global symmetric system of equations:

$$\boldsymbol{Y}_{N\times N}\; \boldsymbol{V}_{N\times P} = \boldsymbol{C}_{N\times P}, \tag{4.39}$$

where N is the number of nodes in the finite element mesh, P is the number of excitations, $\boldsymbol{Y}$ is the global admittance matrix, $\boldsymbol{V}$ is the nodal potentials for each excitation, and $\boldsymbol{C}$ is the current matrix which includes the currents of the finite element nodes.

The off–diagonal entries of the element admittance matrix in Equation (4.36) represents the admittances connected between the nodes of the element (see Figure 4.21), and the diagonal entries of the element matrices calculated in Equation (4.36) are the negative of the sum of the all admittance elements connected to the corresponding node number. For a discrete representation of the imaging domain, the elements are assembled together to represent the whole structure of the impedance network as shown in Figure 4.22.

The global admittance matrix assembled as a new element is added to the admittance network. This process is outlined in the basic steps shown in Figure 4.23. In this process, G is an array which holds the corresponding global node numbers of all the local nodes of the elements and y_e's are the element admittances connected between the element nodes as shown in Figure 4.21.

4.6.3 Normalization of Global Field Equations

In the numerical solution of the potential field problem, there are several variables which directly effect the magnitude of the potential solution. These are the geometric dimensions of the phantom, the conductivity of the liquid in the phantom, and the magnitude of the excitation sources (current/voltage). To avoid working with these extremely high or low values of system variables, the field equations are normalized.

Consider the field equations from the finite element formulation, $\boldsymbol{YV} = \boldsymbol{C}$, the admittance matrix is a function of the phantom dimensions and the conductivity distribution inside the phantom. If the average conductivity, σ_{ave}, and the submerged length of the electrodes length, ℓ_e, are selected as normalization variables, then the admittance matrix is normalized by

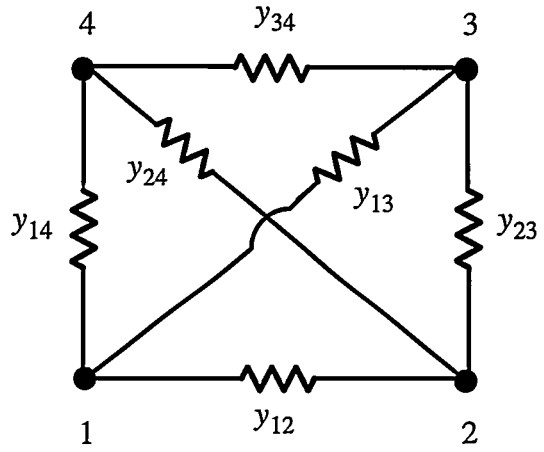

Figure 4.21 Equivalent admittance network of a quadrilateral element: local node numbering and admittance elements (negative of the off–diagonal entries of the element admittance matrix).

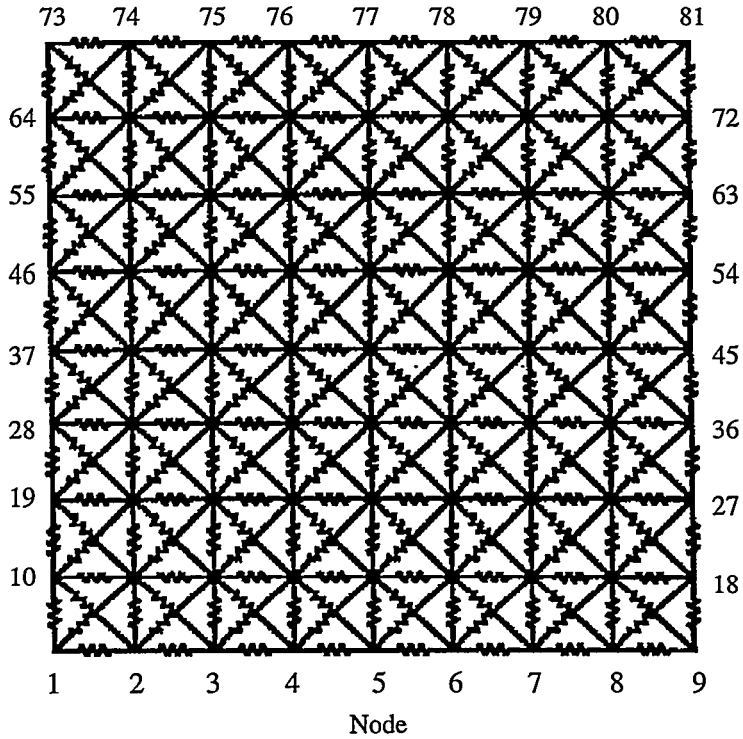

Figure 4.22 Equivalent admittance network of an 8×8 quadrilateral mesh and the global node numbering scheme of the finite element mesh nodes.

step 1. set $Y_o = 0$

step 2. for $e = 1$ to *all elements*
for $\ell_1 = 1$ to *element nodes*
for $\ell_2 = \ell_1 + 1$ to *element nodes*
$g_1 = \min(G(e, \ell_1), G(e, \ell_2))$
$g_2 = \max(G(e, \ell_1), G(e, \ell_2)$
$Y_e(g_1, g_2) = Y_{e-1}(g_1, g_2) + y_e(\ell_1, \ell_2)$
end
end
end

step 3. for $i = 1$ to *all global nodes*
for $j = i + 1$ to *all global nodes*
$Y(i,j) = Y(j,i)$
end
end

step 4. for $i = 1$ to *all global nodes*
y_diag = 0
for $j = 1$ to *all global nodes*
y_diag = y_diag + $Y(i,j)$
end
$Y(i,i) = -$ y_diag
end

step 5. stop

Figure 4.23 Basic steps for assembling the global admittance matrix of the impedance network in Figure 4.22.

$$\underline{Y} = k_y\, Y \tag{4.40}$$

where $k_y = 1/(\sigma_{ave}\ \ell_e)$. On the other hand, the current matrix is also normalized by

$$\underline{C}_p = k_{c,p}\ C_p \tag{4.41}$$

where C_p denotes an $N \times 1$ vector of node currents of the p–th excitation, and the normalization factor is $k_{c,p} = 1/\max|C_p|$. Therefore, once the admittance matrix and the boundary conditions are normalized, the potential solution is automatically calculated in a normalized form. The experimentally measured electrode voltages are also normalized to be consistent with the computational results:

$$\underline{V}_{o,p} = k_{v,p}\ V_{o,p} \tag{4.42}$$

where $V_{o,p}$ denotes the measured electrode voltages vector for the p–th excitation, and the normalization factor is $k_{v,p} = (\ell_e\ \sigma_{ave})/\max|C_p|$.

Thus, the global equations are expressed as a nondimensional linear system:

$$\underline{Y}_{N\times N}\ \underline{V}_{N\times P} = \underline{C}_{N\times P}. \tag{4.43}$$

Since no reference point has been assigned, the normalized global admittance matrix in Equation (4.43) has a rank of $N - 1$. In order to obtain a solution to this linear system, it is necessary to modify the system matrices by assigning a reference potential to a node. To assign a reference potential, the current matrix, $C_{N\times P}$, on the right hand side of Equation (4.43) is modified by setting the corresponding row entries to the reference node potential (In this case an electrode is considered to be a reference voltage. Therefore, the node which belongs to this electrode is selected as a reference node). The global admittance matrix, $Y_{N\times N}$, however, is modified by setting the corresponding diagonal entry to one, and the rest of the corresponding row and the column entries to zero. Therefore, the rank of the global admittance matrix is increased to N. If the modified linear system of equations

are solved, the obtained voltages in $V_{N\times P}$ take values relative to the reference node potential. The modified global admittance matrix, the current matrix, and therefore the voltage matrix after these operations are indicated by a superscript "asterisk," expressing the modified field equations in the form of

$$\underline{Y}^*_{N\times N}\,\underline{V}^*_{N\times P} = \underline{C}^*_{N\times P}. \tag{4.44}$$

To avoid any confusion in later analytical developments of this report, the "under bar" and "asterisk" notation to indicate the normalized and modified matrices will not be used, but these matrices can be assumed to be normalized and referenced to ground potential.

4.6.4 Solution of Linear Equation System

The previous section explained how to obtain a finite element model of the phantom used for imaging conductivity fields. The model given in Equation (4.44) is in the form of a symmetric and a sparse linear system. In the following section, it will be later explained that the solution of the potential function is repetitively used in the inverse calculations. Therefore, it is necessary to efficiently solve the linear system in Equation (4.44) for P independent current excitations.

A fast algorithm for solving the finite element equations for the Newton–Raphson reconstruction method is very important for increasing the performance of the image reconstruction algorithm. Direct methods have the advantage over iterative methods because the the linear system is repetitively solved for all excitations on the right hand side. Woo [30] compared three different methods, the Gaussian elimination method, the Cholesky decomposition method, and the Conjugate gradient method for solving the linear equation sets of three different triangular mesh models containing 77, 149 and 389 nodes. Taking

advantage of full sparsity and symmetry of the finite element matrices, he reduced the decomposition complexity from the cube of the number of nodes $O(N^3)$ to less than the square of the number of nodes $\sim O(N^{1.85})$. He found that using the node–ordering algorithms to reduce the number of *fill–ins* provided a maximum speed–up factor of 32. In addition to general sparse matrix methods, band matrix methods may also be preferable to direct methods because of their easy implementation, when combined with node–ordering methods band–size reduction algorithms.

Instead of solving the system of equations for each excitation pattern, the direct inversion method is used for simultaneous solution of the linear equations. The inverse admittance matrix is obtained by the Gaussian elimination method taking the advantage of the banded structure of the admittance matrix. Therefore, the potential solution is obtained by using the inverse of the admittance matrix as

$$V_{N\times P} = Y_{N\times N}{}^{-1}\, C_{N\times P}. \tag{4.45}$$

Therefore, two operations are completed in a single step. Instead of using the electrode voltages as boundary conditions, it is beneficial to use the measured electrode currents as the Neumann boundary conditions when solving the forward problem because the admittance matrix does not change with the applied boundary conditions for each excitation. It should also be noted that the inverse of the admittance matrix is fully symmetric.

If the finite element mesh is in an array structure and the node numbers are properly numbered (see Figure 4.22), the admittance matrix can be assembled into a band matrix form. For example, the FE mesh used to discretize a square domain in Figure 4.22 designates an 81×81 admittance matrix ($N = 81$) with a half band width of $BW = NI + 2$ (where NI is the number of mesh nodes of the horizontal index of the finite element mesh which contains an 8×8–element array, $NI = 9$).

4.7 Formulation of Newton–Raphson Method

The best iterative method to present rapid convergence (Yorkey's resistive network or YWT method) is explained below for purely resistive or purely capacitive networks. The computational logic includes two parts. The first part is the forward problem (discussed in the previous section) which seeks a solution to electric potential using a given distribution of conductivity. This part was previously explained in Section 4.6. The second part is the inverse problem which uses the calculated boundary voltages in comparison with the measured values to reconstruct the conductivity/permittivity distribution. The theoretical basis for the reconstruction algorithm will be outlined in this section.

4.7.1 Error Measure

In reconstructing images, the true conductivity distribution is not known. To show the performance of the computational algorithms, a comparison between the true and reconstructed images is needed. Unfortunately, there is not any defined measure which correlates the accuracy of the reconstructed image. One measure, defined as the squared error between the observed and computed data, appears to be a reasonable way to show the performance of the reconstruction. Although it does not always provide a good visual comparison, it can be claimed[7] that as the solution approximates to the true conductivity, the computed electrode voltages obtained from the numerical model of the phantom approaches the observed electrode voltages (for the same injected currents). A scalar error function in terms the calculated and the measured electrode voltages is defined as

[7] This claim is based upon the assumption of uniqueness of the problem.

$$\Phi(\sigma) = \frac{1}{2}\{f(\sigma)-V_o\}^T\{f(\sigma)-V_o\}, \tag{4.46}$$

where $f_{EP\times 1}$ and $V_{oEP\times 1}$ are the measured and the computed electrode voltages for a conductivity distribution σ, E and P denote the number of electrodes and the number of independent excitations, and T denotes the transpose of a matrix. Due to its easy differentiability, it will be used in the minimization process described in Section 4.7.2.

Since computation of the error function gives a global measure of reconstruction error, it can be used as a stopping criterion, when the calculated error is less than a certain small number. If Equation (4.46) is properly normalized, its square root is

$$\Phi^{RMS}(\sigma) = \sqrt{\frac{\{f(\sigma)-V_o\}^T\{f(\sigma)-V_o\}}{V_o{}^T V_o}}, \tag{4.47}$$

expressed in the form of a *root mean squared error* (RMS). The RMS error provides the average relative error per electrode. In this report, this error measure is used in the graphs to show the computational performances of the conductivity reconstructions .

4.7.2 Newton–Raphson Minimization

To find a σ–distribution which minimizes $\Phi(\sigma)$, let the derivative of the error function vanish. Thus,

$$\Phi'(\sigma) = [f'(\sigma)]^T\{f(\sigma)-V_o\} = \mathbf{0}, \tag{4.48}$$

where

$$\sigma_{M\times 1} = \left\{ \sigma_1 \; \sigma_2 \; \cdots \; \sigma_m \; \cdots \; \sigma_M \right\}^T. \tag{4.49}$$

The differential of the computed boundary electrode voltages is defined as

$$J = f'(\sigma) = \frac{df(\sigma)}{d\sigma}, \tag{4.50}$$

where $f'(\sigma)$ is called the Jacobian matrix.

Keeping only the linear terms, the Taylor's series expansion of $\Phi'(\sigma)$ around a point σ^k is expressed by

$$\Phi'(\sigma) \cong \Phi'(\sigma^k) + \Phi''(\sigma^k)\, \Delta\sigma^k = \mathbf{0}, \tag{4.51}$$

where the second derivative of the error function $\Phi''(\sigma)$ is called the Hessian matrix given by

$$\Phi''(\sigma^k) = [f'(\sigma^k)]^T f'(\sigma^k) + \left[f''(\sigma^k)\right]^T \left[I_M \otimes \left[f(\sigma^k) - V_o\right]\right], \tag{4.52}$$

where $\otimes$ is the Kronecker matrix product (see for example [98] and [99]), and I_M is an identity matrix of size $M \times M$. The term $f''(\sigma^k)$ is very difficult to calculate explicitly, but often very small relative to $f'(\sigma^k)]^T f'(\sigma^k)$ [100]. Therefore, the Hessian matrix, H, is approximated by

$$H_{M\times M} = \Phi''(\sigma^k) \cong [f'(\sigma^k)]^T f'(\sigma^k). \tag{4.53}$$

An iterative procedure which estimates σ^k is derived. At iteration–k, we have both a current estimate of σ^k and a value for $\Delta\sigma^k$ so that the conductivity estimate is updated for the new value of the conductivities by

$$\sigma^{k+1} = \sigma^k + \Delta\sigma^k, \tag{4.54}$$

where the incremental change $\Delta\sigma^k$ in conductivity variation is calculated by

$$\Delta\sigma^k = -[[f'(\sigma^k)]^T f'(\sigma^k)\ ]^{-1}\ [f'(\sigma^k)]^T \left\{f(\sigma^k) - V_o\right\}, \tag{4.55}$$

where the positive definiteness of the approximate Hessian matrix guarantees that $\Phi(\sigma)$ is minimized. The flow chart of the algorithm is shown in Figure 4.24.

The Newton–Raphson reconstruction method presented herein, in fact, forms the basis of the reconstruction methods developed and used in this report. The overall system uses a forward computation of potential distribution based on assumed conductivity distribution in each element and specified boundary conditions, and a reverse computation of changes in conductivity for each element based on Equation (4.54) which reduces the error between the measured and computed boundary response.

4.7.3 Direct Computation of the Hessian

The Jacobian matrix is calculated by differentiating Equation (4.44) with respect to the conductivity of the j–th element, σ_j, and this procedure is expressed by

$$\frac{\partial f}{\partial \sigma_j} = f' = \boldsymbol{T}\ \mathrm{vec}\left(\frac{\partial}{\partial \sigma_j} \boldsymbol{Y}^{-1}\ \boldsymbol{C}\right) = \boldsymbol{T}\ \mathrm{vec}(\boldsymbol{Q}), \tag{4.56}$$

where vec( ) is an operator which transforms columns of a matrix into a vector. $\boldsymbol{T}$ is an $EP \times NP$ transformation matrix which only extracts the derivatives of the electrode voltages, omitting the calculated values of Q_{ij} for the internal nodes because only the boundary errors are of interest in calculating the error function in Equation (4.46). Since the current matrix is independent of the element conductivities, the result becomes

$$\frac{\partial \boldsymbol{Y}^{-1}}{\partial \sigma_j}\ \boldsymbol{C} = -\ \boldsymbol{Y}^{-1}\ \frac{\partial \boldsymbol{Y}}{\partial \sigma_j}\ \boldsymbol{Y}^{-1}\ \boldsymbol{C} = -\ \boldsymbol{Y}^{-1}\ \frac{\partial \boldsymbol{Y}}{\partial \sigma_j}\ \boldsymbol{V}. \tag{4.57}$$

Therefore, the Jacobian matrix is calculated in terms of the inverse of the admittance matrix, the derivative of the admittance matrix and the computed potentials for the conductivity distribution for the k–th iteration. The majority of computational effort is involved

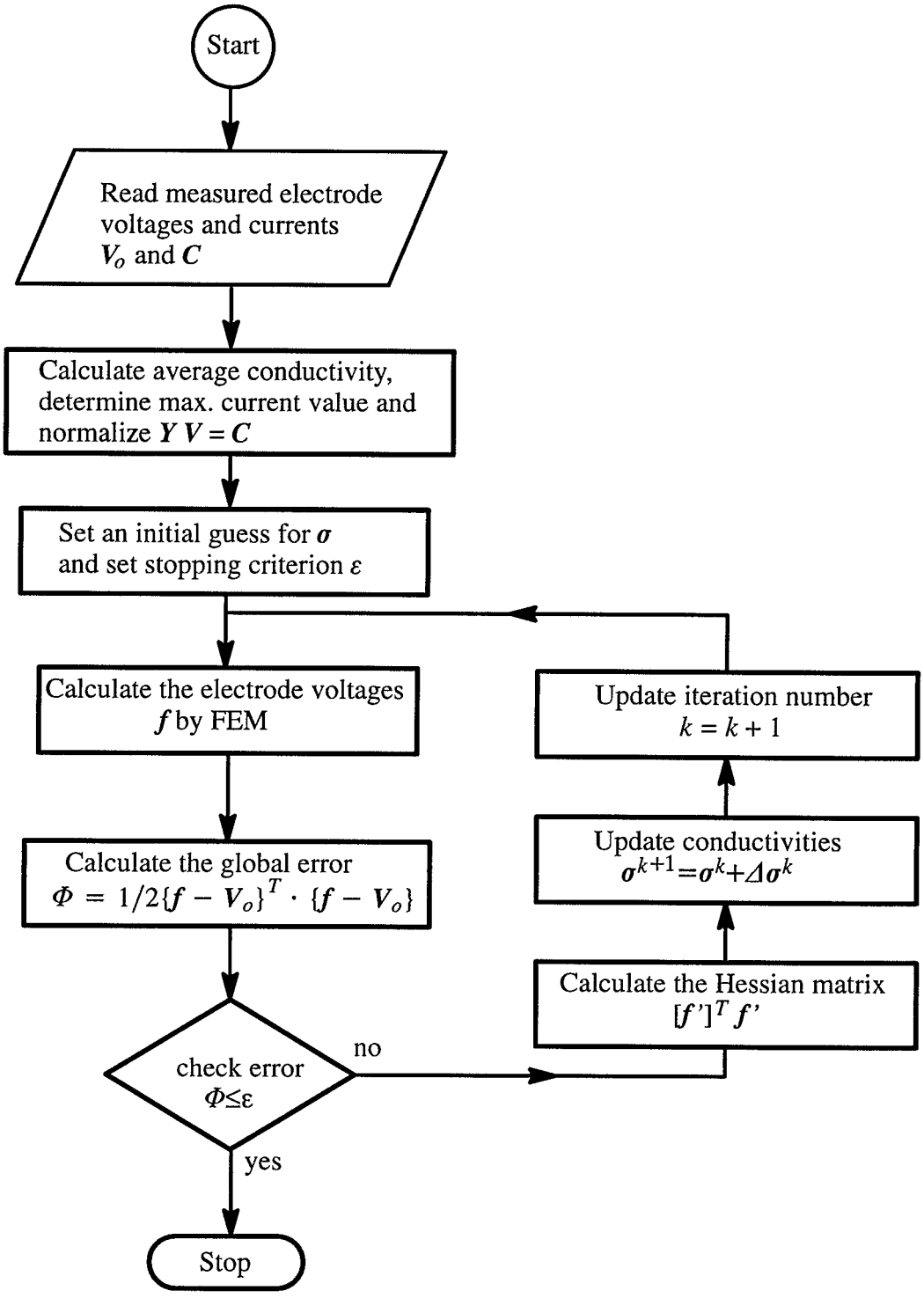

Figure 4.24 Program flow chart of the Newton–Raphson algorithm.

with the Jacobian calculations, and subsequently the Hessian, defined in Equation (4.53). It is found that it is unnecessary to calculate the former and that the latter can be determined in its absence. The numerical details of direct calculation of the Hessian without storing the Jacobian matrix is presented in Appendix B.

4.7.4 Computational Complexity of the Hessian

To date, images obtained by Electrical Impedance Tomography are generally of quite fuzzy and low spatial resolution. To improve the image quality with high accuracy measurements, the imaging domain should be broken into a large number of elements for high resolution images. This, of course, will not only increase the number of unknowns (piecewise constant element conductivity values) of the inverse problem but also will increase the requirement for more measured data and storage for the Jacobian matrix. As an example, if the number of unknown elements is doubled, the memory required to store the Hessian matrix quadruples. Also, CPU time required to reconstruct the Hessian matrix dramatically increases as the number of elements are increased. The number of floating–point arithmetic operations, *FPO,* required to construct the Hessian matrix is expressed in terms of the number of electrodes E, the number of excitations P, and the number of elements M as

$$FPO = M^2 \times (E \times P \times c_1 + c_2) \tag{4.58}$$

where c_1 and c_2 are integer constants representing the number of addition /subtraction and multiplication/division floating–point arithmetic operations. In the algorithm implemented to form the Hessian matrix, $c_1 = 82$ (41 addition/subtraction and 41 multiplication/division) and $c_2 = 24$ (24 addition/subtraction). For a 64–element, 16–electrode system with 34 excitations the number of arithmetic operations $FPO = 129 \times 10^6$ FLOPS are required for each iteration. In computational experiments, the CPU for constructing the

Hessian matrix takes between 80% and 90% of the total CPU of the Newton–Raphson algorithm.

4.7.5 Savings in Computer Memory

In comparing the computer storage requirements for the Jacobian and the Hessian matrices, the Jacobian is a full, nonsymmetric matrix and its storage may become very expensive when the number of elements, electrodes and excitations are large. On the other hand, the Hessian is also a full but a symmetric matrix, and the memory requirement increases with only the number of elements. For example, if an 8×8 finite element structure with 50 excitations and 32 electrodes is considered, the Jacobian matrix will be $32 \times 50 \times 64$ and consume 1.64 MB computer memory (Note that each floating number is a double precision complex number occupying 16 B in computer memory). This is 25 times larger than the required memory of 65 kB for storing $\boldsymbol{H}$ in a 64×64 array. Alternatively, for the same number electrodes and excitations, if the problem is solved for a 16×16 element array, the Jacobian will occupy 6.55 MB of computer memory which is approximately 6 times larger than that of required for $\boldsymbol{H}$ in a 256×256 array occupying only 1.05 MB . When high noise level exists in the experimental measurements, more than four current excitations are desirable and therefore memory requirements will be even larger. For example, for the full 496 independent pair excitations the Jacobian matrix requires 65 MB while $\boldsymbol{H}$ only requires 1.05 MB giving a ratio of 62 times less memory requirement. Furthermore, with proper storage of the upper half of the Hessian matrix these memory savings can be doubled.

For the best, or optimum, current excitations, the computational effort for the two methods is of the same order. However, the new algorithm requires significantly (order of

magnitude) less computer storage and shows no degradation in the convergence relative to the direct computation utilizing the Jacobian.

4.7.6 Ill–Conditioning

Reconstruction of the inverse conductivity problem is inherently ill–conditioned. due to nonlinear nature of the problem. If the conductivity field is represented by pixels, all the pixel conductivities are cross correlated, having their individual effects on the system's boundary response. Woo [30] explained that the cross correlations among the pixels skew the contours of the objective function, defined in Equation (4.46), into a narrow *hyperellipsoid.* The location and the size of the pixels also effect the degree of the ill–conditioning of the problem. Since all the measurements are obtained from the boundary, the conductivity changes of the elements in the interior region of the phantom have a decreasing effect on the measured data. In this case, noise in measurements may be fatal to the stability of solution.

During the minimization of the objective function by the Newton–Raphson method, the ill–conditioning results in a very high condition number of the Hessian matrix. The condition number of a matrix is defined as the ratio of the maximum eigenvalue to the minimum eigenvalue of this matrix by

$$K(A) = \frac{\lambda_{\max}(A)}{\lambda_{\min}(A)}. \tag{4.59}$$

where K is the condition number of any matrix A, $\lambda_{\min}$ and $\lambda_{\max}$ are its maximum and minimum eigenvalues, respectively. The larger the difference between the minimum and the minimum eigenvalues of a matrix, the larger the condition number of the matrix and therefore the more the ill–conditioning occurs (Golub and Van Loan [101]).

If the size of computational mesh elements are are chosen small, the sensitivity decreases and therefore the Hessian matrix becomes very ill–conditioned having eigenvalue variations of, say 10^6 or larger. This results in large errors in solving for the conductivity update in Equation (4.55) due to all system errors including: the noise in the experimental measurements; errors in constructing the specified geometry; errors in the numerical modeling itself.

4.7.7 Regularization of Ill–Conditioned Problem

An ill–conditioned Hessian causes a significant degradation in the performance of iterative methods such as the Newton–Raphson algorithm. Regularization methods basically has a smoothing effect on the solution, improving the condition of the problem, when the guessed starting point is away from the real solution. As the iterative solution converges to the real solution, ill–conditioning becomes relatively less severe, and this artificial smoothing is systematically reduced to avoid any distortion in final results.

Murai and Kagawa [42],[43], and Kagawa et al. [44] used singular value decomposition (SVD) to calculate the eigenvalues of and used Akaike's information criterion (AIC) [41] omitting very small eigenvalues of the Hessian, therefore improving the conditioning of the linear system system of equations. The regularization methods based on coefficient penalty methods (Bayesian regularization methods, see Gottfried and Weissman [102]) were used by Hua et al. [26], [28].

Alternatively, Levenberg [103] and Marquardt [104] suggested a matrix coefficient method whose performance was shown to be better than the SVD method (c.f. Bard [105]) and others. The Levenberg–Marquardt method suggests that instead of directly solving for the conductivity update in Equation (4.55), the conductivity update is calculated from

$$[H + \gamma I]\, \Delta\sigma = B \tag{4.60}$$

where $H = J^T J, B = -J^T(f - V_o)$, and γ is the Marquardt constant which acts like a smoothing parameter bringing the highly spread eigenvalues of the Hessian closer, artificially decreasing its condition number. During the iterations, the Marquardt constant is calculated by

$$\gamma = -2\frac{B^T H B}{B^T B}. \tag{4.61}$$

The Levenberg–Marquardt method eliminates the requirement of highly expensive SVD calculations at every iteration. Yorkey successively implemented and used Marquardt's method for reconstructions from computer simulated data. He reported that for coarse element mesh reconstructions (on an 8×8 model) the conditioning ratio K in Equation (4.59) ranged up to 10^6. The choice of Marqurdt's constant is less critical in perturbing such large–sized elements. However, the choice becomes more critical for more ill conditioned situations such as with noisy data or when computations undertaken on a mesh of smaller–sized elements.

In this research, the Levenberg–Marquardt algorithm is implemented and used throughout all demonstrated results. The choice of Marquardt constant is improved using the information in the gradient vector and the Hessian matrix. Especially, in the very beginning, reconstructing large resistive regions (large sized insulator targets) imbedded in a homogeneous conductivity field was found very difficult to accurately reconstruct. This may be due to the zones of increased sensitivity dominating the less sensitive regions, and this results in the increased condition of the Hessian matrix. Poor choice of Marquardt constant resulted in oscillatory solutions and poor conductivity images.

4.8 Sources of Error

In EIT imaging, the measured boundary voltages are compared to the computed boundary voltages and the difference between these voltage values are minimized by changing the discrete element conductivities of elements. When the squared sum of the differences (the method of least–squares minimization) reaches a minimum then the image is obtained from the computed conductivities. In ideal case, the minimum of this sum is zero. In practice, however, the global error does not reach to zero because of the noise in both experiments and computations.

Basically, the source of error can be categorized into at least the following groups: error in modelling the forward problem; error in the Jacobian matrix calculations; error in placement of nodal element boundaries; error in experimental setup and measurement; computer truncation error.

4.8.1 Error in Modelling the Forward Problem

This error arises when solution to the forward problem is approached by numerical methods (FEM in our case). More accurate solutions are obtained using higher order shape functions as proposed and implemented in Section 4.6. Another way to increase the accuracy is to increase the number of elements. However, an increase in the number of elements also increases the number of unknown conductivities, causing large storage requirements for the inverse solution step (storage of the Jacobian Matrix) and drastically increasing CPU time in the computations. Larger number of elements also increases the numerical errors involved.

4.8.2 Error in the Jacobian Matrix calculations

Considering Equation (4.56), the Jacobian Matrix is calculated using the elements of the inverse of the global admittance matrix, Y^{-1}, the potentials of the nodes, V, and the derivative of the global admittance matrix $\partial Y/\partial \sigma$. Therefore, the error in the Jacobian matrix basically comes from two sources. One part of the error is introduced by the inaccurate modelling the forward solution (error in the admittance network). The other part comes from the numerical error when inverting the large–sized admittance matrix.

The first part of the error may be, at least partially, corrected by methods to be discussed later in this report (PVC method) to improve the forward problem modelling. The second part can only be corrected by using robust matrix inversion algorithms and using high–precision floating numbers.

4.8.3 Error in Placement of Nodal Element Boundaries

At best, the finite element result is an approximation to the real field distribution of conductivities. Obviously, discontinuities in the conductivity would result in perturbations in the electrical field and have an effect on the boundary response to the excitation. With constant–conductivity elements, exact coincidence of the element boundaries with the field discontinuities would yield significantly improved results over the case where the two did not coincide. This, in fact, was the basis for the high degree of accuracy of Yorkey's numerical experiments. Lack of this coincidence would distort the computed field relative to the actual field and increase the errors.

Use of an exponentially–varying conductivity field can significantly improve these types of errors by allowing the exponential shape function to automatically approximate the discontinuous behavior. Thus, if a field boundary is located within an element of the

model, the exponential shape would try to rapidly change the conductivity. The difficulty with this is that under certain circumstances, overflows or under–flows can occur leading to non–convergence of the result. While this latter difficulty has not been a problem in modeling of square geometries using square elements, it has proven a source of difficulty in modeling non–square geometries with quadrilateral elements.

4.8.4 Computer Truncation Error

Computer truncation error can be reduced by using high precision floating numbers. In our reconstruction programs we use double precision floating numbers (16 B for complex and 8 B for real numbers). We have also developed and used algorithms specifically to reduce some of this error.

4.8.5 Error in Experimental Data

This error is related to a number of factors including the digital measurement equipment and measurement techniques used, and the accuracy with which the experimental apparatus is constructed and modeled. The number of digits of measurement and the internal impedance of the voltmeter has a significant role on the measurement accuracy. Sizing and placement of electrodes on the boundary must also be done with care so that the numerical model and the experimental model coincide with a reasonable degree of accuracy.

Another source of error is electromagnetic interference which leads to noise on the signal. Properly shielding the experimental setup and the data acquisition system can prevent or reduce such radio frequency interference noise in data.

4.9 Numerical Simulations

This section describes testing and validating the results of the finite element method developed in Section 4.6 and Yorkey's reconstruction algorithm described in Section 4.7. The "data" used in reconstructions are artificially generated by the implemented version of the finite element solver for ring, annular, and random conductivity patterns.

4.9.1 Reconstruction of Resistive Patterns

Duplication of Yorkey's results required implementation of his method using square elements in the resistive mode only. As Yorkey reported [15], convergence of the error function in Equation (4.46) for an 8×8 array is very rapid as shown in Figure 4.25. Convergence to within 1 part in 10^4 occurs in 12 iterations where the contrast ratio is as large as 10,000:1.

Both real and complex conductivity calculations have been undertaken; however, the real patterns converge much more readily than the complex. Success with complex conductivities was achieved only for contrast ratios of 100:1 or smaller.

Figure 4.26 shows the convergence sequence for a 64–element body with real–conductivity elements of 3:1 contrast ratio distributed in a relatively arbitrary pattern. The quantitative resistivity pattern definition is shown at the center of Figure 4.27, indicating a dense grid for a dimensionless resistivity of 1.0 relative to the continuous media. The original pattern is chosen as uniformly of high conductivity. Gauss elimination was used to perform matrix inversions.

The small square patterns are used to visually represent the degree of variation in resistivity. The dense pattern represents material with high conductivity and low resistivity.

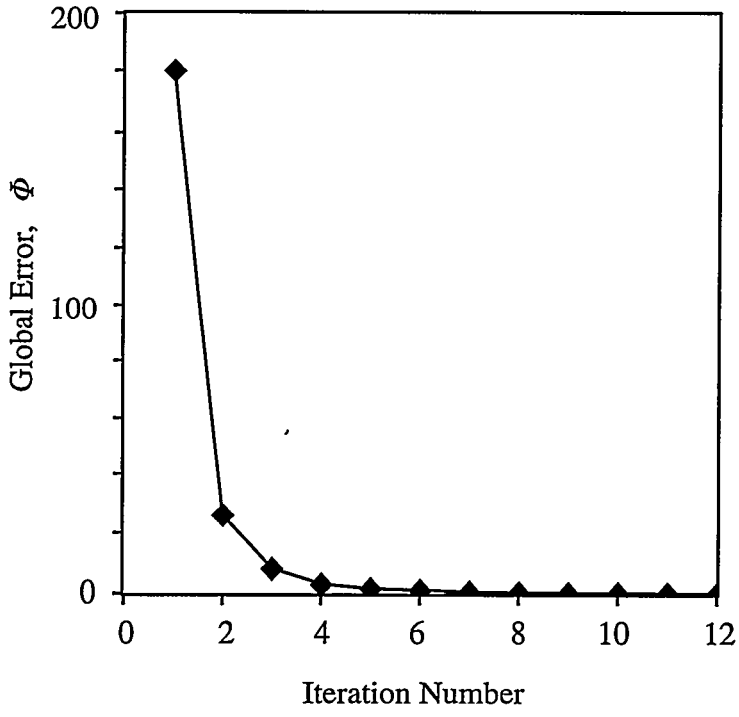

Figure 4.25 Convergence of real conductivity, square–array FEM.

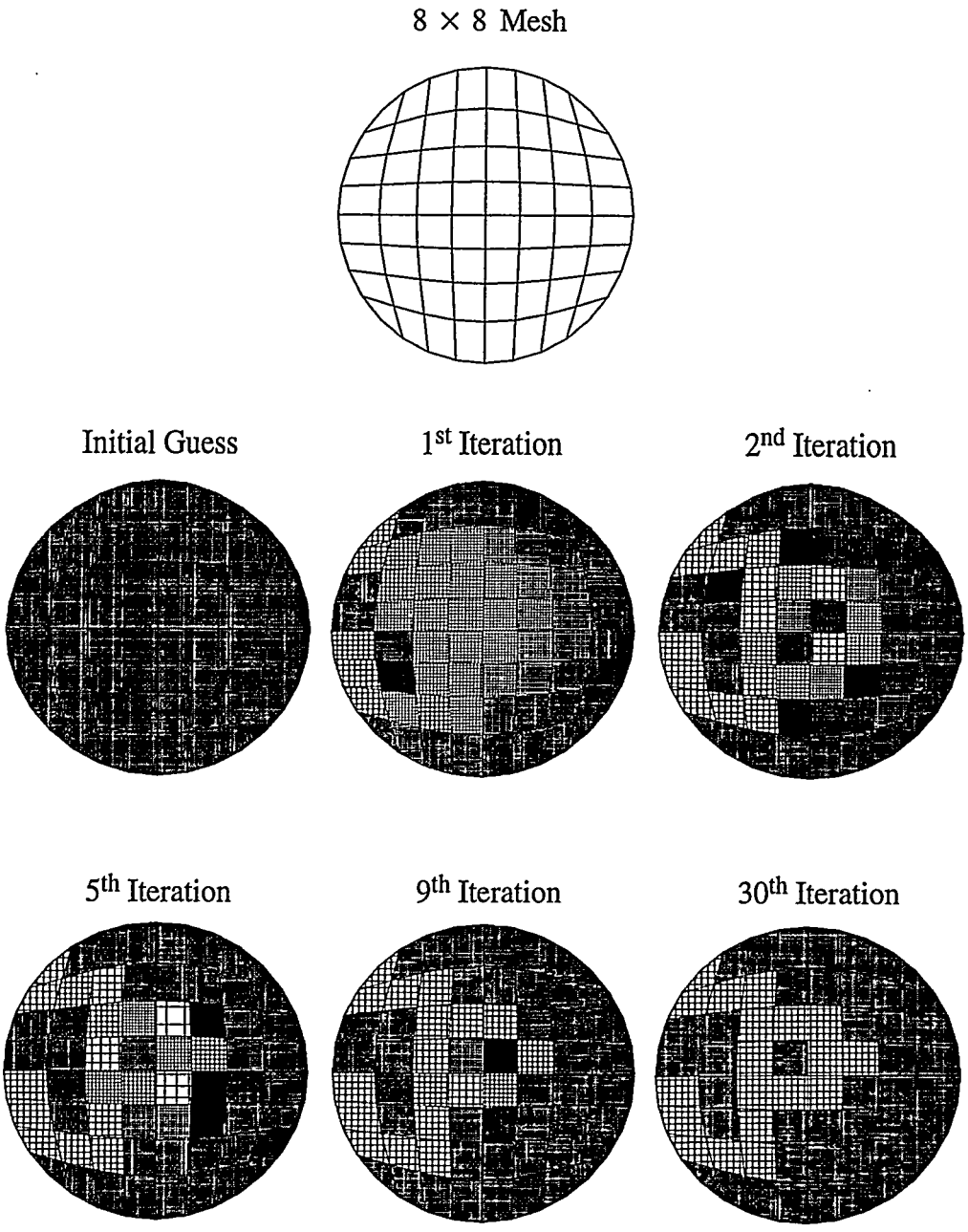

Figure 4.26 Typical convergence sequence for a 64 element array of quadrilateral elements with zero permittivity. Contrast ratio: 3:1.

The less dense the fill pattern, the lower the conductivity (as might be the case with liquid and gas mixtures).

It is seen that there is a relatively rapid convergence for elements near the boundary even though the change is from one extreme to the other. On the other hand, changes in the central region require significantly more computations for convergence due to the extreme lack of sensitivity of regions farthest from the boundaries. Figure 4.27 shows two additional patterns with the number of iterations required for satisfactory convergence. The ring pattern converges much more rapidly than the annular pattern because the zones requiring the greatest changes are nearer the boundary. Furthermore, the central region required no change whereas for the annular geometry, the central zones required maximum change.

Global error for the three cases (arbitrary, ring, and annular) is shown in Figure 4.28 indicating that the more complex the pattern, the larger the number of iterations required for convergence (for a 25–element geometry, convergence within 10^{-6} is generally obtained for contrast ratios up to 100:1 within 15 iterations and convergence was obtained with all real contrast ratios tested up to 10^5:1). Note further that while this iterative procedure is absolutely convergent, if the Jacobian is updated every iteration, this requires extensive computations. By not recomputing the Jacobian every iteration, computational times are shortened but the convergence produces oscillations as seen in the figure whenever the Jacobian is recalculated.

4.9.2 The Effect of Noise in Reconstructions

The question of noise and error generally pose real difficulties in the convergence of an inverse problem to its solution. In the case of the annular geometry, Gaussian noise was added to the "measured" voltages and the problems recomputed. As shown in Figure

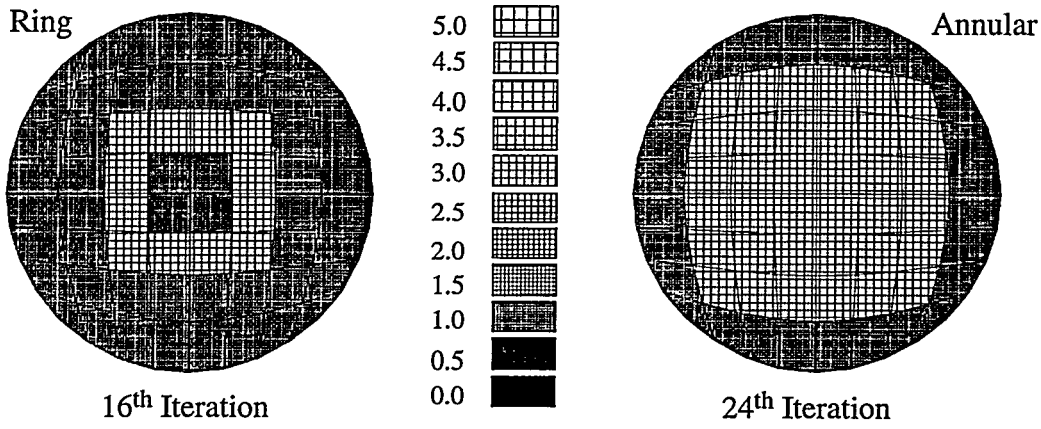

Figure 4.27 Converged patterns and resistivity index for both annular and ring geometries with zero permittivity. Contrast ratio: 3:1.

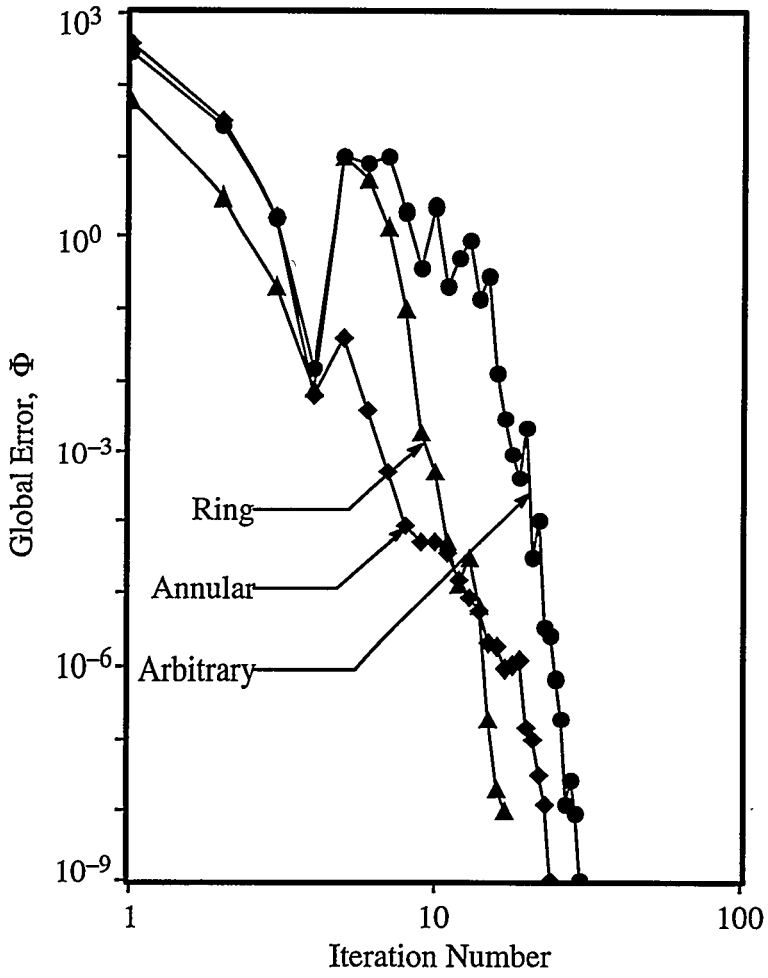

Figure 4.28 Global error for the three patterns tested.

4.29, the global error generally decreases until the effects of the error become important and then become relatively constant. (Again, the rise in error following the fourth iteration is due to a recalculation of the Jacobian).

Global error, however, is not the entire story since the global error can be quite low and local error still significant. Figure 4.30 shows the variation in the local error for each of the four ring layers in the geometry. It is seen that the farther an element is from the boundary where measurements are taken the larger the error. In the case of 1% Gaussian noise, the local error in the inner elements is above 30%. Even in this case, however, the noise has little effect on the visual recognition of the pattern (Figure 4.31).

4.10 Summary

Reconstruction methods for electrical impedance imaging used for imaging two–phase flows have been discussed. Of the methods discussed herein, the Newton–Raphson method is found to be a general and an accurate method which can approximate the conductivity distribution without making any major "a–priori" assumptions. The Newton–Raphson method solves the inverse problem where the internal conductivity field is piecewise approximated and where iterative procedures are used which require computed boundary measurements to converge to measured values which exist due to given boundary excitation. Convergence is undertaken in a manner which minimizes the least squares error between the computations and the measurements.

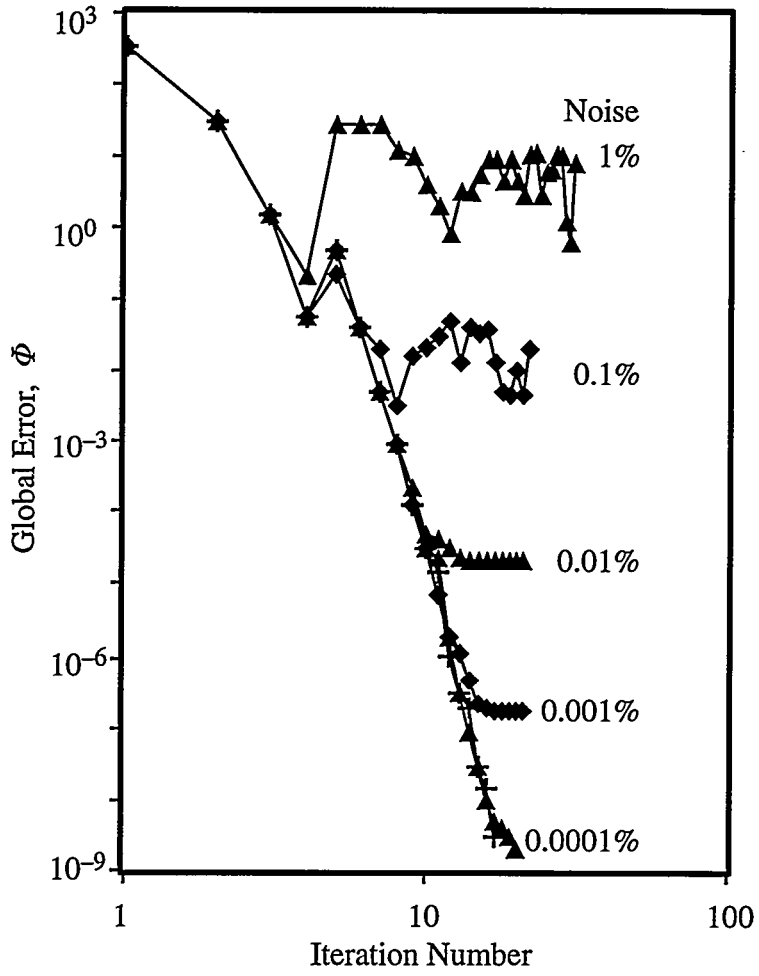

Figure 4.29 Effect of noise on convergence for the annular pattern.

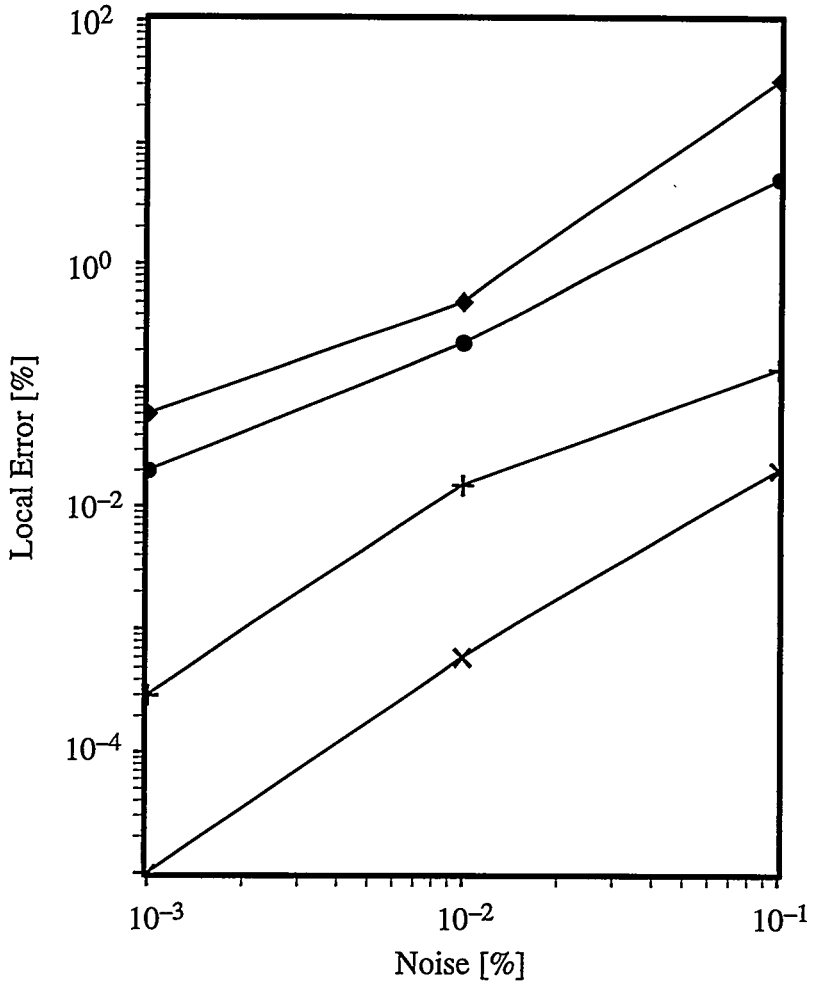

Figure 4.30 Local error for the annular–flow–like geometry: ♦ Inner Cells; • Inner Middle; + Outer Middle; x Outer Cells.

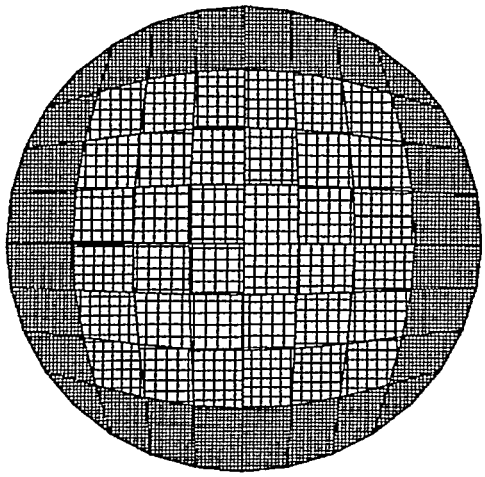

Figure 4.31 Converged annular pattern with 1% Gaussian noise.

Specific conclusions drawn from the test results presented in this chapter are:

- The internal distribution of complex electrical impedance can be piecewise approximated within a body by using only boundary excitation and measurement.
- Square–element FEM modeling of an element–boundary–matching resistive body allows iterative convergence to 1% within 4–5 iterations confirming results of Yorkey [15]. Also, convergence within 0.01% occurs within 12 iterations for all contrast ratios up to 10^5.
- Quadrilateral–element FEM modeling was slower to iterate and more sensitive to contrast ratio, perhaps due to the presence of highly acute or obtuse angles distorting the equivalent square–element conductivity. Local error in a given element was shown to be considerably slower to converge to a reasonable error. Elements farthest from the boundary showed slowest convergence, and more complex situations appear to require more iterations for convergence.
- Complex contrast ratios as large as 10^2 were found to converge using Gauss elimination for matrix inversion. Situations with larger contrast diverged.
- The computational methods utilized appear quite tolerant to Gaussian noise allowing inverse computations to be undertaken with as much as 1% rms noise in boundary "measurements." The global error is found to diverge from the no–noise case and arrive at a relatively constant value dependent on the noise. Even with relatively large local errors, visual discrimination of the patterns was easily possible.

CHAPTER 5

EXTENSIONS TO THE THEORY

5.1 Introduction

The scope of this chapter includes the analytical and numerical developments used in the electrical impedance tomography system designed and built for the Multi–phase Imaging Laboratory at RPI. This EIT system can produce cross sectional images of the distribution of insulating media imbedded in conducting media (basically, binary mixtures having two, widely disparate values of electrical properties). The developments presented herein are extensions to the standard Newton–Raphson algorithm described in Chapter 4. Based on the simulation results obtained using the original version of this algorithm, four major innovations were required to achieve reasonable success in imaging (obtaining a reasonable image resolution, requiring minutes of computational time and at most 16MB of computer memory). These innovations are:

- development of the Block decomposition Method (BDM): to reduce the excessively long computational time requirement in reconstruction. Up to three orders–of–magnitude computational savings can be obtained, thus making iterative convergence to an overall conductivity distribution practical for large number of images which would be required for synthesis of interfacial structures in flowing mixtures;
- development of the Exponential Finite Element Scheme (EFES): to better approximate the effects of conductivity variations in elements. Finite element shape functions using exponential bilinear and biquadratic conductivity models were developed and incorporated in the Block Decomposition Method (BDM);

- development of the method of Preconditioned Voltage Conversion (PVC): to make experimental subspace corrections on boundary (electrode) potentials between finite element computations and measurements so as to account for anomalies such as residual three–dimensional field effects, discreteness in finite element mesh model, errors in constructing the test geometry relative to the design, etc.;
- development of the Layer Reduction Method (LRM): incorporate three–dimensional layers (above and below electrode plane) in a single two–dimensional layer, thereby making three–dimensional images possible through two–dimensional computations.

The theory and implementation of these developments will be presented and discussed in the following sections.

5.2 Overview of Developments

Direct application of the Newton–Raphson method requires extremely lengthy computations and significant computer resources in terms of memory and computer times for large–sized problems. It becomes so extreme that anything significantly greater than a 16×16 element array (256 elements) would require many hours and hundreds of megabytes of storage space for a single image on a Cray Y–MP machine. Two–dimensional computer simulations performed on Institute's IBM 3090D mainframe computer showed computational time grows with 3.3 power of the number of elements being solved. For example, computations on a 16×16 mesh with 50 single pair excitations usually require 20–40 iterations for fully converged images at the expense of approximately an hour. On the other hand, for a typical small–sized problem such as an 8×8 element array, computations require several seconds on the same machine.

Heavy emphasis was therefore placed on improvements reducing computational time requirements. The block decomposition method was developed to perform computations on a coarse mesh to resolve conductivity equivalent to a finer mesh without significantly increasing the computational time. Computations on an 8×8 element array mesh solved for equivalent of a 24×24 element array in about 20 seconds (on IBM 3090D), which can make a reduction of three–orders of magnitudes in computational time. Such improvements mean that impedance images may be practically accomplished on a workstation–sized computer.

A majority of the improvements are made in the finite element solution since the forward problem includes abrupt changes in material properties due to the binary nature of the problem. Using Galerkin's weighted–residual method, the finite element formulation of Poisson's equation for spatial conductivity variations is delineated. The basic finite element method described earlier is reformulated using an exponential conductivity model in each element. The new exponential shape functions utilize first bilinear and then biquadratic exponential conductivity models. Thus, the errors due to the unmodeled rapid conductivity variations in elements are reduced.

In addition to the errors due to conductivity modeling, there are also gradient errors caused by rapid potential change the near the phantom's boundary electrodes. The gradient errors occur because of insufficient discretization where high potential gradients are expected. These errors can be decreased depending on the choice of mesh size, geometry and location of electrodes and a proper choice of excitation patterns used in the data acquisition process. The errors are also partially compensated by using an exponential shape function for field potential variations in each element.

The preconditioned voltage conversion method (PVC) estimates a subspace correction matrix based on the forward solution in the homogeneous case, and converts the measurements of an inhomogeneous field to the computational domain. In addition to the errors associated with discretization, the PVC method also eliminates the errors arising from experimental measurements and numerical modeling. When combined with the PVC method, the exponential finite element scheme developed substantially improved the accuracy of the forward problem, requiring fewer elements near the regions of the phantom's boundary.

Three–dimensional structures cannot be directly modeled because they suffer from the same computational overhead as two–dimensional problems do. For instance, a three–dimensional extension of an 8×8 two–dimensional model with 8 layers ($8 \times 8 \times 8$) would increase the requirements for computational resources (storage, cpu time, etc.) by almost a factor of 1000 while a 16–layer 16×16 model would increase it by almost 10,000–fold. On the other hand, the three–dimensional problem is not complete in terms of the measurements taken. The data set is incomplete so that simultaneous reconstruction of all unknown conductivities in the other layers is not possible. However, note that the three–dimensional model could utilize a single, excited layer with adjacent, unexcited layers to account for the three–dimensionality of both the field potential and the heterogeneities in the media itself. The Layer Reduction method (LRM) was developed to fold these unexcited adjacent layers into the excited layer, making the solution of the whole problem possible in a two–dimensional space.

5.3 Review of Governing Field Equation

The forward problem is described by the governing equation recalled from Chapter 4 as

$$\nabla \cdot (\sigma \nabla \phi) = \sigma \nabla^2 \phi + \nabla \sigma \cdot \nabla \phi = 0, \tag{5.1}$$

where ϕ denotes the electrical potential, and σ denotes the electrical conductivity in the problem region. The differential equation considered herein exhibits a *convection–diffusion* phenomenon, a well–known behavior often met in heat transfer and fluid flow problems [106]. To obtain a numerical solution for ϕ, finite difference or finite element methods can be employed when an analytical solution is not available (for some very special cases such as existence of symmetry in geometry and boundary conditions, an analytical solution using conformal mapping, series expansion methods, or integral methods could be obtained; see Cheney et al. [22], [107], Fuks et al. [24], Churchill et al. [108], Churchill and Brown [109], and Chen and Paoloni [110]).

Serious difficulties are encountered when using both finite difference and finite element methods because of the combination of the essentially *elliptic* and *parabolic* nature of the *diffusion* and the *convection* terms in Equation (5.1) (where the terms $\sigma \nabla^2 \phi$ and $\nabla \sigma \cdot \nabla \phi$ represent the diffusion and the convection terms, respectively[8]). Numerical solution of the resulting set of algebraic equations are difficult to obtain because of a numerical instability which occurs when the convection term dominates the transport of ϕ by diffusion. The problem shows up as unrealistic oscillatory solutions whenever the mesh size ex-

[8] The term $\nabla \sigma \cdot \nabla \phi$ shall be termed the "convection term" herein due to the analytical similarity with the convection term $\bar{v} \cdot \nabla(\,)$ in thermofluid equations where $\bar{v}$ is the fluid velocity field. This term expresses changes due only to an observer moving (i.e., convecting) with the fluid velocity field $\bar{v}$. In some instances the velocity field can be considered to be the gradient of some potential field in which case the two terms are directly analogous.

ceeds a critical value (see, for example, Patankar [106], Hahn et al. [111] and Liu et al. [112]). Overcoming the problem is often computationally expensive.

Numerical prediction of convection–diffusion phenomena started receiving widespread attention of research teams in the 1960s [113]–[115]. Early investigations in this area employed finite difference or finite element methods based on the *central* difference scheme or bilinear shape functions; however, they were limited to pure diffusion problems. With a strong property variation or strong convective transport, development of a special numerical scheme is necessary.

In an early effort, researchers used *upwind* difference schemes to overcome problems of instability. Although upwind difference schemes are not prone to oscillatory solutions, they are less accurate than central difference schemes for cases of weak convective transport. Spalding [116] blended the advantages of both central and upwind difference schemes, and established the *hybrid* difference scheme. Raithby [117] pointed out that locally one–dimensional assumptions made in developing such schemes suffer from severe *false diffusion problems*, especially when the flow varies in a direction at an angle to the grid lines. Results are substantially improved by accounting for the multidimensionality of the flow [106]. Later, Raithby [118] proposed a *skew upstream* differencing scheme which showed a significant reduction in errors caused by false diffusion.

For most practical applications, the finite difference schemes discussed above are limited to regular–shaped geometries. Computational grids created by orthogonal lines which are parallel to the axes of Cartesian or polar coordinate system are difficult to fit into the complex boundaries of a problem domain. Using a special nonorthogonal coordinate system would allow their applicability to irregular–shaped geometries [119], but their extensions to these schemes become rather complicated when multiply connected domains

are encountered. The finite element method, however, has the capability of best handling such geometric complexities. Because of their practical superiority to the finite difference schemes, research on developing special finite element schemes was first started in the mid 1970s.

Use of Galerkin–type finite element methods experience difficulties similar to those which trouble the central difference schemes. Zienkiewicz et al. [120] suggested an upwind finite element scheme similar to finite difference procedures. This was further developed by Christie et al. [121] for one–dimensional problems using piecewise linear and quadratic weighting functions. In this case, upwinding is parametrically controlled depending on the strength of the convection term. Heinrich et al. [122] further extended this approach to two–dimensional problems, and subsequently, Heinrich and Zienkiewicz [123] utilized this scheme for quadrilateral elements. As experienced in hybrid finite difference schemes, false diffusion also afflicts upwind finite element schemes because they are developed based on the concept of straightforward generalizations of one–dimensional ideas. Hughes and Brooks [124], Baliga and Patankar [125], Ramadhyani [126], and Ramadhyani and Patankar [127] proposed streamline upwind schemes to overcome the false diffusion problem. In this concept, each element has a local coordinate system; one axis is aligned with a streamline direction, and the other is normal to that direction. Therefore, a more accurate model of the potential function, ϕ, is locally approximated by an exponential expression which varies in the direction of a strong convective flow. A large collection of papers exists in the literature describing similar ideas which consistently provided satisfactory results [128]–[132].

5.3.1 Galerkin's Weighted Residuals Formulation

This section deals with a complete analysis of the governing field equation for the development of the exponential finite element scheme. The variational principles can be used for the finite element formulation but it is not desirable for the general class of partial differential equations [133]. The Galerkin's weighted–residual method [134] is an equivalent approach and it is easy to apply to Equation (5.1).

Starting with the field equation for a variable–conductivity field, multiply Equation (5.1) by an arbitrary but continuous function W and integrate over the domain of element–e, Ω_e, to obtain the weak form of Equation (5.1):

$$\int_{V(\Omega_e)} W \, \nabla \cdot (\sigma \nabla \phi) \, dV = 0. \tag{5.2}$$

In the weighted–residual method, the parameters of the approximation are determined such that Equation (5.2) is satisfied for every independent choice of the weighting function, W. By partial integration over the element–e, a weak form of Equation (5.2) becomes

$$\int_{V(\Omega_e)} W \, \nabla \cdot (\sigma \nabla \phi) \, dV = \int_{V(\Omega_e)} \nabla \cdot (W \sigma \nabla \phi) \, dV - \int_{V(\Omega_e)} \nabla W \cdot (\sigma \nabla \phi) \, dV \tag{5.3}$$

which vanishes due to the vanishing of the original Equation (5.1). Using Gauss' theorem (see Appendix C),

$$\int_{V(\Omega_e)} W \nabla \cdot (\sigma \nabla \phi) \, dV = \oint_{S(\Omega_e)} (W \sigma \nabla \phi) \cdot d\overline{A} - \int_{V(\Omega_e)} \nabla W \cdot (\sigma \nabla \phi) \, dV = 0. \tag{5.4}$$

Since Equation (5.4) vanishes identically,

$$\int_{V(\Omega_e)} \nabla W \cdot (\sigma \nabla \phi)\, dV = -\oint_{S(\Omega_e)} W\, \overline{q}^e \cdot d\overline{A} \tag{5.5}$$

where the current flux on the element boundary is defined as $\overline{q}^e \equiv -\sigma\ \nabla\phi$. The potential $\phi(x, y, z)$ inside the element–e can be represented by the potentials on the M_c nodes at the corners of the element by[9]

$$\phi(x, y, z) = \sum_{m=1}^{M_c} N_m(x, y, z)\ V_m \tag{5.6}$$

where N's are the interpolation functions. In the Rayleigh–Ritz method, the weighting function W_ℓ is determined as required to minimize the numerical error in closure of Equation (5.1). In this case, $W_\ell = N_\ell$. Since $dV = dxdydz$,

$$\int_{V(\Omega_e)} \nabla W_\ell \cdot (\sigma \nabla \phi)\, dV =$$

$$\int_{V(\Omega_e)} \left(\frac{\partial W_\ell}{\partial x}\bar{i} + \frac{\partial W_\ell}{\partial y}\bar{j} + \frac{\partial W_\ell}{\partial z}\bar{k}\right) \cdot \left(\sigma\frac{\partial \phi}{\partial x}\bar{i} + \sigma\frac{\partial \phi}{\partial y}\bar{j} + \sigma\frac{\partial \phi}{\partial z}\bar{k}\right) dxdydz \tag{5.7}$$

which is

$$\int_{V(\Omega e)} \nabla W_l \cdot (\sigma \nabla \phi)\, dV =$$

$$\int_{V(\Omega_e)} \left(\frac{\partial W_\ell}{\partial x}\sigma\frac{\partial \phi}{\partial x} + \frac{\partial W_\ell}{\partial y}\sigma\frac{\partial \phi}{\partial y} + \frac{\partial W_\ell}{\partial z}\sigma\frac{\partial \phi}{\partial z}\right) dxdydz. \tag{5.8}$$

Writing the potential $\phi(x, y, z)$ in summation form as in Equation (5.6) yields

[9] Note that M_c is 4 for a two–dimensional, first order rectangular element and 8 for a three–dimensional brick element as shown in Figure 5.1.

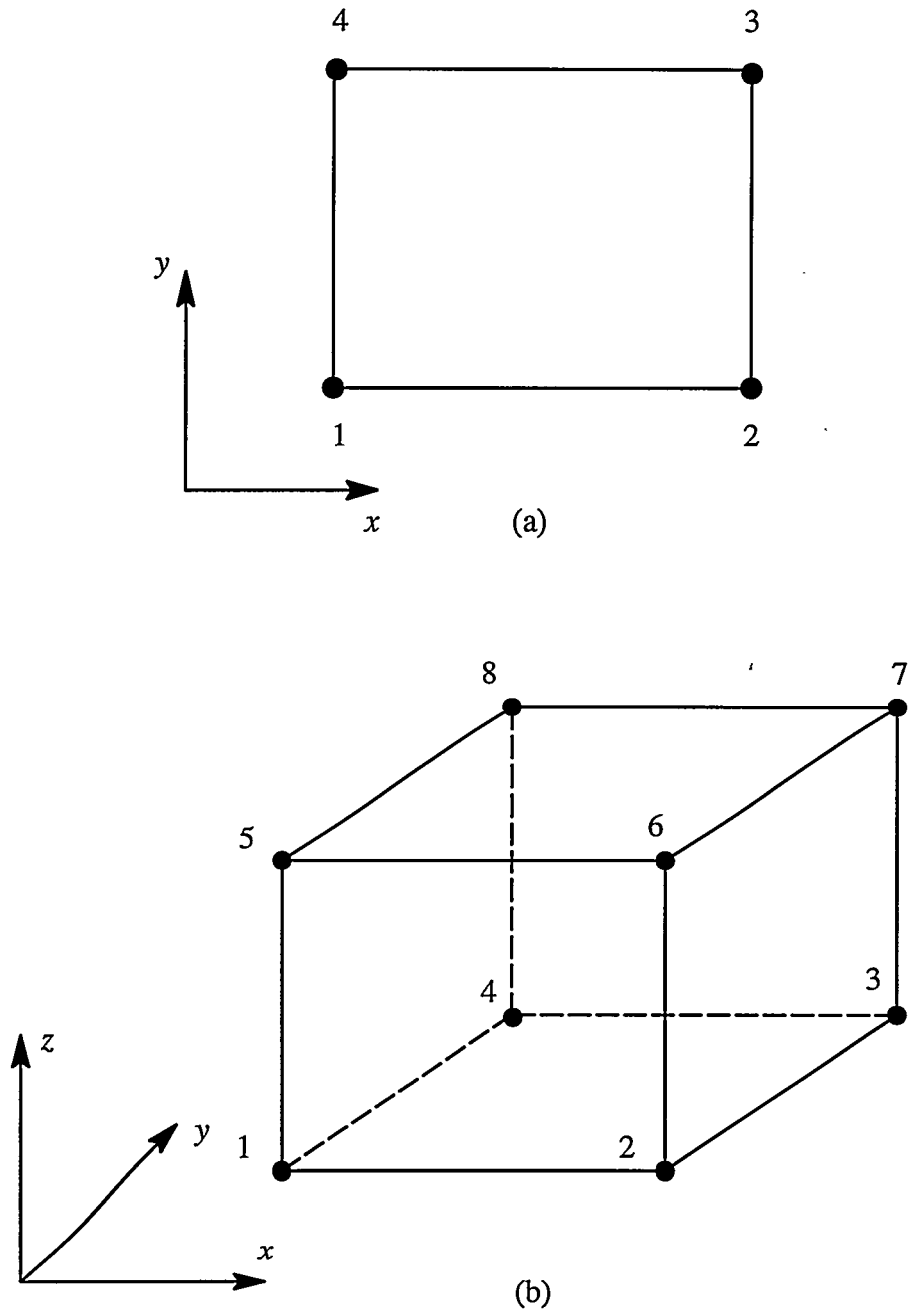

Figure 5.1 Two type of elements used in the finite element model: (a) a two–dimensional rectangular element with four nodes defined on the element corners; (b) a three–dimensional brick element with eight nodes defined on the element corners.

$$\int_{V(\Omega e)} \nabla W_\ell \cdot (\sigma \nabla \phi)\, dV =$$

$$\int_{V(\Omega_e)} \left[\sigma \frac{\partial W_\ell}{\partial x} \sum_{m=1}^{M_c} \left(\frac{\partial N_m}{\partial x} V_m \right) + \sigma \frac{\partial W_\ell}{\partial y} \sum_{m=1}^{M_c} \left(\frac{\partial N_m}{\partial y} V_m \right) + \sigma \frac{\partial W_\ell}{\partial z} \sum_{m=1}^{M_c} \left(\frac{\partial N_m}{\partial z} V_m \right) \right] dxdydz. \tag{5.9}$$

Defining an admittance matrix, $\boldsymbol{Y}$, then allows Equation (5.9) to be written as

$$\int_{V(\Omega e)} \nabla W_\ell \cdot (\sigma \nabla \phi)\, dV = \sum_m Y_{\ell m} V_m \tag{5.10}$$

where

$$Y_{\ell m} \equiv \int_{V(\Omega_e)} \left(\sigma \frac{\partial W_\ell}{\partial x} \frac{\partial N_m}{\partial x} + \sigma \frac{\partial W_\ell}{\partial y} \frac{\partial N_m}{\partial y} + \sigma \frac{\partial W_\ell}{\partial z} \frac{\partial N_m}{\partial z} \right) dxdydz. \tag{5.11}$$

If the weighting function, W_ℓ is chosen as N_ℓ, then Equation (5.11) is written as

$$Y_{\ell m} \equiv \int_{V(\Omega_e)} \left(\sigma \frac{\partial N_\ell}{\partial x} \frac{\partial N_m}{\partial x} + \sigma \frac{\partial N_\ell}{\partial y} \frac{\partial N_m}{\partial y} + \sigma \frac{\partial N_\ell}{\partial z} \frac{\partial N_m}{\partial z} \right) dxdydz, \tag{5.12}$$

and thus voltage–current relation for element–e is expressed by

$$\sum_{m=1}^{M_c} Y_{\ell m} V_m = I_\ell, \tag{5.13}$$

where $\ell = 1, \ldots, M_c$. Also, note that

$$I_\ell \equiv - \int_{S(\Omega_e)} N_\ell \, \bar{q}^e \cdot d\bar{A}, \tag{5.14}$$

where $\bar{q}^e$ is the current flux vector in element–e, and $Y_{\ell m}$ is the (ℓ, m)–th entry of the element stiffness matrix. This element also satisfies Kirchhoff's law with the voltages V_m of the nodes at the corner of the element–e and the net current I_ℓ at the nodes into element–e.

Using the same procedure explained in Section 4.6.2 of Chapter 4, these local element matrices obtained from Equations (5.13) and (5.14) are assembled to from the global admittance matrix and the current matrix to form the global system of equations as $Y_{N\times N}\, V_{N\times P} = C_{N\times P}$.

5.4 General Discussion on Errors in the Finite Element Solution

In iteratively approaching the conductivity distribution by the Newton–Raphson algorithm, numerical errors in the finite element solution to the electrical potential distribution both on the phantom boundary and in its interior region play an important role in the performance of the algorithm. The convergence, stability, and quality of conductivity distribution obtained in these iterations could be significantly improved by reducing these errors. Therefore, development of an accurate numerical model of the phantom is necessary so as to obtain *smooth* convergence and for *undistorted* conductivity images. This section discusses the potential causes of these errors due to discretization and false–diffusion, and suggests some methods to be used for modeling the rod– and plate–electrode test phantoms designed for the EIT system.

The following summarizes the causes of errors which were the primary considerations in developing a finite element model for the inverse problem:

- sensitive boundary regions nearby excited electrodes are prone to high gradient, or discretization, errors since the current densities in the boundary regions are expected to be higher than those of relatively less sensitive interior regions. The magnitude of these errors vary with the choice of proper excitation patterns, electrode geometry, electrode size, etc. Especially, two neighboring electrodes excited in opposite polarities create

very high gradients in the regions between those electrodes, and the elements covering these regions must be properly refined;

- in regions where rapid conductivity variations occur, high gradients of the potential function are also expected. In these regions, the first derivative terms in the governing equation will dominate the second derivative terms, causing a *convection–dominated* potential field. A proper refinement of the elements representing these regions can provide a more accurate approach for these high gradients.

Generally, discretization errors explained herein can be reduced by an adaptive refinement of the finite element mesh. However, satisfying the above considerations causes some difficulties in practical implementation of Yorkey's standard Newton–Raphson method. These difficulties arise from:

- the reconstruction method used being limited by the size of the admittance matrix to avoid highly expensive matrix inversion calculations. The unknown potentials for all the excitation patterns are calculated by inverting the admittance matrix by $\boldsymbol{V} = \boldsymbol{Y}^{-1}\,\boldsymbol{C}$, where using applied electrode currents (Neumann conditions) are easier than using the applied electrode voltages (Dirichlet conditions); thereby, the admittance matrix of the finite element model does not need to be modified for each excitation pattern applied. In addition, the computed inverse of the admittance matrix is a full matrix; therefore, large storage space is required for large number of nodes;
- direct computation of the Hessian matrix requires the inverse of the admittance matrix, and the derivative of the admittance matrix entries with respect to each unknown conductivity parameter (the degrees of freedom describing the conductivity variation in an element). Conductivities of all mesh elements cannot be reconstructed simultaneously because of the limited number of measurements made. Also, perturbing the conductivi-

ties of very small elements increase the ill–conditioning of the problem. Grouping the elements and assigning an unknown parameter for each group of elements can be a solution, but deriving an analytical expression for calculating these derivatives is complex. Using numerical differentiation methods is not an efficient solution as the number of unknown conductivities increases.

Considering these practical limitations, the conventional mesh refinement techniques used in finite element methods cannot be directly applied to large–scale conductivity reconstructions. In addition, although these methods look quite promising for one–dimensional problems, they cannot be practically implemented for two–dimensional inverse problems.

5.4.1 Discretization Error

The gradient, or discretization, error is expected to be remarkably high in current injected regions near the boundary of a phantom. Reductions in this error can be achieved by choosing proper type of elements and a proper mesh density where high potential gradients are expected. In early developments, first order triangular elements are used by Hua [25], Woo [30], Murai and Kagawa [42] and Hussain et al. [135] but the accuracy obtained is not acceptable for the general class of problems with complicated boundaries. Rectangular or quadrilateral elements with bilinear shape functions used by Yorkey [15] may slightly increase the accuracy in the finite element model because of the additional bilinear term in the shape function. In general, applications using triangular or quadrilateral elements with standard shape functions are limited to small–scale problems.

To decrease discretization error, a careful mesh refinement process is usually necessary especially near the phantom boundary. However, the global admittance matrix is used

to uniquely provide a solution to the potential distribution for all excitation patterns. Thus, considering all the excitations at a time, there is not an optimal mesh structure which can reduce discretization errors for all excitation patterns. On the other hand, if a uniform mesh is used, the accuracy of the forward solution is more sensitive to some of these excitation patterns, while it is less sensitive to the others.

If a uniform mesh is used to model the phantom domain, however, the number and the types of elements used for the finite element model of the phantom must be considered. To obtain better results, it its important to determine the critical mesh size or mesh density which causes a discretization error which is no more than the errors expected in experimental measurements. To investigate this, consider a test problem in Figure 5.2(a) which consists of a two–dimensional, one–meter–deep, square homogeneous phantom with conductivity of 1 $(\Omega m)^{-1}$. The phantom is diagonally excited by injecting 1 ampere current into points A and B, where these corner points represent the most critical case of error because of high current density nearby these corner points.

In order to compare the discretization errors due to the type of elements and element densities defined in the finite element model, four different mesh models are used: a 16×16 element array (Mesh I) and a 32×32 element array (Mesh II) with 256 and 1024 quadrilateral elements, respectively, shown in Figures 5.2(b)–(c); a triangular mesh (Mesh III) in Figure 5.2(d) with 512 triangular elements obtained from subdivision of Mesh I; and an adaptively refined triangular mesh (Mesh IV) which consists of 1800 elements and 963 nodes, shown in Figure 5.3(a).

The problem considered herein has an irregular geometry and boundary conditions, and there is not any straightforward analytical solution known. Thus, an approximate solution to the electric potential is obtained from the adaptive mesh (Mesh IV) by using the

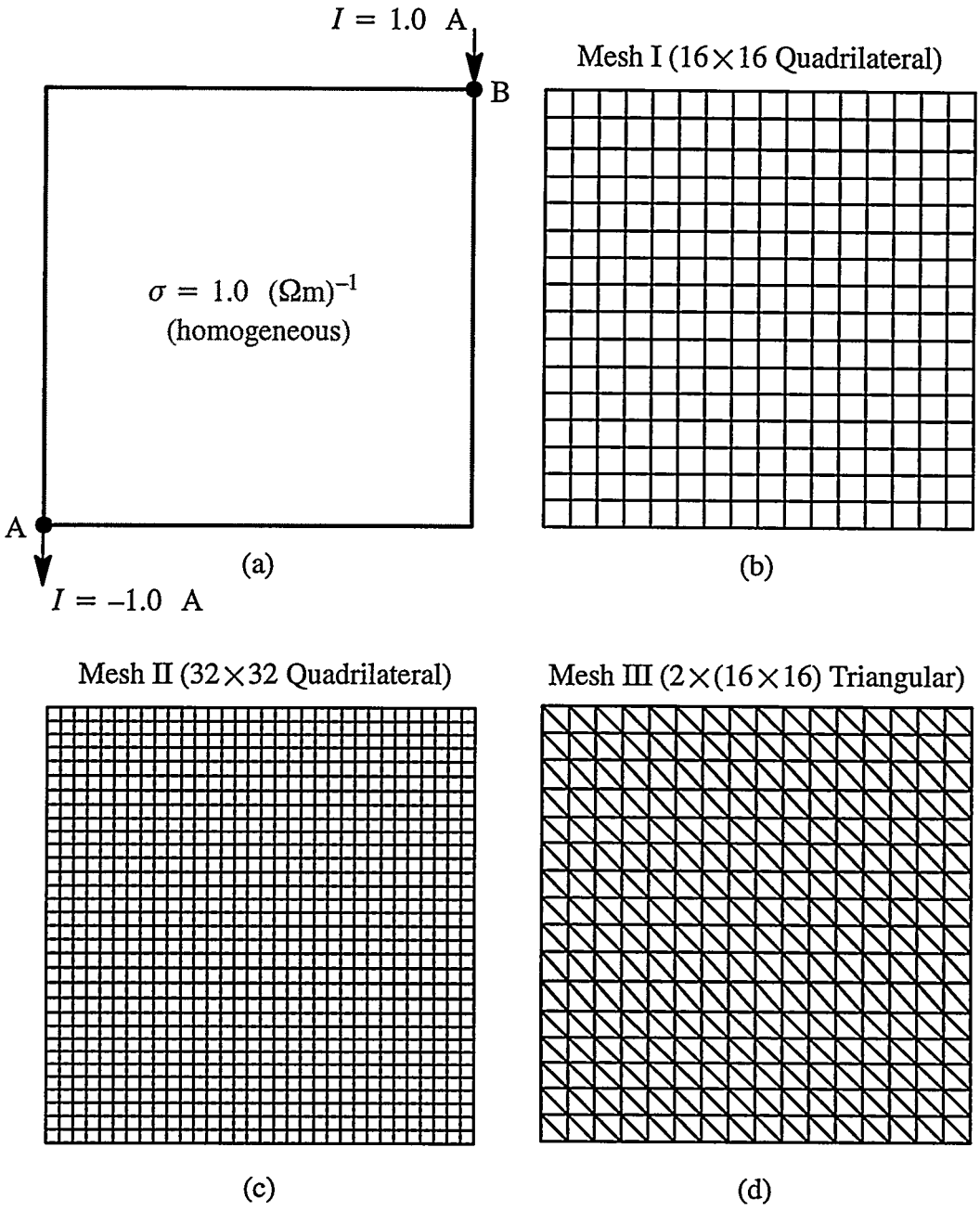

Figure 5.2 **A numerical example to demonstrate gradient errors caused by the finite element discretization of the domain using quadrilateral and triangular elements: (a) a square domain with homogeneous conductivity distribution of 1 $(\Omega m)^{-1}$ diagonally excited by a current source of 1 A; (b) discretization of the domain by a 16×16 quadrilateral mesh; (c) by a 32×32 quadrilateral mesh; (d) subdivision of the mesh in (b) into 512 triangular elements.**

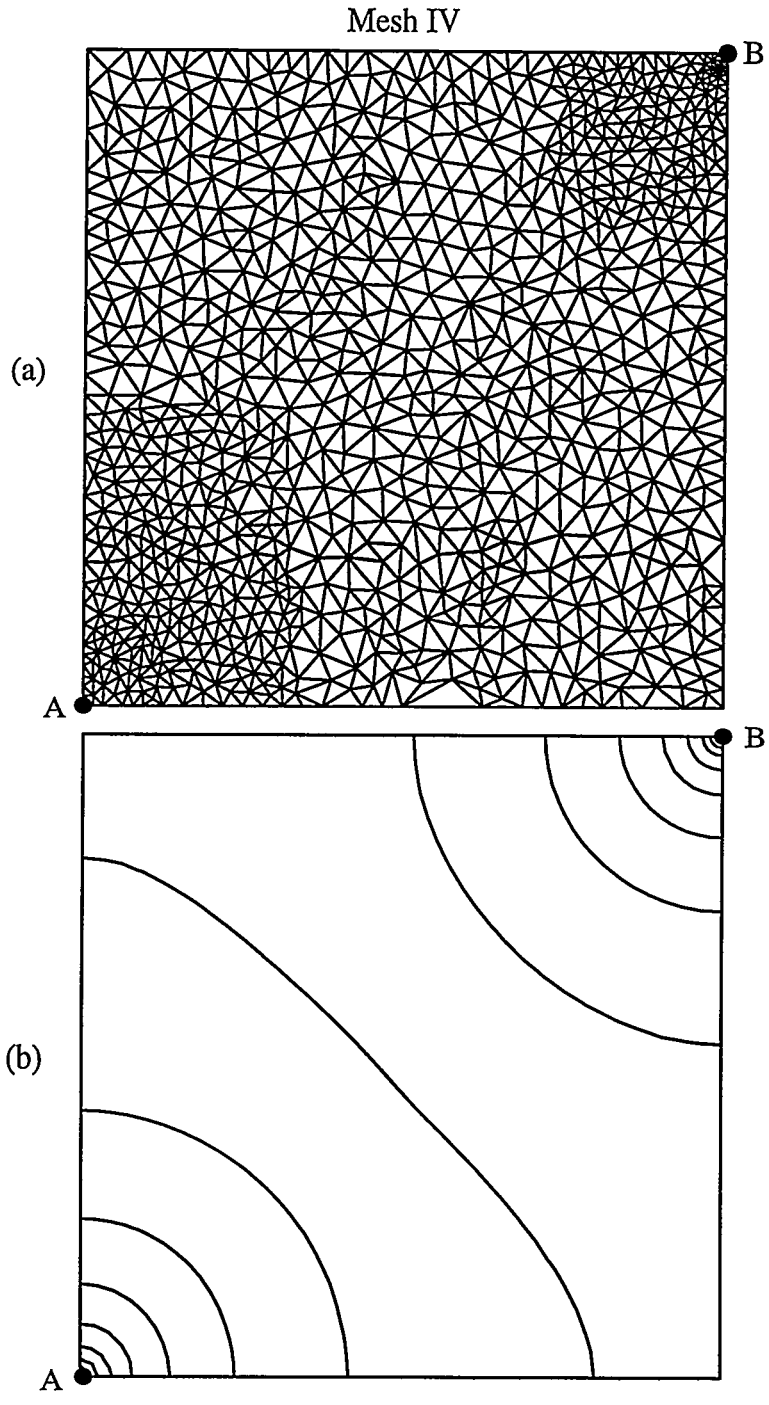

Figure 5.3 **Solution of the electric potential by MICROFLUX 4.0: (a) the finite element mesh used (963 nodes, 1800 elements); (b) equipotential lines. (22 lines with ΔV = 0.3454 Volt intervals, V_{min}= 0, and V_{max}= 7.253 V.)**

mesh generation and solution procedures of the MICROFLUX 4.0 program (see the fine elements near the current injection points A and B in Figure 5.3(a)). The obtained numerical solution can be assumed to be accurate enough, and it can be used to compare with the finite element solutions obtained for the mesh structures given in Figures 5.2(b)–(d). The equipotential lines obtained are shown in Figure 5.3(b).

An examination of the finite element solutions to the electric potential variation on line A–B in Figure 5.4 shows that the discretization error in solution from Mesh I increases both in the excited region near point B and in the interior region of the phantom, and this trend becomes even more critical for the solution obtained from the adaptive mesh, Mesh III, consisting of triangular elements. On the other hand, the solution obtained from Mesh II acceptably well approximates, in both in the interior and the boundary regions, to the solution from Mesh IV. Thus, the discretization errors due to the finite element discretization can be significantly reduced using the 32×32 quadrilateral mesh structure (Mesh III) at the expense of excessive storage and computational effort in the computer. Note that in each case the computed potential only at corner–B varies with the increasing mesh density while the computed potential at corner–A is fixed. This is because the reference node is chosen at corner–A in all cases.

Considering the errors in the numerical results obtained, the triangular elements cause the highest discretization error compared to the results obtained from meshes using the quadrilateral elements. This is because of the lack of the extra bilinear term in the polynomial used to approximate to the electric potential defined in triangular elements. Using higher order terms could reduce discretization errors but it requires a major modification of the entire algorithm including the inverse solution. The mesh using 16×16 element array is still a good approximation if it is combined with an additional numerical error correction

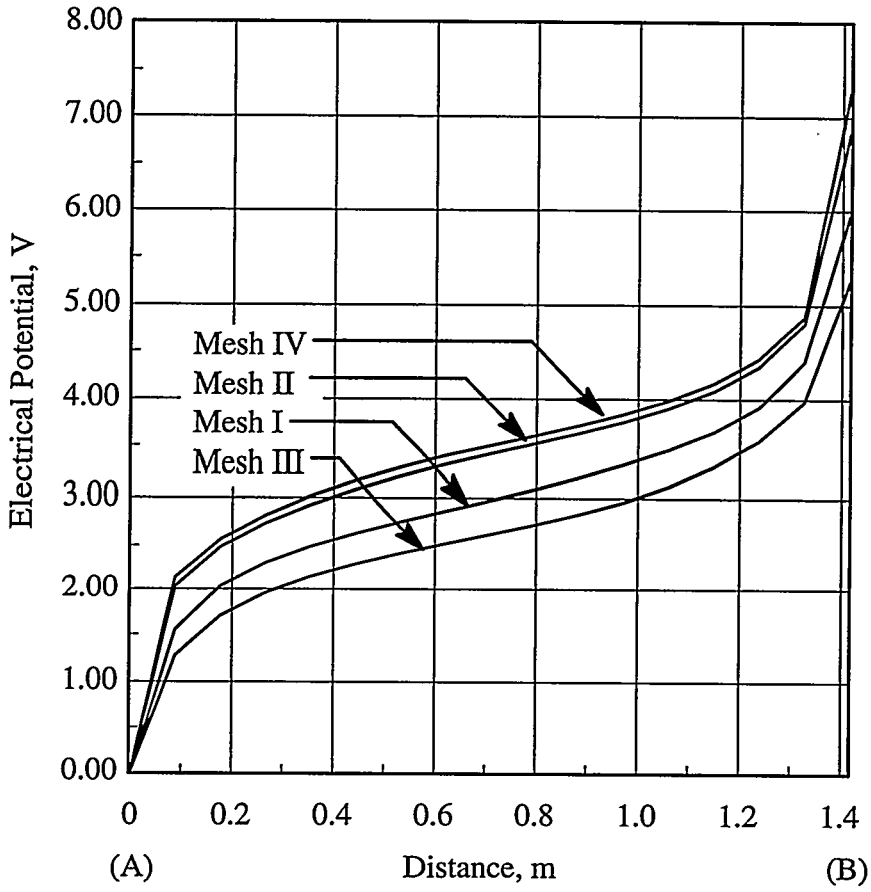

Figure 5.4 Numerical solution of the electric potential along line A–B for four different mesh structures given in Figure 5.2 and Figure 5.3.

technique such as the method of preconditioned voltage conversion (PVC). The theory and implementation of this method will be presented later in Section 5.5.

5.4.2 Errors in Modeling the Convection Term

In addition to the discretization error which occurs in the regions due to rapid variations of the electric potential, the accuracy of the finite element solution also suffers from the solutions of the electric potential with unrealistic oscillations caused by inaccurately modeling the electrical conductivity gradient in the convection term given as $\nabla\sigma \cdot \nabla\phi$ in Equation (5.1). The high gradients of conductivity could be expected anywhere inside the phantom, and the degrees of the standard approximation functions used to approximate the electric potential could not be sufficient enough to handle rapid changes of the potential variations. The following discusses two alternative methods for modeling the convection term and reducing these types of errors will be discussed in Section 5.6.

Two types of errors decreasing the accuracy of the finite element solution of the forward problem will be discussed in detail in the following two sections. These sections also introduce methods developed to eliminate these errors including the development of the method of preconditioned voltage conversion (PVC), and the development of special finite element schemes using exponential bilinear variations and subsequently extension to the finite element scheme (EFES) using biquadratic element conductivity variation.

5.5 Preconditioned Voltage Conversion (PVC)

As previously mentioned in Section 4.8 of Chapter 4, there are a number of features which cannot be modeled exactly without prohibitive computational cost in the solution of the forward problem. Preconditioned voltage conversion (PVC) is a method which was de-

veloped to mitigate much of the effects of such errors. This method is similar to the theory of "space decomposition" and "subspace correction" applied by Xu [136].

5.5.1 Theoretical Development

In the forward solution step, the computational finite element model exhibits a different response than the true model does. This is because such things as the errors due to noise in experimental measurements, the frequency effects of the stray capacitance of the measurement system, gradient error by discretization of the solution domain and geometric description of the electrodes and the phantom cannot be precisely included in the finite element model. The basic idea of the PVC is to find a "preconditioning" matrix, which accounts for these unmodeled features, and using this matrix, modifying the measured electrode voltages at the boundary to match those computed electrode voltages from the finite element model. Once this matrix is determined for a known situation, it is then applied to the unknown cases.

The major concern here is that the voltage matrix in modeling the current–voltage relationship is comprised of both measured boundary voltages and internal voltages, the latter being an unknown in experimental measurements because the measurements are only obtained on the boundary. Nevertheless, the preconditioned problem is now identical to the original problem, the only difference being that the internal voltages are not allowed to be "preconditioned."

The theoretical details can be explained by considering the current–voltage relationship provided by the finite element model as

$$\boldsymbol{Y}_{N\times N}\,\boldsymbol{V}_{N\times P} = \boldsymbol{C}_{N\times P}, \tag{5.15}$$

where Y is the admittance matrix, V is the voltage matrix which includes the potentials of the boundary and the internal nodes for P excitation patterns, and C is the current matrix which includes the current measurements from P excitation patterns assigned to the nodes of the electrodes. For the experimental case, on the other hand, the current–voltage relationship is expressed in the same manner as in Equation (5.15) but with a different admittance matrix as

$$\Gamma_{N\times N}\, V'_{N\times P} = C_{N\times P}, \tag{5.16}$$

where Γ is the true but unknown admittance matrix which includes all experimental features regarding the boundary and internal nodes. The matrix V' is the voltage response to the P excitation currents in C, giving the boundary voltages identical to the voltage measurements on the boundary. Then, since the current matrices are identical in each case, Equations (5.15) and (5.16) are set equal as

$$Y\, V = \Gamma\, V'. \tag{5.17}$$

Now at this point, additional steps are performed to find a relationship between the FE voltage matrix, V, and the experimental voltage matrix, V'. Pre–multiplication of both sides of Equation (5.17) by Y^{-1} yields

$$V = (Y^{-1}\, \Gamma)\, V' = A\, V'. \tag{5.18}$$

If the computation of Y is reasonably accurate, the matrix A should be close to a diagonal matrix so that $A \cong \mathrm{diag}(a_{ii})$ where a_{ii}s are the eigenvalues of A. If Y were exact, it would be identical to the actual admittance matrix, Γ, and matrix A would be an identity matrix. Now, neither Γ nor V' are completely known since the latter includes both

boundary and internal nodal voltages. However, knowing these incomplete terms, the result of carrying out the products in Equation (5.18) is

$$\left[\begin{array}{ccc} V_{11} & \cdots & V_{1P} \\ V_{21} & \cdots & V_{2P} \\ \vdots & \vdots\vdots & \vdots \\ V_{E1} & & V_{EP} \\ \hline V_{(E+1)1} & \cdots & V_{(E+1)P} \\ \vdots & \vdots\vdots & \vdots \\ V_{N1} & \cdots & V_{NP} \end{array}\right] \cong \left[\begin{array}{cccc|ccc} a_{11} & 0 & \cdots & 0 & 0 & \cdots & 0 \\ 0 & a_{22} & \cdots & 0 & 0 & \cdots & 0 \\ \vdots & \vdots & \vdots\vdots & \vdots & \vdots & \vdots\vdots & \vdots \\ 0 & 0 & \cdots & a_{EE} & 0 & \cdots & 0 \\ \hline 0 & 0 & \cdots & 0 & a_{KK} & \cdots & 0 \\ \vdots & \vdots & \vdots\vdots & \vdots & \vdots & \vdots\vdots & \vdots \\ 0 & 0 & \cdots & 0 & 0 & \cdots & a_{NN} \end{array}\right] \left[\begin{array}{ccc} V'_{11} & \cdots & V'_{1P} \\ V'_{21} & \cdots & V'_{1P} \\ \vdots & \vdots\vdots & \vdots \\ V'_{E1} & \cdots & V'_{EP} \\ \hline V'_{(E+1)1} & \cdots & V'_{(E+1)P} \\ \vdots & \vdots\vdots & \vdots \\ V'_{N1} & \cdots & V'_{N1} \end{array}\right] \tag{5.19}$$

where KK represents the starting index of the internal nodes, $E + 1$. Each of the diagonal elements in the matrix are close to unity if the experiment–based model is accurate. Therefore, Equation (5.19) provides a mapping between the measured and computed voltage domain. However, the diagonal terms which belong to the interior nodes remain unknown because of the lack of information due to the noninvasive measurements obtained to reconstruct images. Thus it is assumed that the values from a_{11} to a a_{EE} can be obtained from suitable reference experiments and use the resultant A matrix as a subspace corrector for each subsequent boundary measurement.

5.5.2 Computation of the Subspace Corrector

Since A should be close to an identity matrix, the off–diagonal terms should be orders of magnitude smaller than unity; i.e., A is expected to be a very *stiff* matrix. In practice, it was found that when the A–matrix was based on the homogeneous case the diagonal terms were between 0.97 and 1.01 while the off diagonal terms were all less than 0.03. The same should be true in either the homogeneous case or the target case. It can thus be assumed that $A_h \cong A_t$, where h and t are referred to the homogeneous and target cases respectively.

This is a major assumption in that it allows this method to use the computed values of A as determined from the homogeneous case when computing target conductivity distribution. In this report all measurements are for determining the real part of the conductivity distribution, the only real part of the admittance matrix is considered. The phantom conduction matrix which only includes the electrode nodes can be obtained from the experimental data for any conductivity distribution.

If the preconditioning matrix, A, in Equation (5.19) is considered as a partitioned matrix, let the partition which belongs to the boundary nodes be A_{11}. This partition, A_{11}, is called the *subspace corrector* for eliminating the unmodeled features from the experimental data. The A_{11} matrix can be calculated in a similar way in Equation (5.18) by using the phantom conductance matrix and the phantom resistance matrix. Therefore, the subspace corrector is calculated by

$$A_{11}^{*} = R_p^{*}\, G_p^{*}. \tag{5.20}$$

where R_p^{*} is an $E \times E$ phantom resistance matrix calculated from the electrode voltages and currents extracted from the voltage solution from the finite element model in Equation (5.15) based on specified excitation currents applied to the finite element model with uniform conductivity. The matrix G_p^{*} is the phantom conductance matrix directly calculated from the experimental electrode voltage and current measurements obtained from the phantom with homogeneous conductivity distribution to be described in Section 6.7.3 of (in Chapter 6). Also, superscript "*" used in these matrices indicates that these matrices are conditioned by the reference electrode voltage to make their rank E instead of $E - 1$.

Therefore, let the given experimentally observed voltage data in the upper partition V' be V_1'. Then, V_1' is transformed to the finite element solution domain by

$$V'_{oEP\times 1} = \text{vec}_{(E\times P)\rightarrow(EP\times 1)}\ (A^{*}_{11E\times E}\ V^{*'}_{1\ E\times P}), \tag{5.21}$$

where $\text{vec}_{(E\times P)\rightarrow(EP\times 1)}$ is simply an operator which stacks all the P columns of an $E \times P$ matrix into an $EP \times 1$ vector. Using the *preconditioned* boundary voltage measurements, V_o', the least square error for any conductivity distribution becomes

$$\Phi(\sigma) = \frac{1}{2}\left\{f - V'_o\right\}^T \left\{f - V'_o\right\}, \tag{5.22}$$

and it is minimized to find unknown conductivity distribution.

It indicates that preconditioning the voltage vector with the matrix A^{*}_{11} should eliminate the effect of errors in modeling and computation, and allow the true admittance matrix to be obtained from the measurements.

For the present time, the matrix A^{*}_{11} is determined from the homogeneous case, and then applied to the target cases without any change. To the extent that the elements are insensitive to the internal conductivity distributions, the elements may be expected to correct boundary voltage measurements to compensate all errors in experiments: measurement construction, modeling, numerical, etc. Thus, the "preconditioned" voltage matrix, in the ideal case, is identical to that which has been measured had all errors been eliminated and is computed before image iteration is undertaken. However, for future improvement, it seems reasonable that the matrix A^{*}_{11} can be computed from many different target cases and then a method found to apply the variations of this matrix with conductivity distribution in a way which will let this method being directly applied to the unknown distribution problem.

5.6 Development of the Exponential Finite Element Scheme

One way to accurately represent the overall variable conductivity distribution is to choose *fine* elements where the conductivity function rapidly changes, and coarse elements

where slow changes of conductivity is expected. For example, Figure 5.5(a) illustrates a one–dimensional conductivity problem defined by Equation (5.1) could be represented by M line elements appropriately refined near the regions of rapid variation of conductivity function $\sigma(x)$ (as shown by the heavy curve). Hence, the conductivity variation here is accurately modelled by using mesh refinement. Assume at this point that the conductivity distribution is the distribution at a certain iteration, and the mesh has to be regenerated when a new conductivity distribution obtained after the next iteration. However, re–meshing techniques used after every iteration require a very sophisticated mesh generation and mesh refinement procedures; these procedures are difficult to handle particularly in two– and three–dimensional problems.

An alternative method proposed in this report is to use uniform elements with a special conductivity model function to piecewise model conductivity variation in each element. The solution domain is discretized by a uniform–element mesh, and the conductivity variation is numerically modelled as shown in Figure 5.5(b) by using an exponentially varying conductivity model in element–i defined as $\sigma_i(x) = \sigma_{0,i} \exp\left[a_i\ (x - x_{0,i})\right]$, where $\sigma_{0,i}$ is the conductivity value at the center coordinate, x_i, and a_i is the fitting parameter which represents the slope of the conductivity variation in element–i. Using this exponential model, however, requires development of a special analytical scheme which includes deriving new exponential shape functions used for the finite element procedure.

The linear term in the exponential conductivity model described previously has a limited capability to represent only monotonically increasing or decreasing conductivity variations. This exponential model can further be improved by adding a quadratic term in the exponent as $\sigma_i(x) = \sigma_{0,i} \exp\left[a_{i,1}\ (x - x_{0,i})^2 + a_{i,2}\ (x - x_{0,i})\right]$. The exponential–quadratic conductivity model has ability to represent nonmonotonic variations.

(a)

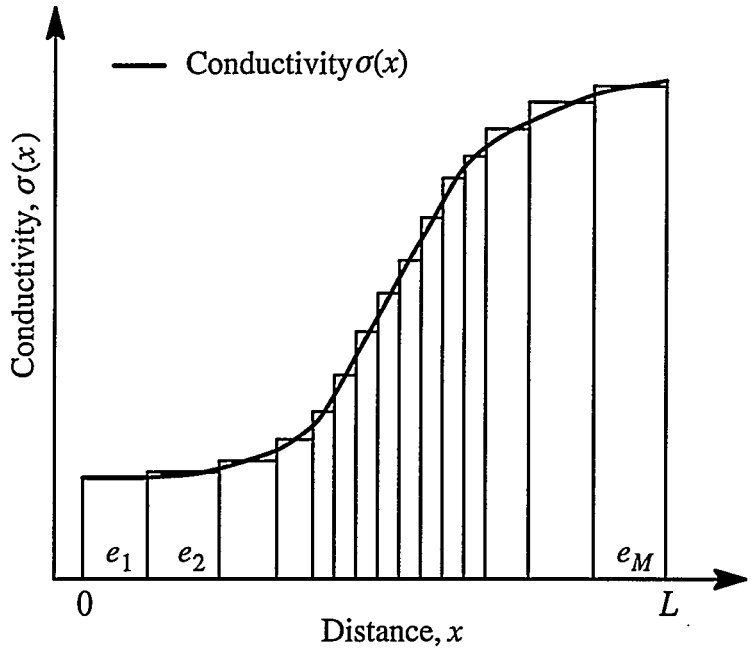

(b)

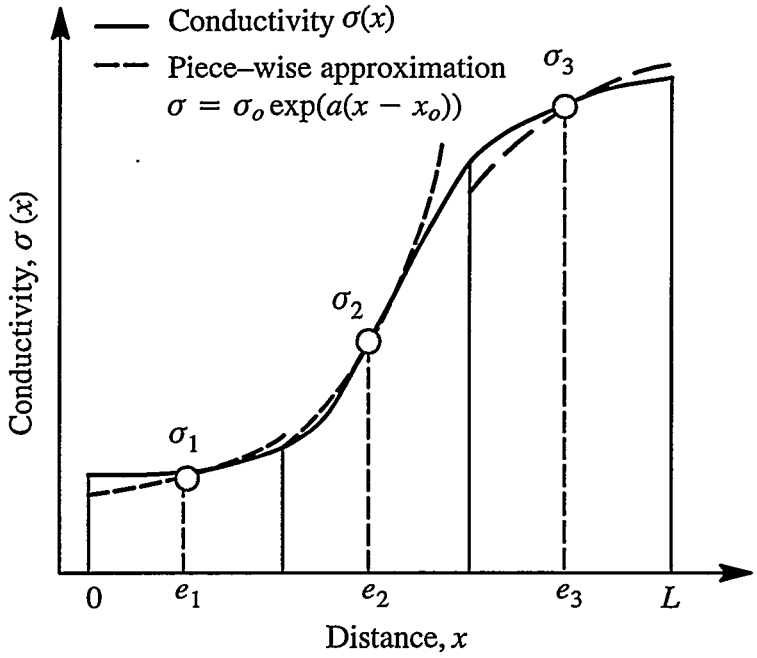

Figure 5.5 **Two methods to properly model the conductivity variation in a one–dimensional context: (a) representation of the conductivity variation by constant–conductivity elements with varying sizes; (b) with uniform–sized elements with varying conductivity in each.**

The problems considered in electrical impedance tomography system are applied to binary gas–liquid mixtures. Whereas, in actuality, the conductivity distribution would be expected to piecewise continuous, the conductivity variation is locally approached by a model function. Especially, for gas–liquid systems to be of interest in this report, the conductivity changes between zero and a finite value. After normalizing the entire conductivity variation relative to the background conductivity, the conductivity distribution takes values between 0.0 and 1.0. Therefore, this variation of conductivity can be piecewise approached by using rectangular elements with exponential conductivity functions.

Exponential functions are selected because of:

- their ability to fit to rapid changes in desired conductivity variations to be fitted;
- their separability property which provides a locally analytical approximation to potential function in each element. Therefore, the potential function can be expressed as a product of functions in each direction of coordinate system.

Therefore, the "exponential scheme" or "exact numerical scheme" developed by Baliga and Patankar [125] is applied in finite element form. This method which, as stated earlier, is known for obtaining solutions which eliminate effects of *false diffusion* in finite element computations, allows for the use of internal, exponentially–shaped conductivity variations in each cell. In this way, the total number of cells required to depict the overall conductivity field may be significantly reduced. Exponential shape functions are derived considering Poisson's equation in one–dimension, finding a locally analytical solution for the potential function for a locally variable conductivity function, and then applying the result to two dimensions. While such models are not unique in possible shape–function selection, they are desirable because of their separable characteristics.

5.6.1 Bilinear Exponential Conductivity Model

The basic one–dimensional expression for the exponential model, introduced in Section 5.4.2, will be extended to analytically two–dimensional problems using a bilinear exponential conductivity model. This model gives two–dimensional conductivity variation as

$$\sigma(x,y) = \sigma_0 \exp\left[a\ (x - x_0) + b\ (y - y_0)\right], \tag{5.23}$$

where the coefficients a and b are parameters to be determined, σ_o is the conductivity at the element reference point (x_o, y_o). The constant conductivity lines for this model are straight lines whose direction is determined by the ratio of a and b.

In defining an exponential function to represent conductivities inside each element, three degrees of freedom per element are introduced instead of one as in the previous version using constant–conductivity elements: a; b; σ_o. If all these parameters are included in the iterative sequence, the memory needed for the Hessian is 9 times bigger than previously required. One way to overcome this difficulty is to investigate which variables have major affect on the convergence. The results based on experimental data have shown that the problem is more sensitive to the central conductivity value σ_o rather directional sensitivity parameters a and b. Thus, the inverse problem is treated as an M–unknown problem, and only the central conductivity for each element in the model is sought by iteration.

5.6.2 Biquadratic Exponential Conductivity Model

It was found that the bilinear shape function was inadequate to properly image curved, discrete domains of zero conductivity, especially if the domain is small relative to the element size. The conductivity value may have an extreme point somewhere inside the element, and this case cannot be represented by a bilinear–exponential function such as giv-

en in Equation (5.23). If the argument of the exponential function in Equation (5.28) is considered to represent characteristic curves along which conductivity is constant, a higher degree argument, say second degree, would allow curved lines of generally circular, elliptic, parabolic or hyperbolic shape along which conductivity would be fixed. Among the models investigated, the following biquadratic exponential conductivity model is suggested:

$$\sigma(x,y) = \sigma_0 \exp[h(x,y)], \tag{5.24}$$

with $h(x,y)$ being a deviation function relative to the element center (x_o , y_o) given as

$$h(x,y) = \begin{Bmatrix} a_1(x-x_0)^2 + a_2(x-x_0) + \\ b_1(y-y_0)^2 + b_2(y-y_0) \end{Bmatrix}, \tag{5.25}$$

where a_1, a_2, b_1 and b_2 are the parameters to be determined which approximately define the global conductivity distribution in the problem domain.

5.6.3 Estimating the Spatial–Sensitivity Parameters of the Conductivity Model

If the conductivity distribution inside an element is known at several points, the slope parameters of the conductivity model can be obtained by using the method of least squares as follows.

Consider the exponential bilinear model in Equation (5.23). To approximate the slopes a and b, define a new coordinate system as

$$\begin{aligned} \bar{x} &= x - x_0 \\ \bar{y} &= y - y_0, \end{aligned} \tag{5.26}$$

where x_o and y_o is the central coordinates of each element. The transformed model is written as

$$\sigma(x,y) = \sigma_o \exp(a\ \bar{x} + b\ \bar{y}). \tag{5.27}$$

A logarithmic transformation yields the linear result

$$f_i \equiv f(\bar{x}_i, \bar{y}_i) = \ln\left[\frac{\sigma_i}{\sigma_0}\right] = a\ \bar{x}_i + b\ \bar{y}_i, \tag{5.28}$$

where the σ_i's are the conductivity values to be fitted at N distinct subspace element coordinates, $(\bar{x}_i, \bar{y}_i)$ obtained from the previous iteration, with σ_o being the central value found from the current iteration.

To obtain a least square fit to N conductivity values, define an error function

$$\Phi(a,b) = \frac{1}{2}\sum_{i=1}^{N}\left[f_i - (a\ \bar{x}_i + b\ \bar{y}_i)\right]^2, \tag{5.29}$$

and then, minimize the error function with respect to the model parameters by

$$\begin{aligned} \frac{\partial \Phi}{\partial a} &= \sum_{i=1}^{N} \bar{x}_i \left[f_i - (a\ \bar{x}_i + b\ \bar{y}_i)\right] = 0 \\ \frac{\partial \Phi}{\partial b} &= \sum_{i=1}^{N} \bar{y}_i \left[f_i - (a\ \bar{x}_i + b\ \bar{y}_i)\right] = 0. \end{aligned} \tag{5.30}$$

A closed form solution to Equation (5.30) is obtained as

$$\begin{aligned} a &= \frac{\sum \bar{x}_i\ \bar{y}_i \sum \bar{y}_i f_i - \sum \bar{y}_i^2 \sum \bar{x}_i f_i}{\left(\sum \bar{x}_i\ \bar{y}_i\right)^2 - \sum \bar{x}_i^2 \sum \bar{y}_i^2} \\ b &= \frac{\sum \bar{x}_i\ \bar{y}_i \sum \bar{x}_i f_i - \sum \bar{x}_i^2 \sum \bar{y}_i f_i}{\left(\sum \bar{x}_i\ \bar{y}_i\right)^2 - \sum \bar{x}_i^2 \sum \bar{y}_i^2}. \end{aligned} \tag{5.31}$$

Similarly, for the exponential biquadratic conductivity model defined in Equations (5.24) and (5.25), exactly the same procedures are applied, and an error function is formed as

$$\Phi(a_1, a_2, b_1, b_2) = \frac{1}{2}\sum_{i=1}^{N}\left[f_i - (a_1\,\bar{x}_i^2 + b_1\,\bar{y}_i^2 + a_2\,\bar{x}_i + b_2\,\bar{y}_i)\right]^2, \quad (5.32)$$

and then, minimizing conditions for Equation (5.32) results in

$$\begin{bmatrix} \sum \bar{x}_i^4 & \sum \bar{x}_i^2\,\bar{y}_i^2 & \sum \bar{x}_i^3 & \sum \bar{x}_i^2\,\bar{y}_i \\ & \sum \bar{y}_i^4 & \sum \bar{x}_i\,\bar{y}_i^2 & \sum \bar{y}_i^3 \\ & \text{Symmetric} & \sum \bar{x}_i^2 & \sum \bar{x}_i\,\bar{y}_i \\ & & & \sum \bar{y}_i^2 \end{bmatrix} \begin{bmatrix} a_1 \\ b_1 \\ a_2 \\ b_2 \end{bmatrix} = \begin{bmatrix} \sum \bar{x}_i^2\,f_i \\ \sum \bar{y}_i^2\,f_i \\ \sum \bar{x}_i\,f_i \\ \sum \bar{y}_i\,f_i \end{bmatrix} \quad (5.33)$$

The slope parameters a_1, a_2, b_1 and b_2 are obtained numerically solving the symmetric linear system in Equation (5.33).

5.6.4 Profile of the Electrical Potential

To develop a new finite element exponential scheme, exponential shape functions are also utilized consistent with the requirement for a general solution to Poisson's equation given in Equation (5.1). As indicated in Baliga and Patankar [125], and Ramadhyani and Patankar [106], the two–dimensional problem can be solved by combining one–dimensional solutions. Thus, one should seek a solution to the one–dimensional problem

$$\frac{d^2\phi}{dx^2} + \frac{\sigma_x}{\sigma}\frac{d\phi}{dx} = 0, \quad (5.34)$$

with the following boundary conditions

$$\begin{aligned} x = 0 \quad & \phi = \phi_0 \\ x = L \quad & \phi = \phi_L, \end{aligned} \quad (5.35)$$

and the solution to the problem in Equation (5.34) will be in the form of

$$\phi(x) = C_0 + C_1 \int e^{-\int p(x)dx} dx, \tag{5.36}$$

where $p(x) \equiv \sigma_x/\sigma$ and where C_0 and C_1 are integration constants. Also, note that for the bilinear model, this ratio in the x–direction is $p(x) \equiv \sigma_x/\sigma = a$, and similarly for the y–direction defined as $p(y) \equiv \sigma_y/\sigma = b$.

Variation of ϕ for different values of the σ_x/σ ratio is shown in Figure 5.6. Note that the variation of ϕ between the boundary values of ϕ_0 and ϕ_L is far from being linear in the presence of a strong convection term, bending in the direction of current flow. This is, of course, because of the one–dimensional current flow case, the potential gradient changes most rapidly in regions of high resistivity or low conductivity. This tendency smoothly approaches a linear variation as the σ_x/σ ratio goes to a limit value of zero. These curves in Figure 5.6 show that using linear trial functions selected for the potential function is a "bad" choice, and therefore a better profile will be in the form of

$$\phi(x) = C_0 + C_1 \exp(-\frac{\sigma_x}{\sigma}x). \tag{5.37}$$

Define $\psi(x) = \exp(-\frac{\sigma_x}{\sigma}x)$, the constants C_0 and C_1 are

$$\begin{aligned} C_0 &= \frac{\phi_0\,\psi(x_2) - \phi_L\,\psi(x_1)}{\psi(x_2) - \psi(x_1)} \\ C_1 &= \frac{\phi_L - \phi_0}{\psi(x_2) - \psi(x_1)}, \end{aligned} \tag{5.38}$$

determined from the boundary conditions in Equation (5.35).

Use of this result yields conductivities which are constant on straight line "characteristics" which do not produce acceptable results in gas–liquid systems. A better result is obtained by allowing the conductivity field to take on biquadratic shapes. These have the

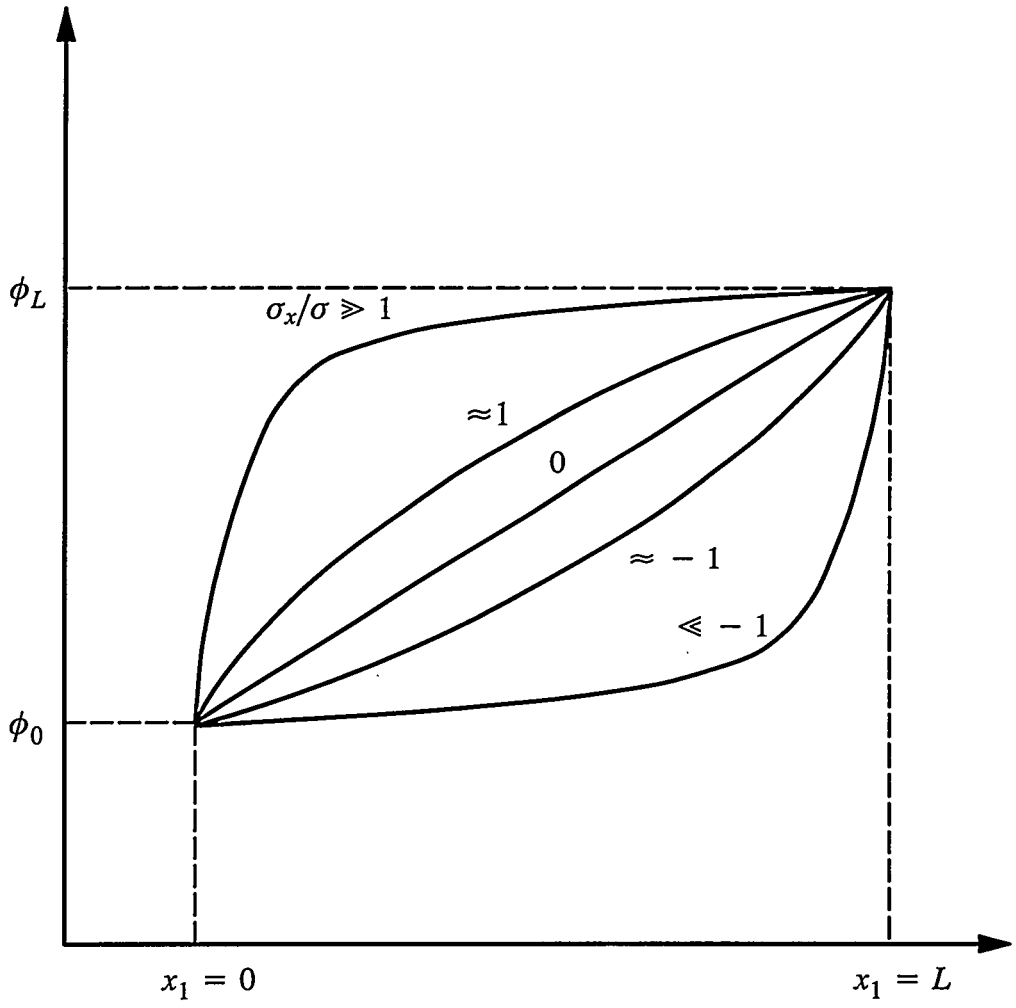

Figure 5.6 **Variation of the potential function for different values of the σ_x/σ ratio.**

potential to simulate circular, elliptic, parabolic or hyperbolic surfaces which divide regions of significantly differing conductivity. Thus, for the quadratic exponential conductivity model in Equations (5.24) and (5.25), rather than being constant, the integration parameter, $p(x)$, becomes

$$p(x) = g_1 + g_2 x, \tag{5.39}$$

where $g_1 = -2a_1x_o + a_2$ and $g_2 = 2a_1$. The profile of the electrical potential in one dimension becomes

$$\phi(x) = C_0 + C_1\psi(x), \tag{5.40}$$

where

$$\psi(x) \equiv \begin{cases} \text{erf}(\tau[x]) & g_2 > 0 \\ \exp(-g_1 x) & \text{for} \quad g_2 = 0 \\ \text{daw}(\tau[x])\exp(\tau^2[x]) & g_2 < 0, \end{cases} \tag{5.41}$$

where erf( ) is the error function, daw( ) is called Dawson's integral defined in Reference [137] as $\text{daw}(x) = \exp(-x^2)\int_0^x \exp(t^2)\,dt \;\; (0 \le x < \infty)$, and with the following definitions

$$\tau(x) \equiv s(x - x_s), \quad \text{where} \quad s \equiv \sqrt{g_2}\ , \ \text{and} \quad x_s \equiv \frac{-g_1}{2g_2}\ . \tag{5.42}$$

Therefore, even in the case of a more complicated conductivity variation, the potential profile can be analytically obtained and be utilized in the development of shape functions.

5.6.5 Development of Shape Functions

Before starting the development of the finite element shape functions, the electrical conduction phenomenon has to be examined, and some assumptions have to be made. Since the steady state electrical conduction problem considered in this study is a linear function of the conduction current, the general solution to the electrical potential can be obtained by implying superposition of the potential profiles in each coordinate direction. Consider, for example, the rectangular element in Figure 5.7. in which the conductivity variation is represented by an exponential bilinear model, and the electrical current density vector assumed constant in both magnitude and direction. An r–n coordinate system is locally defined in this element by defining the r–axis in the gradient direction of the constant conductivity lines shown by a dashed line along the n–axis. The current density vector defined here has an angle θ to the r–direction. If the components of the electric current density J are considered in the r– and n–directions as J_r and J_n, respectively, the potential profiles in each direction can be analytically obtained from integration in Equation (5.36). The potential in the r–direction varies as $\exp(-\frac{\sigma_r}{\sigma} r)$, and in the n–direction as a linear function of n. Then, combining these two profiles in the sense of superposition will give a two–dimensional function with three constants

$$\phi(r,n) = C_1 + C_2 \exp(-\frac{\sigma_r}{\sigma} r) + C_3 n. \qquad (5.43)$$

The two–dimensional analytical solution obtained in Equation (5.43) is flow–directed solution representing the most general case: for instance, if the electrical current is only directed in the normal direction, then the potential profile is a linear variation in the n–direction. On the other hand, if the current is directed in the r–direction, the potential profile is an exponential function. Otherwise, the solution is combination of the two profiles. Note that if the gradient of the conductivity, σ_r, is smoothly decreased to a limit value of

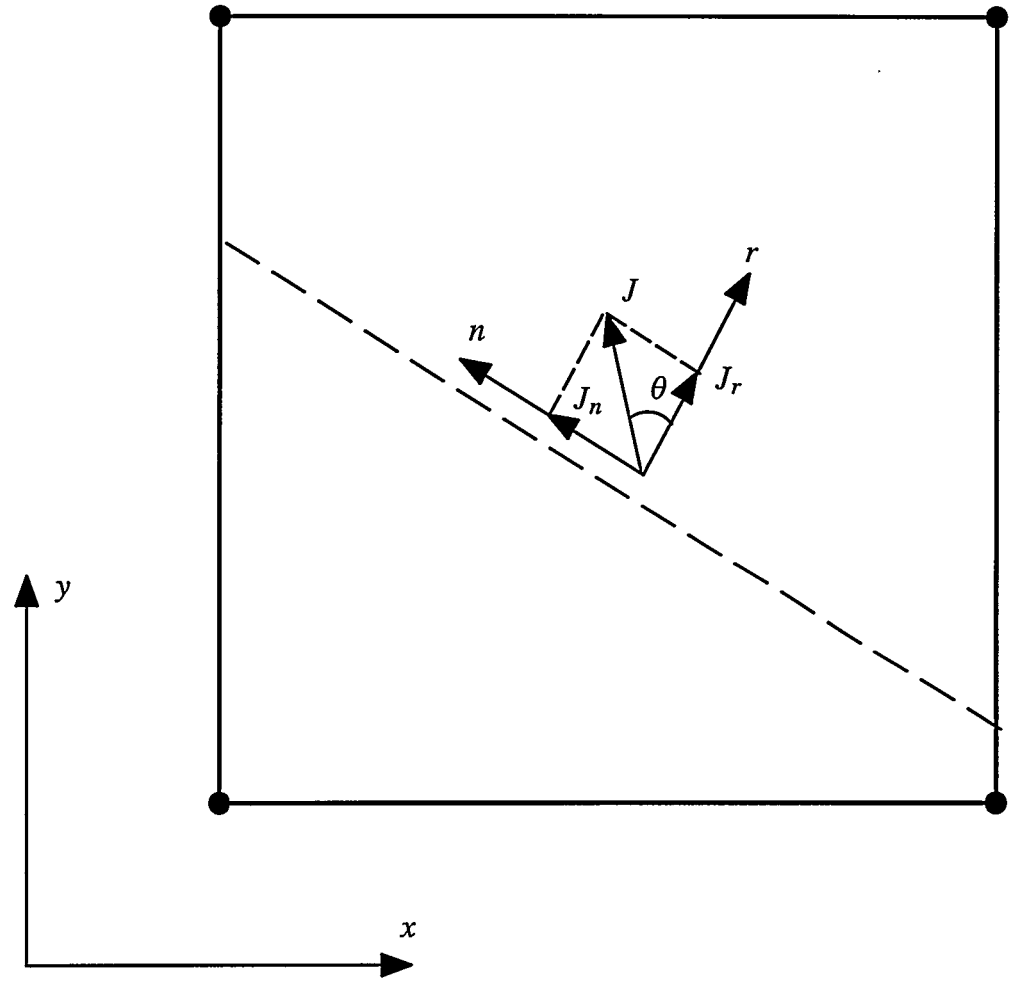

Figure 5.7 **A rectangular element having an exponential bilinear conductivity model (a constant conductivity value on the dashed line) and a locally defined *r–n* coordinate system. The current density is assumed constant having an angle θ to the *r*–axis.**

zero, then the term $\exp(-\frac{\sigma_r}{\sigma}r) \rightarrow 1 - \frac{\sigma_r}{\sigma}r$, and therefore Equation (5.43) smoothly reduces to a linear function of the local coordinates as $\phi(r,n) = C_1 + C_2 r + C_3 n$.

This potential profile in Equation (5.43) was previously developed and used by Raithby [117] for finite element solution of convective flow and heat transfer problems. The potential profile can be considered a suitable shape function with three arbitrary constants and it can be used for triangular elements. For the rectangular elements however an additional term is need. Ramadhyani [126] examined several possibilities for this additional term, and he suggested a potential function used for quadrilateral elements:

$$\phi(x,y,r,n) = C_1 + C_2 \exp(-p_r\, r) + C_3\, n + C_4\, [\exp(-p_x\, x)-1] \\ [\exp(-p_y\, y)-1], \qquad (5.44)$$

where r is the direction of $\nabla\sigma$, σ_r, and n is the direction which is normal to this direction. Both x and y are the Cartesian coordinates. Alternatively, the potential function is expressed in the form of combinations of the solutions in the $x-$ and $y-$directions (Jones et al. [46]) as

$$\phi(x,y) = C_1 + C_2\, \psi(x) + C_3\, \psi(y) + C_4\, \psi(x)\, \psi(y). \qquad (5.45)$$

For an element with a linear exponential conductivity model $\psi(x) = \exp(-ax)$ and $\psi(y) = \exp(-ay)$ obtained from Equation (5.36). Substituting these terms into Equation (5.45) for both $x-$ and $y-$coordinates results in

$$\phi(x,y) = C_1 + C_2 \exp(-ax) + C_3 \exp(-by) + C_4 \exp[-(ax + by)], \quad (5.46)$$

where $\phi(x,y)$ is an approximation to the electric potential function obtained by combining the analytical solution in both directions of the Cartesian coordinate system. Similarly, the

same procedure can be done for a quadratic exponential conductivity model using the terms in Equation (5.41).

If the two–dimensional potential function obtained in Equation (5.45) is chosen as the element shape functions, the potential function may be expressed in terms of these shape functions as

$$\phi(x,y) = \sum_{j=1}^{4} N_j \, V_j, \tag{5.47}$$

where $N = N(x,y)$, and V_j being the corner node potentials for the element. Thus, the potential function inside the element matches potentials, V_j, at four corner–nodes, 1–4, of a rectangular element. Define a function $D(\mu)$ from Equation (5.41)

$$D(\mu) \equiv \frac{\psi(\mu) - \psi(\mu_1)}{\psi(\mu_2) - \psi(\mu_1)}, \tag{5.48}$$

then the element shape functions becomes (Jin [138])

$$N_j = \begin{cases} [1\text{–}D(x)]\ [1\text{–}D(y)] & j = 1 \\ D(x)\ \ [1\text{–}D(y)] & j = 2 \\ D(x)\ \ D(y) & j = 3 \\ [1\text{–}D(x)]\ \ D(y) & j = 4, \end{cases} \quad \text{for} \tag{5.49}$$

and using these shape functions, the admittance matrix entries, $Y_{\ell m}$, of an element e may be calculated as

$$Y_{ij} = \int_{V(\Omega_e)} \sigma \, \nabla N_i \cdot \nabla N_j \, dV. \tag{5.50}$$

In the work describer herein, the result of the integral in Equation (5.50) is numerically computed by using the Gauss–Legendre quadrature formula previously defined in Section

4.6.1. Adequate accuracy is obtained by using a 12 × 12 grid with 12 integration weights selected from Table A.1 in Appendix A.

Computation of the local element matrices, and assembling these local matrices lead directly to the global system of equations previously given in Equation (4.43). The voltage distribution with the given boundary current measurements are obtained for the inverse solution procedure to obtain the σ –distribution. The previously used uniform conductivity field to start the problem could be replaced by a better estimate based on some knowledge base.

5.7 Block Decomposition Method (BDM)

Although the original version of Yorkey's Newton–Raphson method is applied very successfully to certain problems, there are several limitations which may have significant effects on the overall performance of the reconstruction algorithm, such as convergence and resolution of results obtained by using standard finite element methods. Since the standard method uses constant–conductivity elements, difficulties arise when element boundaries are not aligned with target boundaries or where targets are smaller than the elements used. In these cases, the target boundaries cannot be accurately determined. Since the computational time increases dramatically with the number of elements, the method is efficient only for small mesh structures such as 8 × 8 or 16 × 16. The requirement of prohibitive computational resources to obtain reasonable resolution of images, even for two–dimensional geometries, is a major limiting factor for applying this method to a large class of real problems.

In this section, a major new development is described which circumvents the majority of the problems mentioned above. This method is termed the block decomposition method (BDM), and results in a major reduction in computational time compared with the

conventional finite element methods. The conductivity within each element is allowed to vary in a manner that the results can be continuous from element–to–element within the mesh. In this manner, much larger elements may be utilized in the computation while at the same time maintaining the degree of resolution and accuracy usually afforded only by a large number of small mesh elements. In general, the computational times vary even more rapidly than the cube of the number of elements. On the other hand, resolutions equivalent to those obtained with meshes up to 24×24 can thus be calculated by using an 8×8 or a 16×16 BDM model in a matter of several minutes rather than many hours.

The block decomposition method is really a combination of two separate new developments:

- Block decomposition which undertakes outer and inner iterations in a way which reduces computational effort by approximately three orders of magnitude;
- Exponential shape functions for the potential and conductivity fields to allow the conductivity and its first spatial derivative to vary continuously between elements.

In this way, the accuracy and resolution of fine–mesh reconstruction may be approached with a relatively coarse, rapidly converging element structure.

5.7.1 Concept

The concept of block decomposition method is simple. Starting with a uniform conductivity distribution, the best conductivity distribution is iteratively solved in the least–squares sense for a small number of elements. Consider Figure 5.8 showing a typical mesh which consists of 8×8 major elements. Each of these major elements are decomposed into, say, 3×3 or 4×4 subelements. The number of major elements must be chosen so that the measured boundary information is enough to calculate the conductivities of all the

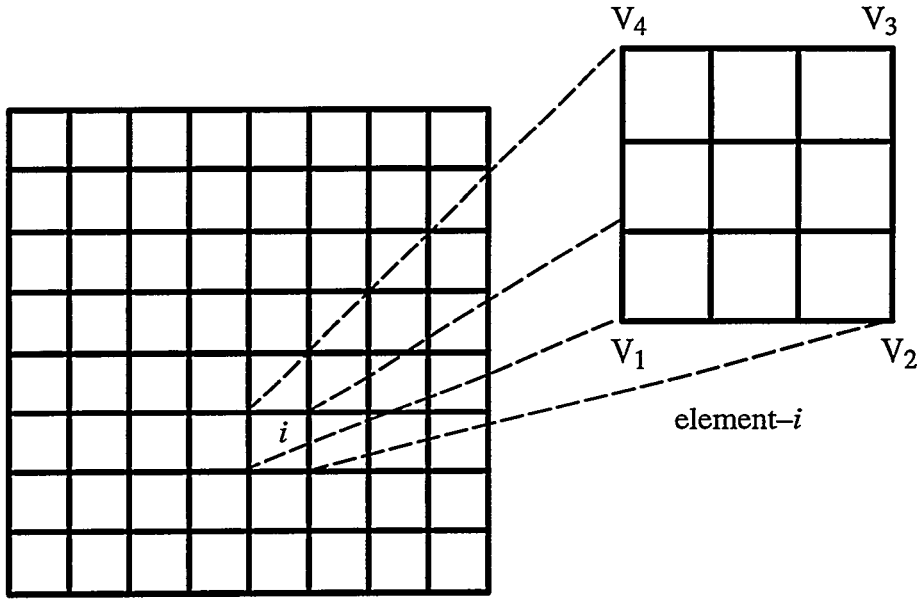

Figure 5.8 **A Coarse mesh and a decomposed major element to show the concept of the block decomposition method. Each major element is decomposed into 3×3 subelements to obtain of a solution which is equivalent to a 24×24 mesh.**

major elements. To reconstruct the conductivity distribution, the first iteration is started with uniform conductivity distribution and the electrical potential is solved inside the problem domain. Then, the potential values on the corners of the major elements are calculated by the forward solver. Using the measured and computed current and voltage data, conductivities of each major elements are next solved independently by using the standard inverse solution procedure. The major elements are then decomposed as in terms of shape functions for both the field potential and the conductivity distribution. Using these subelement conductivities the slopes of the exponential conductivity model are calculated and passed to the global forward solution for the next iteration step. The iterations are continued until the successive changes in the conductivities of the major elements are less than a given tolerance.

5.7.2 Outline of the Block Decomposition Algorithm

The steps of the block decomposition algorithm including three major routines are shown by the flow diagram in Figure 5.9. The two–dimensional cubic spline program fits the conductivities of all subelements obtained in the forward solution step, and interpolates the fitted conductivities in regular intervals at 16×16 locations in each major element of the 8×8 model as shown in Figure 5.10. This produces a 128×128 pixel array which represents the global conductivity distribution to be used for the finite element solution in the next iteration. After a converged conductivity distribution is obtained, the final solution in this pixel array is stored in a file for later use in the post–processing and image display processes.

The routine for the forward solution uses the exponential finite element scheme with the bilinear or biquadratic exponential conductivity shape functions. In this routine, the slopes of the conductivity model are determined by the least–squares method described

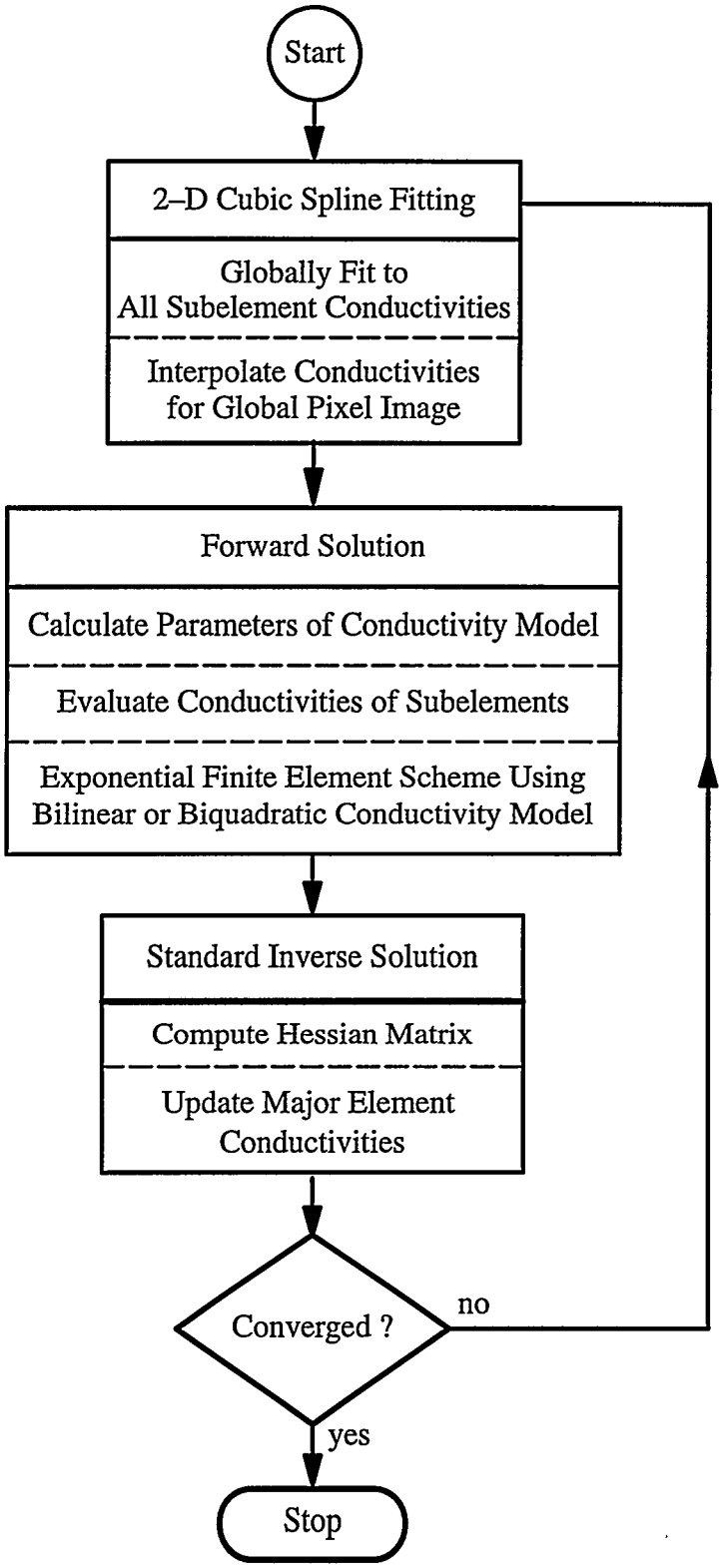

Figure 5.9 Flow Diagram of the Block Decomposition Algorithm.

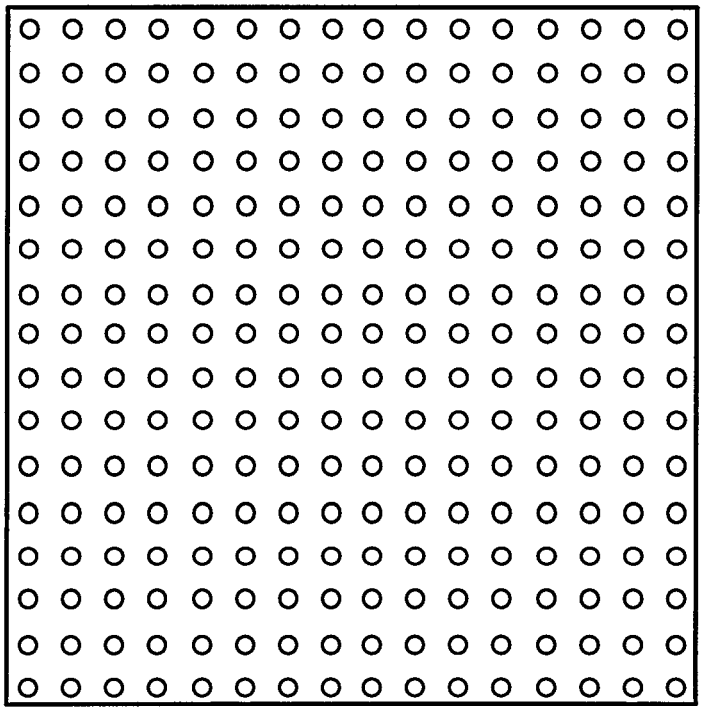

Figure 5.10 A major element and cubic spline interpolation of the fitted conductivity distribution at 16×16 locations represented by o.

in Section 5.6.3 and the conductivities at the center coordinates of the subelements are evaluated by using the selected conductivity model function (see Figure 5.11). Then, the global finite element equations using the exponential shape functions explained in Section 5.6 are assembled and solved to obtain the electrical potential distribution.

The routine for the inverse solution is called after the forward solution step to perform the standard numerical procedures in each Newton–Raphson iteration, including the direct calculation of the Hessian matrix and updating conductivities for each major elements. These procedures are the same as the procedures previously explained in Chapter 4.

Once the computations for any given iteration have been undertaken, there is a conductivity field which is, in effect, piecewise continuous having values of $\sigma_{0_{ij}}$ in each (i,j)–element (64 elements for a 8×8 element model). A cubic spline distribution is also available which exactly matches the major element and subelement conductivity values obtained in the previous iteration (with the exception of the first few iterations where special methods are used to start the problem)

The conductivity values are now assumed to vary exponentially in two directions in each major element according to a bilinear or biquadratic rule given by Equations (5.24) and (5.25). The subscript–0 coordinate values are center coordinates for each of the major elements. The conductivity thus tends to the computed value σ_0 at the center of each major element.

The values of the exponential biquadratic coefficients for the current iteration are determined to give a least squares minimum error fit to the spline conductivity distribution from the previous iteration. This forces the shape to lag one iterative step but allows current central conductivities of each major element to match the value for the current iteration. In

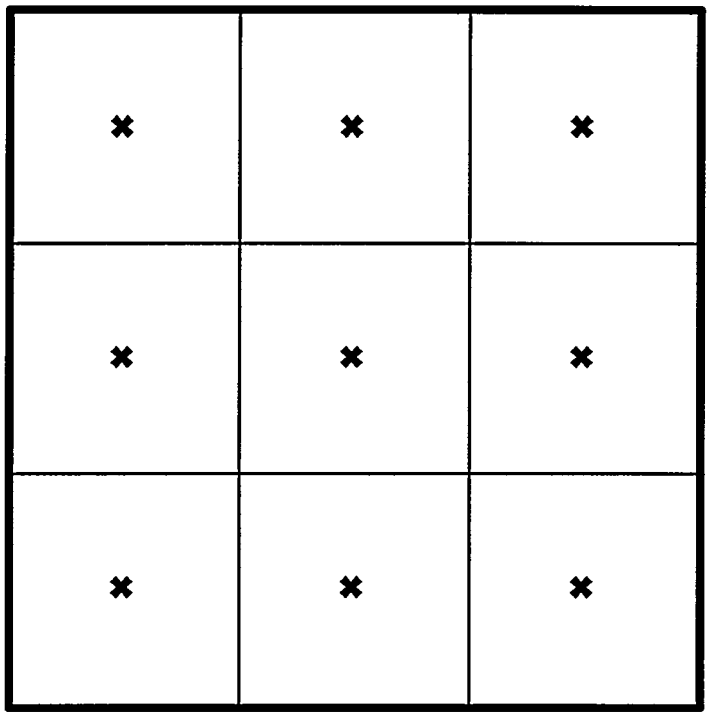

Figure 5.11 Subelements in a major element and the conductivity values of the subelements evaluated at the central coordinates shown by ✖ .

this respect, the resultant biquadratic exponential shape is a hybrid between current and one–step lagged values.

Conductivities are then computed for each of the subspace elements in the overall model using Equations (5.24) and (5.25). Note that only the central subelement (always a 3×3 subspace) in each major element has a value of σ_0 which matches the current iteration.

The spline fit is then updated by evaluating the conductivity at the center of each subspace element from the exponential function and using these values to determine the spline coefficients. For display purposes, conductivity is always computed from the spline fit using a 128×128 overlay to the basic model.

5.8 Extension to Three–dimensional Modeling

In the two–dimensional finite element models considered so far, current distribution inside the phantom is restricted to a single plane or constant in the third dimension. For the conductivity distribution varying along the axial direction, the current flux spreads out in all three dimensions. In actuality, however, with a three–dimensional phantom the potential distribution is not confined to a plane. If additional layers of electrode arrays are placed above and below the cross section of interest, a complete data set to reconstruct the three–dimensional conductivity distribution can be obtained with the additional cost of the electrode channels.

Direct three–dimensional modeling by the described procedures is, however, prohibitive in terms of both storage and computer–time requirements. Since conductivity distribution in three dimensions is complicated, the overall domain cannot be reconstructed in a single step, because of the increasing number of elements, electrodes, and excitations.

To date, there have been only a few papers dealing with three–dimensional electrical impedance tomography. The first three–dimensional finite element reconstruction results based on a synthetically generated data set are presented by Wexler et al. [37]. In order to show the applicability of the double constraint method to three dimensional geological and mineral prospecting problems, they placed electrodes on the top surface of a cubic conductive domain divided into $8 \times 8 \times 8$ cubic elements. They excited a pair of electrodes and took the voltage measurements in different pairs. The potential distribution is computed by the finite element method and used in reconstructions by the double constraint method they originally developed. Although, this method did not suffer from the limitations of storage and speed as the Yorkey's method does, the iterative method provided slowly converging results in 1700 iterations for an $8 \times 8 \times 8$ element structure.

Goble and Isaacson [139] and Goble [140] extended the two–dimensional NOSER method to three dimensions. Using the adaptive method described by Gisser et al. [56], they derived the "best currents" for a three–dimensional, 64–electrode cylindrical phantom which consists of four layers of electrode arrays (each layer having 16 electrodes). Then, they simultaneously applied these best current patterns (in the form of 63 orthogonal "stacked cosines") to all 64 electrodes to obtain data to calculate resistivities in 480 voxels (or volume elements). They compared their three–dimensional method to two–dimensional "slice–by–slice" method. They showed that the computational time required for simultaneous three–dimensional reconstructions is 64 times more than that required for a single two–dimensional slice having 120 voxels. Since one two–dimensional reconstruction is required for each of the four slices, the advantage of using the "slice–by–slice" method is 16:1. They reported, however, that three–dimensional method has the advantage with respect to more accurate target localization and higher target contrast resolution over the "slice–by–slice" method.

Ider et al. [141] developed a method to compensate the three–dimensional effects in the forward solution to the electrical potential problem. By assuming electrodes are placed in a single layer around a cylindrical domain with uniform conductivity distribution in the axial direction, they decomposed the forward problem into a series of 20 finite element solutions by using the Fourier expansion of both the boundary conditions and the potential field in the axial direction. They used this three–dimensional forward solution for the iterative equipotential lines method to reconstruct the conductivity distribution in human organs such as arms or legs.

In the literature reviewed, so far, there has been no attempt made to apply the Newton–Raphson method to three–dimensional problems. Although promising results obtained for simple problems, the methods presented by Wexler and his co–workers, and Ider and his co–workers avoid the closed form calculations in the sensitivity matrix used for the inverse solution. The method presented by Goble and Isaacson provides a one–step–reconstruction of the conductivities of the overall element layers but application to real problems is thus limited because of the requirement for increasing information, and iteration is not available to improve the results.

An alternative is to use the two–dimensional scanning techniques practiced in MRI and X–ray scanner methods making three–dimensional imaging possible without additional sensing layers. These methods utilize a the slice–by–slice scanning technique which may be extended to the finite element method.

5.8.1 Layer Model of the Phantom

Three–dimensional square test geometries using rod or plate electrodes, and their computational finite element grids are shown in Figure 5.12. In this case, the electric

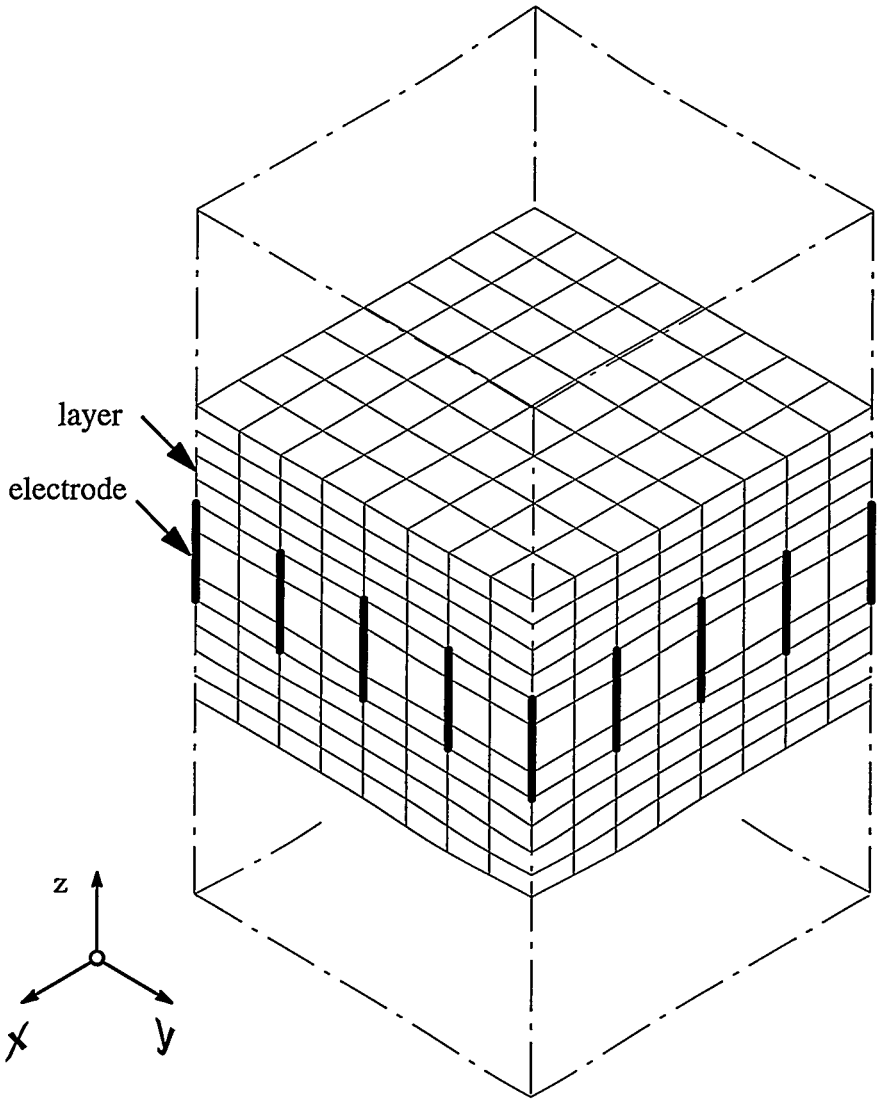

(a)

Figure 5.12 (continued overleaf)

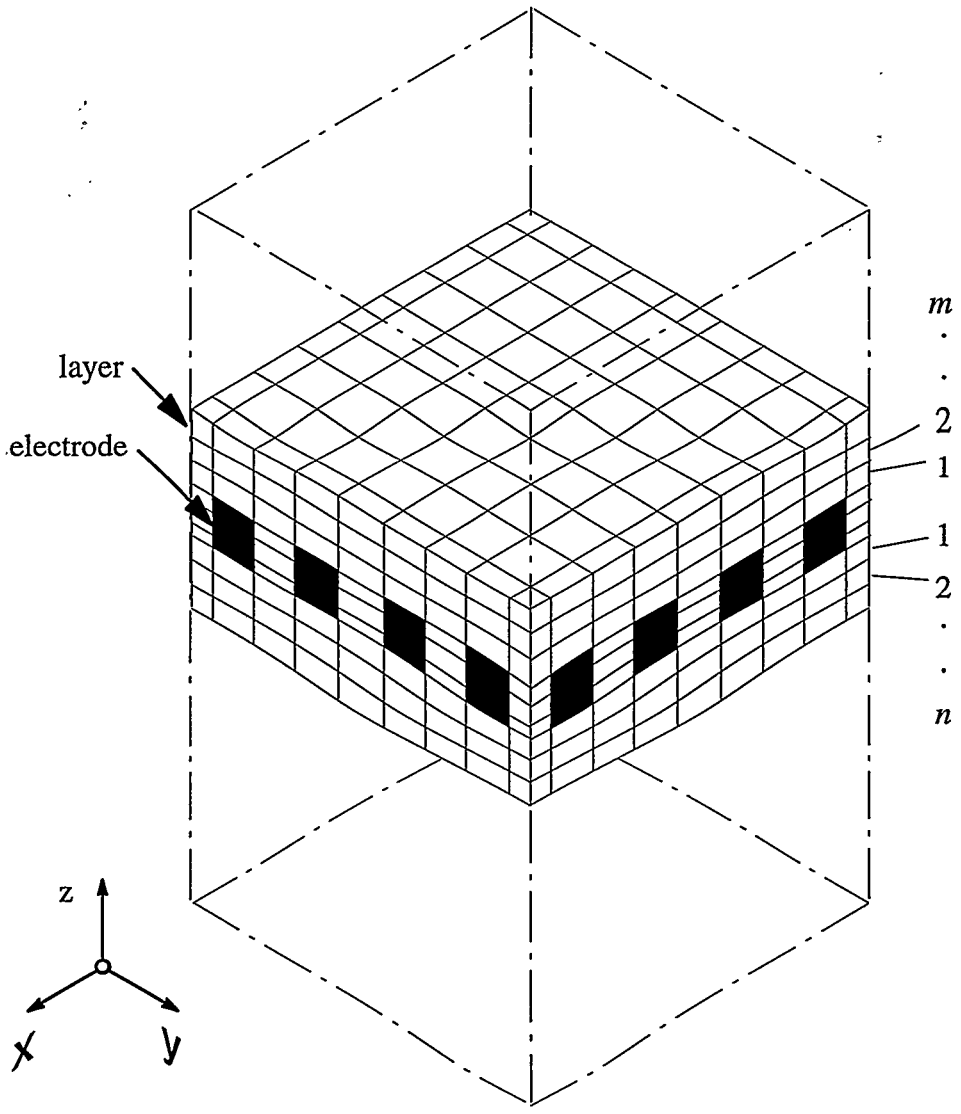

(b)

Figure 5.12 Three–dimensional test phantoms and their computational mesh structures with rectangular brick element layers: (a) a rod–electrode model; (b) plate–electrode model.

current flux is no longer two–dimensional. The magnitude of the three–dimensional distortion varies with the length of the electrodes in relation to the dimensions of the test cell. If the electrode length decreases, the amount of current leakage out of the scan plane will increase causing loss of sensitivity and inaccuracy in modeling using two–dimensional methods.

Figure 5.13(a) shows how the electrical current streamlines are formed when two electrodes are excited in a three–dimensional conductive medium. If the size of the each electrode is L, then we can consider a "uniform–flux" region U whose thickness is d and is less than the size of the electrodes ($d < L$). The relative size of the uniform flux region depends on the ratio d/L. In the point electrode case, for example, this size vanishes and the entire current flux leaks in the nonuniform current region NU. For electrodes which are much larger than the maximum electrode gap in the phantom, the leakage flux can be assumed negligible, and the problem may be considered as two–dimensional.

The three–dimensional phantom domain therefore is divided into two regions as illustrated in Figure 5.13(b). One of these regions is represented by thin layers of three–dimensional rectangular brick elements, each of which has the current density varying in the z–direction, but no excitation. The other is represented by two–dimensional, excited square elements which have only variation of the electrical current flux in the x–y plane at the electrode level. Therefore, the result is a three–dimensional admittance matrix.

It should be noted that a complete data set to reconstruct the overall conductivity distribution in the three–dimensional medium cannot be acquired since the measurements are obtained only at the electrode level. Therefore, the conductivity distribution in the layers below and above the electrode plane should either be known or should be approximated by making certain assumptions. If, for example, the conductivity distribution is uniform in

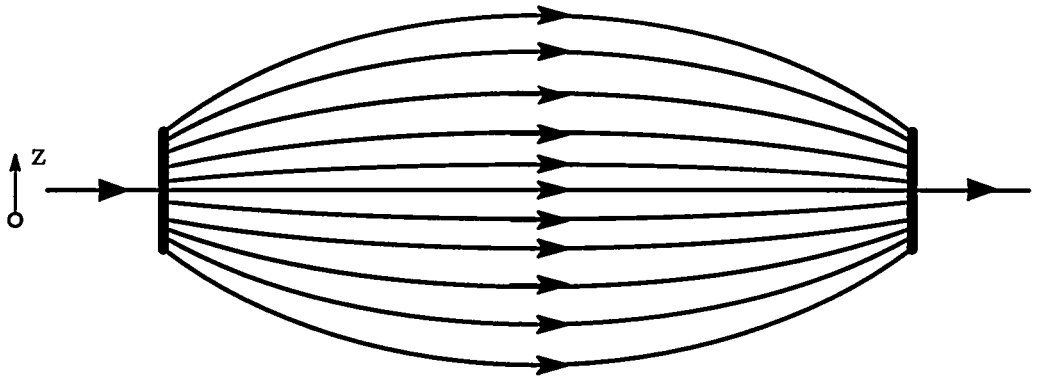

(a)

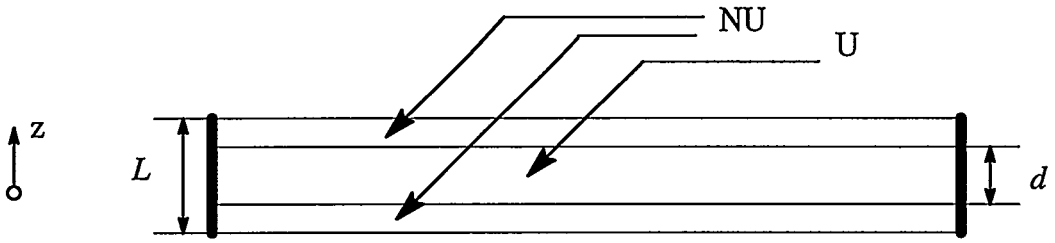

(b)

Figure 5.13 **Three–dimensional electrode model: (a) streamlines of electric current when two opposite electrodes are excited; (b) description of the dimensions of the uniform (U) and the nonuniform (NU) current regions between two opposite electrodes.**

the z–direction, or the length of targets are significantly larger than the length of the electrodes (by a factor of 2 or more), the conductivity distribution of all layers can be chosen equal so that the $\nabla\sigma \cdot \nabla\phi$ term is not modeled in the z–direction. This is a fundamental and major assumption made in the implementation of the three–dimensional reconstruction algorithm.

5.8.2 Layer Reduction Method

The admittance matrix includes some nodes which are not involved in two–dimensional scanning. These may be permanently removed from the algebraic equations by the "Kron reduction" technique (see Kron [142], [143]).

Refer to Figure 5.12. Let the layers be numbered as from 1 to m, starting with the first layer right above the the electrode plane to the topmost one, and from 1 to n starting with the one right below the electrode plane to the the last one at the bottom. The basic idea of the admittance network reduction technique is to start with the outmost layers m and n and recursively collapse the layers onto the previous layers [$(m-1)$–th and $(n-1)$–th layers] until nothing is left but the approximately uniform central layer.

Before the reduction technique is applied, the admittance matrix is a very sparse band matrix with dimensions $N(m+n+1) \times N(m+n+1)$. After collapsing all the layers on the electrode plane we obtain a smaller but a fuller $N \times N$ matrix. However, the off–diagonal terms representing the farthest nodes are weak in relation to the main eigenvalues of the matrix.

Figure 5.14 shows a three–dimensional admittance network layer before and after collapsing onto a lower layer. This yields a planar admittance network in which the prime–numbered nodes are eliminated.

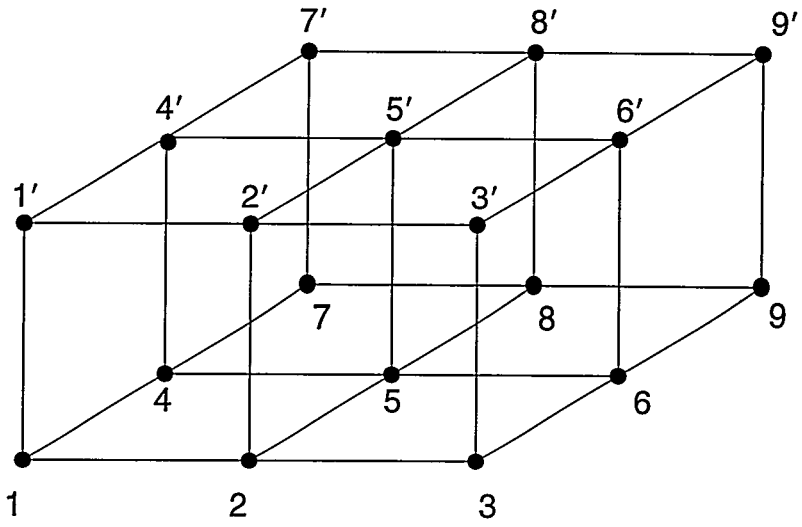

1–layer Network

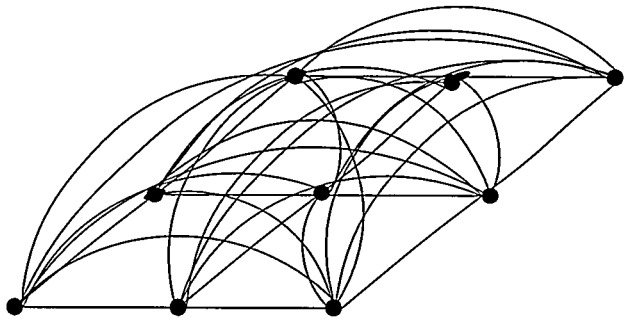

Collapsed Network

Figure 5.14 Reduction of a three–dimensional network into a planar network.

The nodal current equation and the admittance network for a two–layer admittance network with both nonuniform and uniform flux regions is written in the form of a symmetric block matrix

$$\left[\begin{array}{c|c|c} Y_{11}^{2D} + Y_{11}^{3D} & Y_{12}^{3D} & \mathbf{0} \\ \hline Y_{21}^{3D} & 2Y_{22}^{3D} & Y_{12}^{3D} \\ \hline \mathbf{0} & Y_{21}^{3D} & Y_{22}^{3D} \end{array}\right] \left[\begin{array}{c} V_1 \\ \hline V_2 \\ \hline V_3 \end{array}\right] = \left[\begin{array}{c} I^{2D} \\ \hline \mathbf{0} \\ \hline \mathbf{0} \end{array}\right]. \qquad (5.51)$$

The vector V_1 includes the potentials of the nodes in the "uniform flux" region, U, and V_2 and V_3 include the potentials of the nodes in the layer interfaces. Indices 2D and 3D denote the two–dimensional and three–dimensional admittance matrices of the admittance networks, respectively. The diagonal and off–diagonal block matrices are the self and mutual admittance matrices. In this case, the complete reduction of the nodes of the layers requires a two–step Kron reduction yielding

$$Y^{3D} = \left(Y_{11}^{2D} + Y_{11}^{3D}\right) - Y_{12}^{3D}\left(2Y_{22}^{3D} - Y_{12}Y_{22}^{3D^{-1}}Y_{21}^{3D}\right)^{-1} Y_{21}^{3D} \qquad (5.52)$$

and the reduced matrix equation is $Y^{3D}V = C^{2D}$. The method can be applied recursively to more than two layers by eliminating the layers in the similar way described in Equation (5.52).

Simplification. As part of the Newton–Raphson iterative scheme, the Hessian matrix required differentiation of the admittance matrix in terms of the element conductivities. In forming this matrix, variations in the electric current flux in a given element are expected to be insensitive to distant variations in conductivity. Therefore, it can be assumed that small perturbations of the conductivity in element–i only affects its immediate neighbors as

shown in Figure 5.15. The derivative elements of the matrix are thus set to zero except for those corresponding to the adjacent nodes of any given element.

After adding the first layer, the derivative of the admittance matrix of the planar network is approximated by taking the first partial derivative of the admittance matrix with respect to the conductivity of element–i resulting in

$$\frac{\partial \boldsymbol{Y}^{3D}}{\partial \sigma_i} \cong \left(\frac{\partial \boldsymbol{Y}_{11}^{2D}}{\partial \sigma_i} + \frac{\partial \boldsymbol{Y}_{11}^{3D}}{\partial \sigma_i} \right) - \frac{\partial \boldsymbol{Y}_{12}^{3D}}{\partial \sigma_i} \; \boldsymbol{Y}_{22}^{3D^{-1}} \; \boldsymbol{Y}_{21}^{3D}$$

$$+ \boldsymbol{Y}_{12}^{3D} \; \boldsymbol{Y}_{22}^{3D^{-1}} \; \frac{\partial \boldsymbol{Y}_{22}^{3D}}{\partial \sigma_i} \; \boldsymbol{Y}_{22}^{3D^{-1}} \; \boldsymbol{Y}_{21}^{3D} - \boldsymbol{Y}_{12}^{3D} \; \boldsymbol{Y}_{22}^{3D^{-1}} \; \frac{\partial \boldsymbol{Y}_{21}^{3D}}{\partial \sigma_i} \; . \qquad (5.53)$$

Equation (5.53) can be simplified by taking advantage of sparsity and symmetry. This is done by just storing the non–zero entries of $\partial \boldsymbol{Y}^{3D}/\partial \sigma_i$ in a small 16×16 array. This simplification not only saves computational time in the calculations for $\partial \boldsymbol{Y}^{3D}/\partial \sigma_i$ but also significantly reduces the effort for the computation of the Hessian matrix by eliminating the floating point arithmetic operations with the numbers of negligibly small magnitudes.

Number of Layers. In virtually all computations, there are anomalous variations in conductivity due to the fitness of the model and three–dimensional effects in the electrical field are not taken into account, among others. The effect of three–dimensional layering is to reduce these variations thereby presenting a more accurate picture of the actual case. Different situations require different numbers of layers. Typically, variations reduce as the number of layers increases. A simple case of the homogeneous field is shown in Figure 5.16 indicating that for this case little effect is seen in reconstructions when more than three layers are used (in the model shwon in Figure 5.12(a)) for the homogeneous case. However, a slight change in this result is expected for different target situations.

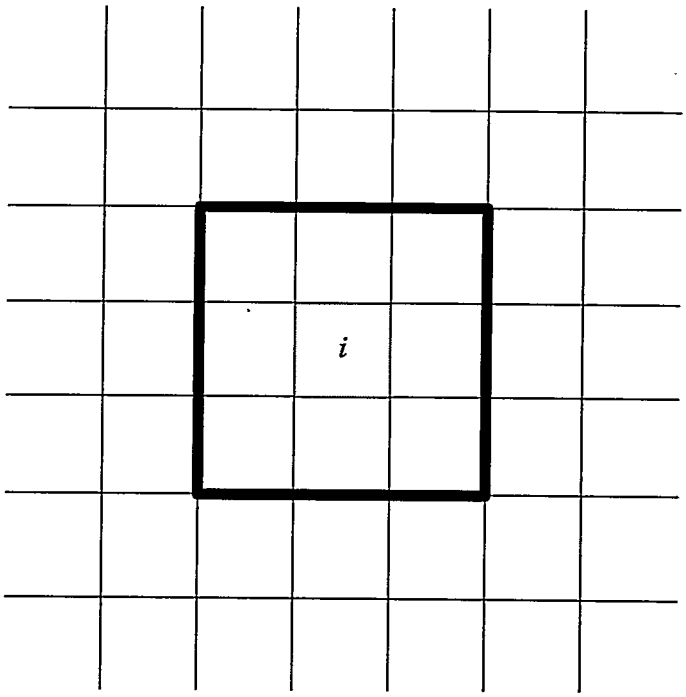

Figure 5.15 The elements (attaching the heavy line) in the neighborhood of the element–i.

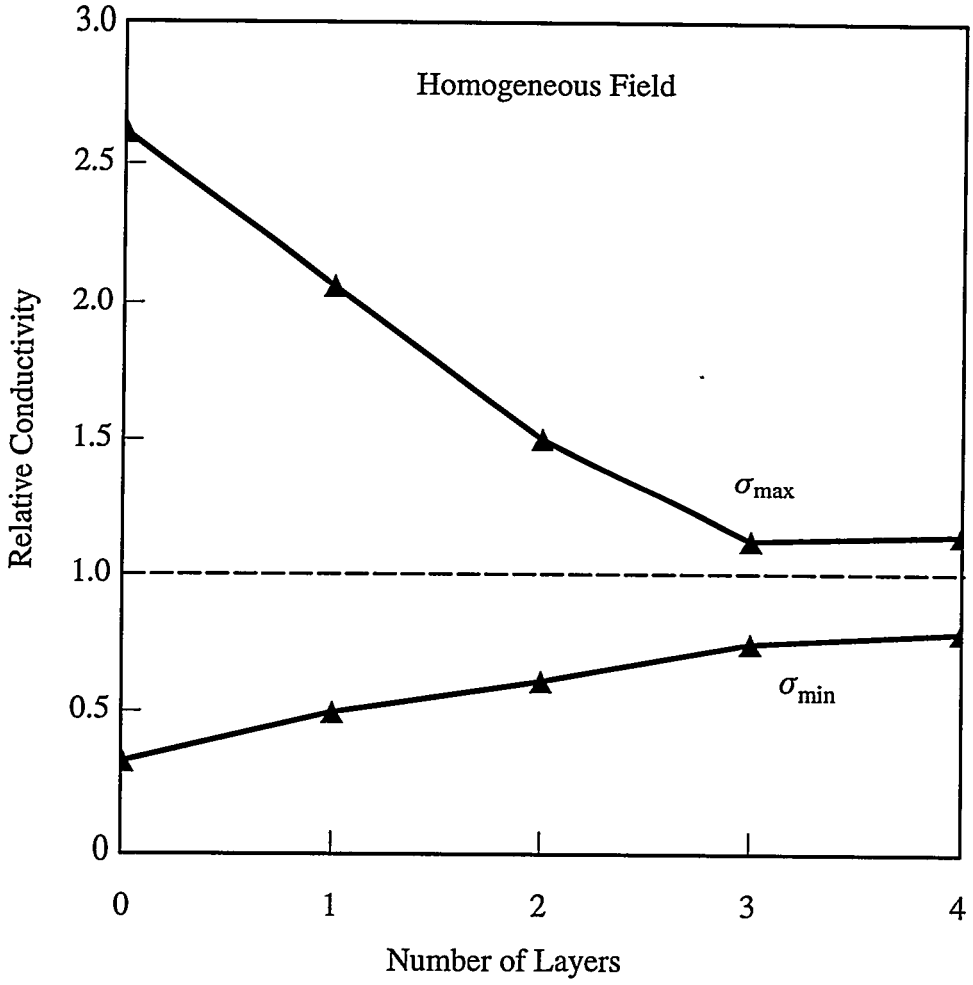

Figure 5.16 Reduction in the anomalous conductivity variations computed as the number of three–dimensional layers increases for the homogeneous field.

5.8.3 Discussion

Using the layer reduction method developed in this section has advantages over using a fully three–dimensional finite element model. If a full three–dimensional model is utilized, the dimension of the admittance matrix dramatically increases as more than the cube of the number of nodes used for the three–dimensional mesh. After inverting the admittance matrix, the inverse of the admittance matrix is a full matrix. For example, consider a three–dimensional finite element model which consists of L element layers and N nodes in each layer. The number of floating point numbers to be stored for the inverse admittance matrix is in the order of $(L + 1)^2 N^2$. On the other hand, since the nodes of the layers above and below the region of interest are eliminated by the layer reduction method, the resulting admittance matrix is still an $N \times N$ matrix; hence, the memory required to store inverse admittance matrix is in the order of N^2. The second advantage is in the matrix inversion calculations: adding more than a certain number of layers makes the inversion of the full $N \times N$ admittance matrix more efficient than directly inverting an $N\,(L + 1) \times N\,(L + 1)$ band matrix.

5.9 Modeling Electrodes

In iterative reconstruction techniques, the error in the boundary potentials arises from experimental, numerical, or modeling. As discussed previously in Chapter 4, measurement error can come from unsteadiness in the excitation source, inaccuracy in measurement of current or voltage, and contact impedances. Geometric tolerance error arises in construction of the phantom, placement of the electrodes, and placement of the target. Numerical error can come from round off, truncation, and computational build–up effects and can be especially troubling in iterative methods. Precise modelling of the phantom depends

on how accurately the actual geometry is constructed and modeled. This is especially true for the electrodes modeled within the coarse finite element model. Using locally analytical methods and higher order approximation functions in the model can significantly improve the accuracy.

Two types of electrode models are of interest and used in the design of the test phantoms. Rod electrodes can easily be modelled by the FEM since the excitation current in the model is injected at a point. However, measurements obtained by using the rod electrodes are less sensitive to conductivity changes because of the rapidly decreasing potential gradient nearby excited electrodes. Therefore, small objects located far from the boundary of the phantom cannot be identified easily. The plate–electrode model is an alternative choice to provide relatively more uniform gradient distribution but an analytical model is difficult to develop for four degrees of freedom with the approximate potential function used in the block decomposition method introduced herein.

The plate electrode phantom is approximately modeled by adding an external domain to that in which the conductivity distribution is found (see Figure 5.17(a)). The conductivities of the shunt–admittance elements, y_s, in the external layer are assumed to be known throughout the inverse solution procedure. However, they need to be considered in the forward solution obtained by the finite element method. Practically, the conductivity value of a stainless steel electrode is very high, in the order of 10^6 $(\Omega m)^{-1}$. Since the conductivity value of the Plexiglass spacers is negligibly low compared to the stainless steel and the liquid with which the phantom is filled, the plate electrodes are modeled by admittance elements using approximately the order of conductivity for the stainless steel by shunting the finite element mesh nodes on the plate electrode geometry as shown in Figure 5.17(b). Therefore, the current injected to the plate electrode is distributed to the other electrode nodes so that all nodes are forced to be the same potential value.

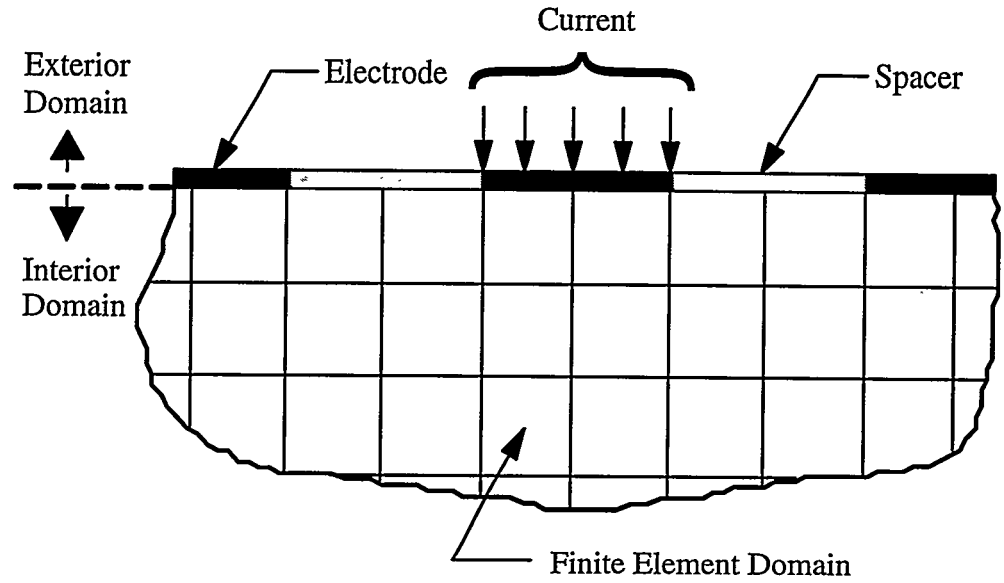

(a)

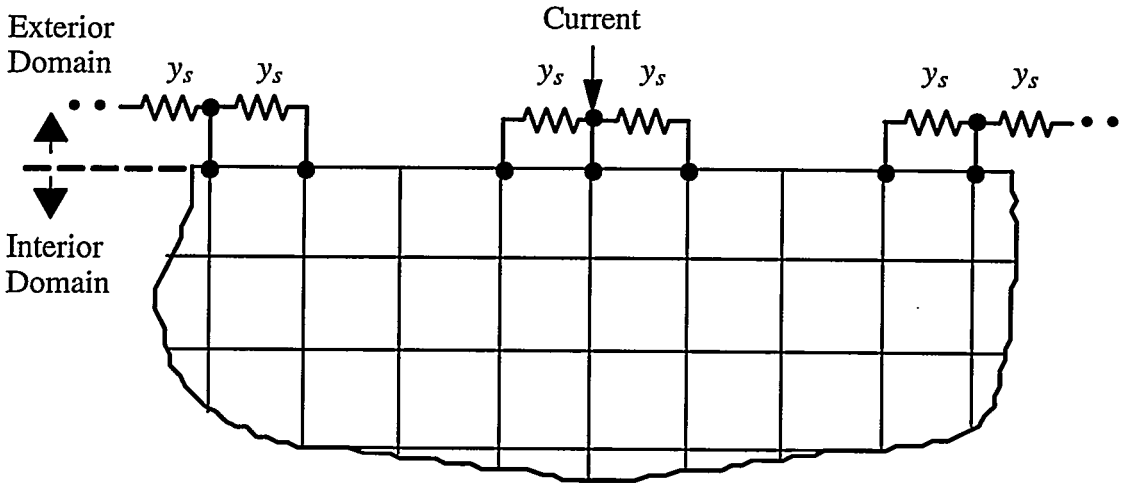

(b)

Figure 5.17 Modeling plate electrodes on a finite element mesh: (a) finite element discretization, plate electrodes and spacer elements on the phantom surface; (b) plate electrodes are represented by admittance elements shunting the finite element mesh nodes on the plate electrodes.

Table 5.1 2–D Computational Resources per iteration.

Problem	Sun IPX	SG INDY
9×9, 15 Excitations, 16 Electrodes (forward)	0.6	0.1
9×9, 15 Excitations, 16 Electrodes (inverse)	20	3.9
16×16, 15 Excitations, 16 Electrodes (forward)	24	5.0
16×16, 15 Excitations, 16 Electrodes (inverse)	198	40
17×17, 31 Excitations, 32 Electrodes (forward)	50	11
17×17, 31 Excitations, 32 Electrodes (inverse)	430	90

Note: Times are in seconds. 9×9 mesh model runs in 2.0 MB. 16×16 mesh model runs in 4.0 MB. 17×17 mesh model runs in 8.0 MB.

5.10 Computational Resources of Computer Programs

With the advent of distributed computing, a centralized mainframe computer to do the imaging computations is no longer used—nor has it to be at least for small three–dimensional models. Rather, either Sun or SGI workstations which are available at Rensselaer's computing system (RCS) are used. Table 5.1 shows that the methods described can undertake a single iteration in a two–dimensional 9 × 9 model of the 16–electrode phantom in approximately four seconds (which includes both forward and inverse computation) on fastest available machine, or approximately seven minutes for 100 iterations. On the other hand, a three–dimensional, 17 × 17 model with 12 layers for the 32–electrode phantom would require approximately 650 seconds per iteration, or 18 hours for a 100–iteration sequence (Table 5.2). However, a six–layer, 9 × 9 model only requires 21 seconds per iteration: a total of 35 minutes for a 100–iteration sequence. From these numbers, one can see that even after seven years of development, truly three–dimensional imaging using the finite element approach is not yet available for using local computing resources.

Table 5.2 3–D Computational Resources per iteration.

Problem	Sun IPX	SG INDY
9×9, 15 Excitations, 16 Electrodes, ±6 Layers (forward)	25	8
9×9, 15 Excitations, 16 Electrodes, ±6 Layers (inverse)	73	13
16×16, 15 Excitations, 16 Electrodes, ±12 Layers (forward)	800	170
16×16, 15 Excitations, 16 Electrodes, ±12 Layers (inverse)	550	110
17×17, 31 Excitations, 32 Electrodes, ±12 Layers (forward)	1200	260
17×17, 31 Excitations, 32 Electrodes, ±12 Layers (inverse)	1900	390

Note: Times are in seconds. 9×9 mesh model runs in 2.0 MB. 16×16 mesh model runs in 4.0 MB. 17×17 mesh model runs in 8.0 MB.

5.11 Summary

This chapter has summarized the theoretical developments of new additions to the basic two–dimensional electrical impedance imaging model. The block decomposition method (BDM) provides a better approximation to the conductivity field. Therefore, fewer numbers of elements are required to improve the solution of the potential field whereas the forward solution accuracy can only be improved by increasing the number of elements. This is not true for the inverse problem. In the latter case, the conductivity is an unknown and a weak approximation to the conductivity variation and so influences the accuracy of the forward solution resulting in slow and unstable decrease of the error function. The block decomposition method subdivides each large element into 3 × 3 smaller elements and in each element the conductivity is interpolated from a global spline fit. The conductivity variation in large elements is considered in the formulation of the shape functions. Therefore, the solution is improved without increasing the number of elements or the number of nodes in the finite element model.

The layer reduction method (LRM) outlined allows the modeling of three–dimensional fields using the basic two–dimensional model as long as the third dimension is not excited and the impedance variations are small in the third dimension. This is a major step forward which reduces the computational effort in three–dimensional imaging by many orders–of–magnitude depending on the size of the model.

In addition to the layer reduction method, the method of preconditioned voltage conversion or the PVC method allows the effects of many sorts of errors to be compensated for by premultiplying the measured voltage matrix by a preconditioning matrix determined by experiment.

CHAPTER 6

EXPERIMENTAL METHODS

6.1 Introduction

The process of using electrical impedance tomography (EIT) to reconstruct a conductivity distribution involves applying electrical excitation patterns and making electrical measurements on the object's boundary. Numerical computation is then used to find the conductivity distribution which provides the "best" comparison between measured and computed boundary response to the excitations. In this research, voltage excitation have been chosen to measure current injection and to measure voltage response on the boundary.

An EIT system is a sophisticated device which employs an aggregate of diverse technologies from analytical and numerical methods to state–of–the–art electronic design techniques. In many EIT applications, the conductivity field has a dynamic behavior in which the conductivity distribution in the cross section of the test region changes in time. Thus, the data acquisition time is constrained by the speed of the change of the conductivity field. In these applications, If the speed and the accuracy of the data acquisition process are not designed properly, there may be significant negative effects on the quality of the image. Thus, it is desirable to design and use a high–speed, high–accuracy data acquisition system which is capable of obtaining all the necessary measurements before a significant change in the conductivity distribution occurs. Such a design would, in effect, produce a stop–motion framing effect by significantly reducing or completely eliminating temporal smear in the image obtained.

Primarily, this chapter focuses on the experimental work which was used to provide useful design information for future development of a high–speed, high–accuracy data acquisition system. Such a system may be used for imaging binary conductivity fields, such as in monitoring gas–liquid flow systems. To determine the limits of capabilities of the proposed imaging system, the new design ideas developed are tested by a low–speed, high–accuracy data acquisition system which is capable of applying desired excitation source signal type and excitation patterns to two– or three–dimensional phantoms with a static conductivity field. This makes it possible to test and verify the numerical and analytical methods as described previously in Chapter 5, and test and verify the experimental techniques useful for the high–speed data acquisition system. These were done so as to investigate the limits of accuracy and resolution of approach to impedance imaging in low–resistivity, gas–liquid systems.

The design details and internal workings of the basic components of the low–speed, high–accuracy data acquisition system, including computer–hardware interfacing, are explained in detail. The ideas developed in designing the data acquisition system are presented following the historical background of other relevant work in the area. The major considerations in the test phantom design, such as modeling of electrodes, and comparison of rod–electrode model to plate–electrode model, are outlined.

6.2 Data Acquisition System for Static Images

The block diagram of an electrical impedance imaging system used for static images is shown in Figure 6.1. Experimental data were obtained with an accurate, low–speed excitation/acquisition system developed for testing the reconstruction methods in realistic noisy conditions. In this system, all experimental functions are controlled by use of a Cannon 486/66MHz PC (Personal Computer). The computations for reconstruction

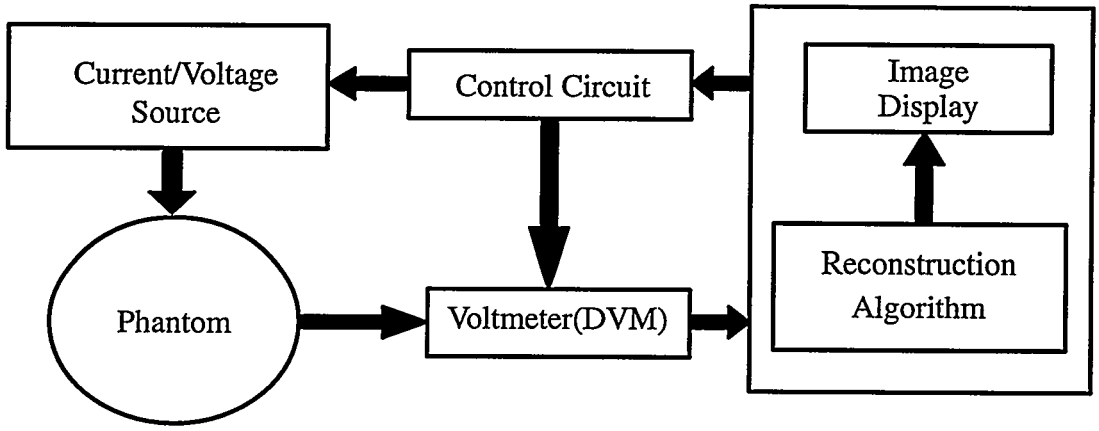

Figure 6.1 A Block diagram representation of an electrical impedance tomography system.

and post–processing of computed conductivity distributions are undertaken using either a Sun/IPX Unix SparcStation or a Silicon Graphics Unix workstation (SGI), both of which are networked to the PC via an Ethernet connection. The post–processing routines to display and enhance computed images use the MATLAB graphics library. The photograph in Figure 6.2 shows the assembly of the basic system components in a data acquisition cabinet. This system provides the voltage and current current data required to reconstruct the resistive component of impedance distribution in a phantom. The system was contained in a laboratory room at a relatively constant temperature of approximately 21°C.

The detailed excitation and the measurement system is shown in Figure 6.3. The functioning of this system includes two basic operations: controlling the multiplexing circuitry (the matrix switching system, Appendix D) and controlling the excitation/measurement instruments. The 486/66MHz PC uses a program called DASCP (Data Acquisition System Control Program, see Appendix E) to control both the matrix switching system via the digital I/O TTL–level control lines and the Hewlett Packard instruments via a GPIB (General Purpose Interface Bus) bus connection. Coaxial cables are used to provide connections to the excitation/measurement system from the fully–guarded 32–channel matrix switching system to the end of each electrode. During measurements, each excitation is provided by a programmable Hewlett–Packard HP–3245A Universal source having a 10V/100 mA output capability and stability of 0.0007% + 85 μV at 10 V over 24–hour period and 90–day current stability of 0.0202% + 3.3 μA at 100 mA at constant temperature. Voltage measurements were obtained using a 10–nV–resolution HP–3458A system multimeter having NIST–traceable internal calibrator. The system could also measure phase with less than 1 ns resolution using zero–crossover comparisons on a 1 GSa/s HP–54510A digital storage oscilloscope. Although the phase measurement capability has not been used for the resistive imaging experiments in this study, the existing system is designed to be

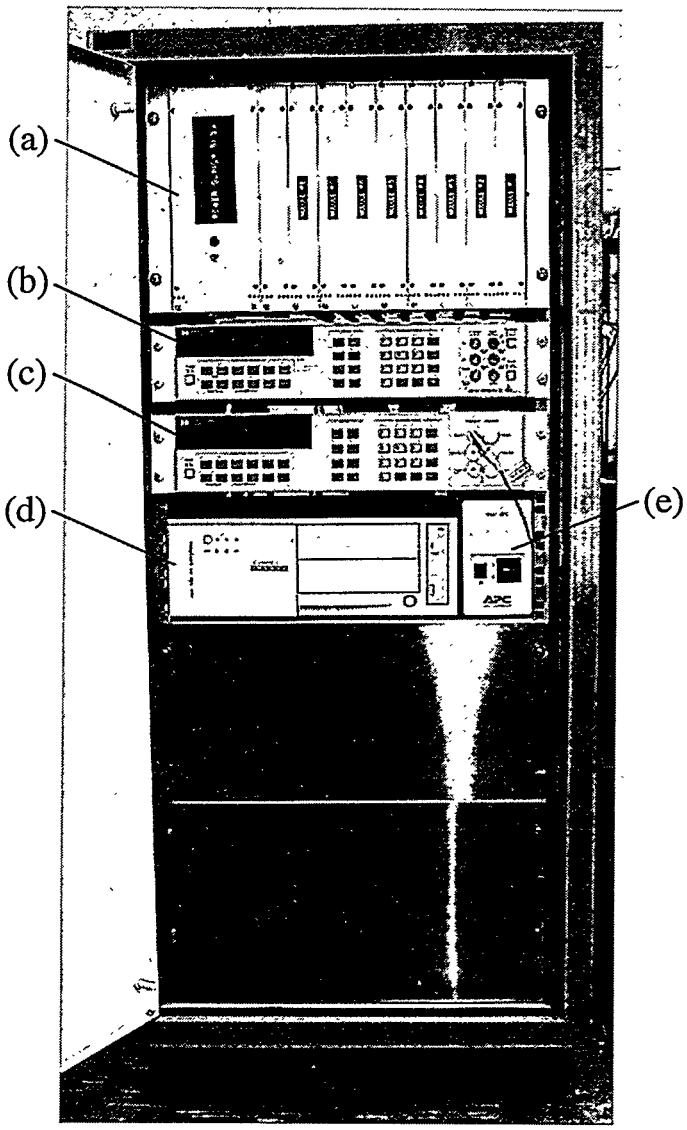

Figure 6.2 The data acquisition system cabinet and its basic components: (a) Matrix switching unit; (b) HP–3458A digital multimeter; (c) HP–3245A digital function generator; (d) Cannon 486/66MHz personal computer; (e) APC 400 backup power supply for the personal computer.

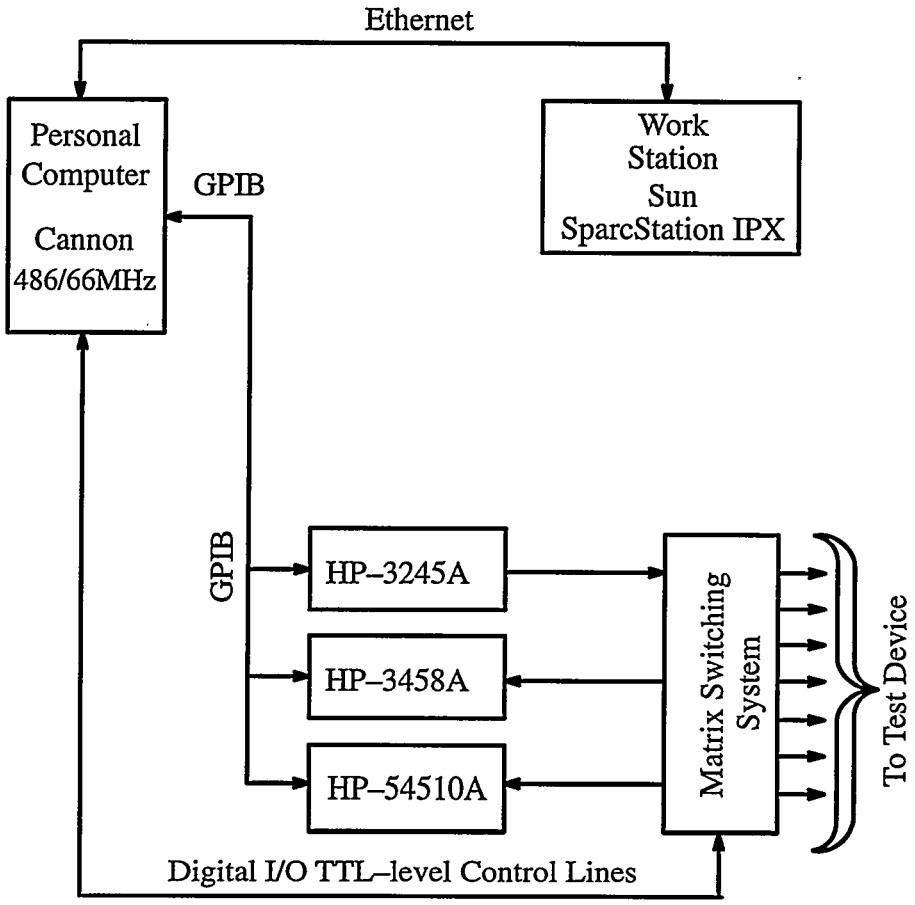

Figure 6.3 Schematic of the high accuracy excitation and measurement system.

capable of providing this facility. The entire process, under programmed computer control, required between 15 and 30 minutes to acquire imaging data using a 32–electrode test phantom.

All switches used in the matrix switching system are shielded relays, which are controlled by TTL–level (Transistor Transistor Logic) signals from the personal computer. Using this switching system, any possible two or multiple combinations of electrodes can be excited and measured simultaneously. Technical details about the electronic design of the matrix switching system are provided in Appendix D.

6.3 Test Phantom

A phantom is a box of some particular shape, perhaps rectangular or cylindrical, which is filled with materials of homogenous resistivity or with a collection of separate materials of different resistances. Phantoms provide controllable mediums which can be used for the calibration and testing of systems that measure target impedance such as EIT systems.

An electrode can be considered to be a transducer which converts the electronic current in a wire to an ionic current in an electrolyte. Contact impedance between the electrode and the medium must be small and known in order to design instruments and reconstruct impedance images. Electrodes must be utilized which are constructed of reasonable materials and sized to interface properly between the metal of the instrument and the ionic conductors in the phantom. They must also be designed to correspond with the geometries capable of being properly modeled numerically. In addition, because in some cases the voltage differences due to the presence of a body in the field are only a few millivolts relative to the homogeneous case, the geometric accuracy of electrode size and placement as

well as the size and the shape of the phantom itself relative to the model being used in the imaging process is quite important.

6.3.1 Plate Electrode Design

There are a number of engineering trade–offs which must be considered when selecting optimal electrodes. Measuring voltages on electrodes different from those to which current is supplied or removed minimizes the effect of contact impedance since without current flow there is no potential drop due to the contact impedance. Another design consideration relates to the size of electrodes. With point–electrode models, the larger an electrode, the larger the error it introduces into a point–electrode model. Furthermore, the smaller the electrode, the larger the high potential field gradients at electrode surface become. Hence, this error increasingly prevents adequate images from being obtained. Furthermore, as electrodes approach each other, they cause an unmodeled current–shunting effect between electrodes, again due to the limited number of elements used in the numerical model for reasons discussed previously.

Electrodes for the three–dimensional phantom were constructed by simply insulating the overall electrode length with shrink–tubing except for a central part which is the desired electrode length. Figure 6.4 shows the photograph of such a three–dimensional 12.7–mm wide plate electrode before (top) and after (bottom) the shrink tube is coated. In this case, a 12.7–mm long tubing section at the center is stripped off to emulate the same effect which a 12.7 $\times$ 12.7–mm plate electrode gives.

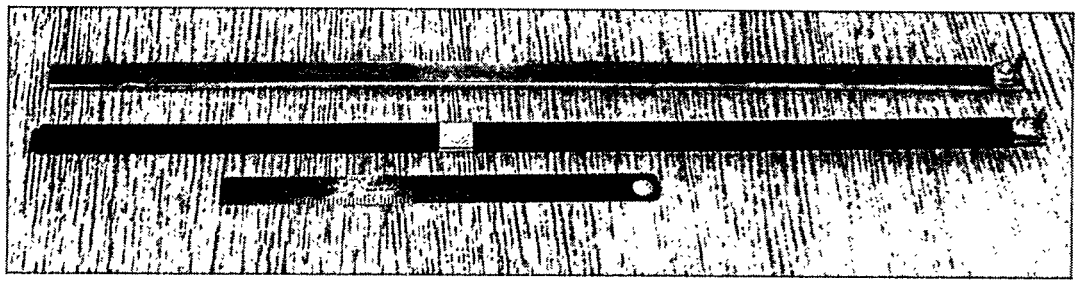

Figure 6.4 Two–dimensional (top) and three–dimensional (bottom) electrodes used for the square phantoms. The electrodes are made of 335–mm–long, 12.7–mm–wide, and 3–mm–thick stainless steel plates. The bare steel plate is first polished, and then coated with insulator shrink tubes. A 12.7–mm–portion at the center is stripped off to simulate a three–dimensional electrode effect.

6.3.2 Phantom Design

Three types of experimental phantoms are designed and constructed to test the reconstruction methods and the hardware. The first design shown in Figure 6.5 stems from an earlier attempt to investigate rod electrodes in variable numbers and locations around the periphery of the phantom. The second design consists of 16 plate electrodes each 25.4 mm wide, used for two–dimensional testing purposes (Figure 6.6). The third design (Figure 6.7) consists of 32 12.7–mm–wide plate electrodes of either two– or three–dimensional design as described in Section 6.3.1. When designing these three phantoms, a caution was taken so that the electrodes are accurately placed, and easily removable from the phantom. Each plate electrode was separated from adjacent electrodes by Plexiglass spacers identical in size to the electrodes themselves.

All of the three phantom designs explained above consist of a glass tank 200 × 200 × 335–mm deep. The stainless steel rod electrodes, each 3.17 mm in diameter, are vertically aligned and equally spaced on the interior wall of the phantom as shown in Figure 6.8. Figure 6.9 illustrates the dimensions and arrangement of the plate electrodes in the 16–electrode phantom. Dimensions were halved those shown in Figure 6.9 for the 32–electrode phantom (compare Figures 6.6 and 6.7).

6.4 Test Objects

Test objects, also called targets, of various geometries and conductivities are used in phantoms to control conductivity distribution in order to test and calibrate the developed EIT imaging system. In this study, since the interest is on imaging gas–liquid systems the insulator (made of Plexiglass or PVC) targets in rectangular and circular shapes in various sizes were used to simulate highly resistive bubbles residing in phantoms filled with water

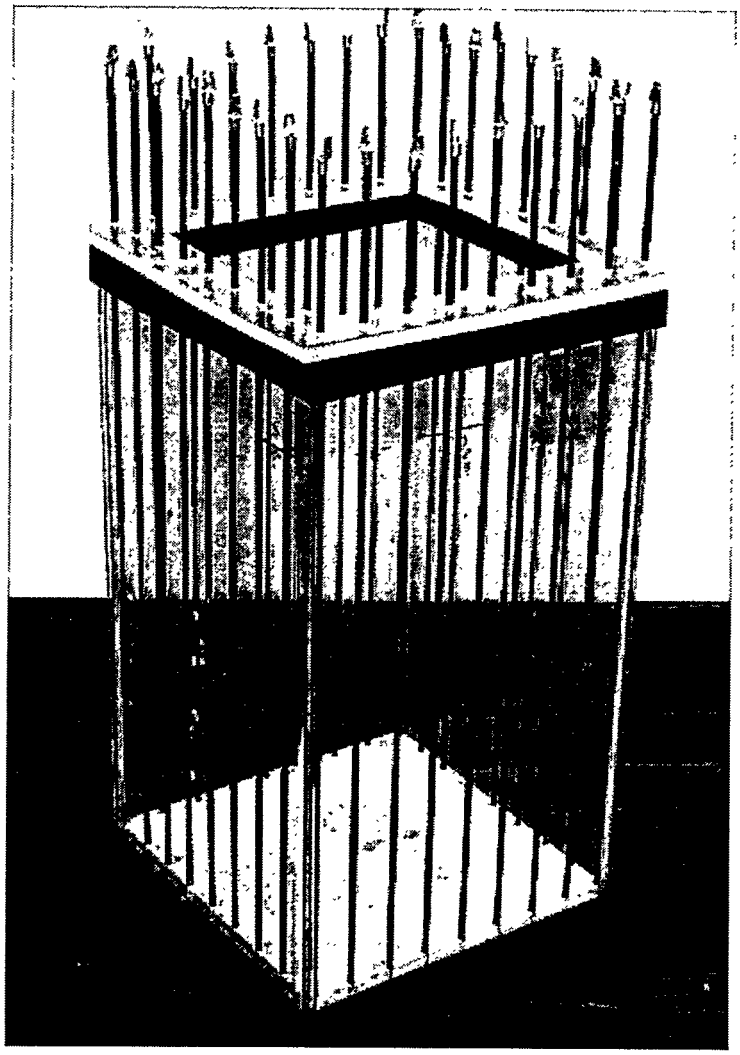

Figure 6.5 **Rod–electrode square phantom used for variable electrode numbers (16/32).**

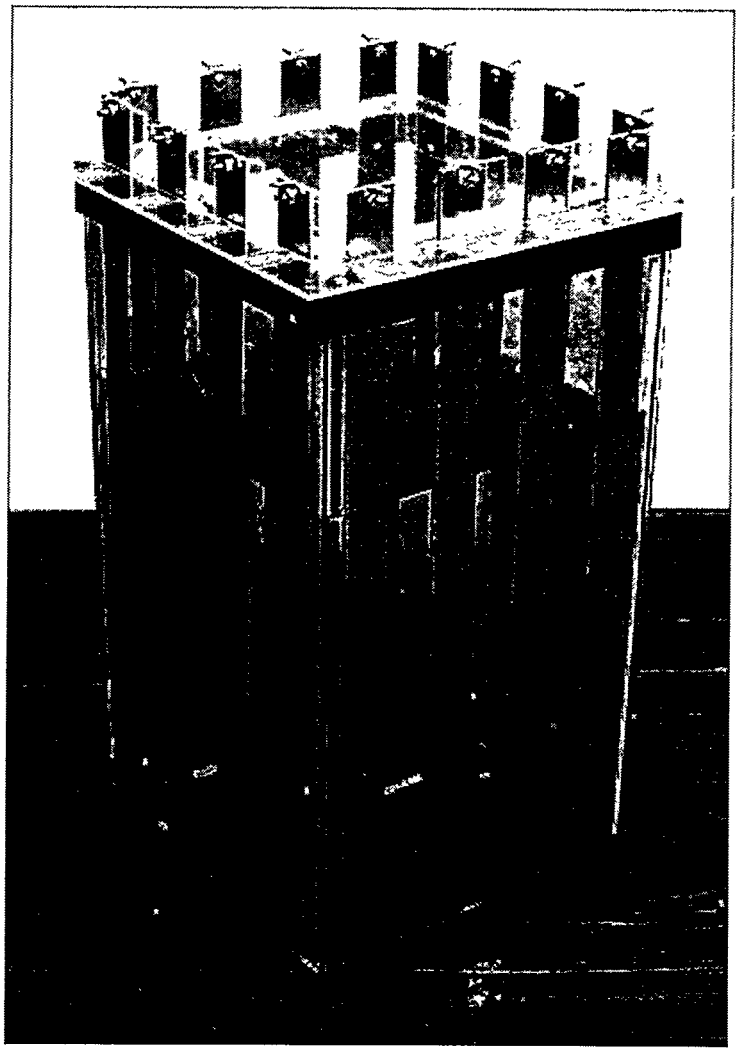

Figure 6.6 Two–dimensional experimental square phantom with 16 plate electrodes.

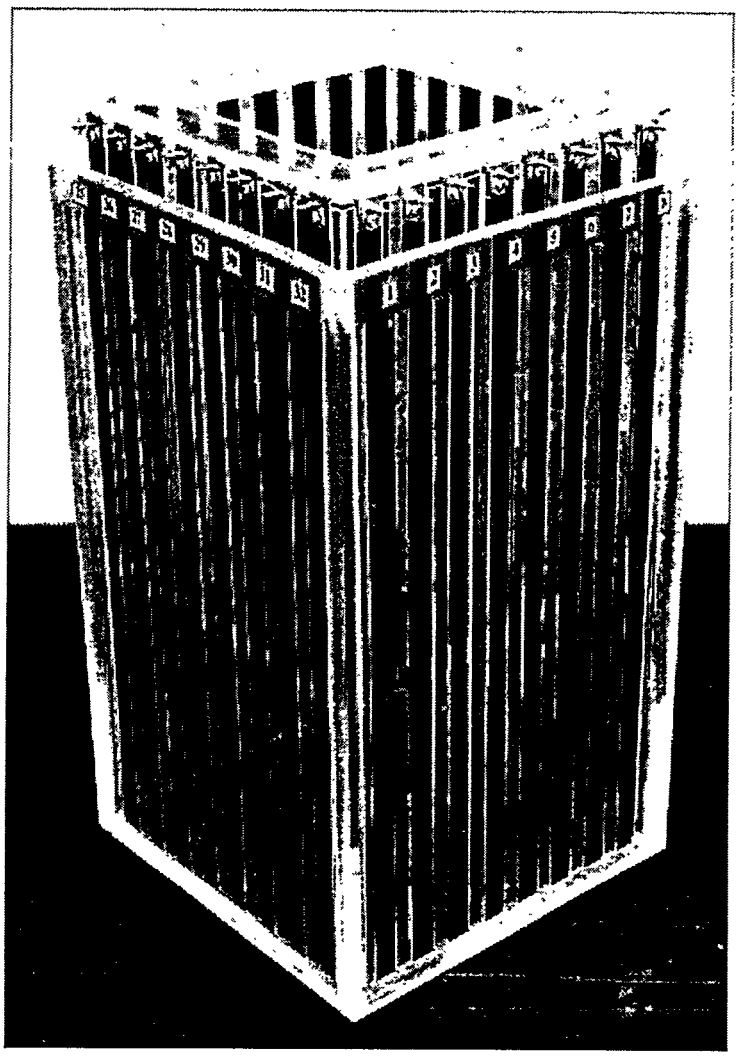

Figure 6.7 Three–dimensional experimental square phantom with 32 plate electrodes.

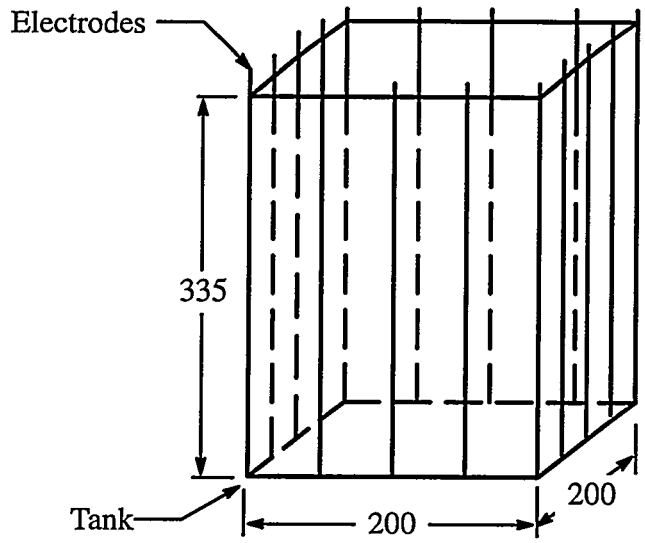

Figure 6.8 **A square tank and 16 rod electrodes, each of which is vertically aligned and placed in equal distances.**

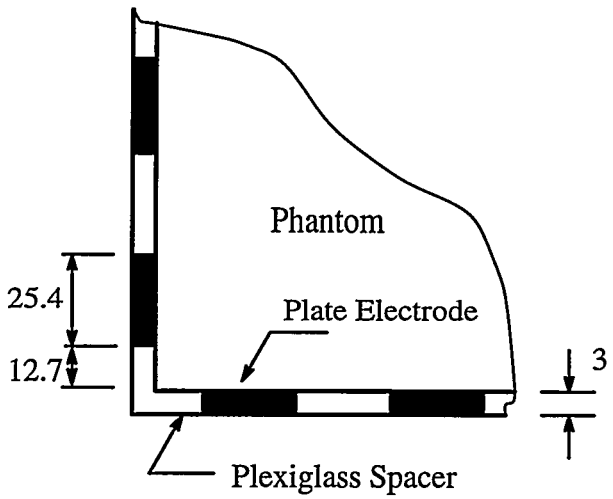

Figure 6.9 **Dimensions and arrangement of the plate electrodes on the interior surface of a square phantom.**

of different conductivity levels. These insulator test objects are shown in the photograph in Figure 6.10.

6.5 Excitation Methods

There are numerous ways in which the current–injecting electrodes are chosen. This section describes the concepts of various excitation methods by which the current is injected and voltages measured.

6.5.1 Background

Early systems, which were virtually all in the biomedical area, used the two–electrode method. The voltage was measured from the same electrodes through which the current was injected. The principal source of error in this measuring system was the voltage drop across the skin contact impedance. Thus, some systems replaced the two–electrode system with a four–electrode data collection method. Then, the current is injected through some electrodes and the voltage recorded through different electrodes. This method minimizes error in voltage measurement due to the skin contact impedances. In spite of the shortcomings of the two–electrode method over the four–electrode method, two–electrode methods are used for their simplicity in geophysics applications, where accuracy in measurement of the resistivity distribution is not as essential as in the biomedical field.

Lytle and Dines [144] applied stepped voltages to all electrodes which would produce a uniform current distribution in a homogeneous media. In a nonhomogeneous media, the currents become nonuniform. They measured the resulting currents at all electrodes and repeated the procedure from several angular directions. Kim and Woo [91] presented a very flexible data collection system, where each of 125 electrodes was programmed separately and various pairs of voltage–injecting and current–measuring electrodes could be selected,

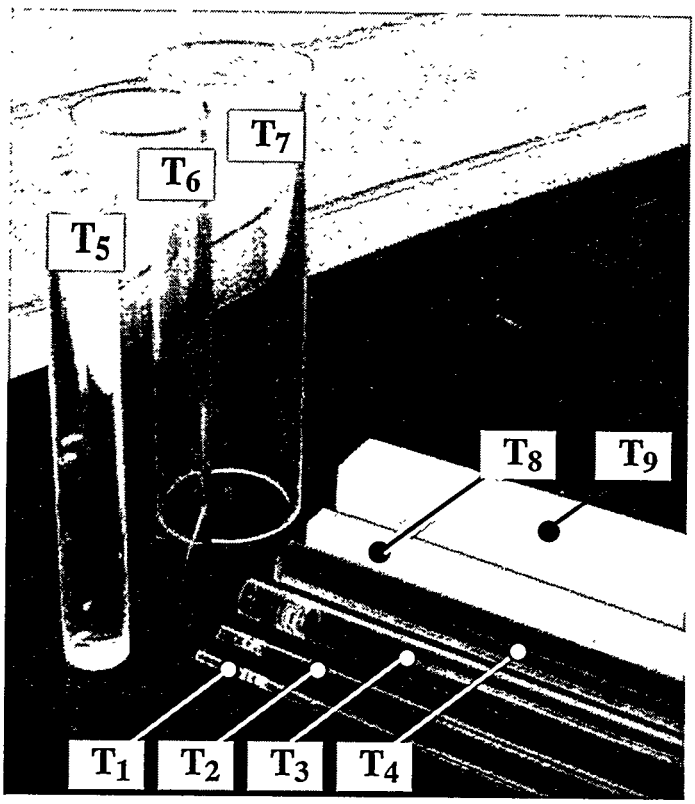

Figure 6.10 Insulator targets in various shapes and sizes: T_1 6–mm; T_2 10–mm; T_3 25.4–mm; T_4 32–mm; T_5 45–mm; T_6 88–mm; T_7 145–mm cylindrical Plexiglass targets; T_8 25.4 × 25.4–mm; T_9 50.8 × 50.8–mm square PVC targets.

to obtain a variety of current distributions. 125 electrodes were arranged in five different columns and each column contained 25 electrodes, all placed in a single plane. This method was used for frontal imaging.

Tasto and Schomberg [145] obtained the voltage–current data points by placing electrodes of different dimensions, insulated from each other, on opposite sides of a tank filled with saline. The object was placed inside the tank. The front of the tank consisted of 20 metallic electrodes. The rear was completely covered with a large metallic electrode. All the electrodes were connected via current meters of negligible internal resistance to a low–frequency AC source. The large electrode was connected to the other pole of the source. All small electrodes had equal potential due to the very low resistance of the current meters. The current was measured for each small electrode and was used to determine the resistance of the current path passing from each small electrode to the large electrode.

6.5.2 Neighboring Method

Brown and Seagar [146], [147] used the neighboring method of data collection. They applied the current through two neighboring electrodes and measured the voltage from all other successive pairs of adjacent electrodes in this four–electrode method.

Figure 6.11(a) shows a data collection system they used for 16 equally spaced electrodes used for a circular cross section, where the current is applied through electrode pair 1–2. The current flows through the circular cross section, with its intensity maximal at the periphery near the current–injecting electrodes and diminishing rapidly towards the opposite side. The equipotential lines are conceptually shown in Figure 6.11(a) and the shaded portion between those that terminate on electrodes 6–7 conceptually represents the resistivity zone for these electrodes. The voltages are measured between the electrode pairs

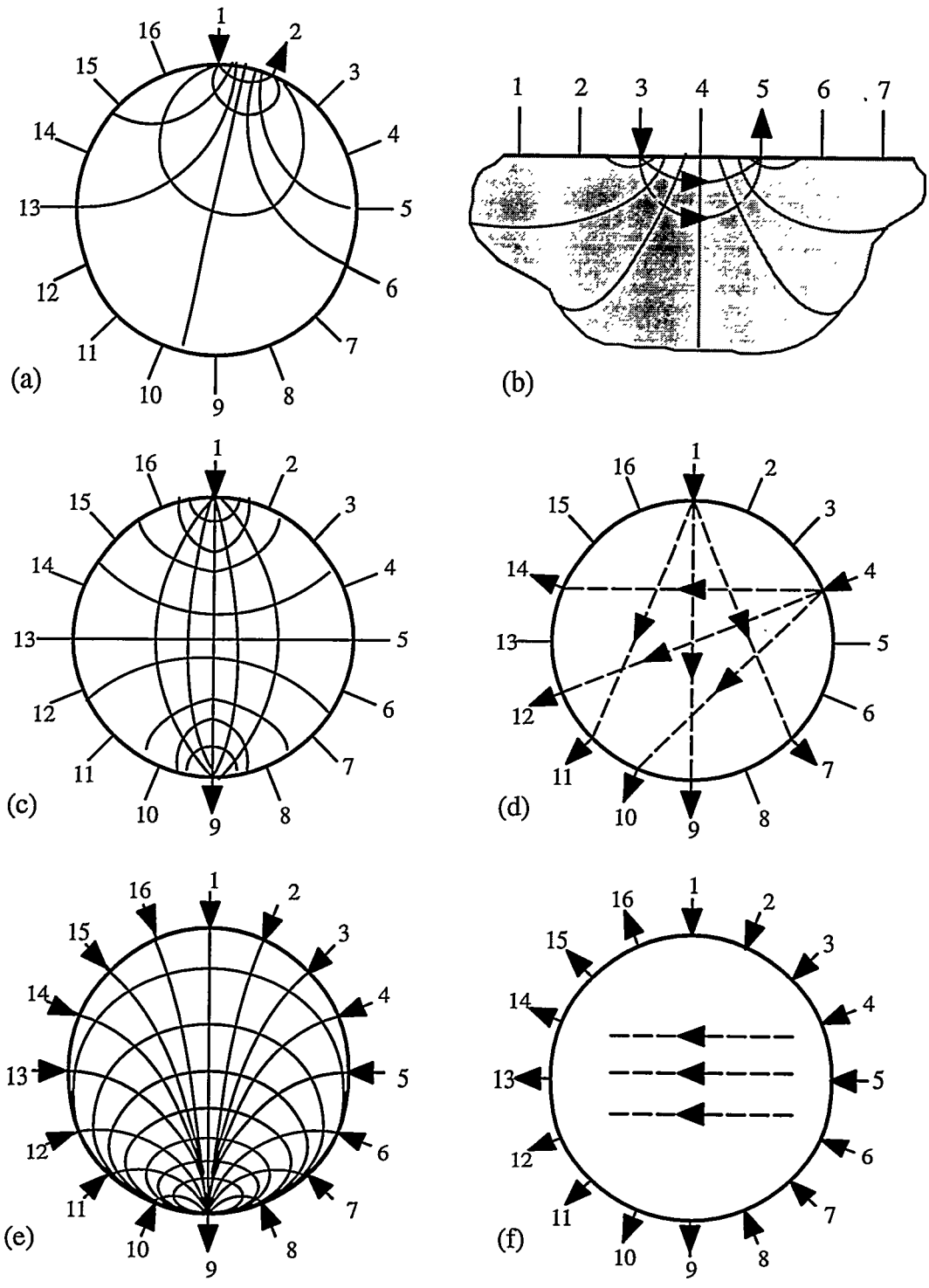

Figure 6.11 Excitation methods: (a) neighboring; (b) linear; (c) opposite; (d) cross; (e) multireference; (f) adaptive (based on Webster [77]).

3–4,4–5,5–6,..., and 15–16. All 13 voltage measurements are independent. Brown and Seagar then changed the current–driving pair to 2–3, and measured the voltages similarly between 13 pairs of adjacent non–excited electrodes. They rotated the excitation current pair through 3–4, 4–5, ..., 16–1 and for each pair, measured the entire set of the voltages between neighboring electrodes. Thus for the 16–electrode system, they obtained $16 \times 13 = 208$ voltage measurements.

Note, however, that not all of these data points are independent, since the reversal of voltage and current electrode pairs would give an identical value of the measured resistivity. Thus because of this reciprocity, only 104 independent measurements are obtained for the above 16–electrode system. Furthermore, note that with adjacent–electrode excitations, the equipotential lines are distributed such that the current flowing through the center regions of the field is minimized, thereby producing extremely small variations in boundary sensitivity to variations in the central regions.

Thus, it is seen that the neighboring method of data collection has a very nonuniform current distribution. Most of the current travels near the peripheral electrodes and hence good sensitivity is obtained at the periphery. This method does not yield good sensitivity at the center because the current density is low there.

6.5.3 Linear Array

The data collection methods considered so far have electrodes placed all around a cross section of an enclosed field. It is not always possible to surround the region of interest with the electrodes, especially in geological applications. Powell et al. [148],[149] used a linear array of electrodes on the top of the surface. They applied a constant current source

between two of the electrodes, and then they measured the voltage between all the adjacent pairs of electrodes, except the current–injecting electrodes.

Figure 6.11(b) shows the equipotential lines for the current injected through a pair of electrodes. The voltage was measured on two intermediate electrodes. An equally spaced 16–electrode system yielded 104 independent data points. The linear array method of data collection has certain disadvantages over the encircling array of electrodes. The current distribution is not specified in a region, and the current density is high only in the region between excited electrodes. Since the current density reduces considerably in a region away from the array, the resolution and sensitivity diminish rapidly as distance from the array increases.

The result shows that the linear array will not detect objects deeper than about half an array length. The voltage measured by the linear array method has a greater variation, and thus the signal–processing circuit is more complicated than that in the encircling array method. Since the current spreads out in all three directions, it is difficult to image one particular plane. The linear array method has advantages because it is easy to remove the electrodes. A linear array can also give very good spatial resolution near the surface.

6.5.4 Opposite Method

Hua [25] also used the opposite method (or 180° method) of data collection. Figure 6.11(c) shows that current was injected through diametrically opposed electrodes. The voltage reference electrode was adjacent to the current–injecting electrodes, the voltages were measured with respect to the reference at all the electrodes, except the current–injecting electrodes. To obtain the next set of data, they switched the current to the next pair of opposite electrodes in the clockwise direction. The voltage reference was also changed ac-

cordingly, and the voltages were similarly measured with respect to the new reference. The entire image set was obtained by switching the oppositely placed current electrodes through 180°, and the voltages measured for each pair of current electrodes with respect to the reference electrode. For 16 electrodes, this method has more uniform current density and hence good sensitivity.

6.5.5 Cross Method

Hua et al. [25] used the cross method of data collection, where the currents are injected between a pair of electrodes separated by large dimensions. Compared to the neighboring method, the current is more uniformly distributed. Figure 6.11(d) shows the data collection system. To collect the data set, they made electrode "0" the current–reference electrode and electrode 1 the voltage–reference electrode. They then applied current successively to electrodes 2, 4,..., 14 and for each current pair measured the voltage with respect to the voltage reference at each electrode except the current electrodes. They then changed the current reference to 3 and the voltage to 2 and applied current through electrodes 5, 7,..., 15 and 1. They repeated the above procedure to measurement of the voltages, and seven different current electrode pairs were selected to give $7 \times 13 = 91$ data points. Another 91 data points could be obtained by changing the voltage and current reference. Thus a 16–electrode system yields a maximum of 182 data points, out of which only 104 are independent measurements. The cross method does not have as good a sensitivity in the periphery as the neighboring method, but has better matrix conditioning and sensitivity over the entire region.

6.5.6 Multi–Reference Method

The data collection methods considered so far use a pair of electrodes through which a single current of constant magnitude is injected, and the voltages are measured across two other electrodes. All the other electrodes are floating. Hua [25] also tried the multi–reference method of data collection, in which he varied the current amplitude in each of many current sources, from 0.0 mA to 5 mA.

Figure 6.11(e) shows that for a system with 16 equally spaced electrodes, currents flow through 15 electrodes simultaneously and are collected by the one remaining electrode, which is grounded. Electrode 1 was initially grounded and they injected current through electrodes 2 through 16 simultaneously. They measured the voltages across each of the electrode 2 through 16 with respect to the reference. They then changed the reference to electrode 2, and injected the current through the remaining 15 electrodes. They measured all the voltages with respect to the new reference. Thus, by varying the references through one cycle and measuring the voltages and current for each different reference, they obtained a complete data set. For a 16–electrode system, they obtained a total of 240 data points, out of which 120 were independent.

To reduce the data collection time and obtain only the independent measurements, approximately eight reference electrodes were used. The current flowed through all the electrodes simultaneously, so the error due to the contact impedance is reduced, if it is assumed to be constant throughout the periphery. In practice, it is not constant, hence the multireference method of data collection introduces error due to contact impedance. For a nonhomogeneous medium of circular cross section, a somewhat uniform current distribution can be obtained by suitable section of the amplitude of current through the current–in-

jecting electrodes. Due to the somewhat uniform current distribution, this method gives good sensitivity.

6.5.7 Optimal Excitation Method

The excitation methods discussed so far (in this section) do not use the "best" or "optimal" current patterns. The optimal current patterns are chosen based on the principle that the applied current is forced to flow into low–conductivity regions to get strong boundary response due to these regions. When the optimal excitation patterns are applied to a phantom, the difference between the boundary measurements for the homogeneous and the nonhomogeneous cases is maximized. A poor selection of excitation pattern can reduce contribution of low–conductivity (or insensitive) regions to the boundary response, causing conductivity information being decimated by the system noise (i.e., low signal–to–noise ratio, SNR).

Finding the best excitation pattern depend on two basic factors: geometry of the boundary surrounding the problem region; distribution of electrical properties such as conductivity and/or permittivity distribution. Since the latter is unknown, the optimal current patterns cannot be derived analytically.

For a special case of a circular disk, Isaacson [55] described an optimal method to calculate the optimal currents. Isaacson showed that the optimal current patterns for a circular object placed in the center of the disk are governed by trigonometric patterns. For given number of electrodes, E, the optimal current patterns are calculated by

$$j_\ell^k = \begin{cases} \cos k\theta_\ell & k = 1, 2, ..., E/2 \\ \sin(k\text{–}E/2)\theta_\ell & k = (E/2) + 1, ..., E\text{–}1, \end{cases} \tag{6.1}$$

where $\theta_\ell = 2\pi\ell/E$ for $\ell = 1, 2, ..., E$.

The optimal currents mentioned above are limited to very special case. Although these current patterns are originally developed for two concentric cylinders, these patterns can be used for circular domains with arbitrary conductivity distributions to maximize sensitivity near the central region.

6.5.8 Adaptive Method

Optimal excitation patterns for arbitrary phantom geometry and conductivity distributions, however, cannot be obtained without using *a–priori* information. Gisser et al. [56] proposed the adaptive data collection method by which almost a uniform current distribution can be obtained by injecting currents of appropriate magnitudes through all the electrodes simultaneously (see Figure 6.11(f)). This method is also called the optimal current method because the concept is to provide a current distribution which maximizes overall sensitivity without knowing the conductivity distribution.

The adaptive method is an interactive method which uses voltage measurements from an actual nonhomogeneous phantom, and calculates a better excitation pattern to distinguish nonhomogeneous distribution from the homogeneous background by comparing these measurements to the voltages computed form a homogeneous model. Starting with any current estimate, the optimal current patterns are iteratively approximated until the change between two iterations is less then the system's measurement precision. Gisser et al. [56] showed that the best current pattern for a circular target centered in a circular phantom follows a cosine curve to give a perfectly uniform current distribution. This method rapidly converges to the best currents typically in five iterations. The adaptive method is known to be the most versatile excitation method among the methods introduced herein. However, an

Table 6.1 Comparison of different data collection methods in terms of their performance (based on Webster [77]).

Data collection method	Current Distribution in the Cross Section	Spatial Resolution and Distinguishability
Neighboring method	Very poor at the center	Poor
Linear array	High only near the surface	Good for depth up to 2 electrode spacing
Opposite method	Uniform	Good
Cross method	Uniform	Good
Multireference method	Very uniform	Very good
Adaptive method	Very uniform	Very good

interactive experimental process must be pursued making the use of method impossible for rapidly changing conductivity fields.

6.5.9 Comparison of Excitation Techniques

The data collection methods discussed are shown in Table 6.1. It is seen that of all the methods, those that utilize multiple sources simultaneously have the best characteristics. Ultimately, this is anticipated to be the method of choice for impedance imaging in general, and for imaging of gas–liquid flows in particular. It should be mentioned, however, that utilization of multiple electrode methods when plate electrodes are used, requires special considerations in modeling in order to obtain reasonable images. A point model does not do a good job in reconstructing data obtained with plate electrodes.

6.5.10 Walsh Excitation Patterns

In general, it appears desirable that the boundary electrodes are excited by independent current sources, and the response is measured by a voltmeter on the electrodes [55],

[150]. For each conductivity distribution, there is an optimal current pattern, related to the eigenvectors of the impedance network. When these eigenvectors are applied as independent current sources for each electrode, the best distinguishability is achieved. However, this is not practical for high–speed imaging systems having framing rates of, say 1000 images per second for flow imaging. This is because accurate current sources do not have sufficiently fast response time to allow variable amplitude patterns to be applied using time scales on the order of milliseconds or tens of microseconds.

To simplify the measurement system and allow the methods developed in this study to be directly applicable high speed systems, independent voltage patterns are applied by means of a single voltage source. Therefore, each excitation pattern is represented by +1 and –1. One possibility for these type of independent vectors is the Walsh–function set. Woo [30] previously reported that the Walsh current patterns actually increase the distinguishability in their experiments. This is because the Walsh functions include both low– and high–frequency spatial variations and correspond to the optimal set for the lowest frequency eigenvectors.

If the number of electrodes is represented by integer powers of 2 (i.e., $E = 2^n$). The applied excitation matrix can be chosen as the columns of the Walsh–Hadamard matrix $\boldsymbol{H}$ whose columns are ordered Walsh functions (see References [152], [153]). The Hadamard matrix (which consists of ordered Walsh functions) is a symmetric $E \times E$ matrix with the property of $\boldsymbol{H}\ \boldsymbol{H}^T = 2^n\ \boldsymbol{I}$. The spatial variation of Walsh functions applied to 16– and 32–electrode systems are shown in Figure 6.12 and Figure 6.13, respectively. In the experiments, only $E - 1$ Walsh functions with zero average are applied to satisfy the Kirchhoff's current law (because all of the Walsh patterns except the first one can satisfy this law).

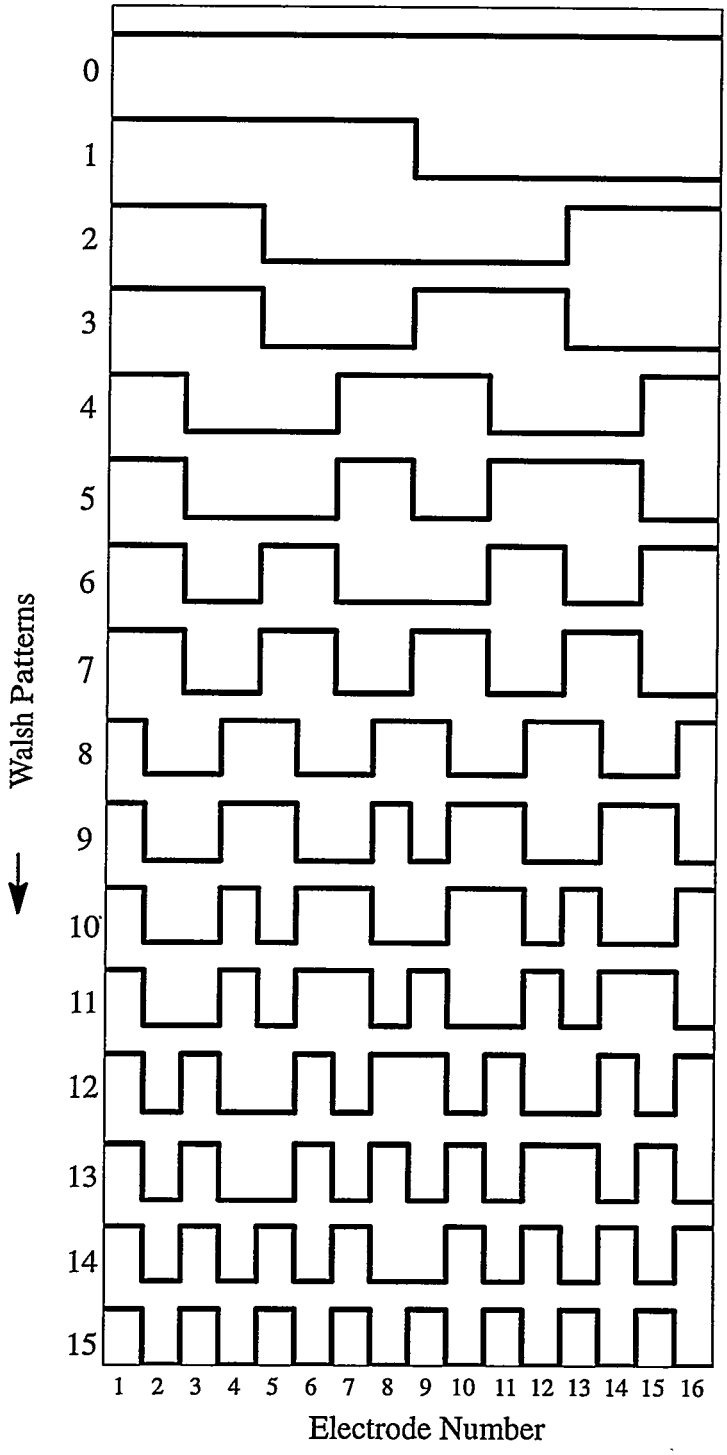

Figure 6.12 Walsh patterns used for excitation of a 16–electrode system.

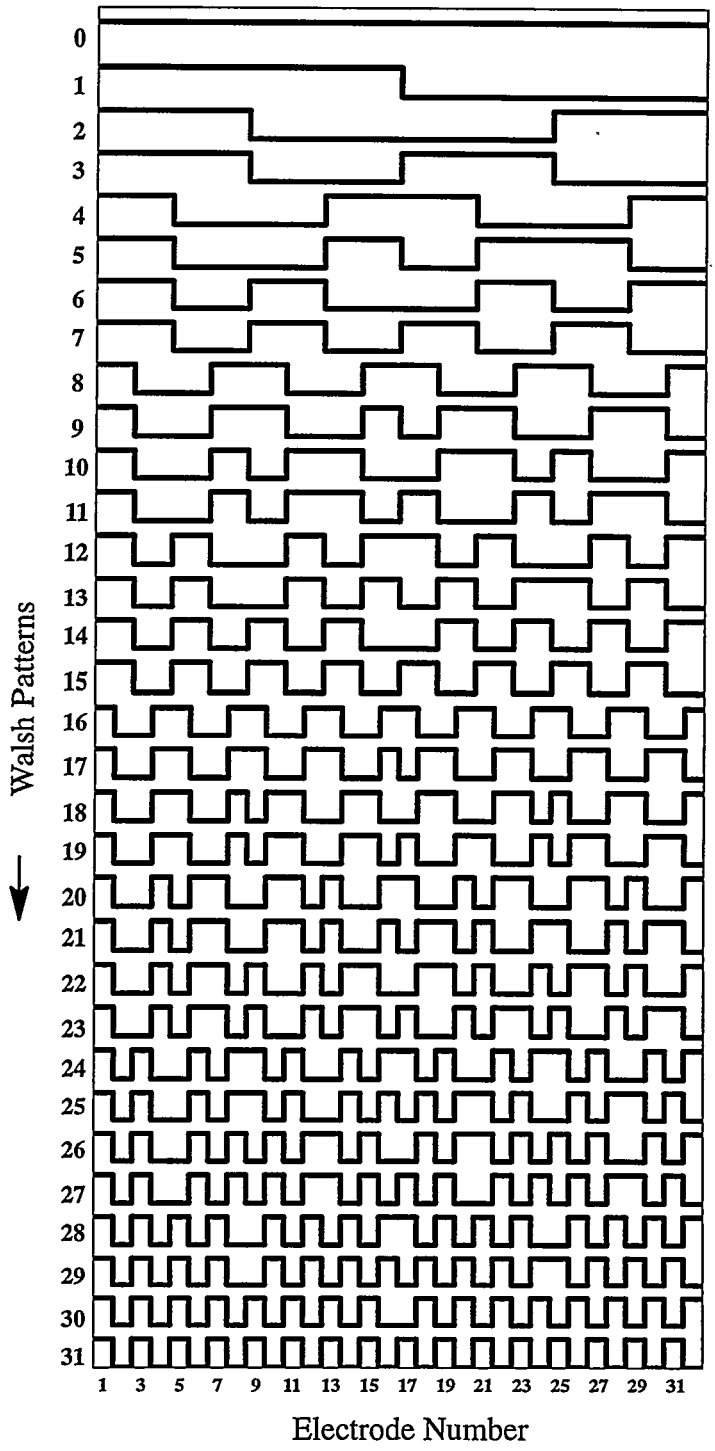

Figure 6.13 Walsh patterns used for excitation of a 32–electrode system.

6.6 Sensitivity

Sensitivity is defined as the relative fractional change of the boundary potential when the conductivity of an element region is perturbed in small magnitudes [77]. All EIT systems suffer from the lack of sensitivity because all measurements are constrained to be taken on the boundary of the unknown body of imaging. This section presents the results of an investigation to determine the sensitivity of the FE mesh using plate and rod electrode models. More specifically, information relative to the following questions is provided:

- How much can sensitivity be increased by using plate electrodes instead of rod–electrodes?
- What is the effect of mesh refinement on sensitivity?
- How does the coarse mesh affect the quality of reconstructed images?
- Can sensitivity be increased by using a proper excitation method?

Using both rod and plate electrodes in the two–dimensional phantoms the conductivity of a chosen conductivity element was varied and the relative change in the boundary voltages was computed from the solution of the forward problem for each case. The mesh was refined by a factor of three or more and the same procedure was repeated to investigate the variation of sensitivity with mesh refinement. A similar technique was used by Murai and Kagawa [42] to determine the fractional change in mean impedance for sensitivity matrix calculations. The variation of the mean impedance is a highly nonlinear function of conductivity but quite linear for small perturbations.

6.6.1 Rod Electrodes versus Plate Electrodes

To compare sensitivities of rod electrode and plate electrode models, the worst case was simulated by choosing the farthest electrodes from the least sensitive central region of the phantom (i.e., the electrodes 1 and 9 diagonally crossing the phantom from the central region). For the homogeneous cases, the conductivity of elements are assigned a constant of 1 $(\Omega m)^{-1}$ and excitation was supplied by injecting 1 A. into electrode pair 9–1. The boundary voltage is first calculated for homogeneous conductivity distribution, and then the boundary voltage is recalculated with the conductivity of the central element increased by a factor of ten. In these computations, the finite element mesh used to model the square phantom geometry is shown in Figure 6.14. Figure 6.14(a) shows a 16×16 square mesh model for the 16 rod–electrode phantom. To have an accurate comparison of two electrode types the same mesh was used but the rod electrodes were replaced by 25.4–mm wide plate electrodes as shown in Figure 6.14(b). Figure 6.15 shows the relative change of the boundary voltage for both models. The results indicated that the maximum sensitivity for both models was near the excited electrodes. This is because the potential gradient is highest near the excited electrodes. From these obtained sensitivity curves, one can conclude that the plate electrode model is approximately 25% more sensitive than the rod electrode model for single pair electrode excitations.

The variation of the sensitivity with the conductivity of the perturbed element is given in Figure 6.16. For small perturbations of the conductivity in the approximate range of 0.1 to 10 times the original value, the sensitivity variation is nearly linear. For larger perturbations, however, the variations becomes highly nonlinear approaching a limit value in both increasing or decreasing directions of σ/σ_o. This explains why the iterative inverse calculations of conductivity values do not converge to their real values for perfect insulator,

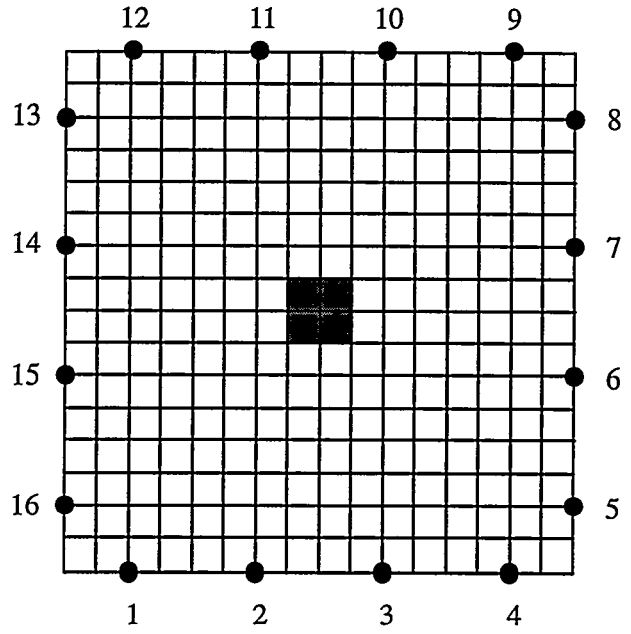

(a)

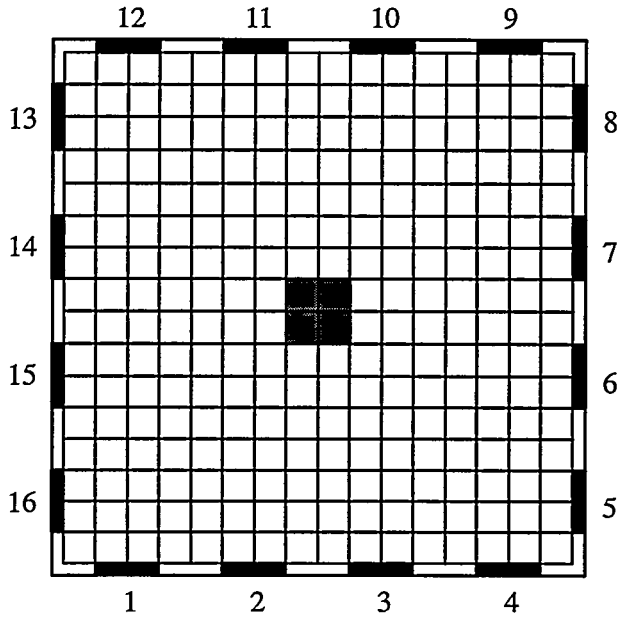

(b)

Figure 6.14 Computational mesh and perturbed elements shaded by gray color at the center of each phantom to compare sensitivities of rod– and plate–electrode phantoms: (a) 16×16 mesh for the rod–electrode phantom; (b) 16×16 mesh for the plate–electrode phantom.

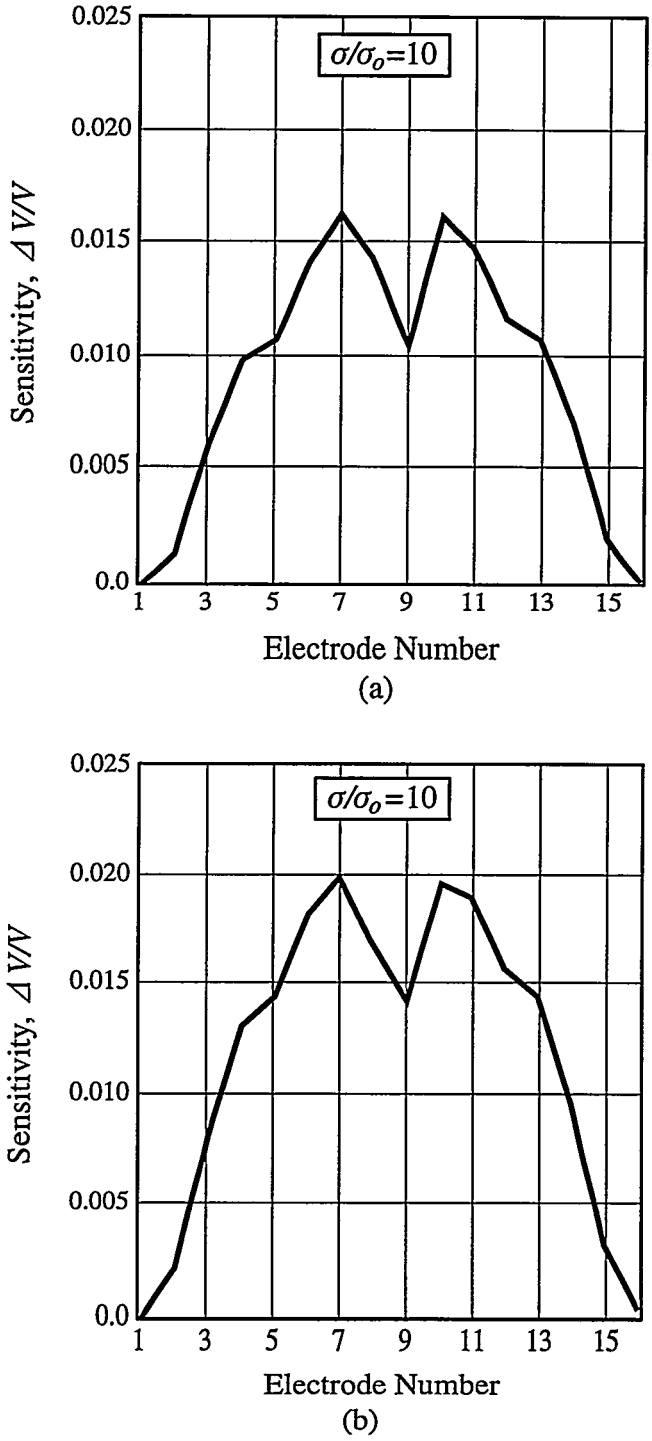

Figure 6.15 Comparison of sensitivity of (a) rod–electrode to (b) plate–electrode phantom with corner–to–corner pair excitation (electrodes 1 and 9 are excited with 1 A).

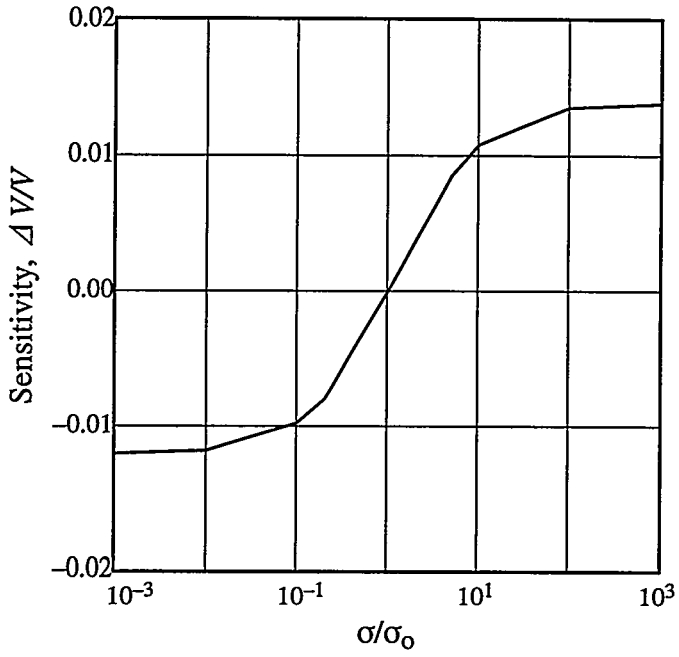

(a)

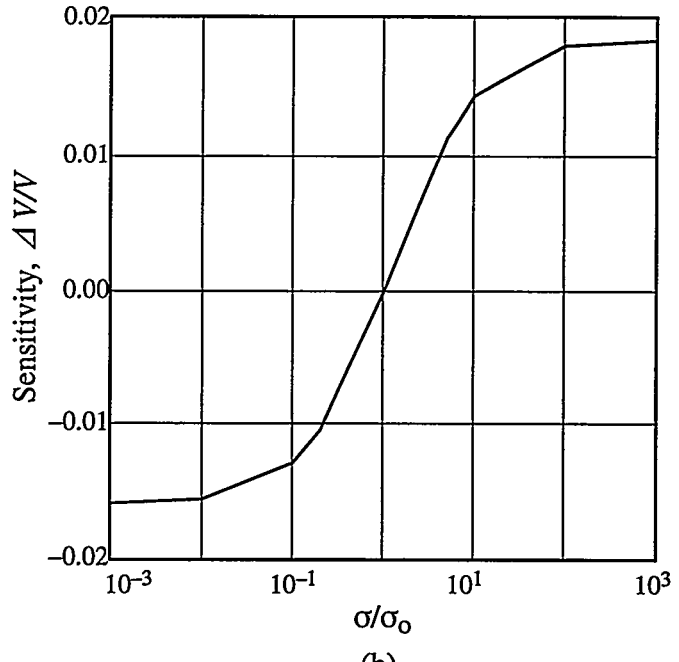

(b)

Figure 6.16 Comparison of sensitivity variation versus changes in the central conductivity: (a) Rod–electrode model; (b) Plate–electrode model.

or perfect conductor targets but, rather, produce contrast ratios which are significantly lower than the true cases.

6.6.2 Numerical Sensitivity vs. Mesh Refinement

The effects of finite element discretization error on sensitivity was investigated. In Figures 6.17(a) and 6.17(b), the refined meshes for the rod– and plate–electrode phantoms are shown, respectively. The shaded areas near the center of the phantoms represent the perturbed conductivity elements. In Figure 6.18, the variation of sensitivity on the boundary is shown as the mesh is refined by a factor of 2, 3 and 4 for the rod–electrode phantom model, and by a factor of 2 and 3 for the plate–electrode phantom model. The results show that the sensitivity slowly converges to a limit as the mesh is refined for the rod electrode model. On the other hand, this convergence for the plate electrode model is so rapid that using the 18×18 mesh does not yield a significantly different result than that of the 27×27 mesh.

6.6.3 Exciting Multiple Electrodes versus an Electrode Pair

It is important to investigate alternative excitation strategies to further increase the sensitivity. Combining adjacent electrodes into two separate groups and exciting them with a voltage source are expected to have an effect of increasing the current density in the interior regions of the phantom.

The sensitivity calculations for multiple electrode excitations are shown in Figure 6.19. These calculations are performed by injecting +1–A excitation currents into each electrode numbered as 1 through 8, and by injecting –1 A into each electrode numbered as 9 through 16 on the 32×32 mesh for the rod–electrode phantom, and on the 27×27 mesh for the plate–electrode phantom (see Figure 6.17). The sensitivity results for rod and plate electrodes are shown in Figures 6.19(a) and (b), respectively. Unlike the results previously

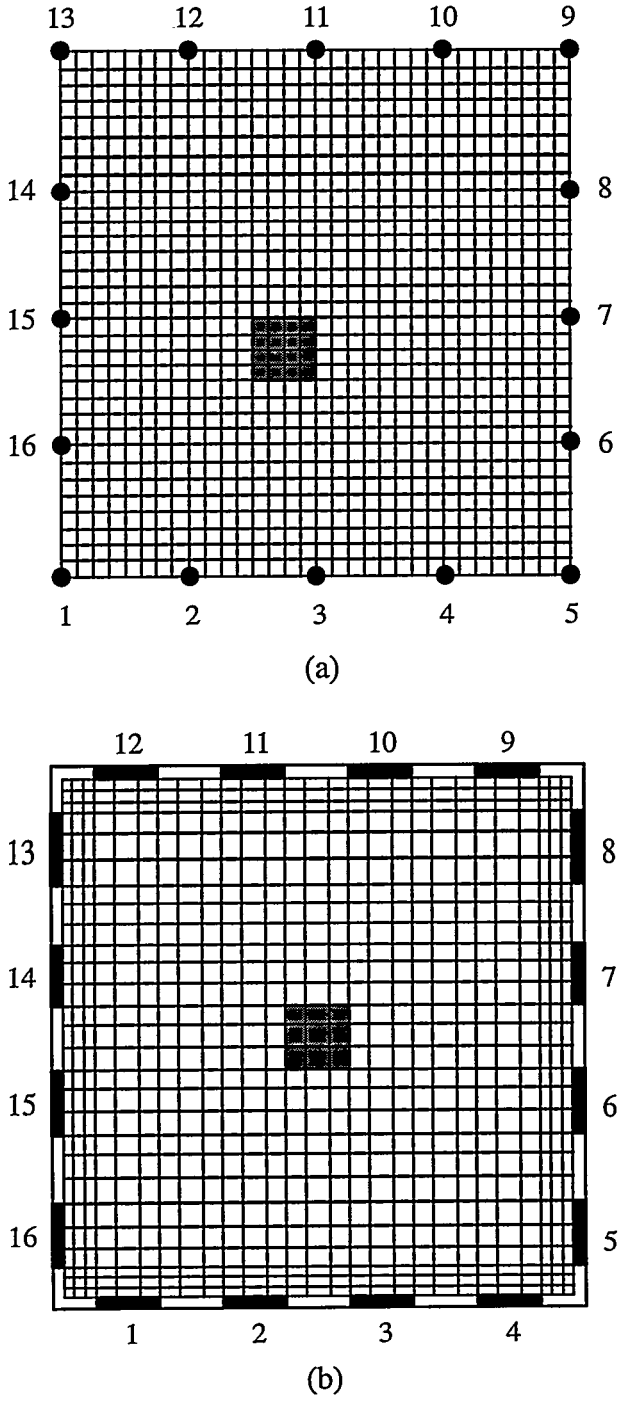

Figure 6.17 Computational mesh and perturbed elements shaded by gray color at the center of each phantom to compare sensitivities of rod– and plate–electrode phantoms: (a) 32×32 mesh for the rod–electrode phantom; (b) 27×27 mesh for the plate–electrode phantom.

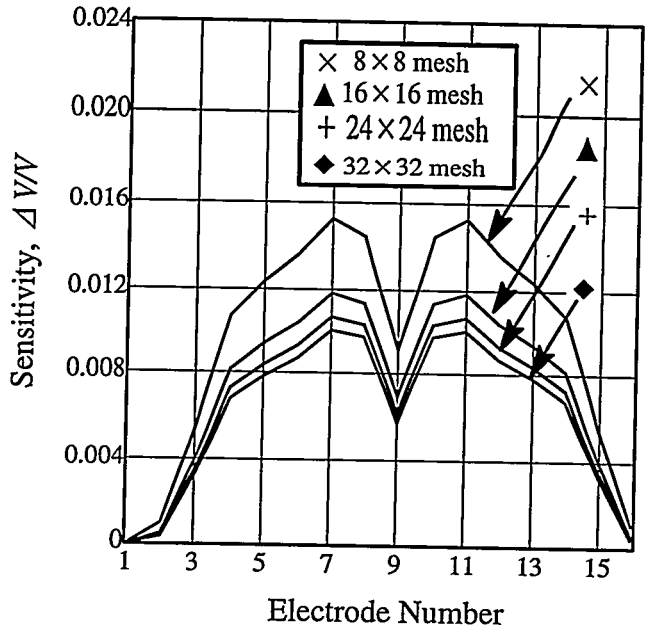

(a)

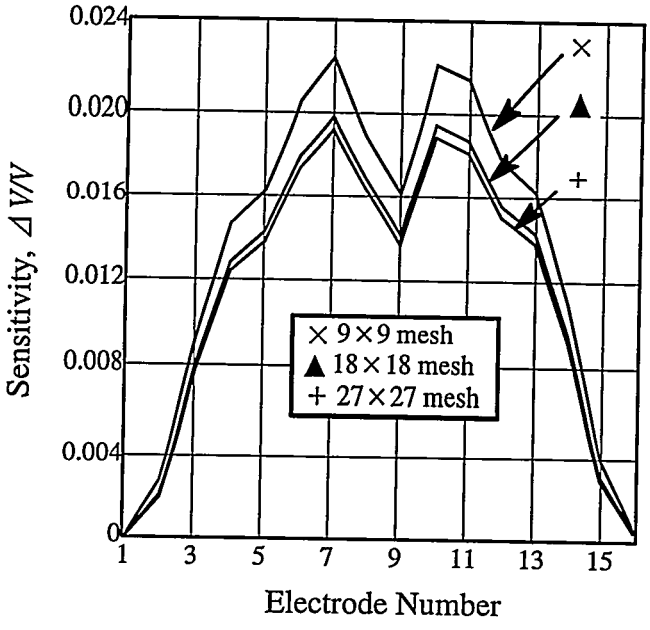

(b)

Figure 5.18 Variation of electrode voltage sensitivity, with single–pair excitation, due to mesh refinement in two models: (a) rod–electrode; (b) plate–electrode.

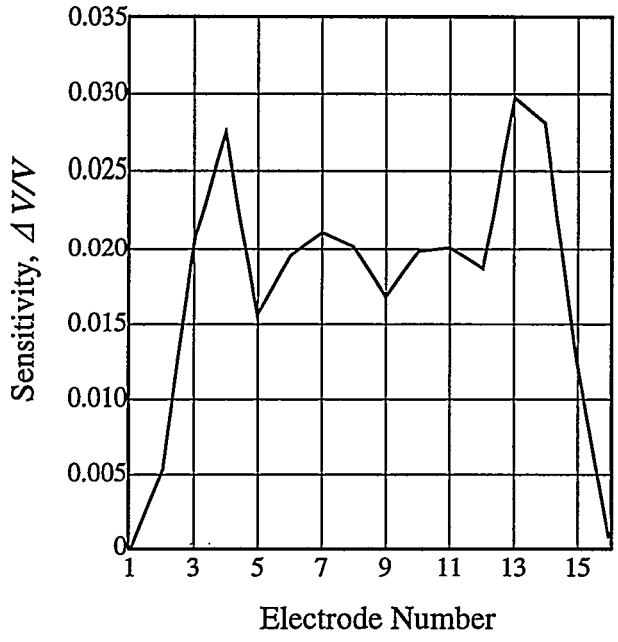

(a)

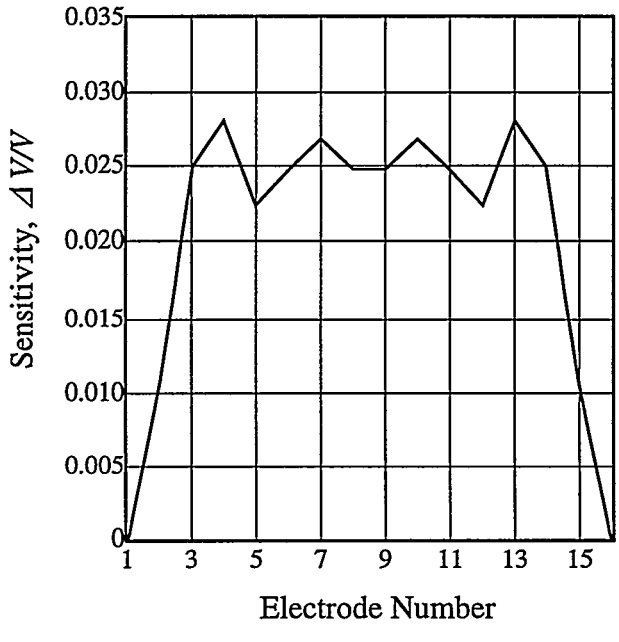

(b)

Figure 6.19 Sensitivity variation when multiple electrodes are excited: (a) rod–electrode model, 32×32 mesh; (b) plate–electrode model, 27×27 mesh.

obtained in Figure 6.15, the results obtained herein show that the difference between the sensitivities of the rod and plate electrodes is very little (compare Figure 6.19(a) to 6.19(b)). However, the plate electrode model has relatively uniform sensitivity variation from electrode to electrode when compared to that of the rod electrodes.

On the other hand, for both the rod and plate electrode models the increase in sensitivity of multiple electrode excitations are significantly higher than those of single pair excitations. Compare Figure 6.19 to Figure 6.18. For the same size of mesh (32×32 for the rod–electrode model and 27×27 for the plate–electrode), the sensitivity of rod electrodes is increased by a factor of three by using multiple electrode excitations. However, the same comparison for the plate–electrode model shows only about a 40% increase.

6.7 Distinguishability

In Chapter 4, it was pointed out that the Hessian matrix may be grossly ill–conditioned with its eigenvalues ranging from over six orders of magnitudes or more. Therefore, in some problems, one might expect to contend with difficulties in correctly imaging small–sized objects near the interior regions farthest away from the boundary electrodes of a phantom. The purpose of this section is to provide a basic theory of distinguishability, and then to introduce an experimental method to increase distinguishability of the data.

6.7.1 Definition

If an object is inserted into a phantom, the changes in observed response (may be either voltage or current depending on the type of excitation) changes relative to the the response observed before the object is inserted into the phantom. In the case of erroneous measurements of boundary response, the magnitude of error plays an important role in distinguishability of the change in conductivity distribution. If the magnitude of this error is

less than the magnitude of the changes in responses, the inserted object is called to be "distinguishable." It is important to provide this measure as a quantitative indicator to determine the minimum detectable size in designing an EIT system. Distinguishability is defined in a vector norm notation by Isaacson [55]. In a continuous excitation case, he defined distinguishability as the ratio of the norm of the differences between two boundary responses to the norm of the excitation source. In the case of current source excitation, let j be the applied current density on the boundary, and v_1 and v_2 be the boundary responses for conductivity distributions σ_1 and σ_2, then the distinguishability is expressed as

$$d(\sigma_1,\sigma_2,j) = \frac{\| v_1(\sigma_1,j) - v_2(\sigma_2,j) \|}{\| j \|}, \tag{6.2}$$

where $\| \cdot \|$ denotes an L^2 norm defined as

$$\| f \| \equiv \left[\int_S |f|^2 \, dA \right]^{1/2} \tag{6.3}$$

where f is any function defined on S.

6.7.2 Optimal Excitation Patterns

Maximizing the distinguishability will minimize the size of the smallest detectable target in an EIT system. In Equation (6.2), for a given phantom geometry, the electrodes sizes and their locations on the phantom boundary, the excitation patterns applied to the electrodes are the main factors influencing the distinguishability measure. From a common sense, the area of electrodes should be enlarged to increase the current density in the insensitive regions of the phantom. However, there is a trade–off between the number of electrodes and their sizes due to space limitation on the boundary. Another alternative for

increasing the distinguishability is to seek optimal current patterns. Therefore, the problem is reduced to an optimization problem as

$$d_{max} = \max_{j} \frac{\| v_1(j) - v_2(j) \|}{\| j \|}. \tag{6.4}$$

In the following two sections the definition in Equation (6.2) is extended to a more general case of discrete electrodes. The specific case related to current excitation source is presented in Woo [30], and Cheney and Isaacson [150]. On the other hand, in this report, voltage excitations by a single voltage source were used in order to simplify the hardware instead of using current sources for each electrode. This necessitates the extension of the same idea for the case of excitations by a voltage source. This extension will be provided in this section.

Excitation by a Current Source. In the case of current source excitation, the response on the boundary is the measured electrode voltages. The current–voltage relationship can be written in a phantom resistance matrix

$$R_{p_{E\times E}}\, C_{e_{E\times P}} = V_{e_{E\times P}}, \tag{6.5}$$

where R_p denotes the phantom resistance matrix, C_e includes excitation currents injected into the electrodes, and V_e includes the measured potentials on the electrodes. If the same current is applied to two both homogeneous and targeted conductivity distributions the results of both cases are expressed as

$$R_p^h\, C_e = V_e^h \tag{6.6a}$$
$$R_p^t\, C_e = V_e^t, \tag{6.6b}$$

where superscripts h and t denote the homogeneous case and target case, respectively. The voltage change on the electrodes (consider the schematic diagram in Figure 6.20(a)) is obtained by the difference between Equation (6.6a) and Equation (6.6b) as

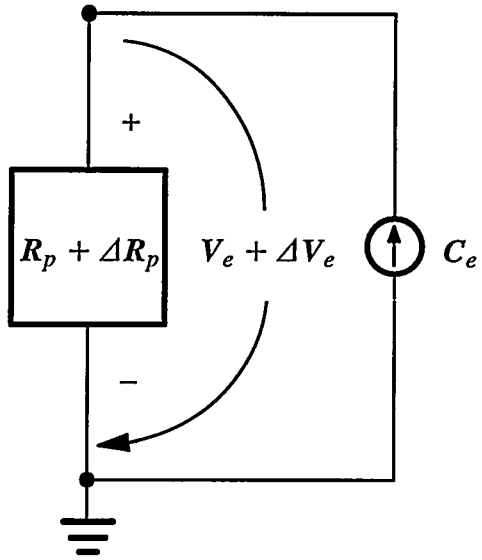

(a)

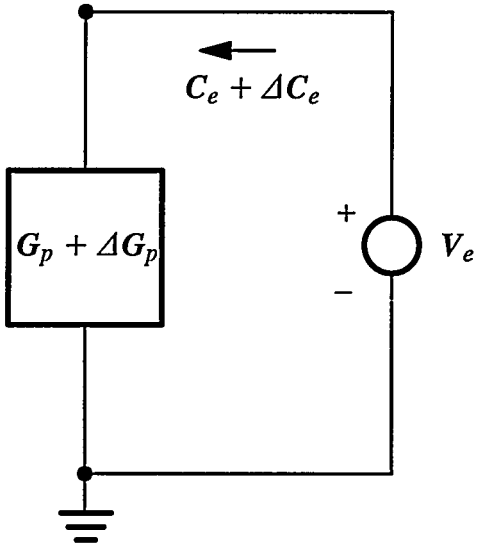

(b)

Figure 6.20 Schematic of excitation of a phantom: (a) by a current source; (b) by a voltage source.

$$\Delta V_e = V_e^h - V_e^t = [R_p^h - R_p^t]\ C_e = \Delta R_p\ C_e \tag{6.7}$$

Thus, the distinguishability for current excitation, is expressed for discrete case of Equation (6.2) by

$$d_c = \frac{\|\Delta V_e\|}{\|C_e\|} = \frac{\|\Delta R_p\ C_e\|}{\|C_e\|} \leq \frac{\|\Delta R_p\|\ \|C_e\|}{\|C_e\|} = \|\Delta R_p\|\,. \tag{6.8}$$

The inequality expression in Equation (6.8) shows that any arbitrary current pattern applied by C_e corresponds to a distinguishability value d_c and this is less than the norm of the matrix representing the resistance changes in the target and homogeneous networks. This maximum distinguishability value can only be achieved by choosing the eigenvectors of matrix ΔR_p as current patterns

$$d_{c,max} = \|\Delta R_p\| \equiv |\lambda_{\max}|, \tag{6.9}$$

where $|\lambda_{max}| = \max\lambda(\Delta R_p)$.

Excitation by a Voltage Source. Similar to the current excitation case, but in a reverse way, the current–voltage relation is expressed by the phantom conductance matrix,

$$G_{p_{E\times E}}\ V_{eE\times P} = C_{eE\times P} \tag{6.10}$$

since the excitation is provided by a constant voltage source (for this case see Figure 6.20(b)). If the similar steps in Equations (6.6a)–(6.6b) and Equation (6.7) are completed for ΔC_e, the inequality in Equation (6.8) turns out to be

$$d_v = \frac{\|\Delta C_e\|}{\|V_e\|} = \frac{\|\Delta G_p\ V_e\|}{\|V_e\|} \leq \frac{\|\Delta G_p\|\ \|V_e\|}{\|V_e\|} = \|\Delta G_p\|\,. \tag{6.11}$$

In this case, the optimal excitation patterns are the eigenvectors of ΔG_p, and maximum distinguishability for voltage excitation patterns are obtained by

$$d_{v,max} = |\lambda_{max}| = \max\lambda(\Delta G_p). \tag{6.12}$$

Note that for optimal excitation, the phantom resistance or conductance matrices are required.

6.7.3 Calculating the Phantom Resistance Matrix

The schematic of the electrode system is shown in Figure 6.21. The input/output current values injected into each electrode are measured through calibrated resistors. These resistors are calibrated by driving a certain amount of known current by a current source. Then, measuring the voltage drop on each resistor, the resistance value is accurately determined from the ratio of voltage value divided by the current value. Accurately knowing resistivity values of the series resistors, the electrode currents are determined from the voltage drop on each resistor.

The relationship between the applied voltages and the currents are expressed by

$$V_s = \left[R_p(\sigma) + R_m\right] C_e \tag{6.13}$$

where $R_p(\sigma)$, R_m and C_e are the phantom impedance matrix, the series resistor transfer impedance matrix (a diagonal matrix) and the electrode current matrix, respectively. The data acquired to reconstructed images is a set of excitation currents of electrodes, for P excitation patterns, and their response on the E electrodes. The source voltages are known patterns, which do not need to be measured in each experiment. Therefore, the relationship between measured electrode voltages and currents is expressed by

$$V_e = R_p(\sigma)\ C_e \tag{6.14}$$

From circuit theory, the system of equations are not solvable unless the reference voltage is introduced to the system (which means that one of the electrodes should be chosen as a

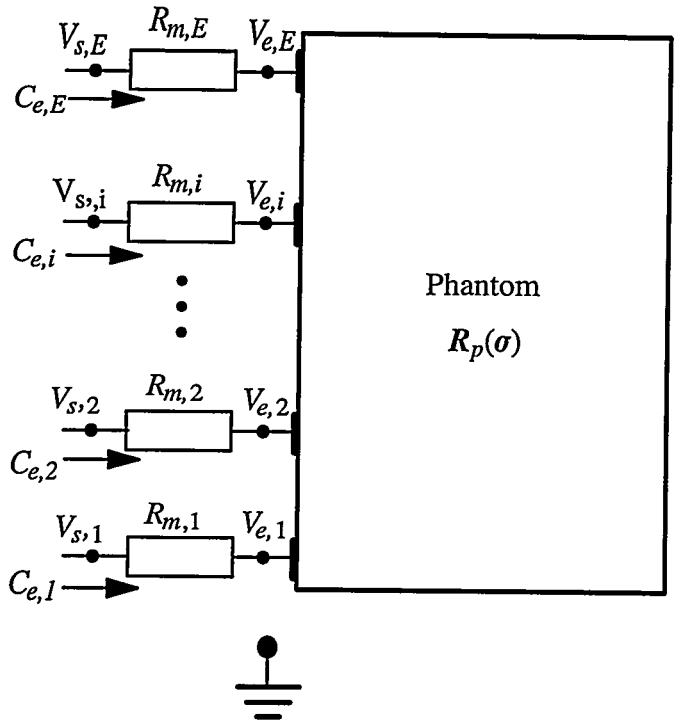

Figure 6.21 Schematic of measuring electrode voltages and currents.

reference electrode with zero potential). This is satisfied allowing the corresponding rows of the electrode voltage and current matrices to be zero. Therefore, we obtain an $(E-1) \times (E-1)$ equation system for each excitation. If the superscript "*" is used to define a reference point in the matrices, the calculation of phantom impedance matrix can be algebraically obtained from the acquired electrode currents and voltages. By setting the reference electrode in Equation (6.14) and multiplying both sides of this equation by the transposed electrode current matrix, the phantom impedance matrix is calculated by

$$\boldsymbol{R}_p^*(\sigma) = \boldsymbol{V}_e^* \, \boldsymbol{C}_e^{*T} \left[\boldsymbol{C}_e^* \, \boldsymbol{C}_e^{*T}\right]^{-1}. \tag{6.15}$$

Since the phantom impedance matrix has a rank of $(E-1)$, the symmetric matrix product $\boldsymbol{C}_e^* \, \boldsymbol{C}_e^{*T}$ obtained is made invertible by setting the diagonal entry to 1 on the row number associated with the selected reference electrode number.

6.7.4 Computation of Eigenvectors

The phantom resistance and conductance matrices are symmetric and self–adjoint matrices. These matrices are calculated from the experimentally applied Walsh pattern excitations and the matrices are differentiated to obtain the distinguishability matrix, $\boldsymbol{D}$ ($\Delta \boldsymbol{R}_p$ or $\Delta \boldsymbol{G}_p$). The eigenvalues and eigenvectors of the distinguishability matrix are computed by singular value decomposition (SVD) [101] as

$$\boldsymbol{D} = \boldsymbol{U} \, \boldsymbol{\Sigma} \, \boldsymbol{V}^T, \tag{6.16}$$

where $\boldsymbol{U}$ and $\boldsymbol{V}$ are orthonormal matrices and $\boldsymbol{\Sigma}$ is a diagonal matrix whose diagonal entries include the singular values of the distinguishability matrix. The columns of $\boldsymbol{U}$ are the eigenvectors of $\boldsymbol{D}$ to be applied as optimal excitation patterns.

The distinguishability matrix defined in Equation (6.16) has eigenvalues ranging between a maximum and minimum value, all being equal or greater than zero as

$$\lambda_1^2 > \lambda_2^2 > \cdots > \lambda_{E-1}^2 \geq 0, \tag{6.17}$$

where each sorted eigenvalue corresponds to one of the $E - 1$ independent excitation patterns (computed eigenvectors of the distinguishability matrix). These excitation patterns contribute to the necessary information with a distinguishability value. For example, the excitation pattern corresponding to λ_1 provides the highest distinguishability, and the second corresponding to λ_2 provides the second highest distinguishability, and so on.

6.7.5 Optimization by Computation

The foregoing ideas on optimization were the basis for developing a system where optimal excitation patterns are determined directly during the experiment and applied to the phantom itself [151]. Conceptually, what this means is that more current is applied to regions of high–resistivity, thereby increasing the sensitivity of normally low–current regions of the phantom. However, it seems that there is no reason why the same concept of optimization cannot be applied *post facto* on data acquired in the standard manner. That is, the data could be obtained using Walsh excitation which include as first harmonics the sine and cosine patterns found optimum by Cheney and Isaacson [150] for a circular target centered in a circular phantom. The $E \times E$ phantom conductance matrix could then be computed in the standard manner for both the targeted and homogeneous cases. Having these two matrices, the difference matrix, $\Delta \boldsymbol{G}$, may be computed along with its eigenvectors which are also optimal voltage patterns guaranteeing to provide the best distinguishability as previously shown. The the current response to $E - 1$ eigenvectors is numerically computed by using Equation (6.10). The obtained current response and the eigenvectors are used in reconstruction process.

In practice, what this means is that the eigenvectors have elements which, in effect, unify the sensitivity over all excitations. Walsh excitations are all applied with equal amplitude. Therefore, excitations which produce most sensitivity are identically weighted with those which produce the least sensitivity. *Postfacto* optimization changes the amplitudes of the experimental data to correspond to the amplitude distribution of the eigenvectors, in effect providing optimal weighting of the data. It will be shown in Chapter 7 that such optimization significantly improves the results of the computed images.

6.8 Effects of Using Multiple Excitations Patterns

An E–electrode model has at most $E(E-1)/2$ possible excitations. Since we use mean–square minimization rather than direct algebraic reduction to converge to an image, we need not use as many excitations (equations) as we have elements.

Figure 6.22 shows that the image reconstruction error *per unit excitation*[10] typically decreases by a factor of six as the number of excitations increases from 16 to 120, the maximum number of independent excitations for this 16–electrode phantom. The plate electrode model has a 40% improvement under similar conditions. In practice, the *total* reconstruction error increases slightly up to 32 excitations then remains relatively constant.

6.9 Effect of Liquid Conductivity

The electrode–liquid contact impedance of an electrode is also another factor which may especially become more critical when the electrodes are in contact with high concentrations of saline solution. Schwan [154] and Geddes et al. [155], [156] previously reported that the contact impedance mainly depends on the current density, the frequency of the applied excitation signal, and the conductivity or concentration of the saline solution.

10. The per unit excitation error is the total excitation error, ϕ, divided by the number of excitations.

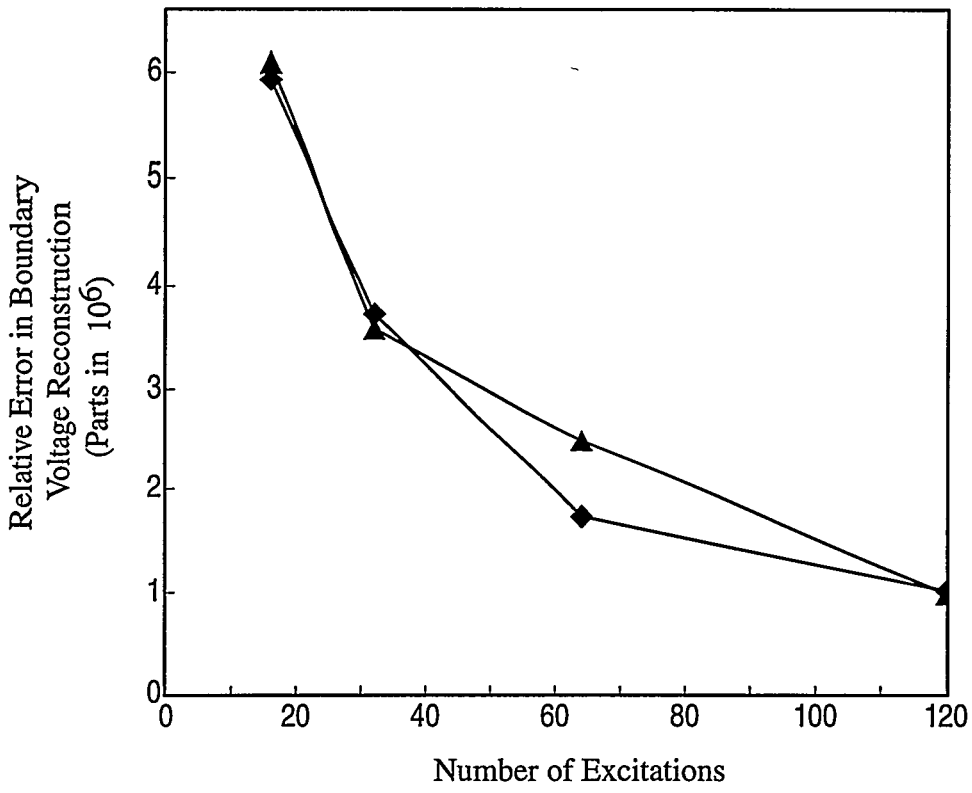

Figure 6.22 RMS error in boundary reconstruction per unit excitation for the 16–rod–electrode phantom: ● homogeneous; ▲ nonhomogeneous.

An analytical model for the behavior of contact impedance is very complex and it cannot be easily calculated *a priori* (see Onaral and Schwan [157], [158], and Onaral et al. [159]). Newell et al. [160] described a quantitative method for rapid assessment of contact impedances of electrodes in a two–dimensional phantom. For situations when the electrode–liquid contact impedances are significantly high, these impedances have to be determined and properly modeled in the numerical model of the phantom for the forward solution in reconstruction process (see Cheng et al. [54], [161], and Somersalo et al. [162]).

Contact impedance concerns are very critical for biomedical applications dealing with typically 0.9% saline solution, having conductivity value of about 30,000 μS/cm. Due to the power limitations of the excitation sources, low concentrations of saline solution within 50–1000 μS/cm conductivity range were used in the experiments presented this study and the effects of contact impedance are unknown.

It had been anticipated, however, that addition of salt to the water would degrade the experiment due to contact impedance. The lack of sensitivity with distilled water, however, required that we look for an optimum where decreased error due to increased current flow might, at first, reduce overall error which might then increase due to contact impedance effects. The data in Figure 6.23 taken with stainless steel electrodes show that there does not appear to be an optimum although there was a reproducible localized maximum in reconstruction error near 70 μS/cm. We have no idea of the cause of this effect but now, typically, use conductivity values either in the range near 150–200 μS/cm, or near 1000 μS/cm, the power limit for signal generator and geometry.

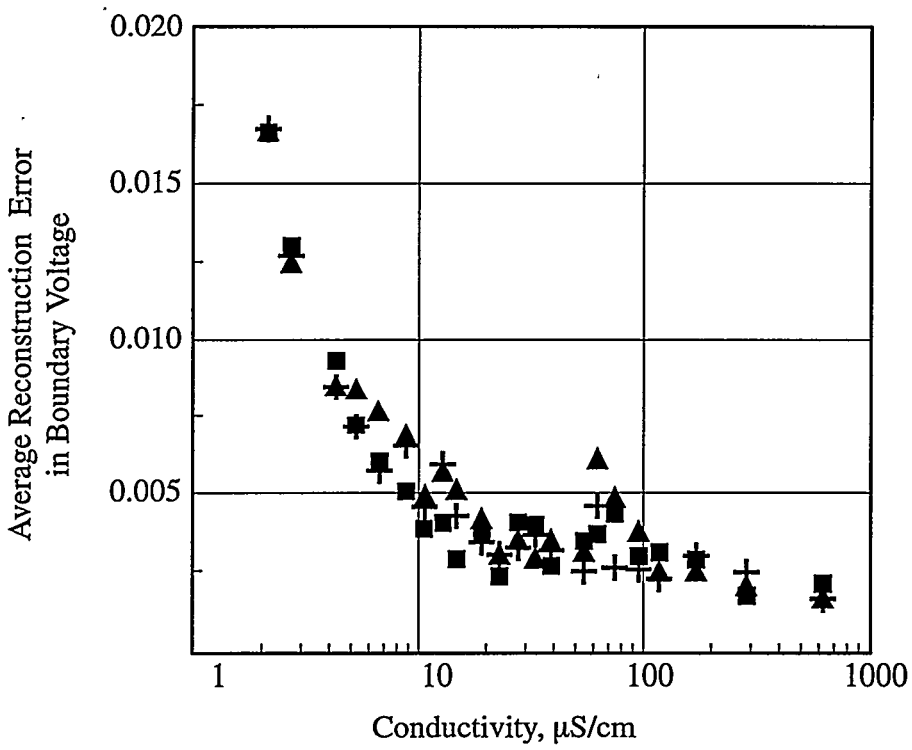

Figure 6.23 Liquid conductivity effect on reconstruction error. Different symbols represent different repeatability sets taken over several months time.

6.10 Noise in Measurements

During the data acquisition procedure, the digital voltmeter is required to make many voltage measurements. These measurements, depending on the chosen type of the source (current or voltage source), are a set of electrode voltage values and voltage drops on series resistors used for current measurements. Sequential readings of constant voltage signal (this reading may be the rms value of a sinusoidal signal or the peak value of a square pulse signal, to be explained later) exhibits some random variation. These variations comes from different sources: the noisy test environment (radio frequency (RF) interference noise), the finite resolution of the digital multimeter and signal waveform generator, etc. In this section, the statistical behavior of these variations is investigated and the sequential averaging technique (SAT) is developed to eliminate noise in measurements.

6.10.1 Frequency Considerations

Unchanging electric currents or extremely slowly changing currents cause charges to flow in the body, and their presence and distribution can be significant. Their frequency of change is essentially zero, and the electric and magnetic fields associated with them decrease steadily with distance but do not change much with time. The fields set up by such currents are able to cause ions to flow in the same direction yielding additional effects which are not accounted for properly in the modeling. Also, associated electrode polarization makes impedance measurements difficult to undertake at very low frequency.

At high frequencies there will be interaction with the target, and stray capacitors become increasingly important. Furthermore, over a few MHz, space charge effects become important and microwave transmission modes begin to dominate. Thus, frequencies used in impedance imaging are generally in the range of a few dozen Hz up to several

hundred kHz, or even a MHz. Voltage can be applied to a pair of electrodes and the resulting current measured, or a constant current can be forced to flow and the resulting voltage measured.

6.10.2 Excitation Signal

Virtually, all impedance tomography systems in use today utilize sinusoidal excitation signal. Direct acquisition folds noise into the alternating current rms averaging process. Alternately frequency locking methods may be used to eliminate noise effects to achieve 100 Hz slot noise levels $\sim$100 dB less than the signal level itself. Such methods, however, do not lend themselves to high speed imaging where data must be obtained on millisecond time scales or less. Rather, a phase–timed method illustrated in Figure 6.24 is adopted. Square–pulse signal is used as excitation, since this is exactly what would be obtained using high speed switching methods in real–time systems.

Measurements are taken at the quarter–wave point as determined by the zero crossover and the excitation frequency. Figure 6.25 shows an oscillograph of a 1 kHz square–pulse excitation signal with zero–to–peak magnitude of 25 mV. This low signal magnitude is specifically chosen to clearly show the noise in the signal.

Unfortunately, there are some undesirable effects which should be considered when choosing the frequency of the excitation signal. Capacitive and inductive effects are inherent in the signal waveform generator, the digital multimeter, and the connection wires of the data acquisition system. Typically, these effects exhibit the behavior of an oscillating L–C circuit on the square–pulse signal, distorting the pulse from its ideal square shape. For low frequencies, these oscillations quickly die off before the multimeter is triggered at quarter–wave point and their effects are small in measurements as seen in the oscillograph

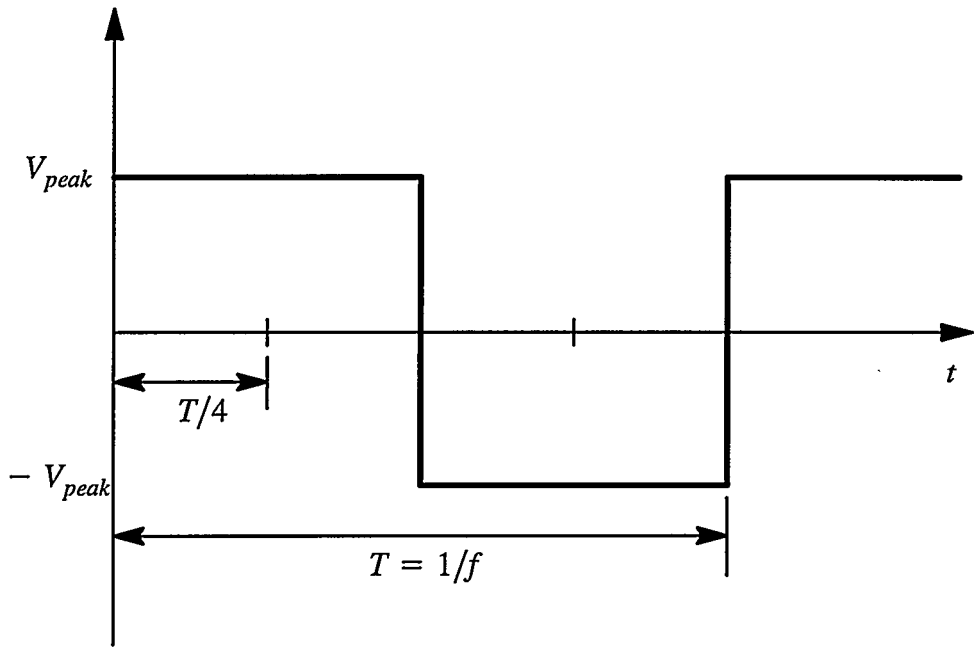

Figure 6.24 Square pulse type excitation signal with duty cycle of 50%. The peak of the pulse is measured by triggering the voltmeter at T/4. This minimizes the unwanted effects of signal decaying due to the impedance of the load and the data acquisition circuitry.

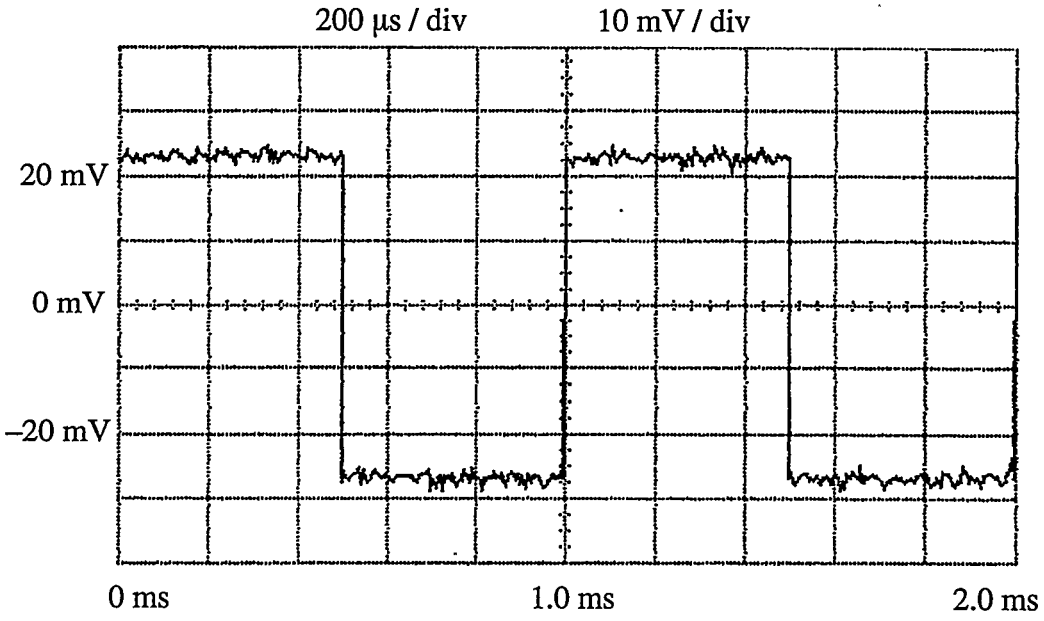

Figure 6.25 Oscillograph of a 1–kHz square–pulse obtained from the signal wavefom generator loaded by the phantom impedance.

of a 100 Hz square–pulse in Figure 6.26(a). However, in higher frequency ranges this effect appears as a decaying pulse characteristic as seen in the oscillograph of a 1–kHz square–pulse in Figure 6.26(b). This effect is a nonissue in the 100 Hz range but it may cause considerable variations in measurements at frequency ranges from hundreds of kHz to a tens of MHz, considered for high data acquisition speeds. Especially, at high frequency applications the measurements may become very sensitive to detection of zero–crossing point.

To investigate the characteristic of the noise source involved in the measurements, a large number of measurements (here, a population of 10,000 data points were assumed to be a reasonable size) were obtained by the digital voltmeter. In this case, the peak of a 1–volt–square–pulse signal was measured. For convenience, the measured data are normalized by the mean calculated from the overall data set. The histogram of these measurements is shown in Figure 6.27. The same type of histograms have been obtained for various peak values, and they all have showed the similar Gaussian distribution pattern but with different standard deviations. The standard deviation changes depending on the signal magnitude and the selected voltmeter range where the signal magnitude falls. Table 6.2 shows the measurements of peak of a 1–kHz square–pulse at various peak values using various voltage ranges of the digital multimeter (DMM). In these measurements, the signal waveform generator was loaded by the impedance of the phantom to depict the real conditions of the data acquisition process.

6.10.3 Sequential Averaging of Measurements

The sequential averaging technique is based on averaging independently collected samples. The standard deviation of the averaged samples decreases by a factor of the reciprocal of the square root of the number of collected samples $\sigma_n = \sigma/\sqrt{n}$ [163]. When an

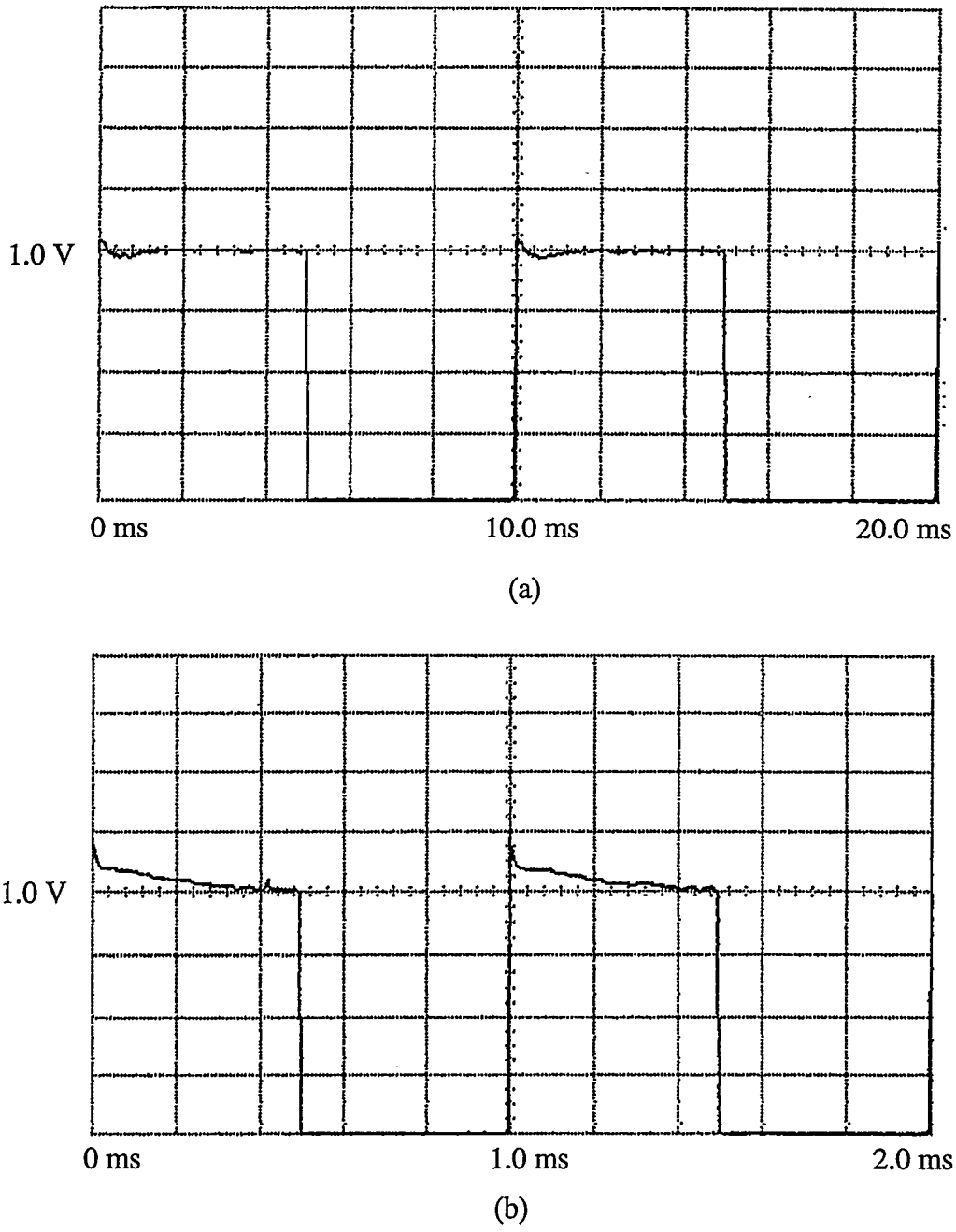

Figure 6.26 Oscillographs showing the effect of frequency on excitation signal: (a) a 100 Hz square–pulse of 1V (zero–to–peak); (b) a 1–kHz square–pulse of 1V (zero–to–peak).

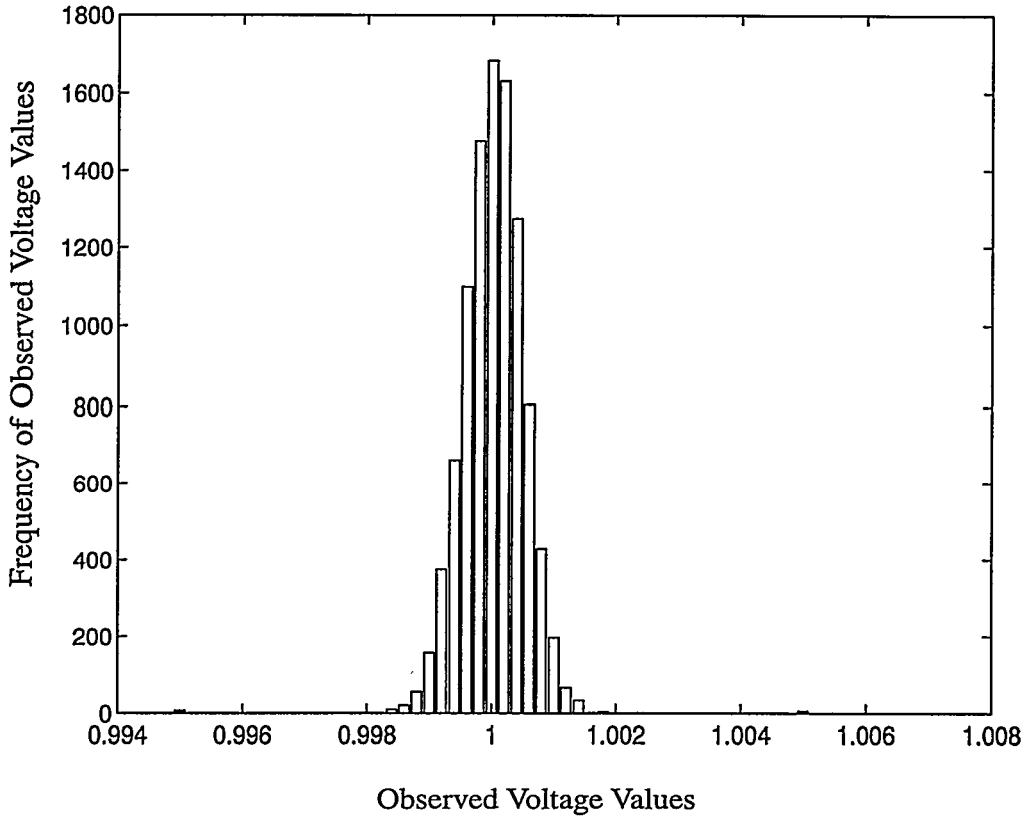

Figure 6.27 Frequency distribution obtained from 10,000 voltage measurements of the peak of square–pulses (all measurements are normalized by the average of the entire data set).

Table 6.2 Experimental measurements of peaks of square–pulse with various magnitudes and measurement errors in different voltage ranges of the voltmeter.

Expected (Volt)	Average (Volt)	Standard dev. (Volt)	CV (x 100 %)	Range
2.5000E–02	2.4769E–02	3.4319E–04	1.3855E–02	0.1 V
5.0000E–02	4.9968E–02	3.7606E–04	7.5259E–03	0.1 V
7.5000E–02	7.5023E–02	4.5139E–04	6.0166E–03	0.1 V
1.0000E–01	9.9857E–02	4.9910E–04	4.9981E–03	0.1 V
2.5000E–01	2.4998E–01	8.2116E–04	3.2848E–03	1 V
5.0000E–01	4.9951E–01	9.2064E–04	1.8431E–03	1 V
7.5000E–01	7.4970E–01	6.8237E–04	9.1019E–04	1 V
1.0000E+00	1.0007E+00	8.0642E–03	8.0584E–03	1 V
2.5000E+00	2.5065E+00	3.2217E–02	1.2853E–02	10 V
5.0000E+00	5.0160E+00	9.6349E–02	1.9208E–02	10 V
7.5000E+00	7.5147E+00	1.0779E–01	1.4344E–02	10 V
1.0000E+01	1.0013E+01	9.4168E–02	9.4050E–03	10 V

Note: Where CV is the coefficient of variation defined as the ratio of the standard deviation of the measurements to the average of the measurements.

infinite number of independent samples are averaged, the average converges to the true value of the signal.

This method was developed to predict the mean of a signal (gives a Gaussian probability distribution) with unknown population size and standard deviation of signal. In this case the data is measured and averaged until the variation of the calculated mean stays in user–defined control limits. To show how averaging improves the accuracy of the measurements, a set of 1,000 data samples (collected by the test system) were examined. Of this population, first, the approximate mean is calculated. The procedure was repeated every time the new data was measured. Then, the average of the new population is calculated and

normalized by the true average (calculated average of 10,000 samples). As the population size was increased the the moving average value converged to the expected value. As seen from the plot of moving averages in Figure 6.28, after 70 data measurements the moving average stayed inside the upper and lower control limits (LCL and UCL). After this point, stopping is decided by the user if this error is acceptable. The above example is given to show that averaging eliminates a certain part of the error. If more precision is required, then the control limits are narrowed so that more measurements are obtained.

In the case of an unknown population size, standard deviation, and of course the true value, it is not possible to predict the relative error of the measurement as the averaging proceeds by adding more samples to the averaged population. Therefore, an automated algorithm was required to predict the relative error. In addition, since this is a random process, there was also a need to set a confidence level.

An alternate method was derived to obtain steady state data with any desired degree of accuracy. Alternating measurements acquired were considered as two separate blocks. After the n–th reading in this measurement sequence the relative error between the averages of each block, ε_n, and an error comparison indicator, η_n, are given by

$$\varepsilon_n = \frac{\bar{x}_{n,1} - \bar{x}_{n,2}}{0.5(\bar{x}_{n,1} + \bar{x}_{n,2})} \tag{6.18}$$

and

$$\eta_n = \left(\frac{\varepsilon_n}{\sigma_n/\bar{x}_n}\right) \tag{6.19}$$

where the subscripts n, 1 and n, 2 refer to the average after the n–th measurement for blocks 1 and 2 respectively and where $\bar{x}_n$ is the average of the two blocks taken together. Then, let ν be the number of of readings required to obtain $\varepsilon_n \leq 10^{-r}$, where r specifies the de-

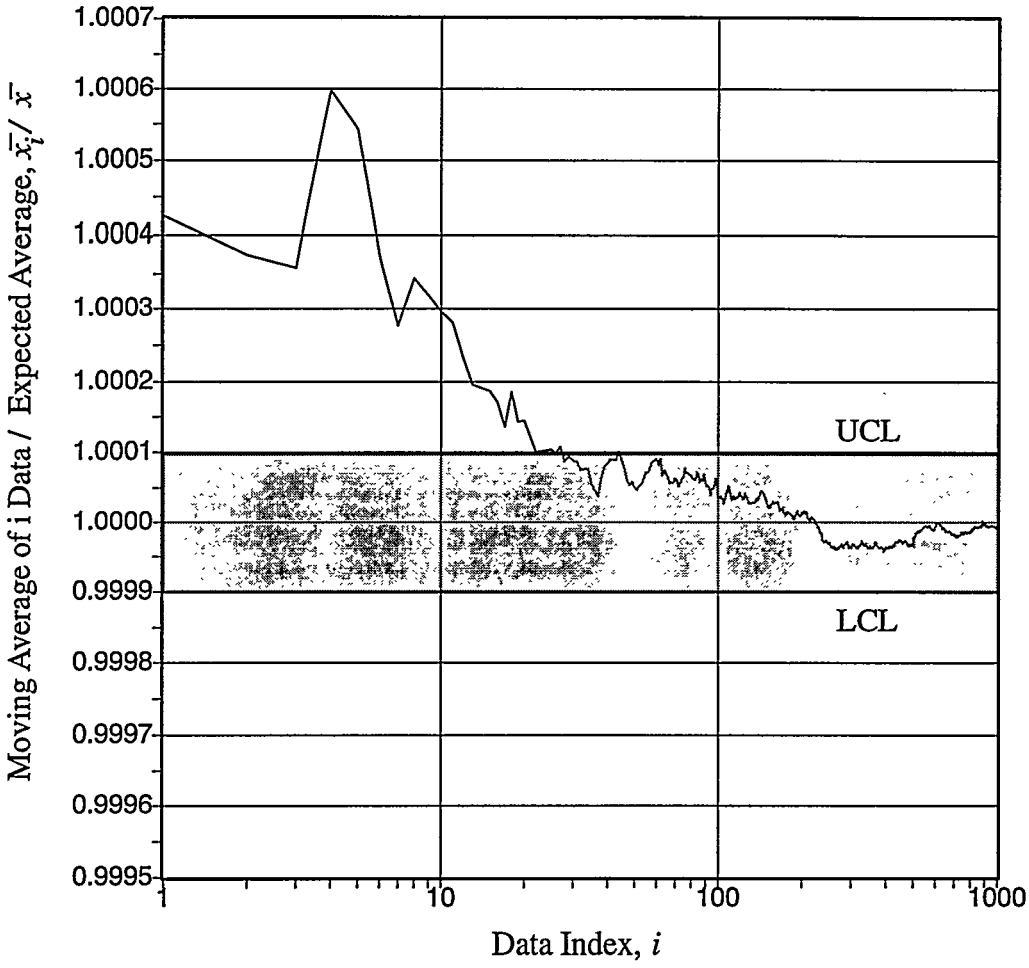

Figure 6.28 Convergence of the moving average to the known average value of the data set. If enough number of data are obtained, the moving average stays in specified control limits (UCL : Upper Control Limit, LCL: Lower Control Limit).

sired convergence, with confidence given by the probability level. Results, of course, depend on the overall signal–to–noise level of the system. As seen in Figure 6.29, if it is desired to achieve a measurement convergence to within 10% (η) of the relative standard deviation of the data with confidence level of 70% (P), one needs to acquire 100 data points ($\nu + 1$) in each block. Also, from Figure 6.30, a set of 600 data points are needed to be acquired for for convergence within 10% error comparison indicator (η) with a confidence level of 99% (P). Typical noise levels $\sigma/\bar{x}$ in the system were between –40 dB and –60 dB in the voltage range of interest. Data were taken in sufficient numbers to ensure accuracy within 1 part in 1,000 relative to the standard deviation giving overall signal–to–noise ratios (SNR) of 60 to 80 dB in measurements.

6.11 Outline of the Data Acquisition Process

For all experimental measurements, the data acquisition control program (DASCP) was used (for more details see Appendix E). The DASCP program has two main purposes: to control the data acquisition hardware in assigning excitation patterns, and to acquire the necessary measurements for the image reconstruction program. The DASCP program was written in the QBASIC language utilizing the library of subroutines of the Keithley–MetraByte GPIB board and the Keithley–MetraByte PIO–96 control board which were used to control the Hewlett Packard instruments and the matrix switching system, respectively. The flow diagram of the computer program is given in Figure 6.31. The program is divided into two distinct interactive units called BLOCK–A and BLOCK–B. The main program which sequentially executes the procedures in BLOCK–A is shown in boxes A–1 through A–5. BLOCK–B assigns excitation patterns and obtain measurements by executing the procedures in boxes B–1 through B–5. BLOCK–B also shares procedure in box B–5 with

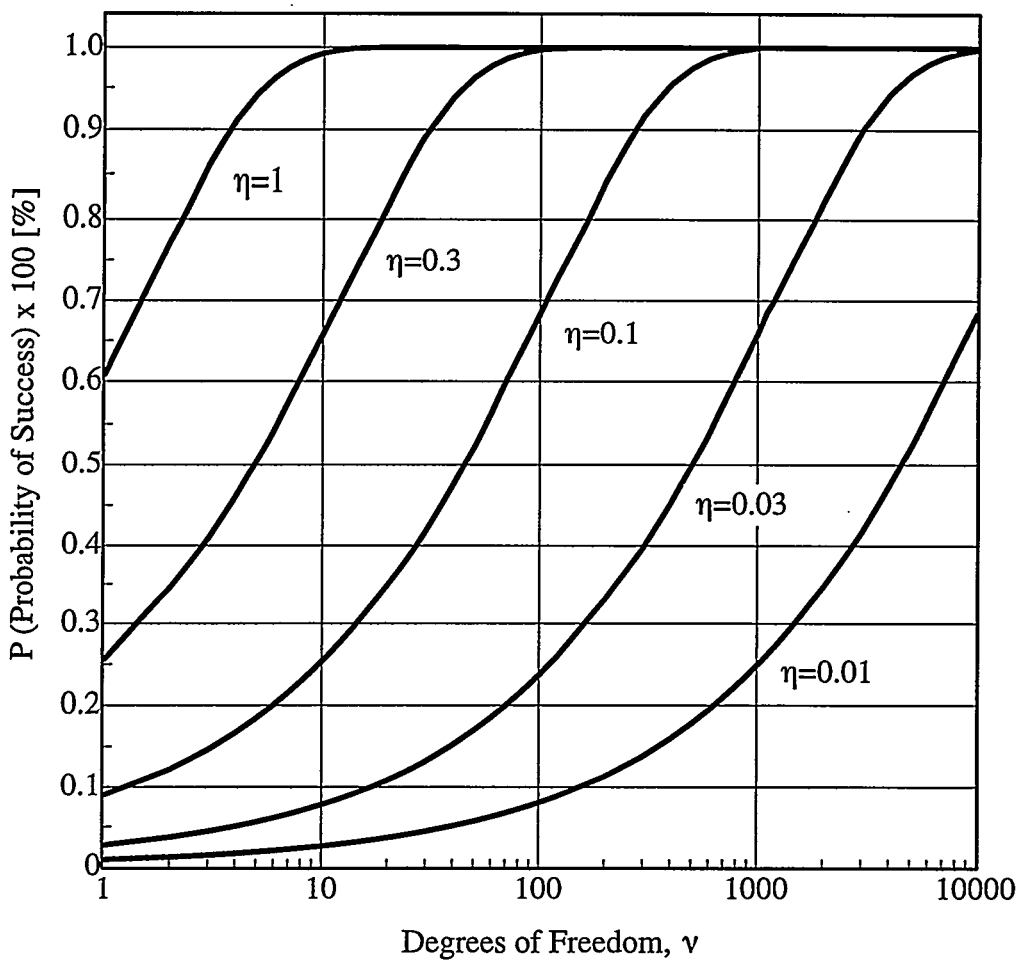

Figure 6.29 Probability versus the number of degrees of freedom for different error comparison indicator (η) levels.

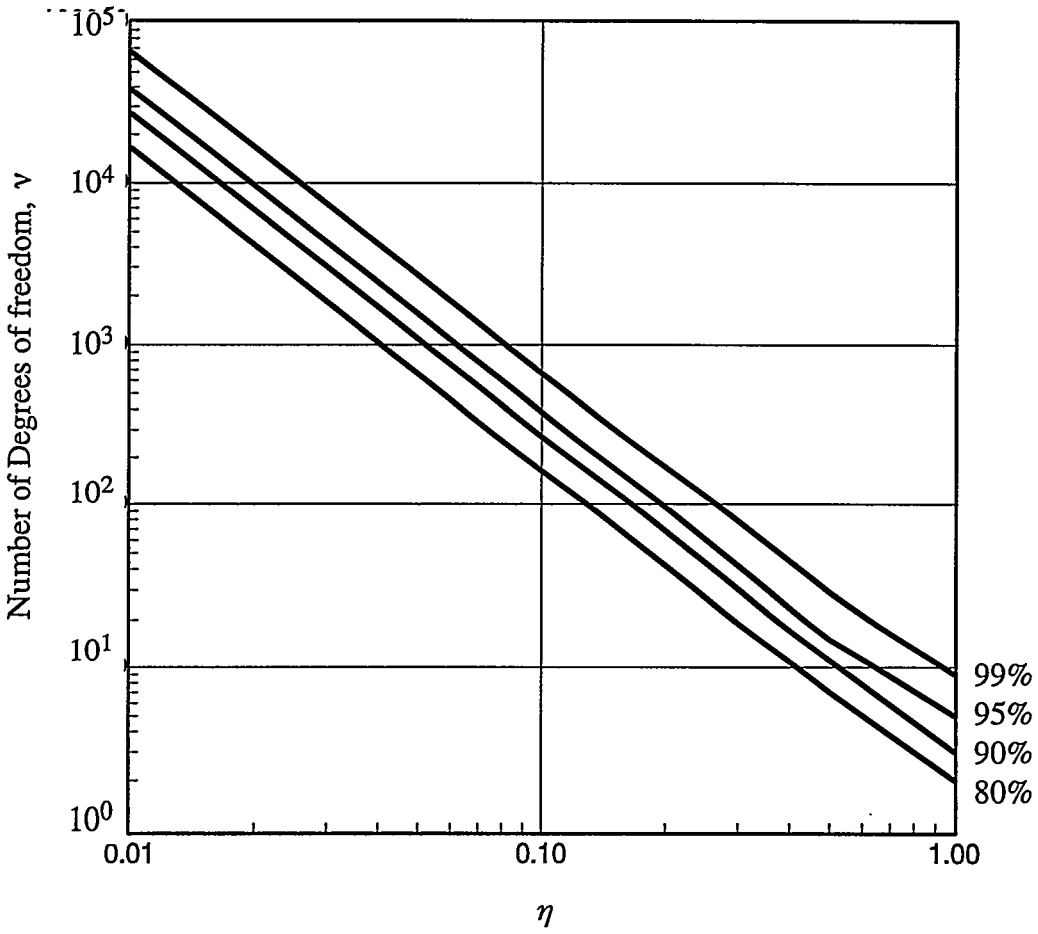

Figure 6.30 The number of degrees of freedom versus the error comparison indicator for the different confidence levels.

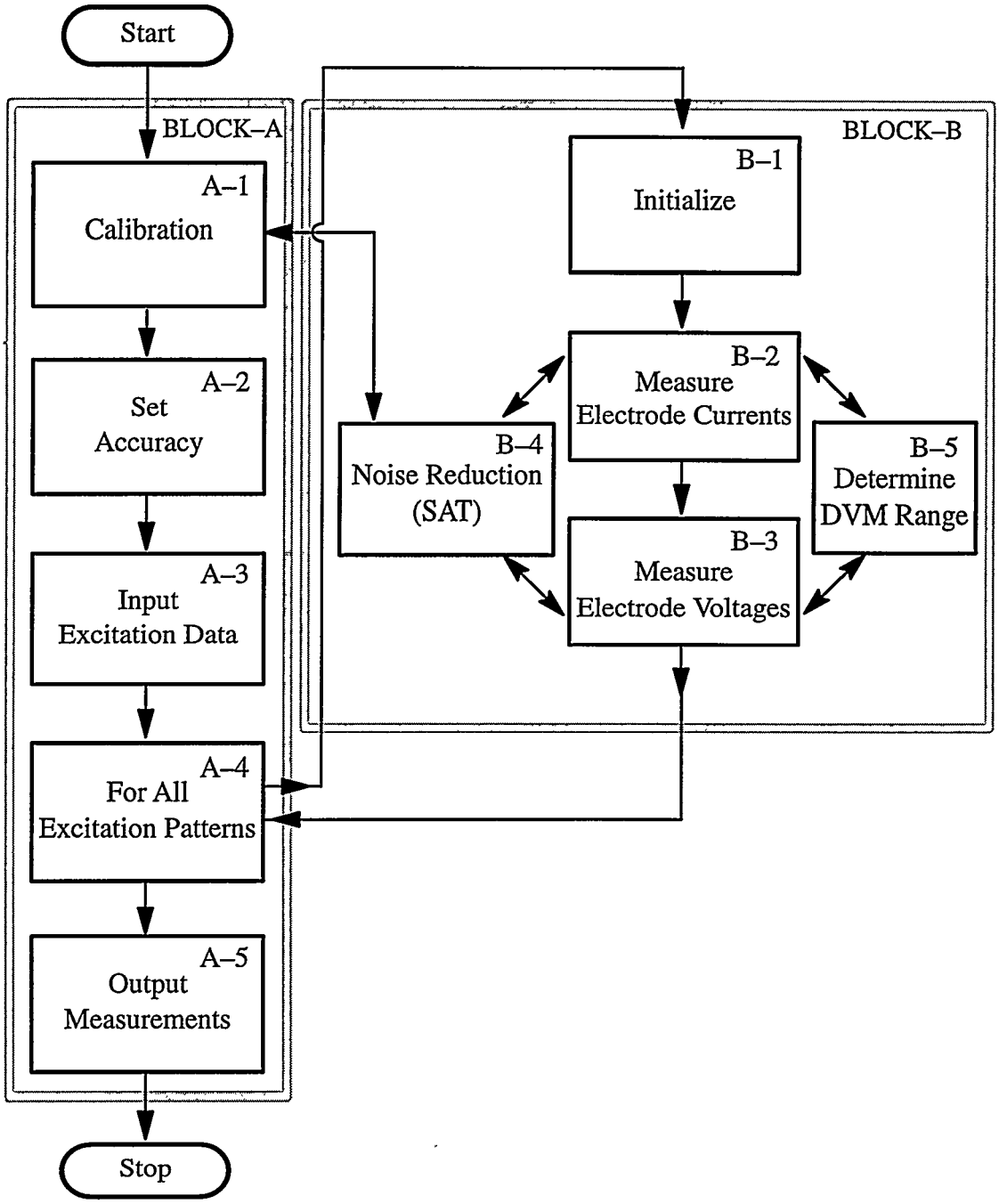

Figure 6.31 Flow diagram for the procedures of the data acquisition control program (DASCP): the single–sided arrows indicate execution sequences; the double–sided arrows indicate subroutine calls.

BLOCK–A while calibrating the series resistors used for electrode current measurements. The following sections give a detailed outlook for how each one of these boxes functions.

6.11.1 Calibration (A–1)

The accuracy of the measurement instruments and excitation sources steadily degrades after time of calibration and with the changing ambient temperature. For the former, the instrument is sent to its manufacturer at regular intervals, recommended by the manufacturer, to be externally calibrated. For the latter, the instrument can be auto–calibrated before starting any set of measurements.

The second step of calibration is concerned with the series resistors used to measure injected electrode currents. The injected electrode currents are obtained by measuring the voltage drop on the resistors of a known value of about 100 Ω, each connected in series in the electrode channel as shown by the schematic diagram in Figure 6.21. Since temperature change has quite an effect on these resistance values (about 1%), they should also be accurately measured if the data acquisition system is switched off for several minutes or longer. Initially, the resistance of each channel was directly measured by operating the DMM in the ohmmeter mode. However, this was found inappropriate because the resistance measurement also included the lead resistance of connection wires including the paths on the PC boards. The lead resistance in the system was measured for 32 channels, and all had different values between 0.5–0.7 Ω because each channel has a different length of connection wires and paths on the PC boards. A more accurate way is to measure the resistance value by injecting a known current to the channel and to measure the voltage drop in the resistor and to calculate the resistance value from the voltage/current ratio. Since the internal impedance of the DVM is very high (10 MΩ) compared with the 100–Ω resistor, the amount of current in the measurement path is negligible causing no voltage drop in the lead resistance.

Thus, by this technique, the series resistors can be precisely measured within a tolerance of 1:10,000 by utilizing the noise reduction technique provided by B–4.

6.11.2 Accuracy (A–2)

The measurement accuracy ($\varepsilon = 10^{-r}$) for the sequential averaging technique is specified by the user at this stage of the program. It should be always remembered that there is a trade–off between the data acquisition time and the accuracy of the measurements. A requirement of a very high accuracy dramatically increases the data acquisition time depending on the level of noise which is in the measurements. A reasonable data collection time for 32–channel measurements is about 30–50 sec/excitation with an accuracy of 1:1,000 ($r = 3.0$). For the system used, each voltage measurement requires about 30–90 readings depending on its magnitude.

6.11.3 Data Input (A–3)

This procedure provides an interaction between the user and the program. The number of channels to be used, the filename which includes the number of excitations, the excited channel numbers and their excitation polarities, and the filename of the calibrated series resistances, the name of the output file is entered by the user at this stage of the program.

6.11.4 Application of Excitation Patterns (A–4)

This procedure interacts with BLOCK–B for every excitation to be assigned to the phantom. This procedure provides the electrode numbers and their polarities to BLOCK–B, details of which will be explained later.

6.11.5 Data Output (A–5)

After all measurements are obtained, all the electrode voltages and currents are saved in a user defined file to be used in the image reconstruction program.

6.11.6 Initialization (B–1)

A new excitation pattern is applied when requested by A–4. A new excitation means that the switching sequence changes. All switches are first opened, then those required for the desired excitation are closed. This is undertaken by interaction between the digital I/O card in the computer and the matrix–switching cards.

6.11.7 Measurements (B–2 and B–3)

The measurements are obtained by controlling the switches of the matrix switching system to establish necessary the connections to the proper nodes to read voltages by the DVM. The electrode currents are measured by simply measuring the voltage drops in the resistors, and dividing these measured voltage drops by the resistance value as voltage/resistance ratio.

In measuring the electrode voltages, two different procedures are used depending on the type of excitation patterns. If all the electrodes are simultaneously excited, as in the case of applied Walsh voltage patterns, the voltage value between the terminals of the voltage source is first measured and then the electrode voltages are calculated by subtracting the measured voltage drops from the terminal voltage of the excitation source. If a single or multiple pairs of electrodes are excited, the unexcited electrodes do not carry any excitation current, and thus there is no voltage drop in their series resistors. In this case, a reference

electrode is selected and all the electrode voltages are measured relative to the selected reference electrode.

Care must be taken in selecting the reference electrode; because only the magnitude of the applied alternating excitation signal is measured not its polarity. For each applied excitation pattern, the electrode having a minimum potential value is determined first, and then all the electrode voltages are measured relative to this reference electrode voltage (thus, all the measured potential differences are guaranteed to be positive).

6.11.8 Determine Range (B–4)

The magnitude of the voltage is unknown and the range of measurement for the DVM has to be set before each measurement. It is unfortunate that for time–locked voltage measurements the DVM's measurement range is not automatically determined by the DVM itself as in rms measurement of a sinusoidal voltage signal. The expected voltage values in the EIT system fall in the 4 voltage ranges (12 mV – 120 mV), (120 mV – 1.2 V) and (1.2 V – 12V), and the measured voltage is determined by a single measurement (no averaging) before the noise reduction procedure is activated.

6.11.9 Noise Reduction (B–5)

After the voltage range is determined, more voltage measurements are made and sequentially averaged (as explained in Section 6.10.3) until the relative variation of measurements is equal to or less than the accuracy level defined by the user in procedure A–2.

6.12 Summary

The purpose of the work presented in this chapter was to determine the best possible imaging measurements which could be achieved using carefully controlled experimental methods. This chapter summarized an historical survey of developments achieved in experimental methods including excitation and measurement methods.

A number of innovations in experimental methods included in this chapter to make the designed EIT system a viable imaging utility for both two– and three–dimensional gas–liquid phase imaging. The sensitivity of the numerical model to changes in the number of elements showed that a plate–electrode model is considerably superior to a rod–electrode model for imaging. Reasons for this were provided. Finally, It was demonstrated that the resolution of targets could be optimized by choosing current or voltage distributions which are eigenvectors of the conductance or resistance matrices respectively.

It is shown that Walsh functions can be used as excitation patterns to benefit from their easy–to–apply characteristics using a single voltage source as well as increasing the sensitivity of the result. The square–pulse–type excitation signal was utilized for the excitation because using frequency–locking measurements are more advantageous than rms measurements used by others and do not average the system noise combined with the signal. A sequential averaging technique was developed to eliminate the Gaussian noise in all the measurements. This has a distinct advantage over rms measurement where rectified noise cannot be eliminated.

CHAPTER 7

EXPERIMENTAL RESULTS

7.1 Introduction

In Chapter 5 and Chapter 6, the theory, analytical, numerical developments and implementation of the proposed methods for imaging conducting media were explained in detail but no results was presented. The objective of this chapter, however, is to present a set of experimental results reconstructed from a group of test data acquired by using the electrical impedance imaging system designed and built at the Rensselaer Multiphase Imaging Laboratory. When presenting these results, the sequence of these experiments are arranged so that the claimed effects and improvements due to all developed methods can be evaluated and justified. These results presented herein will provide a baseline for the long–term objective which is to obtain images at an approximate rate of 1000 ips (images per second) in gas–liquid flow systems. The following summarizes the contents of this study.

First, an algorithm is described to determine the "best contour" for determining the size and shape of a target. This algorithm indicates that below a certain contrast level the image broadens relative to the actual size of the body. It is shown that this behavior is at least dependent on whether the shapes are two–dimensional or three–dimensional. It is also shown that multiple targets within the field will produce different contrast ratios relative to the homogeneous background and that differential discrimination provided by the "best–contour" algorithm is required to properly image each target separately.

The experiments undertaken in this study are broken into three separate groups to demonstrate imaging capabilities of the overall system:

- design, measurement, and numerical methods comparisons;
- resolution limits and comparisons;
- two– and three–dimensional size, number, and location comparisons.

The first group of experiments presents results to demonstrate comparisons and effects of various design properties and measurement techniques such as using a different number of electrodes and electrode type (rod and plate electrode models), excitation methods and patterns (exciting single pair and multiple electrodes), and magnitude measurements of applied signal type (rms of a sinusoidal and averaged peak of a square–pulse wave signal). This part also deals with investigating effects of all computational methods including three different finite element schemes using constant and exponentially varying conductivity assumption within each block element, the preconditioned voltage correction (PVC) method , and optimization of the excitation patterns previously developed to obtain images in a reasonable quality. Comparisons are provided for images obtained with both rod– and plate–electrode geometries demonstrating the superiority of the latter. It is shown that imaging using a 256–element model (16×16) provides superior imaging to a 9×9 model but at the expense of both increased background noise and significantly increased computational time but that the finer model is required to separate multiple, small images which are close together.

The second group of experiments demonstrate the limits of resolution of both centered targets and two separated identical targets in both longitudinal and diagonal directions inside the 16–plate–electrode phantom. This group of experiments describes the methods used to energize the field using Walsh functions, simultaneous excitation of boundary electrodes and the methods utilized to optimize the results with regard to the accuracy of the data acquired. The methods previously introduced in Chapter 6 for analyzing eigenvalues

of the imaging system to determine system's ability to distinguish minimum size were utilized to demonstrate the resolution of the overall imaging system to be easily one part in 375 with possible resolution as fine as 1:570.

Finally, the third group of experiments presents the computational results to show the capability of the system to image cases of both single and multiple insulating targets with changing size, geometry and location placed in two– and three–dimensional phantoms. The results presented herein show the ability of the system to image a "moving" three–dimensional shape and show that not only is the discrimination level dependent on the contrast level, but also dependent on whether it is cylindrical or spherical.

It should be noted that most numerical methods are undertaken in the space–time continued by sequentially reducing element size or increments sufficiently small to eliminate any further demonstrable effect due to diminishing size. The degree to which computational assets increase with increasing number of model elements has already been discussed showing a very real limitation imposed by available resources. A large part of this chapter, therefore, shall be devoted to demonstrating the degree to which the number of elements is "adequate" in a somewhat qualitative sense rather than sufficient in number to preclude further changing in results. The latter would have required resources very much larger than available at this date and indeed, generally available to workers who may choose to utilize these methods in future times.

7.2 Identification of Target Boundaries: the "Best Contour" Algorithm

The test cases studied in this report include determination of electrical conductivity distribution in binary mixtures such as insulating targets inserted in conductive liquid. This binary conductivity variation is approached by the two–dimensional cubic spline method

used in the block decomposition algorithm. The computed distribution is a relief map stored in a 128 × 128 pixel array to be used later in post–processing and image display.

Conventionally, either a grey or color scale image can be displayed on the computer's screen to discriminate boundaries between two different electrical conductivity/resistivity values describing both shape and location of targets. While grey scale images are useful, they themselves provide a form of discrimination to the data. This is seen in Figures 7.1 and 7.2. The former has a 256–level grey scale adapted from a 256–color original and so does not change linearly or monotonically with intensity. The original targets shown in the upper left of Figure 7.1 include three cylindrical insulators 6.3–, 12.7– and 19.0–mm in diameter. The unadulterated grey image, derived from a color image, is shown in the upper right. This image definitely shows three targets but at differing intensity. When a sharp, two–level discriminator is applied to each target individually, differential discrimination, the actual size and shape of the targets may be accurately shown. The discrimination level is found to differ, however, for each target. Similar results are seen for Figure 7.2 where the targets are square rather than round. The grey–scale image this time is monotonic. It is obvious that there are three targets, their contrast diminishing with the size of the target, but without good shape or size differentiation in the image. Differential discrimination again shows the individual targets with reasonable representation of the size.

When displaying and evaluating the computed conductivity/resistivity results, the previous experience shows neither a grey–scale image nor a contour plot alone is a good choice to be used for display purposes because of the following reasons:

- The boundaries of small and large targets existing altogether cannot be clearly identified due to large differences in contrast levels corresponding to each target. If a linear, grey–scale image is used, the targets with high contrast level can be clearly identified

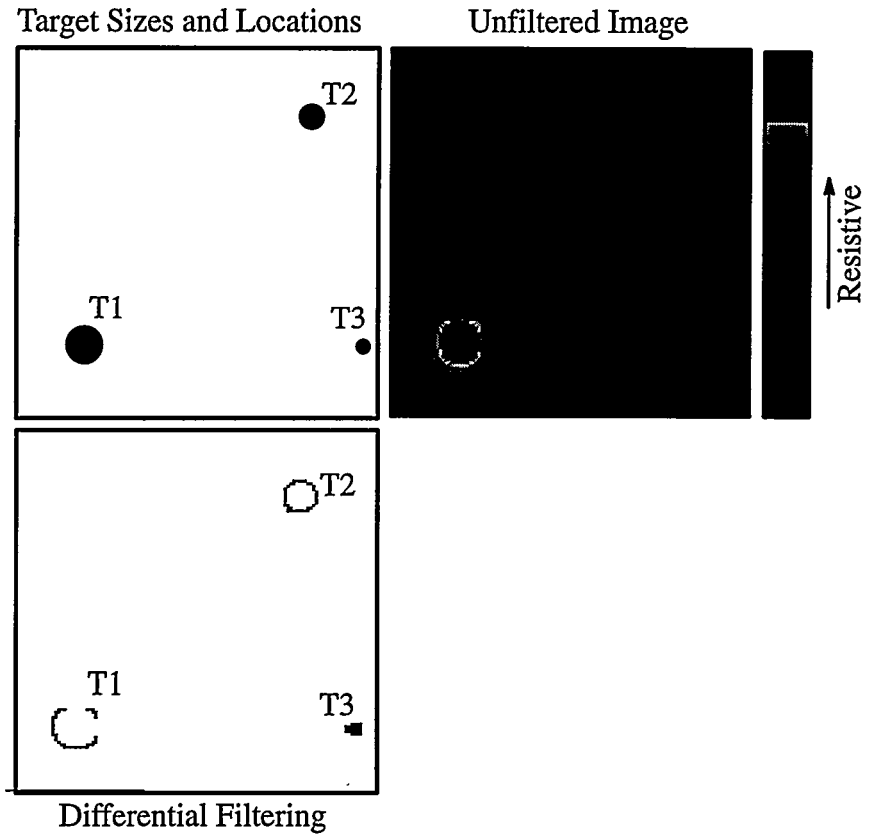

Figure 7.1 **A test image of three insulating cylindrical targets of differing sizes: (T1) 19.0–, (T2) 12.7– and (T3) 6.3–mm in diameter. Data were obtained from a two–dimensional, 16–plate–electrode phantom.**

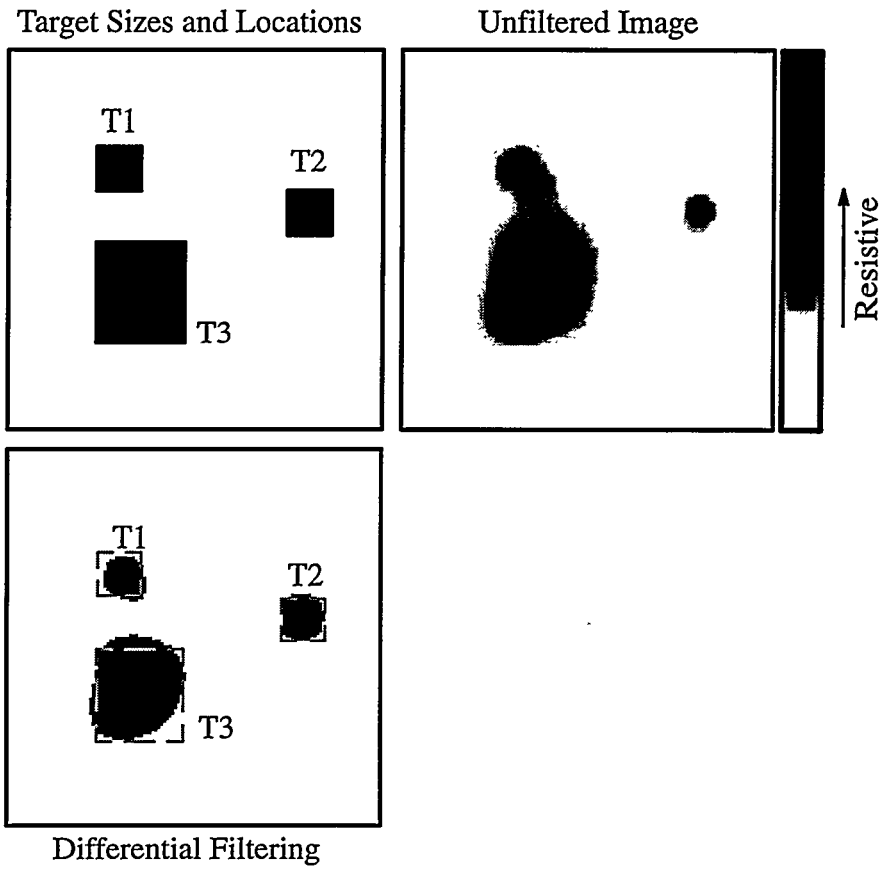

Figure 7.2 **A test image of three randomly located insulating square targets of differing sizes: 25.4×25.4–mm (T1), 25.4×25.4–mm (T2); 50.8×50.8–mm (T3). Data were obtained from a two–dimensional, 16–plate–electrode phantom.**

whereas low contrast–targets cannot. Therefore, the low–contrast targets are difficult to see due to decreasing contrast level although in reality they have the same conductivity value as the high–contrast targets have;

- A contour plot obtained by using a linear scale is also not a good choice because the low–contrast targets will not be resolved very accurately, and also it is not clear which contour lines should be picked to display actual shape of each target.

It is expected that the above mentioned difficulties arising in identifying target boundaries is mainly caused by the nonlinear nature of the inverse conductivity problem and the assumption is used in its implementation. The image computed for a discrete target is not itself discrete but continuous due to the computational methods.

Since the inverse conductivity problem is inherently nonlinear, the measurements obtained on the electrodes are insensitive to the targets which are small in size and placed away from the electrodes. In this case, the computed conductivity values do not converge to their actual resistivity values. Generally, decreasing target size and increasing distance from the phantom's boundary where the measurement electrodes are placed result in lower computed resistivity or lower target contrast levels relative to those of placed near electrodes.

What is needed, and what has not been undertaken previously, is a good, quantitative method of using differential discrimination for target identification. For this, there is no theory. Rather, it is observed that the sharpness of any given image varies with the contrast ratio. Targets with either small size or distant location relative to the electrode boundary will have low contrast relative to the background. Those with large size or close proximity to electrodes will have higher contrast. Figure 7.3 shows this typical case illustrated in one dimension. In this figure, C_{max} is the maximum (resistivity) contrast level of

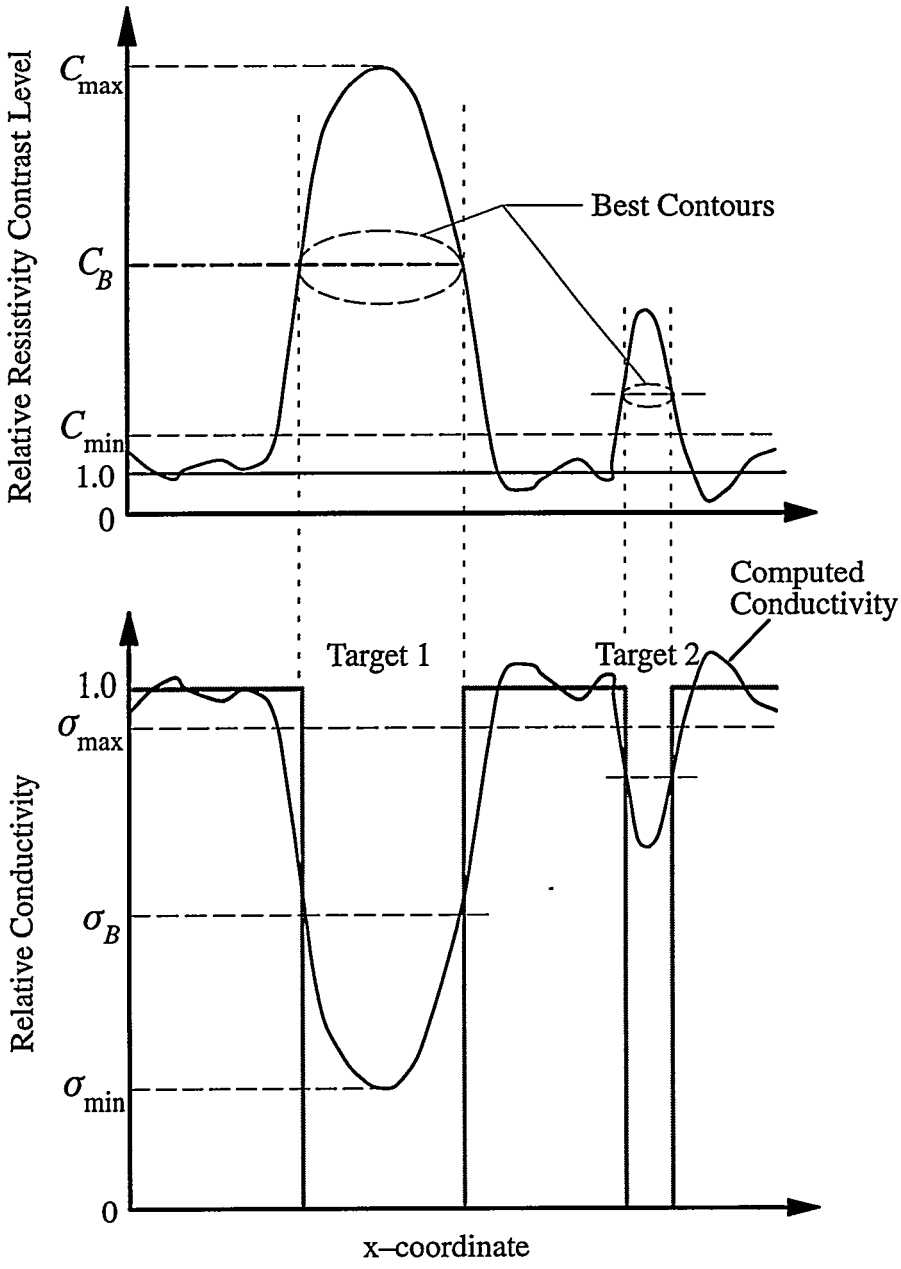

Figure 7.3 **One–dimensional illustration of the relative conductivity and resistivity map for two different targets. Each target has a maximum contrast, C_{max}, corresponding to minimum conductivity, and its corresponding best contour level, C_B, matching to the actual size of the target. Everything above a minimum contrast level, C_{min}, is identified as a target.**

the target, and C_B is the "best contrast" or the "best contour" level of this target. Due to the variations on the background resistivity value, there is a minimum level, $C_{\min}$, chosen as the noise level. Every contrast level above $C_{\min}$ should belong to a possible target.

From these observations, it was suspected that the discrimination level per target, different for each target in any image, will depend on the contrast level. This forms the basis for an empirical development wherein a large number of images obtained from distinct test cases are topologically examined for distinguishing qualities in the following manner:

- *Normalization:* All conductivities are normalized in the model to that of the continuum field and stored in a 128 × 128–pixel map.
- *Target Identification:* Using the normalized resistivity map, the local maximum, $C_{\max}$, of any contour on the relief map greater than the noise level, $C_{\min}$, is identified as a target;
- *Segmentation and Labeling:* Local maxima and their surrounding contours are examined and contrast levels of the surrounding pixels which stay between $C_{\max}$ and $C_{\min}$. are determined and labeled corresponding to the target number. The pixels which do not belong to a target are labeled "zero;"
- *Determine the Best Contour Level:* Starting at each local maximum, each lower closed contour is examined to determine that contour which has identically the *same area* as the known target. This contour is termed "best contour," C_B and in this way each target has a contrast pair $C_{\max}$ and C_B.

Figure 7.4 shows the "best contour" level relative to maximum contrast ratio, each differenced to unity, the homogeneous level. These data were determined from separate imaging undertaken on cylindrical targets, either singly or multiply, in the two–

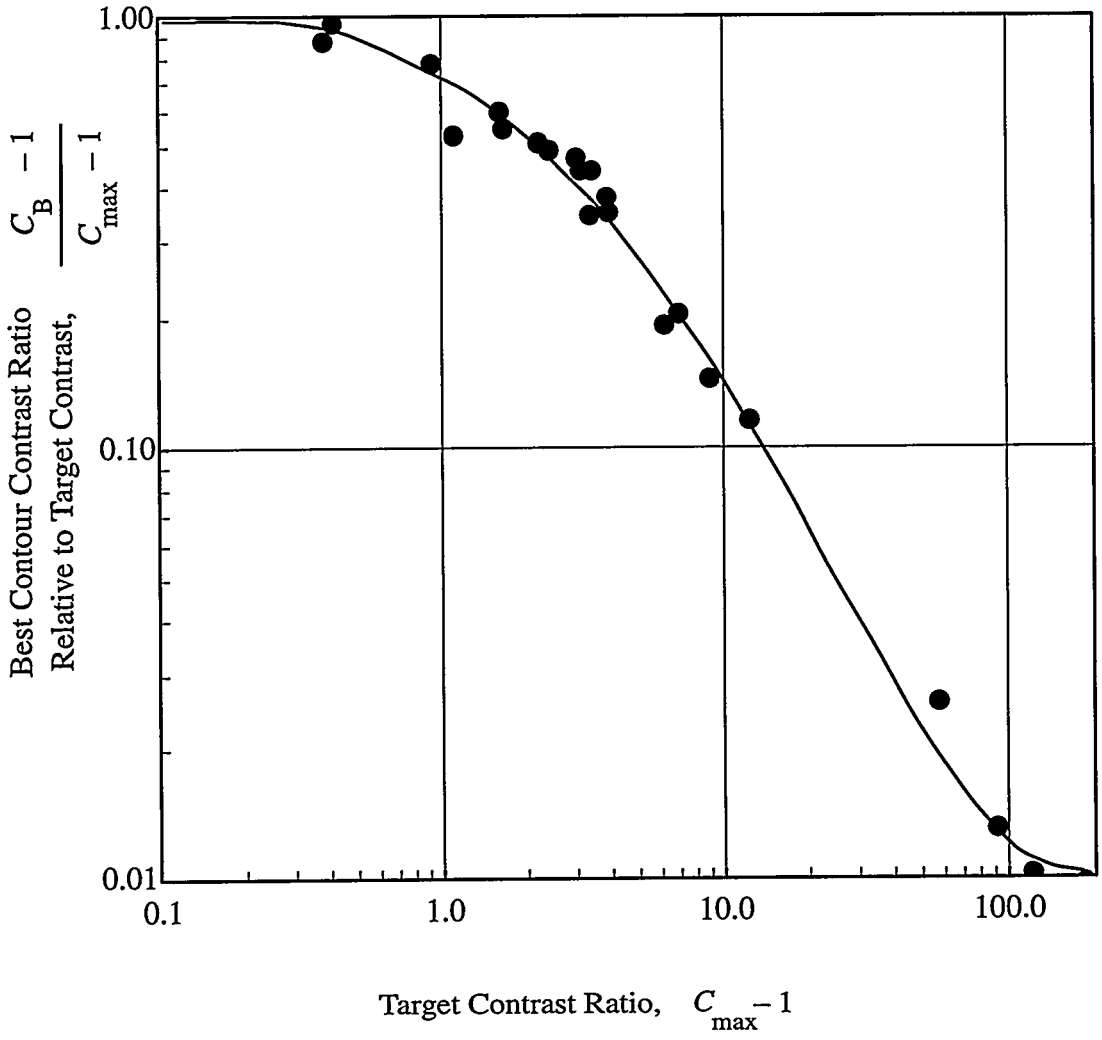

Figure 7.4 Correlation of differential discrimination level for individual targets taken from multiple–target images: ● All 2–D data.

dimensional, plate–electrode phantom. The least–squared polynomial fit shown in the figure was used for differential discrimination of the data shown herein. Figure 7.5 demonstrates that the "best contrast" level remains relatively constant being between 2.2 and 2.6 times higher than homogeneous as long as the maximum contrast level exceeds the homogeneous by approximately a factor of four or five. Once the maximum contrast for the target drops below approximately four times the homogeneous, the best contour decreases logarithmically to the homogeneous level as target contrast decreases.

Figure 7.6(a) explains these results. In the low–contrast region, lower contrast is accompanied by broadening of the affected zone (a broader image) relative to the actual size of the target. Such a target is best imaged by a contour closer to the peak. On the other hand, Figure 7.6(b) shows that a target having high contrast level is imaged best by a contour near the base of the relief, slightly above the homogeneous level. What this really means is that while a very small target produces a discernable variation in the boundary potentials relative to the background, the difference is not sufficient to produce a sharp contrast. Rather, its effect becomes spread throughout, quite possibly an artifact of the modeling rather than the information base itself.

The fact that small or poorly defined targets have broadened relief contours means that they are expected to produce a worse representation of the true shape due to the decreasing slope of the relief. A small error in determining the best contour contrast level can cause the image shape and/or size to change markedly.

7.2.1 Application of the "Best Contour" Algorithm

Figure 7.7 shows the results of applying the empirical "best contour" differential discriminator to data for two different cases, corresponding to those shown in Figure 7.6: a

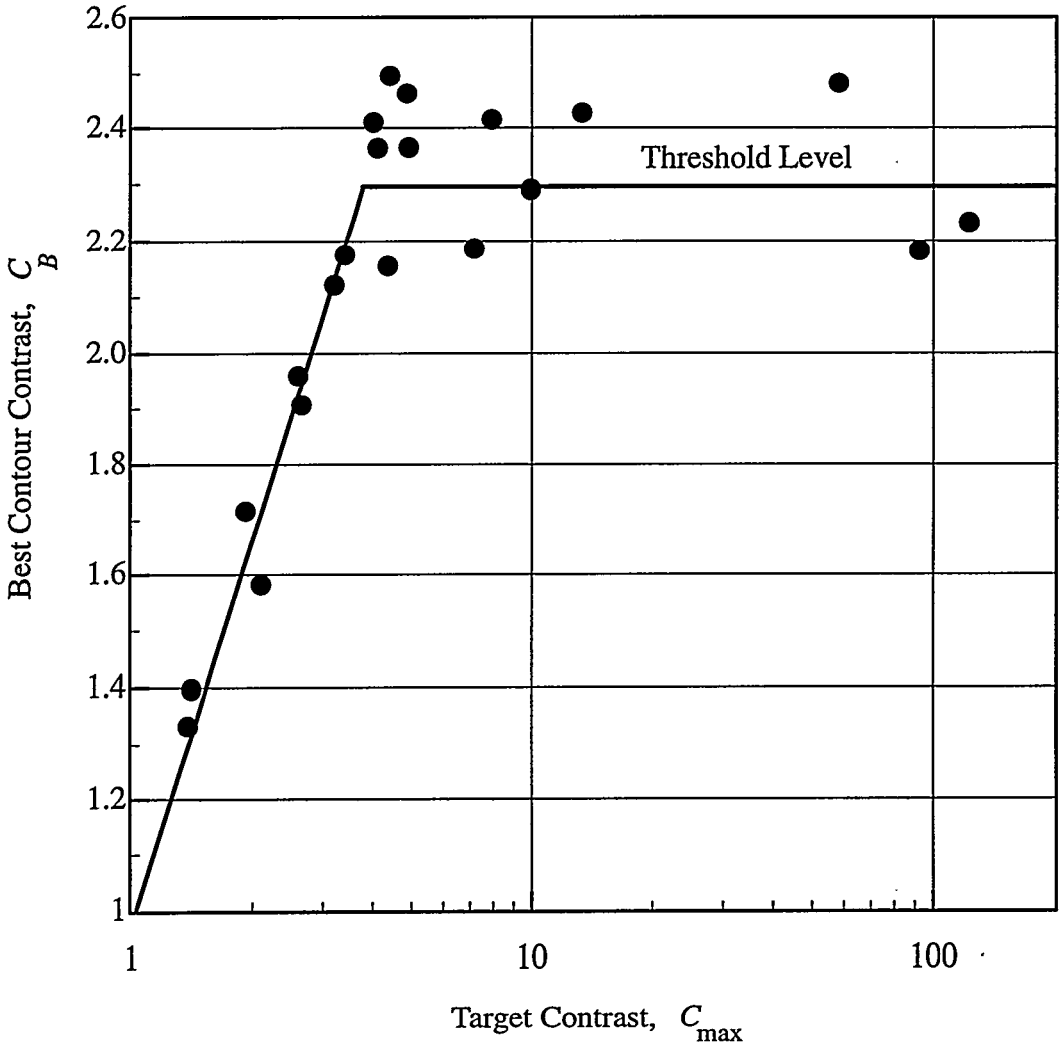

Figure 7.5 Correlation of differential discrimination level for individual targets taken from multiple–target images: ● All 2–D data.

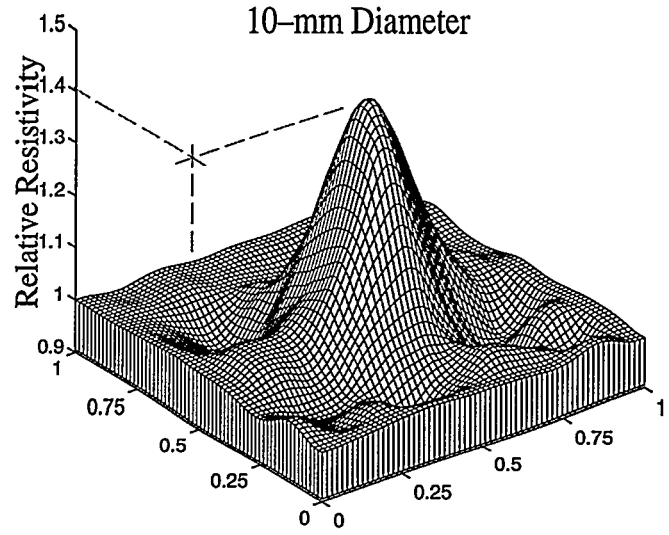

(a)

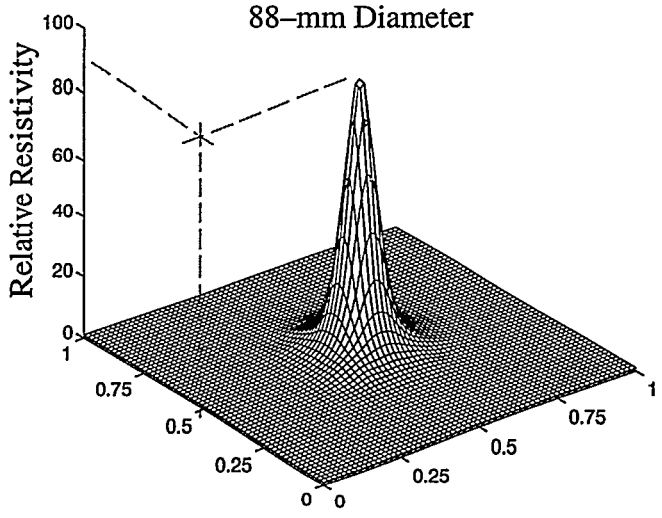

(b)

Figure 7.6 **Relief plots of relative resistivity computed for circular targets located at the center of the 16–plate–electrode phantom with 190 μS/cm conductivity: (a) 10–mm diameter; (b) 88–mm diameter. Computations were carried out on a 9×9 mesh.**

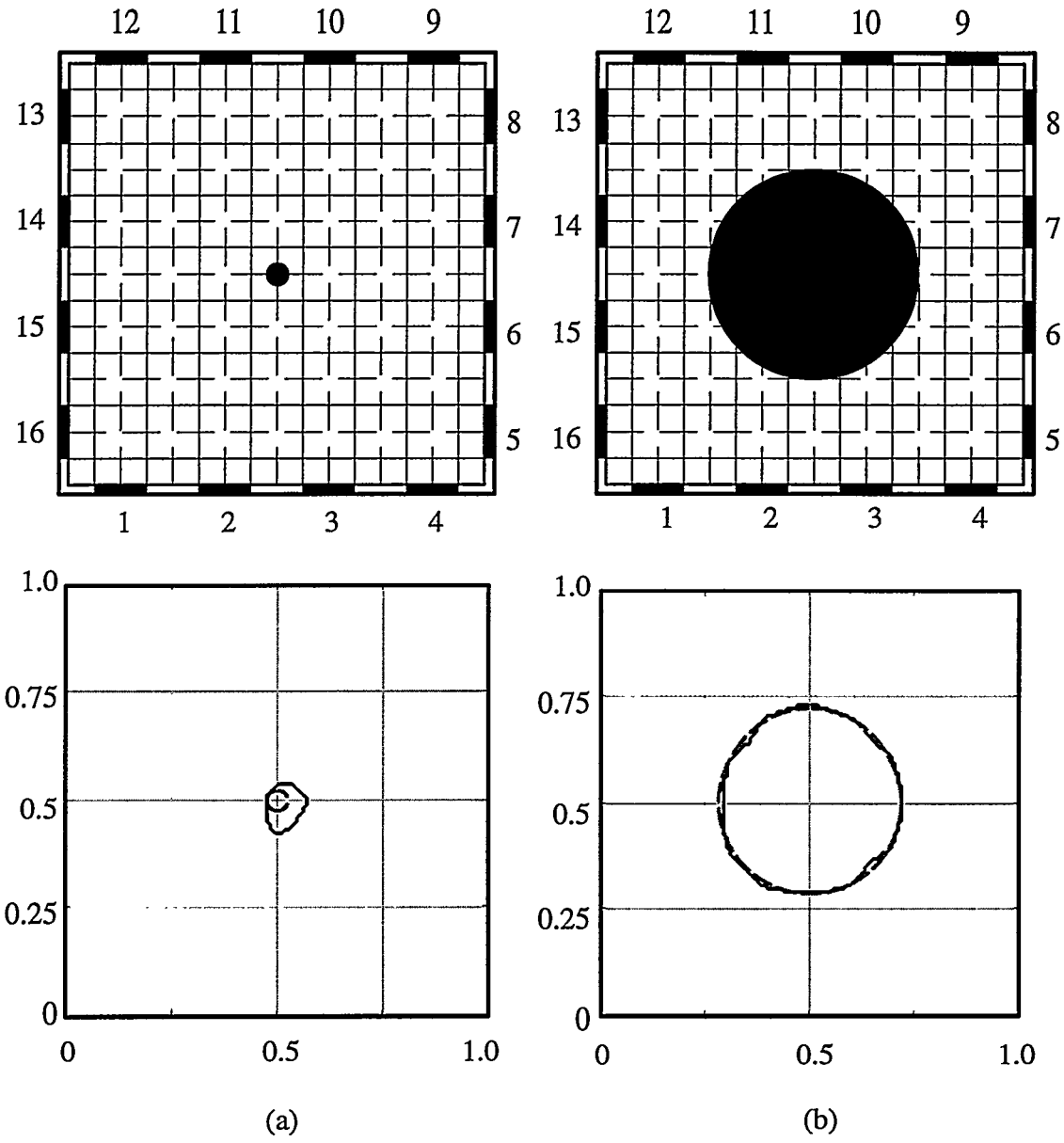

Figure 7.7 The "best contour" for different targets: (a) 10–mm diameter located at the center; (b) 88–mm diameter located at the center.

small and a large central target. In both cases the 16–plate–electrode experimental data were computed on a 9 × 9 mesh model using the best contour algorithm shown in Figure 7.4. The 10–mm–diameter image shown in Figure 7.7(a) is larger than the actual target, for reasons previously discussed, whereas the 88–mm–diameter target shown in view (b) is smaller[11]. Two square target images are shown in Figure 7.8. The 75–mm square target is imaged with rounded corners when in the center whereas it become misshapen when imaged near the corner. Both locations, however, are depicted with reasonable accuracy.

7.3 Comparisons and Effects of Experimental Methods Developed

The results of electrical impedance imaging can be affected by several features such as design, experimental measurement techniques, and accuracy of numerical modelling of the problem. When designing an efficient and an accurate imaging system, it is critical to know how these features such as number of electrodes, type of electrodes used, and applied excitation signal and excitation patterns affect the results. This section will present the results of a comparative study dealing with investigating these features.

The results of this study to be presented herein show that the new improvements in design and experiments not only can be utilized for improving the efficiency and speed of the existing static imaging system, but these results also provide new ideas for a future development and design of a high–speed flow imaging system as well.

7.3.1 Standard Test Case

For the experiments conducted for comparisons of experimental methods (to be presented in this section) and the comparisons of numerical methods (to be presented in Section 7.4), it is necessary to describe a standard test case which can provide valid and

[11] Here, and in all subsequent figures, a grey, dashed contour is shown. This contour represents the actual target boundary, size and location, and it is included for comparison purposes.

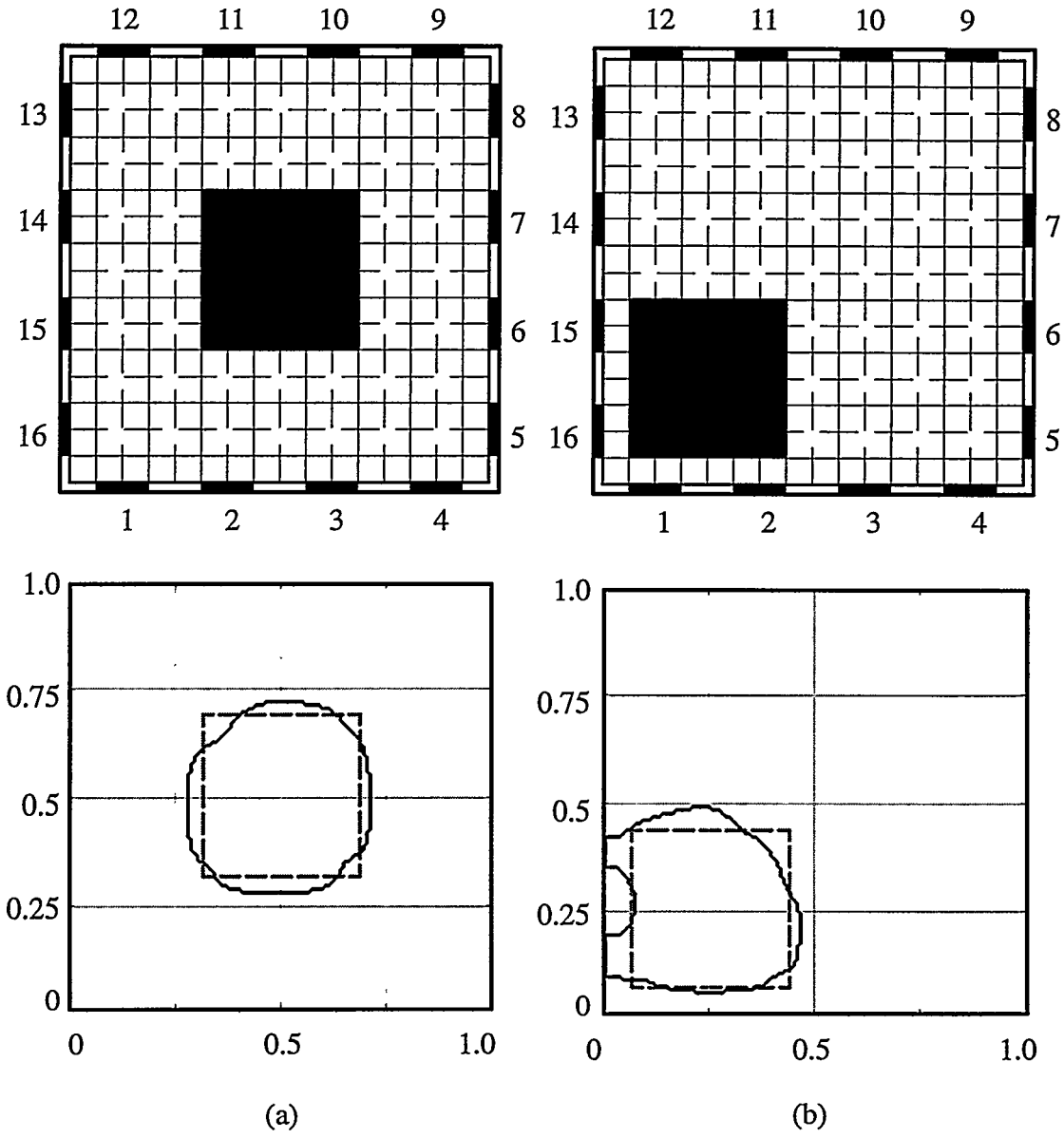

Figure 7.8 The "best contour" for different targets: (a) 75–mm square target located at the center; (b) 75–mm square target located at (50, 50).

unbiased comparisons. Especially, the following criteria were considered, in introducing a standard test case, to evaluate the quality of the results:

- distinguishability of different targets from each other;
- identification of targets located in insensitive, central regions of the phantom;
- identification of varying target sizes.

In addition, it is also required that the imaging domain (the phantom's interior region surrounded by the measuring electrodes) should have the same area and geometry as well as identical experimental conditions, such as liquid conductivity and room temperature etc., regardless of the number and geometry of the electrodes used in data acquisition process.

Considering all of the aforementioned criteria, a standard test case consisting of two insulating cylindrical targets of 45–mm (T1) and 32.8–mm diameter (T2) is defined. In this test case, the targets are placed on the phantom's horizontal at coordinates (75,100) and (150,100) (coordinates are in millimeters) respectively in a 200×200–mm, two–dimensional square phantom. The location of these targets on finite element mesh models of two–dimensional 16– and 32–electrode phantoms using with two different electrode models (rod and plate electrodes) and their electrode numbering are shown in Figure 7.9. The experimental data for all test cases were acquired for the same test conditions at room temperature of $21 \pm 3\ ^{\circ}C$ and water conductivity of $190 \pm 5\ \mu S/cm$.

7.3.2 Electrode Type: Rod versus Plate Electrodes

The size, number, geometry and location of electrodes placed around the phantom periphery has significant effects on acquiring useful information to determine the phantom's internal conductivity distribution. A bad choice of electrode model and design greatly degrades the quality of images reconstructed. Furthermore, in the reconstruction

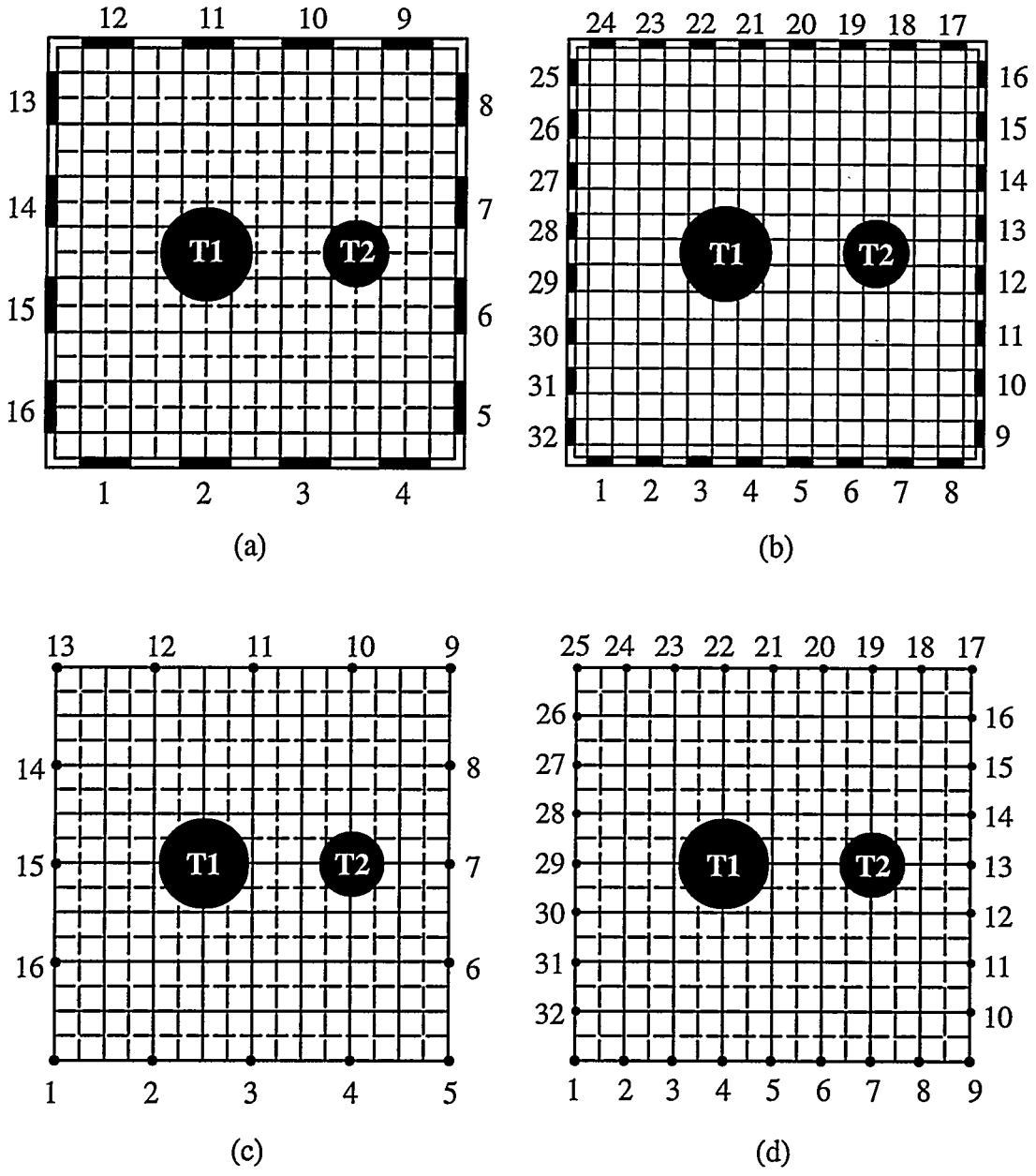

Figure 7.9 **A standard test case of two cylindrical insulating targets placed in four different two–dimensional phantoms with their finite element mesh models and numbering of electrodes used in comparisons: (a) 16–plate–electrode phantom; (b) 32–plate–electrode phantom; (c) 16–rod–electrode phantom; (d) 32–rod–electrode phantom. The target dimensions are 45–mm (T1) and 32.8–mm (T2) in diameter. The solid lines in the mesh indicate the basic mesh and the dashed lines indicate the refined mesh.**

process, the analytical model of electrodes utilized in the numerical model of the phantom is a critical matter of investigation for using this information to precisely determine the geometry and location of targets.

In designing electrodes of an imaging system, certain trade–offs have to be considered. One is that the selected electrode geometry should maximize phantoms distinguishability, i.e., maximize the signal–to–noise ratio of measurements. A theoretical study of Gisser et al. [56] showed that the signal–to–noise ratio of the voltage/current measurements obtained on the phantom's boundary is a function of electrode size. They claimed that the signal–to–noise ratio is degraded approximately as the square root of the fraction of the circumference covered by the electrodes placed on the periphery of a 30–cm–diameter circular phantom decreases. On the other hand, if the electrode area is increased, the gap between the electrodes decreases. The increase of a substantial amount of highly conductive electrode material on the boundary of the phantom results in an effective short circuit called "shunting effect" which was first recognized by Yorkey [15]. The presence of increasing "shunting effect" on the boundary may reduce the applied current density in the interior regions of the phantom, causing decreasing distinguishability and signal–to–noise ratio. However, no current will flow between closely–spaced electrodes of identical potential suggesting that proper shaping of the boundary potential distribution may obviate any negative effects of shunting.

The results of reconstructions using the data obtained through carefully prepared experiments showed that the conductivity images computed from data acquired from the 16–plate–electrode phantom yielded superior results in both target contrast and target discrimination compared with the results from the 16–rod–electrode phantom. Figure 7.10 shows the relief, contour and best contour plots, respectively, computed to 70 iterations. The left and right columns in this figure are for the 16–rod–electrode and the 16–plate elec-

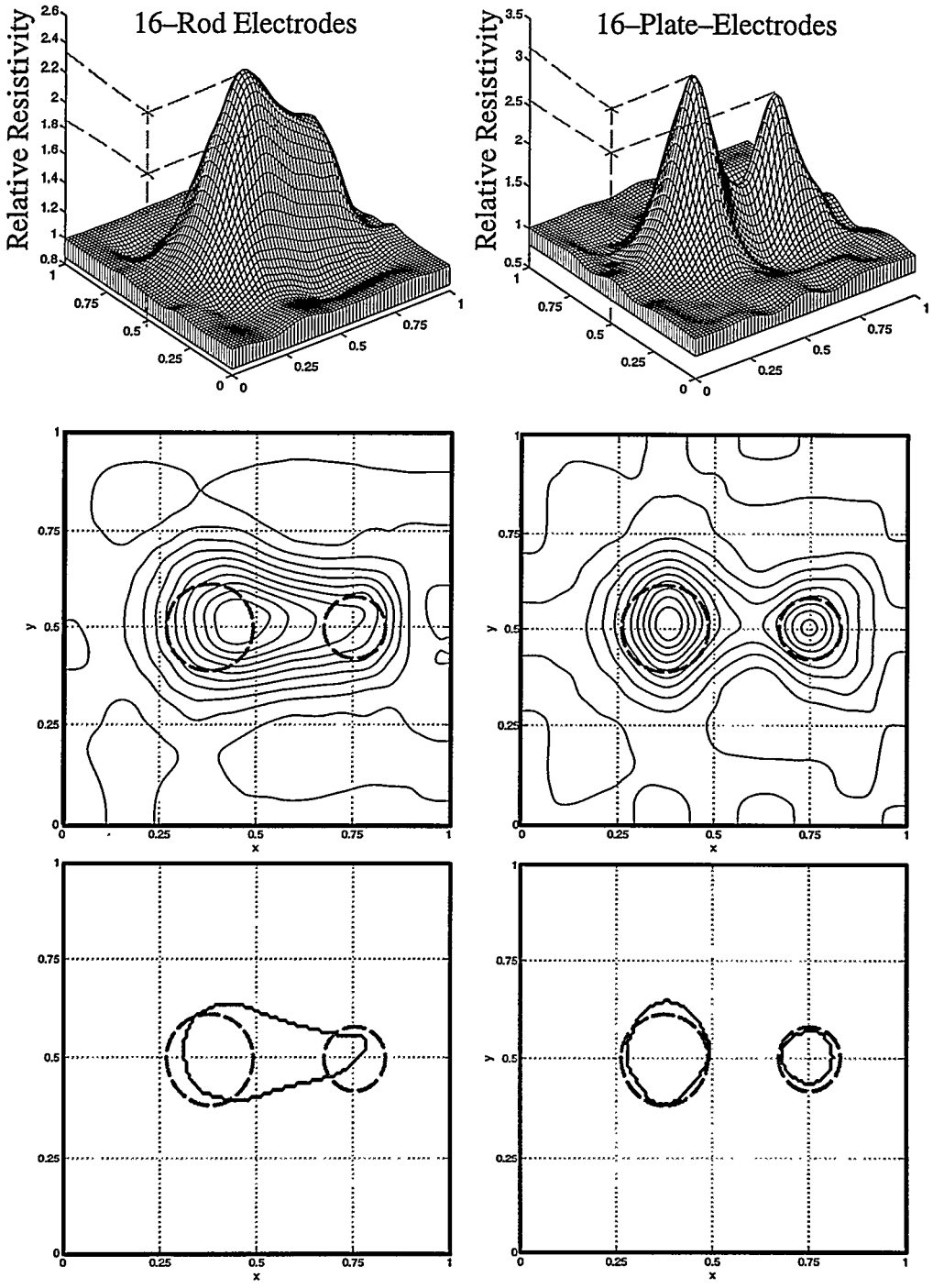

Figure 7.10 Relief, contour and best contour plots for comparing the 16–rod–electrode phantom (left column) and the 16–plate–electrode phantom (right column). Computations were carried out on an 8×8 mesh for the rod and on a 9×9 mesh for the plate–electrode phantom.

trode phantoms respectively. All the computations were carried out on a 8 × 8 mesh for the rod–electrode phantom and a 9 × 9 mesh for the plate–electrode phantom. Fifteen Walsh functions were used as excitations in each case as described in Chapter 6. The applied signal type was 10–Volt (peak–peak) square–pulse signal. All of the voltage and current measurements on the electrodes were obtained with a block convergence, r, of 1 part in 1000 (i.e., the sequential measurements were split into two blocks and each block was averaged until the relative error between the two blocks was less than or equal to one part in 1000 with a confidence level of 99%). From the relief plots in Figure 7.10, the contrast ratios are 2.3:1 for T1 and 1.82:1 for T2 for the rod–electrode phantom, and 3.1:1 for T1 and 2.5:1 for T2 for the plate–electrode phantom[12]. The contrast is thus ~50% lower in the rod–electrode phantom than in the plate–electrode phantom. As for the discriminations of targets, the "best contour" plots in Figure 7.10 showed that the two targets were well discriminated from each other for the plate electrodes while the results were unsatisfactory for the rod electrodes. Further iterations in reconstructions did not significantly change these computed values.

The effect of mesh refinement in reconstructions with the same experimental data yielded a slight improvement in the results of both electrode types. Figure 7.11 shows that refining the mesh to 16 × 16, computations carried out to 50 iterations result in some improvements in contrast ratios for both electrode types by approximately 20%. Contour plots show a slight increase in the background conductivity variation for the rod electrodes relative to the coarse mesh computations while this variation remained the same for the plate electrodes. There is also a slight improvement in the target discrimination for the rod electrodes and no significant improvement was obtained for the plate electrodes. This reaffirms the results of Chapter 6 indicating the plate–electrode model to be superior to that using rod electrodes

[12] In each contour plot, contour lines are assigned in equal intervals between maximum and minimum relative resistivity values. In all presented results in this report, either 10 or 20 contour lines are used.

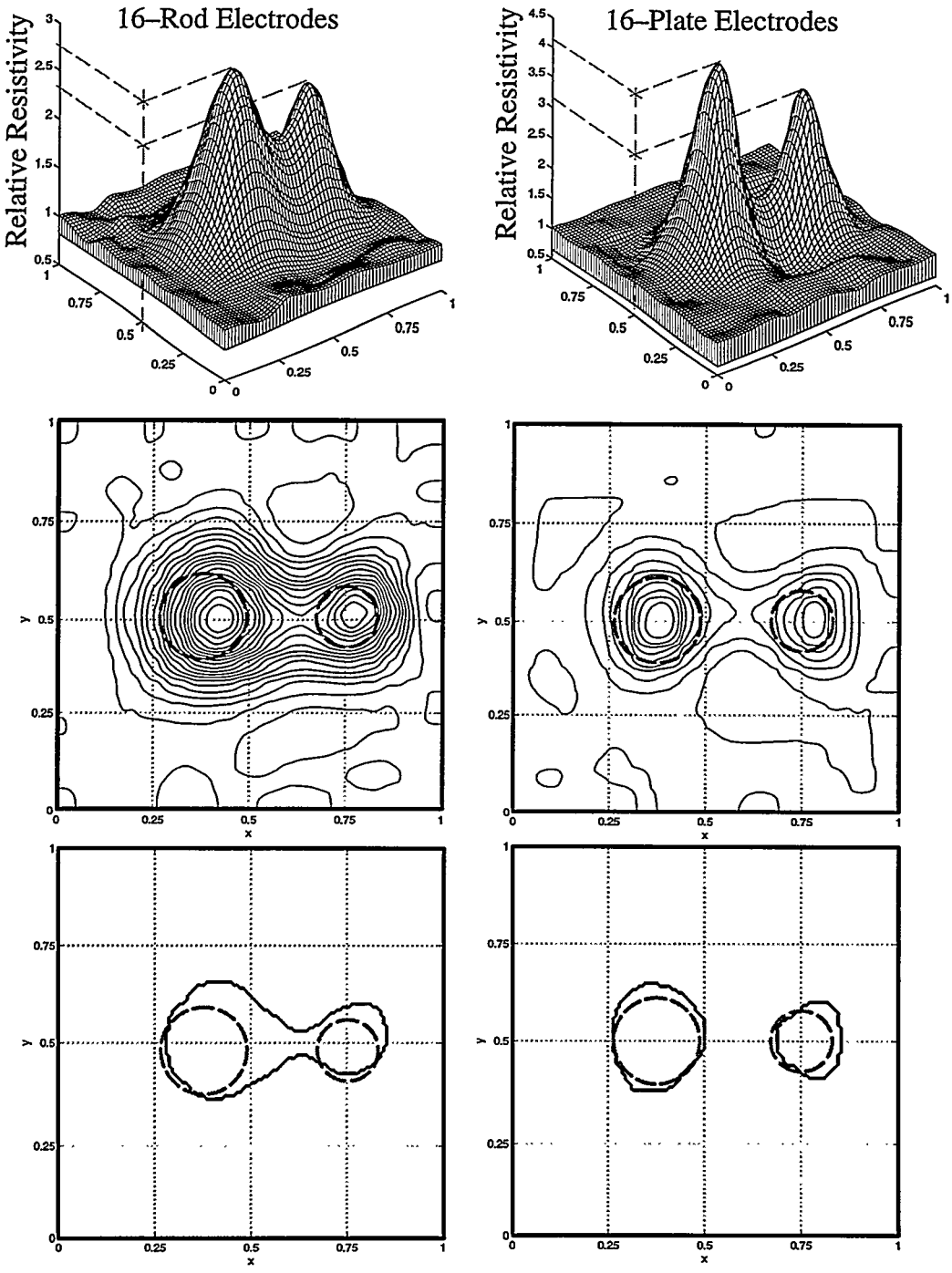

Figure 7.11 The same results presented in Figure 7.10, but all computations in this case were carried out on a 16×16 mesh model for both the rod and the plate–electrode phantom.

7.3.3 Number of Electrodes: 16 versus 32 Electrodes

Although the theory of electrical impedance imaging is well developed for smooth, continuous conductivity distributions, due to both cost and practical reasons, there are certain limitations on the system such as finite number of electrodes and finite precision of measurements obtained on the boundary of the phantom. For a given conductivity distribution differing from a homogeneous background, different excitation patterns have different abilities to distinguish this conductivity difference. However, there exists an optimum set of excitation patterns, also known as the "best" patterns, which can best distinguish variations of conductivity from a uniform background. These best patterns are discretely applied to a finite number of electrodes of the imaging system using measurement instruments having a limited capability of obtaining measurements in a finite precision. The limitations of these measurements should be well understood by the designer of an EIT system. This section investigates the effects of increasing number of electrodes in the imaging system developed.

A thorough theoretical basis for these limitations in terms of spectral properties of certain pseudo–differential operators are established by Gisser, Isaacson, Newell and their Rensselaer co–workers in [55], [56], [78]. They showed that for a given measurement precision and the conductivity contrast ratio of the smallest inhomogeneous area in the center of a circular phantom, there is a minimum number of electrodes which can uniquely resolve conductivity of the smallest area. This minimum number of electrodes is proportional to the square root of the conductivity contrast ratio and inversely proportional to the square root of the measurement precision. That means that the larger the contrast ratio and the measurement precision, the larger the number of electrodes can be used to uniquely resolve the conductivity in the area selected. In other words, if the system resolution has to be improved, both the number of electrodes and the precision of the measurements should also be in-

creased. Using the number of electrodes less than the minimum required number will cause loss of resolution near the center of the phantom, otherwise the results will not be significantly improved. Also, choosing the mesh size smaller than the minimum detectable area the system can distinguish causes severe ill–conditioning in reconstruction.

Figure 7.12 shows the effects of increasing number of electrodes on a rod–electrode phantom from 16 electrodes (left column) to 32 (right column) with measurement accuracy of $r = 3.0$. Computations were carried out to 70 iterations on an 8×8 mesh model. The results in this figure are very poor and the targets cannot be identified. Contrary to these results, if the relief and contour plots in Figure 7.13 are considered, it can be seen that the increasing number of electrodes can improve the resolution of two targets if the number of mesh elements is quadrupled to 16×16 mesh (computations to 50 iterations).

The last two figures show clearly that a model with insufficient mesh elements may not be adequate to obtain reasonable results. For instance, with only a 17×17 model, results for the 32–plate–electrode phantom are worse than those for the 16–plate–electrode phantom shown in Figure 7.14. This shows the quandary of the finite element modeling since processing to a 34×34 model is computationally prohibitive, estimated at more than several days on a Silicon Graphics INDY workstations. As a result it is not possible to tell if these poor results with the 32–plate–electrode phantom is due to shunting or to the model. Later results will show, however, that it is the model which is at fault and that the computational limitations may, in fact, be circumvented.

7.3.4 Excitation Patterns: Walsh–Function vs. Single Electrode Pair Excitations

Adaptive excitation techniques described in Gisser et al. [56] are considered to be the best excitation methods for increasing distinguishability and for eliminating the other

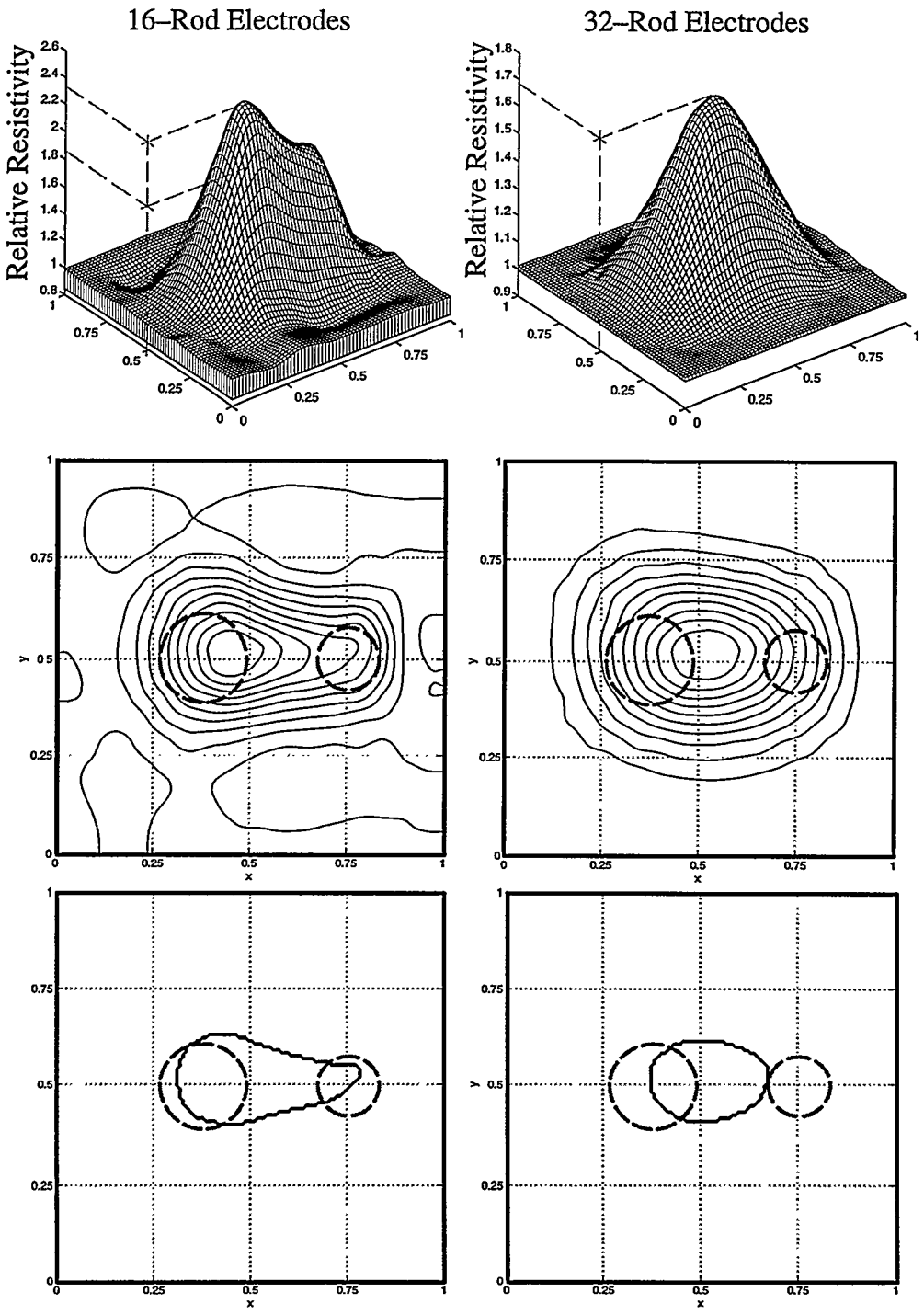

Figure 7.12 Relief, contour, and best contour plots for comparing the 16–rod–electrode phantom and the 32–rod–electrode phantom. Computations were carried out on a 8×8 mesh model.

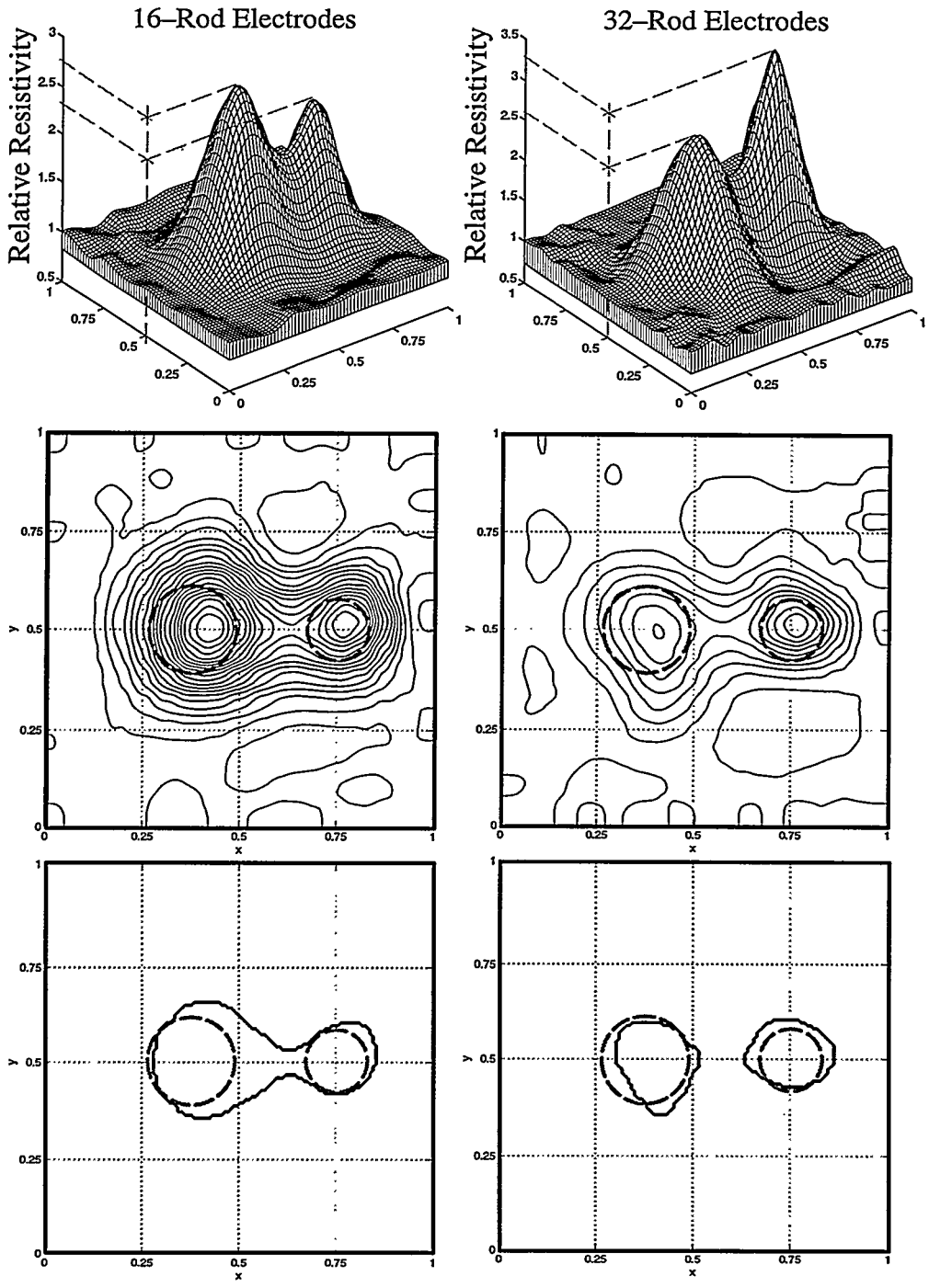

Figure 7.13 The same case presented as in Figure 7.12 but the computations in this case were carried out on a 16×16 mesh model.

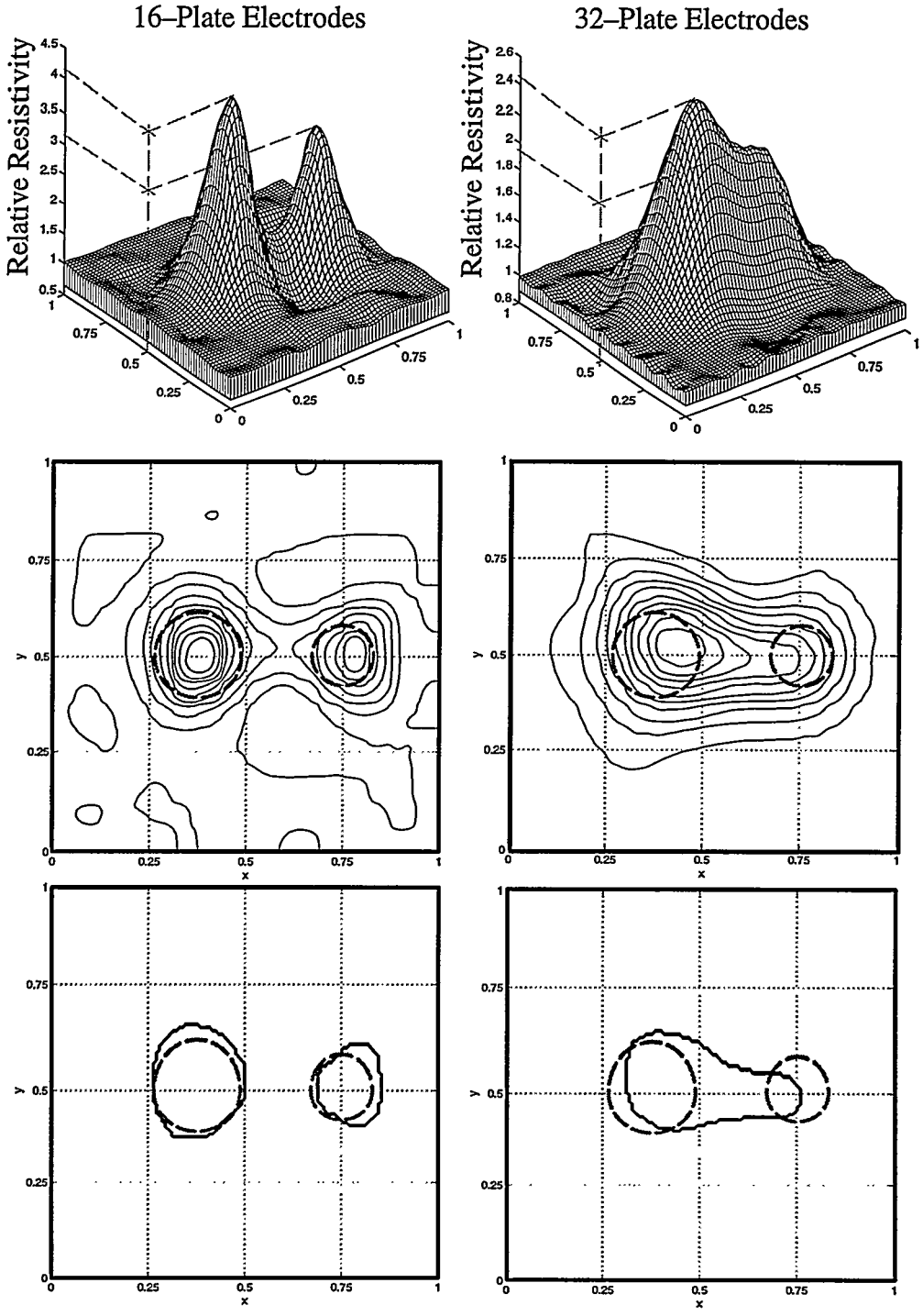

Figure 7.14 Relief, contour, and best contour plots for comparing the 16–plate–electrode phantom and the 32–plate–electrode phantom. Computations were carried out on a 16×16 for the 16–electrode phantom and 17×17 for the 32–electrode phantom.

undesired effects. The adaptive techniques, however, require jointly iterative measurement and computational procedures, and they are not suitable for imaging periods on the order of milliseconds or less in which the conductivity field changes very rapidly. Instead, Walsh–function excitation patterns may be adopted because they require no *a priori* computations and they require relatively simple measurement hardware. In what follows, it is shown that the Walsh–function excitation patterns which might, in a 16–plate–electrode system, be viewed as analog multiplexing of eight paired excitations for each Walsh pattern, give excellent results compared to the results obtained using single pair excitation patterns. Thus, on a 16–electrode system a complete Walsh–function set is comprised of 15 separate patterns, each containing the equivalent of eight pair of excitations for an equivalent total of $(16 \times 15)/2 = 120$ excitations. This walsh–function set is obtained, however, in only 12% of the time equal to obtain a complete paired set. This time saving is a major consideration.

An experimental procedure was prepared to investigate the results of obtaining a partial set of paired excitations in the same time as it takes to obtain a complete Walsh set. The partial paired set including diagonal and cross electrode pairs was chosen to maximize the system sensitivity. The 16–plate–electrode phantom is used in all of the experiments. To approximate the low and the high spatial excitation patterns as described in the best excitation patterns, a combination of 8 diagonal and 7 cross electrode pairs (a total of 15 excitations) are selected. Therefore, the excited diagonal and the cross electrode pairs can provide a relatively uniform sensitivity distribution in both the central and the boundary regions of the phantom, respectively.

The electrode numbers of the selected pairs are shown in Table 7.1. The excited electrode pairs are selected as follows: In the diagonal electrode pair excitations, for each excitation, one of the first 8 electrodes was selected and excited with the negative

Table 7.1 Electrode numbers of the diagonal and cross electrode pairs used in the 15 single pair excitation patterns applied to the 16–plate–electrode phantom shown in Figure 7.9(a).

	Diagonal Pairs								Cross Pairs						
Exc	1	2	3	4	5	6	7	8	9	10	11	12	13	14	15
Neg	1	2	3	4	5	6	7	8	1	3	5	7	10	12	1
Pos	9	10	11	12	13	14	15	16	4	6	8	10	13	15	14

Note: Where the symbols stand for:
Exc: the excitation number;
Neg: the electrode number excited with the negative polarity;
Pos: the electrode number excited with the positive polarity.

polarity, and the next 7 electrodes were skipped and the 8th electrode was selected and excited with positive polarity. In cross electrode pair excitations, starting with the first electrode, the selected electrode was excited with negative polarity, and then two electrodes were skipped, and the 3rd electrode was selected and excited with negative polarity. For the next pair two electrodes were skipped and the third electrode is selected as a negative polarity electrode and so on.

The acquired data for 15 single pair excitations and the Walsh excitation patterns were reconstructed on a 9×9 mesh for the 16–plate electrode phantom to 70 iterations. The relief and contour plots for this case are shown in Figure 7.15. The measurements in both test cases were obtained within an accuracy of 1 part in 1000 ($r = 3.0$). The results obtained for the single pair excitation patterns are found to be very poor compared to those for the Walsh excitation patterns. The targets showed low contrast ratios of 2.1:1 for the single pair excitation case and the targets were not separated from each other. This emphasizes the dramatic time savings of using Walsh patterns without sacrificing image quality.

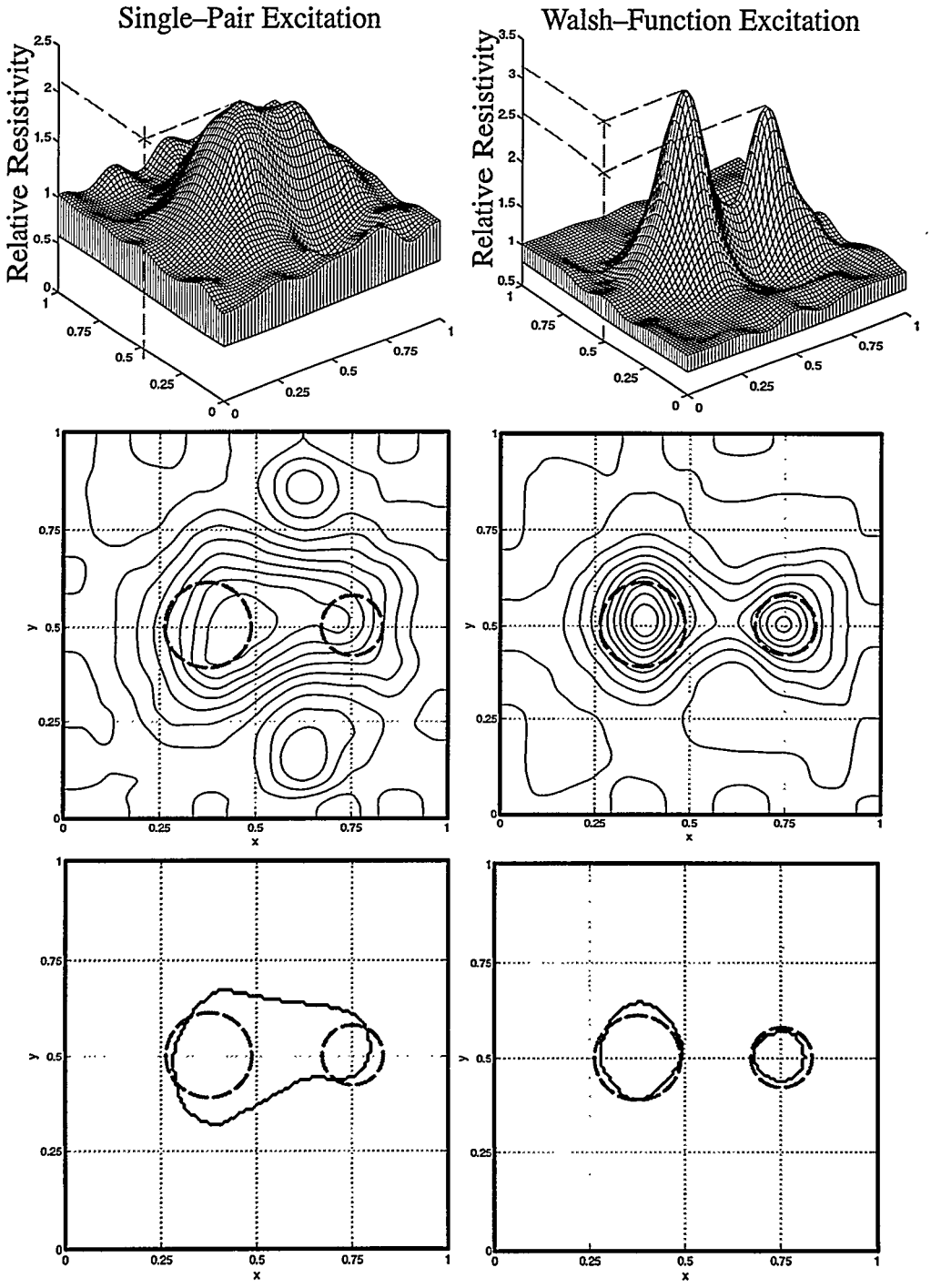

Figure 7.15 Relief and contour plots for the results obtained under equal data acquisition and computed for single pair excitations (left column) and the Walsh pattern excitations (right column) applied to a 16–plate–electrode phantom. All of the computations were carried out on a 9×9 mesh.

Not only are the time savings substantial, but also computations are undertaken with only 12% of the data with voltage and current matrices only 12% the size of those required with a complete paired set. Computational savings are also substantial.

Figure 7.16 shows the result of increasing the number of elements in the mesh model to 16×16 computed to 50 iterations. The mesh refinement in this case slightly improved both the target contrasts and separability of the targets in the single pair excitation case. The contrast ratios increase 14% and 30% relative to the coarse mesh reconstruction for the single pair and the Walsh excitation cases respectively. Background conductivity variation in the single pair excitation case slightly increased relative to the coarse mesh reconstruction while it remained the same for the Walsh patterns. The results shown in this figure indicate that reconstructions using single electrode–pair excitations were significantly affected by the finite element discretization errors. On the other hand, the results obtained from the Walsh excitations remained relatively immune to these errors.

7.3.5 Excitation Signal: Sinusoidal versus Square–Pulse

In this section, the performance of the measurement methods and two applied excitation signal types are investigated. Two alternate signal types were proposed earlier. The first one uses sinusoidal voltage signals and measures rms values of electrode voltages and currents. However, the second one using square–pulse excitation signals gives the choice of setting the measurement error in the beginning and the data is averaged until the variation of the averaged values reaches the defined measurement accuracy level. The data acquisition time, therefore, can be reduced by using averaged peak measurements of square–pulse signals with a selected, constant accuracy level in all measurements. Therefore, repeating unnecessary measurements can be greatly avoided. As the accuracy is sacrificed, the data acquisition time can be reduced significantly.

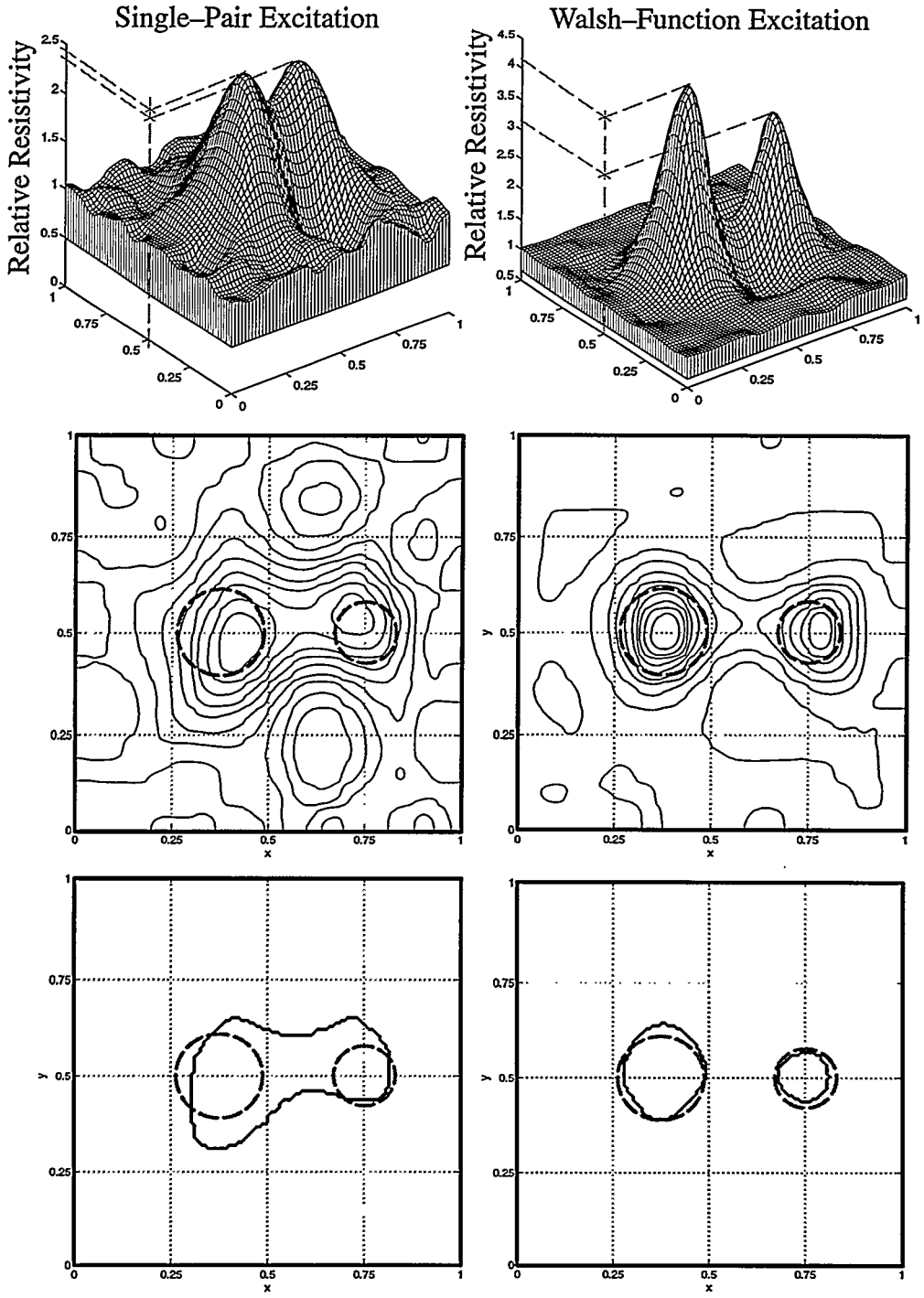

Figure 7.16 Relief contour and best contour plots for single pair (left column) and Walsh pattern excitations (right column) applied to a 16–plate–electrode phantom. No computer optimized patterns are used. All of the computations were carried out on a 16×16 mesh.

The results computed on 9×9 and 16×16 mesh models presented in the order of applied signal types of sinusoidal and square–pulse, and increasing accuracy in the measurements as $r = 2.0, 2.5, 3.0, 3.5$ and 4.0. In all experiments the Walsh–function excitation patterns were applied to the 16–plate electrode phantom under the same experimental conditions. Comparison of excitations by using sinusoidal signal and square–pulse signal excitation for varying measurement error, effects of computations to 70 iterations on a 9×9 mesh, 16–plate–electrode phantom are provided. Relief, contour, and best contour plots for each case are shown in Figure 7.17, Figure 7.18, and Figure 7.19 respectively. Results are shown for the rms measurements in (a), and for the square–pulse with different accuracy levels in (b) through (f) respectively in each figure. In the same manner, Figure 7.20, Figure 7.21, and Figure 7.22 shows the results computed to 50 iterations from the same data for the 16×16 mesh.

Reconstructions using data obtained by the two measurement methods introduced herein shows that both methods have the ability to take measurements to depict the two–target test case in a reasonable accuracy but with slightly differing contrasts and shapes as well as differing data acquisition speeds. The results using square–pulse excitation signal yielded fluctuating target contrasts which are especially noticeable for the accuracy levels of $r = 2.0$ and 2.5. It is suspected that this unrealistic increase or decrease in contrast ratios is simply related to the fluctuation tolerated in measured data. In retrospect, accuracy levels selected as 3.0 or higher could reduce this fluctuation yielding similar results.

There is factor which can significantly affect the magnitude of target contrasts. That is the mesh model used in reconstructions. Examining the relief plots in Figures 7.17 and 7.20, it is seen that computed target contrasts consistently increased for both excitation signal types and for all accuracy levels when 16×16 mesh model is used in reconstructions. Using a fine mesh model showed different effects when different accuracy levels were

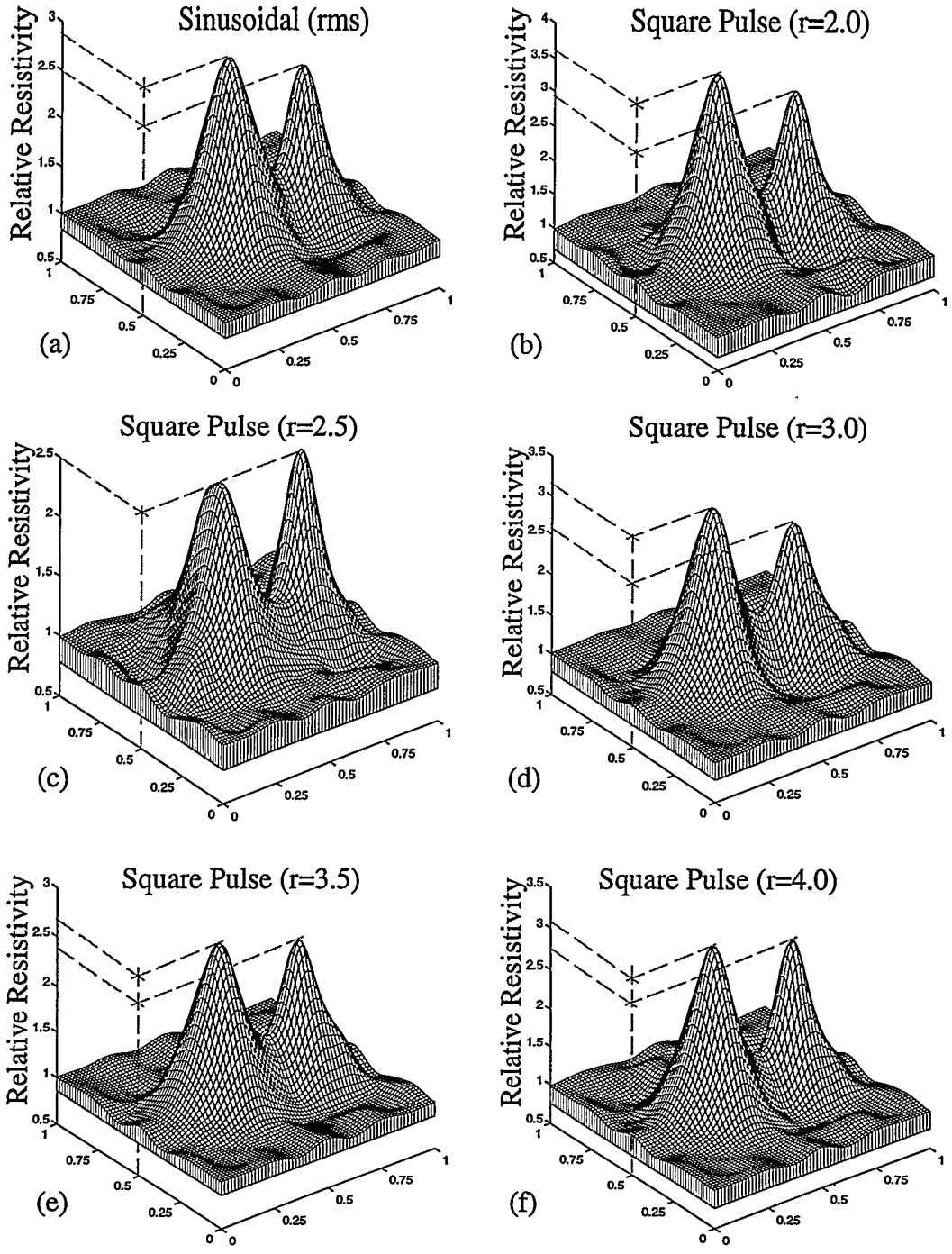

Figure 7.17 Relief plots for comparing measurement methods; (a) rms measurements of sinusoidal signals (rms); (b)–(f) averaged peak measurements of square–pulse signals. The computations carried out on a 9×9 mesh model of the 16–plate–electrode phantom.

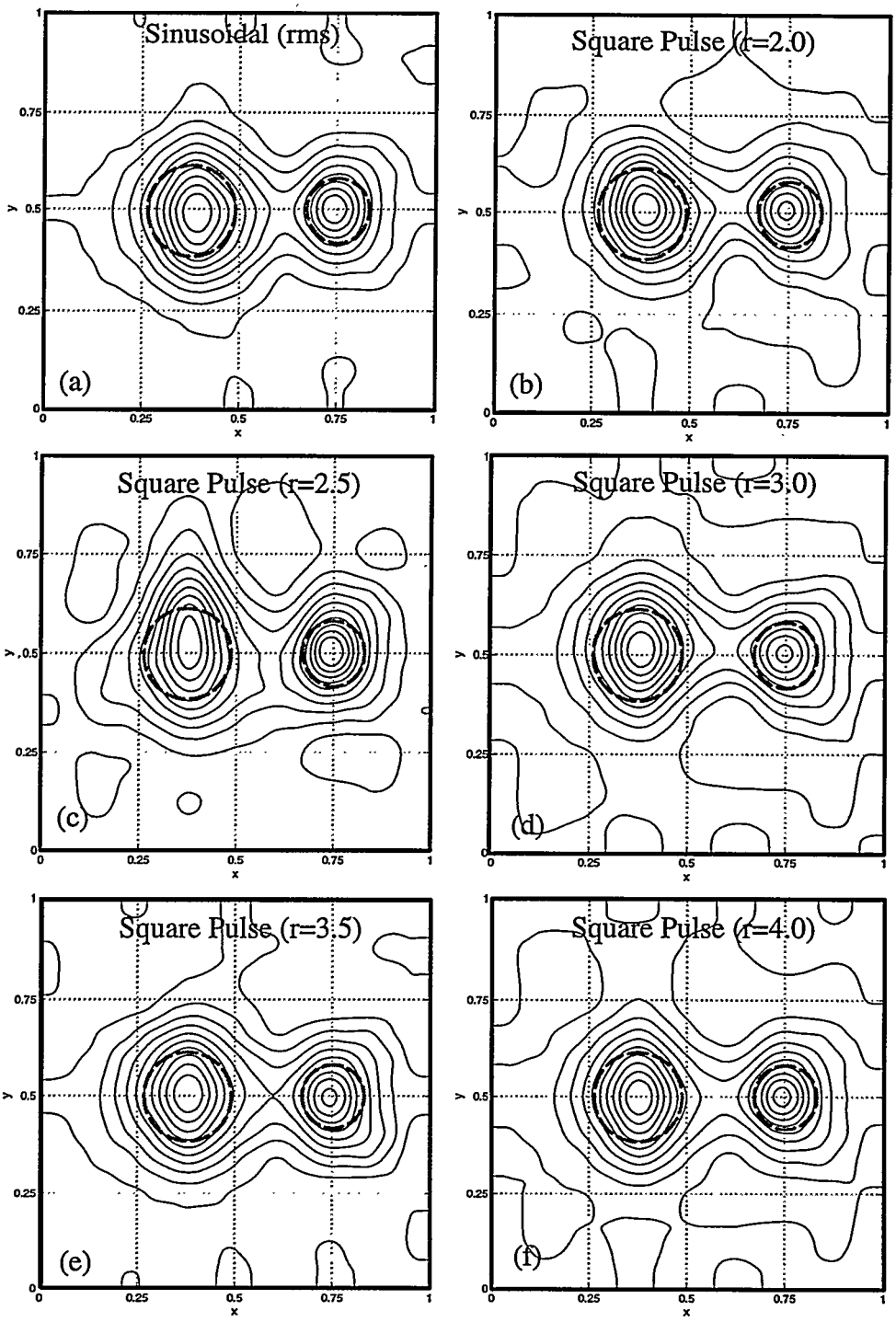

Figure 7.18 Contour plots given in Figure 7.17: (a) rms measurements of sinusoidal signals (rms); (b)–(f) averaged peak measurements of square–pulse signals. The computations carried out on a 9×9 mesh model of the 16–plate–electrode phantom.

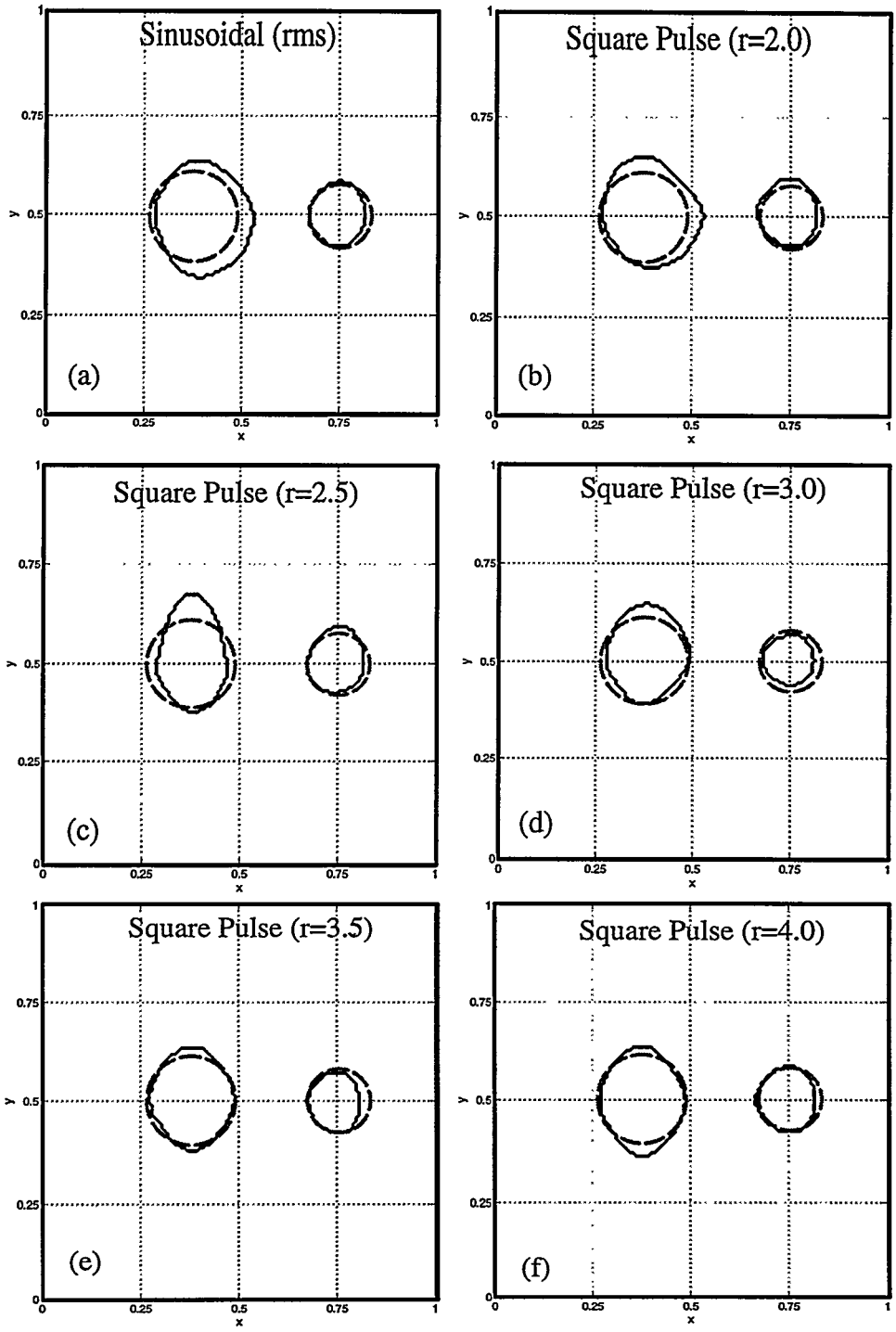

Figure 7.19 Best contour plots given in Figure 7.18: (a) rms measurements of sinusoidal signals (rms); (b)–(f) averaged peak measurements of square–pulse signals. The computations carried out on a 9×9 mesh model of the 16–plate–electrode phantom.

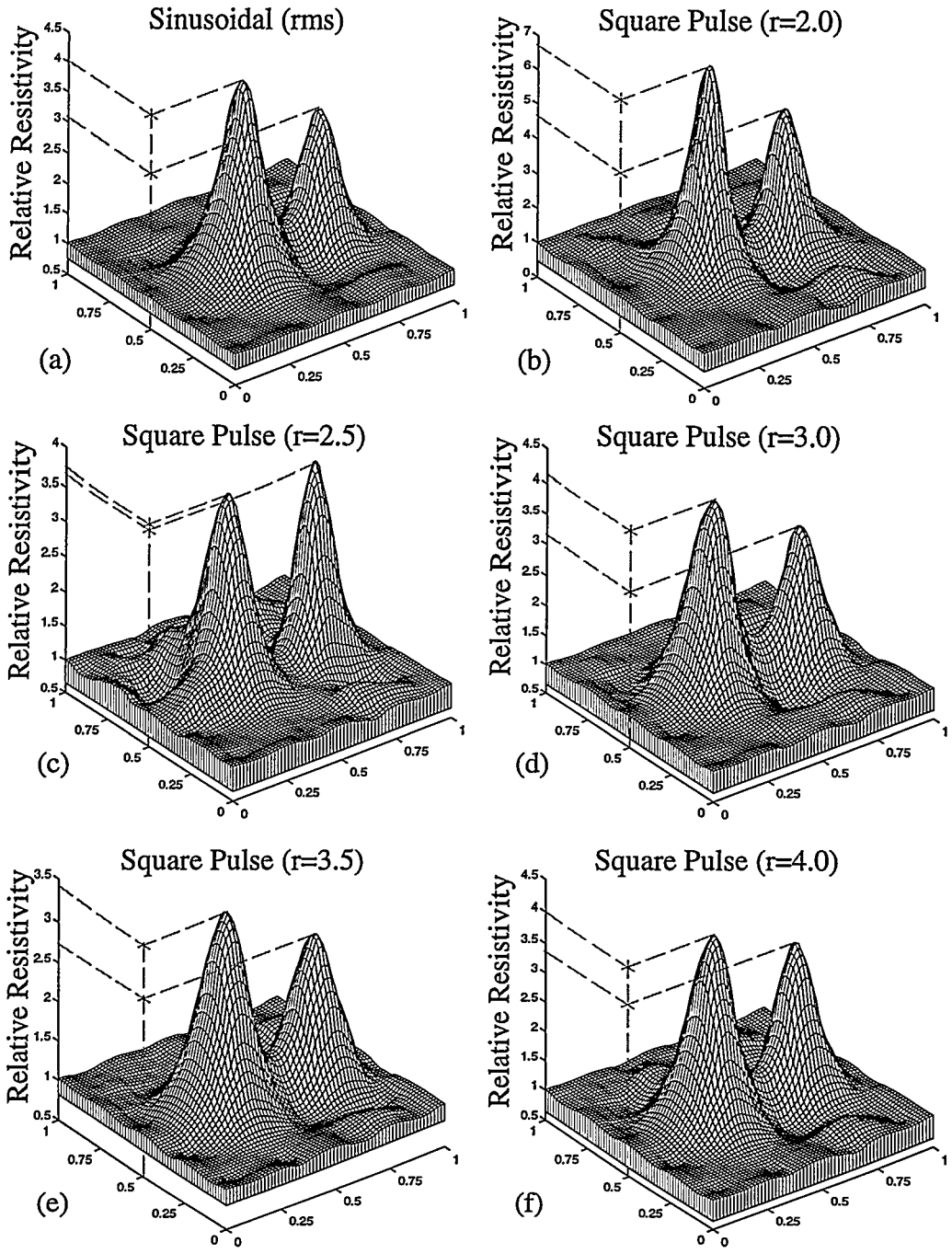

Figure 7.20 Relief plots for comparing measurement methods: (a) rms measurements of sinusoidal signals (rms); (b)–(f) averaged peak measurements of square–pulse signals. The computations carried out on a 16×16 mesh model of the 16–plate–electrode phantom.

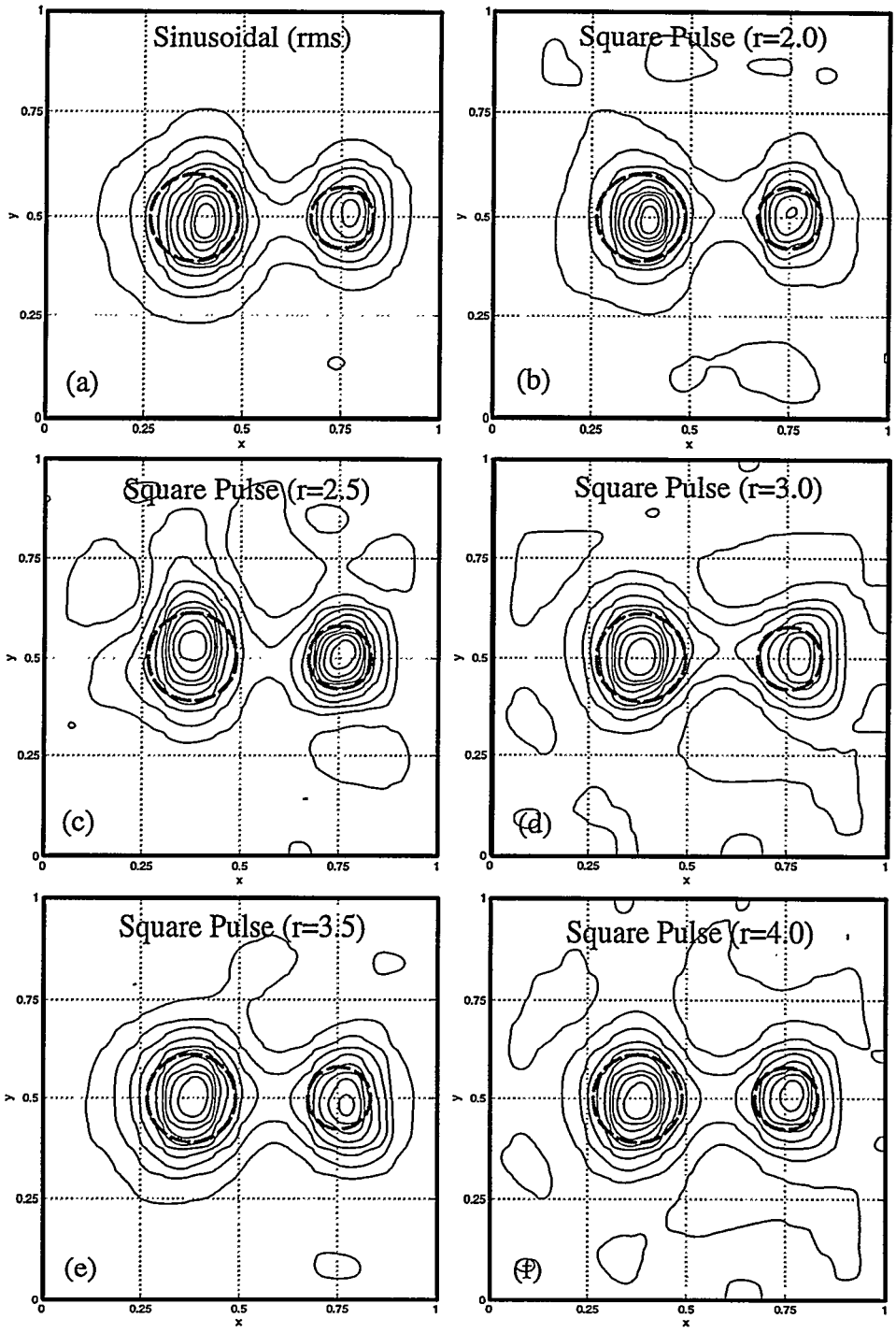

Figure 7.21 Contour plots given in Figure 7.20: (a) rms measurements of sinusoidal signals (rms); (b)–(f) averaged peak measurements of square–pulse signals. The computations carried out on a 16×16 mesh model of the 16–plate–electrode phantom.

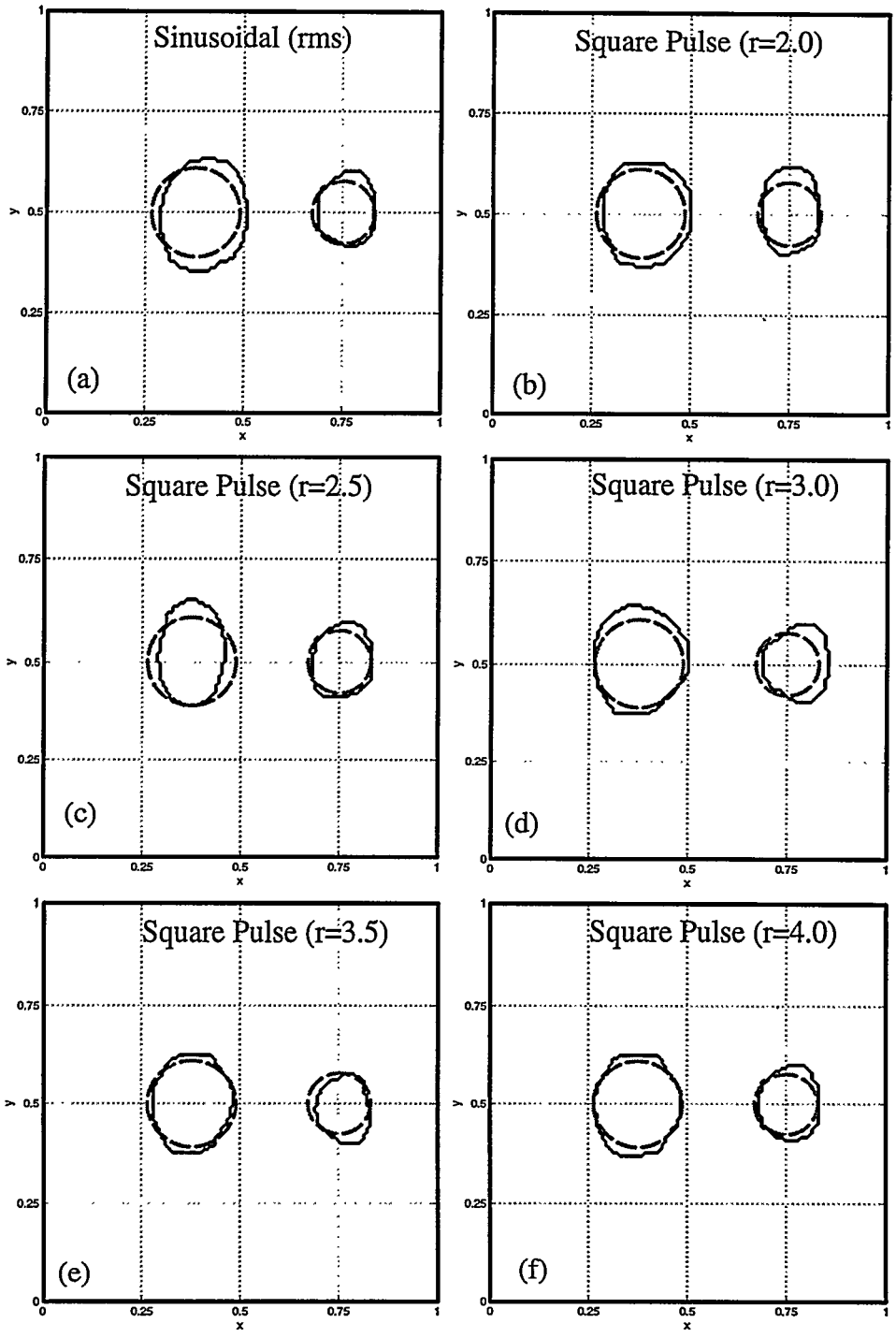

Figure 7.22 Best contour plots given in Figure 7.21: (a) rms measurements of sinusoidal signals (rms); (b)–(f) averaged peak measurements of square–pulse signals. The computations carried out on a 16×16 mesh model of the 16–plate–electrode phantom.

selected: target contrasts increased as high as 90% (in accuracy level of 2.0) when fine mesh model is used, and this increase goes down to 30% as the accuracy level is increased to 3.0 or higher. In conclusion, using a fine mesh model in reconstructions may amplify this undesired, unrealistic contrast level fluctuations due to noisy measurements but it can improve the results if the measurement accuracy is improved.

Figure 7.23 shows that to obtain data with a higher degree of accuracy than with $r = 3.0$, the the time required increases very rapidly as the accuracy criterion is increased. From a practical standpoint, the data acquisition times indicate that little is to be gained by increasing r beyond a value of 3.0, the accuracy index with which most data reported herein were obtained.

7.4 Comparisons and Effects of Computational Methods Developed

The effects and improvements due to the design and the experimental techniques were presented for the standard test case in detail. The results presented however were not fully exposed to the effects of all of the numerical and analytical techniques developed. This section concentrates on investigating the effects of these developments. Results presented herein are basically composed of three groups. The first group shows the effects and improvements in conductivity images when the Preconditioned Voltage Conversion (PVC) method (described in Chapter 5, Sect. 5.5) is used. The second group shows that additional improvements in reconstructions can be obtained by using the computer optimized excitations rather than the direct measurements acquired by the data acquisition system. Finally, the third group includes comparisons of three different finite element schemes: constant, bilinear– and biquadratic–exponential conductivity variation within each major element.

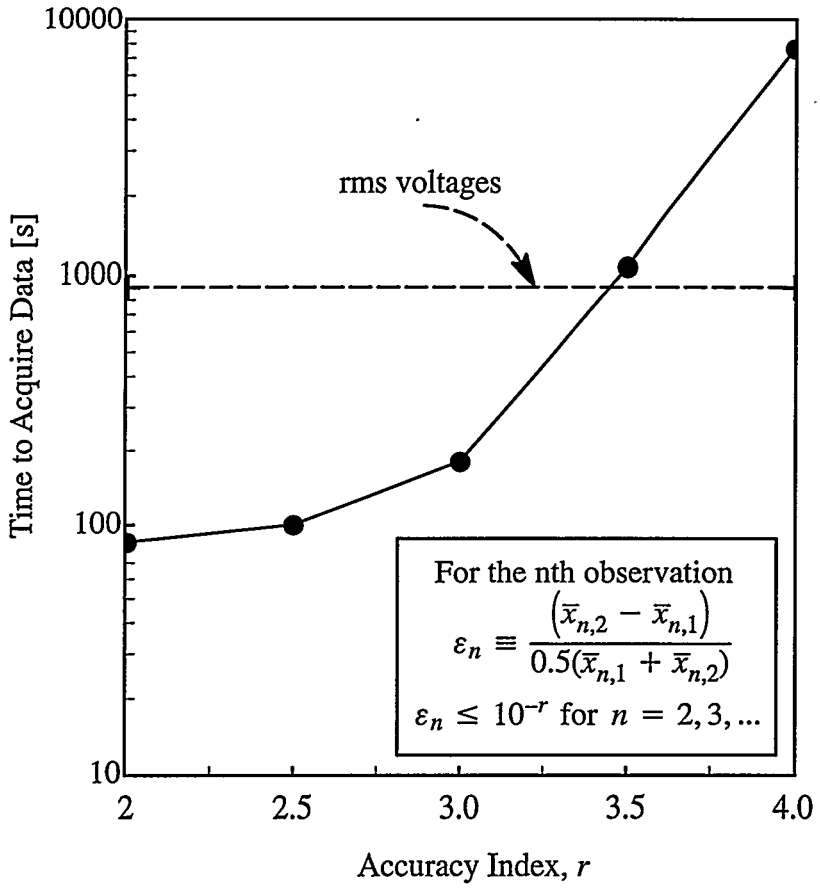

Figure 7.23 Time required to obtain a complete set of imaging data at a given accuracy level.

7.4.1 Improvements by Using the PVC Method

The results presented herein demonstrate the effects of applying PVC to the 16–plate–electrode phantom experiments with both 9×9 and 16×16 finite element mesh densities. Figure 7.24 demonstrates the improvements obtained when the PVC method was used in the reconstructions on a 9×9 mesh model. Considering these results, it can be noticed that the relief, contour and best contour plots with the case using the PVC method (shown in the right column) are considerably better than the results obtained by using the uncorrected data (shown in the left column). There is much less noise, contrast is better and target separation improves.

The same data used for the results in Figure 7.24 was also reconstructed in the same manner on a 16×16 mesh model. These results are shown in Figure 7.25. In this case, the target contrasts for both cases increased about 30% relative to the reconstructions using a coarse mesh. Again, PVC yields improvements for the 16×16 model as seen for the 9×9 model. Similar results are obtained in any set of data examined.

It was previously mentioned when developing the PVC method that the "A" preconditioning matrix should ideally be a diagonal matrix. In fact, it was found that the A–matrix used for preconditioning the measured boundary voltages (as determined from the homogenous case) had diagonal values, a_{ii} in the range $0.970 \leq a_{ii} \leq 1.1$ where the off–diagonal terms were in the range of $|a_{ij}| \leq 0.03$, where $i \neq j$. This confirms the assumptions stated in its development.

It is clear that PVC markedly improved the results of raw imaging. Indeed, without PVC, some images are impossible to obtain.

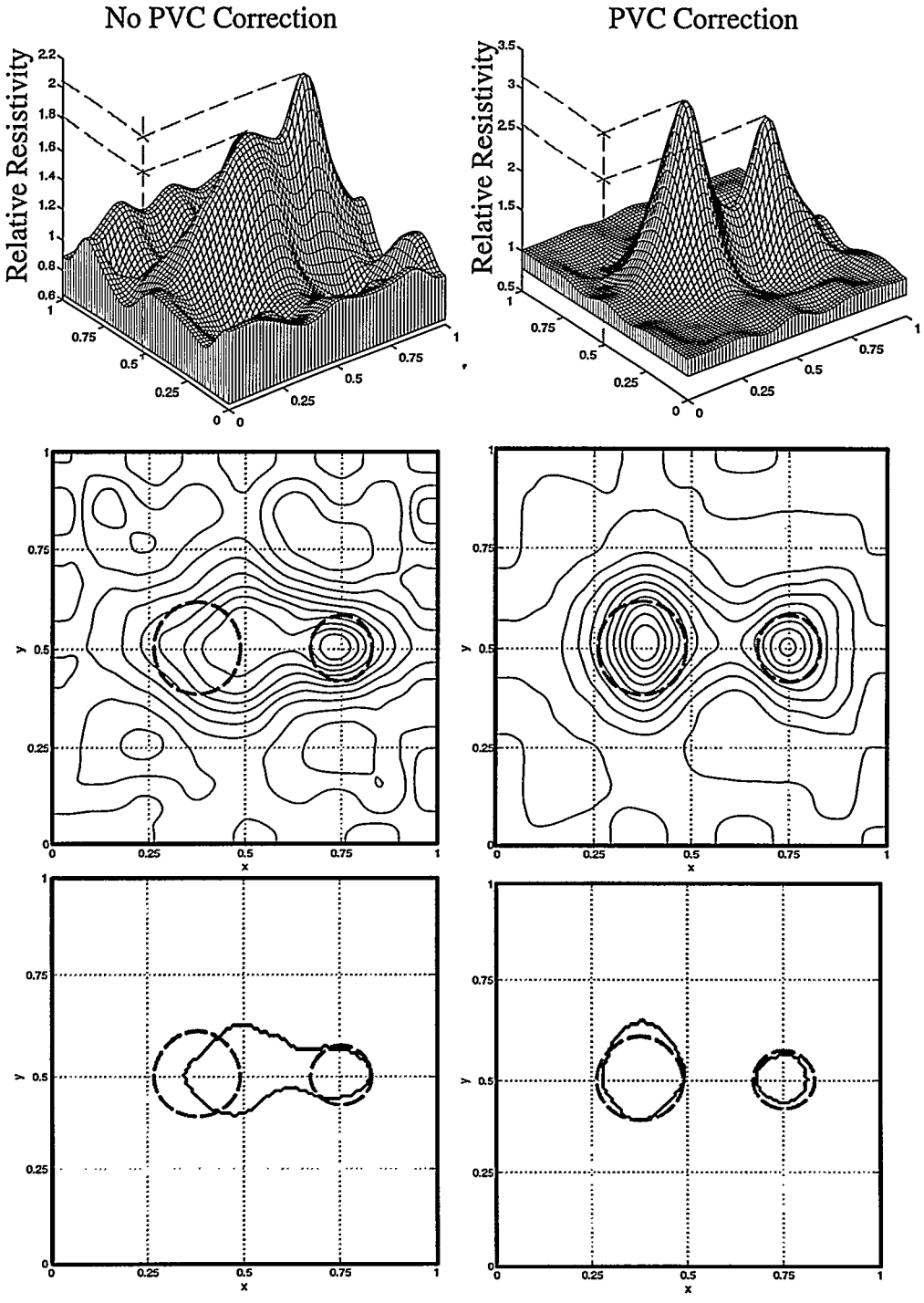

Figure 7.24 Relief, contour and best contour plots showing the improvements in the computations when the PVC method is used. The computations were carried out on a 9×9 mesh model of the 16–plate–electrode phantom.

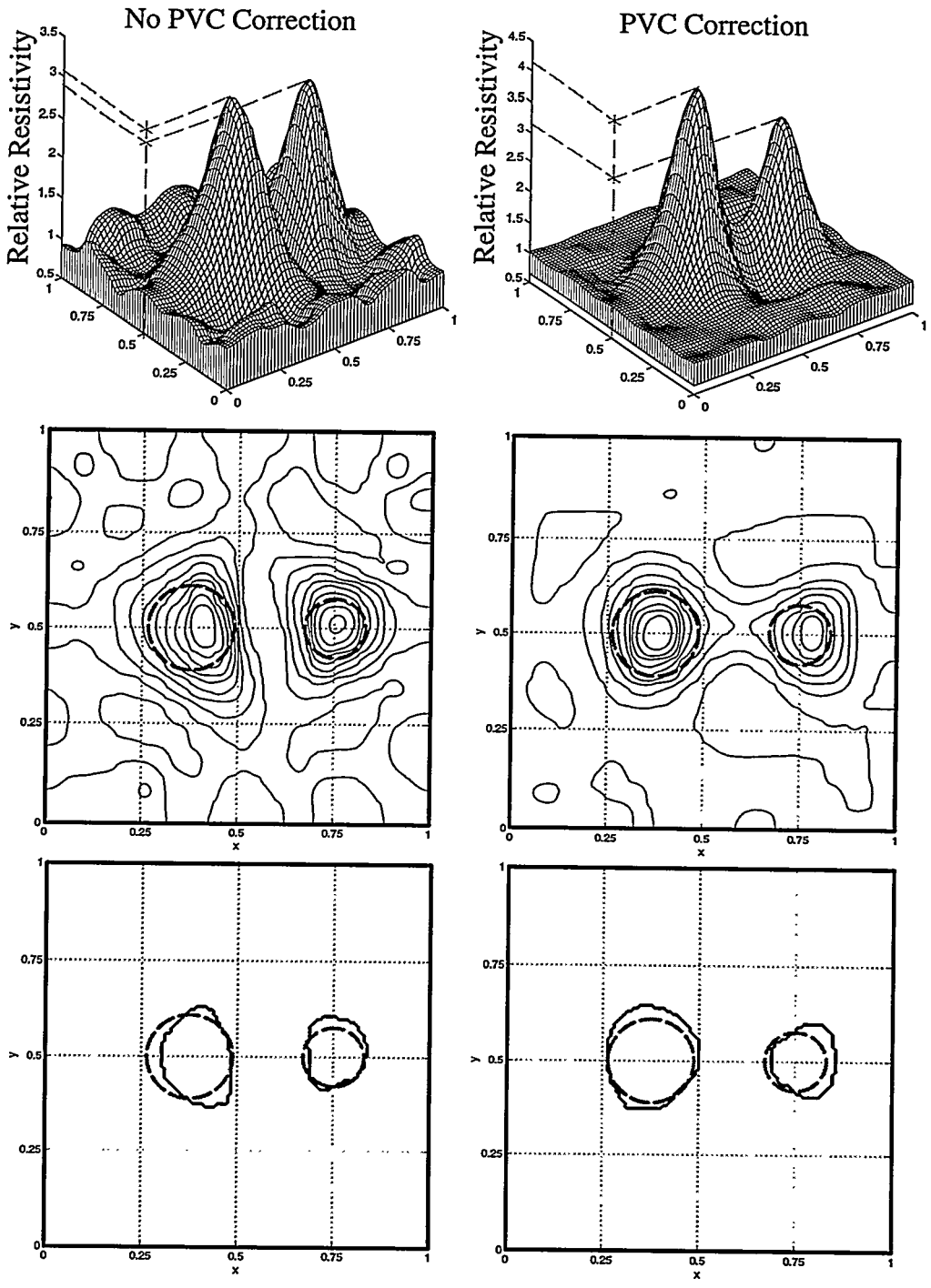

Figure 7.25 **The same case as in Figure 7.24 but the computations in this case were carried out on a 16×16 mesh model of the 16–plate–electrode phantom.**

7.4.2 Recapitulation

The results presented so far, all using directly measured boundary excitation voltages, have shown some improvements in reconstructions. None of them completely considered the effects of all design and modeling features. Before presenting results showing the effects of the optimized patterns it would be quite helpful to reconsider what conclusions have been drawn from the previous results.

Rod– versus Plate–Electrodes. Use of the 16–plate–electrode phantom produced significantly better results than the 16–rod–electrode phantom when models of 16×16 or fewer elements were used. However, similar improvements were not observed in 32–plate–electrode phantom. Rather, it was seen that increasing the number of electrodes from 16 to 32 worsened the results unless a finer mesh was used for analysis, an impracticality in the case of the 32–plate electrodes and a 34×34 model.

Pair– versus Walsh–Excitation. Walsh excitation of all electrodes simultaneously produced significantly better results than the single electrode pairs.

Measurement Type and Accuracy. Accuracy levels of 1 part in 1000 ($r = 3.0$) or higher yielded nearly identical results to those obtained from rms measurements but took only 20% of the time to acquire data. Increasing the accuracy index, r, beyond a value of 3.0 had a little measurable effect on image quality but took more time to acquire data.

Preconditioned Voltage Conversion. PVC produced significant improvements in image quality yielding good target separation where none existed without the use of PVC. Imaging without PVC sometimes failed completely.

From the foregoing comparisons, it was seen that the best results were obtained with the following criteria:

1. Plate electrode phantom using Walsh–function excitation;

2. Averaged peak voltage measurements with an accuracy index $r = 3.0$;

3. Preapplied voltage conditioning (PVC).

Therefore, unless otherwise stated, all further results presented will be utilize these conditions.

7.4.3 Improvements Using the Computer Optimized Boundary Excitations

The initial attempt of using optimized patterns showed that the reconstructions with the absence of the PVC method failed or yielded very poor results. This is because of all the errors which go into computation of the phantom conductance matrix. Computing optimized patterns using the difference conductance matrices of homogeneous and nonhomogeneous cases in the absence of PVC severely suffered from these errors.

Computer optimization occurs when each excitation is numerically diminished proportionally with the eigenvalues of the difference conductance matrix. This modulation is, in effect, a post–facto application of optimization according to the method of Gisser et al. [56]. It was shown that this second treatment of the data, following PVC, added significant further improvements to the image results. Noise levels were further reduced, contrast ratios further enhanced, and target separation and identification improved or made possible when PVC alone failed.

It will be shown that significant improvements are found when computer optimized patterns are applied to both rod– and plate–electrode phantoms having 16 and 32 electrodes and for 8×8, 9×9, 16×16 and 17×17 element models. In all results presented herein, the effects on the results relative to the mesh refinement will also be discussed.

Using Rod Electrodes. The computational results obtained on an 8×8 and a 16×16 mesh models for the 16–electrode phantom are shown in Figures 7.26 and 7.27. A close examination on the relief, contour and the best contour plots shows that use of computer optimized excitation patterns clearly improves the images but the final results are still not satisfactory.

Increasing the number of electrodes further improves the situation. Both 8×8 and a 16×16 mesh models of the 32–rod–electrode phantom are shown in Figures 7.28 and 7.29. In this case, it could be concluded that increasing the number of electrodes makes the results even worse in the coarse mesh reconstructions. This is an indication that if the number of rod electrodes is increased, the discretization error due to inaccurate modeling of these close electrodes expected to increase. In contrast to the coarse mesh model, considerably better results were seen in the fine mesh reconstructions. Furthermore, computerized boundary optimization increased the contrasts of both targets by about a factor of two but little or no improvement in the shapes of the targets.

Using 16 Plate Electrodes. Figures 7.30 and 7.31 show the computed results for 9×9 and 16×16 mesh models of the 16–plate–electrode phantom. It seems that computer optimizing the boundary measurements has the ability to decrease the noise levels in both coarse and fine mesh reconstructions. The best contour plots indicate no significant difference in determining the target contours. However, the contrast increased by a factor of 1.6 and 2.5 in coarse and fine mesh cases respectively.

Using 32 Plate Electrodes. Results for a 17×17 mesh model are shown in Figure 7.32, the unoptimized results being identical to those shown in Figure 7.14 for the 32–plate–electrode phantom. Because of the geometric constraint of these phantom no coarse mesh results are presented. The results of the 32–plate–electrode phantom seen in

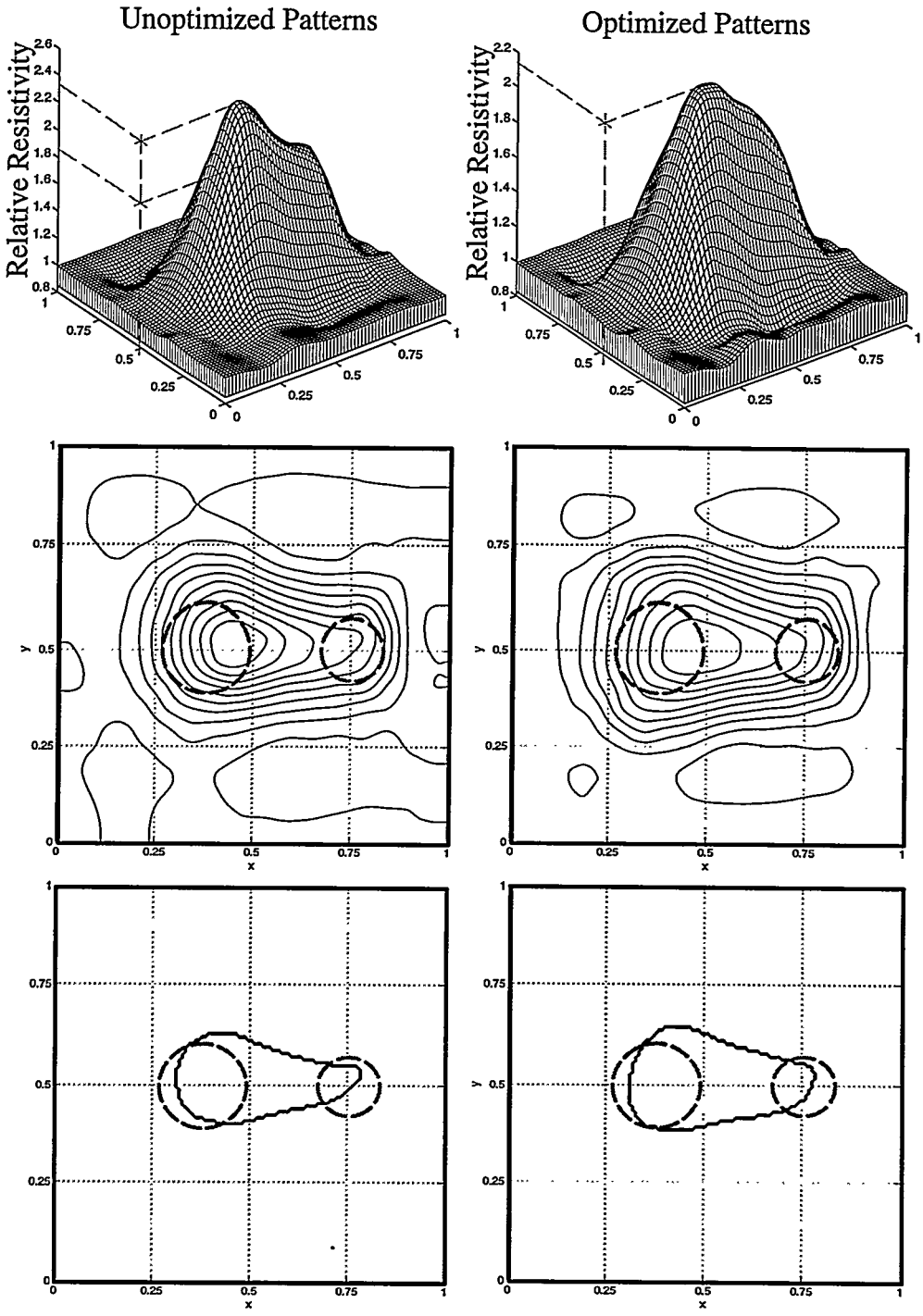

Figure 7.26 Relief, contour, and best contour plots for comparing reconstructions without (left column) and with (right column) applying the computer of unoptimized excitation patterns. The computations were carried out on an 8×8 mesh model of the 16–rod–electrode phantom.

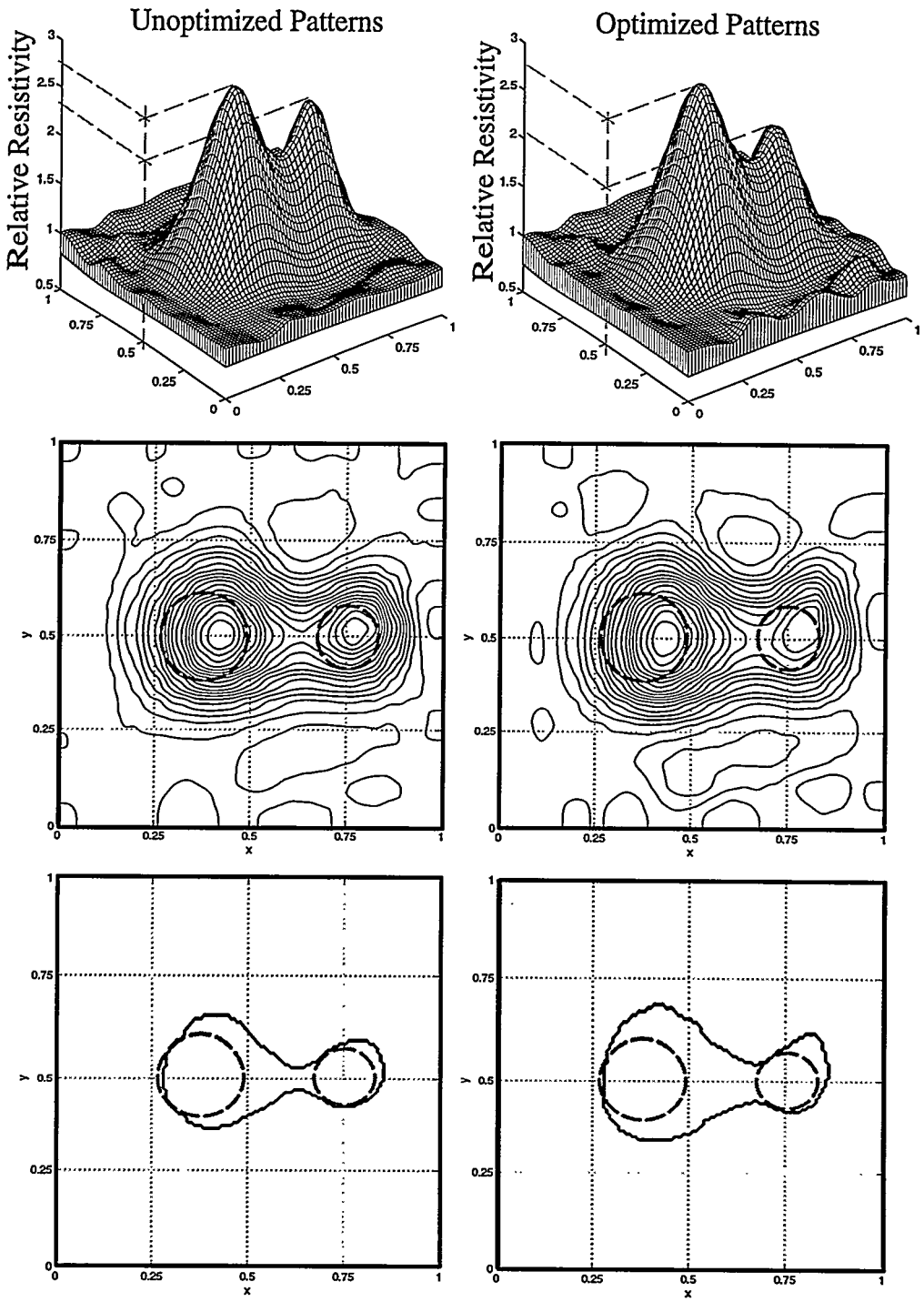

Figure 7.27 The same case as in Figure 7.26 but the computations in this case were carried out on a 16 × 16 mesh model of the 16–rod–electrode phantom.

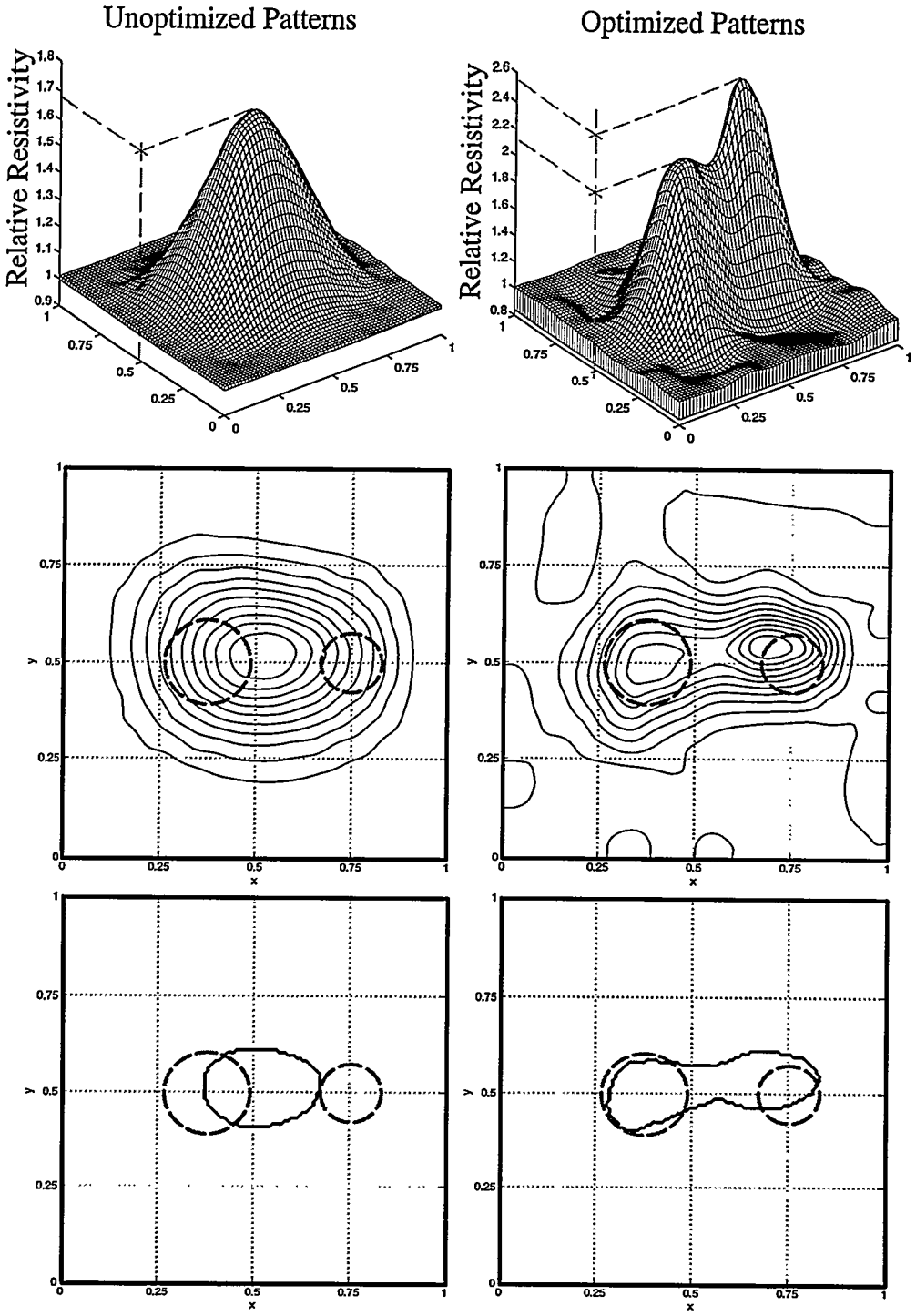

Figure 7.28 Relief, contour, and best contour plots for comparing reconstructions without (left column) and with (right column) applying the computer of unoptimized excitation patterns. The computations were carried out on an 8×8 mesh model of the 32–rod–electrode phantom.

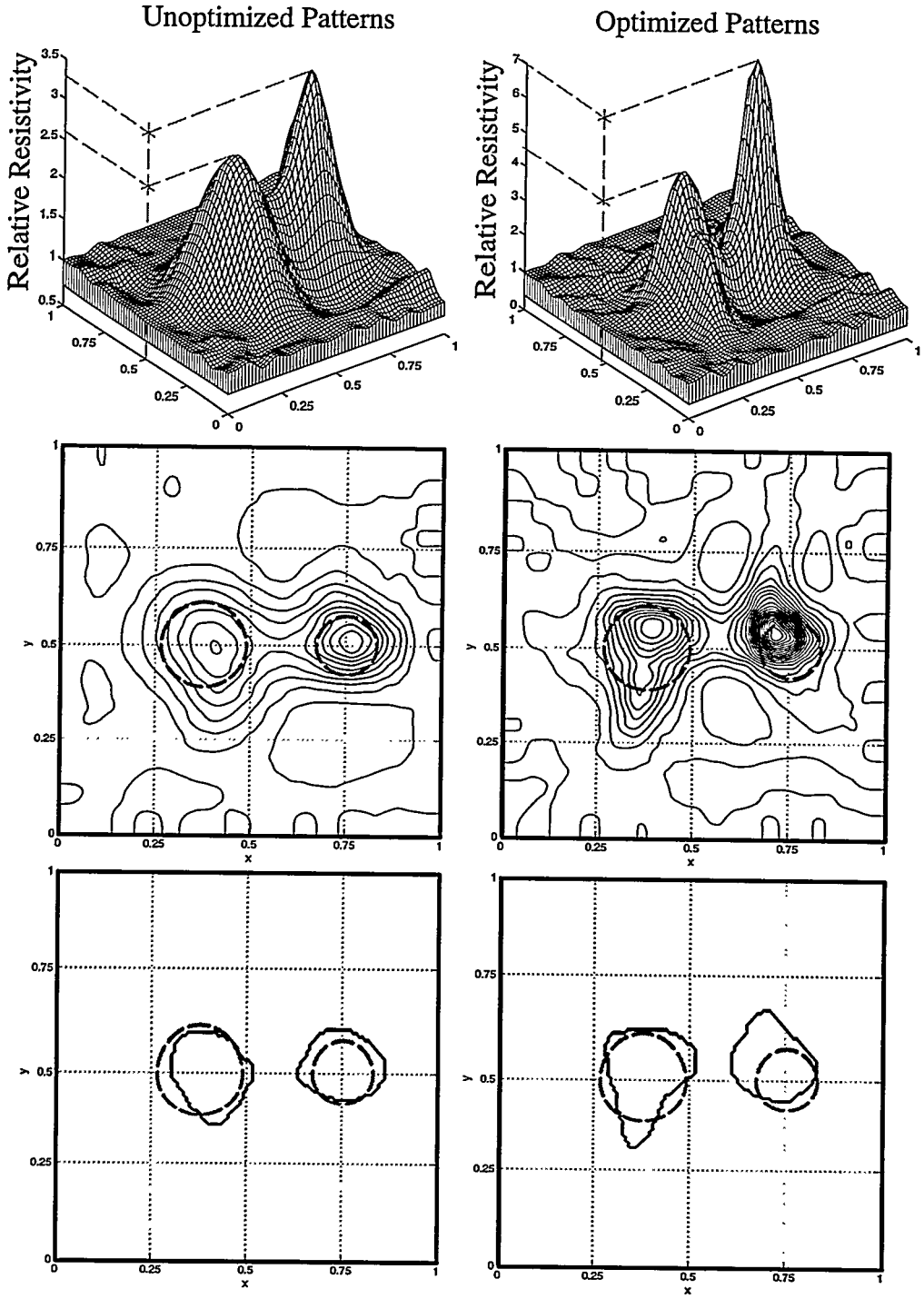

Figure 7.29 The same case as in Figure 7.28 but the computations in this case were carried out on a 16 × 16 mesh model of the 32–rod–electrode phantom.

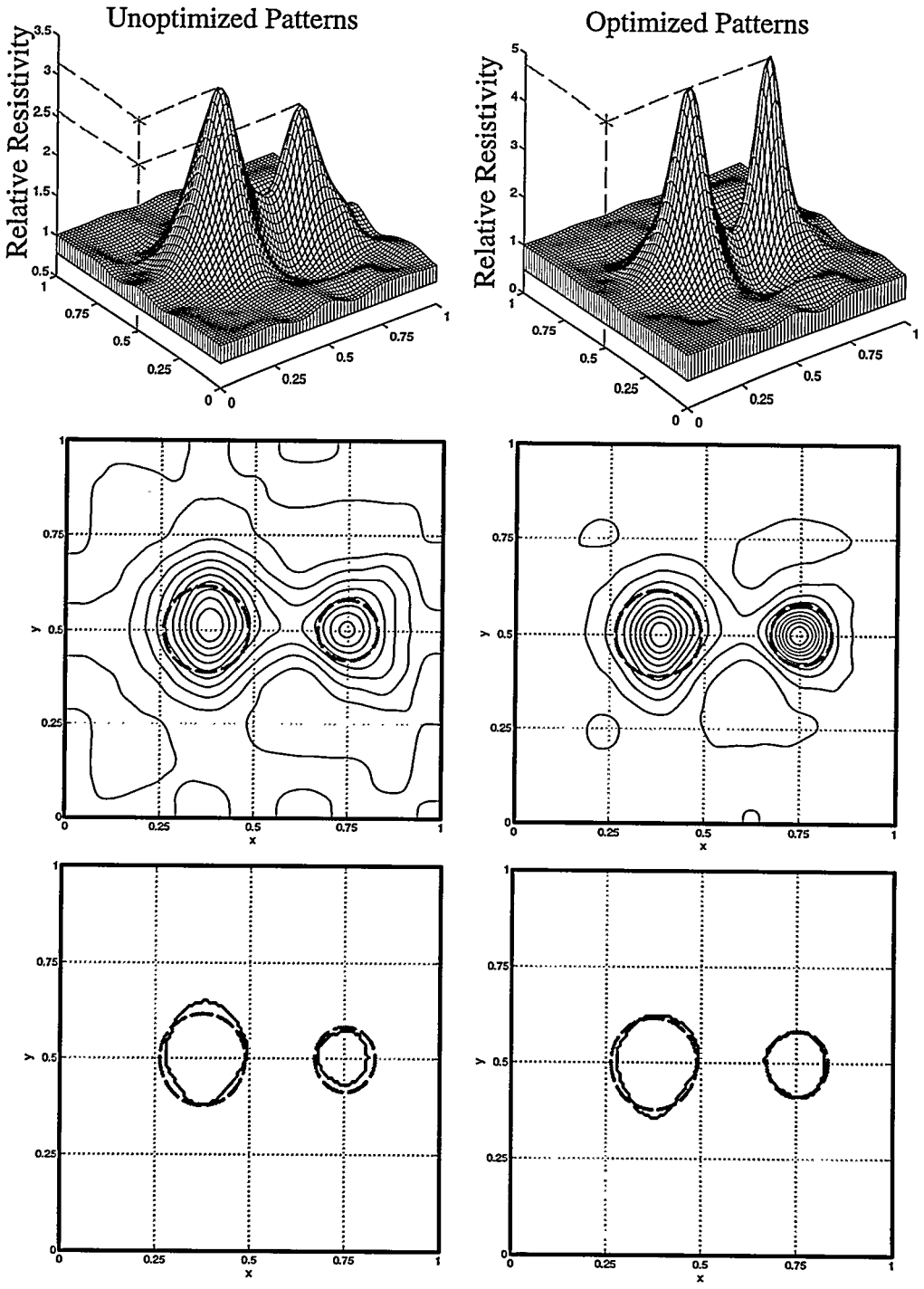

Figure 7.30 Relief, contour, and best contour plots for comparing reconstructions without (left column) and with (right column) applying the computer of unoptimized excitation patterns. The computations were carried out on an 9×9 mesh model of the 16–plate–electrode phantom.

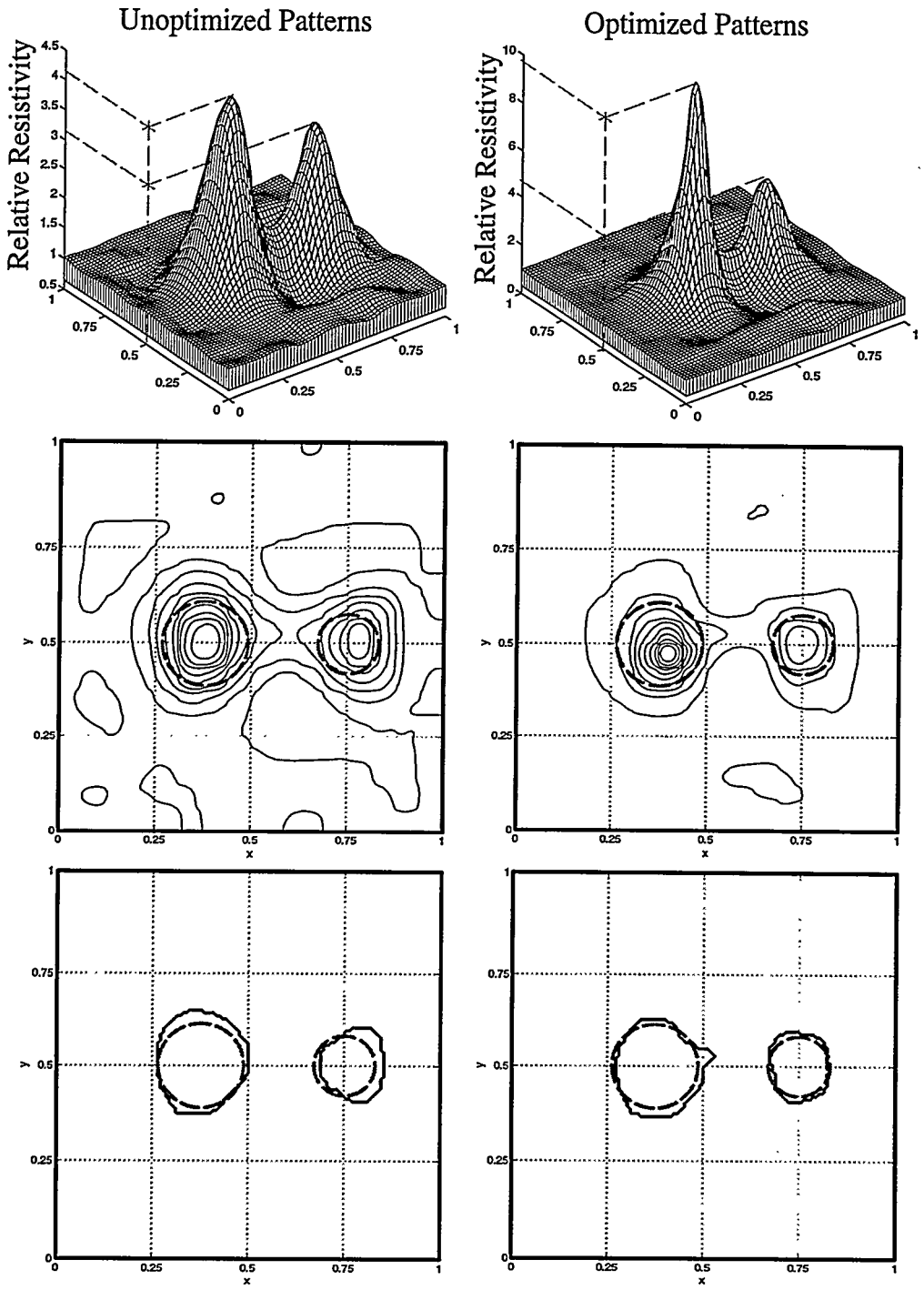

Figure 7.31 The same case as in Figure 7.30 but the computations in this case were carried out on a 16 × 16 mesh model of the 16–plate–electrode phantom.

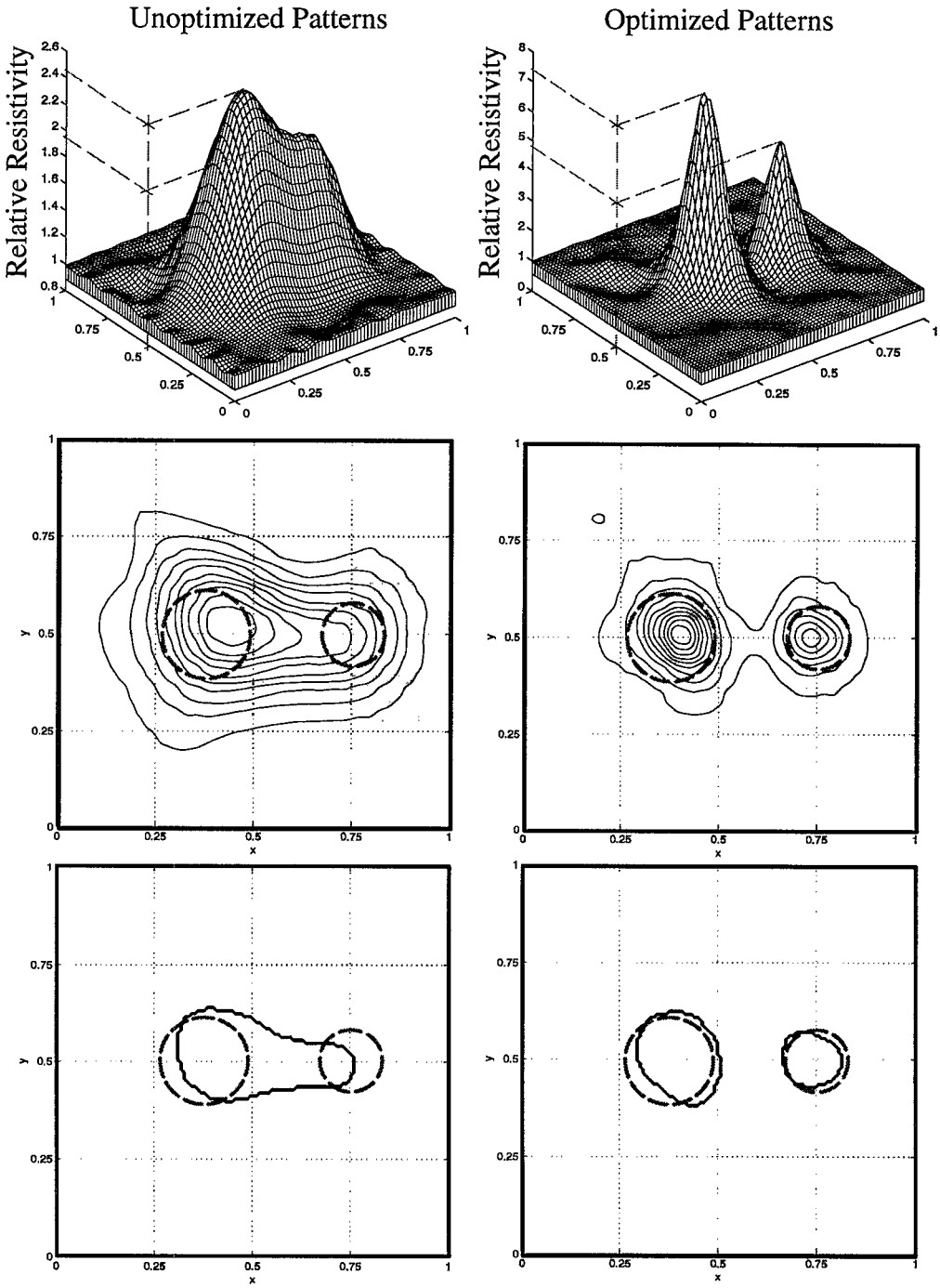

Figure 7.32 Relief, contour, and best contour plots for comparing reconstructions without (left column) and with (right column) applying the computer of unoptimized excitation patterns. The computations were carried out on a 17×17 mesh model of the 32–plate–electrode phantom.

this figure yielded quite a different behavior than the 16–plate electrode phantom did. Without the applied optimized excitation patterns, the two targets could not be distinguished separately and the maximum peak of the target contrast ratio was as low as 2.4. Optimization increased target contrast ratio by a factor of 3, and the targets were perfectly separated with very low background noise. This definitely shows the benefit of using computer optimized boundary excitations.

It can be seen that under all cases examined, computerized optimization significantly, even dramatically, improved image quality. *All further results presented in this report will include computer optimization of boundary measurements along with the other methods identified in Section 7.4.2 unless specifically stated otherwise.*

7.4.4 Finite Element Schemes: Constant, Bilinear– and Biquadratic–Exponential

Images computed on 9×9 and 16×16 finite element mesh models of the 16–plate–electrode phantom are shown in Figure 7.33. The number of iterations for the coarse and fine mesh reconstructions were 50 and 70, respectively (no changes in results in the case was noted for further iterations in each case). The contour and the best contour plots are shown in Figures 7.34 and 7.35. The best contour plot for the constant conductivity model is not included in Figure 7.35 since it does not apply.

The relief plots shown in Figure 7.33 indicate that two targets can be identified both in their contrasts and locations by using all three finite element schemes in both fine and coarse mesh reconstructions. However, use of the contour plots shown in Figure 7.34 yield conductivities which are constant on straight line "characteristics" as seen in Figures 7.34(a), (b), (c) and (d). This is not a difficulty when rectangular shapes are imaged, but proves to be a difficulty with curved surfaces when the shapes become small. A better result

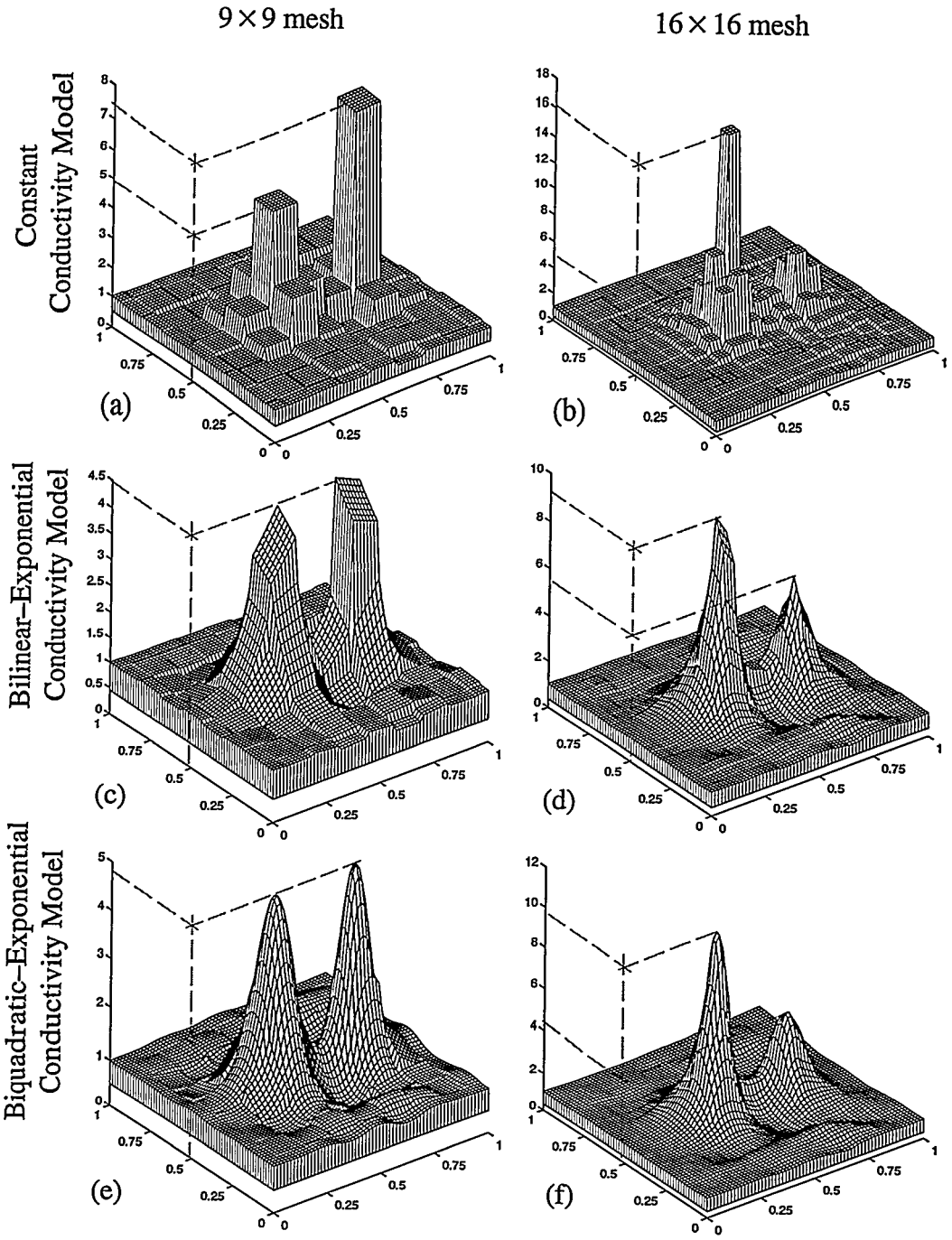

Figure 7.33 Relief plots for comparing reconstructions with different finite element schemes; (a), (b) constant: (c), (d) bilinear– and (e), (f) biquadratic–exponential schemes. The left and right columns show the 9×9 and 16×16 mesh computations carried out with both the computer optimized patterns and the PVC method applied.

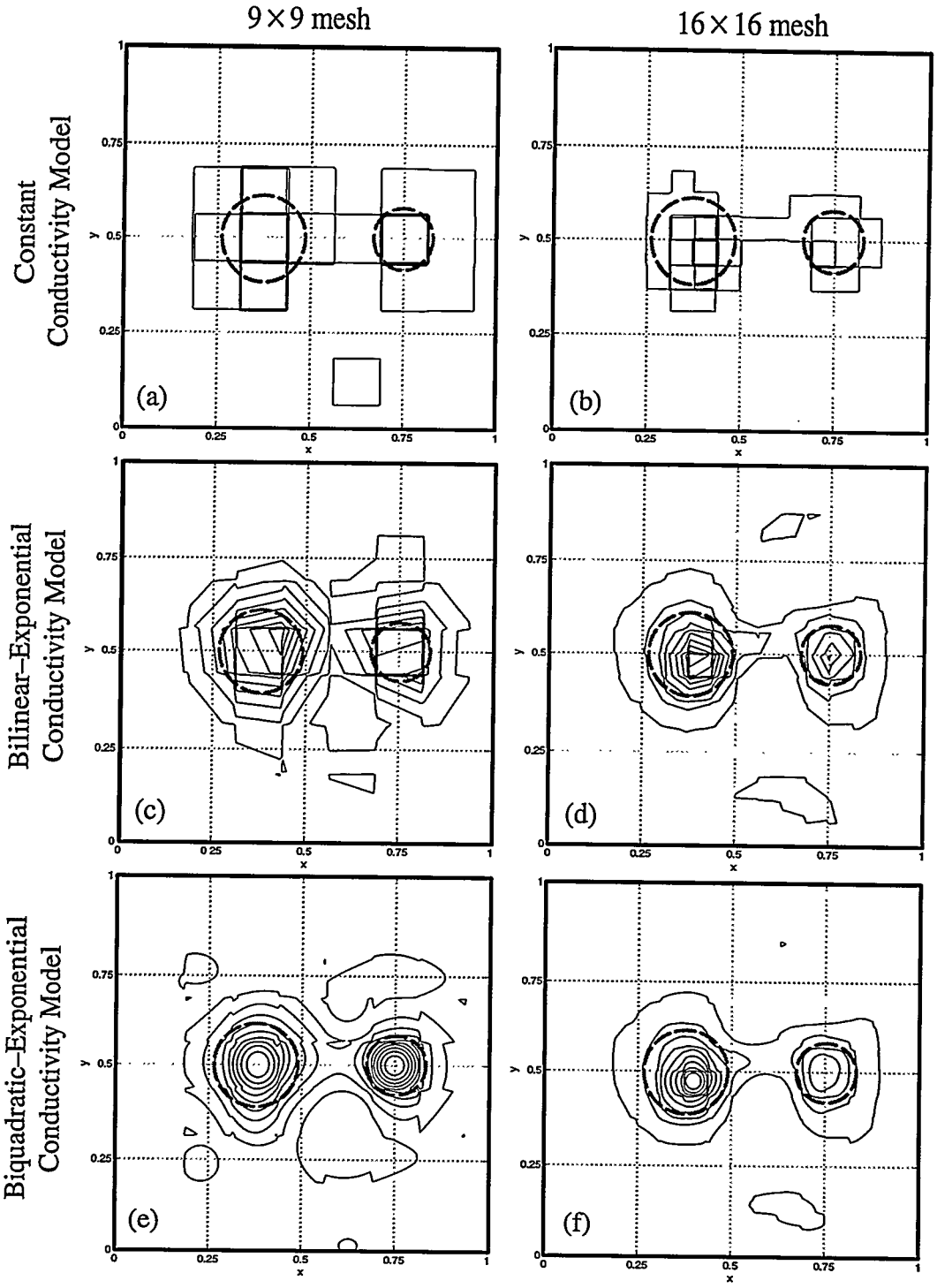

Figure 7.34 Contour plots of the relief plots in Figure 7.33 for comparing the reconstructions with different finite element schemes: (a), (b) constant; (c), (d) bilinear– and (e), (f) biquadratic–exponential schemes.

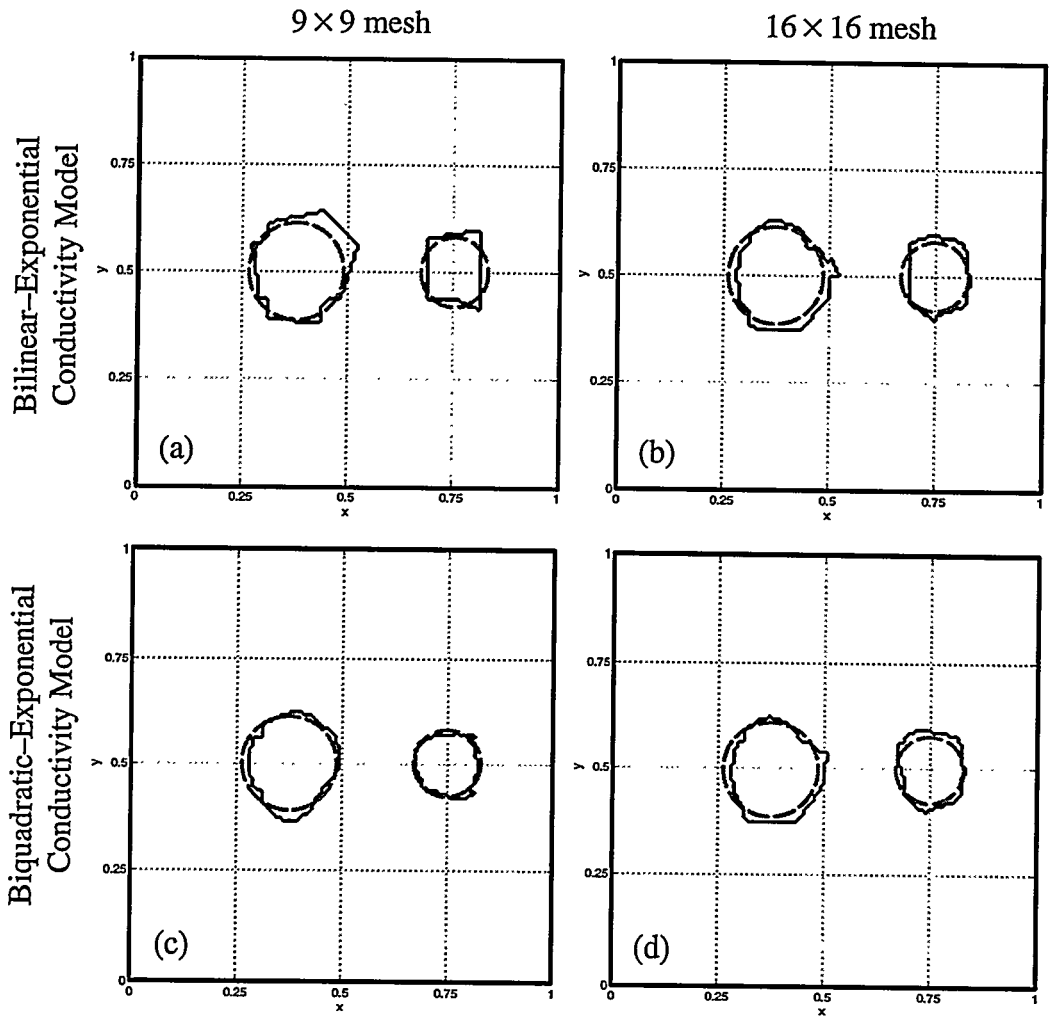

Figure 7.35 **Best contour plots obtained from the contour plots in Figure 7.34 for comparing the reconstructions with different finite element schemes: (a), (b) bilinear– and (c), (d) biquadratic–exponential schemes. The plot for the constant conductivity model is excluded since the best contour algorithm does not apply for this case.**

is obtained by allowing the conductivity field to take on exponentially biquadratic shapes as shown in Figures 7.34(e) and (f). These have the potential to simulate circular, elliptic, parabolic or hyperbolic surfaces which divide regions of significantly differing conductivity.

Results seen in Figures 7.35(c) and (d) appear to be better than those same data are evaluated using a bilinear–exponential conductivity model in Figures 7.35(a) and (b). However, as shown in the Figures 7.33(d) and (f), it is clearly seen that a 16×16 element model is required to obtain reasonable curvature and replication of the actual boundaries of two cylindrical targets.

7.4.5 Overall Comparisons Using the 16–Plate–Electrode Phantom

Finally, the relief plots seen in Figure 7.36 depicts a complete summary of experimental and numerical developments applied to the 16–plate–electrode phantom. The first row of relief plots demonstrates these effects of optimized patterns on 9×9 and 16×16 mesh models for rms voltage measurements of applied sinusoidal signals used in the Walsh excitations. The second through sixth rows show the same effects for the averaged peak measurements of applied square–pulse signals for measurement accuracy levels of r=2.0, 2.5, 3.0, 3.5 and 4.0, respectively. The contour plots and the best contour plots associated to these results respectively shown in Figures 7.37 and 7.38.

It is seen from these results that fine mesh reconstructions slightly increase the contrast levels of the targets. The contour plots for each of these cases show that background conductivity variations decrease and the target contours improve. Additional improvements in target contrast levels, target boundaries and background conductivity variations can be obtained by applying optimized excitation patterns and by increasing the measure-

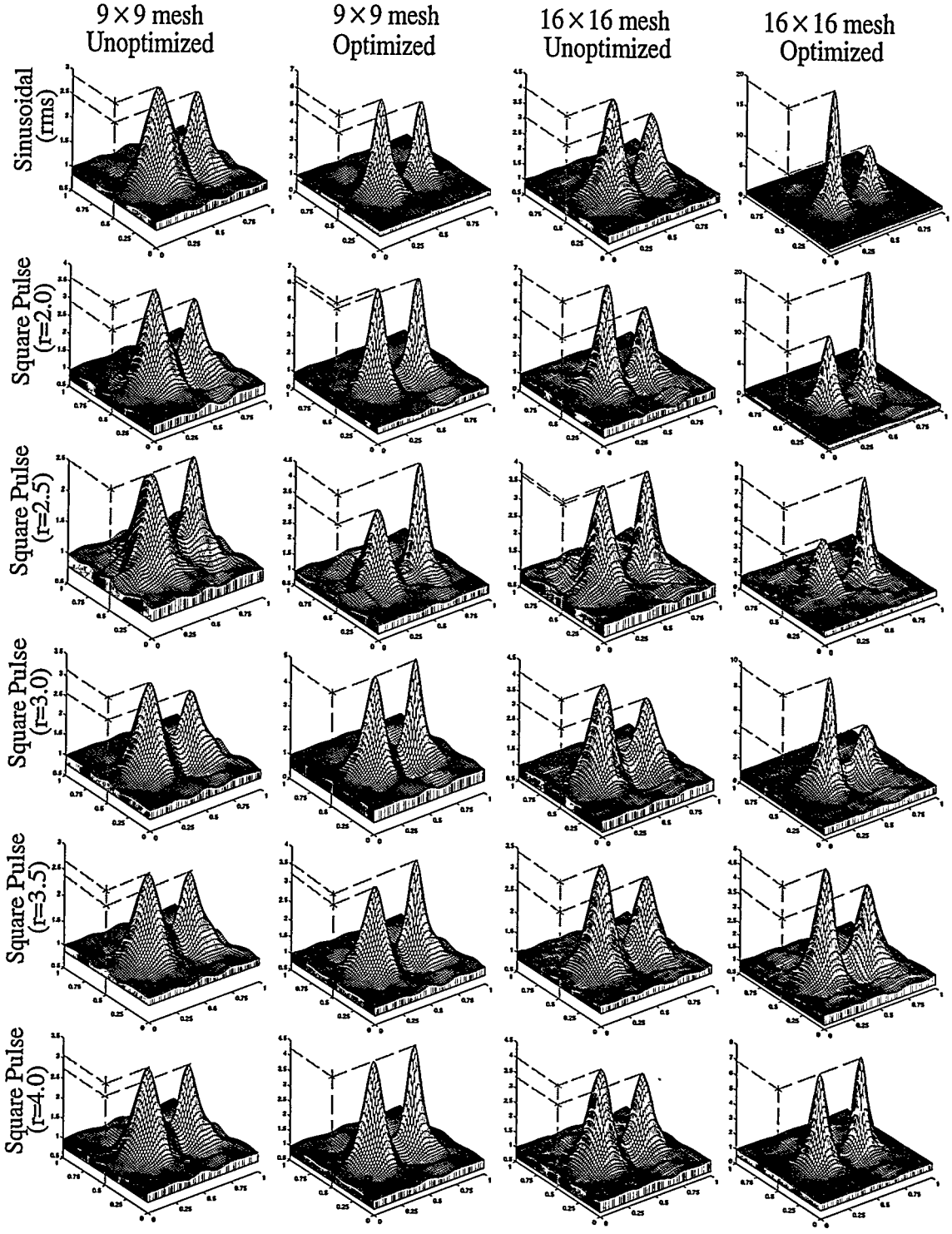

Figure 7.36 Relief plots for comparing the computations with unoptimized and optimized excitation patterns applied to a 9×9 and 16×16 mesh models of the 16–plate–electrode phantom with respect to the sinusoidal and the square pulse signals and varying measurement error.

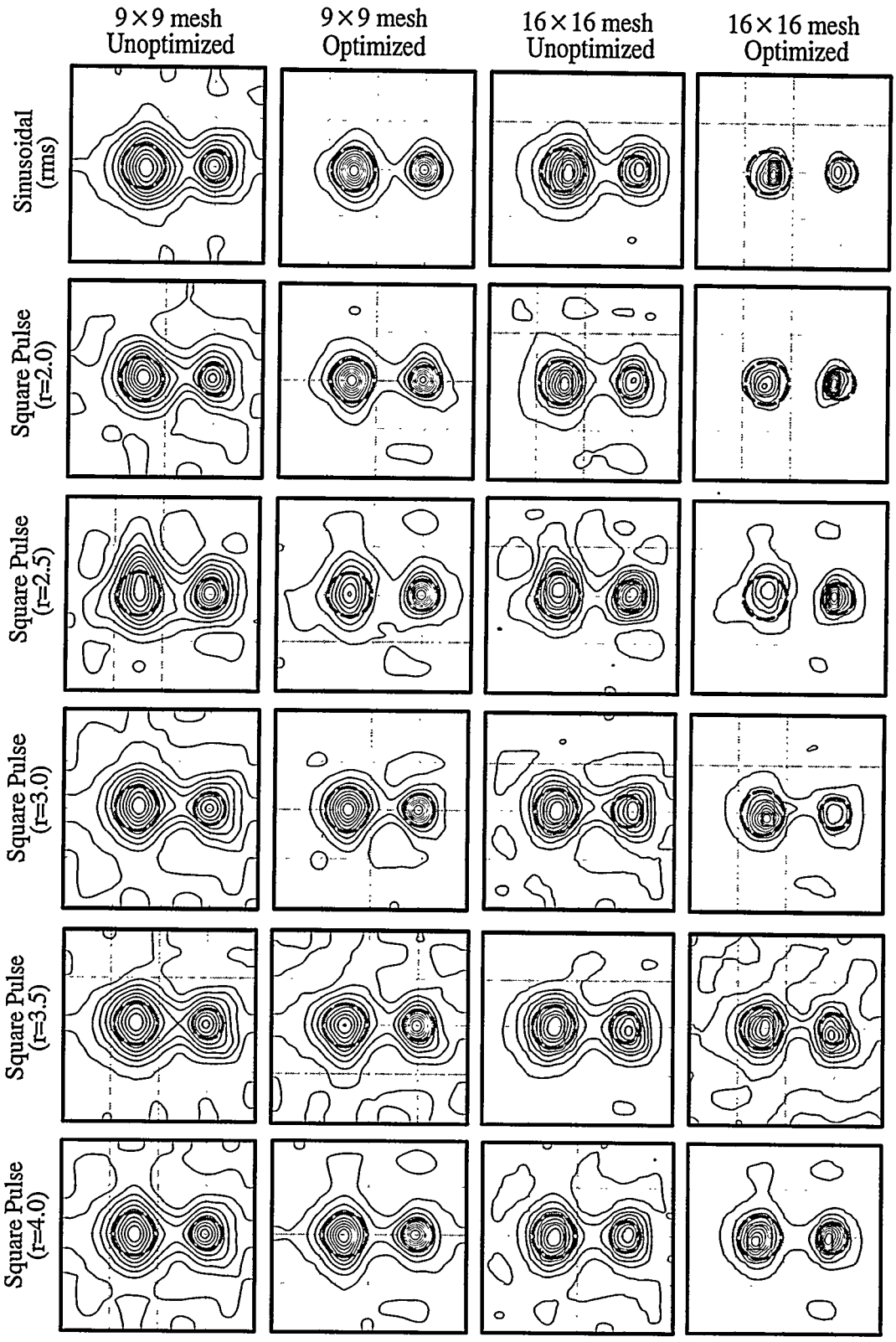

Figure 7.37 Contour plots of the relief plots in Figure 7.36.

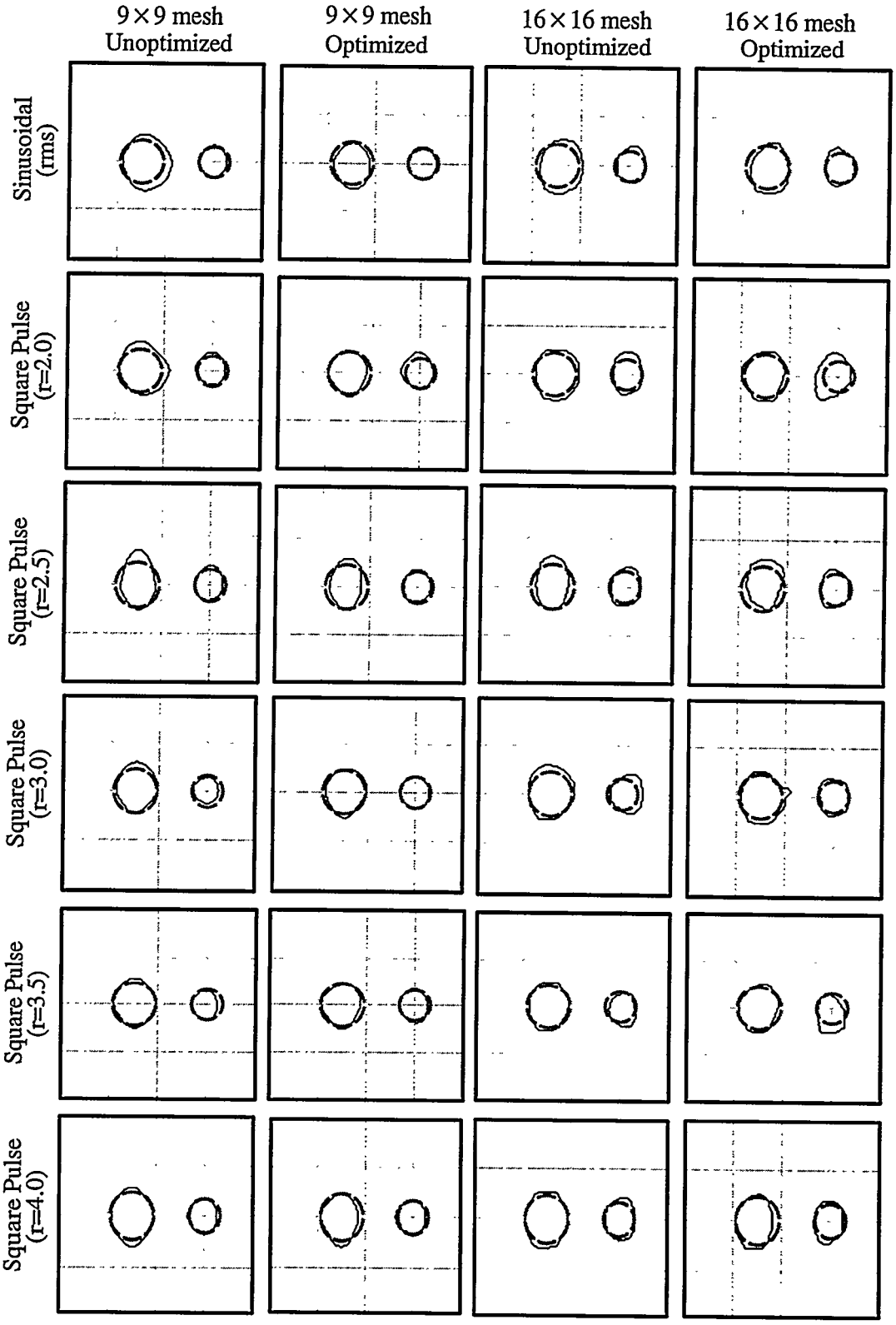

Figure 7.38 Best contour plots obtained from the contour plots in Figure 7.37.

ment accuracy. The best contour plots of 16 × 16 mesh, optimized case and accuracy level of r=3.0 are identical to the results of rms measurements.

7.5 Limits of Resolution

This section introduces experimental methods based on eigenvalue analysis which were applied to the two–dimensional 16–plate–electrode test phantom to provide the resolution limits of noisy measurements allowing different levels of measurement accuracy in the data acquisition system.

7.5.1 Review of Basic Concept

Isaacson, Newell and their Rensselaer coworkers [24], [55], [78], [150] developed analytical methods to determine the limits of resolution (which they termed distinguishability) for circular targets located centrally in a circular phantom excited with a current source. They suggested that two conductivities σ_1 and σ_2 could be resolved from each other in a system having a noise level of ε if the L^2 norm of the voltage difference vector for the two cases divided by the norm of the current vector was greater than this measurement error, ε. Their suggestion was extended to the system designed in this study showing that this condition becomes equivalent to examining the eigenvalues of the matrix formed by subtracting two conductance matrices: e.g., $\lambda_{target} - \lambda_{homog} > \Delta\lambda_{homog}$ where $\Delta\lambda_{homog}$ are the anticipated variations in the eigenvalues of the homogeneous case due to normal experimental variations. If the eigenvalues indicate that a target should be distinguishable, then inability to compute an image must be due to the manner in which the data were evaluated rather than in the data themselves.

7.5.2 Eigenvalues of Homogeneous Phantom

Consider a sequence of imaging data sets obtained for the homogeneous case. Ideally, if there were no measurement error, identical conductance matrices would be obtained for each set. In reality, however, there will be random errors in the measurements which lead to random fluctuations in computed conductance values for each element from set–to–set.

If the fluctuation matrix is denoted as $\delta \boldsymbol{G}$ representing the difference between any two homogeneous conductance matrices, then there will be a set of eigenvalues $\lambda(\delta \boldsymbol{G})$ which represent the limits of distinguishability for any target situation. That is, unless the target produces given eigenvalues which vary from the homogeneous fluctuation set by more than $\lambda(\delta \boldsymbol{G})$, no possibility of imaging the target exists and the information is said to be lost. If only part of the target case eigenvalue set does not exceed the homogeneous set by more than $\lambda(\delta \boldsymbol{G})$, some information is lost, and incomplete and/or inaccurate distinguishability of the target is obtained.

The effects of measurement error may be seen by examining eigenvalue decay plots for the 16 plate–electrode phantom for the three different measurement accuracy levels of $r = 2.0$, 3.0 and 4.0. To produce experimental data, a homogeneous phantom was filled with tap water and excited by the Walsh voltage patterns, and then 10 sets of data were repeatedly acquired. The conductivity of the tap water is measured as 190 μS/cm (where S is Siemens defined as $\mathrm{S} \equiv \Omega^{-1}$) by a 1 μS/cm–resolution, OMEGA CDH–70 hand–held conductivity meter which is capable of making measurements in 0–20.0 mS/cm conductivity range. To produce a sufficiently large population size, these 10 independent data sets were first paired, and then $(10 \times 9)/2 = 45$ independent difference conductance matrices, $\delta \boldsymbol{G}$, were computed. Finally, eigenvalue decay plots were produced from the com-

puted conductance fluctuating matrices yielding $\lambda_j(\delta G_i)$ (where $i = 1, ..., 45$ and $j = 1, ..., 15$). Recall that the computed conductance matrices, and hence the eigenvalues, were normalized relative to the phantom size and the water conductivity used inside the phantom by multiplying by a factor of $1/(\ell_e \sigma_{water})$, where ℓ_e is the submerged electrode length (the water height inside the phantom in these experiments was $\ell_e = 0.3$ m).

Figure 7.39 shows two things. First, Figure 7.39(a) shows the variation in the eigenvalues of the averaged homogeneous conductance matrix itself. If differences are taken between any randomly–selected conductance matrix and the average of all conductance matrices, the resulting eigenvalues represent the distinguishability limits relative to noise in the homogeneous system. These averaged variations to a confidence level of 99% are shown in Figure 7.39 and are:

$$r = 2.0,\ \delta\lambda \cong 0.0488,\ \frac{\delta\lambda}{\lambda_{\max}} \cong 1.49\%;$$

$$r = 3.0,\ \delta\lambda \cong 0.00663,\ \frac{\delta\lambda}{\lambda_{\max}} \cong 0.242\% \text{ (min. level of acceptable accuracy)};$$

$$r = 4.0,\ \delta\lambda \cong 0.00533,\ \frac{\delta\lambda}{\lambda_{\max}} \cong 0.194\%.$$

Variations in the relative eigenvalue differences are approximately $\pm 10\%$ of the differences themselves. Thus, for $r = 3.0$, the eigenvalue variations can be expected to be between 0.218% and 0.266%. Similarly, for the case of $r = 4.0$, the eigenvalue variations can be expected to be between 0.175% and 0.213%. Based on the Isaacson criterion of examining the largest eigenvalue, the ultimate resolution of the system should therefore be between one part in 375 (worst case for $r = 3.0$ or 1/0.00266) and one part in 570 (best case for $r = 4.0$ or 1/0.00175) at a confidence level of 99%.

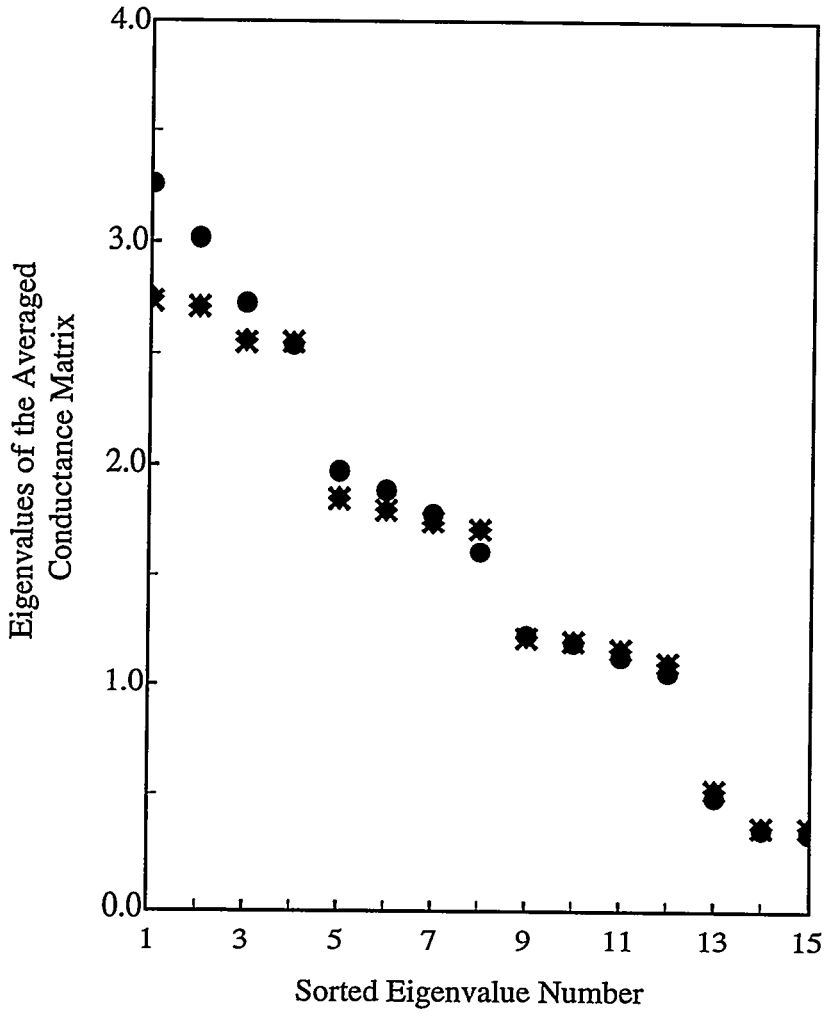

(a)

Figure 7.39 (continued overleaf)

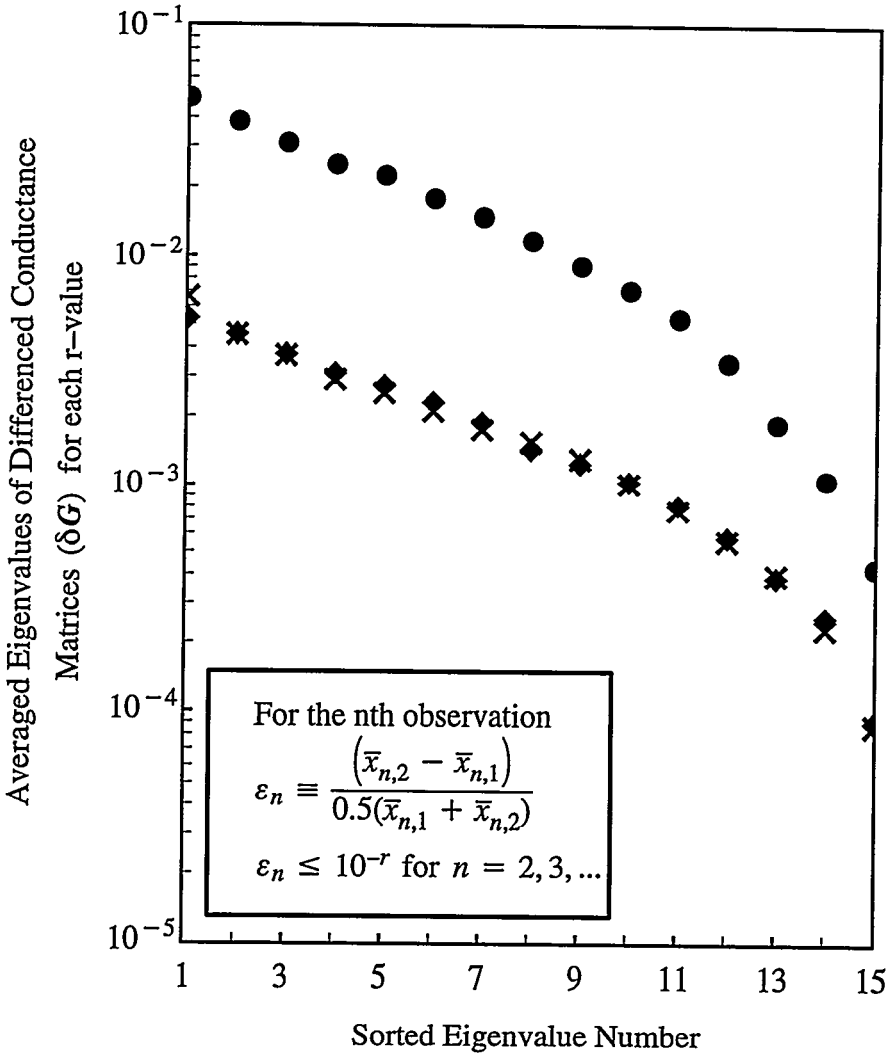

(b)

Figure 7.39 Eigenvalues for the homogeneous case: (a) eigenvalues of the averaged and normalized conductance matrices; (b) averages of eigenvalues of 45 differenced matrices formed by differencing individual conductance matrices from 10 sets of data. ● r=2.0; × r=3.0; ◆ r=4.0.

The accuracy to which data are acquired can have a significant effect on the resolution of a given target. Figure 7.40 shows that the distinguishability (maximum eigenvalue of the fluctuating difference of conducting matrix, $\max\lambda(\delta G)$, improves by approximately one order of magnitude as the data acquisition exponent r increases from 2.0 to 3.0. Further increase has little effect but to increase the data acquisition time (Figure 7.23). It was this result, when combined with the previously described results, which justified the use of $r = 3.0$ in the majority of other data.

7.5.3 Effect of Model on Minimum Detectable Target Size

Sensitivity eigenvalues were obtained for the matrices created by comparing the homogeneous case and the nonhomogeneous case. The latter was created by placing cylindrical insulator targets of different diameters at the center of the phantom where the lowest sensitivity is expected. Five distinct target diameters were selected as $D_t = 6.0, 10.0, 25.0,$ 45.0, and 88.0 mm. Throughout the experiments, the data acquisition error tolerance was equal or less than 1:1000 (i.e., $\varepsilon \leq 10^{-r}$, $r = 3.0$) and the water conductivity was 190 μS/cm.

Figure 7.41 shows the normalized eigenvalues of the distinguishability matrix of the 16 plate–electrode two–dimensional phantom. The results indicate that all the selected target sizes are distinguishable from the homogeneous conductivity background. However, the eigenvalues corresponding to the target diameters 6.0 mm and 10.0 mm are very close to each other. Thus, one could conclude that even if these two targets are distinguishable from the background, their sizes may not be clearly visible in the reconstructions. Based on the results, it can be said that for a given measurement error tolerance of 1:1000 the minimum detectable size is at least as small as 6.0 mm. This gives a demonstrated resolution of 6:200 or slightly above 3% linear resolution for the given measurement accuracy.

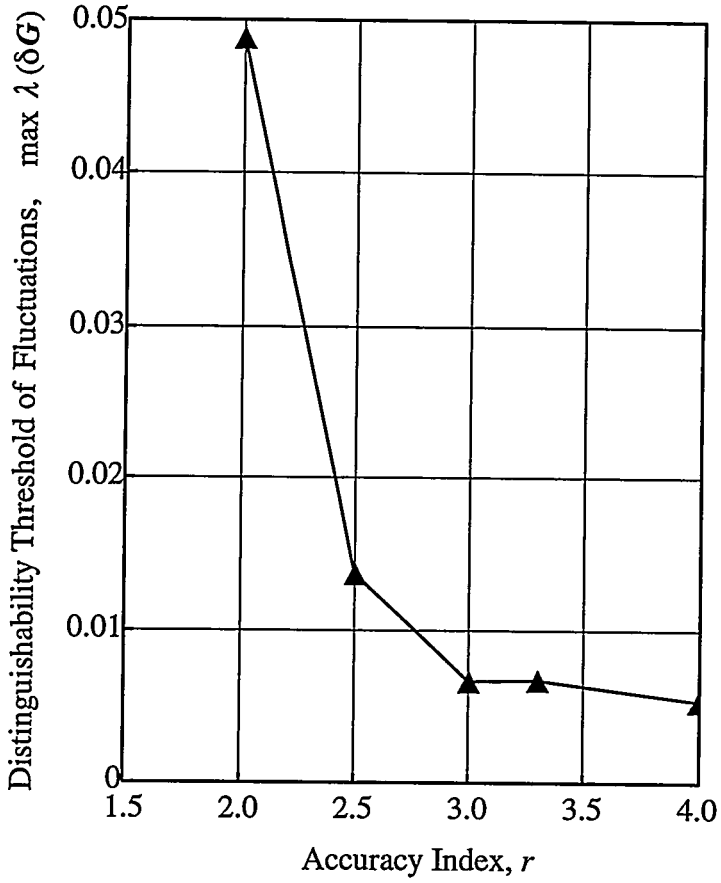

Figure 7.40 Effect of choice of measurement accuracy on the distinguishability threshold for the 16 plate–electrode phantom. Data represent the range of variation in the maximum eigenvalue of the conductivity matrix for the homogeneous case.

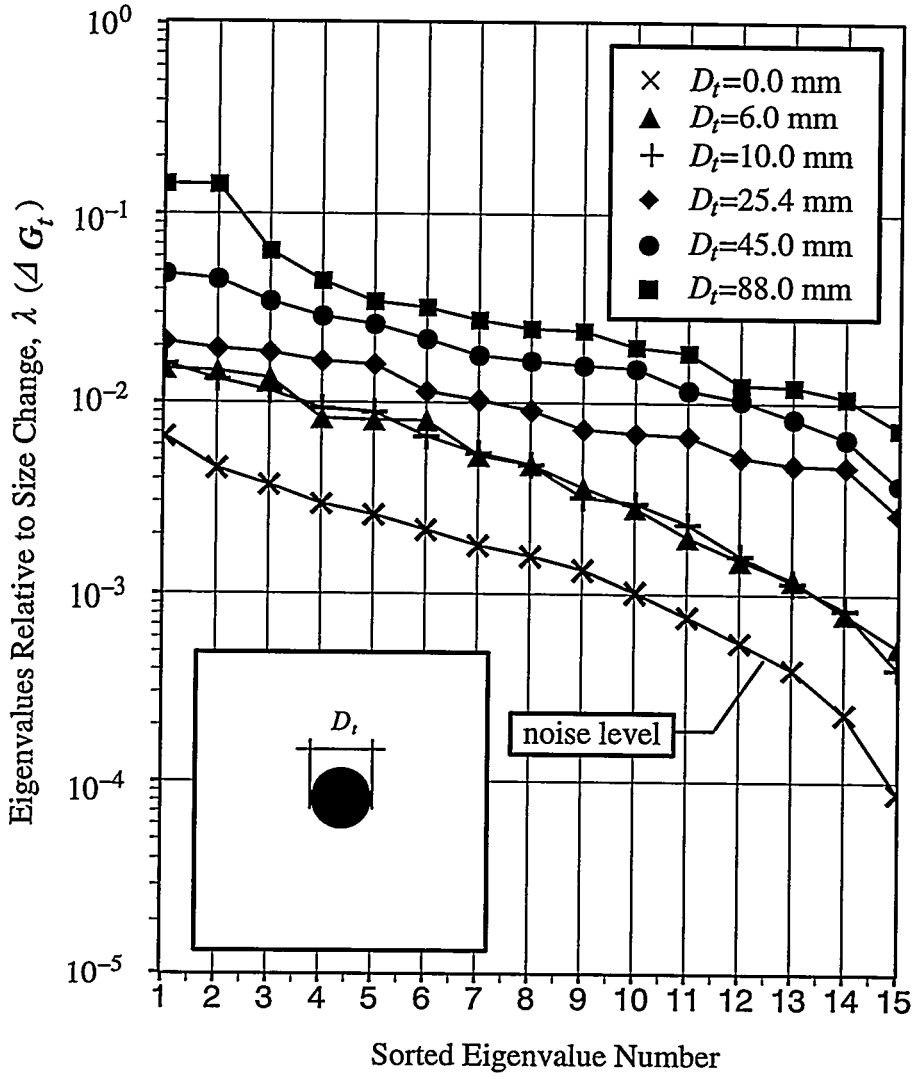

Figure 7.41 Eigenvalue decay plots of the sensitivity matrix for different sized cylindrical insulator targets placed at the center of the 16–plate–electrode phantom.

The limit of resolution between a small target and the homogeneous medium is estimated by cross plotting the distinguishability as a function of target diameter as shown in Figure 7.42(a). Noise bands may be placed on both the homogeneous distinguishability and on any target data. If these noise bands do not intersect, than the two may be resolved. The limit of resolution at the 99% confidence level is when the two 99% noise bands just touch. This situation is shown in Figure 7.42(b) for the case of $r = 3$ where only the range of 10–mm diameter and smaller targets of Figure 7.42(a) has been shown. From this comparison, a diameter in the vicinity of 0.7 mm should be resolvable within a 99% confidence. This corresponds to a linear resolution of 0.7/200 or 1/286 in substantive agreement with the previously stated resolution.

The reason for the lack of discrimination for small targets is that as the target gets smaller, not only does the contrast between the homogeneous background and the target diminishes, but, as discussed previously in Section 7.2, the computed target image area spreads out over the phantom. This can be seen by examining the relative resistivity relief plots in Figure 7.43 for 6, 10, 25.4, 45, and 88–mm diameter targets respectively obtained with a 9×9 block mesh model. The contrast ratio for the largest target size is near 90:1 while that for the smallest target size is only in the range of approximately 1.3:1. Figure 7.44 shows the results of duplicating the central–target computations using a 16×16 mesh and may be directly compared with Figure 7.43. Discrimination and contrast level improves in all cases, the contrast in the 88–mm circular centered target increasing to approximately 270 times the homogeneous values.

7.5.4 Effect of Model on Successively Separating Two Targets

Based on the size test explained in Section 7.5.3, if reasonably large targets are used, one can expect that measurements from these two targets can provide reasonably high

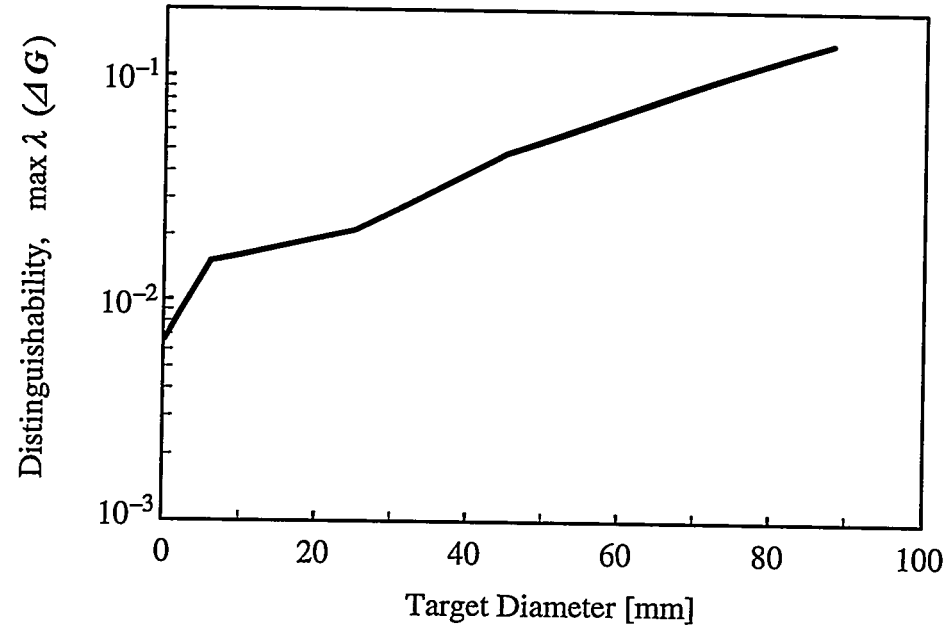

(a)

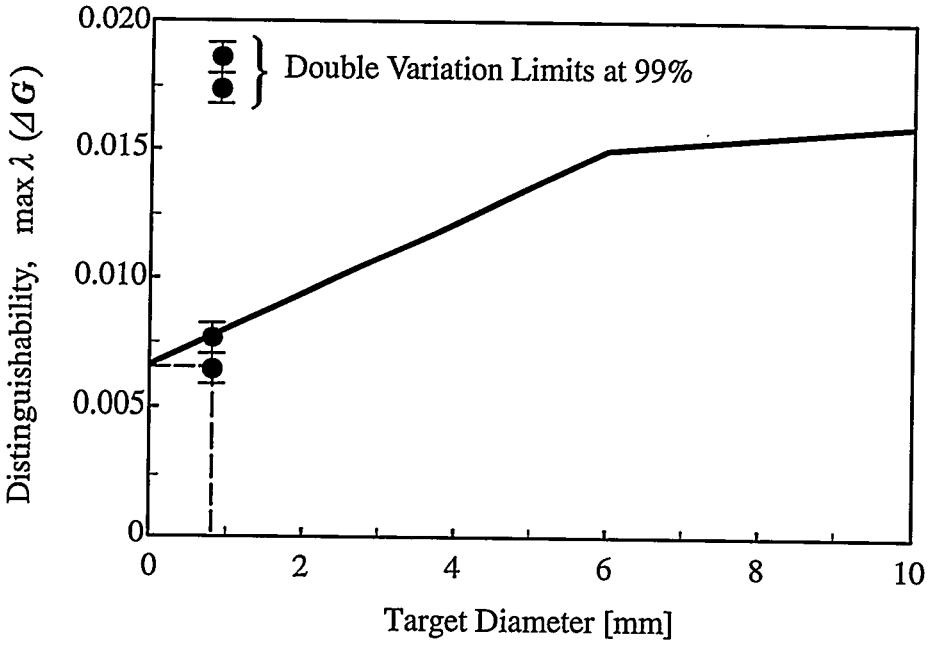

(b)

Figure 7.42 Distinguishability for central–target tests: (a) Figure 7.41 cross plotted as a function of target diameter; (b) region of small diameter distinguishability taken from (a) showing the expected minimum size for a distinguishable centrally–located cylindrical target.

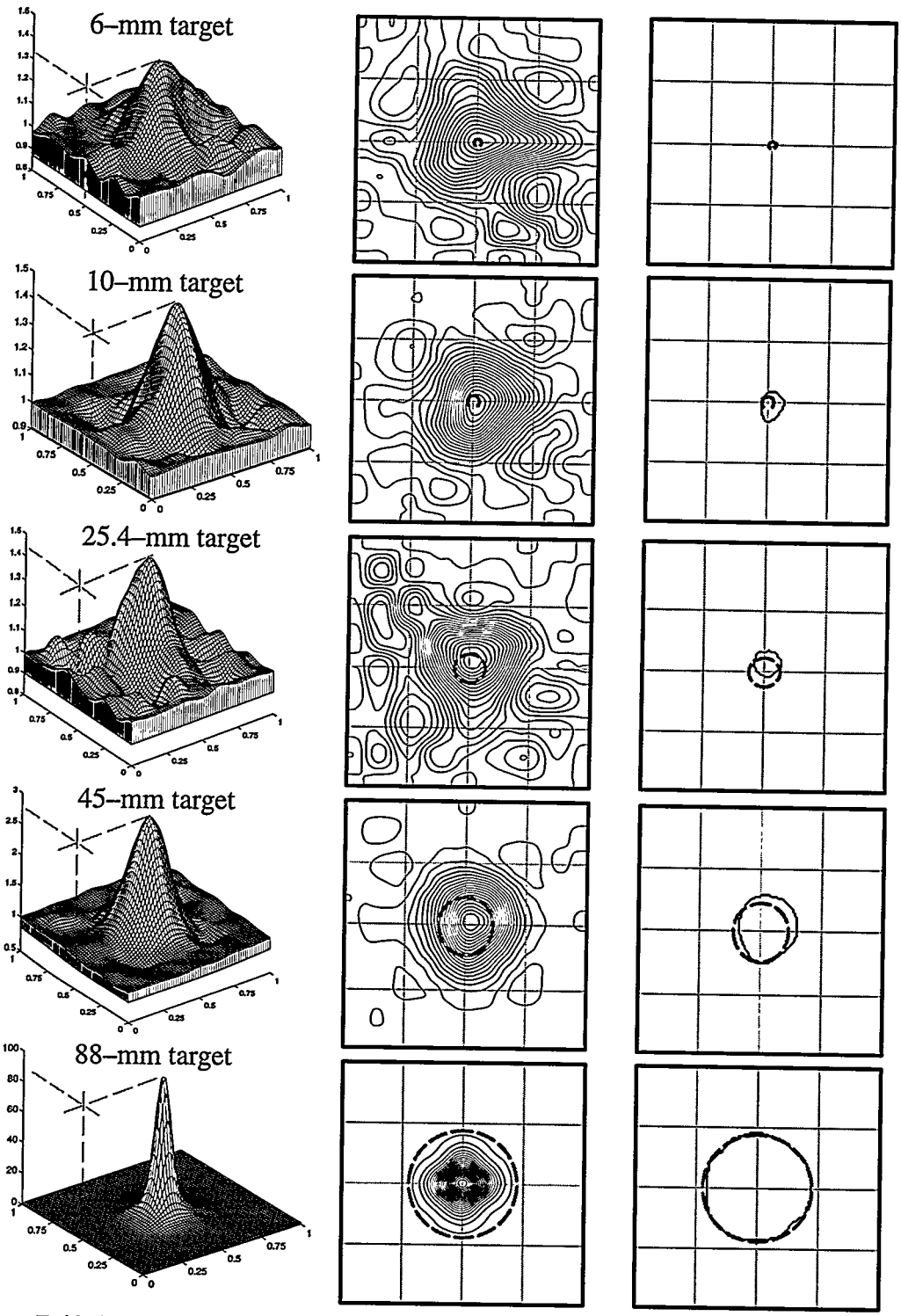

Figure 7.43 Relief, contour and best contour relative resistivity plots for distinguishability tests on centrally–located circular targets. Data obtained in the two–dimensional, 16–plate–electrode phantom and calculated using boundary optimization on a 9×9 mesh.

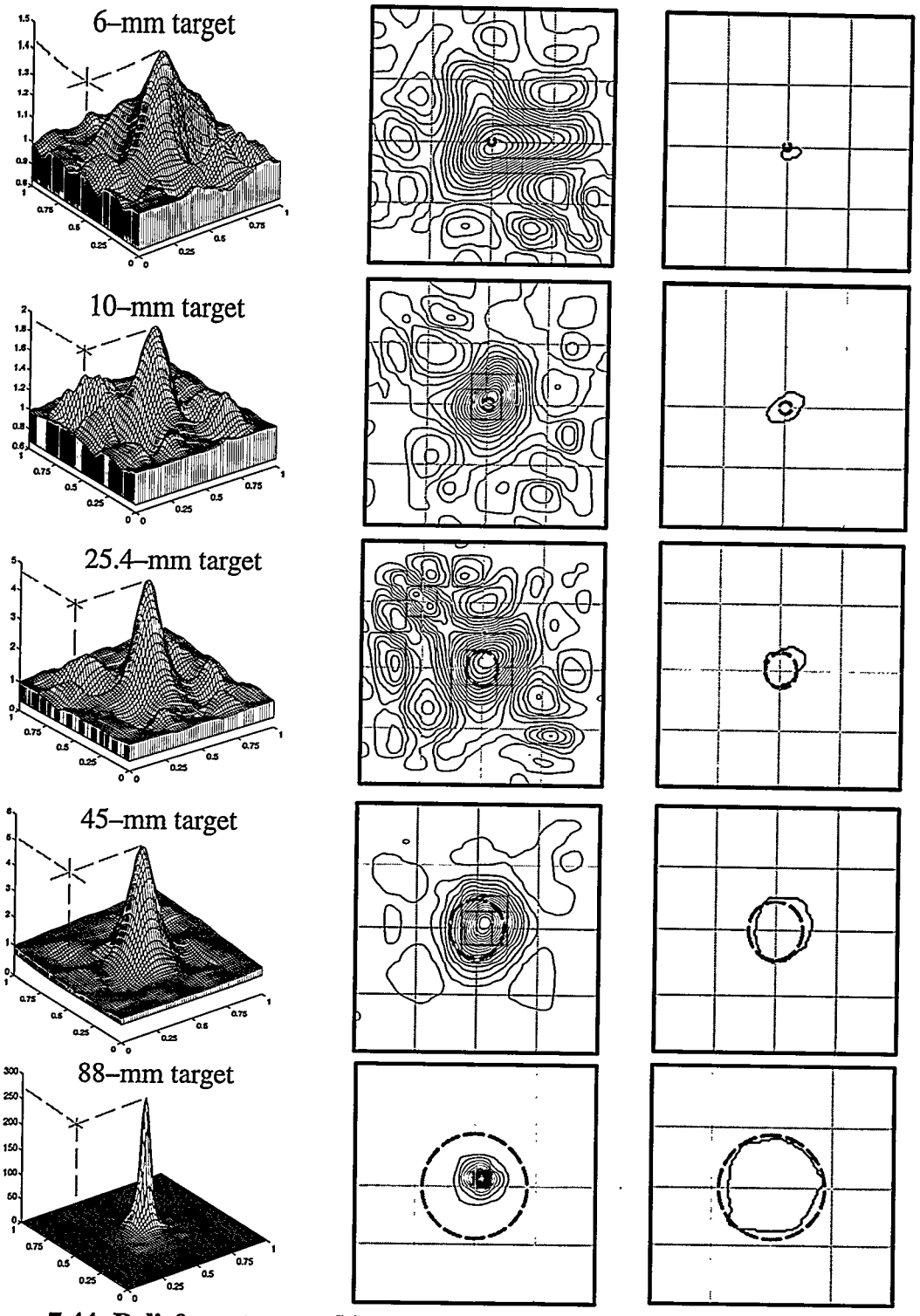

Figure 7.44 Relief, contour and best contour relative resistivity plots for distinguishability tests on centrally–located circular targets. Data obtained in the two–dimensional, 16–plate–electrode phantom and calculated using boundary optimization on a 16×16 mesh.

distinguishability to correctly locate the targets inside the phantom. However, the reconstructed results from these data may result in merged images when two targets are placed close to each other. If, for example, two cylindrical insulator targets are successively separated either in the longitudinal or in the diagonal direction inside the phantom, each case having a different separation distance between two targets yields eigenvalues of the distinguishability matrix relative to the homogeneous. However, this eigenvalue set only refers to differences from homogeneous and does not show anything relative to the change in separation itself.

There is another method which can be considered to determine the distinguishability of the targets when they are separated by moving them from one position to another. Let the distance between two targets be d_t. For each position, let the distances be $d_{t,0}$, $d_{t,1}$, $d_{t,2}$ and so on. Considering the first position as a reference position (when two targets are attached to each other), let the distinguishability matrix corresponding to conductivity change due to the position change from k to $k + 1$ be $\Delta \boldsymbol{G}_k$. The eigenvalues of $\Delta \boldsymbol{G}_k$ is $\lambda(\Delta \boldsymbol{G}_k)$, and is termed the separation sensitivity plot.

Two sets of experiments were completed, one for longitudinal separation and one for diagonal separation. In the first case, two 32.8–mm diameter cylindrical insulator targets were placed at the center of the phantom filled with 190 μS/cm tap water. The distance between two targets was successively increased in 25.4–mm intervals, as $d_t = 0.0$, 25.4, 50.8, 76.2, 101.6 and 127.0 mm, in the horizontal direction. The actual position of the targets for each separation distance is shown in Figure 7.45

Figure 7.46 shows the differential distinguishability results for two 32.8–mm–diameter targets displaced in increments of 25.4 mm. This represents an extension of Isaacson's concept for multiple, off–center targets. Variations for the touching case virtually

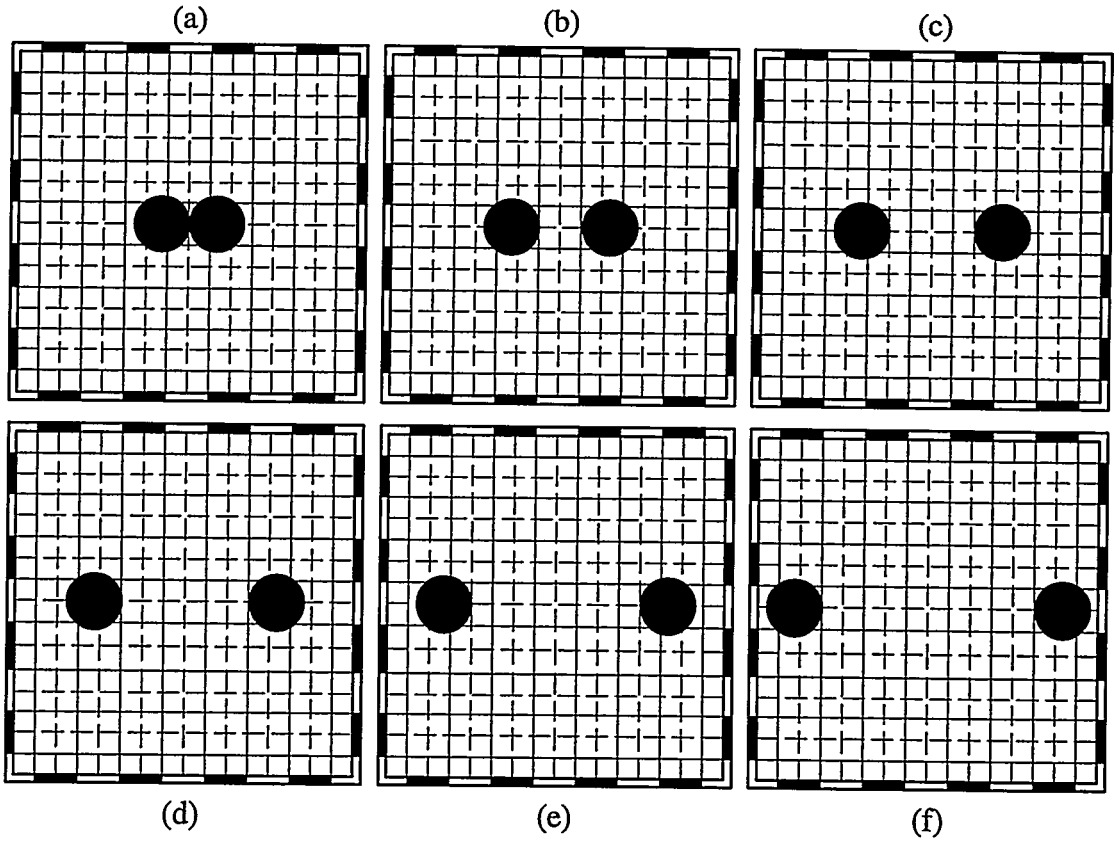

Figure 7.45 Actual locations of two 32.8–mm–diameter cylindrical insulator targets successively separated by 25.4–mm intervals along the longitudinal direction in the 16–plate–electrode phantom: separation distances are (a) 0.0–mm; (b) 25.4–mm; (c) 50.8–mm; (d) 76.2–mm; (e) 101.6–mm; (f) 127–mm.

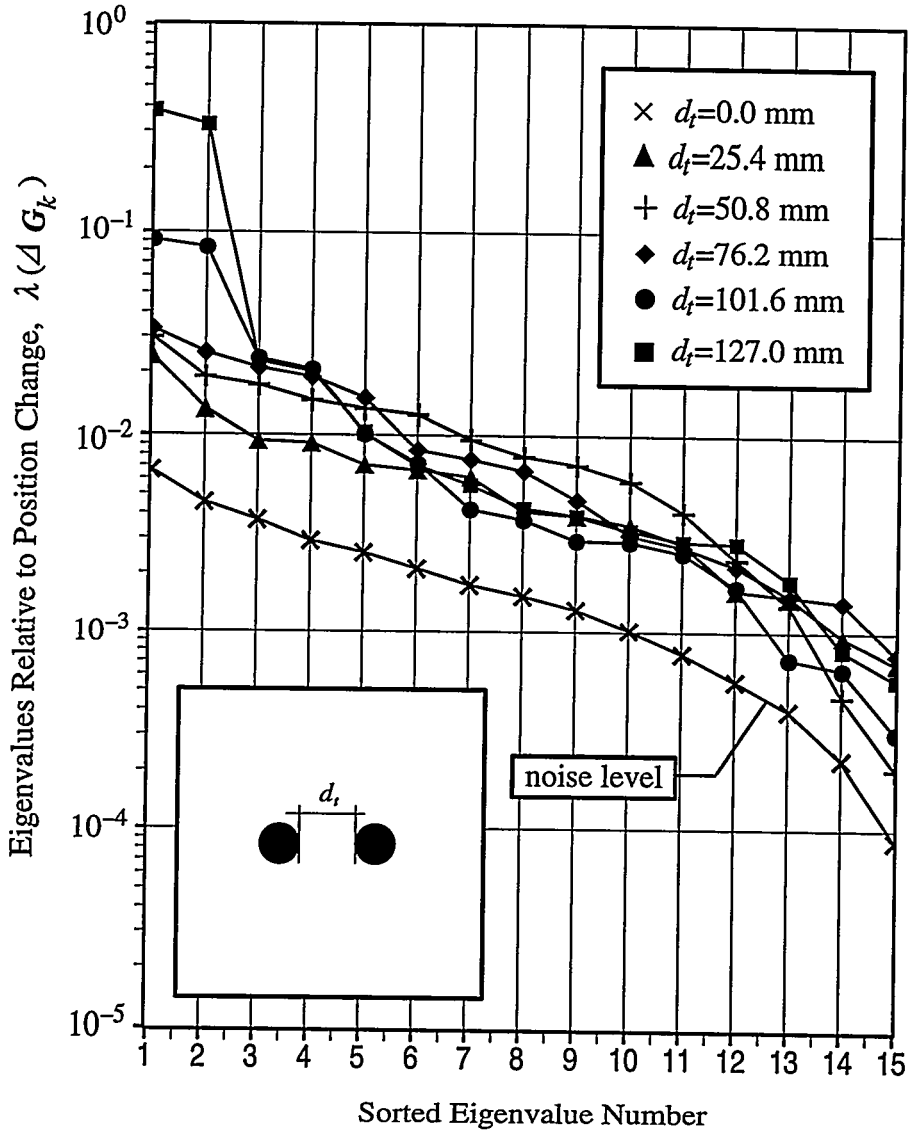

Figure 7.46 Eigenvalue decay plots of two cylindrical targets successively separated in the longitudinal–direction (lower left to upper right) inside the 16–plate–electrode phantom. The normalized eigenvalues are relative to a position change from k to k+1.

duplicate the eigenvalue variation measured in the homogeneous case and represents the noise level similar to the results shown in Figure 7.41. Figure 7.46 results indicate that separation at the one–diameter level should be able to distinguished. However, when the relief plot of the image computed on a 9×9 mesh and shown in Figure 7.47 is examined it is seen that the images at one–diameter separation are still merged. Note also that the best contour plot (9×9 mesh) for the case where the targets are touching (Figure 7.48) indicates that the target appears to be oblong horizontally. Computing the same results using a 16×16 mesh makes the targets clearly separated as seen in the relief and contour plots in Figure 7.49. The best contour algorithm which was also applied to these situations yields results as seen in Figure 7.50. From the eigenvalue decay plots shown in Figure 7.46 the data is sensitive to at least longitudinal separation of 25.4 mm and this can be depicted by using a 16×16 mesh model.

In the diagonal separation case, the same two 32.8–mm–diameter cylindrical insulator targets were first placed at the center of the phantom filled with the tap water of 190 μS/cm. The distance between two targets was successively increased in 35.9–mm intervals, as $d_t = 0.0, 35.9, 71.8, 107.8, 143.7$ and 179.6 mm along the diagonal direction (lower left to upper right). The actual positions of the targets for each separation distance is shown in Figure 7.51

Results in this case are similar to the previous case. Figure 7.52 shows the differential eigenvalue variations indicating that the separation of targets by 35.9 mm should be distinguishable. The separation, however, does not show up in the relief plots when computed on a 9×9 mesh as can be seen in Figure 7.53. Again the two targets when touching appear as an oblong solid and 35.9 mm separation of two targets could not be depicted as seen in Figure 7.54. Improvement may be obtained by using a 16×16 mesh as seen in

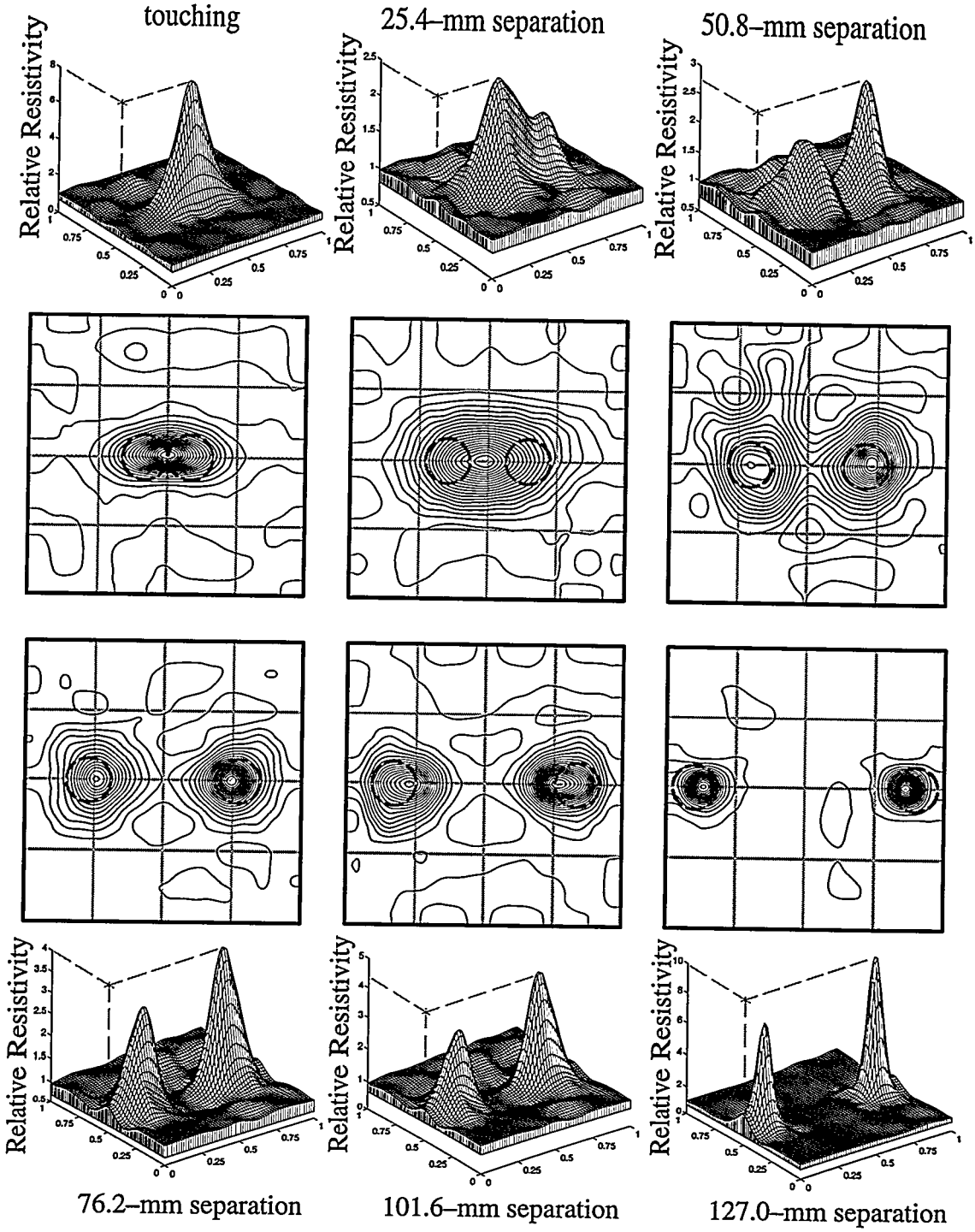

Figure 7.47 Relief plots of the normalized impedance for two 32.8–mm diameter targets separated symmetrically by various distances perpendicular to the phantom boundary (Figure 7.45). Data obtained in the 16–plate–electrode phantom with water conductivity of 190 μS/cm and reduced using a 9 × 9 mesh model.

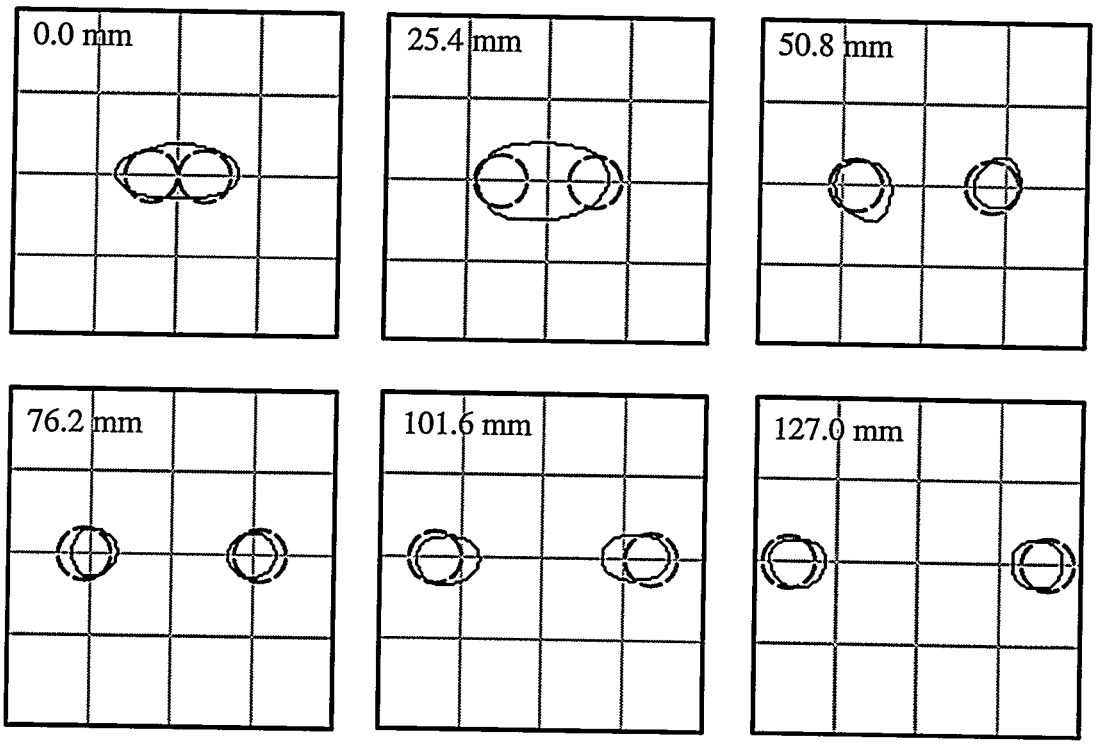

Figure 7.48 Results of the best contour algorithm applied to the horizontal separation distinguishability test results shown in Figure 7.47.

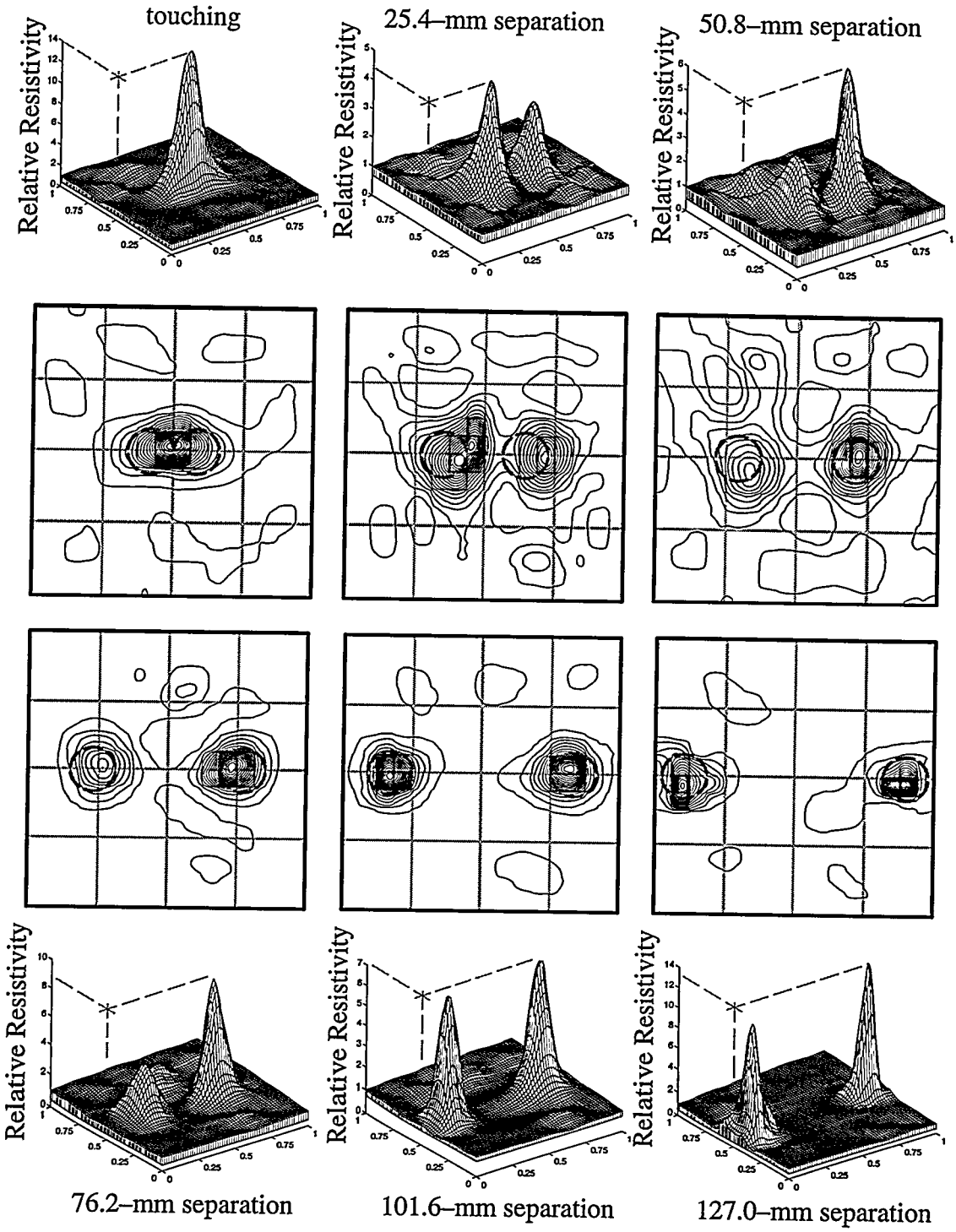

Figure 7.49 Relief and contour plots of relative resistivity for separability test as shown in Figure 7.45. Data calculated using boundary optimization on a 16 × 16 mesh.

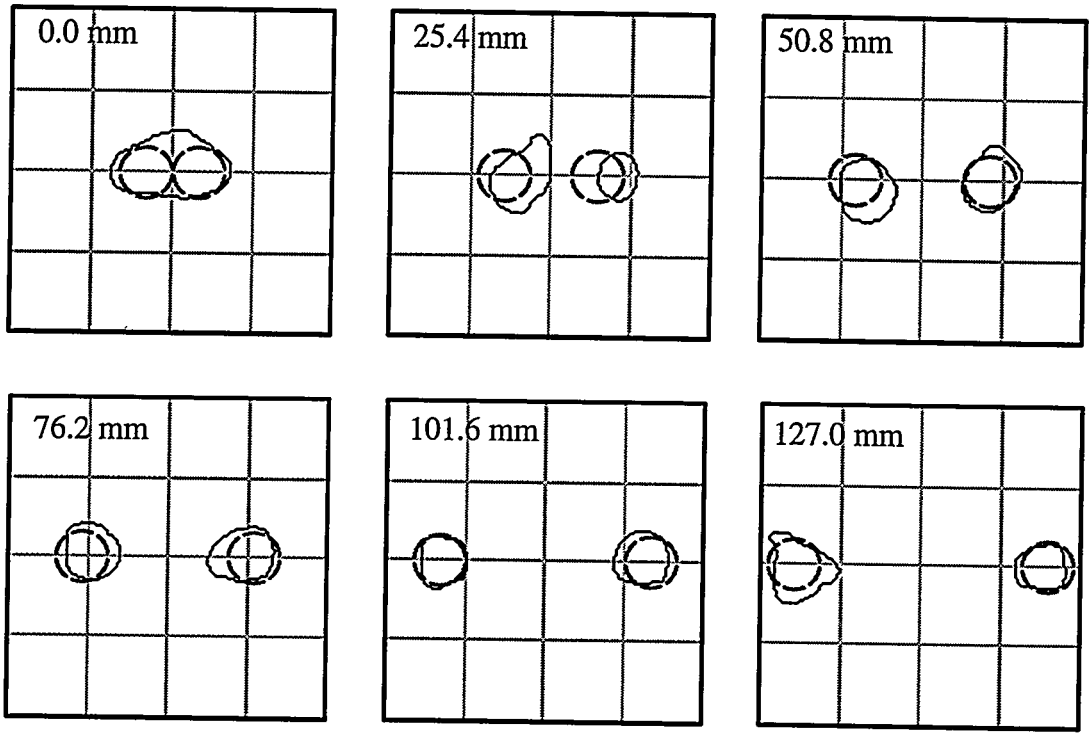

Figure 7.50 Results of the best contour algorithm applied to the horizontal separation distinguishability test results shown in Figure 7.49: 16×16 mesh.

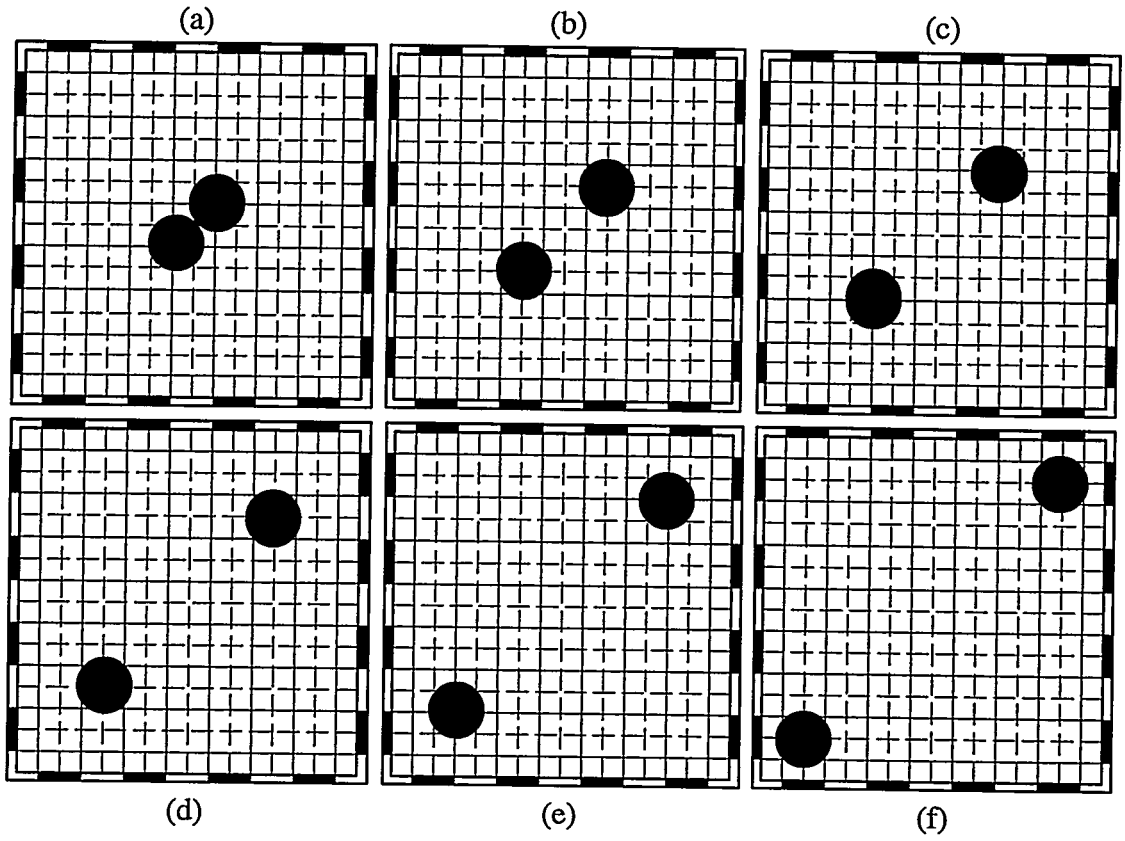

Figure 7.51 Actual locations of two 32.8–mm–diameter cylindrical insulator targets successively separated by 35.9–mm intervals along the diagonal direction in the 16–plate–electrode phantom: separation distances are (a) 0.0–mm; (b) 35.9–mm; (c) 71.8–mm; (d) 107.8–mm; (e) 143.7–mm; (f) 179.6–mm.

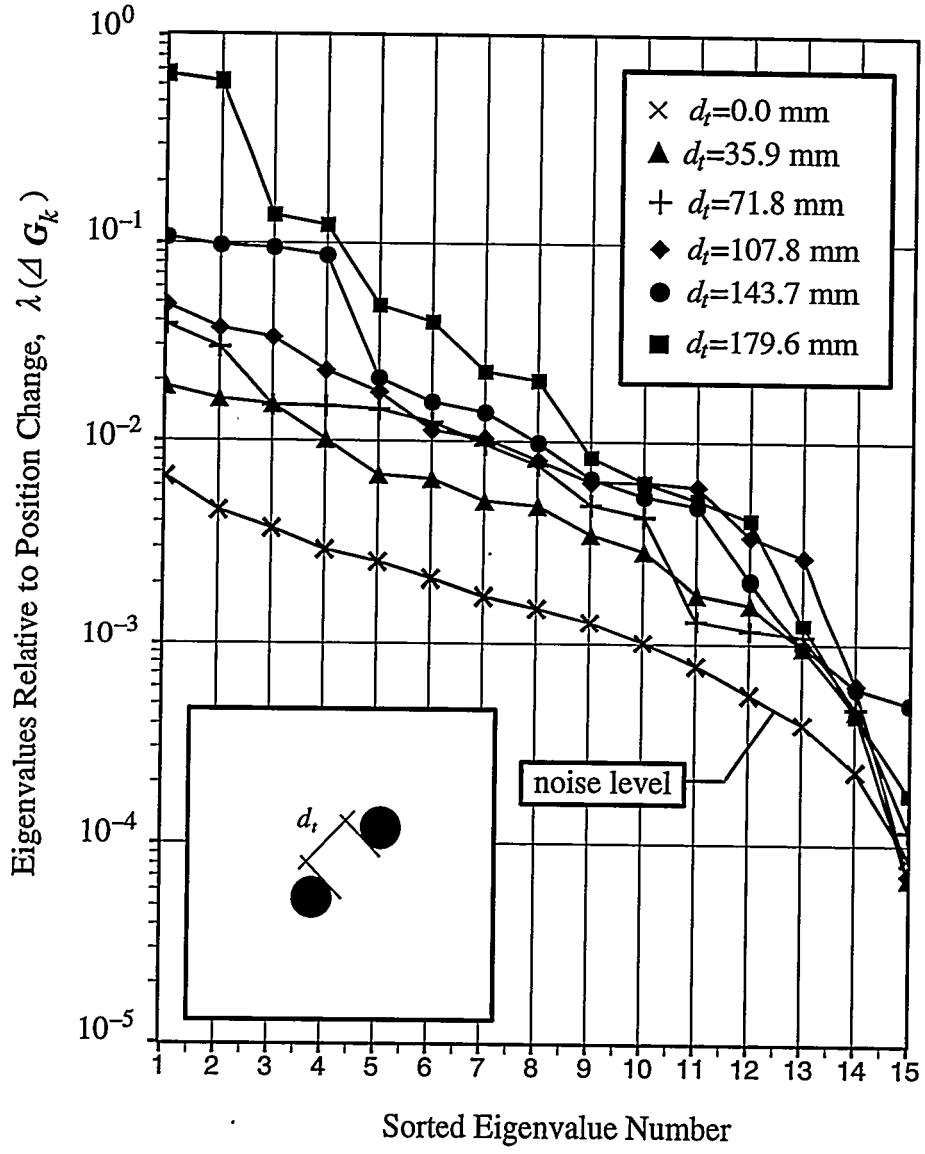

Figure 7.52 Eigenvalue decay plots of two cylindrical targets successively separated along the diagonal direction (lower left to upper right corner) inside the 16–plate–electrode phantom. The normalized eigenvalues are relative to a position change from k to k+1.

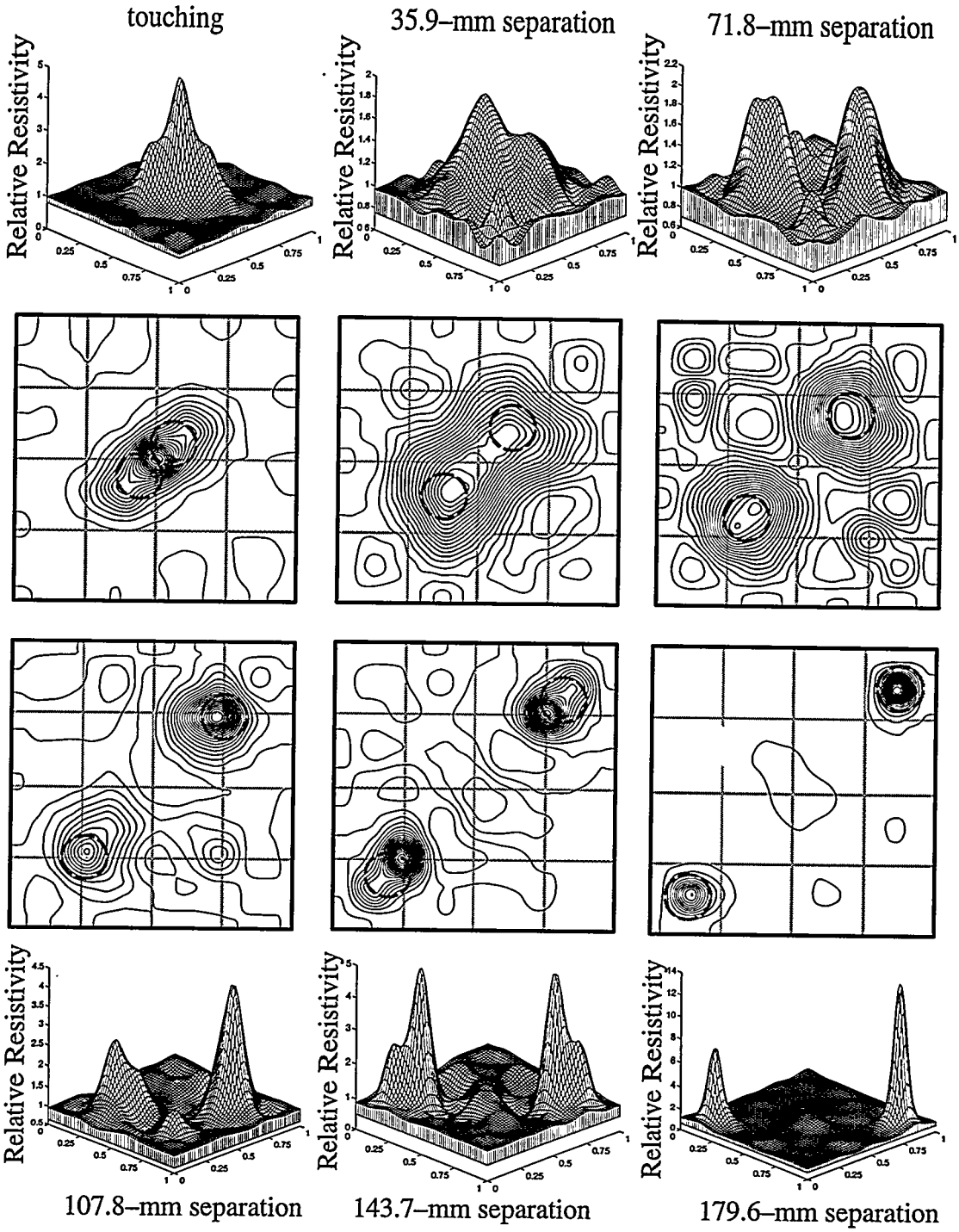

Figure 7.53 Relief plots of the normalized impedance for two 32.8–mm diameter targets separated symmetrically by various distances along the diagonal (Figure 7.51). Data obtained in the 16–plate–electrode phantom with water conductivity of 190 μS/cm and reduced using a 9×9 mesh model.

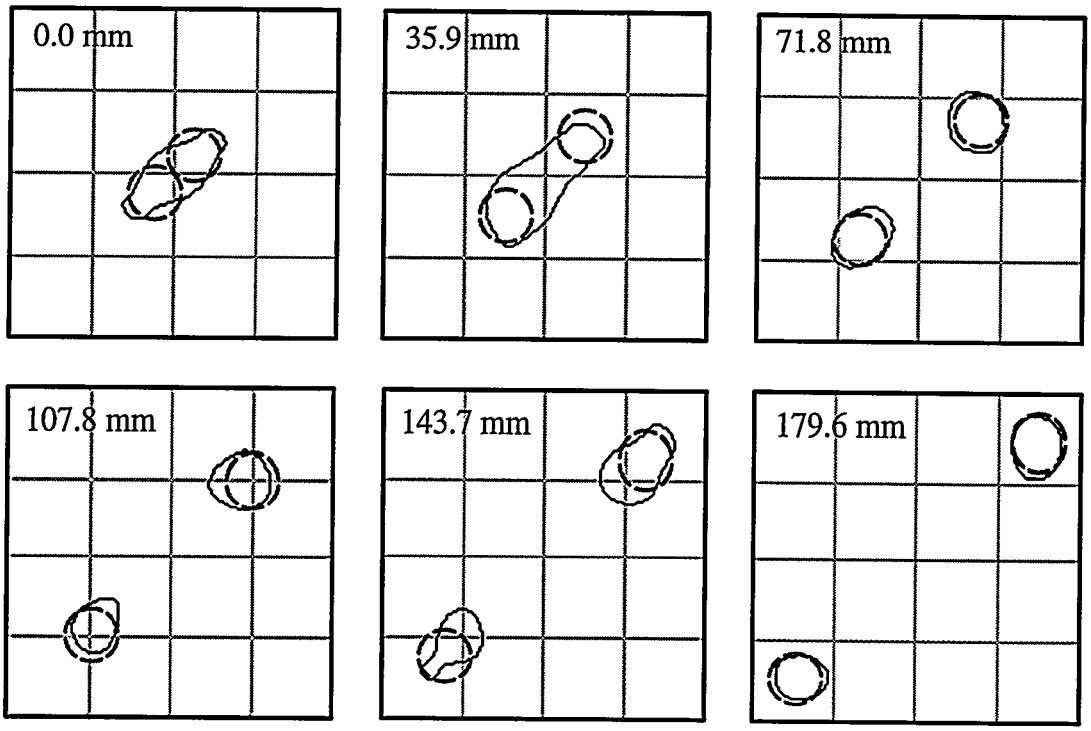

Figure 7.54 Results of the the best contour algorithm applied to the diagonal separation distinguishability test results shown in Figure 7.53: 9×9 mesh.

Figures 7.55 and 7.56. In all cases the size, shape and location of the resultant images are reasonably accurate.

7.5.5 Size and Shape Resolution

What has become apparent in the foregoing discussion of the results presented herein is that, even with excellent contrast between the target and the homogeneous background, there is a smooth variation in the computed conductivity field. This is in part due to the used model which, rather than being a binary model, is instead a continuous one wherein the conductivity is assumed to vary exponentially with a biquadratic exponent. As a result, it is impossible to determine the exact size and/or shape of any target with this model as it currently exists. It is also partly due to the limited sensitivity of the boundary variations to target conductivity variations as described before. This lack of actual size discrimination is not unique to this method and is one of the reasons why most impedance imaging results are shown as bit–mapped images using some type of grey scale which may or may not be linear. Using such a scale masks wholly or partially the continuous nature of the computations which are at odds with the phenomena being imaged.

7.6 Multiple Two–Dimensional Targets with Differing Size and/or Position

The results presented in this section are intended to present the capability of the system in obtaining images of two dimensional targets of different rectangular and circular shapes placed in various locations inside the phantom. All experimental and numerical procedures presented herein uses the best capabilities as described previously. These include:

- 16–plate–electrode phantom;
- Walsh–function excitation patterns;

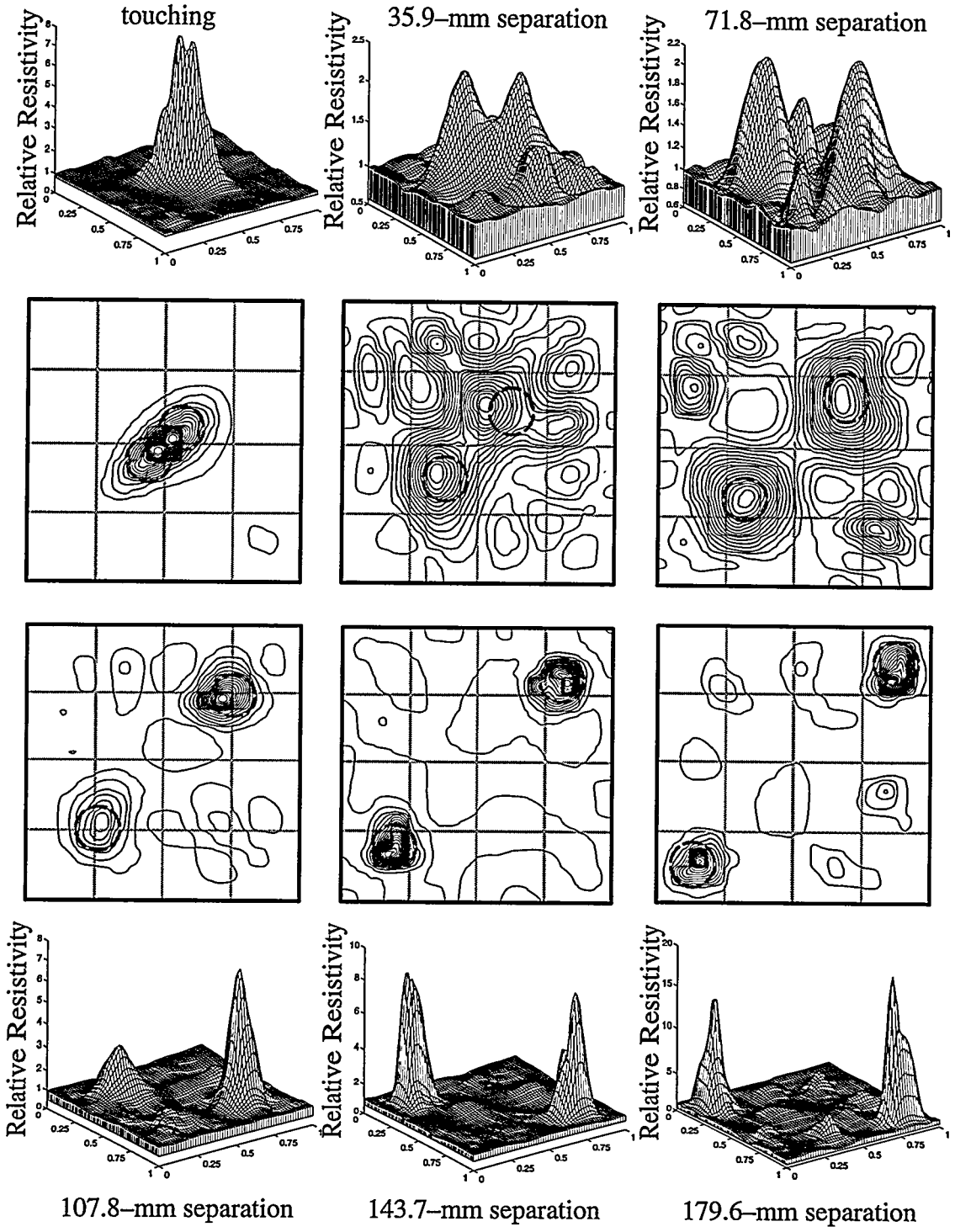

Figure 7.55 Relief and contour plots of relative resistivity for separability tests of Figure 7.51. Data obtained in the 16–plate–electrode phantom with water conductivity of 190 μS/cm and reduced using a 16 × 16 mesh.

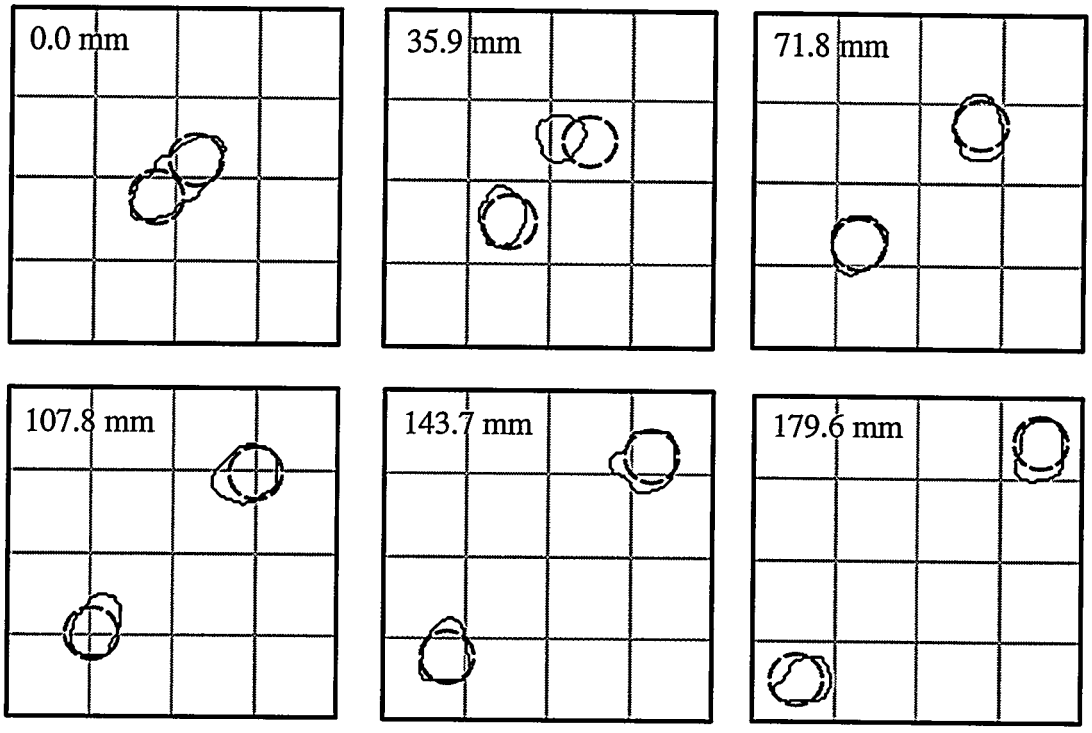

Figure 7.56 The best contour algorithm applied to the diagonal separation distinguishability test results shown in Figure 7.55: 16 × 16 mesh.

- biquadratic–exponential finite element scheme;
- the PVC method;
- computer optimized excitation patterns (unless the opposite is specifically mentioned).

7.6.1 Best Contour

Figure 7.57 shows three identical 32.8–mm diameter targets in a homogeneous bath. The use of a grey scale image makes the image appear to be excellent in both discrimination and resolution, in spite of the variations in the dark grey continuum. However, when the relief and contour plots are examined for a very similar condition in Figure 7.58, it becomes obvious that the grey–scale imaging produces a *de–facto* visual discrimination which is not representative of the actual situation. This figure shows three fairly large circular targets of differing size (25.4–, 32.8–, and 45–mm diameter) and variable locations, (150, 75), (125, 137.5) and (62.5, 75) respectively (x–y coordinate locations in mm from the lower left corner of the phantom). It is obvious that the contrast ratio for each target is different, varying in relation to the target sensitivity. Note that the smallest target, being closer to the boundary, could produce a more sensitive response than if it were in the location of the 32.8–mm diameter target but since both targets have approximately the same contrast ratio it is seen that the contrast depends not only on size but on location as well. Imaging with the best–contour algorithm produces reasonable results for all three targets. Recalling the results of Figure 7.1 which also used differential filtering, it appears that the method is reasonable for a fairly wide range of sizes and locations of circular targets.

It would appear, then, that the differential filtering "best–contour" algorithm might be expected to work reasonably well for targets having curved boundaries, but not as well for targets having sharp demarcations in their shape. In retrospect, this appears to make

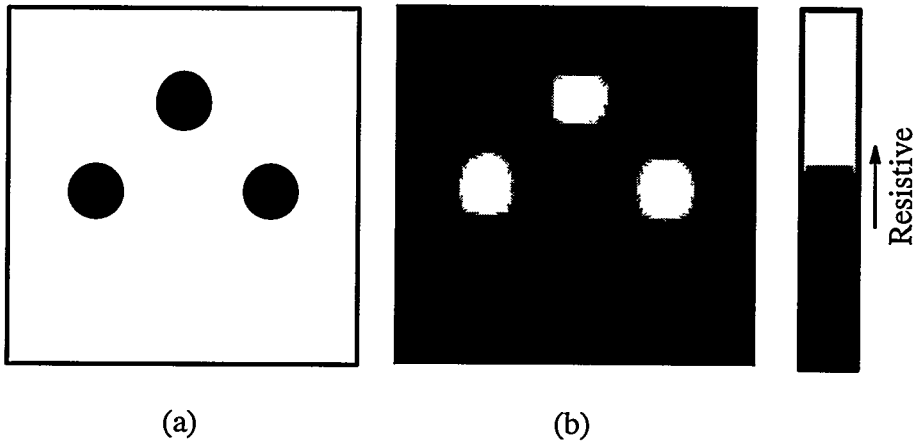

Figure 7.57 Three 32.8–mm diameter cylindrical insulator targets located in the two–dimensional 16–plate–electrode phantom: (a) the actual geometries and locations; (b) reconstructed image.

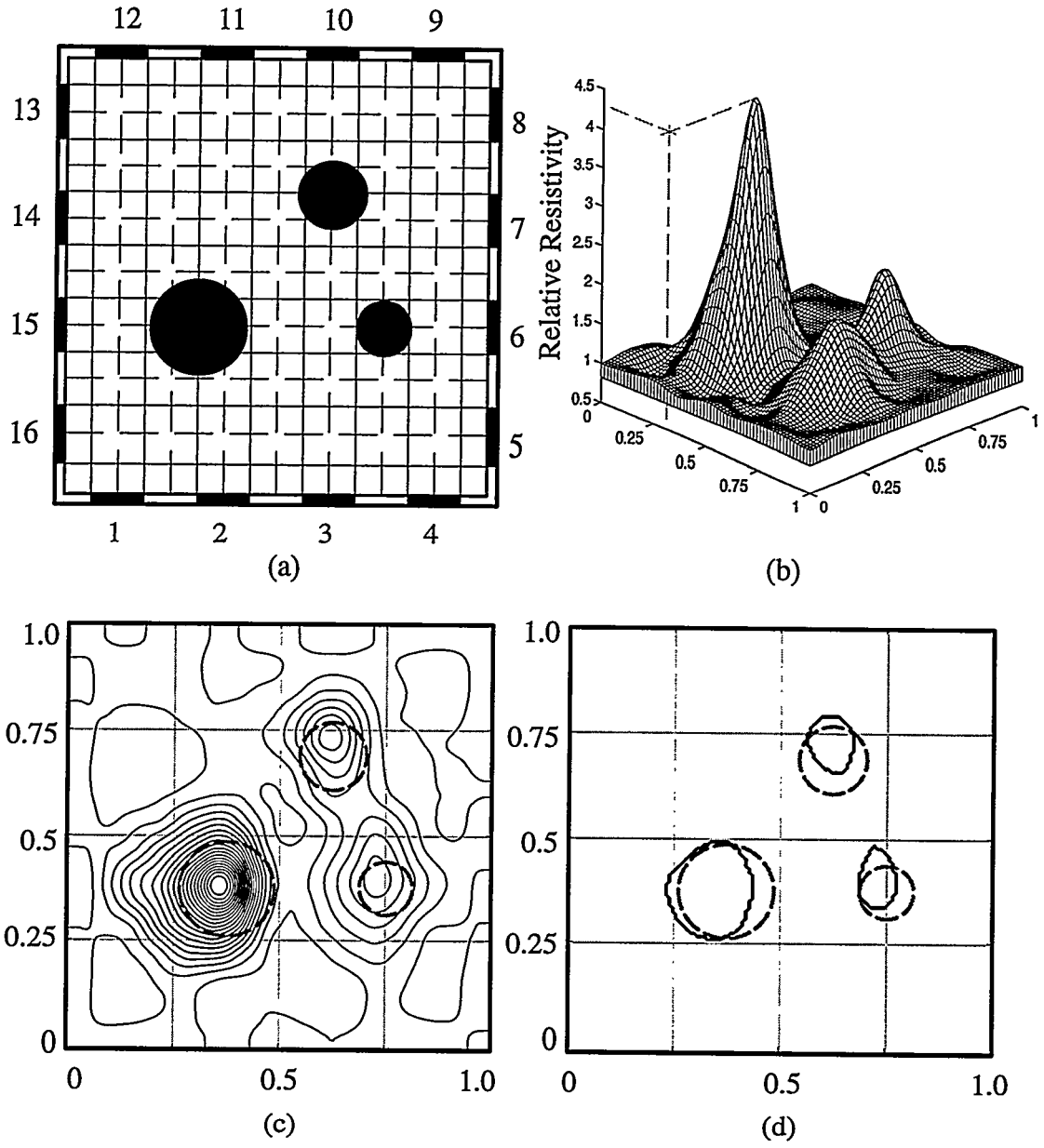

Figure 7.58 Imaging of three differently–sized circular targets (25.4–mm, 32.8–mm and 45–mm diameters) located randomly: (a) actual location; (b) relief map of relative resistivity; (c) resistivity contour map; (d) "Best contours" from Figure 7.4.

sense since the conductivity shape function adopted in the block decomposition model was devised to produce a continuous approximation to a physical situation having sharp changes in field properties, and to do so in a manner which produced characteristic curves of quadratic type: e.g., lines of constant conductivity would be represented by generalized quadratics, such as circles, ellipses, parabolas and hyperbolas.

7.6.2 Comparisons of Effects

It was previously stated that computational requirements for impedance imaging using these methods are intensive. Thus, as few computational assets as necessary to obtain the basic information required are desirable and were used herein. Much of what has previously been shown to demonstrate that electrical impedance imaging is a potentially useful tool in binary media was computed using a 9 × 9 mesh.

A six–target case computed to 100 iterations is shown in Figure 7.59. In this case the targets are cylindrical and located as follows: 25.4 mm, (37.5, 100); 32.8 mm at locations (75, 50), (162.5, 62.5), (162.5, 125), (112.5, 150); 45 mm, (100, 100) respectively. Data were obtained on the 16–electrode phantom with water conductivity of 190 μS/cm and computations undertaken on a 9 × 9 mesh without optimizing the excitation pattern. Computed conductivity was 170 μS/cm, 11% lower than that measured with the hand–held meter. While it is obvious from both relief and contour maps that the targets exist, and are located at approximately the correct position, the contrast at 100 iterations is low and the best–contour algorithm can not separate the targets.

A direct comparison of the effect of the number of iterations is seen by examining Figure 7.60(a) relative to Figure 7.59. It is seen that the contrast is slightly lower and the results give much less definition of the targets at 70 iterations compared with 100. Further-

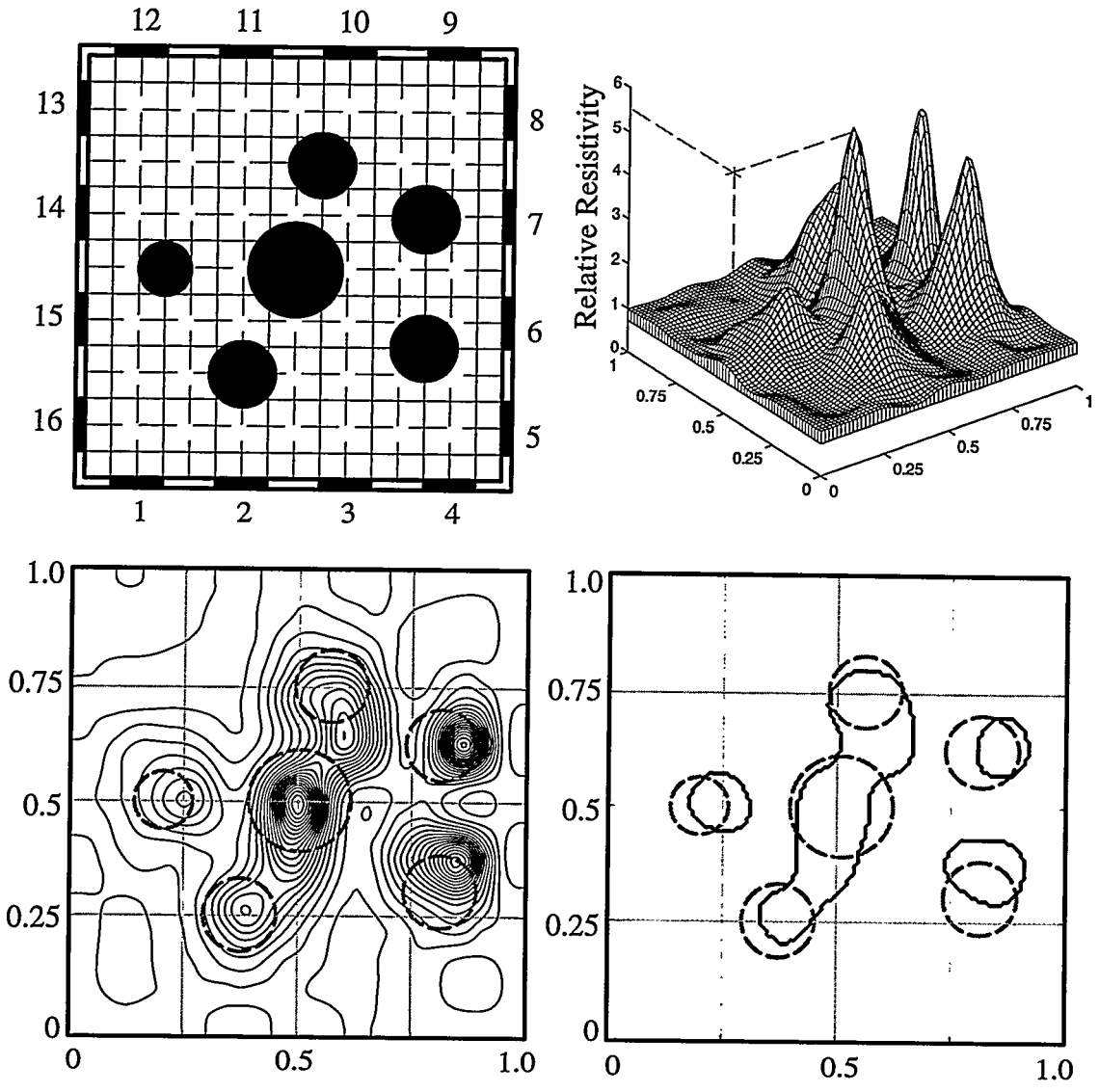

Figure 7.59 Image of six targets in the 16–plate–electrode phantom computed without using optimized excitation patterns: 190 μS/cm conductivity, 100 iterations, 9×9 mesh model.

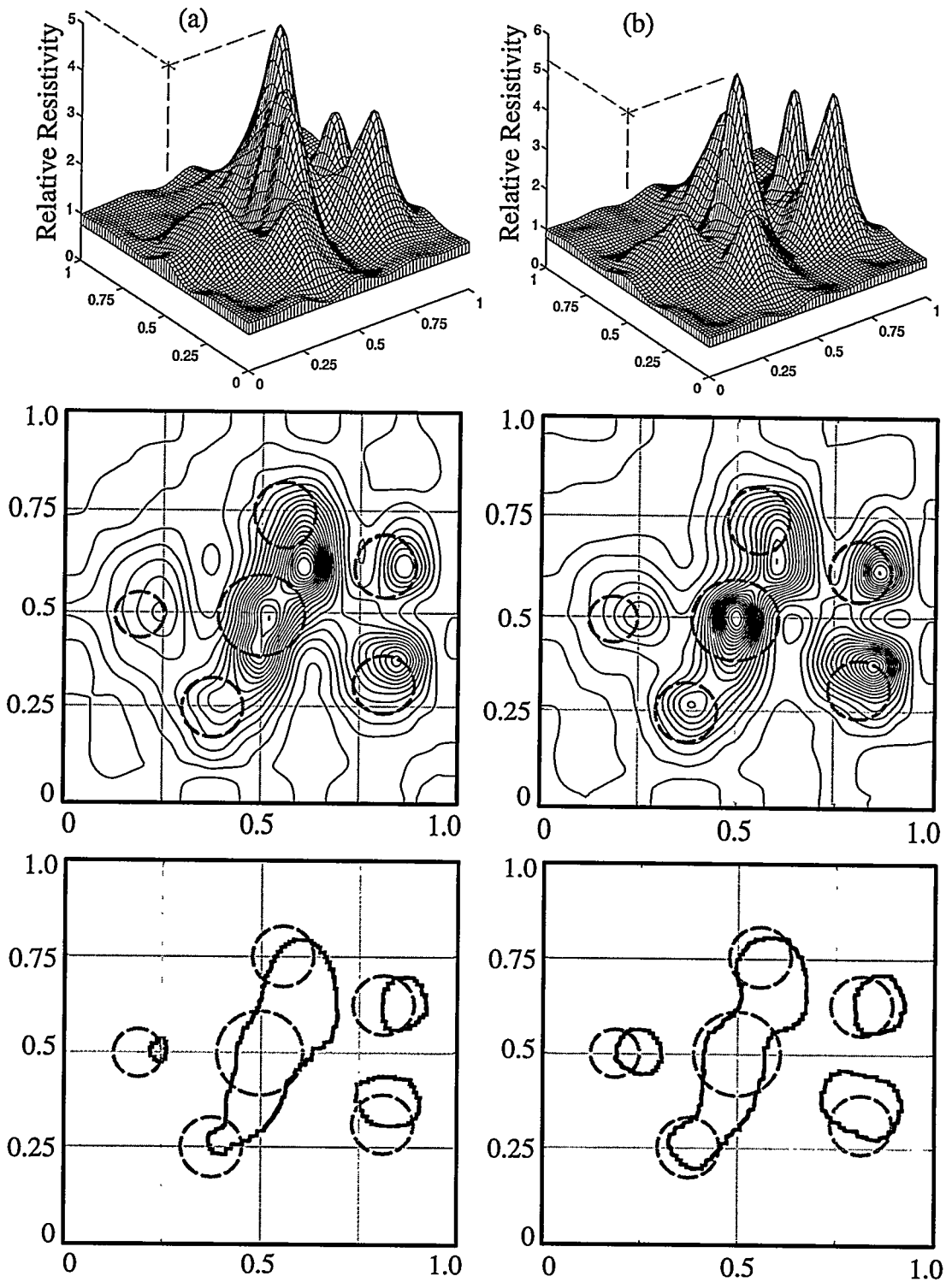

Figure 7.60 Effect of computed excitation pattern optimization on the six–target case shown in Figure 7.59 at 70 iterations: (a) not optimized; (b) optimized.

more, by comparing Figure 7.60(b) with (a), both computed to 70 iterations on a 9×9 mesh, it is confirmed that computer optimization of the boundary excitation patterns provides somewhat better definition, giving results which appear fully equivalent to the unoptimized computations at 100 iterations.

The effect of increasing the number of mesh elements from 9×9 to 16×16 for multiple targets may be seen by comparing the results in Figure 7.61 with those in Figure 7.59. In this case, computed to only 40 iterations, the relief map has been truncated to show the definition of the lower–contrast elements in comparison with the noise in the system. No optimization of excitation patterns was used in computations for this figure. The results show clear definition of all six targets although both size and location leave something to be desired. Maximum contrast for this was significantly improved over the 9×9 mesh case.

Using computer optimized boundary excitations and carrying out the computations to 100 iterations on a 16×16 mesh, the achieved results shown in Figure 7.62. The maximum contrast ratio has now increased to approximately 32:1 while the contrast of the center element increases from about 5.5:1 to nearly 22:1. The actual locations of the six targets is seen to be accurate and the noise relative to the contrast is negligible. The best contour algorithm (using the correlation data in Figure 7.4), however, still can not fully distinguish between all six targets and even picks up one which is spurious as seen in Figure 7.63.

What is concluded from this case is that the best contour algorithm cannot give fully satisfactory results where numerous targets exist as in the previous case since the contrast level of the large target at the center is not significantly higher than those of smaller targets. This is partly due to the fact that the the sensitivity of the excitations to the central region diminishes due to the isolation effects of the surrounding targets. Therefore, the contrast of the centered target broadens (see the relief plot in Figure 7.62) causing best contour lines

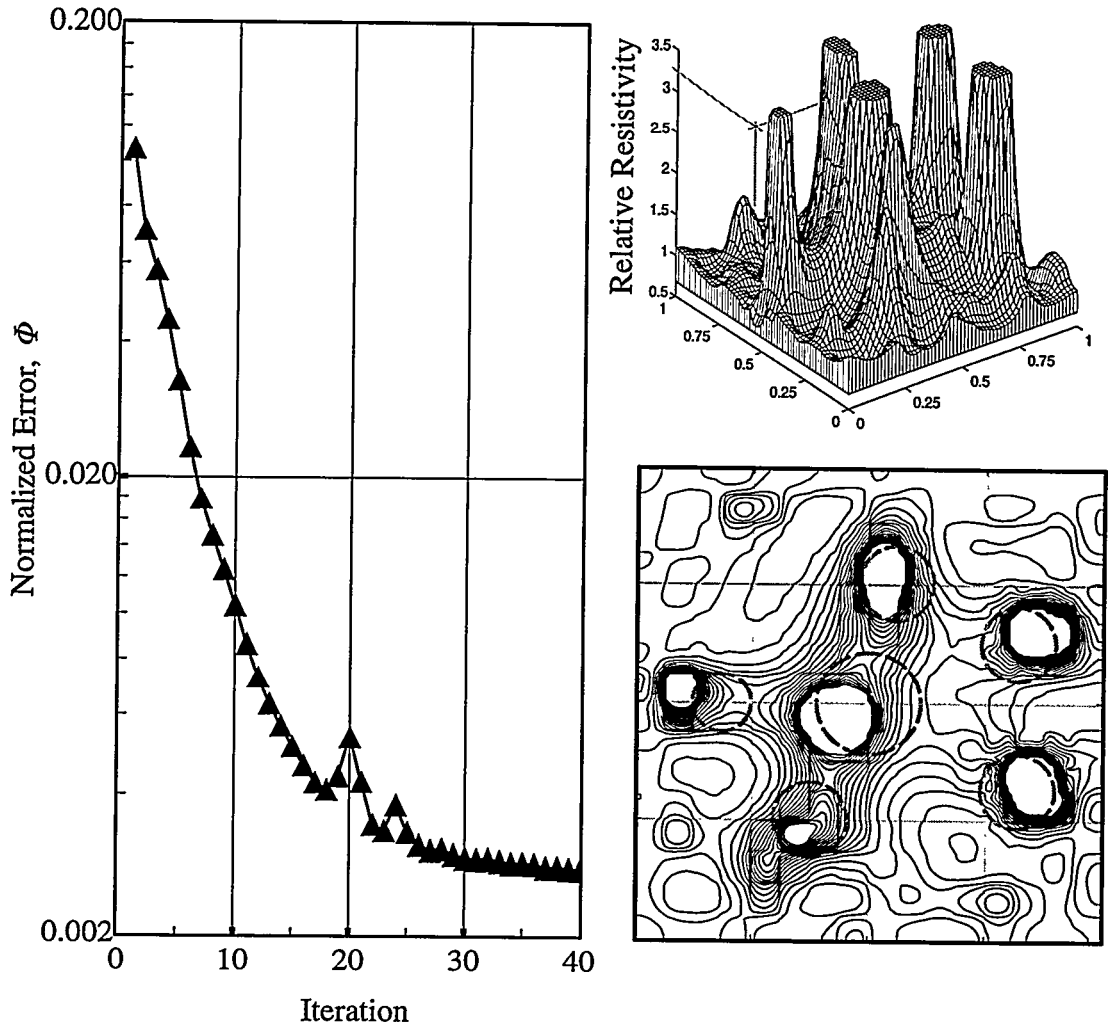

Figure 7.61 Effect of mesh size on imaging of the six–target case shown in Figure 7.59 showing the convergence pattern with contour relief map and contour plot at 40 iterations. Computation undertaken without pattern optimization on a 16×16 mesh.

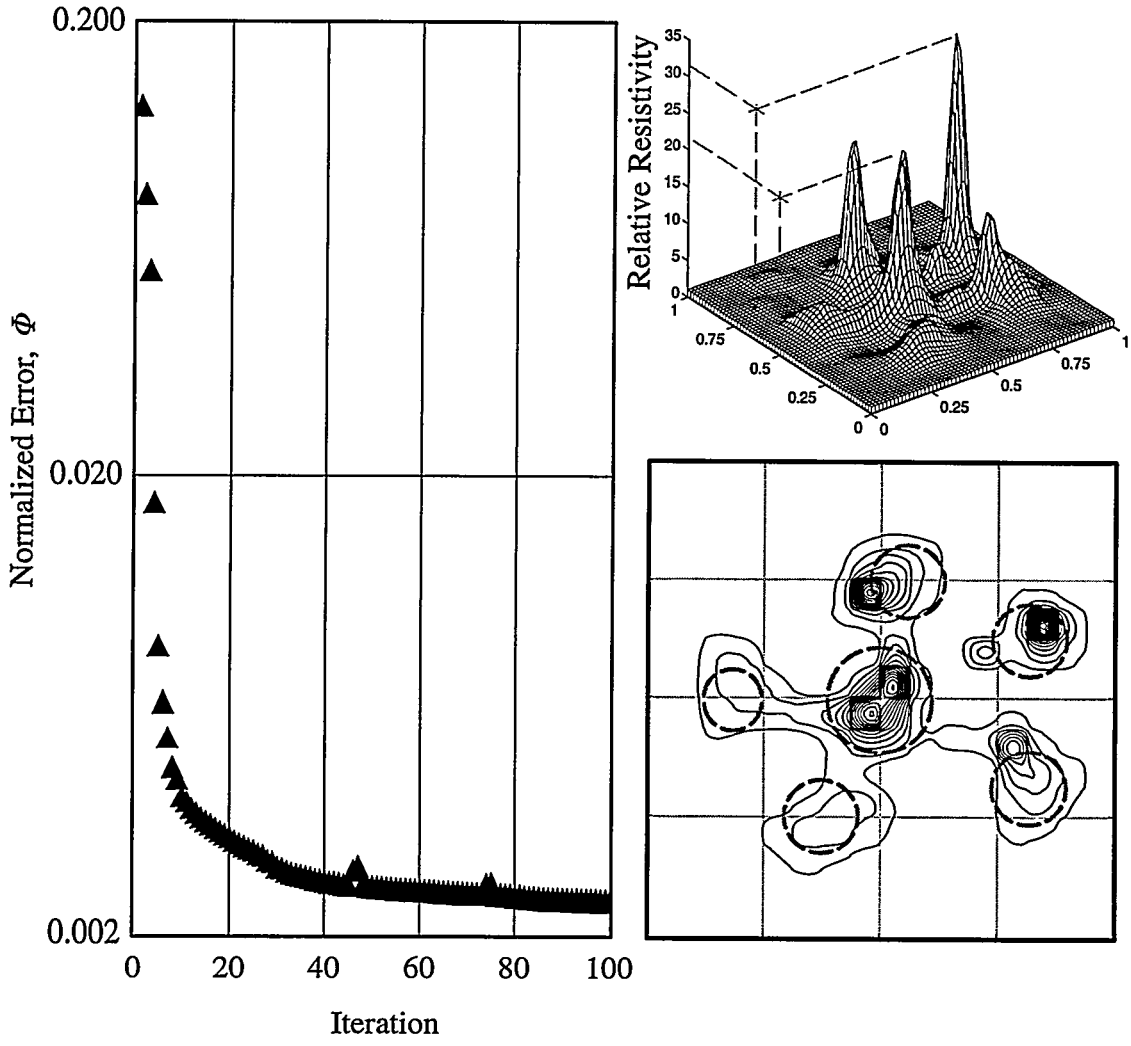

Figure 7.62 Six–target pattern shown in Figure 7.59 computed with optimized excitation patterns on a 16×16 mesh to 100 iterations.

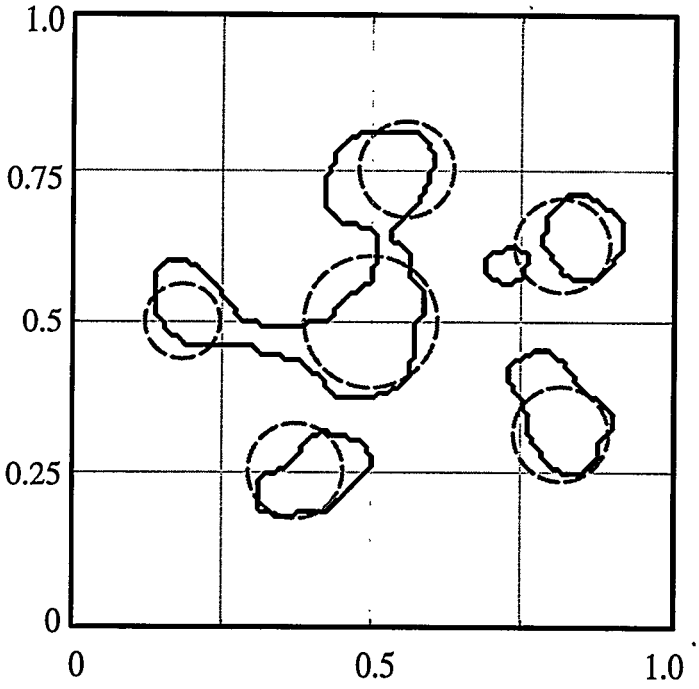

Figure 7.63 Best contour correlation in Figure 7.4 is applied to the computed image of Figure 7.62.

merging with the smaller targets. The best contours levels of all six targets can be slightly improved by varying the threshold level defined in Figure 7.5. Figure 7.64 shows the best contours determined using different threshold levels of 2.2, 2.6, 3.0, 3.4, 3.6 and 3.8 when target contrast more than 5.0. As the threshold level is increased beyond 3.0 (which was previously used as 2.4) all the targets started separating, but with a poor shape resolution.

7.7 Three–Dimensional Targets

The analytical model is basically a two–dimensional model, limited by the basic assumption made in layering that the impedance is constant in the third dimension. This allows only for slowly varying impedances in the depth direction when three–dimensional electrodes are used. Nevertheless, it is interesting to see how well the methods developed may apply to three–dimensional objects. Computations on quasi–two–dimensional shapes in the three–dimensional such as truncated cylinders, glass flasks, etc., produce virtually identical results to those previously described. True three–dimensional objects do not, however, fare as well.

7.7.1 Best Contour

Best–contour correlation plots for three–dimensional objects are shown in Figures 7.65 and 7.66. Included in this figure are all the data taken in the 16–plate–electrode, three–dimensional phantom using both two– and three–dimensional targets: cylinders of various sizes; a 250–ml glass flask having a neck diameter of 26 mm, and a conical body with sections of 54 mm, 80 mm and 88 mm located at the electrode centerplane; spheres of 60–mm (tennis balls filled with plaster of Paris) and 115–mm diameter (plastic ball filled with plaster of Paris), all centered in the electrode plane.

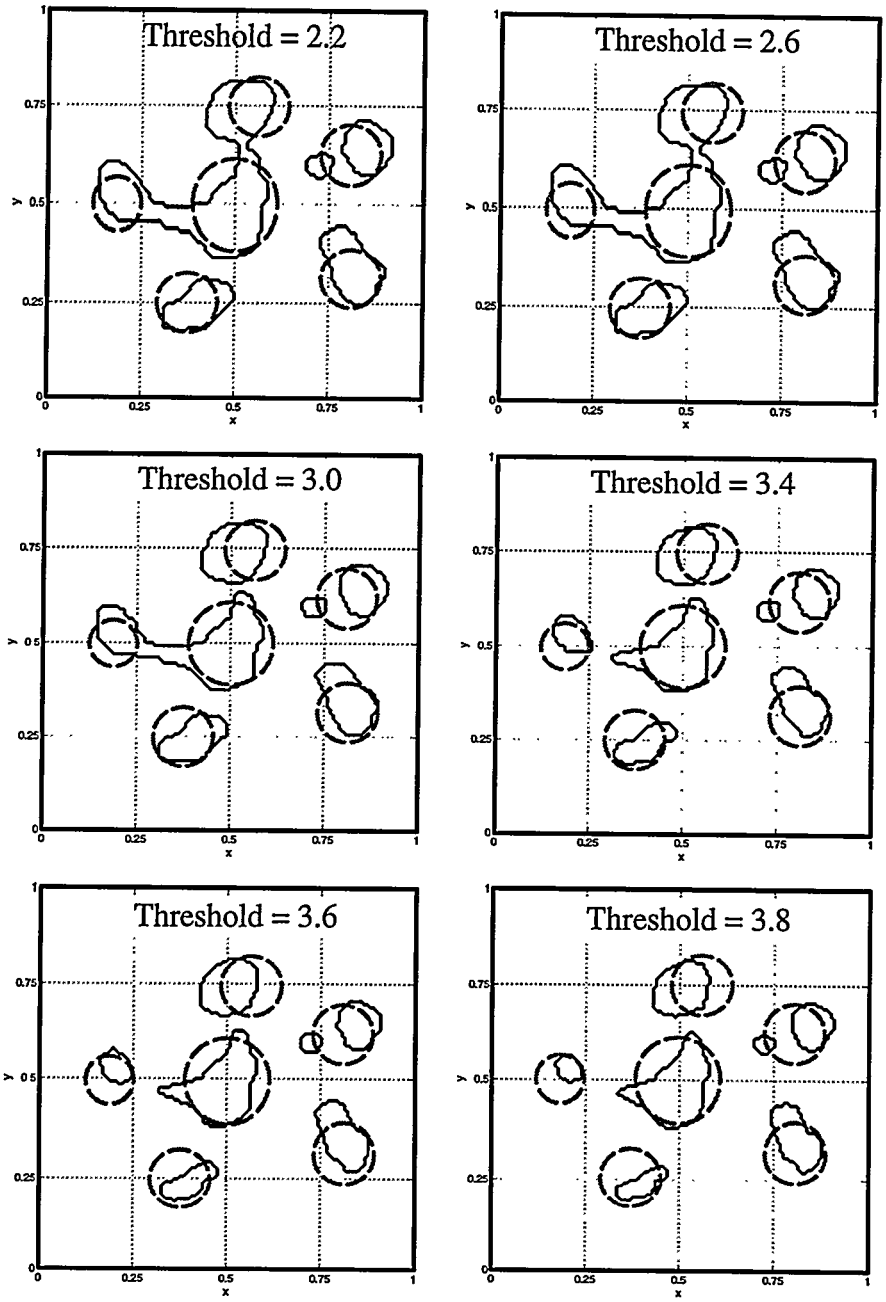

Figure 7.64 Best contour correlation in Figure 7.5 applied to the computed image of Figure 7.62 for different threshold levels: 2.2, 2.6, 3.0, 3.4, 3.6 and 3.8.

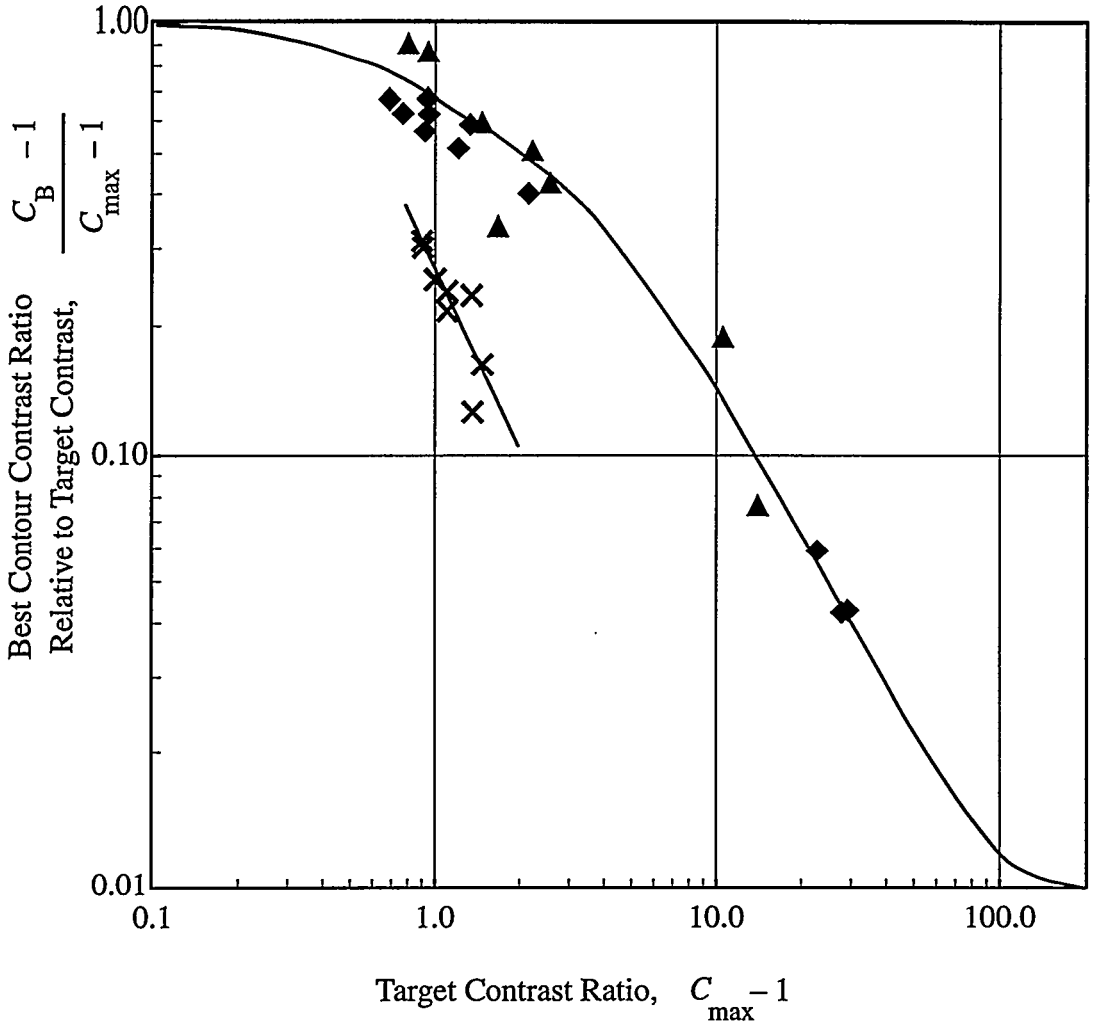

Figure 7.65 Correlation of differential discrimination level for individual targets taken from multiple–target images: ◆ 3–D cylinder data; ▲ 3–D flask data; × 3–D sphere data (60–mm and 115–mm diameter).

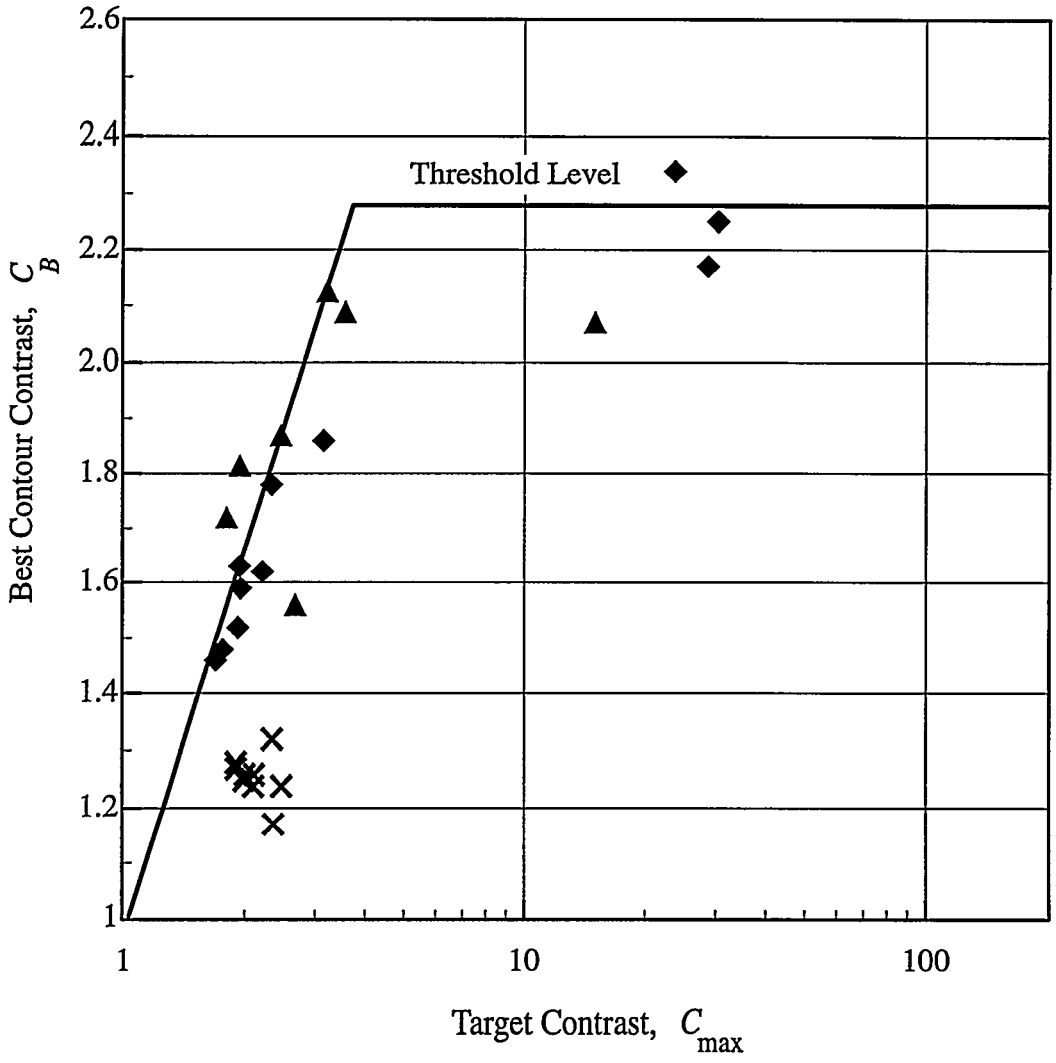

Figure 7.66 Correlation of differential discrimination level for individual targets taken from multiple–target images: ◆ 3–D cylinder data; ▲ 3–D flask data; × 3–D sphere data (60–mm and 115–mm diameter).

Figure 7.67 and 7.68 show all the data together. What is noted is that the spherical targets behave somewhat differently from the two–dimensional and quasi–three–dimensional data. In fact, these all have best contours which are between 20% and 30% above the homogeneous (Figure 7.68). It is suggested that this is due to the shunting effect of the fluid above and below these plainly three–dimensional targets, making them appear more conductive than they are in fact. When Figures 7.5 and 7.66 are compared, both two–dimensional shapes in both the two–dimensional phantom (as shown in Figure 7.5) and the three–dimensional phantom and quasi–three–dimensional shapes in the three–dimensional phantom (as shown in Figure 7.66) fall on approximately the same curve (Figure 7.67) even though the two–dimensional phantom is for the former and the three–dimensional phantom for the latter.

7.7.2 Imaging

Two spheres (tennis balls filled with plaster) were located in a horizontal plane of the 200 × 200–mm phantom at locations (50,100) and (150, 100) relative to the corner at a depth of 150 mm when the liquid depth was 300 mm. Conductivity was 190 μS/cm. The 25.4–mm high exposed portion of the electrodes (Figures 6.7 and 6.4 in Chapter 6) were also centered at the 150–mm height. Calculations for the 16–plate–electrode, three–dimensional phantom were undertaken with optimized boundary excitation using 6 layers above and 6 layers below the central layer (see the discussion of the layer model in Section 5.8.1 of Chapter 5). Each layer was 25.4–mm in thickness. Computations were undertaken on a 9 × 9 element mesh. Figure 7.69 shows the results obtained. The location of the spheres is depicted closer to the walls than the actual locations. Furthermore, the contrast ratios for the two spheres as seen in the resistivity relief map are relatively low, slightly less than 2.0.

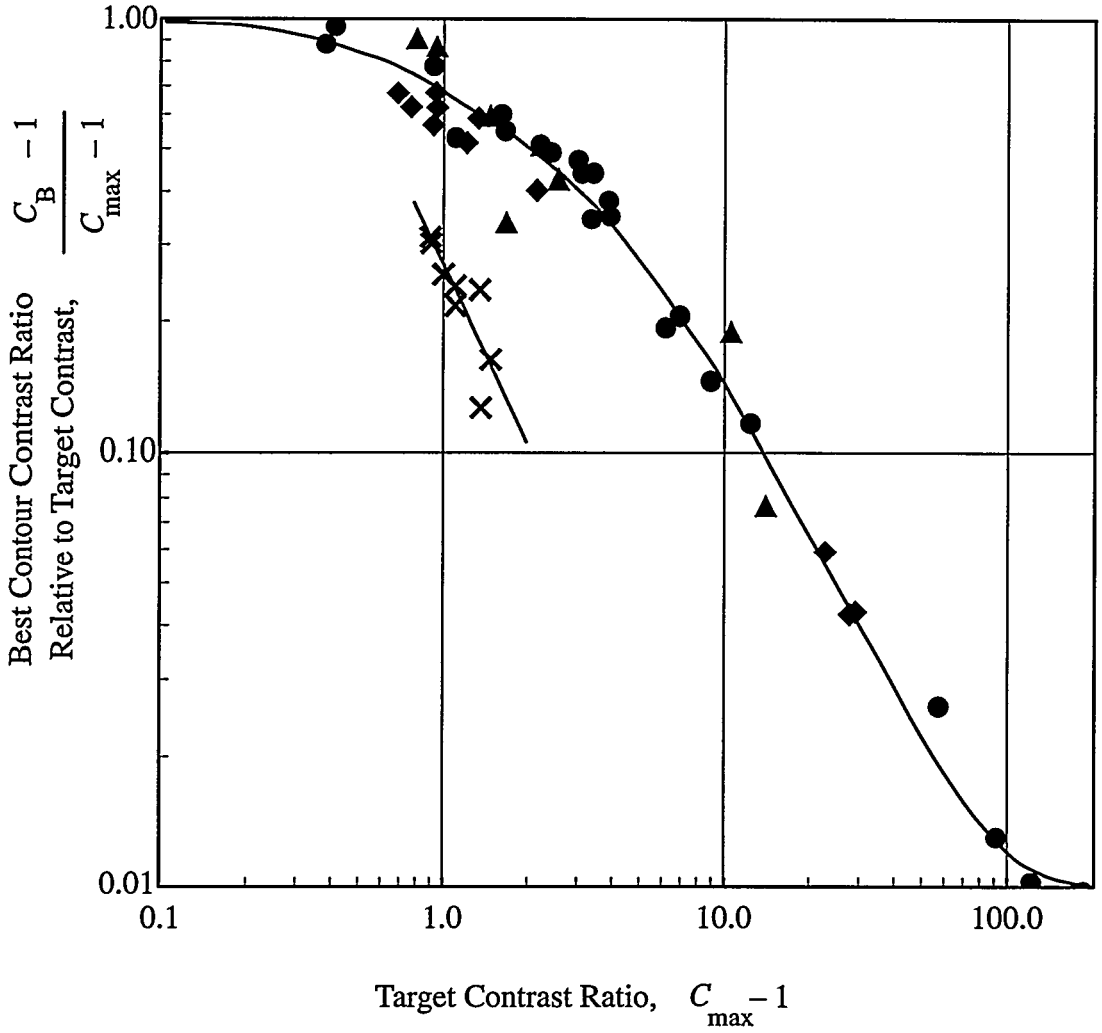

Figure 7.67 Correlation of differential discrimination level for individual targets taken from multiple–target images: ● 2–D data; ◆ 3–D cylinder data; ▲ 3–D flask data; × 3–D sphere data (60–mm and 115–mm diameter).

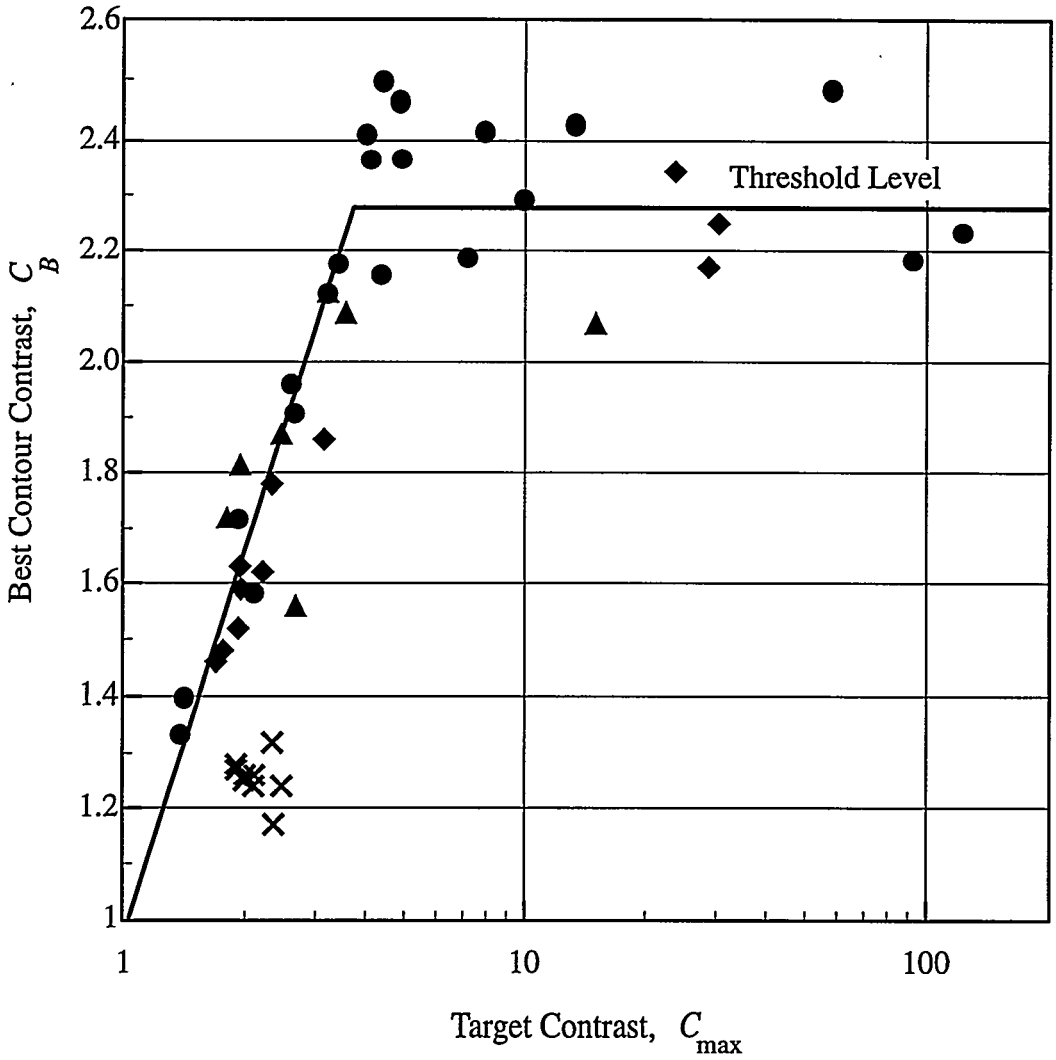

Figure 7.68 Correlation of differential discrimination level for individual targets taken from multiple–target images: ● 2–D data; ◆ 3–D cylinder data; ▲ 3–D flask data; × 3–D sphere data (60–mm and 115–mm diameter).

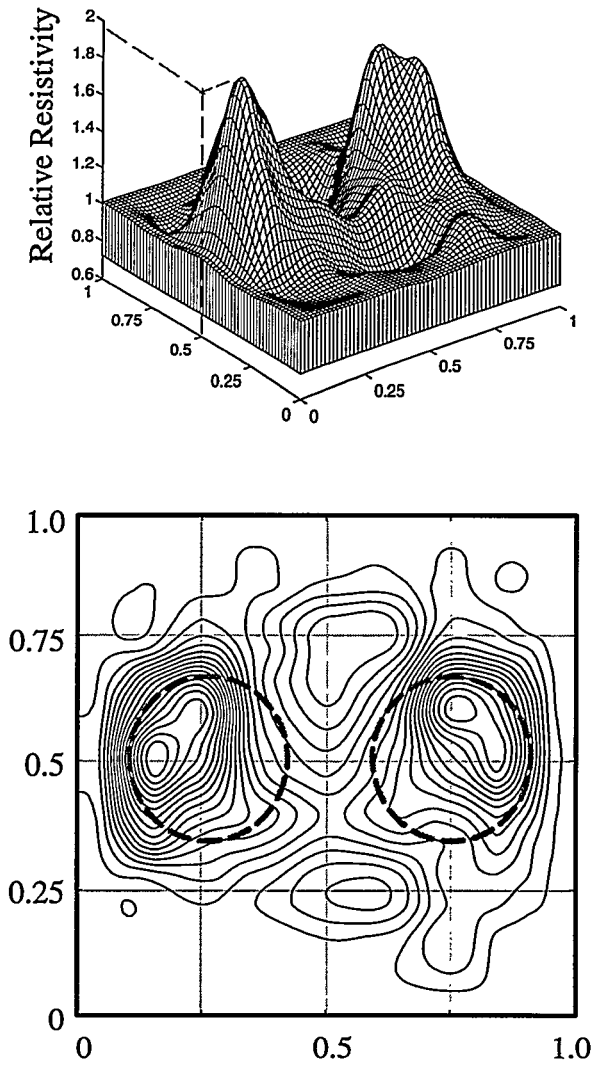

Figure 7.69 Imaging of two 60–mm diameter spheres located at 150–mm height in 300–mm of water in the three–dimensional, 16–plate–electrode phantom, computed to 30 iterations. Conductivity was 190 µS/cm.

The same experiment was repeated in the 32–plate–electrode phantom with the results as seen in Figure 7.70. The larger number of electrodes provides slightly better contrast and lower noise, and slightly better definition of the actual locations as seen by comparison with the dashed, light grey circles shown in the figures.

When the same 16–plate–electrode experiment is again repeated but with a higher water conductivity of approximately 1000 μS/cm, the results are considerably better (Figure 7.71). (The conductivity was the upper limit possible without overloading the excitation source.) In this case, with higher sensitivity provided by more than five–times increase in current flow, imaging produces locations and sizes which are more accurately depicted although still somewhat flattened in shape. Note that the center of each peak in the relief map is almost exactly centered while the best contour shape is not because of the flattened contours. Note too that the contrast ratios for the two spheres, computed to the same number of iterations, has increased slightly over that of Figure 7.69.

A similar experiment was undertaken but with three spheres located as shown in Figure 7.72 at positions (50, 50), (100, 150) and (150, 50). Optimized computations were undertaken to 30 iterations on a 9 × 9 mesh model. The highest contrast ratio was approximately 3:1. Maxima of all three peaks were almost exactly at the proper locations but the best contours showed shapes somewhat distorted from the true shape of the spheres.

Finally, a single, 60–mm diameter sphere was positioned at seven different vertical locations along the (100,100) line in the phantom as shown in Figure 7.73, these locations spanning the electrode imaging volume. The sequence of approaching positions occurred as follows: sphere top tangent to the bottom of the measuring volume; sphere top tangent to the center plane of the measuring volume; sphere top tangent to the top of the measuring

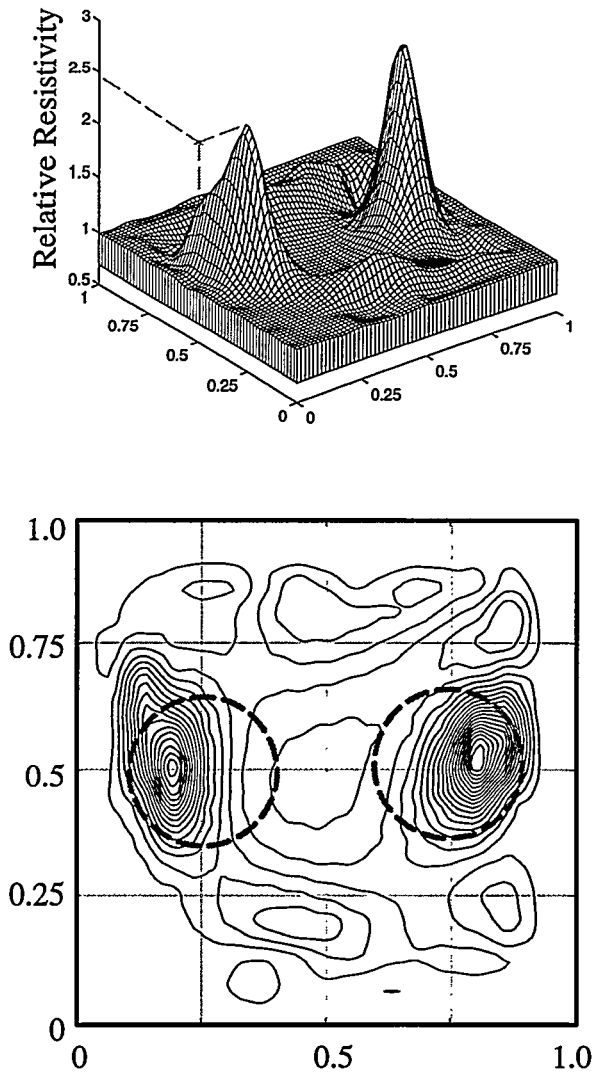

Figure 7.70 Identical to Figure 7.69 except that the data were obtained in the 32–plate–electrode phantom.

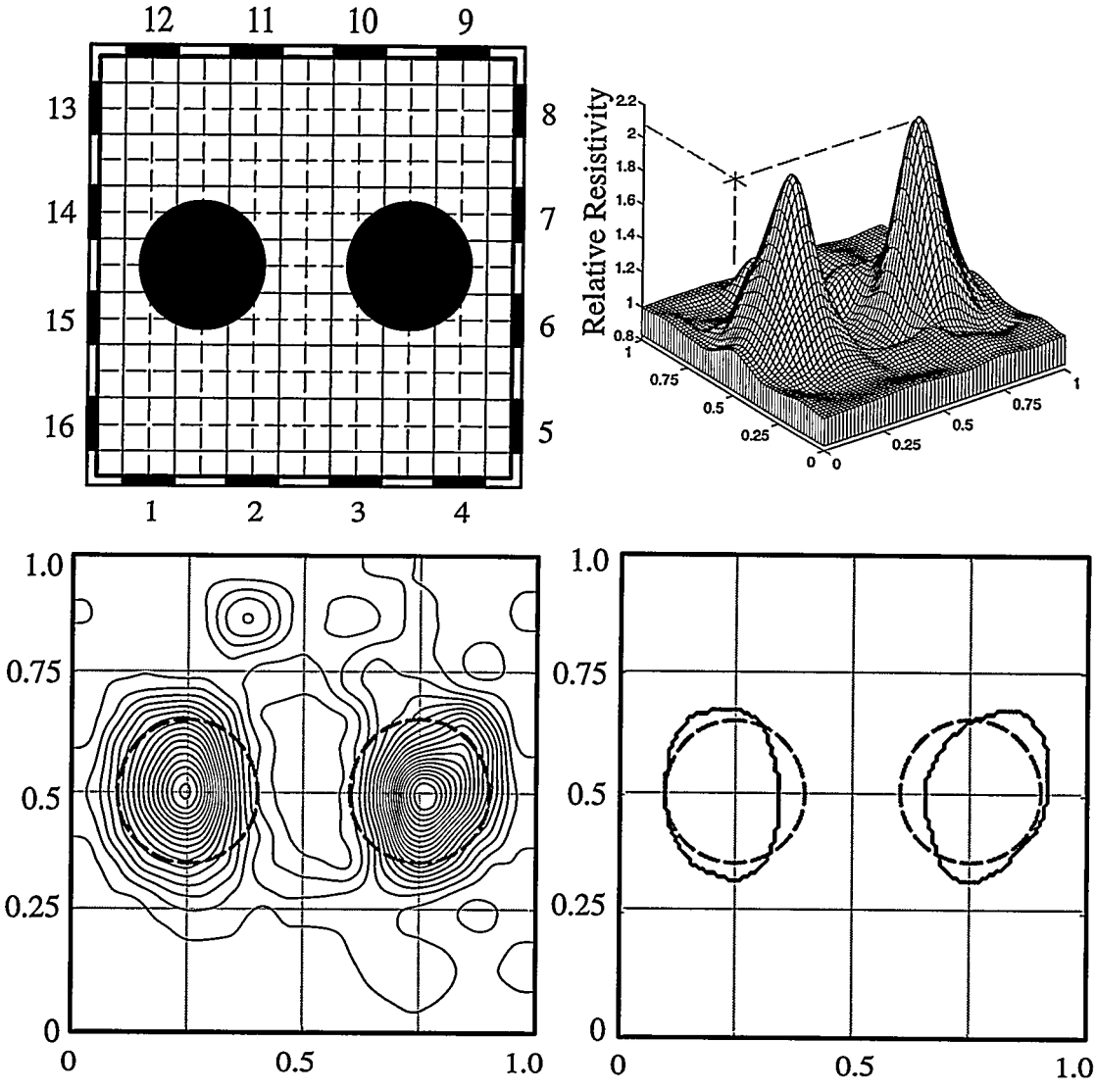

Figure 7.71 Image of two 60–mm diameter spheres located at the 150–mm depth in the 3–D, 16–plate–electrode, 200 × 200–mm phantom at cross section locations (50, 100) and (150, 100). Images were computed to 30 iterations on a 9 × 9 element model. Water conductivity 1000 µS/cm.

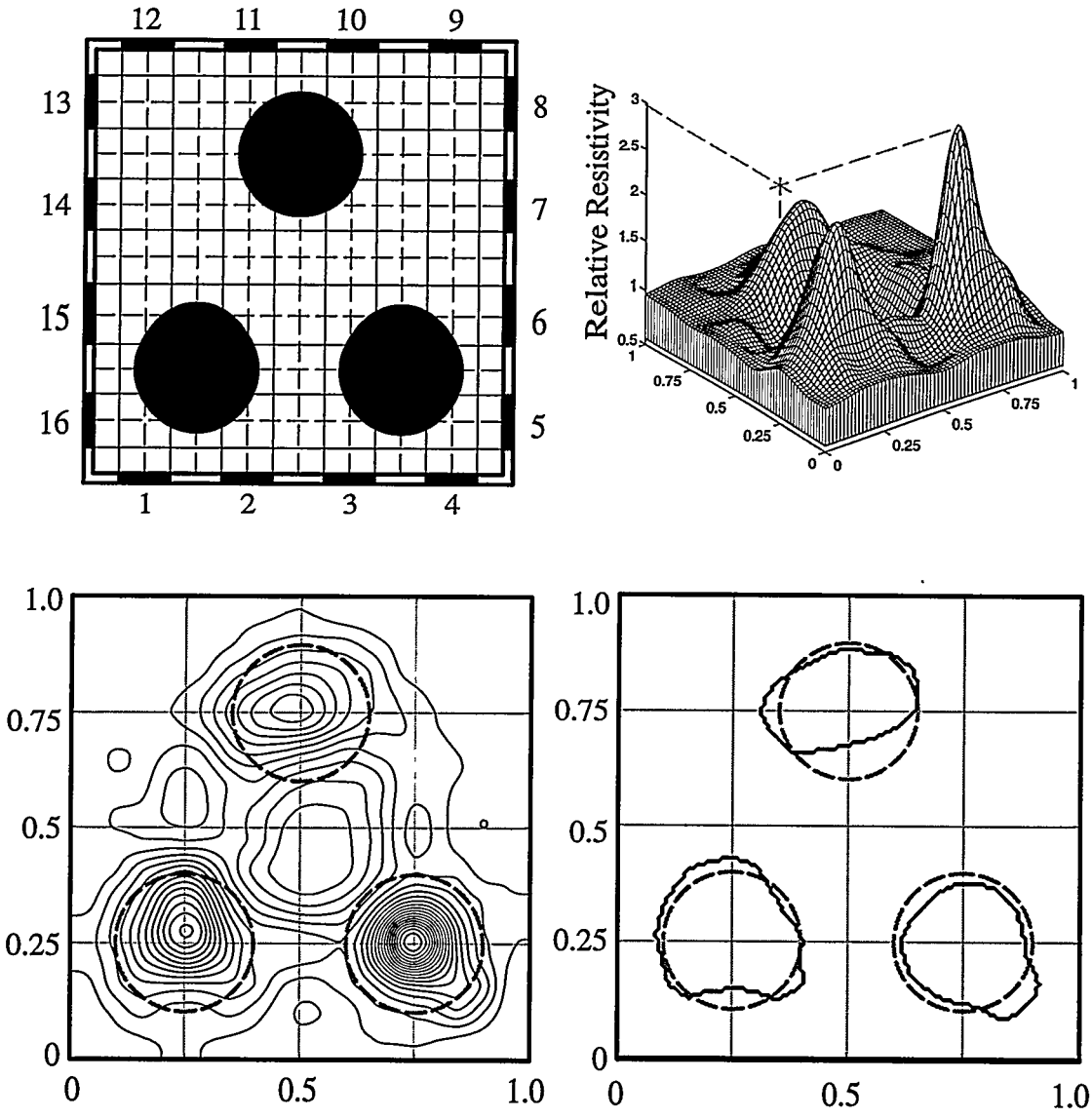

Figure 7.72 Image of three 60–mm–diameter spheres in the 3–D, 16–plate–electrode phantom computed to 30 iterations on a 9 × 9 mesh model. Water conductivity 1000 μS/cm.

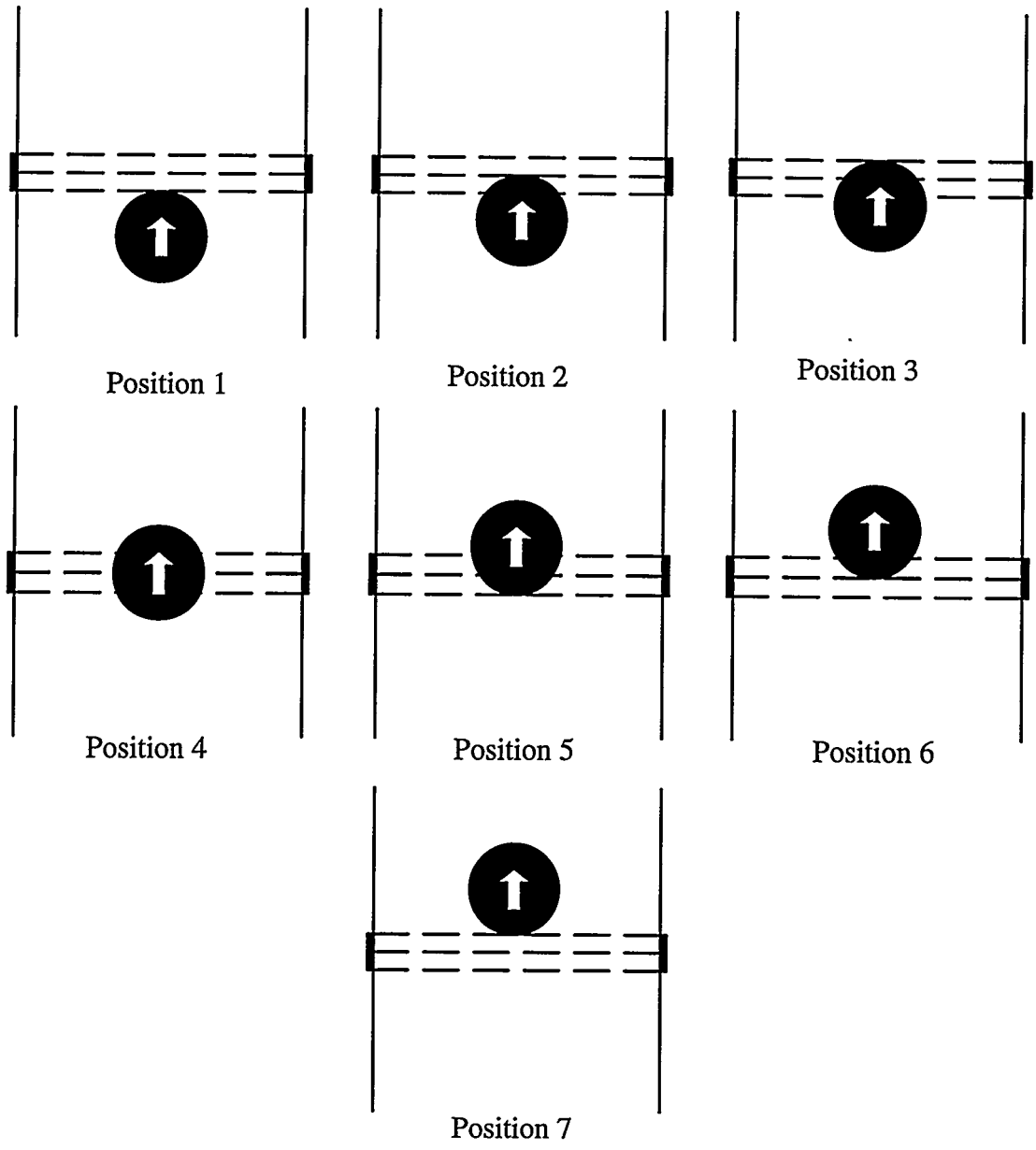

Figure 7.73 A 60–mm–diameter tennis ball moved in upward direction in the center of the three–dimensional phantom and data is collected in each of position.

volume; sphere centered in the measuring volume. The departing sequence was symmetric with the approach.

The results of the imaging of these locations are displayed in Figure 7.74. An accurate depiction of the sphere size and locations would result in an ellipsoidal shape due to the finite height of the imaging volume. The actual result is a somewhat misshapen ellipsoidal shape with the location of the image of the sphere at its lowest location, image and Position 1, not depicted accurately. Nevertheless, the results show that it might be expected to image moving three–dimensional shapes with reasonable accuracy if the measurement accuracy is also maintained.

7.8 Summary

This chapter has presented in detail electrical impedance images of binary, multiply–connected fields computed by using experimental measurements. These measurements were obtained for various test cases of differently–sized insulating targets placed in a homogenous conducting medium. Both two– and three–dimensional test phantoms were designed and utilized to investigate the imaging methods. The ultimate application would apply to liquid–gas flowing systems. The results included:

- an empirical method called the "best contour" algorithm to determine the best contour level used to depict the best shape of targets;
- a demonstration of the effects of all the experimental, design, analytical and numerical developments previously proposed for reconstructions;
- a demonstration of the resolution and distinguishability limits of the imaging system;

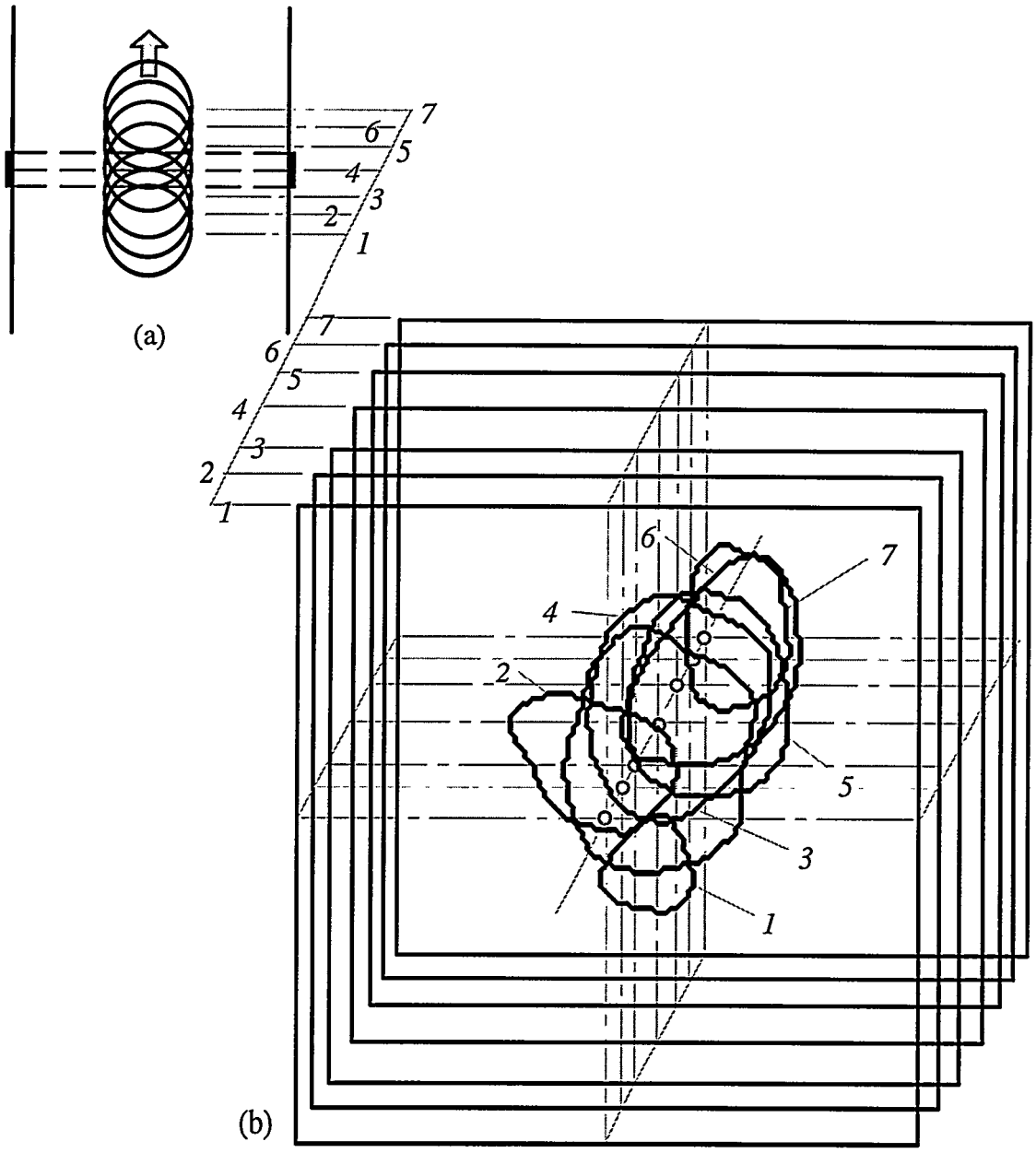

Figure 7.74 Sequential imaging of a 60–mm–diameter sphere as it moves through the 16–plate–electrode phantom's 3–D imaging volume with a 9×9 element model and all optimizations: (a) schematic of moving sphere locations; (b) sequential images taken at those locations. Water conductivity 1000 μS/cm.

- a demonstration showing that by combining all the proven best methods, images of insulator targets in various size, shape, and/or locations can be visualized in both two– and three–dimensional phantoms;
- a demonstration that a three–dimensional target can be imaged as it moves in three–dimensional space;
- a demonstration that increasing the system conductivity can significantly enhance the accuracy of three–dimensional images.

The "best contour" algorithm used differential discrimination wherein each "recognized target" was subject to a binary filter whose level was a function of the maximum contrast ratio for that target. The algorithm was calibrated using separate experiments where the "best contour" was chosen to match exactly the cross sectional area of the target. Application of the best contour algorithm demonstrated the following:

- Differing target sensitivity produced varying contrast ratio images of identical targets at differing locations and similar contrast ratio images of differing targets at differing locations.
- Targets producing contrast ratios larger than approximately 4:1 relative to the homogeneous background, were best imaged by the contrast contour at approximately the 2.3:1 level. That is, the base of the relief did not change significantly while the maximum contrast increased to computed values close to 300:1.
- Targets producing contrast ratios smaller than approximately 4:1 had their images spread out more and more over the surrounding field as the contrast diminished with the best contour level decreasing logarithmically with the maximum contrast of that target. This explains why it becomes increasingly difficult to obtain the true size of a very small target.

Considering the results due to all experimental and design features the following effects in results were observed:

- Use of rod and plate electrodes in the phantom showed significantly different results on images: coarse mesh reconstructions using unoptimized boundary data for the 16–plate–electrode phantom yielded superior results when compared to those for the 16–rod–electrode phantom. Fine mesh reconstructions, under identical conditions, improved very little for the rod electrodes but showed considerable improvement for plate electrodes.

- Increasing the number of electrodes from 16 to 32 improved the 16 × 16–model image for rod electrodes and decreased the 17 × 17–model resolution for plate electrodes. This may be due to increased shunting of current between adjacent plate electrodes, or simply due to the coarse mesh of the model. In any event, application of computer optimization of excitation patterns reversed this effect and demonstrated that the plate–electrode results yielded much better results relative to the rod electrodes under all similar circumstances.

- Measurements obtained from multiply–excited electrodes showed substantially better results relative to those obtained from single–pair electrodes when the same time and number of excitations were used. Due to the low sensitivity for the latter, very poor images were obtained.

- Data obtained by taking single rms measurements from sinusoidal source signals showed almost identical images as those obtained at an accuracy level of 1 part in 1000 or greater for averaged peak measurements of square–pulse source signals. Data acquisition time for rms measurements were, however, ten times greater than those for

1:1000 accuracy. Further increase in data accuracy resulted in little change in target distinguishability.

Computational requirements for the iterative reconstruction of inverse conductivity problem involving huge Hessian matrices and their inverses, made large models and truly three–dimensional impedance tomography impractical. Thus heavy emphasis was placed on detaining image of excellent quality using small models. Considering the results due to the application of the computational developments, the following conclusions were obtained:

- Improvements obtained by using the biquadratic–exponential conductivity model in the forward finite element scheme showed remarkably better results relative to the others using constant and bilinear–exponential models in both coarse and fine mesh reconstructions. Results of the biquadratic conductivity model computed on a 9×9 mesh were found almost identical but slightly better than the results of bilinear model computed on a 16×16 mesh. This shows that the biquadratic–exponential conductivity model has the ability to accurately resolve target boundaries of parabolic, elliptic and even hyperbolic shapes even when a coarse mesh model is used;

- There are many errors in the overall imaging system including construction inaccuracies, experimental errors in electrical excitations and measurements, coarseness and lack of details in the numerical model. All these errors may combine to completely eliminate the possibility of obtaining an image. Many of these factors may be accounted for "preconditioning" the voltage measurements to account for the accumulation of errors. The use of the preconditioned voltage conversion (PVC) method made differences in many cases between a quality image and no image at all.

Results were demonstrated for a centrally–located, cylindrical target resolution of 6 parts in 200. Distinguishability data indicates that an ultimate resolution of one part in between 375 and 570 should be obtainable with 99% confidence with relative error limits between 10^{-3} and 10^{-4} on boundary measurements. Two 32.8–mm diameter targets, when separated along either a perpendicular or diagonal centerline in the phantom, were not distinguishable from each other with a 9×9 mesh model but were clearly identifiable with a 16×16 mesh model.

Imaging of truly three–dimensional objects in the three–dimensional phantom was also demonstrated. Clearly, increasing the conductivity to the limits the system could handle to yield more than a factor of five increase in the three–dimensional phantom current flow produced superior results to those taken with lower conductivity: This was true in both the 16–electrode and the 32–electrode test devices. The results with higher current flow produced images of spherical targets of almost exact location and size but with slightly distorted shapes. The distortion is assumed due to the three–dimensional current flow which is not accounted for in computational model. A sequential image of a moving sphere produced reasonable results in light of the foregoing conclusions.

Finally, from all the foregoing, it is clear that the images are in the data. It remains now to determine the best analytical and computational methods of extracting the information to produce meaningful results.

CHAPTER 8

CONCLUSIONS AND RECOMMENDATIONS

8.1 Summary

The material presented in this report summarized the effort expended in the course of developing a finite element electrical impedance imaging system for obtaining images of binary mixtures of fluids, such as liquid and gas, using electrical measurements obtained on the boundary.

Introductory material in Chapter 1 provided an overview for inverse problems arising from various fields of engineering, and described inverse problems within the context of mathematics. Issues related to ill–posedness and regularization of inverse problems were also briefly discussed.

Chapter 2 provided a literature survey which included a historical background of the work previously undertaken in the area of electrical impedance imaging, and then outlined the contributions which have been made to this area.

Chapter 3 presented an extended overview which places impedance imaging in perspective relative to other imaging methods, and provided detailed background information for alternative imaging techniques. First, these alternative methods were introduced. Then, the basic principles of each were explained, including X–ray computerized tomography, nuclear magnetic resonance tomography, ultrasonic imaging, neutron tomography, radiation scattering tomography, electrical impedance tomography. Finally, comparisons of these methods in terms of their cost, their capabilities of speed and resolution were pro-

vided, and the practical applicability of these these methods for imaging binary mixtures of flows in real time was discussed.

Chapter 4 summarized the theory of basic electrical impedance methods. The concept of electrical impedance imaging was first explained and then a discussion of the minimum number of boundary measurements required to uniquely calculate the conductivity distribution was provided. Starting with Maxwell's equations, the field equation governing the electrical conduction problem (forward problem) in conductive and dielectric medium was derived. Background theory and historical developments of available reconstruction methods including the backprojection method, capacitive imaging methods, perturbation method, double constraint method, Newton–Raphson method (Yorkey's method), NOSER method, and compensation theorem method, were discussed along with their basic principles, advantages and disadvantages. The basic finite element formulation of the forward problem for solution of the field equation was also presented. Of the methods introduced, Yorkey's method appeared to be potentially more accurate relative to the others. Details regarding formulation and full implementation of this algorithm were explained. Various sources of error affecting experimental measurements and reconstruction procedures were also identified. Finally, Yorkey's algorithm was tested on various resistive patterns with the effects of simulated Gaussian noise added to the data.

Chapter 5 introduced several analytical and numerical innovations which can also be considered as extensions to the basic Newton–Raphson algorithm to be used for both two– and three–dimensional conductivity imaging. The majority of the effort undertaken in this chapter was placed on developing a more accurate finite element model of the forward solution. First, the governing field equation was reviewed for a more general case having a variable conductivity model within each mesh element, and then a more detailed finite element method using Galerkin's weighted residual formulation was outlined. Nu-

merical errors (in the forward solution) due to discretization and the convection term in the field equation were discussed in detail. A method called "preconditioned voltage conversion" (PVC) was introduced. It was then explained that this method is capable of eliminating a significant portion of discretization error caused by using a coarse finite element mesh model as well as other errors in the overall imaging system. On the other hand, errors due to the "convection" term can be reduced by finite element schemes using linear– or bilinear–exponential conductivity models implemented within the block decomposition method (BDM). In addition to these, errors caused by unmodeled z–directional distortion of current streamlines due to using finite–size electrodes in three–dimensional phantoms were discussed. A layer reduction method (LRM) was described which is able to provide a more realistic finite element model, and is able to eliminate the errors caused by z–directional distortion of current streamlines, thereby making quasi–three–dimensional imaging possible.

Chapter 6 summarized various experimental features used in the development of static, high–accuracy data acquisition system. This included a detailed description of mechanical design, and computer interfacing of the data acquisition hardware and its components such as the matrix switching unit, test phantoms, and test objects. Information regarding numerical sensitivity calculations of both point– and plate–electrode experiments, and description of plate electrode modeling as implemented herein were discussed. An extended historical background comparing various excitation and measurement techniques was provided including the neighboring method, cross method, opposite method, multi–reference method, adaptive method, and the linear array. Mathematical background for distinguishability and distinguishability calculation methods extended to cases of current or voltage source excitations were presented. Numerical sensitivity calculations were presented to demonstrate comparisons of using rod or plate electrodes in the finite element

model. The effect of liquid conductivity on imaging accuracy was also discussed along with a discussion on measurement noise and noise reduction methods. The data acquisition computer program and its procedures using all of these developments were also explained.

Finally, Chapter 7 summarized a set of computational results obtained to compare the effects of all experimental and numerical methods developed. Some aspects on displaying computed images were discussed and then the "best contour" algorithm used to identify boundaries of insulator targets was described. In the first part of this chapter, all experimental features compared including the use of rod– and plate–electrodes, varying electrode number (16 and 32 electrodes), single–pair excitations versus Walsh–pattern–excited electrodes. Also shown were data and image comparing the use of single rms measurements of sinusoidal boundary signals and averaged peak measurements of square–pulse boundary signals. The the effects of numerical developments are demonstrated including three different finite element schemes, improvements obtained by using the PVC method and improvements obtained by applying computer optimized boundary excitations. Experimental methodologies for determining the resolution limits of the imaging system were then presented. The basic concept of eigenvalue experiments was first summarized, and then the variation of eigenvalues of difference conductance matrices of the two–dimensional, 16–plate–electrode homogeneous phantom were used to determine the system's noise level. Eigenvalue sets of centrally–located insulator cylindrical targets of various diameters were compared to the noise level to demonstrate the capability of the measurements for distinguishing minimum size of 6–mm diameter targets. Similar experiments were conducted for successive separation of two identical 32.8–mm–diameter cylindrical insulator targets in both longitudinal and diagonal directions. Another subsequent group of experiments demonstrated that the imaging system is capable of identifying single, multiple insulator targets in various size, geometry and locations placed in a homogeneous field inside

the 16–plate–electrode phantom. It was shown that the imaging system is also capable of accurately imaging single and multiple 60–mm–diameter spherical targets located in the electrode plane. In addition, it was shown that if a set of sequential data measurements were obtained for a 60–mm–diameter spherical target passing through the electrode scanning plane, sequential set of images can be reconstructed by using the layer reduction method showing an approximately ellipsoidal image sequence through the 25.4–mm high measuring volume.

8.2 Major Accomplishments

There have been a number of major modeling innovations required to achieve reasonable success in imaging of binary mixtures (mixtures having basically two, widely disparate sets of electrical properties). The basic method required first the development of the basic finite element model required patterned on the YWT method. This allowed us to obtain and utilize the Jacobian (sensitivity matrix) which in turn allows element conductivities to be perturbed in a manner which decreases the overall error between computed and measured response to the boundary excitation, and to converge to a minimum error. In this we have duplicated results previously presented by Yorkey and his coworkers. Innovations which have been necessary to enable us to image binary fluids in an acceptable manner include:

1. Determined methods to directly computate the Hessian matrix rather than indirectly through the Jacobian resulting in an order–of–magnitude savings in computational resources;

2. Developed a method of undertaking preconditioned voltage conversion (PVC) of experimental boundary data which enabled us to make subspace corrections between fully converged computations and measurements which will account for

analytical, numerical and experimental anomalies such as residual three–dimensional field effects, discreteness in the model, errors in constructing the test geometry relative to the design, etc.;

3. Developed a block decomposition model for the field to be imaged thus reducing the computational times by three orders of magnitude and making iterative convergence to an overall conductivity distribution more practical for large numbers of two–dimensional images such as would be required for real–time synthesis of interfacial structure. This model incorporates the following attributes:

   - use of exponential shape functions to define the behavior of the field potential within individual finite elements and especially adjacent to electrodes;
   - use of biquadratic exponential shape functions to define the variations of electrical conductivity within each finite element relative to that at the element center;
   - improved modeling of the electrodes themselves in the case of plate electrodes;

4. Developed a layer reduction method for folding unexcited three–dimensional image layers into an equivalent two–dimensional layer thereby making real quasi–three–dimensional images possible;

5. Determined the numerical sensitivity as affected by the number of elements in the finite element model and the limits of contrast sensitivity in the model;

6. Determining the boundary excitation patterns which optimize the resolution of the imaging system.

These developments allow imaging data to be obtained and images to be computed with a minimum of experimental and numerical effort.

Additional developments which have had an important and enabling effect on our ability to clearly and accurately image single and multi–sized binary targets in homogeneous media involve

7. Clearly determined that plate electrodes were superior to rod (point) electrodes for use in exciting the phantom and obtaining images;

8. Adoptation of the use of multiply–excited, plate electrodes for significantly increased sensitivity, similar to that of Newell et al. [52] and Fuks et al. [24];

9. Determination of error variation with fluid conductivity and demonstration of lack of contact impedance effect on the data for conductivities of the continuous field below 1000 μS/cm;

10. Use of incomplete measurement sequences combined with Walsh–function boundary excitation to minimize the acquisition effort and demonstrate methods which will be utilized in high–speed imaging;

11. Extended Isaacson's distinguishability concepts [55] to experimental data through the use of differential eigenvalues to determine the minimum target sizes and multiple target separations which should be amenable to accurate imaging.

12. *Post–facto* application of boundary excitation pattern optimization to experimental data to significantly improve quality of images obtained;

13. Differential filtering of targets of varying sensitivity to allow simultaneous imaging of multiple targets of differing size and location;

14. Development of a "best contour" algorithm for explicitly determining the boundary of any discrete component based on its contrast ratio in the image.

This report described the details of these accomplishments, all of which were integral in the success we have obtained, some enabling and some incremental, in obtaining accurate images of single and multiple, two–dimensional and three–dimensional insulating targets in a homogeneous conducting medium.

8.3 Conclusions

The *first major conclusion* that can be drawn from this work is that accurate excitation and measurement of boundary voltages and currents appears to be sufficient to obtain images of the real conductivity distribution of a binary, multiply connected field within a measuring volume. Figure 8.2 shows just two examples of this while at the same time showing the imaging of a very small object of 6–mm diameter inside a 200–mm square tank, a demonstrated linear resolution of three parts in 100. Furthermore, we have shown that the quality of these images, and in fact the ability to obtain an image itself, is heavily dependent on both excitation/measurement techniques and the theoretical and numerical implementation of imaging algorithms. It is shown in this report that electrical impedance imaging method *has the potential* of being both fast and cost effective in comparison with alternative methods.

The *second major conclusion* drawn is that at this point, even after seven years of development effort, considerably more work must be expended before the the potential becomes reality. It has been found that excellent images of objects within a homogeneous region can be obtained with a demonstrated linear resolution of six parts in 200, and potential resolution based on distinguishability results perhaps better than one part in more than five hundred; however, the ability to correctly determine the boundary of the object depends on its shape, its relationship to the finite element geometry, the algorithm(s) chosen to represent the conductivity behavior within the elements, the image enhancement algorithms uti-

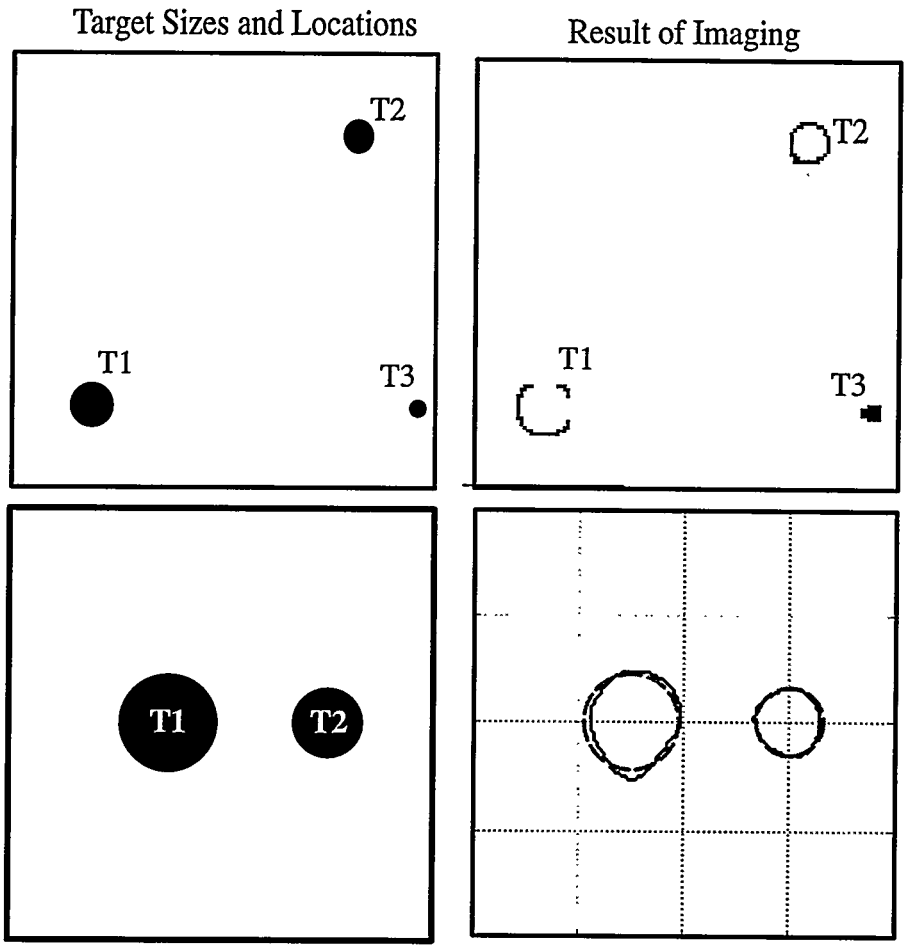

Figure 8.1 Examples of imaging of various targets of differing positions and sizes. Dashed grey circles indicate actual size and position of targets.

lized to treat the image before reconstructive iteration, and even the basic numerical model itself. Furthermore, the limits of resolution implied by the distinguishability data can probably approached only with an accurate, discrete–property, adaptive mesh, field computation model rather than using a conductivity continuum as undertaken herein. This will require a significant new development effort.

Specific conclusions may be drawn from this study as itemized below. Selected figures from previous chapters are reproduced as an aid to the reader.

1. It is impossible using the Newton–Raphson, finite element, inverse computations methods developed herein to obtain perfect delineation of target contrast (ratio of target conductivity to background conductivity) if it varies by more than approximately a factor of ten from the homogeneous values and that computational, S–curve saturation ultimately occurs with increasing true contrast.

2. The computed boundary sensitivity to perturbations diminishes as the size of the elements used in the model decreases making our model increasingly ill posed as the number of elements used to represent a given situation increases. Nevertheless, this model was judged as that having the best potential to ultimately yield accurate phase boundary images.

3. The computational times for conductivity reconstructions using Newton–Raphson methods increase with 3.3 power of the number of elements used in the model, thus limiting the use of large number of elements in practical situations, especially three–dimensional models.

4. Numerous methods were utilized to minimize the compute times and resources. In particular, block decomposition reconstruction methods developed in this program yielded the ability to rapidly compute a converged image with a reasonable accuracy and resolution. A 50 iterations, two–dimensional, 16×16 mesh model using 16–plate–electrodes now requires approximately 37.5 minutes (45 seconds/iteration) on a Silicon Graphics INDY Unix workstation.

5. In comparison with a constant conductivity element model or one using a bilinear exponential shape function, the use of a biquadratic–exponential conductivity shape

function with the plate–electrode model produced excellent results seen in Fig. 8.3 for the case of the two circular–target case shown in Fig. 8.2.

6. Phase–timed (PT) boundary measurement methods (measuring the peak of square–pulse signals) using an accuracy of one part in 1000 is an excellent alternate to frequency locking methods (measuring rms of sinusoidal signals). PT was found to produce images as accurate as low–noise rms methods and is ten times faster. PT methods also have the advantage of eliminating broad–band noise and is more suited to high–speed applications.

7. Increasing liquid background conductivity has the effect of increasing the current magnitude and therefore improving the signal–to–noise ratio of the data and ultimately reducing the overall error in any image as seen in Fig. 8.4. No effect of liquid–electrode contact impedance was noted in the range of conductivities utilized.

8. The computed relative contrast (resistivity relative to the background) of any insulating target is not only a function of the model itself, but also of the target size and location within the field of interest. This is clearly shown in the relief and contour maps of Fig. 8.5 where targets identical to those shown in the two–target image of Fig. 8.2 have differing contrasts.

9. An algorithm was required and developed to determine the actual contrast ratio depicting the true size of a given object (Figure 8.6). behavior once the conductivity contours are known. Applying this algorithm to the two–target case yields reasonable results seen in Fig. 8.7. Figure 8.8 demonstrates that this algorithm works for circular targets of various sizes from 6–mm to 88 mm in diameter. Even with one of the most difficult challenges, imaging numerous targets of differing size and locations, Figure 8.9 shows that the targets can be imaged if the correct contrast ratio is utilized.

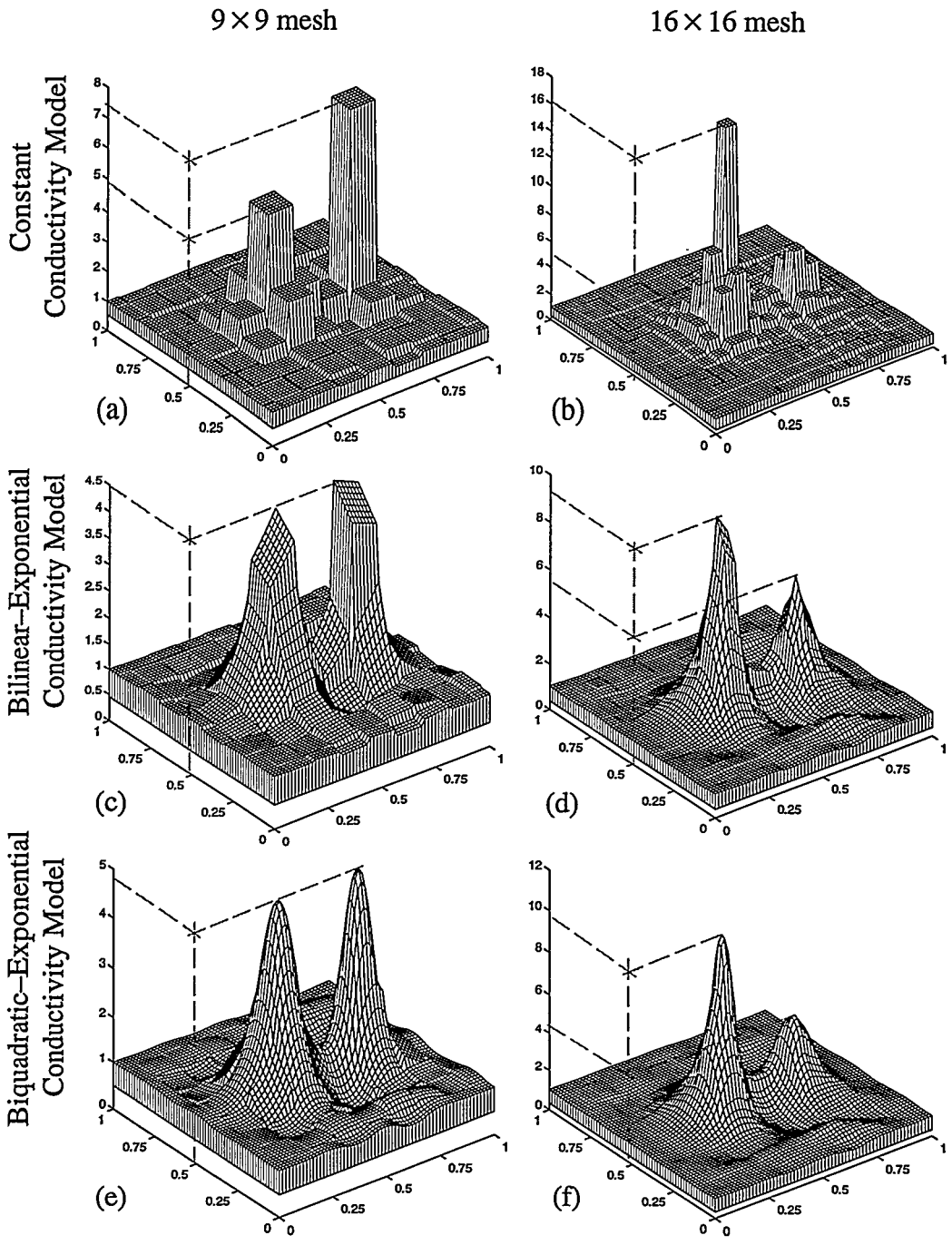

Figure 8.2 Comparison of element conductivity shape functions; (a), (b) constant: (c), (d) bilinear– and (e), (f) biquadratic–exponential schemes.

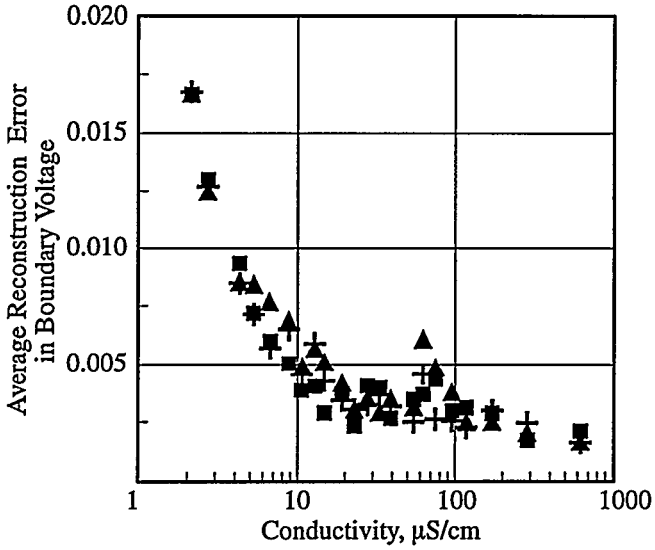

Figure 8.3 Liquid conductivity effect on reconstruction error.

10. Numerous different methods were utilized to improve experimental measurements. Some of the most significant include:

    - increasing the number of single–pair electrode excitations up to a point;
    - increasing the number of electrodes;
    - using multiple simultaneous excitations of electrodes rather than sequential single–pair excitation;
    - using the Preconditioned Voltage Conversion (PVC) method to correct noise and modeling errors. In many cases made the difference between obtaining a good image and no image at all;
    - using *post–facto* boundary measurement optimization to increase sensitivity of measurements.
    - correcting for quasi–three–dimensional effects in two–dimensional reconstructions using finite–length, boundary–electrode elements and a new layer model.

11. Use of Walsh–function excitations patterns (alternate, plus/minus, constant amplitude, electrode excitation) not only yielded superior results compared with single–

Figure 8.4 Two–target case of Fig. 8.2 showing relief and contour relative conductivity maps.

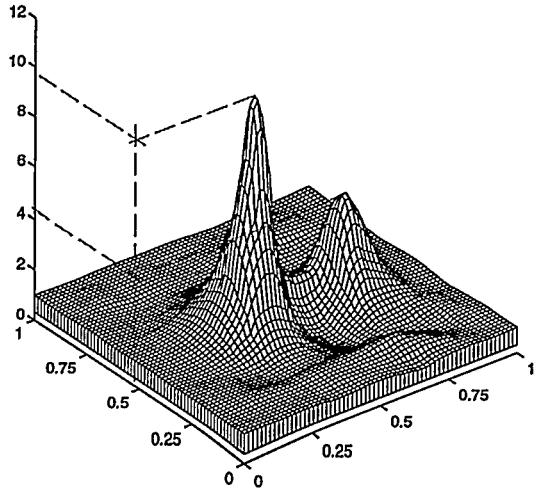

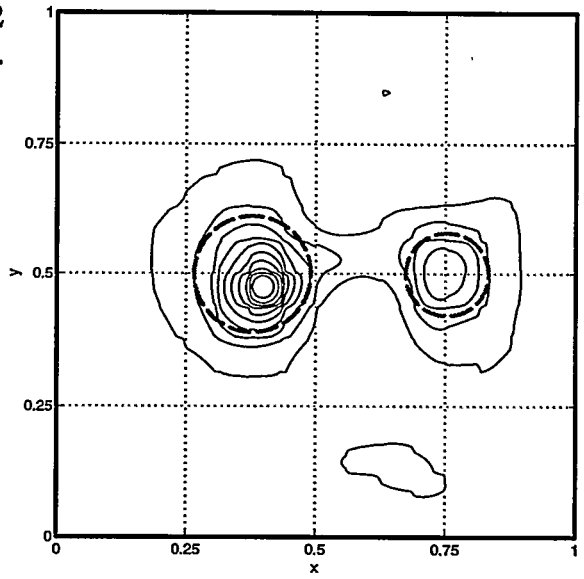

Figure 8.5 Correlation of differential discrimination level for individual targets taken from multiple–target images: ● 2–D data; ◆ 3–D cylinder data; ▲ 3–D flask data; × 3–D sphere data (60–mm and 115–mm diameter).

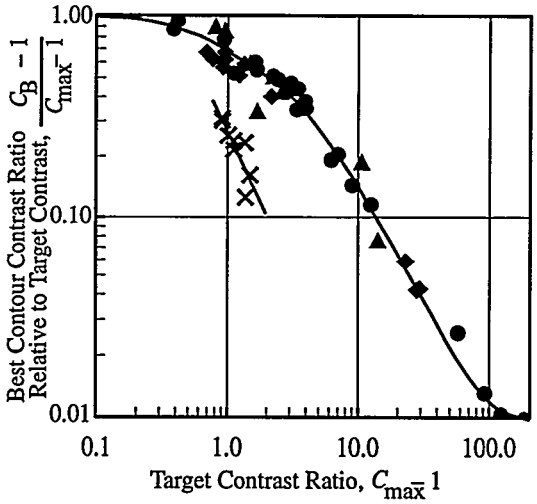

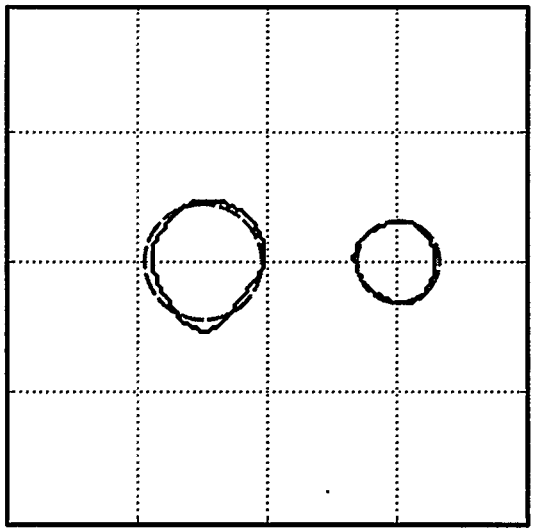

Figure 8.6 Application of best contour result from Fig. 8.6 as applied to the two–target case of Fig. 8.2.

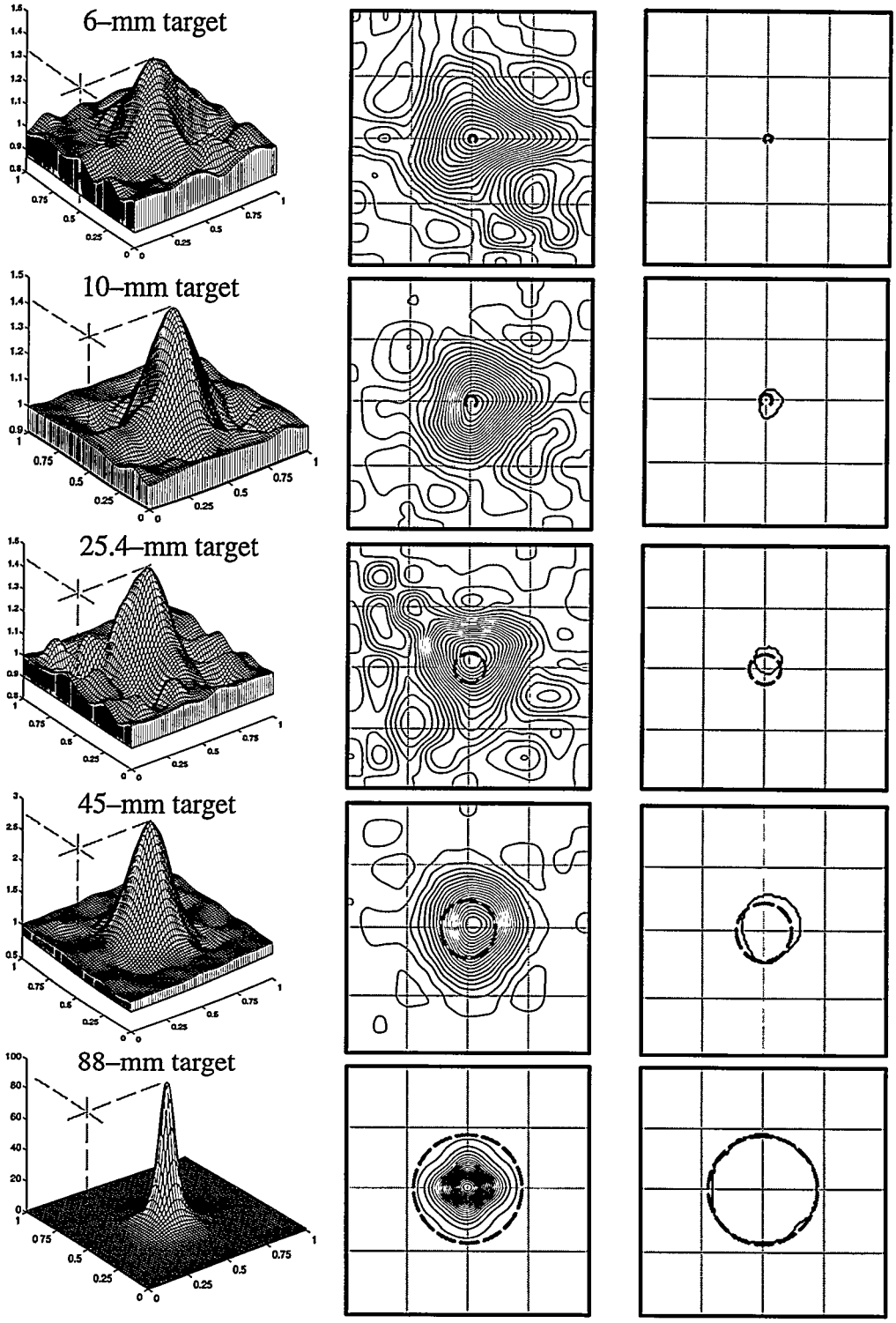

Figure 8.7 Relief, contour and best contour relative resistivity plots for distinguishability tests on centrally–located circular targets. Dashed grey scale circles depict actual target size and location.

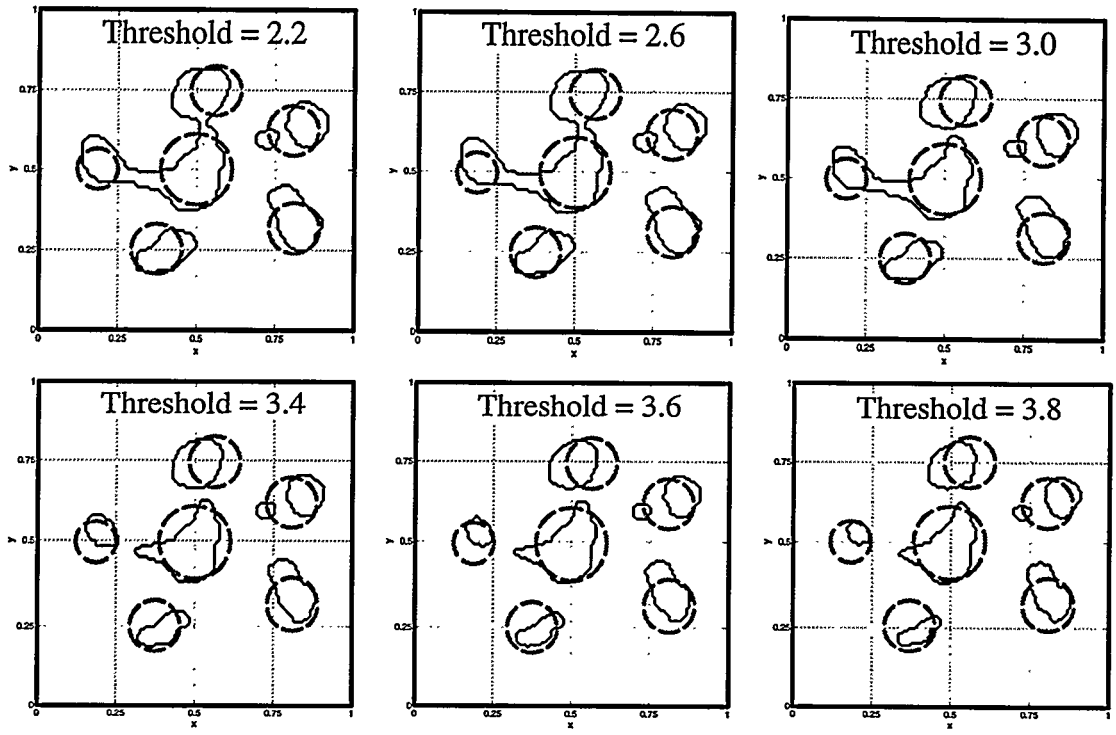

Figure 8.8 Best contour algorithm applied to six targets of differing size using differing contrast threshold: 2.2, 2.6, 3.0, 3.4, 3.6 and 3.8.

pair excitation acquired in the same amount of time, but also allowed phantom conductance matrices to be computed more accurately.

12. Plate electrodes were consistently better than rod electrodes in producing quality, low–noise images, the former failing in many instances to produce anything acceptable or simply failing to produce any converged image. Figure 8.10 depicts typical results comparing the two test geometries.

13. Multiple targets which are very close together or touching may not be separated in the image but the degree of separation required for separation is small as shown in Fig. 8.11.

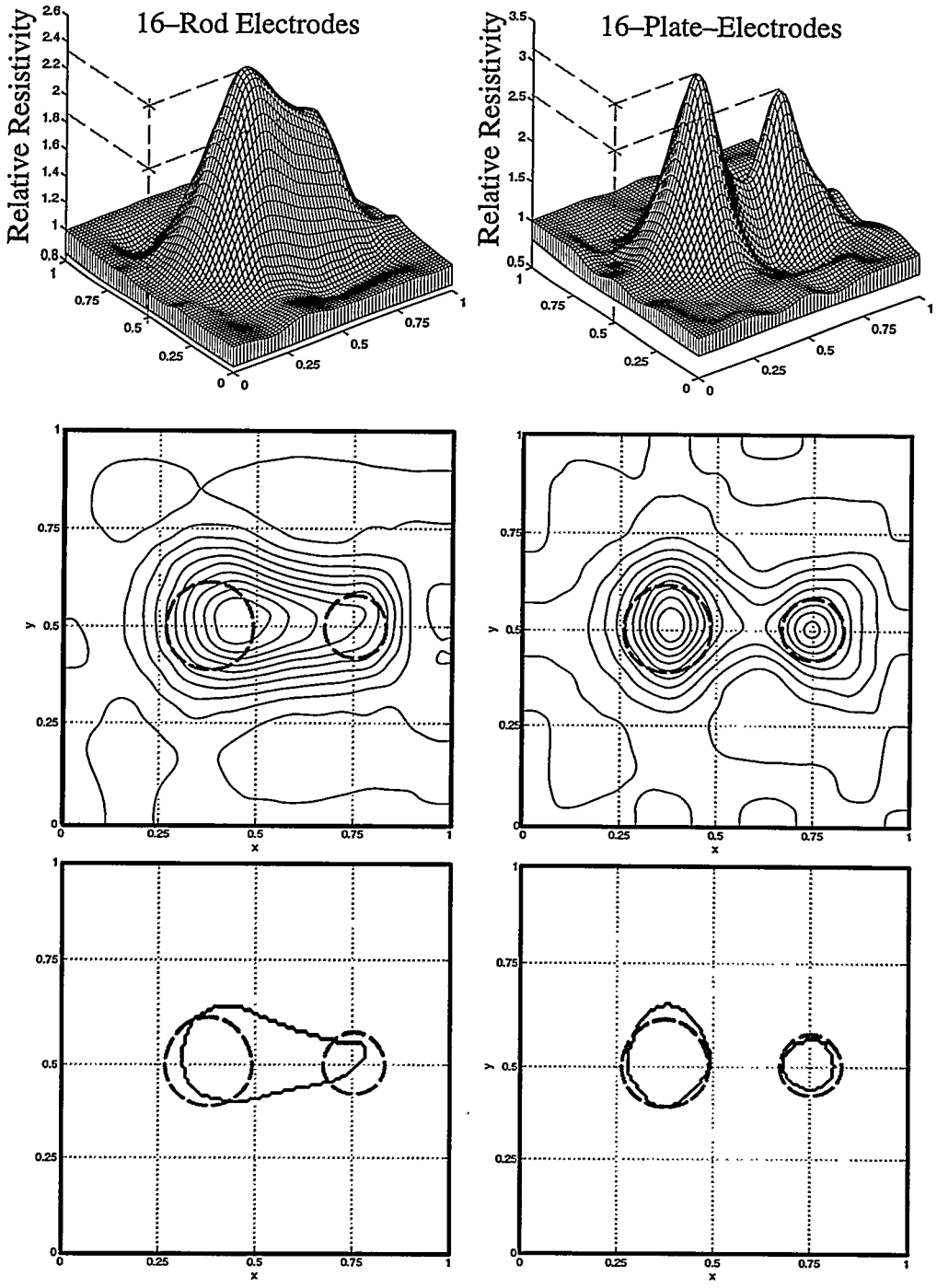

Figure 8.9 Relief, contour and best contour plots for the two–target case shown in Fig. 8.2 comparing the 16–rod–electrode phantom (left column) and the 16–plate–electrode phantom.

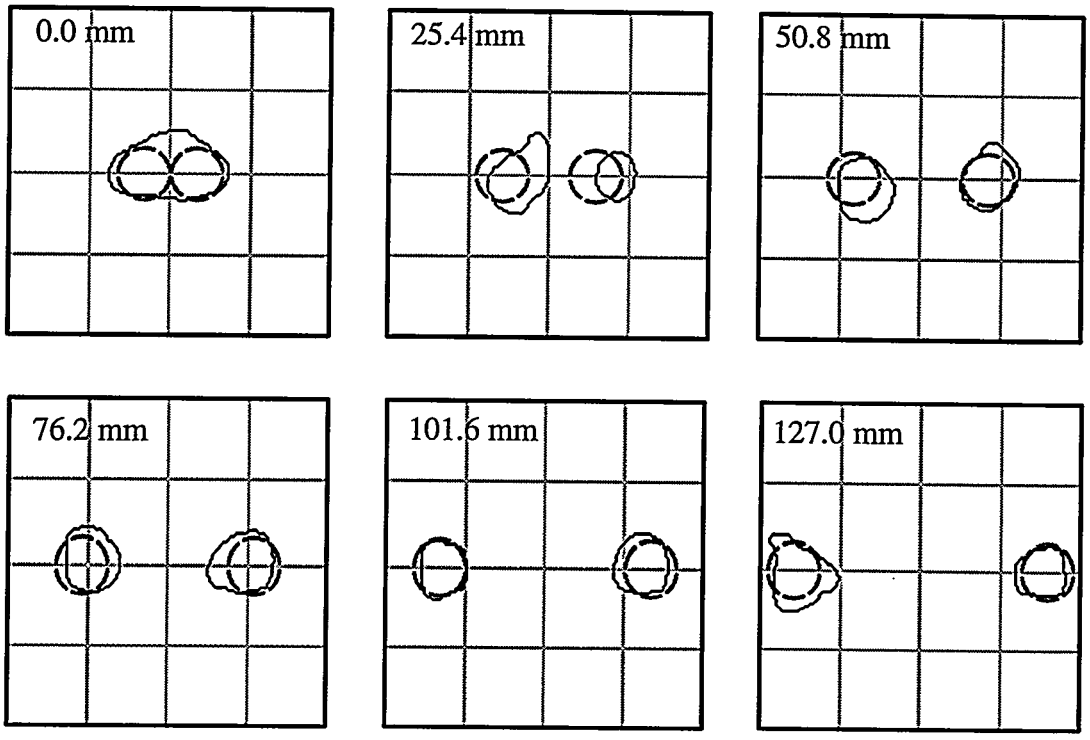

Figure 8.10 Horizontal distinguishability test results for various amounts of separation.

14. While strictly applicable only to two–dimensional or quasi–three–dimensional situations, images were obtained of two spherical targets shown in Fig. 8.12, the contours being flattened due to three–dimensional current flow not accounted for in the model.

15. The first, crude images of a moving target were obtained showing that sequential slicing of a three–dimensional target (Fig. 8.13) may be possible to build three–dimensional images.

16. In comparison with other electrical impedance imaging methods described in the literature, it is concluded that the finite element model, among of all those known and examined to date, provides the best possibility of those currently in existence of yielding the best quality (size, shape and position of targets) impedance images of binary media.

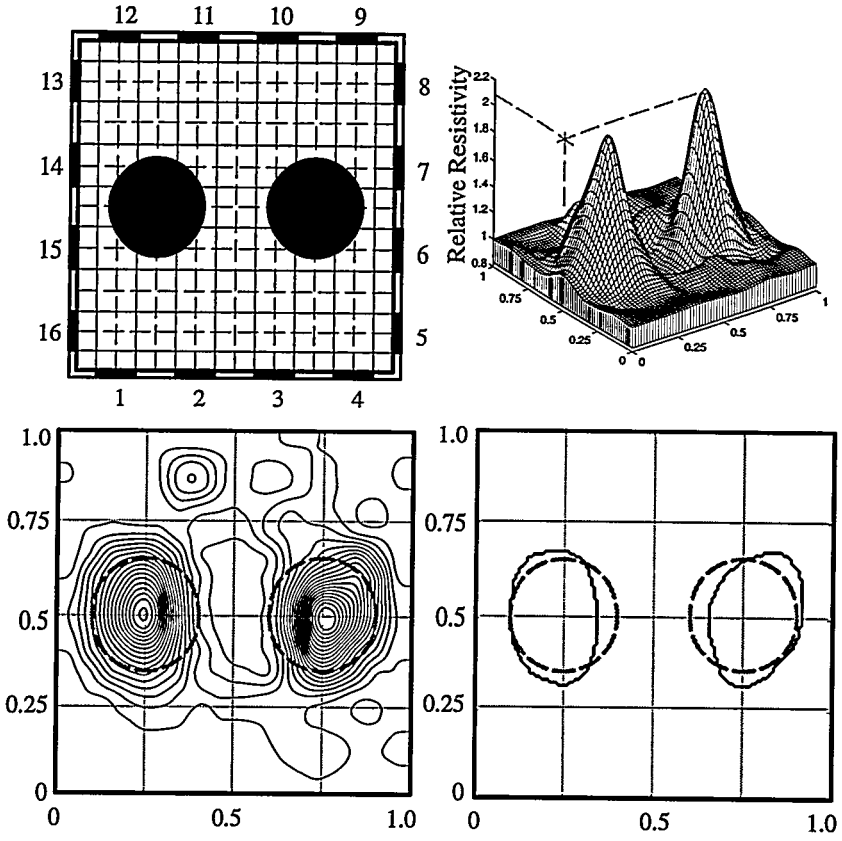

Figure 8.11 Image of two 60–mm diameter spheres centered vertically in the imaging plane of the three–dimensional phantom.

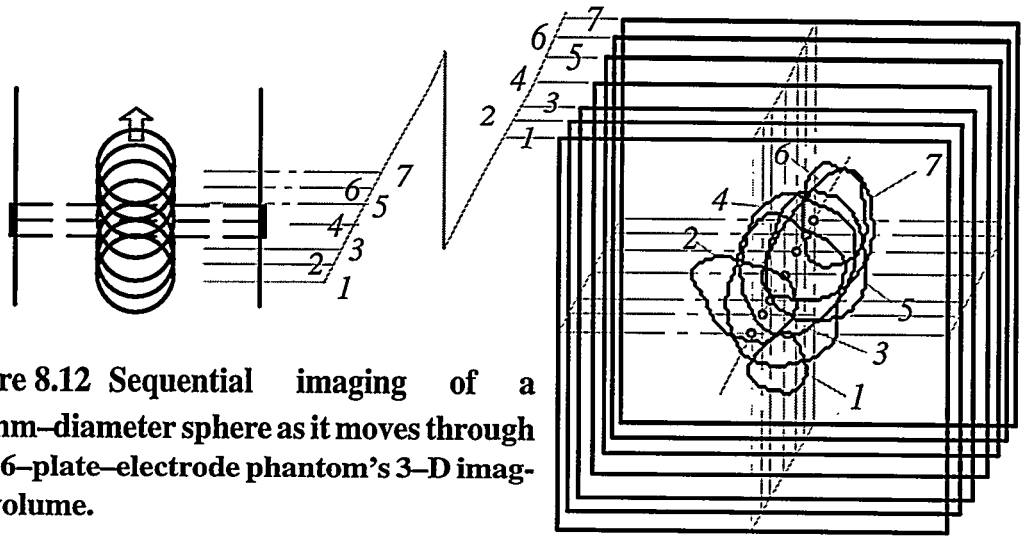

Figure 8.12 Sequential imaging of a 60–mm–diameter sphere as it moves through the 16–plate–electrode phantom's 3–D imaging volume.

17. It is further concluded that the finite element model has limitations which will mean its ultimate replacement by a true binary field model where the limitations associated with best contour algorithms no longer limit the accuracy of the results.

18. In general, it is concluded that the information necessary to obtain accurate images of three–dimensional binary media is available using electrical impedance imaging methods described herein, and that these methods should allow image framing rates of at least 1000 images per second using relatively inexpensive electronics. Faster imaging should be possible limited only by the cost and accuracy of available high–speed data acquisition hardware.

8.4 RECOMMENDATIONS FOR FUTURE WORK

The research undertaken in electrical impedance imaging (EII) has put the Rensselaer Multiphase Imaging Laboratory at the forefront of the low–cost imaging field with capabilities which in most cases far surpass those currently extant. However, there is still much left to be done for the goal of using EII for interfacial reconstruction of gas–liquid flows to become a reality. It is recommended that future research should place the emphasis particularly on software development, and design of a high–speed data acquisition system. In the near term, the finite element model will be the work house of electrical impedance imaging in this field. For liquid–gas system imaging, a truly three–dimensional result will ultimately be needed and this will probably require one of the new generation of vector machines. This section outlines major developmental items which are necessary to further improve performance of the finite element schemes and iterative reconstruction schemes.

8.4.1 Two–Dimensional, Continuous Conductivity Model

8.4.2 Generalized geometry

This research report presents a detailed summary of the exponential finite element scheme for rectangular or brick elements. These elements however are limited to accurately representing only rectangular geometries. The first recommendation is to:

1. *Extend the exponential finite element scheme to quadrilateral (2–D) and/or tetrahedral or hexahedral (3–D) elements to represent more general boundary geometries.*

8.4.3 Adaptive mesh

Although the biquadratic–exponential conductivity function does not represent the most general case, this model has probably reached its ultimate limit of applicability. Because of the criterion which is necessary for obtaining a closed form solution to the potential function inside each element, exponential functions are very attractive because of both their separability in each coordinate direction and their ability to approximate discontinuity in conductivity variations. Considering a bicubic or a higher order exponential model is not recommended because closed solutions for such models do not exist. Rather, the conductivity distribution could be first estimated by using the existing block decomposition algorithm, and then the mesh coordinates could be moved to the contours where very rapid conductivity variations occur.

2. *Develop an adaptive, mesh–moving scheme which can place element boundaries along the edges of "large" discontinuities in the field.*

8.4.4 Reactive–continuum modeling

Since only continuous conducting media are considered herein, such media being in electrical contact with the boundary, the ultimate extension to this method will involve the ability to completely image a field where the continuum may, in fact, be nonconducting. This would be enabling for imaging of resistive media surrounded by purely reactive media. Therefore, the recommendation is to:

3. *Extend the methods developed to consider both the resistive and reactive parts of the electrical field to enable the entire field to be determined under circumstances where the reactive field surrounds or contains, at least in part, the resistive field.*

8.4.5 Three–Dimensional, Continuous Conductivity Model

8.4.6 Variable–conductivity layer model

The original idea in developing the layer reduction method was to provide reconstructions from a single scan. However, a single scan data set does not contain the conductivity information in layers below and above the scanning plane and so variable conductivity in the axial dimension could not be considered. While this was adequate for three–dimensional objects having slowly varying axial conductivity, it was not adequate where the variations were large or rapid. Thus, although successful results were obtained for 60–mm–diameter spherical targets, this method did not produced the same successful results when smaller spherical targets such as 32–mm–diameter spheres were used. Therefore, the next step should:

4. *Improve element conductivity model (in brick or quadrahedral elements) which can also model conductivity variation in the phantom's axial direction (z–direction).*

8.4.7 Automatic Tomographic Capability

The development of three–dimensional imaging methods has as its goal the computation of true tomographs using slices which can then be pieced together to display the whole field. Such layering tomography is characteristic of every tomographic method currently in existence such as magnetic resonance and x–ray tomography methods. Whether approximate three–dimensional methods are used or true three–dimensionality is developed, slice tomography must be developed. Therefore:

5. *Automate the layer reduction method to develop a three–dimensional, slice–by–slice, tomographic and three–dimensional reconstruction capability which uses multiple–scan data acquired in successive time intervals as the conductivity field passes through the scanning plane.*

8.4.8 True Three–Dimensional Model

Faster, more powerful computers continue to become available. The limiting factor for using currently reported methods in three–dimensions was the 3.3 power variation of computer time and storage required as the size of the model gets larger. Thus, taking a 16 x 16 model into the third dimension by the same factor increase the compute time by approximately 10,000 times. The availability of new vector machines having large numbers of parallel processors, coupled with further improvements and innovations, may make true three–dimensional imaging possible. Therefore,

6. *Begin development of both software and hardware for a truly three–dimensional imaging FEM system adapting the current methodology to advanced, high speed, vector computers.*

8.4.9 True binary modeling

In the longer term, a true three–dimensional model which can handle a combination of continuous and discontinuous conductivities will be required. The continuous field capability will be needed where imbedded discontinuities are so small as to make the field a quasi–homogeneous mixture such as a froth, foam or slurry. The discontinuous field is required to image large imbedded discontinuities such as large bubbles in a foam or slurry, or large liquid masses or columns imbedded in a gaseous continuum such as inverted annular flow. The size of discrete elements is a consideration because it is generally where the elements are large that they present impediments to interfacial energy or momentum transfer. Otherwise, discrete elements simply make the flow appear as homogeneous with mixture properties somewhere between those of the continuum and discrete phase.

Such a model was attempted early on in the research program being discussed but was found to be inherently unstable within the confines of our FE model due in part to the lack of coincidence of the phase boundaries with the element boundaries. However, in the long run, this type of computational system will be required and its implementation will immediately eliminate the necessity of heuristic algorithms such as the best contour method of shape determination. Thus, under conditions where the discreteness is both important and limiting in some form of multiphase behavior, the last two recommendations are:

7. *Develop a true binary model using piecewise analytic solutions for potential field variations near electrode and conductivity field discontinuities occur.*

8. *Develop a combination model which can handle both fields with a variable conductivity continuum and discontinuous fields capable of handling pure conductors or pure insulators.*

REFERENCES

[1] Roy, D. N. G., *Methods of Inverse Problems in Physics*, CRC Press, Boca Raton, FL, 1991.

[2] Ovacik, L., *Extensions To The Finite Element Method For The Analysis Of Inverse Problems In Electromagnetic Devices*, PhD thesis, Rensselaer Polytechnic Institute, Troy, New York, 1998.

[3] Glasko, V. B., *Inverse Problems of Mathematical Physics*, Translated by A. Bincer, American Institute of Physics (AIP), New York, NY, 1988.

[4] Hadamard, J. S., *Lectures on Cauchy's Problem in Linear Partial Differential Equations*, Dover Publications, New York, NY, 1952.

[5] Baumeister, J., *Stable Solution of Inverse Problems*, Friedr. Vieweg and Sohn, Braunschweig, Germany, 1987.

[6] Tikhonov, A. N., and Goncharsky, A. V. (Editors), *Ill–Posed Problems in the Natural Sciences*, MIR Publishers, Moscow, U.S.S.R., 1987.

[7] Sakagami, T., Kubo, S., and Ohji, K., "A Hierarchical Inversion Scheme for Reconstructing a Three–Dimensional Internal Crack from an Electric Potential Distribution," *Int. J. Pres. Ves. & Piping*, Vol. 44, 1990, pp. 35–47.

[8] Kubo, S., and Ohji, K., "Identification of a Source Crack in a Pipe Using Data Base of Electric Potential Distribution," *Proc. 6th Int. Conf.*, Pergamon Press, Kyoto, Japan, July/August 1991, pp. 717–722.

[9] Hoole, S. R. H., Subramaniam, S., Saldanha, R., Coulomb, J. L. and Sabonnadiere, J. C., "Inverse Problem Methodology and Finite Elements in the Identification of Cracks, Sources, Materials, and Their Geometry in Inaccessible Locations," *IEEE Trans. Mag.*, Vol. 27, No. 3, May 1991, pp. 3433–3443.

[10] Dines, K. A., and Lytle, R. J., "Analysis of Electrical Conductivity Imaging," *Geophysics,* Vol. 46, 1981, pp. 1025–1036.

[11] Price, L. R., "Electrical Impedance Computed Tomography (ICT): A New CT Imaging Technique," *IEEE Trans. Nucl. Sci.*, Vol. 26, No. 2, April 1979, pp. 2736–2739.

[12] Barber, D. C., and Brown, B. H., "Applied Potential Tomography," *J. Phys. E: Sci. Instrum.*, Vol. 17, 1984, pp. 723–733.

[13] Barber, D. C., and Brown, B. H., "Recent Developments in Applied Potential Tomography–APT," *Proc. 9th Int. Conf. Inform. Med. Imag*, Washington, D.C., June 1985, pp. 106–121.

[14] Seagar, A. D., Barber, D. C., and Brown, B. H., "Electrical Impedance Imaging," *IEE Proc.*, Vol. 134, Pt. A, No. 2, 1987, pp. 201–210.

[15] Yorkey, T. J., *Comparing Reconstruction Methods for Electrical Impedance Tomography*, Ph.D. Thesis, Department of Electrical Computer Engineering, University of Wisconsin, Madison, WI, August 1986.

[16] Yorkey, T. J., "Electrical Impedance Tomography with Piecewise Polynomial Condutivities," *J. Comp. Phys.*, Vol. 91, 1990, pp. 344–360.

[17] Yorkey, T. J., Webster, J. G., and Tompkins, W. J., "An Optimal Impedance Tomographic Reconstruction Algorithm," *Proc. 8th Annu. Int. Conf. IEEE Eng. Med. Biol. Soc.*, 1986, pp. 339–342.

[18] Yorkey, T. J., Webster, J. B., and Tompkins, W. J., "Errors Caused by Contact Impedance in Impedance Imaging," *Proc. 7th Annu. Int. Conf. IEEE Eng. Med. Biol. Soc.*, 1985, pp. 632–637.

[19] Yorkey, T. J., and Webster, J. G., "A Comparison of Impedance Tomographic Reconstruction Algorithms," *Clin. Phys. Physiol. Meas.*, Vol. 8, suppl. A, 1987, pp. 55–62.

[20] Yorkey, T. J., Webster, J. G., and Tompkins, W. J., "An Improved Perturbation Technique for Electrical Impedance Imaging with Some Criticisms," *IEEE Trans. Biomed. Eng.*, Vol. 34, No. 11, November 1987, pp. 898–901.

[21] Yorkey, T. J., Webster, J. G., and Tompkins, W. J., "Comparing Reconstruction Algorithms for Electrical Impedance Tomography," *IEEE Trans. Biomed. Eng.*, Vol. 34, No. 11, November 1987, pp. 843–852.

[22] Cheney, M., Isaacson, D., Newell, J. C., Simske, S. and Goble, J., "NOSER: An Algorithm for Solving Inverse Conductivity Problem," *Int. J. Imag. Sys. and Tech.*, Vol. 2, 1990, pp. 66–75.

[23] Fuks, L. F., *Reactive Effects in Impedance Imaging*, PhD Thesis, Department of Electrical and Computer Systems Engineering, Rensselaer Polytechnic Institute, Troy, NY, May 1989.

[24] Fuks, L. F., Cheney, M., Isaacson, D., Gisser, D. G., and Newell, J. C., "Detection and Imaging of Electrical Conductivity and Permittivity at Low Frequency," *IEEE Trans. Biomed. Eng.,* Vol. 38, No. 11, November 1991, pp. 1106–1110.

[25] Hua, P., *Modeling and Reconstruction Methods for Electrical Impedance Tomography*, PhD Thesis, Department of Electrical and Computer Engineering, University of Wisconsin, Madison, WI, 1990.

[26] Hua, P., Woo, E. J., Webster, J. G., and Tompkins, W. J., "Iterative Reconstruction Methods Using Regularization and Optimal Current Patterns in Electrical Impedance Tomography," *IEEE Trans. Med. Imag.,* Vol. 10, No. 4, December 1991, pp. 621–628.

[27] Hua, P., Woo, E. J., Webster, J. G., and Tompkins, W. J., "Improved Methods to Determine Optimal Currents in Electrical Impedance Tomography," *IEEE Trans. Med. Imag.,* Vol. 11, No. 4, December 1992, pp. 488–495.

[28] Hua, P., Woo, E. J., Webster, J. G., and Tompkins, W. J., "Using Compound Electrodes in Electrical Impedance Tomography," *IEEE Trans. Biomed. Eng.,* Vol. 40, No. 1, January 1993, pp. 29–34.

[29] Hua, P., Woo, E. J., Webster, J. G., and Tompkins, W. J., "Finite Element Modeling of Electrode–Skin Contact Impedance in Electrical Impedance Tomography," *IEEE Trans. Biomed. Eng.,* Vol. 40, No. 4, April 1993, pp. 335–343.

[30] Woo, E. J., *Finite Element method and Reconstruction Algorithms in Electrical Impedance Tomography*, PhD Thesis, Department of Electrical and Computer Engineering, University of Wisconsin, Madison, WI, August 1990.

[31] Woo, E. J., Hua, P., Webster, J. G., and Tompkins, W. J., "Measurung Lung Resistivity Using Electrical Impedance Tomography," *IEEE Trans. Biomed. Eng.*, Vol. 39, No. 7, July 1992, pp. 756–760.

[32] Woo, E. J., Hua, P., Webster, J. G., Tompkins, W. J., and Pallas–Areny. R., "Walsh Function Current Patterns and Data Synthesis for Electrical Impedance Tomography," *IEEE Trans. Med. Imag.,* Vol. 11, No. 4, December 1992, pp. 554–559.

[33] Starzyk, J. A., and Dai, H., "Element Evaluation in the Resistive Networks," *Proc. 28th Midwest Symp. Circuits Systems,* Louisville, KY, 1985, pp. 178–181.

[34] Santosa, F., and Vogelius, M., "A Backprojection Algorithm for Electrical Impedance Imaging," *Technical Note, BN–1081*, Institute for Physical Science & Technology, Univ. of Maryland, Collage Park, MD, July 1988.

[35] Huang, S. M., Stott, A. L., Green, R. G. and Beck, M. S., "Electronic Transducers for Industrial Measurement of Low Value Capacitances," *J. Phys. E: Sci. Instrum.*, Vol. 21, 1988, 242–250.

[36] Beck, M., and Williams, R., "Looking into Process Plant," *The Chem. Eng.*, No. 478, July 1990, pp. 14–15.

[37] Wexler, A., Fry, B., and Neiman, M. R., "Impedance–Computed Tomography Algorithm and System," *Appl. Opt.,* Vol. 24, No. 23, 1985, pp. 3985–3992.

[38] Kohn, R. V., and McKenney, A., "Numerical Implementation of a Variational Method for Electrical Impedance Tomography," *Courant Institute of Mathematical Sciences*, private communication, New York, NY, 1989.

[39] Kim, Y., Tompkins, W. J., and Webster, J. G., "Medical Body Imaging Using Electrical Impedance and Nonlinear Reconstruction," *Ann. Northwest Bioeng. Conf.*, Vol. 10, 1982, pp. 298–303.

[40] Kim, Y., Webster, J. G., and Tompkins, W. J., "Electrical Impedance Imaging of the Thorax," *J. Microwave Power,* Vol. 18, No. 3, 1983, pp. 245–257.

[41] Akaike, H., "A New Look at Statistical Model Identification," *IEEE Trans. Auto. Cont.*, Vol. 19, No. 6, December 1974, pp. 716–723.

[42] Murai, T., and Kagawa, Y., "Electrical Impedance Computed Tomography Based on a Finite Element Model," *IEEE Trans. Biomed. Eng.*, Vol. 32, No. 3, March 1985, pp. 177–184.

[43] Murai, T., and Kagawa, Y., "Boundary Element Iterative Techniques for Determining the Interface Boundary Between Two Laplace Domains–a Basic Study of Impedance Plethysmography as an Inverse Problem," *Int. J. Num. Meth. Eng.*, Vol. 23, No. 1, 1986, pp. 35–47.

[44] Kagawa, Y., Murai, T., and Matsumoto, O., "Finite Element Iterative Technique for Determining the Interface Boundary Between Laplace and Poisson Domains–Characteristic Analysis of Field Effect Transistor," *Int. J. Num. Meth. Eng.,* Vol.19, 1983, pp. 315–329.

[45] Jones, O. C., Lin, J. T., and Ovacik, L., "Investigation of Electrical Impedance Imaging for Two–Phase, Gas–Liquid Flows," *Chem. Eng. Comm.*, Vol. 118, 1992, pp. 299–325.

[46] Jones, O. C., Lin, J. T., Ovacik, L. and Shu, H., "Impedance Imaging Relative to Gas–Liquid Systems," *Nucl. Eng. Design,* Vol. 141, 1993, pp 159–176.

[47] Jones, O. C., "Developments in Impedance Imaging of Two–Phase Flows," *Pro. Int. Conf. on Multiphase Flows.* Tsukuba, Japan, September 1991, pp. 24–27.

[48] Jones, O.C., Lin, J. T., and Ovacik, L., "Electrical Impedance Imaging in Two–Phase, Gas–Liquid Flows: 1. Initial Investigation," *Pro. Int. Conf. on Inverse Design Concepts and Optimization in Engineering Sciences–III,* Washington, DC, October 1991, pp. 111–122.

[49] Lin, J. T., Suzuki, H., Ovacik, L., Jones, O. C., Newell, J. C., and Cheney, M., "Use of Electrical Impedance Imaging in Two–phase, Gas–Liquid flows," *Proc. 7th Annu. Rev. of Prog. in Appl. Computational Electromagnetics,* U. S. Naval Postgraduate School, Monterey, CA, March 1991, pp. 18–22.

[50] Lin, J. T., Ovacik L., Jones, O. C., and Newell, J. C., and Cheney, M., and Suzuki, H., 1991, "Use of Electrical Impedance Imaging in Two–Phase, Gas–Liquid flows," *1991 National Heat Transfer Conference,* Minneapolis, July 1991, pp. 28–31.

[51] Kohn, R.V., and Vogelius, M., "Relaxation of a Variational Method for Impedance Computed Tomography," *Comm. Pure Appl. Math.,* Vol. 40, 1987, pp. 745–777.

[52] Newell, J. C., Gisser, D. G., and Isaacson, D., "An Electric Current Tomograph," *IEEE Trans. Biomed. Eng.*, Vol. 35, No. 10, October 1988, pp. 828–833.

[53] Isaacson, D., and Cheney, M., "Current Problems in Impedance Imaging," *Inverse Problems in Partial Differential Equations*, D. Coliton, R. Ewing, and W. Rundell, (Editors), SIAM, Philadelphia, PA, 1990, pp. 141–148.

[54] Cheng, K. –S., Isaacson, D., Newell, J. C., and Gisser, D. G.,"Electrode Models for Electric Current Computed Tomography," *IEEE Trans. Biomed. Eng.,* Vol. 36, No. 9, September 1989, pp. 918–924.

[55] Isaacson, D., "Distinguishability of Conductivities by Electric Current Computed Tomography," *IEEE Trans. Med. Imag.*, Vol. 5, No. 2, June 1986, pp. 91–95.

[56] Gisser, D. G., Isaacson, D., and Newell, J. C., "Current Topics in Impedance Imaging," *Clin. Phys. Physiol. Meas.*, Vol. 8, Suppl. A, 1987, pp. 39–46.

[57] Goodenough, D., and Weaver K. E., "Overview of Computed Tomography," *IEEE Trans. Nucl. Sci.*, Vol. 26, No. 1, February 1979, pp. 1662–1667.

[58] Valk, J., MacLean, C., and Algra, P. R., *Basic Principles of Nuclear Magnetic Resonance Imaging*, Elsevier Science Publications, The Netherlands, 1985.

[59] Robb, R. A., *Three–Dimensional Biomedical Imaging,* Vol. I–II, CRC Press, Boca Raton, FL. 1985.

[60] Kak, A. C., and Slaney, M., *Principles of Computerized Tomographic Imaging*, IEEE Press, New York, NY, 1988.

[61] Cho, Z. H., Jones, J. P., and Singh, M., *Foundations of Medical Imaging*, John Wiley & Sons, New York, NY, 1993.

[62] Pfister, G., Schatz A. K., and Siegel, C., "Nondestructive Testing of Materials and Components by Computerized Tomography with Fast and Thermal Reactor Neutrons," *Nucl. Sci. Eng.*, Vol. 110, 1992, pp. 303–315.

[63] Hussein, E. M. A, and Meneley, D. A., "Single–Exposure Neutron Tomography of Two–Phase Flow," *Int. J. Multiphase Flow*, Vol. 12, No. 1, 1986, pp. 1–34.

[64] Hussein, E. M. A, Meneley, D. A., and Banerjee, S., "On the Solution of the Inverse Problem of Radiation Scattering Imaging," *Nucl. Sci. Eng.*, Vol. 92, 1986, pp. 341–349.

[65] Halow, J. S., Fashing, G.E., and Nicoletti, P., "Preliminary Capacitance Imaging Experiments of a Fluidized Bed," *Proc. AIChE Sym. Ser.,* Vol. 86, No. 276, 1990, pp. 41–50.

[66] Huang, S., *Capacitance Transducers for Concentration Measurement in Multi–Component Flow Processes*, Ph.D. Thesis, Department of Instrumentaiton and Analytical Science, UMIST, Manchester, U.K., 1986.

[67] Huang, S. M., Plaskowski, A. B., Xie, G. C., and Beck, M. S., "Tomographic Imaging of Two–Component Flow using Capacitance Sensors," *J. Phys. E: Sci. Instrum.*, Vol. 22, 1989, pp. 173–177.

[68] Huang, S. M., Xie, C. G., Thorn, R., Snowden, D., and Beck, M. S., "Design of Sensor Electronics for Electrical Capacitance Tomography," *IEE Proc. G, Electron. Circuits & Syst.*, Vol. 139, No. 1, February 1992, pp. 83–88.

[69] Xie, C. G., Plaskowski, A., and Beck, M. S., "8–Electrode Capacitance System for Two–Component Flow Identification. Part 1: Tomographic Flow Imaging," *Science,* Vol. 136, Suppl. A, No.4, 1989, pp. 173–183.

[70] Xie, C. G., Plaskowski, A., and Beck, M. S., "8–Electrode Capacitance System for Two–Component Fluid Flow Identification, Part 2: Tomographic Flow Imaging," *IEE Proc.*, Pt. A., Vol. 136, No. 4, July 1989, pp. 184–190.

[71] Xie, C. G., Huang, S. M., Hoyle, B. S., Thorn, R., Lenn, C., Snowden, D. and Beck, M. S., "Electrical Capacitance Tomography for Flow Imaging: System Model for Development of Image Reconstruction Algorithms and Design of Primary Sensors," *IEE Proc. G, Electron. Circuits & Syst.*, Vol. 139, No. 1, 1992, pp. 89–98.

[72] Shi, T. M., Xie, C. G., Huang, S. M., Williams, R. A., and Beck, M. S., "Capacitance–Based Instrumentation for Multi–Interface Level Measurement," *Meas. Sci. Technol.*, Vol. 2, 1991, pp. 923–933.

[73] Dickin, F. J., Zhao, X. J., Abdullah M. Z., and Waterfall, R. C., "Tomographic Imaging of Industrial Process Equipment Using Electrical Impedance Sensors," *Proc. 5th Conf. Sensors and Their Applications*, Edinburg, Scotland, September 1991, pp. 215–220.

[74] Dickin, F. J., Hoyle, B. S., Hunt, A., Huang, S. M., Ilyas, O., Lenn, C., Waterfall, R. C., Williams, R. A., Xie, C. G., and Beck, M.S., " Tomographic Imaging of Industrial Process Equipment–Review of Needs and Methods," *Proc. 5th Conf. Sensors and Their Applications*, Edinburg, Scotland, September 1991, pp. 191–196.

[75] Dickin, F. J., Hoyle, B. S., Hunt, A., Huang, S. M., Ilyas, O., Lenn, C., Waterfall, R. C., Williams, R. A., Xie, C. G. and Beck, M. S., "Tomographic Imaging of Industrial Process Equipment: Techniques and Applications," *IEE Proc. G, Electron. Circuits & Syst.*, Vol. 139, No. 1, 1992, pp. 72–82.

[76] Griffiths, H., "The Importance of Phase Measurement in Electrical Impedance Tomography," *Phys. Med. Biol.*, Vol. 32, No. 11, 1987, pp. 1435–1444.

[77] Webster, J. G. (Editor), *Electrical Impedance Tomogrphy*, Adam Hilger, New York, NY, 1989.

[78] Gisser, D. G., Isaacson, D., and Newell, J. C., "Electric Current Computed Tomography and Eigenvalues," *SIAM J. Appl. Math.*, Vol. 50, No. 6, 1990, pp. 1623–1634.

[79] Bradshaw, M. D. and Byatt, W. J., *Introductory Engineering Field Theory*, Prentice–Hall, Englewood Cliffs, NJ, 1967.

[80] Uhlmann, G., "Inverse Boundary Value Problems for First Order Perturbations of the Laplacian" *1993 AMS–SIAM Summer Seminar on the Mathematics of Tomography, Impedance Imaging and Integral Geometry, June 7–18, 1993, Mount Holyoke College, Massachussetts,* E. T. Quinto, M. Cheney, and P. Kuchment (Editors), American Mathematical Society: Providence, RI, Vol. 30, 1993, pp. 245–258.

[81] Isakov, V., "On Uniqueness in the Inverse Conductivity Problem with ne Boundary Measurement," *1993 AMS–SIAM Summer Seminar on the Mathematics of Tomography, Impedance Imaging and Integral Geometry, June 7–18, 1993, Mount Holyoke College, Massachussetts,* E. T. Quinto, M. Cheney, and P. Kuchment (Editors), American Mathematical Society: Providence, RI, Vol. 30, 1993, pp. 105–114.

[82] Barber, D. C., Brown, B. H., and Freeston, I. L., "Imaging Spatial Distributions of Resistivity using Applied Tomography," *Elec. Lett.*, Vol. 19, October 1983, pp. 933–935.

[83] Barber, D. C., and Brown, B. H., "Recent Developments in Applied Potential Tomography," *Information Processing in Medical Imaging,* S. Bacharach (Editor), 1986, pp. 446–462.

[84] Barber, D. C., and Seagar, A. D., "Fast Reconstruction of Resistance Images," *Clin. Phys. Physiol. Meas.*, Vol. 8, Suppl. A, 1987, pp. 47–54.

[85] Seagar, A. D., Barber, D. C., and Brown, B. H., "Theoretical Limits to Sensitivity and Resolution in Impedance Imaging," *Clin. Phys. Physiol. Meas.*, Vol. 8, Suppl. A, 1987, pp. 13–31.

[86] Eyuboglu, B. M., *Development and Application of Electrical Impedance Tomography for Thoracic Imaging,* PhD Thesis, Department of Medical Physics and Clinical Engineering, University of Sheffield, U.K., 1988.

[87] Santosa, F., and Vogelius, M., "A Backprojection Algorithm for Electrical Impedance Imaging," *SIAM J. Appl. Math.,* Vol. 50, No. 1, 1990, pp. 216–243.

[88] Breckon, W. R., and Pidcock, M. K., "Mathematical Aspects of Impedance Imaging," *Clin. Physiol. Meas.* Vol. 8, Suppl. A, 1987, pp. 77–84.

[89] Kotre, C. J., "A Sensitivity Coefficient Method for the Reconstruction of Electrical Impedance Tomograms," *Clin. Phys. Physiol, Meas.*, Vol. 10, 1989, pp 275–281.

[90] Ider Y. Z., Altan, C., Atalar, E., and Gencer N. G., "Electrical Impedance Imaging System Applicable to Objects of Arbitrary But Known Boundary," *Proc. 9th Annu. Int. Conf. IEEE Eng. in Med. and Bio. Soc.*, 1987, pp. 1427–1428.

[91] Kim, Y., and Woo, H. W., "A Prototype System and Reconstruction Algorithms for Electrical Impedance Techniques," *Clin. Physiol. Meas.* Vol. 8, Suppl. A, 1987, pp. 63–70.

[92] Lingenfelter, A. A., *Two Forward Solvers for Electric Current Computed Tomography,* M.S. Thesis, Rensselaer Polytechnic Institute, Troy, New York, NY, August 1988.

[93] Eggleston, M. R., Schwabe, R. J., Isaacson, D., and Coffin, L. F., "The Application of Electric Current Computed Tomography to Defect Imaging in Metals," Review of Progress in Quantitative NDE, Plenum Publishing, 1989.

[94] Jain, H., Isaacson, D., Edic, P. M., and Newell, J. C., "Electrical Impedance Tomgraphy of Complex Distributions with Noncircular Boundary," *IEEE Trans. Biomed. Eng.,* Vol. 44, No. 11, November 1997, pp. 1051–1060.

[95] Edic, P. M., Isaacson, D., Saulnier, G. J., Jain, H., and Newell, J. C., "An Iterative Newton–Raphson Method to Solve the Inverse Admittivity Problem," *IEEE Trans. Biomed. Eng.,* Vol. 45, No. 7, July 1998, pp. 899–908.

[96] Geselowitz, D. B., "An Application of Electrocardiographic Lead Theory to Impedance Plethysmography," *IEEE Trans. Biomed. Eng.*, Vol. 18, No. 1, January 1971, pp. 38–41.

[97] Stroud, A. H., and Secrest, D., *Gaussian Quadrature Formulas,* Prentice–Hall, Eaglewood Cliffs, NY, 1966.

[98] Eisele, J. A, and Mason, R. M., *Applied Matrix and Tensor Analysis*, Wiley–Interscience, New York, NY, 1970.

[99] Brewer, J. W., "Kronecker Products and Matrix Calculus in System Theory," *IEEE Trans. Circ. Sys.*, Vol. 25, No. 9, September 1978, pp. 772–781.

[100] Gupta, N. K., and Mehra, R. K., "Computational Aspects of Maximum Likelyhood Eastimation and Reduction in Sensitivity Function Calculations," *IEEE Trans. Auto. Cont.*, Vol. 19, No. 6, December 1974, pp. 774–783.

[101] Golub, G. H., and Van Loan C. F., *Matrix Computations*, Johns Hopkins University Press., Baltimore, MD, 1983.

[102] Gottfried, H. G., and Weisman, J., *Introduction to Optimization Theory*, Prentice Hall, Englewood Cliffs, NJ, 1973.

[103] Levenberg, K., "A Method for the Solution of Certain Non–Linear Problems in Least Squares," *Quart. Appl. Math.,* Vol. 2, 1944, pp. 164–168.

[104] Marquardt, D. W., "An Algorithm for Least–Squares Estimation of Nonlinear Parameters," *SIAM J. Appl. Math.* Vol. 11, 1963, pp. 431–441.

[105] Bard, Y., "Comparison of Gradient Methods for the Solution of Nonlinear Parameter Estimation Problems," *SIAM J. Num. Anal.*, Vol. 7, 1970, pp. 157–186.

[106] Patankar, S. V, *Numerical Heat Transfer and Fluid Flow*, Taylor & Francis, Washington, DC, 1980.

[107] Cheney, M, Isaacson, D., and Isaacson, E. L., "Exact Solutions to a Linearized Inverse Boundary Value Problem," *Inverse Problems*, Vol. 6, 1990, pp. 923–934.

[108] Churchill, R. V., Brown, J. W., and Verhey, R. F., *Complex Variables and Applications*, 3rd Edit., MacGraw–Hill, New York, 1974.

[109] Churchill, R. V., and Brown, J. W., *Fourier Series and Boundary Value Problems,* 4th Edit., MacGraw–Hill, New York, 1987.

[110] Chen, Z. Q., and Paoloni, F. J., "An Integral Equation Approach to Electrical Conductance Tomography," *IEEE Trans. Med. Imag.*, Vol. 11, No. 4, December 1992, pp. 570–576.

[111] Hahn, S. Y., Bigeon, J., and J. C. Sabonnadiere, "An 'Upwind' Finite Element Method for Electromagnetic Field Problems in Moving Media," *Int. J. Num. Meth. Eng.*, Vol. 24, 1987, pp. 2071–2086.

[112] Liu, Z., Eastham, A. R. and Dawson, G. E., "A Novel Finite Element Method for Moving Conductor Eddy Current Problems," *IEEE Trans. Mag.,* Vol. 29, No. 6, November 1993, pp. 2449–2451.

[113] Roberts, K. V., and Weiss, N. O., "Convective Difference Schemes," *Math. Comp.*, Vol. 20, 1966, pp. 272–299.

[114] Gosman, A. D., Pun, W. M., Runchal, A. K., Spalding, D. B., and Wolfshtein, M., *Heat and Mass Transfer in Recirculating Flows*, Academic Press, London, U.K., 1969.

[115] Roache, P. J., *Computational Fluid Dynamics*, Hermosa, Albuquerque, NM, 1976.

[116] Spalding, D. B., "A Novel Finite Difference Formulation for Differential Expressions Involving Both First and Second Derivatives," *Int. J. Num. Meth. Eng.*, Vol. 4, 1972, pp. 551–559.

[117] Raithby, G. D., "A Critical Evaluation of Upstream Differencing Applied to Problems Involving in Fluid Flow," *Comp. Meth. Appl. Mech. Eng.*, Vol. 9, 1976, pp. 75–103.

[118] Raithby, G. D., "Skew Upstream Differencing Schemes for Problems Involving Fluid Flow," *Comp. Meth. Appl. Mech. Eng.*, Vol. 9, 1976, pp. 153–164..

[119] Karki, K. C., Patankar, S. V., "Calculation Procedure for Viscous Incompressible Flows in Complex Geometries," *Num. Heat Trans.*, Vol. 14, 1988, pp. 295–307.

[120] Zienkiewicz, O. C., Gallagher, R. H., and Hood, P., "Newtonian and Non–Newtonian Viscous Incompressible Flow. Tempature Induced Flows. Finite Element Solu-

tions," *2nd Conf. Mathematics of Finite Elements and Applications*, Brunel University, 1975.

[121] Christie, I., Griffiths, D. F. and Mitchell, A. R., "Finite Element Methods for Second Order Differential Equations with Significant First Derivatives," *Int. J. Num. Meth. Eng.*, Vol. 10, 1976, pp. 1389–1396.

[122] Heinrich, J. C., Huyakorn, P. S., and Zienkiewicz, O. C., "An 'Upwind' Finite Element Scheme for Two–Dimensional Convective–Transport Equation," *Int. J. Num. Meth. Eng.*, Vol. 11, 1977, pp. 131–143.

[123] Heinrich, J. C., and Zienkiewicz, O. C., "Quadratic Finite Element Schemes for Two–Dimensional Convective–Transport Problems," *Int. J. Num. Meth. Eng.*, Vol. 11, 1977, pp. 1831–1844.

[124] Hughes, T. J. R., and Brooks, A., "A Multi–Dimensional Upwind Scheme with No Cross Wind Diffusion," *Proc. of a Symp. on Finite Element Methods for Convection Dominated Flows, ASME Winter Annu. Meet.*, New York, NY, 1979, pp. 19–35.

[125] Baliga, B. R., and Patankar, S. V., "A New Finite–Element Formulation for Convection–Diffusion Problems," *Num. Heat Trans.*, Vol. 3, 1980, pp. 393–409.

[126] Ramadhyani, S., *Solution of the Equations of Convective Heat, Mass, and Momentum Transfer by the Finite–Element Method Using Quadrilateral Elements*, PhD Thesis, University of Minesota, Mineapolis, MN, 1979.

[127] Ramadhyani, S., and Patankar, S. V., "Solution of the Convection–Diffusion Equation by a Finite–Element Method Using Quadrilateral Elements," *Num. Heat Trans.*, Vol. 8, 1985, pp. 595–612.

[128] Hughes, T. J. R. , Liu, W. K., and Brooks, A., "Finite Element Analysis of Incompressible Viscous Flows by the Penalty Function Formulation," *J. Comp. Phys.*, Vol. 30, 1970, pp. 1–60.

[129] Parakash, C., "An improved Control Volume Finite–Element Method for Heat and Mass Transfer, and for Fluid Flow Using Equal–Order Velocity–Pressure Interpolation," *Num. Heat Trans.*, Vol. 9, 1986, pp. 253–276.

[130] Hookey, N. A., Bailga, B. R., and Prakash, C., "Evaluation and Enhancements of Some Control Volume Finite–Element Methods—Part. 1. Convection–Diffusion Problems," *Num. Heat Trans.*, Vol. 14, 1988, pp. 255–272.

[131] Hookey, N. A., Bailga, B. R., and Prakash, C., "Evaluation and Enhancements of Some Control Volume Finite–Element Methods—Part. 2. Fluid Flow Problems," *Num. Heat Trans.*, Vol. 14, 1988, pp. 273–293.

[132] Araseki, H., "Finite Element Method for Thermal Hydraulic Analysis Using Equal–Order Interpolation," *Num. Heat Trans.*, Part B., Vol. 19, 1991, pp. 153–174.

[133] Carey, G. F., and Oden, J. T., *Finite Element Computational Aspects*: Vol. III, Prentice–Hall, Englewood Cliffs, NJ, 1984.

[134] Wait, R., and Mitchell, A. R., *Finite Element Analysis and Applications*, John Wiley & Sons, New York, NY, 1985.

[135] Hussain, M. A., Noble, B., and Becker, B., "Computer Simulation of an Inverse Problem for Electric Current Computed Tomography Using a Uniform Triangular Discretization," *Proc. 11th Annu. Conf. IEEE Eng. in Med. and Bio. Soc.*, 1989, pp. 448–450.

[136] Xu, J., "Iterative Methods by Subspace Decomposition and Subspace Correction," *SIAM Review,* Vol. 34, No. 4, 1992, pp. 581–613.

[137] Abramowitz, M., and Stegun, I. A., *Handbook of Mathematical Functions*, Applied Mathematics Series, Vol. 55 (National Bureau of Standards), Dover Publications, New York, NY, 1968.

[138] Jin, J., *The Finite Element Method in Electromagnetics*, John Wiley & Sons, New York, NY, 1993.

[139] Goble, J., and Isaacson, D., "Optimal Current Patterns for Three–Dimensional Electric Current Computed Tomography," *Proc. 11th Annu. Conf. IEEE Eng. in Med. and Bio. Soc.*, 1989, pp. 463–464.

[140] Goble, J. C., *The Three–Dimensional Inverse Problem in Electric Current Computed Tomography*, PhD Thesis, Department of Computer Science, Troy, NY, December 1990.

[141] Ider, Z. and Gencer, N. G., Atalar, E. and Tosun, H., "Electrical Impedance Tomography of Translationally Uniform Cylindrical Objects with General Cross Sectional Boundaries," *IEEE Trans. Med. Imag.*, Vol. 9, No. 1, March 1990, pp. 49–59.

[142] Kron, G., *Tensor Analysis of Networks*, John Wiley & Sons, Inc., New York, NY, 1939.

[143] Kron, G., *Diakoptics: The Piecewise Solution of Large–Scale Systems*, MacDonald & Co. (Publishers) Ltd., London, U.K., 1963.

[144] Lytle, R. J., and Dines, K. A., *An Impedance Camera: A System for Determining the Spatial Variation of Electrical Conductivity*, UCRL–52413, Lawrance Livermoore Lab. Livermoore, CA, 1978.

[145] Tasto, M., and Schomberg, H., "Object Reconstruction from Projections and Some Non–Linear Extensions," *Pattern Recognition and Signal Processing*, C. H. Chen (Editor), Austria, 1978.

[146] Brown, B. H., and Seagar, A. D., "Applied Potential Tomography: Data Collection Problems," *Proc. IEE Int. Conf. on Electric and Magnetic Fields in Medicine and Biology*, pp. 79–82, 1985.

[147] Brown, B. H., and Seagar, A. D., "The Sheffield Data Collection System," *Clin. Phys. Physiol. Meas.*, Vol. 8, Suppl. A, 1987, pp. 91–97.

[148] Powell, H. M., Barber, D. C., and Freeston, I. L., "Impedance Imaging Using Linear Electrode Arrays," *Proc. IEE Int. Conf. on Electric and Magnetic Fields in Medicine and Biology*, 1985, pp. 88–92.

[149] Powell, H. M., Barber, D. C., and Freeston, I. L., "Impedance Imaging Using Linear Electrode Arrays," *Clin. Phys. Physiol. Meas.*, Vol. 8, Suppl. A, 1987, pp. 109–118.

[150] Cheney, M., and Isaacson, D., "Distinguishability in Impedance Imaging," *IEEE Trans. Biomed. Eng.*, Vol. 39, No. 8, August 1992, pp. 852–860.

[151] Gisser, D. G., Isaacson, D., and Newell, J. C., "Theory and performance of adaptive Current tomography System," *Clin. Phys. Physiol. Meas.*, Vol. 9, Suppl. A, 1988, pp. 35–41.

[152] Beauchamp, K. G., *Applications of Walsh and Related Functions*, Academic Press, London, U.K., 1984.

[153] Gonzales, R. C., and Woods, R. E., *Digital Image Processing*, Addison–Wesley, Reading, MA, 1993.

[154] Schwan, H. P., "Determination of Biological Impedances," *Phys. Tech. Bio. Res.*, Vol. 6, 1963, pp. 323–407.

[155] Geddes, L. A., Foster, K. S., Reilly, J., Voorhees, W. D., Bourland J. D., Ragheb, T., and Fearnot, N. E., "Rectification Properties of an Electrode–Electrolyte Interface Operated at High Sinusaoidal Current Density," *IEEE Trans. Biomed. Eng.*, Vol. 34, No. 9, September 1987, pp. 669–672.

[156] Geddes, L. A., Da Costa, C. P., and Wise, G., "The Impedance of Stainless–Steel Electrodes," *Med. Biol. Eng.* Vol. 9, 1971, pp. 511–521.

[157] Onaral, B., and Schwan, H. P., "Linear and Nonlinear Properties of Platinum Electrode Polarisation. Part I: Frequency Dependence at Very Low Frequencies," *Med. & Biol. Eng. & Comput.,* Vol. 20, 1982, pp. 299–306.

[158] Onaral, B., and Schwan, H. P., "Linear and Nonlinear Properties of Platinum Electrode Polarisation II: Time Domain Analysis," *Med. & Biol. Eng. & Comput.,* Vol. 21, 1983, pp. 210–216.

[159] Onaral, B., Sun, H. H. and Schwan, H. P., "Electrical Properties of Bioelectrodes," *IEEE Trans. Biomed. Eng.*, Vol. 31, No. 12, December, 1984, pp. 827–832.

[160] Newell, J. C., Isaacson, D., and Gisser, D. G., "Rapid Assesment of Electrode Characteristics for Impedance Imaging," *IEEE Trans. Biomed. Eng.*, Vol. 37, No. 7, July 1990, pp. 735–738.

[161] Cheng, K. –S., Simske, S. J., Isaacson, D., Newell, J. C., and Gisser, D. G., "Errors Due to Measuring Voltage on Current–Carrying Electrodes in Electric Current Computed Tomography," *IEEE Trans. Biomed. Eng.,* Vol. 37, No. 1, January 1990, pp. 60–64.

[162] Somersalo, E., Cheney, M., and Isaacson, D., "Existence and Uniqueness for Electrode Models for Electric Current Computed Tomography," *SIAM J. Appl. Math.*, Vol. 52, No. 4, 1992, pp. 1023–1040.

[163] Mendenhall, W., *Introduction to Probability and Statistics*, 3rd Edit., Duxbury Press, Belmont, CA, 1971.

[164] Morrison, R., *Guarding and Shielding Techniques in Instrumentation,* John Wiley & Sons, NY, New York, 1986

[165] Keitley MetraByte Corporation, *1991 PIO–96 User's Manual.*

APPENDIX A

NUMERICAL INTEGRATION BY GAUSS–LEGENDRE QUADRATURE

A.1 Numerical Integration Formula

One–dimensional integral in interval [–1, 1] is numerically calculated by

$$\int_{-1}^{1} f(x)dx = \sum_{m=1}^{N} w_m f(x_m) \tag{A.1}$$

where x_m and w_m denote Gauss points and their corresponding weights. N is the number of Gauss points selected based on the polynomial degree (p) of $f(x)$. For $N = (p + 1)/2$ Gauss points the integration is calculated without any error; when $(p + 1)$ is odd, one should pick the nearest larger integer as $N = p/2 + 1$. Table A.1 lists Gauss points and their corresponding weights up to 12 points with 15 decimal points of accuracy.

Table A.1 Gauss–Legendre quadrature: weights and abscissas [97]

x_m	w_m
$N=2$	
±0.57735 02691 89626	1.00000 00000 00000
$N=3$	
±0.77459 66692 41483	0.55555 55555 55556
0.00000 00000 00000	0.88888 88888 88889
$N=4$	
±0.86113 63115 96053	0.34785 48451 37454
±0.33998 10435 84856	0.65214 51548 62546
$N=5$	
±0.90617 98459 38664	0.23692 68850 56189
±0.53846 93101 05683	0.47862 86704 99367
0.00000 00000 00000	0.56888 88888 88889
$N=6$	
±0.93246 95142 03152	0.17132 44923 79170
±0.66120 93864 66265	0.36076 15730 48139
±0.23861 91860 83197	0.46791 39345 72691
$N=7$	
±0.94910 79123 42759	0.12948 49661 68870
±0.74153 11855 99394	0.27970 53914 89277
±0.40584 51513 77397	0.38183 00505 05119
0.00000 00000 00000	0.41795 91836 73469

$N = 8$

±0.96028 98564 97536	0.10122 85362 90376
±0.79666 64774 13627	0.22238 10344 53375
±0.52553 24099 16329	0.31370 66458 77887
±0.18343 46424 95650	0.36268 37833 78362

$N = 9$

±0.96816 02395 07626	0.08127 43883 61574
±0.83603 11073 26636	0.18064 81606 94857
±0.61337 14327 00590	0.26061 06964 02936
±0.32425 34234 03809	0.31234 70770 40003
0.00000 00000 00000	0.33023 93550 01260

$N = 10$

±0.97390 65285 17172	0.06667 13443 08688
±0.86506 33666 88985	0.14945 13491 50581
±0.67940 95682 99024	0.21908 63625 15982
±0.43339 53941 29247	0.26926 67193 09996
±0.14887 43389 81631	0.29552 42247 14753

$N = 11$

±0.97822 86581 46057	0.05566 85671 16174
±0.88706 25997 68095	0.12558 03694 64905
±0.73015 20055 74049	0.18629 02109 27734
±0.51909 61292 06812	0.23319 37645 91991
±0.26954 31559 52345	0.26280 45445 10247
0.00000 00000 00000	0.27292 50867 77901

$N = 12$

±0.98156 06342 46719	0.04717 53363 86512
±0.90411 72563 70475	0.10693 93259 95318
±0.76990 26741 94305	0.16007 83285 43346
±0.58731 79542 86617	0.20316 74267 23066
±0.36783 14989 98180	0.23349 25365 38355
±0.12523 34085 11169	0.24914 70458 13403

APPENDIX B

DIRECT COMPUTATION OF THE HESSIAN MATRIX

B.1 Introduction

In the process of reconstructing the conductivity distribution by the Newton–Raphson method, the majority of computational effort involves computation of the Jacobian, and subsequently the Hessian previously defined by Equation (4.53) (see Chapter 4). The work presented herein suggests a new scheme which directly forms the Hessain matrix without storing the Jacobian itself. Therefore, commensurate order–of–magnitude saving in computer memory can be obtained, especially when large number of excitations and electrodes are required for the imaging system.

Let $\boldsymbol{H}$ denote the Hessian matrix expressed previously as

$$\boldsymbol{H}_{M\times M} \equiv \left[\boldsymbol{J}^{T}_{M\times EP} \cdot \boldsymbol{J}_{M\times EP}\right]_{M\times M}, \tag{B.1}$$

where E is the total number of electrodes, P is the number of excitation patterns, and M is the number of elements. Then, define $\boldsymbol{B}$ as

$$\boldsymbol{B}_{M\times 1} \equiv -\boldsymbol{J}^{T}_{M\times EP}\left\{f(\sigma^{k})_{EP\times 1} - \boldsymbol{V}_{oEP\times 1}\right\}_{EP\times 1}. \tag{B.2}$$

Thus, the conductivity update for the k–th iteration can be expressed by the linear system:

$$\boldsymbol{H}_{M\times M}\,\Delta\sigma^{k}_{M\times 1} = \boldsymbol{B}_{M\times 1}. \tag{B.3}$$

The correction term for the conductivity of each element for is determined by

$$\Delta\sigma^{k}_{M\times 1} = \boldsymbol{H}^{-1}_{M\times M}\,\boldsymbol{B}_{M\times 1}. \tag{B.4}$$

If the matrix $\boldsymbol{H}$ and vector $\boldsymbol{B}$ in Equation (B.4) can be directly calculated, the Jacobian itself is not needed for inverse calculation, only its square. If the square of the Jacobian, $\boldsymbol{H}$, can be computed directly, considerable storage savings can be obtained. In the following section, the direct computation of the Hessian matrix as well as the right hand side vector will be explained.

B.1.1 Formulation of the Direct Hessian Computation Scheme

Confirming the Jacobian itself is not needed for the inverse calculation, recall that the Jacobian matrix is defined by

$$J^k \equiv \frac{\partial f^k}{\partial \sigma}. \tag{B.5}$$

Since Equation (B.5) is a derivative of one matrix with respect to another, the Jacobian matrix consisting of M vectors given by

$$J_{EP\times M} = \left[J_{1_{EP\times 1}},\ J_{2_{EP\times 1}}, \cdots, J_{m_{EP\times 1}}, \cdots,\ J_{M_{EP\times 1}}\right], \tag{B.6}$$

where

$$J_{m_{EP\times 1}} = \frac{\partial f_{EP\times 1}}{\partial \sigma_m} \quad \text{for} \quad m = 1,\ldots,M. \tag{B.7}$$

Each $EP \times 1$ vector in Equation (B.6) can be calculated for element–m by

$$J_{m_{EP\times 1}} = \left\{\text{Tran}_{NP\to EP}\left[\text{vec}\left(-Y^{-1}_{N\times N}\frac{\partial Y_{N\times N}}{\partial \sigma_m}V_{N\times P}\right)_{N\times P}\right]_{NP\times 1}\right\}_{EP\times 1}, \tag{B.8}$$

where vec( ) is an operator which stacks the columns of the $N \times P$ matrix into an $NP \times 1$ array, and $\text{Tran}_{NP\to EP}$ is the transition matrix which transforms from the array $NP \times 1$, size of all nodes, N, for all current excitations, P, into the array of size $EP \times 1$ having all measured electrodes for all current excitations. Matrices Y and V denote the global admit-

tance matrix and the voltage matrix obtained from the finite element structure. These operators used herein demonstrate the mathematical concept of the computations. However, in implementation of these operations requires consideration of sparsity by which further computational savings can then be achieved.

Consider the term in the parentheses of Equation (B.8), the last two matrices are multiplied and the j–th column which corresponds to the j–th excitation is obtained as

$$\text{column } j \text{ of } \left[\left[\frac{\partial \boldsymbol{Y}_{N\times N}}{\partial \sigma_m}\boldsymbol{V}_{N\times P}\right]_{N\times P}\right] = \left\{\begin{array}{l} \sum_{\beta=1}^{N} y'_{m_{1\beta}}\, V_{\beta j} \\ \sum_{\beta=1}^{N} y'_{m_{2\beta}}\, V_{\beta j} \\ \vdots \\ \sum_{\beta=1}^{N} y'_{m_{i\beta}}\, V_{\beta j} \\ \vdots \\ \sum_{\beta=1}^{N} y'_{m_{N\beta}}\, V_{\beta j} \end{array}\right\}_{N\times 1}, \tag{B.9}$$

where $V_{\beta j}$ is the voltage on the node–β for the j–th excitation, and $y'_{m_{i\beta}}$ is the derivative of the admittance from node–i to node–β with respect to the conductivity of element–m; i.e.,

$$y'_{m_{i\beta}} \equiv \text{element of } \left[\left(\frac{\partial \boldsymbol{Y}_{N\times N}}{\partial \sigma_m}\right)_{N\times N}\right]_{i,\beta}. \tag{B.10}$$

Continuing for one step further, the multiplication of the three matrices inside the parentheses of Equation (B.8) can then be expressed as

$$\text{column } j \text{ of } \left\{\left[\boldsymbol{Y}_{N\times N}^{-1}\frac{\partial \boldsymbol{Y}_{N\times N}}{\partial \sigma_m}\boldsymbol{V}_{N\times P}\right]_{N\times P}\right\} = \left\{\begin{array}{l} \sum_{\alpha=1}^{N} y_{1,\alpha}^{-1} \sum_{\beta=1}^{N} y'_{m_{\alpha\beta}} V_{\beta,j} \\ \sum_{\alpha=1}^{N} y_{2,\alpha}^{-1} \sum_{\beta=1}^{N} y'_{m_{\alpha\beta}} V_{\beta,j} \\ \vdots \\ \sum_{\alpha=1}^{N} y_{i,\alpha}^{-1} \sum_{\beta=1}^{N} y'_{m_{\alpha\beta}} V_{\beta,j} \\ \vdots \\ \sum_{\alpha=1}^{N} y_{N,\alpha}^{-1} \sum_{\beta=1}^{N} y'_{m_{\alpha\beta}} V_{\beta,j} \end{array}\right\}_{N\times 1}, \tag{B.11}$$

where $y_{i,\alpha}^{-1}$ is the (i,α)–th entry of the inverse of the global admittance or the global impedance matrix which results from the finite element structure. If the computational procedure given in Equation (B.11) is repeated for all the excitations and the element conductivities, an $NP \times M$ partitioned matrix $\boldsymbol{Q}$ is obtained as

$$\boldsymbol{Q}_{NP\times M} = \begin{bmatrix} q_{1,1} & q_{1,2} & & q_{1,M} \\ q_{2,1} & q_{2,2} & \vdots & q_{2,M} \\ \vdots & \vdots & q_{j,m} & \vdots \\ q_{P,1} & q_{P,2} & & q_{P,M} \end{bmatrix}_{NP\times M}, \tag{B.12}$$

where each partition $\boldsymbol{q}_{j,m}$ is an $N \times 1$ vector computed by Equation (B.11) for excitation–j and element–m, respectively. Note that the inverse problem considered herein only requires the boundary information, and each vector $\boldsymbol{q}$ given in Equation (B.12) includes the derivative information for both the boundary and the internal nodes, while only the boundary nodes are required to form the Jacobian. Therefore, the extra information is omitted by defining an operator which only picks up the electrode nodes, and the vector $\boldsymbol{J}_{m_{EP\times 1}}$ in Equation (B.8) is obtained as

$$J_{m_{EP\times 1}} = -\begin{Bmatrix} \mathrm{Tran}_{N\to E}\left(q_{1,m}\right) \\ \mathrm{Tran}_{N\to E}\left(q_{2,m}\right) \\ \vdots \\ \mathrm{Tran}_{N\to E}\left(q_{P,m}\right) \end{Bmatrix}_{EP\times 1}. \tag{B.13}$$

Finally, by calculating J_m's for each element, the upper diagonal of the symmetric Hessian matrix, H, in Equation (B.1) and the right hand side vector, B, in Equation (B.2) are computed by

$$H_{ij} \equiv (J^T \cdot J)_{ij} = \sum_{e=1}^{EP} J_{i,e}\ J_{j,e}, \tag{B.14}$$

and

$$B_j = -\sum_{e=1}^{EP} \left(f_e - V_{0,e}\right) J_{j,e}, \tag{B.15}$$

where e is the index for excitation and electrodes given by

$$e = (e_b - 1) \cdot E + e_a, \tag{B.16}$$

and where e_a is the electrode index, from 1 to E, and e_b is the excitation index, from 1 to P.

To obtain a more explicit form, Equation (B.13) is substituted into Equations (B.14) and (B.15), and rearranging results in

$$H_{ij} = \sum_{e=1}^{EP} \left[\sum_{\alpha=1}^{N} y^{-1}_{nl(e_a),\alpha} \sum_{\beta=1}^{N} y'_{i_{a\beta}} V_{\beta,e_b}\right]_e \left[\sum_{\alpha=1}^{N} y^{-1}_{nl(e_a),\alpha} \sum_{\beta=1}^{N} y'_{j_{a\beta}} V_{\beta,e_b}\right]_e, \tag{B.17}$$

and

$$B_j = \sum_{e=1}^{EP} \left(f_e - V_{0,e}\right) \left[\sum_{\alpha=1}^{N} y^{-1}_{nl(e_a),\alpha} \sum_{\beta=1}^{N} y'_{j_{a\beta}} V_{\beta,e_b} \right]_e, \tag{B.18}$$

where $nl(e_a)$ is the node number of electrode index e_a. Note that the node numbers which correspond to the electrodes are determined *a priori* and stored in array $nl(e_a)$ so that only the necessary rows of $\boldsymbol{Q}$ in Equation (B.12) are computed; thereby, unnecessary computations for the rows corresponding to the internal rows are avoided.

So far, the implementing of the numerical procedure for direct computation of the square of the Jacaobian has been presented but the computational efficiency was ignored. Yorkey et al. [21] pointed out that the inverse of the admittance matrix, $\boldsymbol{Y}$,$^{-1}$ and the voltage matrix, $\boldsymbol{V}$, are full matrices but the derivative of the admittance matrix, $\partial \boldsymbol{Y}/\partial \sigma_m$, is sparse. When four–node quadrilateral elements are utilized in the finite element model, only 16 nonzero entries contribute to matrix $\partial \boldsymbol{Y}/\partial \sigma_m$. Thus, if a special scheme is employed in the computation of Equation (B.9), floating point operations with these zero entries in $\partial \boldsymbol{Y}/\partial \sigma_m$ can be mostly avoided regardless of the size of the admittance matrix, $\boldsymbol{Y}$.

Considering only the nonzero entries of the derivative of the admittance matrix, $\partial \boldsymbol{Y}/\partial \sigma_m$, a further improvement is possible by modifying Equations (B.17) and (B.18) as

$$H_{ij} = \sum_{e=1}^{EP} \left\{ \left[\sum_{\alpha=1}^{4} y^{-1}_{nl(e_a),ni(\alpha)} \sum_{\beta=1}^{4} y'_{i_{ni(\alpha),ni(\beta)}} V_{ni(\beta),e_b} \right]_e \cdot \left[\sum_{\alpha=1}^{4} y^{-1}_{nl(e_a),nj(\alpha)} \sum_{\beta=1}^{4} y_{j_{nj(\alpha),nj(\beta)}} V_{nj(\beta),e_b} \right]_e \right\} \tag{B.19}$$

and

$$B_j = \sum_{e=1}^{EP} \left(f_e - V_{0,e}\right) \cdot \left[\sum_{\alpha=1}^{4} y^{-1}_{nl(e_a),nj_{(\alpha)}} \sum_{\beta=1}^{4} y'_{j_{nj(\alpha),nj(\beta)}} V_{nj(\beta),e_b} \right]_e, \qquad \text{(B.20)}$$

where $ni(\alpha)$ and $ni(\beta)$ are node numbers of the neighborhood of element i, where α and β are dummy variables from 1 to 4, $nj(\alpha)$ and $nj(\beta)$ are node numbers of the neighborhood of element j, where α and β are also dummy variables from 1 to 4. Note too that $V_{ni(\beta),e_b}$ is the voltage on the node of $ni(\beta)$ for excitation e_b, $V_{nj(\beta),e_b}$ is the voltage on the node of $nj(\beta)$ for the excitation e_b, $y'_{i_{ni(\alpha),ni(\beta)}}$ is the derivative of the admittance from node $ni(\alpha)$ to node $ni(\beta)$ with respect to the conductivity of element i, $y'_{j_{nj(\alpha),nj(\beta)}}$ is the derivative of the admittance from node $nj(\alpha)$ to node $nj(\beta)$ with respect to the conductivity of element j, and $y^{-1}_{nl(e_a),ni(\alpha)}$ is the element having the coordinates (node of the electrode e_a, node on $ni(\alpha)$) in the inverse of the admittance matrix, $\boldsymbol{Y}^{-1}$.

From Equations (B.19)–(B.20) the matrix $\boldsymbol{H}_{M\times M}$ and the vector $\boldsymbol{B}_{M\times 1}$ can be constructed directly without storing the $EP \times M$ Jacobian matrix.

APPENDIX C

SOME USEFUL VECTOR IDENTITIES AND INTEGRAL THEOREMS

C.1 Introduction

This appendix summarizes the vector calculus identities and theorems occasionally used in formulation of electromagnetic quantities for this study. The symbols used below do not refer to specific physical quantities; bold letters such as $\overline{A}$, $\overline{B}$, $\overline{C}$, $\overline{D}$, etc. are generic symbols for vectors, and U and V are for scalar quantities.

C.2 Vector Identities

$$\overline{A} \cdot \overline{B} \times \overline{C} = \overline{B} \cdot \overline{C} \times \overline{A} = \overline{C} \cdot \overline{A} \times \overline{B} \tag{C.1}$$

$$\overline{A} \times (\overline{B} \times \overline{C}) = \overline{B}\ (\overline{A} \cdot \overline{C}) - \overline{C}\ (\overline{A} \cdot \overline{B}) \tag{C.2}$$

$$(\overline{A} \times \overline{B}) \times \overline{C} = \overline{B}\ (\overline{A} \cdot \overline{C}) - \overline{A}\ (\overline{B} \cdot \overline{C}) \tag{C.3}$$

$$\overline{A} \times (\overline{B} \times \overline{C}) + \overline{B} \times (\overline{C} \times \overline{A}) + \overline{C} \times (\overline{A} \times \overline{B}) = 0 \tag{C.4}$$

$$(\overline{A} \times \overline{B}) \cdot (\overline{C} \times \overline{D}) = (\overline{A} \cdot \overline{C})\ (\overline{B} \cdot \overline{D}) - (\overline{B} \cdot \overline{C})\ (\overline{A} \cdot \overline{D}) \tag{C.5}$$

$$(\overline{A} \times \overline{B}) \times (\overline{C} \times \overline{D}) = (\overline{A} \times \overline{B} \cdot \overline{D})\ \overline{C} - (\overline{A} \times \overline{B} \cdot \overline{C})\ \overline{D} \tag{C.6}$$

$$\nabla \times \nabla U = 0 \tag{C.7}$$

$$\nabla\ (U + V) = \nabla U + \nabla V \tag{C.8}$$

$$\nabla\ (UV) = U\ \nabla V + V\ \nabla U \tag{C.9}$$

$$\nabla \cdot (U\ \overline{A}) = \overline{A} \cdot \nabla U + U\ \nabla \cdot \overline{A} \tag{C.10}$$

$$\nabla \times (U\ \overline{A}) = \nabla U \times \overline{A} + U\ \nabla \times \overline{A} \tag{C.11}$$

$$(\overline{A} \cdot \nabla)\ U = \overline{A} \cdot (\nabla U) \tag{C.12}$$

$$\overline{B} \cdot (\overline{A} \cdot \nabla)\ \nabla U = \overline{A} \cdot (\overline{B} \cdot \nabla)\ \nabla U \tag{C.13}$$

$$(\overline{A} \cdot \nabla)\ (\overline{B} \cdot \nabla)\ U = \nabla U\ (\overline{A} \cdot \nabla) \cdot \overline{B} + \overline{A}\ (\overline{B} \cdot \nabla) \cdot \nabla U \tag{C.14}$$

$$\nabla \cdot \nabla \times \overline{A} = 0 \tag{C.15}$$

$$\nabla \times \nabla \times \overline{A} = \nabla\ (\nabla \cdot \overline{A}) - \nabla^2 \overline{A} \tag{C.16}$$

$$\nabla \cdot (\overline{A} + \overline{B}) = \nabla \cdot \overline{A} + \nabla \cdot \overline{B} \tag{C.17}$$

$$\nabla \times (\overline{A} + \overline{B}) = \nabla \times \overline{A} + \nabla \times \overline{B} \tag{C.18}$$

$$\nabla\ (\overline{A} \cdot \overline{B}) = \overline{A} \times (\nabla \times \overline{B}) + \overline{B} \times (\nabla \times \overline{A}) + (\overline{A} \cdot \nabla)\ \overline{B} + (\overline{B} \cdot \nabla)\ \overline{A} \tag{C.19}$$

$$\nabla \cdot (\overline{A} \times \overline{B}) = \overline{B} \cdot \nabla \times \overline{A} - \overline{A} \cdot \nabla \times \overline{B} \tag{C.20}$$

$$\nabla \times (\overline{A} \times \overline{B}) = \overline{A}\ \nabla \cdot \overline{B} - \overline{B}\ \nabla \cdot \overline{A} + (\overline{B} \cdot \nabla)\ \overline{A} - (\overline{A} \cdot \nabla)\ \overline{B} \tag{C.21}$$

$$(\overline{A} \cdot \nabla)\ (\overline{B} \cdot \overline{C}) = \overline{B} \cdot (\overline{A} \cdot \nabla)\ \overline{C} + \overline{C}\ (\overline{A} \cdot \nabla)\ \overline{B} \tag{C.22}$$

C.3 Integral Theorems

Divergence Theorem:

$$\int_v \nabla \cdot \overline{A}\ dv = \oint_S \overline{A} \cdot d\overline{S} \tag{C.23}$$

Corollaries of the divergence theorem:

$$\int_v \nabla U\ dv = \oint_S U\ d\overline{S} \tag{C.24}$$

$$\int_v \nabla \times \overline{A}\ dv = -\oint_S \overline{A} \times d\overline{S} \tag{C.25}$$

Stoke's theorem:

$$\oint_{\ell} \overline{A} \cdot d\overline{\ell} = \int_{S} (\nabla \times \overline{A}) \cdot d\overline{S} \tag{C.26}$$

Corollary of Stoke's theorem:

$$\oint_{\ell} U \, d\ell = \int_{S} \nabla U \times d\overline{S} \tag{C.27}$$

Greens's theorem:

$$\oint_{v} \left(U \, \nabla^2 V - V \nabla^2 U \right) dv = \int_{S} \left(U \frac{\partial V}{\partial n} - V \frac{\partial U}{\partial n} \right) dS \tag{C.28}$$

APPENDIX D

MATRIX SWITCHING SYSTEM DESIGN

D.1 Introduction

This appendix summarizes the electronic design results undertaken to complete the imaging measurement. The high accuracy system including detailed circuit board design and layout, noise reduction methods, computer interfacing, phase measurement, and accuracy considerations are explained in detail.

D.2 Detailed Circuit Diagrams and PC Board Layouts

The original concept for the electronic system was to have been an extension of methods used in the biomedical area. Figure D.1 shows the system block diagram of one unit of the matrix switching system.

The matrix switching system is comprised of 160 shielded switches for 32 channels: 32 each for switching excitation high signals; 32 each for low signals to any or all of 32 electrodes on the phantom test device; 32 $\times$ 2 each for switching high side voltage measurement to either side of the current–measuring resistors; and 32 for switching the low–side of the digital voltmeter or oscilloscope to any electrodes. All switches are CP Clare DSS3 shielded relays, which are controlled by a TTL–level signal from the IBM personal computer through a Keithey Metrabyte PIO–96 (96–channel digital input/output control board). Using this switching system, any two electrodes can be excited and the responses of the other two electrodes in all possible combinations can be measured. A schematic diagram of the matrix switching system is shown in Figure D.2.

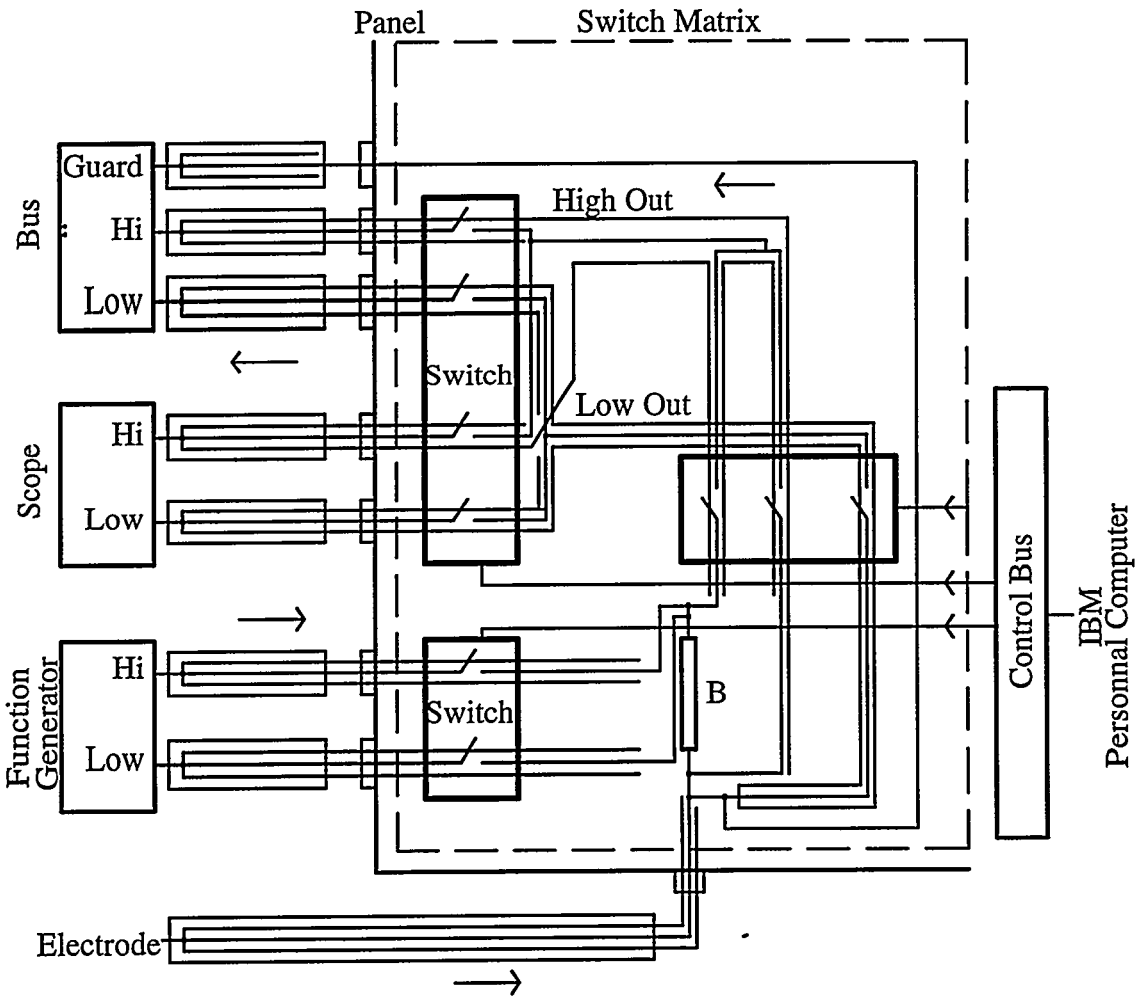

Figure D.1: Block diagram of the matrix switching system.

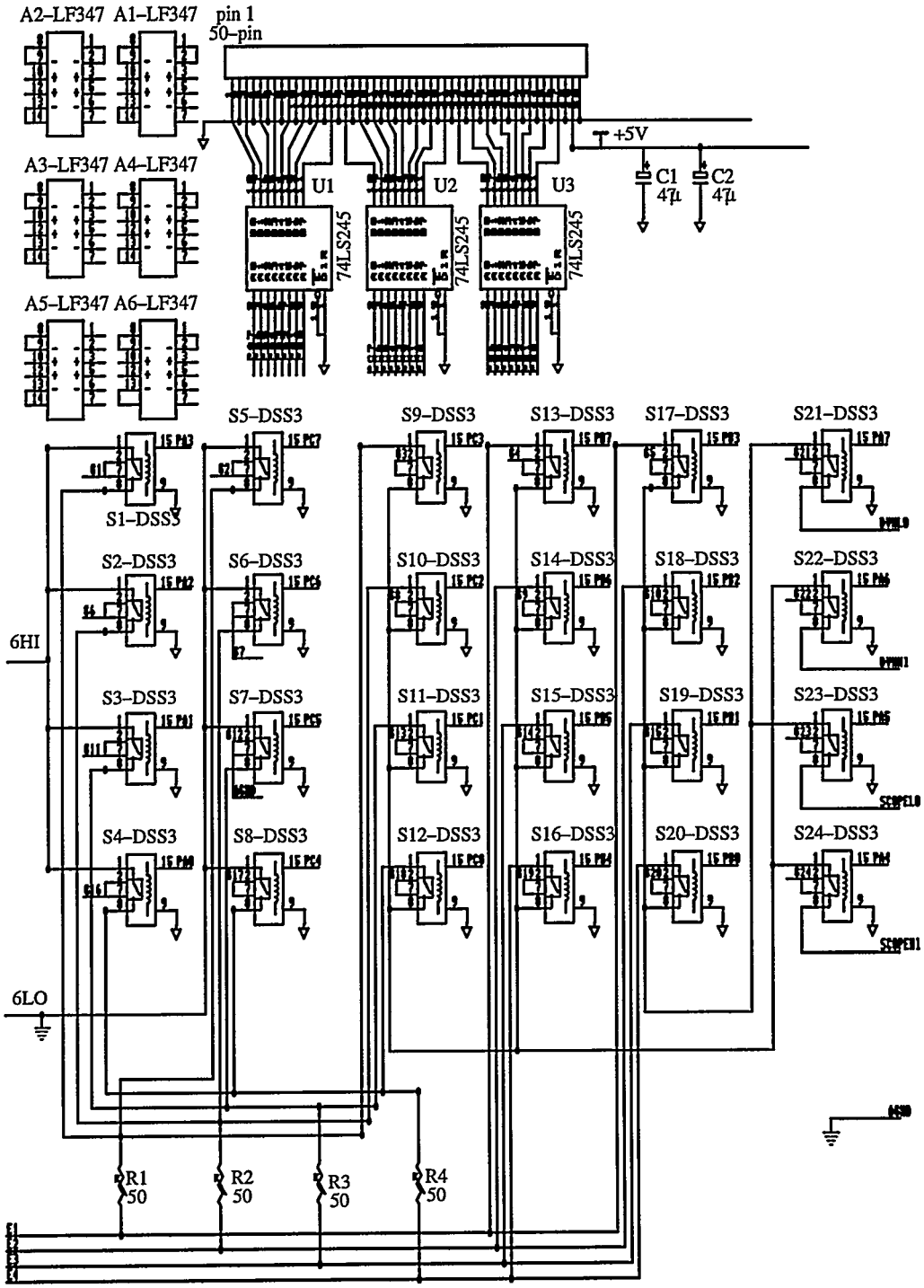

Figure D.2: Schematic diagram of the matrix switching system.

In order to obtain high signal to noise ratio, the layout of the printed–circuit–board (PCB) is designed carefully. All considerations of noise reduction are applied in the PCB design. Figure D.3 shows PCB configuration while Figure D.4 and Figure D.5 show the component–side and solder–side layout of PCB.

D.2.1 Noise Reduction

Our object is to design a high accuracy, static switching matrix system. High sensitivity measurements are subject to common mode noise (CMN). Normally, CMN is avoided by breaking the ground loop and employing other methods like grounding, guarding, shielding, decoupling, driven guarding, etc.. The reader is directed to Reference [164] for an excellent discussion of these factors summarized below.

BBB– Shielding against noise in systems involves shielding against both capacitive (electric) and inductive (magnetic) coupling in the system.

CCC– The copper surface of the PC board will also be largely given over to the ground plane to maximize overall shielding effects.

DDD– "Decoupling" provides means to dissociate circuit functions from the power bus serving that circuit.

D.2.2 Sources of Noise in the Electronic System

The measurement of low level signals in a test system environment can best be accomplished with careful attention to the details of grounding and shielding. The following are major sources of noise coupling into these systems: conductivity–coupled noise; coupling through a common impedance; electric– and magnetic–field coupled noise.

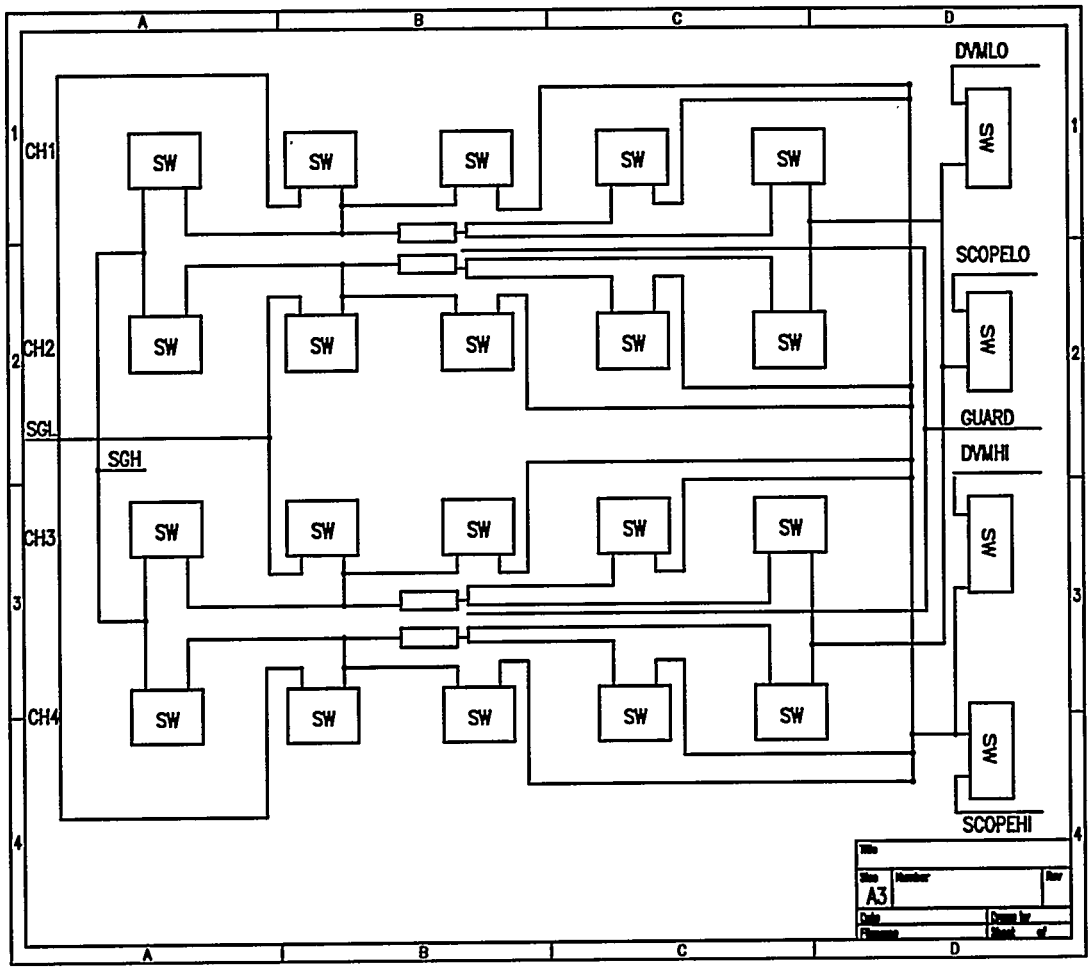

Figure D.3: Printed circuit board configuration.

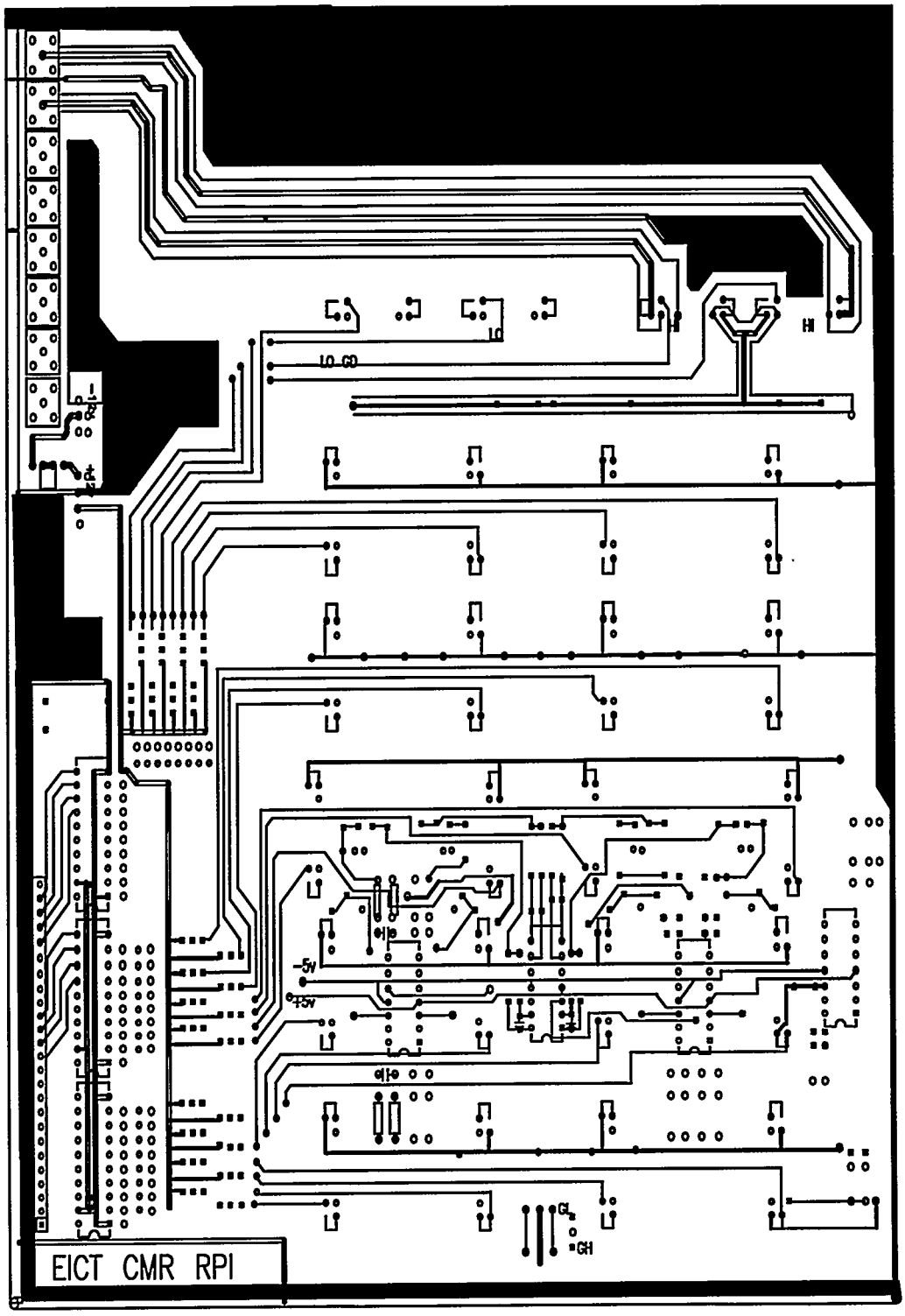

Figure D.4: PC board layout of the component side of the high accuracy circuit as modified to be compatible with cabinets ordered for the system.

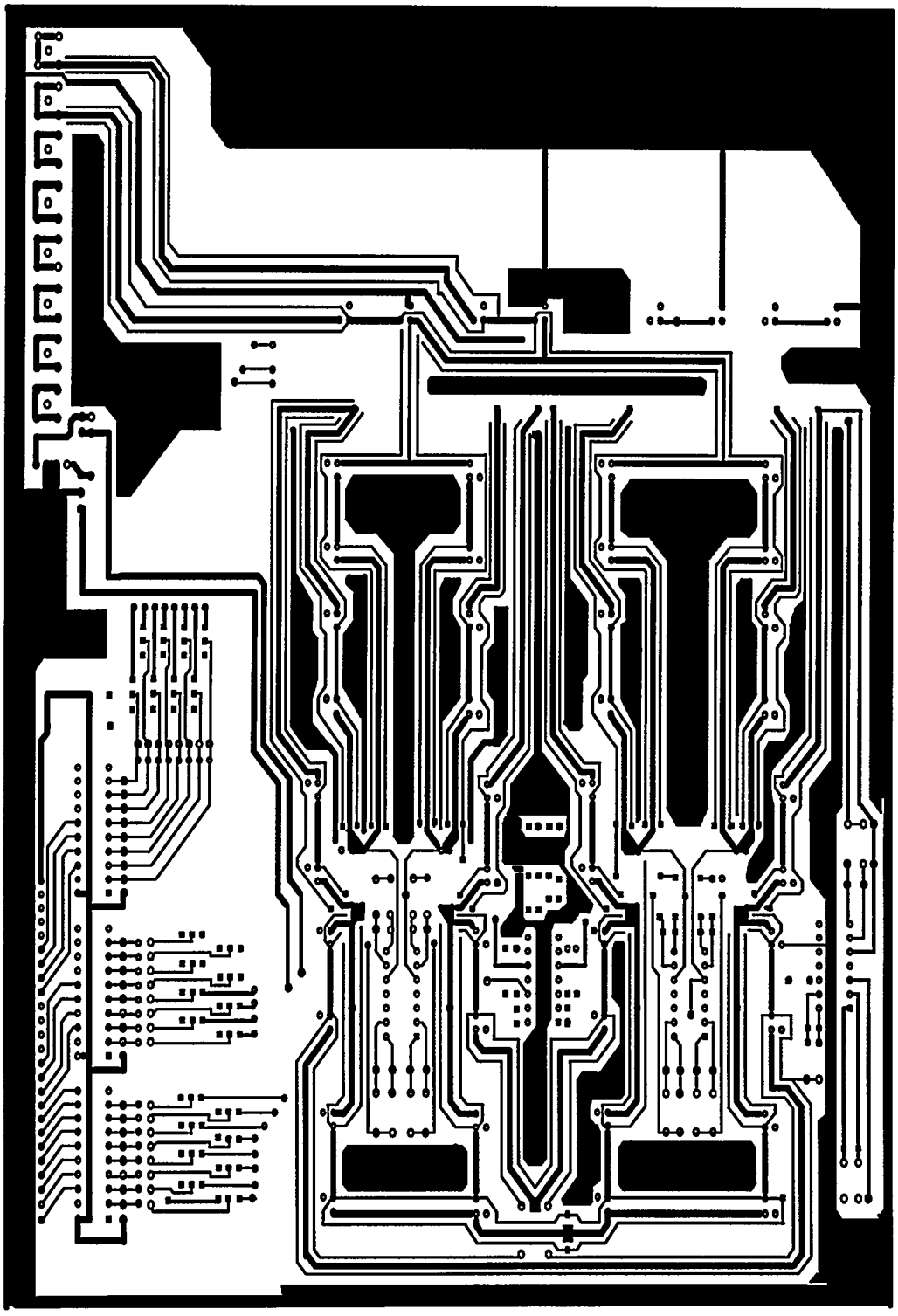

Figure D.5: PC board layout of the solder–side of the high accuracy circuit as modified to be compatible with cabinets ordered for the system.

The following common noise reduction techniques apply to single point systems and multipoint systems: grounding; guarding; shielding; decoupling; driven guard. There are discussed in turn.

D.2.3 Grounding

The design objectives of a grounding system are:

- to minimize the noise voltage generated by currents from two or more circuits flowing through a common ground impedance;
- to avoid creating ground loops that are susceptible to magnetic fields and differences in ground potential.

D.2.4 Single Point Grounding to Avoid Creating Ground Loops

Lower frequency, high sensitivity measurements are subject to common mode noise. This noise can be avoided by breaking the ground loop with a floating input. The parallel single point ground is the most desirable configuration for frequencies in the audio range. This configuration eliminates cross coupling between ground currents through different circuits, avoids creating ground loops, and provides good low–frequency grounding for frequencies lower than 1 Mhz.

D.2.5 Separate Ground Returns

For practical reasons, most systems require three separate ground returns. Signal grounds should be separated from hardware grounds and from noisy grounds such as those emanating from digital circuitry. Separate ground returns, carefully designed to avoid ground loops, can reduce mutual interface.

D.2.6 Wide Ground System

The ground distribution system is designed to be as wide as possible everywhere on the PC board. In addition, each signal line on the PC board is separated by a ground line.

D.2.7 Surrounding the Signal Conductor with a Ground Shield

The coupling noise from one conductor to the other is a result of the capacitance between the conductors and expressed as

$$V_n = j\omega RCV_s, \tag{D.1}$$

where V_n is the noise voltage, V_s the signal voltage, ω the frequency, and RC the coupling time constant between the two conductors.

If the capacitance, C, is reduced, then the noise voltage coupled into the conductor would be reduced. Surrounding the signal conductor with a grounded shield and a uniform electric field reduces the noise voltage on the signal conductor. Lines can be isolated by running ground conductors parallel to critical or noise–generating lines. These ground lines then act as a shield.

Since inductive noise coupling is proportional to the loop area cutting the magnetic flux of the noise, receiver circuits can be best protected against magnetic fields by decreasing the area of the receiver loop. For maximum protection against induced noise at low frequencies, the shield should not be one of the signal conductors. So, one end of the circuit must be isolated from the ground.

D.2.8 Guarding

A guarded instrument has an additional shield between the low and ground, effectively increasing the low to ground–leakage–impedance. The guard terminal should be connected closely to the low terminal so that the guard terminal and the low terminal are at or close to being at identical the same voltages. Therefore, no common mode (CM) current goes through any of the source resistance. The guard increases the resistance and decreases the total capacitance. It shunts the CM current paths with typical rejection of 160 dB (DC), and 140 dB (AC).

D.2.9 Driven Guard

The signal line connects to the driven guard line through a buffer amplifier at the source. At the receiving end, the guarding line is left floating. Thus providing a "Faraday" shield between the guarding line and signal line. In this way, the effect of distributed capacitance of the cable is greatly reduced. Guarding is not only provided to the external cables, but each signal line on the PC board is run between two guard lines throughout, these guard lines being driven by the same buffer amplifier as the external guard. In addition, the guarding is carried through all the switches by connecting the guard lines to the internal r–f shield of each switch.

D.2.10 Tree Switching Model to Reduce the Stray Capacitance and Cross–Talk

Tree switching is often used to reduce the stray open switch capacitance in systems resulting from connecting the unused relays in parallel in the system. This method is utilized in this design.

D.2.11 Decoupling

In practice, decoupling includes adding decoupling and power–entry capacitors, and utilizing appropriate printed–circuit board (PCB) layout. Good decoupling decreases radiated and conducted emission from equipment and minimizes susceptibility to noise. Methods include:

- Leaving as much copper as possible on the PCB;
- Using decoupling capacitors and placing them close to their respective components. These capacitors reduce noise and minimize voltage change due to load variation;
- Keeping the Vcc and ground traces reasonably close together;
- Reducing loop areas, which always corresponds to a reduction of inductances and vice–versa;
- Keeping the highest–current solid state device(DIPs) as close as possible to the power entry point in order to minimize ground noise;
- Using additional edge connector pins for ground.

D.2.12 Floating Measurements

Measurements with differences between grounds, or common mode voltages, are called floating measurements and are said to "float" by the amount of common mode voltage. An ideal floating measurement would be insensitive to the common mode signals. It would measure only the normal mode input, no matter how much common mode noise it had. A floating meter, like HP–3458A DVM, can reduce the effects of common mode voltages and is utilized for this work.

D.3 Computer Interfacing

The whole system is controlled by an IBM personal computer. Matrix switching is controlled by IBM compatible personal computer (PC) through a MetraByte's PIO–96, 96–channel digital input/output (I/O) board (see Reference [165]). Measurement instruments are controlled through MetraByte's GPIB interface card. MetraByte's PIO–96 is a high density parallel digital I/O card that allows up to 96 TTL/DTL/CMOS compatible digital I/O lines to be controlled by an IBM PC/XT/AT . The board consists of 4 industry–standard 8255 Programmable Peripheral Interface (PPI) chips each providing three 1–B ports: PA, PB, and PC (8 bits each). The PC port can be further subdivided into 2 nybble–wide (4 bit) ports. Each of the PA, PB, PC–upper and PC–lower ports can be programmed through the 8255 write–only control register, and each can be either an input or output port. After power up or whenever the computer's hardware RESET line is asserted, all 8255 lines are cleared to the digital input state on all ports. All of the standard features of the 8255 PPI are supported including operation in Modes 0, 1 and 2. Mode 0 means basic I/O, all ports are I/O ports; Mode 1 means strobed I/O, part of the PC port controls data transfer; Mode 3 means bidirectional I/O on PA only, part of the PC controls data transfer. Each digital output line has a sink current capability of 1.7 mA (one standard, or four LS TTL loads). Each 8255 uses four consecutive I/O addresses so that the PIO–96 requires a contiguous block of 16 I/O addresses. The base I/O address can be set on any 16 bit boundary in the PC's I/O address range of 200–3FO Hex (100–3FO Hex for PC/AT) by a switch. More than one PIO–96 may be installed in a computer; provided they are set to different base addresses, there is no conflict with memory because no memory addresses are used.

Each 8255 uses a 50 pin double row 0.1 in. header for its 24 I/O connections. This allows for a ground drain wire using standard flat insulation displacement cable (50 way 0.05", centers) between each I/O pin to provide maximum shielding and minimize cross

talk. Power from the computer's +5 V is also brought out on 1 pin of each connector. These pins are mainly intended for use with pull up resistors etc., but may also be used them for powering accessories as long as computer's available power ratings are observed (taking into account other adapter boards) and as long as each connector pin current limit rating is one Ampere (1.0 A).

The DVM, function generator and oscilloscope are connected to computer through the GPIB interface. GPIB is used to set up these instruments, control the whole measuring process and obtain data from DVM and scope. In order to obtain high accuracy, calibrate instruments are calibrated for every excitation, and effective data are obtained by using the oversampling method to ensure the average reading has settled to the maximum resolution of the instrument.

D.3.1 Phase–Sensitive Measurement

Using the 32–channel high–accuracy static system, the phase difference between the exciting and responding signals can be measured. Two measurement system signals (i.e., excitation and response signals) are sent to HP–54510A Digitizing Oscilloscope first, then program the oscilloscope settings and acquisition over the GPIB. The most important point is that the oscilloscope digitizes two channel signals simultanously, the exciting signal and the responding signals. After digitizing, two wave forms, data are transferred to controller computer. Comparing those two sets data, allows the phase information to be obtained from zero voltage cross–over points in each signal. While this method is slow, it is suitable to low–cost static measurement system.

D.3.2 Accuracy

Several experiments were undertaken to test the system accuracy. The results revealed that the accuracy of the data acquisition system is better then 0.5% with the target impedance around 200 kΩ. When the target impedance increased, the resolution decreased. This phenomena is caused by low input impedance (10 MΩ) of digital voltmeter. Data are recorded and ensemble–averaged until the per–measurement variation in the average is reduced below one part in 10^r where r is controlled by the experiment. This error is verified by performing nodal averaging of the reconstructed images with results having the same order of magnitude error in comparison with measurements.

In addition, the FFT's (fast Fourier transform) of the original signal (Figure D.6) were compared with the corresponding signal (Figure D.7) after passing through the excitation/measurement system. The two FFT's yielded the same result showing that the measurement system introduces no spurious noise or signals. These FFT's also show general signal broadband noise to be in the order of –80 dB.

D.3.3 Software

The PIO–96 is programmed using simple 8 bit I/O port commands e.g. BASIC's INP and OUT command. Three ports were set to output mode. When one of the pins is low, the switch controlled by this pin closes. When it is high, the switch opens. The basic control command is the following:

```
10 out &H303, &H80

20 out &H300, control–word1

30 out &H301, control–word2.
```

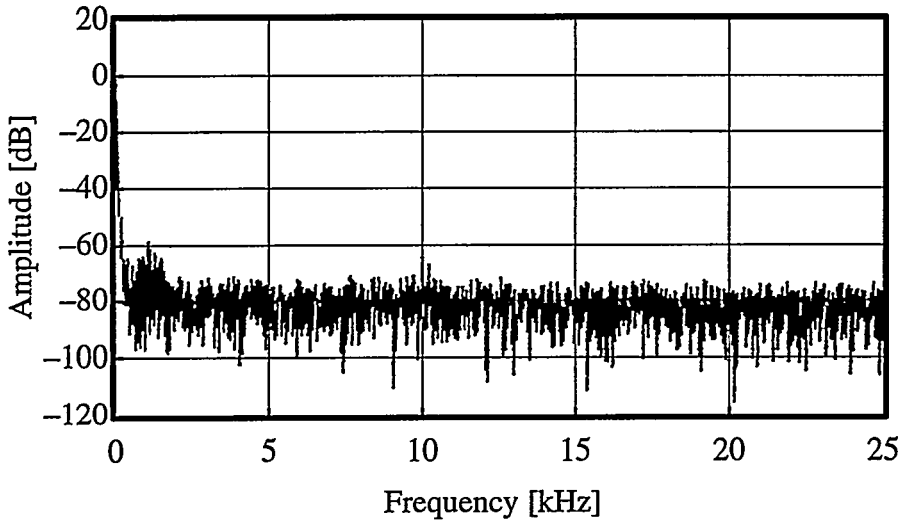

Figure D.6: FFT of the original signal.

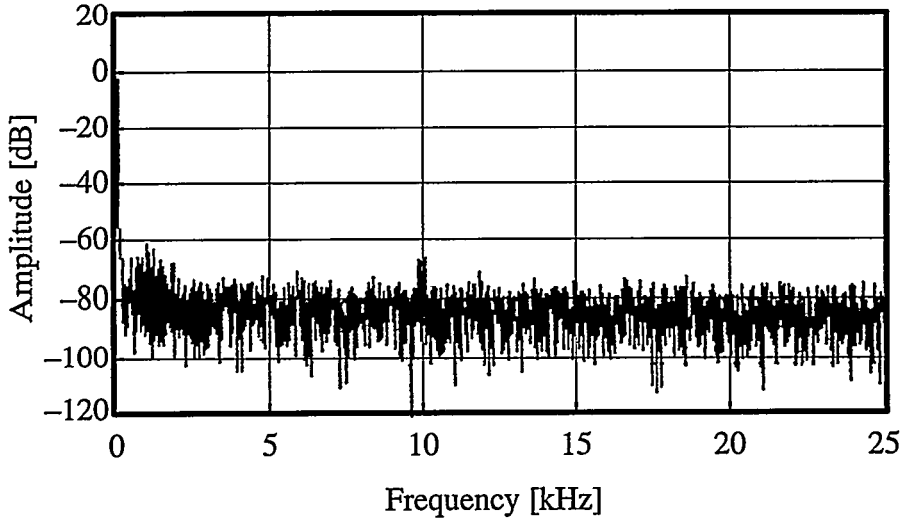

Figure D.7: FFT of the signal after passing through the measurement system.

- 40 out &H302, control–word3.

Turning these switches on/off is effected by different control–words, thereby selecting different combinations of switching for excitation and measurement. The measurement controlling software is listed in Appendix E.

APPENDIX E

PROGRAM LISTING

E.1 Listing of the Data Acquisition System Control Program (DASCP)

```
' ************************************************************************
' DATA ACQUIZATION CONTROL PROGRAM FOR HIGH ACCURACY SYSTEM
' ************************************************************************
' APPLIES MULTIPLE ELECTRODE AND WALSH EXCITATION PATTERNS
'
' Version 1.0   April 20, 1994 (By Hongjun Shu)
' Version 1.1   May 10, 1995 (By Levent Ovacik)
' Version 1.2   July 05, 1997 (By Levent Ovacik)
' ************************************************************************

DIM CTRWA(32), ctrwb(32), ctrwbl(32), ctrwc(32), Ctrwah(32), Ctrwal(32), dati(128), R(32),
RDROP(32), CTRHT(32), CtrLT(32)
DIM Ha(32), hp(32), hc(32), SUM(128, 32), DAT1(1000), DAT2(1000), IHCE(32, 32), ILCE(32, 32),
TEMP(32), IMT(32), rdgs(1000), stdc(32)
DIM CB(34)
' THE T-DISTRIBUTION TABLE FOR 99% CONFIDENCE LEVEL
DATA 63.657,9.925,5.841,4.604,4.032,3.707,3.499,3.355,3.250,3.169
DATA 3.106,3.055,3.012,2.977,2.947,2.921,2.898,2.878,2.861,2.845
DATA 2.831,2.819,2.807,2.797,2.787,2.779,2.771,2.763,2.756,2.750
DATA 2.704,2.660,2.617,2.576
d$ = SPACE$(40)
DMMADDR% = 22
FGADDR% = 9
CALL INITIALIZE(21, 0)
CLS : KEY OFF
' READ THE t-DISTRIBUTION TABLE
FOR I = 1 TO 34
READ CB(I)
NEXT I
DATMAX = 1000
EPSMAX = 10 ^ (-3.00001)
RUNMODE = 0  ' SET 0 FOR CONTINUOS RUNNIG MODE
NEXPT = 10
NR = 2
R$ = STR$(NR)
FOR I = 1 TO 32
R(I) = 0!
NEXT I
```

```
' SCREEN SETTINS
 SCREEN 0: COLOR 15, 1:
 CLS : KEY OFF
 CALL SEND(FGADDR%, "RESET", STATUS%)
 CALL SEND(FGADDR%, "APPLY SQV 10.", STATUS%)
 CALL SEND(FGADDR%, "FREQ 1000", STATUS%)
 CALL SEND(DMMADDR%, "RESET", STATUS%)
 CALL SEND(DMMADDR%, "PRESET NORM", STATUS%)
 CALL SEND(DMMADDR%, "LFILTER ON", STATUS%)
 CALL SEND(DMMADDR%, "DISP OFF", STATUS%)
 CALL SEND(DMMADDR%, "BEEP OFF", STATUS%)
 CALL SEND(DMMADDR%, "DELAY .25E-3", STATUS%)
 CALL SEND(DMMADDR%, "LEVEL 0,AC", STATUS%)
 CALL SEND(DMMADDR%, "SLOPE POS", STATUS%)
 CALL SEND(DMMADDR%, "MEM OFF", STATUS%)
 CALL SEND(DMMADDR%, "INBUF ON", STATUS%)
 INDAT$ = STRING$(50, 0)      'Array to hold strinG returned by ENTER
 STAT$ = STRING$(70, 0)       'StrinG to hold status information
' Set time out to 1 second(s)
 CALL SETTIMEOUT(1000)
' Set up error handler
' ON ERROR GOTO 10000
2
 CLS : LOCATE 10, 15: PRINT "*************************************************"
 LOCATE 5, 23: PRINT "Static Switching Measurement System"
 LOCATE 12, 15: PRINT "  0————————FUNCTION GENERATION CONFIGRATION"
 LOCATE 13, 15: PRINT "  1————————STARTING MEASUREMENT"
5
 LOCATE 15, 15: PRINT "*************************************************"
 PRINT
 INPUT "         PLEASE SELECT 0/1                  > ", MODE
 IF MODE = 0 THEN GOSUB 20000
 IF MODE = 1 THEN GOTO 10
 GOTO 5
10
 INPUT "         PLEASE SELECT DVM/SCOPE(1/2)         > ", idors
 IF idors <> 1 AND idors <> 2 THEN
 PRINT "INPUT ERROR. TRY AGAIN"
 GOTO 10
 END IF
 INPUT "         PLEASE INPUT SAVING DATA FILENAME :   > ", outname$
 outname$ = "C:\GPIB\DATA\" + outname$
' ================================================
15
 INPUT "         PLEASE INPUT CHANNEL NUMBER(/16/32)   > ", ichannel
 IF ichannel <> 16 AND ichannel <> 32 THEN
 PRINT "INPUT ERROR:TRY AGAIN"
```

```
 GOTO 15
 END IF
22
 INPUT "        PLEASE INPUT CHANNEL RESISTORS FILENAME > ", FILERES$
 OPEN FILERES$ FOR INPUT AS #15
 FOR ICHAN = 1 TO 32 STEP 32 / ichannel
 INPUT #15, ii, R(ICHAN)
 NEXT ICHAN
 CLOSE #15
 INPUT "        PLEASE INPUT EXCITATION PATERN FILENAME > ", FILENAME$
 OPEN FILENAME$ FOR INPUT AS #5
 INPUT #5, itime
 PRINT USING "        THE NUMBER OF EXCITATIONS          > ### "; itime
 FOR J = 1 TO itime
 INPUT #5, IMT(J)
 FOR I = 1 TO IMT(J)
 INPUT #5, IHCE(J, I)
 NEXT I
 FOR I = 1 TO IMT(J)
 INPUT #5, ILCE(J, I)
 NEXT I
 NEXT J
 CLOSE #5
 INPUT "        press any key to continue     ", a
24
 FOR id = 1 TO NEXPT
 outname1$ = outname$ + LTRIM$(STR$(id))
 OPEN outname1$ FOR OUTPUT AS #3
25 '==========INITIALIZE PIO BOARD==========
 FOR K = 1 TO itime        'LOOP FOR THE NUMBER OF EXCITATIONS
 FOR I = 1 TO 32
 dati(I) = 0!
 NEXT IGOSUB 1300
 CLSLOCATE 2, 2: PRINT "Excitation : "; K;
 LOCATE 25, 60: PRINT "EXPERIMENT NO. : "; id
 LOCATE 1, 30: PRINT "Channel Current Values"
 LOCATE 3, 2: PRINT "Measuring Channel : "
' ========= GET THE CONTROL WARD A==========
 GOSUB 1200
 FOR I = 1 TO 8
 OUT &H300 + (I – 1) * 4, Ctrwah(I – 1)
 NEXT I
 FOR M = 1 TO 1000000
 NEXT M  ' delay for stable
' ========= GET THE CURRENT VALUE==========
 FOR J = 1 TO IMT(K)
 TEMP(J) = IHCE(K, J)
```

```
TEMP(J + IMT(K)) = ILCE(K, J)
NEXT J
CURMOD = 1
SUMC = 0!
FOR J = 1 TO IMT(K) * 2
412
LOCATE 3, 22: PRINT TEMP(J)
lm = TEMP(J)
Lb = FIX((lm – 1) / 16)
La = lm – Lb * 16 – 1
La = FIX(La / 4)
lc = lm – Lb * 16 – La * 4
ctrwc(Lb * 4 + La) = &HFF – 2 ^ (8 – lc)
ctrwb(Lb * 4 + La) = &HFF – 5 – 2 ^ (8 – lc)
OUT &H302 + (Lb * 4 + La) * 4, ctrwc(Lb * 4 + La)
OUT &H301 + (Lb * 4 + La) * 4, ctrwb(Lb * 4 + La)
' ==============PIO PORTC=========================
FOR M = 1 TO 10000              'delay for stable
NEXT M
JROW = 4
I = 0
GOSUB 900
dati(TEMP(J)) = SUM(K, 0) / R(TEMP(J))   'current value
RDROP(TEMP(J)) = SUM(K, 0)
stdc(TEMP(J)) = STDEV / R(TEMP(J))
JROW = 4 + J
JCOL = 5
IF J > IMT(K) THEN
JROW = 4 + J – IMT(K)
JCOL = 45
vdrop = ABS(SUM(K, 0))
dati(TEMP(J)) = –dati(TEMP(J))
RDROP(TEMP(J)) = –SUM(K, 0)
IF (J – IMT(K)) = 1 THEN
vdropmin = vdrop
indmin = TEMP(J)
END IF
IF vdrop < vdropmin THEN
vdropmin = vdrop
indmin = TEMP(J)
END IF
END IF
SUMC = SUMC + dati(TEMP(J))
LOCATE JROW, JCOL:
PRINT USING "I[##] =  ##.######^^^^ ##.##^^^^"; TEMP(J); dati(TEMP(J)), stdc(TEMP(J))
OUT &H302 + (Lb * 4 + La) * 4, &HFF
OUT &H301 + (Lb * 4 + La) * 4, &HFF
```

```
LOCATE 3, 40: PRINT USING "Sum. : ##.######^^^^"; SUMC
NEXT J
FOR ii = 1 TO 100000
NEXT ii
CURMOD = 0
PRINT
' ==============================
413
CLS
LOCATE 2,1
PRINT"_____"
LOCATE 1, 2: PRINT "Excitation : "; K
LOCATE 1, 30: PRINT "Electrode Potential Values"
LOCATE 3, 2: PRINT "Reference Electrode : "; indmin
LOCATE 5, 2: PRINT " Elec.|   Ave.   |  St.Dev."
LOCATE 6, 2: PRINT "_____|_____|_____"
IF ichannel = 32 THEN
LOCATE 5, 41: PRINT " Elec.|   Ave.   |  St.Dev."
LOCATE 6, 41: PRINT "_____|_____|_____"
END IF
' MEASURE THE SOURCE VOLTAGE
VPMIN = 1000!
VNMIN = 1000!
FOR I = 1 TO IMT(K) * 2
INDEX = TEMP(I)
VVDROP = ABS(RDROP(INDEX))
IF (I <= IMT(K)) THEN
IF (VVDROP < VPMIN) THEN
IF (INDEX <> 5) AND (INDEX <> 21) AND (INDEX <> 29) THEN
IPMIN = INDEX
VPMIN = VVDROP
END IF
END IF
END IF
IF (I > IMT(K)) THEN
IF (VVDROP < VNMIN) THEN
INMIN = INDEX
VNMIN = VVDROP
END IF
END IF
NEXT I
hm = IPMIN
lm = INMIN
I = hm
Hb = FIX((hm - 1) / 16)
Ha = hm - Hb * 16 - 1
Ha = FIX(Ha / 4)
```

```
hc = hm – Hb * 16 – Ha * 4
Lb = FIX((lm – 1) / 16)
La = lm – Lb * 16 – 1
La = FIX(La / 4)
lc = lm – Lb * 16 – La * 4
ctrwc(I) = &HFF – 2 ^ (4 – hc)
ctrwb(I) = &HFF – idors
ctrwbl(I) = &HFF – 4 * idors – 2 ^ (8 – lc)
IF Hb * 4 + Ha = Lb * 4 + La THEN
ctrwbl(I) = ctrwbl(I) – idors
ctrwb(I) = ctrwbl(I)
END IF
LOCATE 3, 50: PRINT USING "High = ## Low = ## "; hm; lm
OUT &H302 + (Hb * 4 + Ha) * 4, ctrwc(I)
OUT &H301 + (Hb * 4 + Ha) * 4, ctrwb(I)
OUT &H301 + (Lb * 4 + La) * 4, ctrwbl(I)
GOSUB 900
OUT &H302 + (Hb * 4 + Ha) * 4, &HFF
OUT &H301 + (Lb * 4 + La) * 4, &HFF
OUT &H301 + (Hb * 4 + Ha) * 4, &HFF
IE = 0
FOR I = 1 TO 32 STEP 32 / ichannel
IE = IE + 1
IF (RDROP(I) < 0!) THEN
SUM(K, I) = –RDROP(I)
ELSE
SUM(K, I) = (VSOURCE + ABS(RDROP(IPMIN)) + ABS(RDROP(INMIN))) – RDROP(I)
END IF
PRINT #3, USING "## ##  ##.######^^^^ ##.######^^^^ ##.######^^^^ "; K; IE; SUM(K, I); dati(I);
stdc(I) 'write  excitation electrode VOLTAGE & current value
NEXT I
NEXT K
895
CLOSE #3
' ========== initialization of PIO==========
GOSUB 1300
IF RUNMODE <> 0 THEN
1120
INPUT " PLEASE PRESS <1> FOR THE NEXT EXPERIMENT  > ", IRUN
IF IRUN = 1 THEN 1122
GOTO 1120
END IF
1122
NEXT id
STOP
' >>>>>>>>>>>>>>>>>>>>>>>>>>>>>>>>>>>>>>>>>>>>>>>>>>>>>>>>>>>>>>>>>>>>>>>>
900
```

```
' SUBROUTINE TO GET DATA FROM DVM
' DETERMINE THE VOLTAGE RANGE
 CALL SEND(DMMADDR%, "DSAC .01", STATUS%)
 GOSUB 1100
 VMAX = ABS(VMEAS)
 IF VMAX < 1000 THEN
 IF VMAX <= .012 GOTO 123
 END IF
 CALL SEND(DMMADDR%, "DSAC .1", STATUS%)
 GOSUB 1100
 VMAX = ABS(VMEAS)
 IF VMAX < 1000 THEN
 IF VMAX <= .12 GOTO 123
 END IF
 CALL SEND(DMMADDR%, "DSAC 1", STATUS%)
 GOSUB 1100
 VMAX = ABS(VMEAS)
 IF VMAX < 1000 THEN
 IF VMAX <= 1.2 GOTO 123
 END IF
 CALL SEND(DMMADDR%, "DSAC 10", STATUS%)
 GOSUB 1100
 VMAX = ABS(VMEAS)
 IF VMAX > 1000 THEN STOP
123
 SLAST$ = VSCALE$
 IF (VMAX <= .012) THEN VSCALE$ = ".01"
 IF (VMAX > .012) AND (VMAX <= .12) THEN VSCALE$ = ".1"
 IF (VMAX > .12) AND (VMAX <= 1.2) THEN VSCALE$ = "1"
 IF (VMAX > 1.2) AND (VMAX <= 12) THEN VSCALE$ = "10"
 IF SLAST$ <> VSCALE$ THEN
 CALL SEND(DMMADDR%, "DSAC " + VSCALE$, STATUS%)
 END IF
 SUM(K, I) = 0!
 NN = NR
 FOR III = 1 TO NN
 VMEAS = 0!
 GOSUB 1100
 DAT1(III) = VMEAS
 NEXT III
 FOR III = 1 TO NN
 VMEAS = 0!
 GOSUB 1100
 DAT2(III) = VMEAS
 NEXT III
 SUM1 = 0!
 SUM2 = 0!
```

```
FOR IM = 1 TO NN
SUM1 = SUM1 + DAT1(IM)
SUM2 = SUM2 + DAT2(IM)
NEXT IM
AVE1 = SUM1 / NN
AVE2 = SUM2 / NN
STD1 = 0!
STD2 = 0!
FOR IM = 1 TO NN
STD1 = STD1 + ((AVE1 – DAT1(IM))) ^ 2
STD2 = STD2 + ((AVE2 – DAT2(IM))) ^ 2
NEXT IM
STD1 = SQR(STD1 / (NN – 1))
STD2 = SQR(STD2 / (NN – 1))
STD12 = SQR((STD1 ^ 2 + STD2 ^ 2) / NN)
IF STD12 <= 1E–20 THEN STD12 = 1E–20
ZCONF = CB(2 * (NN – 1))
LOCATE 25, 1: PRINT USING " NO. OF AVERAGES: #####   EPSILON: #.####^^^^"; NN; EPSILON;
XAVE = (AVE1 + AVE2) / 2!
STDEV = SQR((STD1 ^ 2 + STD2 ^ 2) / 4! / NN)
EPSILON = STDEV / XAVE
IF (ZCONF * STD12 / 2! / XAVE <= EPSMAX) THEN
ELSE
DO UNTIL (ZCONF * STD12 / 2! / XAVE <= EPSMAX)
NN = NN + 1
IF (NN > DATMAX) THEN
CALL INITIALIZE(21, 0)
IF CURMOD = 1 THEN BEEP: RETURN 412
IF CURMOD = 0 THEN BEEP: RETURN 413
END IF
NU = 2 * (NN – 1)
IF NU > 120 THEN ZCONF = CB(34)
IF NU <= 120 THEN ZCONF = CB(33)
IF NU <= 60 THEN ZCONF = CB(32)
IF NU <= 40 THEN ZCONF = CB(31)
IF NU <= 30 THEN ZCONF = CB(NU)
VMEAS = 0!
GOSUB 1100
DAT1(NN) = VMEAS
VMEAS = 0!
GOSUB 1100
DAT2(NN) = VMEAS
SUM1 = SUM1 + DAT1(NN)
SUM2 = SUM2 + DAT2(NN)
AVE1 = SUM1 / NN
AVE2 = SUM2 / NN
STD1 = 0!
```

```
STD2 = 0!
FOR IM = 1 TO NN
STD1 = STD1 + ((AVE1 – DAT1(IM))) ^ 2
STD2 = STD2 + ((AVE2 – DAT2(IM))) ^ 2
NEXT IM
STD1 = SQR(STD1 / (NN – 1))
STD2 = SQR(STD2 / (NN – 1))
STD12 = SQR((STD1 ^ 2 + STD2 ^ 2) / NN)
IF STD12 <= 1E–20 THEN STD12 = 1E–20
EPSILON = ABS((AVE1 – AVE2) / (AVE1 + AVE2))
XAVE = (AVE1 + AVE2) / 2!
STDEV = SQR((STD1 ^ 2 + STD2 ^ 2) / 4! / NN)
EPSILON = STDEV / XAVE
LOCATE 25, 1: PRINT USING " NO. OF AVERAGES: #####  EPSILON: #.####^^^^"; NN; EPSILON;
LOOP
END IF
SUM(K, I) = XAVE
IF CURMOD = 0 THEN
VSOURCE = XAVE
IF IE <= 16 THEN
XROW = 6 + IE
YCOL = 1
ELSE
XROW = 6 + IE – 16
YCOL = 40
END IF
LOCATE XROW, YCOL: PRINT USING " ##  ##.######^^^^ ##.######^^^^ ";
hm; SUM(K, I);  STDEV
FOR jj = 1 TO 500000
NEXT jj
END IF
RETURN
' ================================================
1100
' SUBROUTINE FOR DMM PROTOCOL
CALL SEND(DMMADDR%, "TRIG LEVEL", STATUS%)
CALL ENTER(d$, LENGHT%, DMMADDR%, STATUS%)
' Test for error in ENTER
IF STATUS% <> 0 THEN
BEEP
CALL INITIALIZE(21, 0)
IF CURMOD = 1 THEN RETURN 412
IF CURMOD = 0 THEN RETURN 413
END IF
d$ = LEFT$(d$, LENGHT%)
VMEAS = VAL(d$)
RETURN
```

```
1200
' CACULATE THE CONTROL WARD A
 FOR I = 1 TO IMT(K)
 hm = IHCE(K, I)
 Hb = FIX((hm – 1) / 16)
 Ha = hm – Hb * 16 – 1
 Ha = FIX(Ha / 4)
 hc = hm – Hb * 16 – Ha * 4
 lm = ILCE(K, I)
 Lb = FIX((lm – 1) / 16)
 La = lm – Lb * 16 – 1
 La = FIX(La / 4)
 lc = lm – Lb * 16 – La * 4
 CTRHT(Hb * 4 + Ha) = 2 ^ (8 – hc)
 CtrLT(Lb * 4 + La) = 2 ^ (4 – lc)
 CTRHT(Hb * 4 + Ha) = &HFF – CTRHT(Hb * 4 + Ha)
 CtrLT(Lb * 4 + La) = &HFF – CtrLT(Lb * 4 + La)
 IF Ha + Hb * 4 = La + Lb * 4 THEN
 CTRHT(Hb * 4 + Ha) = CTRHT(Hb * 4 + Ha) AND CtrLT(Lb * 4 + La)
 CtrLT(La + Lb * 4) = CTRHT(Hb * 4 + Ha)
 END IF
 Ctrwah(Hb * 4 + Ha) = Ctrwah(Hb * 4 + Ha) AND CTRHT(Hb * 4 + Ha)
 Ctrwal(Lb * 4 + La) = Ctrwal(Lb * 4 + La) AND CtrLT(Lb * 4 + La)
 NEXT I
 FOR I = 1 TO 8
 Ctrwah(I – 1) = Ctrwah(I – 1) AND Ctrwal(I – 1)
 NEXT I
 RETURN
1300
' ====================initialization PIO==============
 FOR I = 0 TO 7            '8 BOARDS FOR INITIALIZING
 OUT &H303 + 4 * I, &H80
 OUT &H300 + 4 * I, &HFF
 OUT &H301 + 4 * I, &HFF
 OUT &H302 + 4 * I, &HFF
 NEXT I
 FOR I = 0 TO ichannel – 1
 CTRWA(I) = &H0
 ctrwb(I) = &HFF
 ctrwc(I) = &HFF
 Ctrwah(I) = &HFF
 Ctrwal(I) = &HFF
 dati(I + 1) = 0
 NEXT I
 RETURN
' ==================END==================
 END
```

```
' Error Processing
1460
 CALL SEND(DMMADDR%, "STATUS", STATUS%)       'Request status
 CALL ENTER(d$, LENGHT%, DMMADDR%, STATUS%)
' Test for error in ENTER
 IF STATUS% <> 0 THEN PRINT " The data from DMM is not right !!": STOP
 d$ = LEFT$(d$, LENGHT%)
 STAT$ = d$
 PRINT STAT$
 IF (MID$(STAT$, 22, 1) <> "1") GOTO 1460
 PRINT
' SRQ received cancel timer
 TIMER OFF
' Enter and print the SRQ1 of the DMM
 CALL SEND(DMMADDR%, "SPOLL 22", STATUS%)'Request serial poll byte
 CALL ENTER(d$, LENGHT%, DMMADDR%, STATUS%)
' Test for error in ENTER
 IF STATUS% <> 0 THEN PRINT " The data from DMM is not right !!": STOP
 d$ = LEFT$(d$, LENGHT%)
 srq1 = VAL(d$)' Read serial poll byte
 PRINT "The SPOLL byte returned from the 196 = "; srq1
 PRINT
 IF srq1 = 88 GOTO 2400
 IF srq1 = 80 GOTO 2600
 PRINT "WHAT'S GOING ON ???"
 STOP
2400
 PRINT "MEASUREMENT COMPLETE AND METER IS READY FOR COMMAND"
 PRINT
 RETURN
2600 PRINT "METER READY FOR COMMAND"
 PRINT
 RETURN
4000
' ************ EXIT DUE TO TIME OUT WAITING FOR SRQ ***************
 PRINT "PROGRAM TIMED OUT WAITING FOR A SRQ"
 STOP
10000
' ************************ Error handler ***************************
 IF (ERR = 57 OR ERR = 68 OR ERR = 75) GOTO 10100
 PRINT "BASIC Error In Line "; ERL; "Error Number = "; ERR
 STOP
10100
 PRINT "IEEE Error In Line "; ERL; "Error Number = "; ERR
 CALL SEND(DMMADDR%, "STATUS", STATUS%)       'Request status
 CALL ENTER(d$, LENGHT%, DMMADDR%, STATUS%)
' Test for error in ENTER
```

```
 IF STATUS% <> 0 THEN PRINT " The data from DMM is not right !!": STOP
 d$ = LEFT$(d$, LENGHT%)
 STAT$ = d$ 'Return status string
 PRINT STAT$
 STOP
20000
 WAVEFORM$ = "FU1"
 HZNUM$ = "FR100HZ"
 AMPL$ = "AM10VO"
 OFF$ = "OF0MV"
 PHASE$ = "PH0DE"
21000
 CLS
 LOCATE 8, 20:  PRINT "*********************************************"
 LOCATE 9, 20:  PRINT "*  CONFIGERATION FUNCTION GENERATION  *"
 LOCATE 10, 20: PRINT "*   0——EXIT                          *"
 LOCATE 11, 20: PRINT "*   1——WAVE FORM                     *"
 LOCATE 12, 20: PRINT "*   2——FREQUENCY                     *"
 LOCATE 13, 20: PRINT "*   3——AMPLITUDE                     *"
 LOCATE 14, 20: PRINT "*   4——OFFSET                        *"
 LOCATE 15, 20: PRINT "*   5——PHASE                         *"
 LOCATE 16, 20: PRINT "*   6——SELFTEST                      *"
 LOCATE 17, 20: PRINT "*   7——AMPLITUDE CALIBRATION         *"
 LOCATE 18, 20: PRINT "*********************************************"
22100
 a$ = INKEY$
 IF a$ = "0" THEN GOTO 22000
 IF a$ = "1" THEN GOSUB 21100
 IF a$ = "2" THEN GOSUB 21200
 IF a$ = "3" THEN GOSUB 21300
 IF a$ = "4" THEN GOSUB 21400
 IF a$ = "5" THEN GOSUB 21500
 IF a$ = "6" THEN GOSUB 21600
 IF a$ = "7" THEN GOSUB 21700
 GOTO 22100
21100
 I = 12: J = 30
 LOCATE I, J:     PRINT "*********************************************"
 LOCATE I + 1, J: PRINT "*   CONFIGERATION WAVEFORM           *"
 LOCATE I + 2, J: PRINT "*   0——DC                            *"
 LOCATE I + 3, J: PRINT "*   1——SINE                          *"
 LOCATE I + 4, J: PRINT "*   2——SQUARE                        *"
 LOCATE I + 5, J: PRINT "*   3——TRANGLE                       *"
 LOCATE I + 6, J: PRINT "*   4——RAMP UP                       *"
 LOCATE I + 7, J: PRINT "*   5——RAMP DOWN                     *"
 LOCATE I + 8, J: PRINT "*   6——AUX. TTL                      *"
 LOCATE I + 9, J: PRINT "*********************************************"
```

```
21010
 a$ = INKEY$
 IF a$ < "0" OR a$ > "6" THEN GOTO 21010
 WAVEFORM$ = "FU" + a$
 PRINT WAVEFORM$
 RETURN 21000
21200
 I = 13: J = 30
 LOCATE I, J:     PRINT "*******************************************"
 LOCATE I + 1, J: PRINT "*   CONFIGURATION FREQUENCY               *"
 LOCATE I + 2, J: PRINT "*                                         *"
 LOCATE I + 3, J: PRINT "*   PLEASE INPUT HZ NUMBER(HZ)            *"
 LOCATE I + 4, J: PRINT "*                                         *"
 LOCATE I + 5, J: PRINT "*                                         *"
 LOCATE I + 6, J: PRINT "*                                         *"
 LOCATE I + 7, J: PRINT "*******************************************"
 LOCATE I + 4, J + 5: INPUT HZNUM$
 HZNUM$ = "FR" + HZNUM$ + "HZ"
 RETURN 21000
21300
 I = 14: J = 30
 LOCATE I, J:     PRINT "*******************************************"
 LOCATE I + 1, J: PRINT "*   CONFIGERATION AMPLITUDE               *"
 LOCATE I + 2, J: PRINT "*   1——1 MV                               *"
 LOCATE I + 3, J: PRINT "*   2——10 MV                              *"
 LOCATE I + 4, J: PRINT "*   3——100 MV                             *"
 LOCATE I + 5, J: PRINT "*   4——1 V                                *"
 LOCATE I + 6, J: PRINT "*   5——10 V                               *"
 LOCATE I + 7, J: PRINT "*******************************************"
21310
 a$ = INKEY$: IF a$ = "" THEN GOTO 21310
 IF a$ = "1" THEN AMPL$ = "AM1MV": RETURN 21000
 IF a$ = "2" THEN AMPL$ = "AM10MV": RETURN 21000
 IF a$ = "3" THEN AMPL$ = "AM100MV": RETURN 21000
 IF a$ = "4" THEN AMPL$ = "AM1VO": RETURN 21000
 IF a$ = "5" THEN AMPL$ = "AM10VO": RETURN 21000
 GOTO 21310
21400
 I = 15: J = 30
 LOCATE I, J: PRINT "*******************************************"
 LOCATE I + 1, J: PRINT "*   CONFIGURATION DC OFFSET           *"
 LOCATE I + 2, J: PRINT "*                                     *"
 LOCATE I + 3, J: PRINT "*   PLEASE INPUT OFFSET NUMBER(MV)    *"
 LOCATE I + 4, J: PRINT "*                                     *"
 LOCATE I + 5, J: PRINT "*                                     *"
 LOCATE I + 6, J: PRINT "*                                     *"
 LOCATE I + 7, J: PRINT "*******************************************"
```

```
 LOCATE I + 4, J + 5: INPUT OFF$
 HZNUM$ = "OF" + OFF$ + "MV"
 RETURN 21000
21500
 I = 16: J = 30
 LOCATE I, J: PRINT "*****************************************"
 LOCATE I + 1, J: PRINT "*   CONFIGURATION PHASE              *"
 LOCATE I + 2, J: PRINT "*                                    *"
 LOCATE I + 3, J: PRINT "*   PLEASE INPUT PHASE DEGREE        *"
 LOCATE I + 4, J: PRINT "*                                    *"
 LOCATE I + 5, J: PRINT "*                                    *"
 LOCATE I + 6, J: PRINT "*                                    *"
 LOCATE I + 7, J: PRINT "*****************************************"
 LOCATE I + 4, J + 5: INPUT PHASE$
 PHASE$ = "PH" + PHASE$ + "DE"
 RETURN 21000
21600
 RETURN 1000
21700
 I = 18: J = 30
 LOCATE I, J: PRINT "*****************************************"
 LOCATE I + 1, J: PRINT "*   AMPLITUDE CALIBRATION            *"
 LOCATE I + 2, J: PRINT "*                                    *"
 LOCATE I + 3, J: PRINT "*   PLEASE WAIT A FEW SECONDS        *"
 LOCATE I + 4, J: PRINT "*                                    *"
 LOCATE I + 5, J: PRINT "*                                    *"
 LOCATE I + 6, J: PRINT "*                                    *"
 LOCATE I + 7, J: PRINT "*****************************************"
 FOR I = 1 TO 1000:
 FOR J = 1 TO 100: NEXT J
 NEXT I
 RETURN 21000
22000
 ' Set time out to 10 seconds
 PRINT #1, "TIME OUT 10" '=======================================
 PRINT #1, "clear 17"
 PRINT #1, "output 17;OOF1"
 PRINT #1, "output 17;beep"
 RETURN 2
'=========================================================
```

E.2 Listing of the Data Acquisition System Calibration Program

```
' CALIBRATION PROGRAM FOR DATA ACQUISITION SYSTEM
' MULTIPLE ELECTRODE AND WALSH EXCITATION
 DIM CTRWA(32), CTRWB(32), CTRWBL(32), CTRWC(32), CTRWAH(32), CTRWAL(32),
 DATI(128), r(32), CTRHT(32), CTRLT(32)
 DIM HA(32), hp(32), HC(32), SUM(128, 32), A(100), IHCE(32, 32), ILCE(32, 32), TEMP(32), IMT(32)
 DIM CB(34), DAT1(1000), DAT2(1000)
' THE T-DISTRIBUTION TABLE FOR 99% CONFIDENCE LEVEL
 DATA 63.657,9.925,5.841,4.604,4.032,3.707,3.499,3.355,3.250,3.169
 DATA 3.106,3.055,3.012,2.977,2.947,2.921,2.898,2.878,2.861,2.845
 DATA 2.831,2.819,2.807,2.797,2.787,2.779,2.771,2.763,2.756,2.750
 DATA 2.704,2.660,2.617,2.576
 EPSMAX = .0005
 NR = 2
 r$ = STR$(NR)
' READ THE t-DISTRIBUTION TABLE
 FOR I = 1 TO 34
 READ CB(I)
 NEXT I
' SCREEN SETTINGS
 CLS : KEY OFF
 SCREEN 0: COLOR 15, 1:
 d$ = SPACE$(30)
 DMMADDR% = 22
 fgaddr% = 9
 CALL INITIALIZE(21, 0)
 INDAT$ = STRING$(50, 0)      'Array to hold string returned by ENTER
 STAT$ = STRING$(70, 0)       'StrinG to hold status information
' Set time out to 5 seconds
 CALL SETTIMEOUT(3000)
' Set up error handler
 ON ERROR GOTO 10000
2
 CLS : LOCATE 10, 15: PRINT "**************************************************"
 LOCATE 12, 20: PRINT "Static Switching Measurement"
 LOCATE 14, 15: PRINT "  0————————FUNCTION GENERATION CONFIGRATION"
 LOCATE 15, 15: PRINT "  1————————STARTING MEASUREMENT"
5
 LOCATE 17, 15: PRINT "**************************************************"
 INPUT "          PLEASE SELECT 1/0                > ", MODE
 IF MODE = 0 THEN GOSUB 20000
 IF MODE = 1 THEN GOTO 10
 GOTO 5
10
 LOCATE 18, 1: PRINT :
```

```
 INPUT "          PLEASE SELECT DVM/SCOPE(1/2)          > ", IDORS
 IF IDORS <> 1 AND IDORS <> 2 THEN
 PRINT "INPUT ERROR. TRY AGAIN"
 GOTO 10
 END IF
 LOP = 10
 INPUT "          PLEASE INPUT SAVING DATA FILENAME :    > ", OUTNAME$
 OUTNAME$ = "C:\GPIB\BASIC\" + OUTNAME$
 OPEN OUTNAME$ FOR OUTPUT AS #3
' ===============================================
15
 INPUT "          PLEASE INPUT CHANNEL NUMBER(/16/32)    > ", ICHANNEL
 IF ICHANNEL <> 16 AND ICHANNEL <> 32 THEN
 PRINT "INPUT ERROR:TRY AGAIN"
 GOTO 15
 END IF
22
 INPUT "          PLEASE INPUT EXCITATION PATERN FILENAME > ", FILENAME$
 OPEN FILENAME$ FOR INPUT AS #5
 FILENAME$ = "C:\GPIB\BASIC\" + FILENAME$
 INPUT #5, ITIME
 PRINT "          THE NUMBER OF EXCITATIONS          >", ITIME
 FOR J = 1 TO ITIME
 INPUT #5, IMT(J)
 FOR I = 1 TO IMT(J)
 INPUT #5, IHCE(J, I)
 NEXT I
 FOR I = 1 TO IMT(J)
 INPUT #5, ILCE(J, I)
 NEXT I
 NEXT J
 CLOSE #5
 INPUT "          press any key to continue          ", A
 CLS
24
 PRINT "++++++++++++++++++++++++++++++++++++++++++++++++++"
 PRINT "  MEASURING THE SERIAL CHANNEL RESISTOR VALUES"
 PRINT "++++++++++++++++++++++++++++++++++++++++++++++++++"
' ==========initialization of PIO==========
 GOSUB 1300
25
' ==============init PIO BOARD==================
 FOR K = 1 TO ITIME  'LOOP FOR THE NUMBER OF EXCITATIONS
 FOR I = 1 TO 32
 DATI(I) = 0
 NEXT I
' ============initialize the meter and function generator=====
```

```
' DIGITAL MULTIMETER
 CALL SEND(DMMADDR%, "RESET", STATUS%)
 CALL SEND(DMMADDR%, "PRESET NORM", STATUS%)
 CALL SEND(DMMADDR%, "LFILTER ON", STATUS%)
 CALL SEND(DMMADDR%, "DISP OFF", STATUS%)
 CALL SEND(DMMADDR%, "BEEP OFF", STATUS%)
 CALL SEND(DMMADDR%, "DELAY .25E-3", STATUS%)
 CALL SEND(DMMADDR%, "LEVEL 0,AC", STATUS%)
 CALL SEND(DMMADDR%, "SLOPE POS", STATUS%)
 CALL SEND(DMMADDR%, "INBUF ON", STATUS%)
' FUNCTION GENERATOR
 CALL SEND(fgaddr%, "APPLY SQI .002", STATUS%)
 CALL SEND(fgaddr%, "FREQ 1000", STATUS%)
' ========= GET THE CONTROL WARD A==========
 GOSUB 1300
 GOSUB 1200
 FOR I = 1 TO 8
 OUT &H300 + (I - 1) * 4, CTRWAH(I - 1)
 NEXT I
' ========GET THE CURRENT VALUE===============
 CURMOD = 1
 FOR J = 1 TO IMT(K)
 TEMP(J) = IHCE(K, J)
 TEMP(J + IMT(K)) = ILCE(K, J)
 NEXT J
 FOR J = 1 TO IMT(K) * 2
 LM = TEMP(J)
 LB = FIX((LM - 1) / 16)
 LA = LM - LB * 16 - 1
 LA = FIX(LA / 4)
 LC = LM - LB * 16 - LA * 4
 CTRWC(LB * 4 + LA) = &HFF - 2 ^ (8 - LC)
 CTRWB(LB * 4 + LA) = &HFF - 5 - 2 ^ (8 - LC)
 OUT &H302 + (LB * 4 + LA) * 4, CTRWC(LB * 4 + LA)
 OUT &H301 + (LB * 4 + LA) * 4, CTRWB(LB * 4 + LA)
' ===============PIO PORTC=======================
 FOR M = 1 TO 2000:              'delay for stable
 NEXT M
 412
 GOSUB 900
 r(TEMP(J)) = SUM(K, 0)
 OUT &H302 + (LB * 4 + LA) * 4, &HFF
 OUT &H301 + (LB * 4 + LA) * 4, &HFF
 NEXT J
 NEXT K
' Write  current measurement resistor values
 IE = 0
```

```
 FOR I = 1 TO 32 STEP 32 / ICHANNEL
 IE = IE + 1
 PRINT #3, USING "### ###.######"; I; r(I)
 NEXT I
895
 CLOSE #3
 GOSUB 1300
 STOP
900
' SUBROUTINE TO GET DATA FROM DVM
' DETERMINE THE VOLTAGE RANGE
 CALL SEND(DMMADDR%, "DSAC .01", STATUS%)
 GOSUB 1100
 VMAX = ABS(VMEAS)
 IF VMAX < 1000 THEN
 IF VMAX <= .012 GOTO 123
 END IF
 CALL SEND(DMMADDR%, "DSAC .1", STATUS%)
 GOSUB 1100
 VMAX = ABS(VMEAS)
 IF VMAX < 1000 THEN
 IF VMAX <= .12 GOTO 123
 END IF
 CALL SEND(DMMADDR%, "DSAC 1", STATUS%)
 GOSUB 1100
 VMAX = ABS(VMEAS)
 IF VMAX < 1000 THEN
 IF VMAX <= 1.2 GOTO 123
 END IF
 CALL SEND(DMMADDR%, "DSAC 10", STATUS%)
 GOSUB 1100
 VMAX = ABS(VMEAS)
 IF VMAX < 1000 THEN
 IF VMAX <= 1.2 GOTO 123
 END IF
123
 SLAST$ = VSCALE$
 IF (VMAX <= .012) THEN VSCALE$ = ".01"
 IF (VMAX > .012) AND (VMAX <= .12) THEN VSCALE$ = ".1"
 IF (VMAX > .12) AND (VMAX <= 1.2) THEN VSCALE$ = "1"
 IF (VMAX > 1.2) AND (VMAX <= 12) THEN VSCALE$ = "10"
 IF SLAST$ <> VSCALE$ THEN
 CALL SEND(DMMADDR%, "DSAC " + VSCALE$, STATUS%)
 END IF
 SUM(K, I) = 0!
 NN = NR
 FOR iii = 1 TO NN
```

```
GOSUB 1100
DAT1(iii) = VMEAS
GOSUB 1100
DAT2(iii) = VMEAS
NEXT iii
SUM1 = 0!
SUM2 = 0!
FOR IM = 1 TO NN
SUM1 = SUM1 + DAT1(IM)
SUM2 = SUM2 + DAT2(IM)
NEXT IM
AVE1 = SUM1 / NN
AVE2 = SUM2 / NN
STD1 = 0!
STD2 = 0!
FOR IM = 1 TO NN
STD1 = STD1 + ((AVE1 – DAT1(IM))) ^ 2
STD2 = STD2 + ((AVE2 – DAT2(IM))) ^ 2
NEXT IM
STD1 = SQR(STD1 / (NN – 1))
STD2 = SQR(STD2 / (NN – 1))
STD12 = SQR((STD1 ^ 2 + STD2 ^ 2) / NN)
IF STD12 <= 1E–20 THEN STD12 = 1E–20
Z = ABS(AVE1 – AVE2) / STD12
XAVE = (AVE1 + AVE2) / 2!
STDEV = SQR((STD1 ^ 2 + STD2 ^ 2) / 4! / NN)
EPSILON = STDEV / XAVE
ZCONF = CB(NN – 1)
LOCATE 25, 1: PRINT USING " NO. OF AVERAGES: #####   EPSILON: #.####^^^^"; NN; EPSILON;
IF (ZCONF * STD12 * .5 / XAVE <= EPSMAX) THEN
ELSE
DO UNTIL (ZCONF * STD12 * .5 / XAVE <= EPSMAX)
NN = NN + 1
IF (NN > 1000) THEN
IF CURMOD = 1 THEN BEEP: RETURN 412
END IF
NU = NN – 1
IF (NU) > 120 THEN ZCONF = CB(34)
IF (NU) <= 120 THEN ZCONF = CB(33)
IF (NU) <= 60 THEN ZCONF = CB(32)
IF (NU) <= 40 THEN ZCONF = CB(31)
IF (NU) <= 30 THEN ZCONF = CB(NU)
GOSUB 1100
DAT1(NN) = VMEAS
GOSUB 1100
DAT2(NN) = VMEAS
SUM1 = SUM1 + DAT1(NN)
```

```
 SUM2 = SUM2 + DAT2(NN)
 AVE1 = SUM1 / NN
 AVE2 = SUM2 / NN
 STD1 = 0!
 STD2 = 0!
 FOR IM = 1 TO NN
 STD1 = STD1 + ((AVE1 – DAT1(IM))) ^ 2
 STD2 = STD2 + ((AVE2 – DAT2(IM))) ^ 2
 NEXT IM
 STD1 = SQR(STD1 / (NN – 1))
 STD2 = SQR(STD2 / (NN – 1))
 STD12 = SQR((STD1 ^ 2 + STD2 ^ 2) / NN)
 IF STD12 <= 1E–20 THEN STD12 = 1E–20
 Z = ABS(AVE1 – AVE2) / STD12
 XAVE = (AVE1 + AVE2) / 2!
 STDEV = SQR((STD1 ^ 2 + STD2 ^ 2) / 4! / NN)
 EPSILON = STDEV / XAVE
 LOCATE 25, 1: PRINT USING " NO. OF AVERAGES: #####  EPSILON: #.####^^^^"; NN; EPSILON;
 LOOP
 END IF
 SUM(K, 0) = XAVE / .001
 IF ICHANNEL = 16 THEN
 XCOL = 1: YROW = 3 + (TEMP(J) + 1) / 2
 END IF
 IF ICHANNEL = 32 THEN
 IF TEMP(J) <= 16 THEN
 XCOL = 1: YROW = 3 + TEMP(J)
 ELSE
 XCOL = 40: YROW = 3 + TEMP(J) – 16
 END IF
 END IF
 LOCATE YROW, XCOL:
 PRINT USING " Chan.: ###    Res[OHM]: ###.######"; TEMP(J); SUM(K, 0): BEEP:
 CALL SEND(DMMADDR%, "CLEAR22", STATUS%)
 RETURN
1100
' SUBROUTINE FOR DMM PROTOCOL
 CALL SEND(DMMADDR%, "TRIg LEVEL", STATUS%)
 CALL ENTER(d$, LENGHT%, DMMADDR%, STATUS%)
' Test for error in ENTER
 IF STATUS% <> 0 THEN
 BEEP
 CALL INITIALIZE(21, 0)
 IF CURMOD = 1 THEN RETURN 412
 END IF
 d$ = LEFT$(d$, LENGHT%)
 VMEAS = VAL(d$)
```

```
 RETURN
'=============================================================
1200
' CACULATE THE CONTROL WARD A
 FOR I = 1 TO IMT(K)
 HM = IHCE(K, I)
 HB = FIX((HM – 1) / 16)
 HA = HM – HB * 16 – 1
 HA = FIX(HA / 4)
 HC = HM – HB * 16 – HA * 4
 LM = ILCE(K, I)
 LB = FIX((LM – 1) / 16)
 LA = LM – LB * 16 – 1
 LA = FIX(LA / 4)
 LC = LM – LB * 16 – LA * 4
 CTRHT(HB * 4 + HA) = 2 ^ (8 – HC)
 CTRLT(LB * 4 + LA) = 2 ^ (4 – LC)
 CTRHT(HB * 4 + HA) = &HFF – CTRHT(HB * 4 + HA)
 CTRLT(LB * 4 + LA) = &HFF – CTRLT(LB * 4 + LA)
 IF HA + HB * 4 = LA + LB * 4 THEN
 CTRHT(HB * 4 + HA) = CTRHT(HB * 4 + HA) AND CTRLT(LB * 4 + LA)
 CTRLT(LA + LB * 4) = CTRHT(HB * 4 + HA)
 END IF
 CTRWAH(HB * 4 + HA) = CTRWAH(HB * 4 + HA) AND CTRHT(HB * 4 + HA)
 CTRWAL(LB * 4 + LA) = CTRWAL(LB * 4 + LA) AND CTRLT(LB * 4 + LA)
 NEXT I
 FOR I = 1 TO 8
 CTRWAH(I – 1) = CTRWAH(I – 1) AND CTRWAL(I – 1)
 NEXT I
 RETURN
1300
' ====================initialization PIO==============
 FOR I = 0 TO 7          '8 BOARDS FOR INITIALIZING
 OUT &H303 + 4 * I, &H80
 OUT &H300 + 4 * I, &HFF
 OUT &H301 + 4 * I, &HFF
 OUT &H302 + 4 * I, &HFF
 NEXT I
 FOR I = 0 TO ICHANNEL – 1
 CTRWA(I) = &H0
 CTRWB(I) = &HFF
 CTRWC(I) = &HFF
 CTRWAH(I) = &HFF
 CTRWAL(I) = &HFF
 DATI(I + 1) = 0
 NEXT I
 RETURN
```

```
' ================END=====================
 END
' error processing
1460
 CALL SEND(DMMADDR%, "STATUS", STATUS%)        'Request status
 CALL ENTER(d$, LENGHT%, DMMADDR%, STATUS%)  'Read character strinG from the 196
 IF STATUS% <> 0 THEN PRINT " The data from DMM is not right": STOP
'  Test for error in ENTER
 STAT$ = LEFT$(d$, LENGHT%)
 PRINT STAT$
 IF (MID$(STAT$, 22, 1) <> "1") GOTO 1460
 PRINT
'  SRQ received cancel timer
 TIMER OFF
'  Enter and print the SRQ of the DMM
 CALL SEND(DMMADDR%, "SPOLL 22", STATUS%)  'Request serial poll byte
'  Read serial poll byte
 CALL ENTER(d$, LENGHT%, DMMADDR%, STATUS%) 'Read character strinG from the 196
 IF STATUS% <> 0 THEN PRINT " The data from DMM is not right": STOP
'  Test for error in ENTER
 d$ = LEFT$(d$, LENGHT%)
 SRQ = VAL(d$)
 PRINT "The SPOLL byte returned from the 196 = "; SRQ
 PRINT
 IF SRQ = 88 GOTO 2400
 IF SRQ = 80 GOTO 2600
 PRINT "WHAT'S GOING ON ???"
 STOP
2400
 PRINT "MEASUREMENT COMPLETE AND METER IS READY FOR COMMAND"
 PRINT
 RETURN
2600
 PRINT "METER READY FOR COMMAND"
 RETURN
4000
'  ***********  EXIT DUE TO TIME OUT WAITING FOR SRQ  ***************
 PRINT "PROGRAM TIMED OUT WAITING FOR A SRQ"
 STOP
10000 '************************  Error handler  ***************************
 IF (ERR = 57 OR ERR = 68 OR ERR = 75) GOTO 10100
 PRINT "BASIC Error In Line "; ERL; "Error Number = "; ERR
 STOP
10100
 PRINT "IEEE Error In Line "; ERL; "Error Number = "; ERR
 CALL SEND(DMMADDR%, "STATUS", STATUS%)        'Request status
 CALL ENTER(d$, LENGHT%, DMMADDR%, STATUS%)  'Read character strinG from the 196
```

```
 IF STATUS% <> 0 THEN PRINT " The data from DMM is not right": STOP
' Test error in ENTER
 STAT$ = LEFT$(d$, LENGHT%) 'Return status stringG
 PRINT STAT$
 STOP
20000
 WAVEFORM$ = "FU1"
 HZNUM$ = "FR100HZ"
 AMPL$ = "AM10VO"
 OFF$ = "OF0MV"
 PHASE$ = "PH0DE"
21000 CLS
 LOCATE 8, 20:  PRINT "*********************************************"
 LOCATE 9, 20: PRINT "*  CONFIGERATION FUNCTION GENERATION   *"
 LOCATE 10, 20: PRINT "*   0——EXIT                           *"
 LOCATE 11, 20: PRINT "*   1——WAVE FORM                      *"
 LOCATE 12, 20: PRINT "*   2——FREQUENCY                      *"
 LOCATE 13, 20: PRINT "*   3——AMPLITUDE                      *"
 LOCATE 14, 20: PRINT "*   4——OFFSET                         *"
 LOCATE 15, 20: PRINT "*   5——PHASE                          *"
 LOCATE 16, 20: PRINT "*   6——SELFTEST                       *"
 LOCATE 17, 20: PRINT "*   7——AMPLITUDE CALIBRATION          *"
 LOCATE 18, 20: PRINT "*********************************************"
22100
 A$ = INKEY$
 IF A$ = "0" THEN GOTO 22000
 IF A$ = "1" THEN GOSUB 21100
 IF A$ = "2" THEN GOSUB 21200
 IF A$ = "3" THEN GOSUB 21300
 IF A$ = "4" THEN GOSUB 21400
 IF A$ = "5" THEN GOSUB 21500
 IF A$ = "6" THEN GOSUB 21600
 IF A$ = "7" THEN GOSUB 21700
 GOTO 22100
21100
 I = 12: J = 30
 LOCATE I, J:     PRINT "*********************************************"
 LOCATE I + 1, J: PRINT "*   CONFIGERATION WAVEFORM            *"
 LOCATE I + 2, J: PRINT "*   0——DC                             *"
 LOCATE I + 3, J: PRINT "*   1——SINE                           *"
 LOCATE I + 4, J: PRINT "*   2——SQUARE                         *"
 LOCATE I + 5, J: PRINT "*   3——TRANGLE                        *"
 LOCATE I + 6, J: PRINT "*   4——RAMP UP                        *"
 LOCATE I + 7, J: PRINT "*   5——RAMP DOWN                      *"
 LOCATE I + 8, J: PRINT "*   6——AUX. TTL                       *"
 LOCATE I + 9, J: PRINT "*********************************************"
21010
```

```
 A$ = INKEY$
 IF A$ < "0" OR A$ > "6" THEN GOTO 21010
 WAVEFORM$ = "FU" + A$
 PRINT WAVEFORM$
 RETURN 21000
21200
 I = 13: J = 30
 LOCATE I, J:     PRINT "*******************************************"
 LOCATE I + 1, J: PRINT "*   CONFIGERATION FREQUENCY                *"
 LOCATE I + 2, J: PRINT "*                                          *"
 LOCATE I + 3, J: PRINT "*   PLEASE INPUT HZ NUMBER(HZ)             *"
 LOCATE I + 4, J: PRINT "*                                          *"
 LOCATE I + 5, J: PRINT "*                                          *"
 LOCATE I + 6, J: PRINT "*                                          *"
 LOCATE I + 7, J: PRINT "*******************************************"
 LOCATE I + 4, J + 5: INPUT HZNUM$
 HZNUM$ = "FR" + HZNUM$ + "HZ"
 RETURN 21000
21300
 I = 14: J = 30
 LOCATE I, J:     PRINT "*******************************************"
 LOCATE I + 1, J: PRINT "*   CONFIGERATION AMPLITUDE                *"
 LOCATE I + 2, J:  PRINT "*   1——1 MV                               *"
 LOCATE I + 3, J:  PRINT "*   2——10 MV                              *"
 LOCATE I + 4, J:  PRINT "*   3——100 MV                             *"
 LOCATE I + 5, J:  PRINT "*   4——1 V                                *"
 LOCATE I + 6, J:  PRINT "*   5——10 V                               *"
 LOCATE I + 7, J:  PRINT "*******************************************"
21310
 A$ = INKEY$: IF A$ = "" THEN GOTO 21310
 IF A$ = "1" THEN AMPL$ = "AM1MV": RETURN 21000
 IF A$ = "2" THEN AMPL$ = "AM10MV": RETURN 21000
 IF A$ = "3" THEN AMPL$ = "AM100MV": RETURN 21000
 IF A$ = "4" THEN AMPL$ = "AM1VO": RETURN 21000
 IF A$ = "5" THEN AMPL$ = "AM10VO": RETURN 21000
 GOTO 21310
21400
 I = 15: J = 30
 LOCATE I, J:     PRINT "*******************************************"
 LOCATE I + 1, J: PRINT "*   CONFIGERATION DC OFFSET                *"
 LOCATE I + 2, J: PRINT "*                                          *"
 LOCATE I + 3, J: PRINT "*   PLEASE INPUT OFFSET NUMBER(MV)         *"
 LOCATE I + 4, J: PRINT "*                                          *"
 LOCATE I + 5, J: PRINT "*                                          *"
 LOCATE I + 6, J: PRINT "*                                          *"
 LOCATE I + 7, J: PRINT "*******************************************"
 LOCATE I + 4, J + 5: INPUT OFF$
```

```
 HZNUM$ = "OF" + OFF$ + "MV"
 RETURN 21000
21500
 I = 16: J = 30
 LOCATE I, J:     PRINT "*******************************************"
 LOCATE I + 1, J: PRINT "*   CONFIGERATION PHASE                   *"
 LOCATE I + 2, J: PRINT "*                                         *"
 LOCATE I + 3, J: PRINT "*   PLEASE INPUT PHASE DEGREE             *"
 LOCATE I + 4, J: PRINT "*                                         *"
 LOCATE I + 5, J: PRINT "*                                         *"
 LOCATE I + 6, J: PRINT "*                                         *"
 LOCATE I + 7, J: PRINT "*******************************************"
 LOCATE I + 4, J + 5: INPUT PHASE$
 PHASE$ = "PH" + PHASE$ + "DE"
 RETURN 21000
21600
21700
 I = 18: J = 30
 LOCATE I, J:     PRINT "*******************************************"
 LOCATE I + 1, J: PRINT "*   AMPLITUDE CALIBRATION                 *"
 LOCATE I + 2, J: PRINT "*                                         *"
 LOCATE I + 3, J: PRINT "*   PLEASE WAIT A FEW SECONDS             *"
 LOCATE I + 4, J: PRINT "*                                         *"
 LOCATE I + 5, J: PRINT "*                                         *"
 LOCATE I + 6, J: PRINT "*                                         *"
 LOCATE I + 7, J: PRINT "*******************************************"
 FOR I = 1 TO 1000:
 FOR J = 1 TO 100: NEXT J
 NEXT I
 RETURN 21000
22000
' Set time out to 10 seconds
 CALL SEND(DMMADDR%, "TIME OUT 10", STATUS%)
' ====================================
 CALL SEND(fgaddr%, "clear 17", STATUS%)
 CALL SEND(fgaddr%, "OOF1", STATUS%)
 CALL SEND(fgaddr%, "beep", STATUS%)
 RETURN 2
' ============================================================
```

E.3 Excitation Data for DASCP

There are two files which include the information for applying the Walsh–excitation patterns to either of the 16– and 32–electrode phantoms. Either of these data files named `walsh16.ptn` and `walsh32.ptn` (for the 16– and 32–electrode systems, respectively) are supplied to DASCP as input. The input data for these files are given in Table E.1 and Table E.2. The integer number in the first row of each data file denotes the number of excitations to be performed by DASCP. The first integer number in the following rows indicates the number of channels to be excited with the positive voltage polarity. The following integer numbers in the same row are the channel numbers to be excited. The first group of channel numbers are excited by the positive polarity. The data format used herein is however not limited to only Walsh patterns but also the system is capable of exciting any number of channels in any given order of voltage polarity.

Table E.1 The *walsh16.ptn* file data for exciting 16 channels.

15																
8	1	3	5	7	9	11	13	15	17	19	21	23	25	27	29	31
8	1	3	5	7	25	27	29	31	9	11	13	15	17	19	21	23
8	1	3	5	7	17	19	21	23	9	11	13	15	25	27	29	31
8	1	3	13	15	17	19	29	31	5	7	9	11	21	23	25	27
8	1	3	13	15	21	23	25	27	5	7	9	11	17	19	29	31
8	1	3	9	11	21	23	29	31	5	7	13	15	17	19	25	27
8	1	3	9	11	17	19	25	27	5	7	13	15	21	23	29	31
8	1	7	9	15	17	23	25	31	3	5	11	13	19	21	27	29
8	1	7	9	15	19	21	27	29	3	5	11	13	17	23	25	31
8	1	7	11	13	19	21	25	31	3	5	9	15	17	23	27	29
8	1	7	11	13	17	23	27	29	3	5	9	15	19	21	25	31
8	1	5	11	15	17	21	27	31	3	7	9	13	19	23	25	29
8	1	5	11	15	19	23	25	29	3	7	9	13	17	21	27	31
8	1	5	9	13	19	23	27	31	3	7	11	15	17	21	25	29
8	1	5	9	13	17	21	25	29	3	7	11	15	19	23	27	31

Table E.2 The *walsh32.ptn* file data for exciting 32 channels.

31
16 1 2 3 4 5 6 7 8 9 10 11 12 13 14 15 16 17 18 19 20 21 22 23 24 25 26 27 28 29 30 31 32
16 1 2 3 4 5 6 7 8 25 26 27 28 29 30 31 32 9 10 11 12 13 14 15 16 17 18 19 20 21 22 23 24
16 1 2 3 4 5 6 7 8 17 18 19 20 21 22 23 24 9 10 11 12 13 14 15 16 25 26 27 28 29 30 31 32
16 1 2 3 4 13 14 15 16 17 18 19 20 29 30 31 32 5 6 7 8 9 10 11 12 21 22 23 24 25 26 27 28
16 1 2 3 4 13 14 15 16 21 22 23 24 25 26 27 28 5 6 7 8 9 10 11 12 17 18 19 20 29 30 31 32
16 1 2 3 4 9 10 11 12 21 22 23 24 29 30 31 32 5 6 7 8 13 14 15 16 17 18 19 20 25 26 27 28
16 1 2 3 4 9 10 11 12 17 18 19 20 25 26 27 28 5 6 7 8 13 14 15 16 21 22 23 24 29 30 31 32
16 1 2 7 8 9 10 15 16 17 18 23 24 25 26 31 32 3 4 5 6 11 12 13 14 19 20 21 22 27 28 29 30
16 1 2 7 8 9 10 15 16 19 20 21 22 27 28 29 30 3 4 5 6 11 12 13 14 17 18 23 24 25 26 31 32
16 1 2 7 8 11 12 13 14 19 20 21 22 25 26 31 32 3 4 5 6 9 10 15 16 17 18 23 24 27 28 29 30
16 1 2 7 8 11 12 13 14 17 18 23 24 27 28 29 30 3 4 5 6 9 10 15 16 19 20 21 22 25 26 31 32
16 1 2 5 6 11 12 15 16 17 18 21 22 27 28 31 32 3 4 7 8 9 10 13 14 19 20 23 24 25 26 29 30
16 1 2 5 6 11 12 15 16 19 20 23 24 25 26 29 30 3 4 7 8 9 10 13 14 17 18 21 22 27 28 31 32
16 1 2 5 6 9 10 13 14 19 20 23 24 27 28 31 32 3 4 7 8 11 12 15 16 17 18 21 22 25 26 29 30
16 1 2 5 6 9 10 13 14 17 18 21 22 25 26 29 30 3 4 7 8 11 12 15 16 19 20 23 24 27 28 31 32
16 1 4 5 8 9 12 13 16 17 20 21 24 25 28 29 32 2 3 6 7 10 11 14 15 18 19 22 23 26 27 30 31
16 1 4 5 8 9 12 13 16 18 19 22 23 26 27 30 31 2 3 6 7 10 11 14 15 17 20 21 24 25 28 29 32
16 1 4 5 8 10 11 14 15 18 19 22 23 25 28 29 32 2 3 6 7 9 12 13 16 17 20 21 24 26 27 30 31
16 1 4 5 8 10 11 14 15 17 20 21 24 26 27 30 31 2 3 6 7 9 12 13 16 18 19 22 23 25 28 29 32
16 1 4 6 7 10 11 13 16 17 20 22 23 26 27 29 32 2 3 5 8 9 12 14 15 18 19 21 24 25 28 30 31
16 1 4 6 7 10 11 13 16 18 19 21 24 25 28 30 31 2 3 5 8 9 12 14 15 17 20 22 23 26 27 29 32
16 1 4 6 7 9 12 14 15 18 19 21 24 26 27 29 32 2 3 5 8 10 11 13 16 17 20 22 23 25 28 30 31
16 1 4 6 7 9 12 14 15 17 20 22 23 25 28 30 31 2 3 5 8 10 11 13 16 18 19 21 24 26 27 29 32
16 1 3 6 8 9 11 14 16 17 19 22 24 25 27 30 32 2 4 5 7 10 12 13 15 18 20 21 23 26 28 29 31
16 1 3 6 8 9 11 14 16 18 20 21 23 26 28 29 31 2 4 5 7 10 12 13 15 17 19 22 24 25 27 30 32
16 1 3 6 8 10 12 13 15 18 20 21 23 25 27 30 32 2 4 5 7 9 11 14 16 17 19 22 24 26 28 29 31
16 1 3 6 8 10 12 13 15 17 19 22 24 26 28 29 31 2 4 5 7 9 11 14 16 18 20 21 23 25 27 30 32
16 1 3 5 7 10 12 14 16 17 19 21 23 26 28 30 32 2 4 6 8 9 11 13 15 18 20 22 24 25 27 29 31
16 1 3 5 7 10 12 14 16 18 20 22 24 25 27 29 31 2 4 6 8 9 11 13 15 17 19 21 23 26 28 30 32
16 1 3 5 7 9 11 13 15 18 20 22 24 26 28 30 32 2 4 6 8 10 12 14 16 17 19 21 23 25 27 29 31
16 1 3 5 7 9 11 13 15 17 19 21 23 25 27 29 31 2 4 6 8 10 12 14 16 18 20 22 24 26 28 30 32